Computational Insights into Organic and Organometallic Catalysis

A Thesis submitted for the degree of

Doctor of Philosophy

Trinity Term 2019

Xinglong Zhang

St Catherine's College

Department of Chemistry

University of Oxford

To my family.

Author's declaration

This thesis describes the work carried out by the author in the Department of Chemistry, University of Oxford, under the supervision of Professor Robert S. Paton. No part of this thesis has previously been submitted for a degree at either this University or elsewhere. The work of other authors has been freely drawn upon and is duly acknowledged in the text.

Xinglong Zhang

Oxford, UK. Sept 2019

Acknowledgements

When I was a little kid, I had always wanted to become a scientist. It was however beyond my imagination that I would be required to write a thesis − a book full of my personal research. This to present day I have accomplished. It is unquestionable that I can never achieve this feat without the help and support of the many people in my life and it is appropriate that I acknowledge these wonderful people who have helped make this a reality.

I would like to thank my DPhil supervisors, Prof. Robert Paton and Prof. John McGrady, without whom this thesis would not be possible. I thank Rob for providing the highest level of guidance possible and giving me a lot of freedom in my research. From him, I learn how to think critically about my own work and how to be independent. In addition to being very knowledgeable, perhaps most importantly, Rob is a perspicacious person whose charisma, humility and approachability have been a source of inspiration. The same can be said for John, who kindly agreed to become a joint supervisor after Rob left Oxford. John has provided me with a lot of support when I was struggling with graduate school problems.

Much of this thesis describes work in collaboration with the experimental groups. I am in fact very fortunate to work with some of the best groups in their respective fields. At the start, I was learning and being rather slow with regard to progress, but the amount of patience rendered to me in these situations has been almost limitless. I thank Prof. Ross Denton (Nottingham) and Prof. Debabrata Maiti (Indian Institute of Technology, Bombay) for giving me the opportunities to work on these wonderful projects and their group members for productive collaborations.

I would also like to thank Prof. Israel Fernández and Prof. Michael Willis for kindly acting as my thesis examiners; I have very much enjoyed the whole session of insightful and fruitful discussion. In particular, Prof. Fernández has proposed numerous helpful suggestions that make this thesis a better version of itself.

I thank the Paton and McGrady group members for the discussion, support and companionship throughout my DPhil journey. A special word of thanks goes to David Ascough, with whom I have shared many discussions on science and research problems and from whom I have learned many things. The shared memory with everyone will serve as a source for reminiscences many years down the road.

I am also fortunate to be part of the Theory and Modelling in Chemical Sciences (TMCS) CDT programme. I was privileged to work under Prof. Fredrick Manby and Prof. Adrian Molholland at Bristol for a short rotation project where I learned about projection-based wavefunction-in-density functional theory (WF-in-DFT) embedding. I was also fortunate to work with and learn from their excellent post-doctoral scholar, Dr. Simon Bennie, who taught me many skills in my early foray into computational chemistry.

Indeed, there are many people in my undergraduate institution who have motivated and inspired me to where I am today. In particular, Dr. James Keeler is always so kind to me whenever I ask for recommendation letters, from applying to Ph.D programmes to scholarships and lectureships. Dr. David Bosworth and Robert Dillon have also been very kind whenever I need references. I cannot thank them enough for their support of and confidence in me.

It is very important that I thank and acknowledge the Agency for Science, Technology and Research (A*STAR) in Singapore for the generous support and funding throughout

my studies; this thesis would not be possible without the financial support from A*STAR. In addition, my mentor at A*STAR, Dr. Michael Sullivan, has also provided much support and mentorship throughout my research journey and I am grateful to him for all his guidance.

Lastly, I thank my parents for their unwavering love throughout my life. I also want to thank my wonderful wife, Qianting, who has always been so loving, supportive and understanding of me. I owe her so much that she has to endure the times being apart from me while I complete my DPhil studies. One thing that I have regretted is the time lost being away from our son, Austin, and missing out much of his social and intellectual developments. I hope this thesis will serve as an inspiration to him.

锲而舍之，朽木不折；锲而不舍，金石可镂。

— 荀子《劝学》

Abstract

This thesis presents computational studies of some catalytic systems in both organic and organometallic chemistry using density functional theory (DFT). With these studies, we show how electronic structure theory such as DFT can complement experimental studies in elucidating and unravelling complex mechanisms. In **Chapter 1**, we give an overview of the theoretical background governing computational quantum chemistry and electronic structure theories. We then look at how theory is translated to the quantitative study of chemical reactivity and selectivity through simple transition state theory. Chapters 2 and 3 look at organocatalysis. In **Chapter 2**, we discuss computational work on the oxidant-promoted, hole-catalysed cyclobutanation between two unsymmetrical olefins (Scheme 0 (a)). Chemoselectivity (of reacting olefins), regioselectivity and stereoselectivity (of product formations) were explored. **Chapter 3** discusses the mechanistic investigation of a novel bifunctional hydroxyphosphine catalyst, coupling with terminal phenylsilane reductant, in catalytic Staudinger reduction of azide to amine (Scheme 0 (b)). Chapters 4 to 7 look at the catalytic C–H bond functionalisations using transition-metal catalysts. In **Chapter 4**, we discuss Pd-catalysed δ-selective C(sp^3)–H arylation of α-amino acids (Scheme 0 (c)). In **Chapter 5** and **Chapter 6**, we look at the mechanisms underlying Pd-catalysed *meta*-selective C(sp^2)–H allylation using unbiased internal olefin as an allyl surrogate and alkynylation via inverse Sonogashira coupling using trialkylsilylated bromoalkyne, respectively (Scheme 0 (d)). In **Chapter 7**, we look at using different transition metal catalysts to effect the regiodivergent C(sp^2)–H arylation of isoquinolone (Scheme 0 (e)). **Chapter 8** gives some concluding remarks regarding the field of computational chemistry in organic and organometallic catalyses and some outlook to the future of chemistry using other computational tools apart from those used in this thesis.

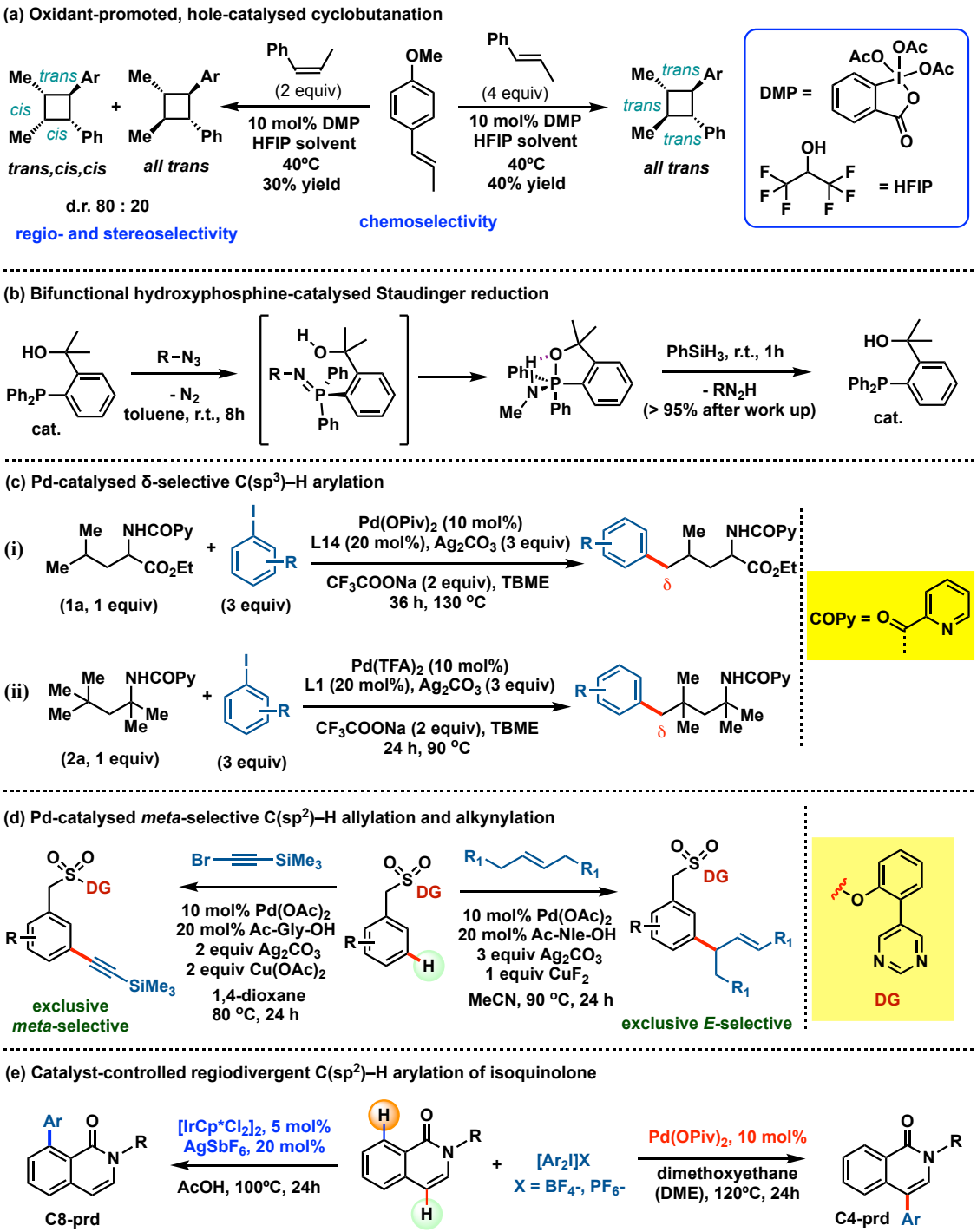

Scheme 0. Overview of the organic and organometallic systems studied in this thesis.

Keywords: Density functional theory (DFT), theoretical investigations, calculations, catalysis, mechanisms, cyclobutanation, Staudinger reduction, C–H functionalisation.

Table of contents

List of Schemes

Chapter 5

Chapter 6

Chapter 7

List of Figures

Chapter 2

Chapter 3

Chapter 4

Chapter 5

Chapter 6

Chapter 7

List of Tables

List of Abbreviations

Ac	Acetate/acetyl
aq.	aeueous
atm	atomosphere
Bu	Butyl
ca.	*circa.*
CMD	Concerted metallation deprotonation
Cp*	Pentamethyl cyclopentadiene
DCE	Dichloroethane
DCM	Dichloromethane
DFT	Density functional theory
DG	Directing group
DME	Dimethoxyethane
DMP	Dess-Martin periodinane
ESP	Electrostatic potential
Et	Ethyl
ET	Electron transfer
eq.	Equivalent(s)
GGA	Generalized gradient approximation
KIE	Kinetic Isotopic Effect
HF	Hartree-Fock
HFIP	Hexafluoroisopropanol
HOMO	Highest Occupied Molecular Orbital
HTFA	Trifluoroacetatic acid
hr	Hour(s)
IRC	Intrinsic reaction coordinate
KIE	Kinetic isotope effect
LUMO	Lowest unoccupied molecular orbital
MM	Molecular mechanics
MPAA	Mono-protected amino acid
NBO	Natural bonding orbital
NCI	Non-covalent interaction

NGA	Non-separable gradient approximation
NMR	Nuclear magnetic resonance
OA	Oxidative addition
PCM	Polarizable continuum model
PES	Potential energy surface
PG	Protecting group
Ph	Phenyl
QM	Quantum mechanics
quant.	Quantitative
quasi-RRHO	quasi-Rigid Rotor Harmonic Oscillator
RDTS	Rate-determining Transition State
RE	Reductive elimination
rel.	Relative
rt	Room temperature
SCF GIAO	Self-consistent filed gauge-invariant atomic orbital
SET	Single electron transfer
SMD	Solvation Model based on Density
SOMO	Singly occupied molecular orbital
TBME	tert-butyl methyl ether
^{t}Bu	tert-butyl
TDI	Turnover-frequency determining Intermediate
TDTS	Turnover-frequency determining Transition State
TFA	Trifluoroacetate
TM	Transition metal
TOF	Turnover-frequency
TS	Transition state
TST	Transition state theory

List of Appendices

Never trust an experimental result until it has been confirmed by theory.

— Arthur Stanley Eddington

1

Theoretical Background

1.1 Computational Chemistry

Computational chemistry is a branch of chemistry where theoretical study of physics and chemistry are implemented in computer programs to simulate and understand chemical reactions that occur both in laboratory settings and in biological systems, using techniques ranging from kinetics and thermodynamics calculations, electronic structure analysis and spectroscopy simulations, amongst many others. Within this field, computer simulations are routinely used to understand and explain chemical reactivity; in some cases, these simulations can predict remarkable and hitherto unperceived chemical phenomena.[1–3] Today, computational chemistry has become an indispensable tool in understanding reaction mechanisms in chemical reactions and catalysis.[4,5] The advent and continued development of computational chemistry has been fuelled by paralleled development in theoretical methods and computational architecture. We should note that computational chemistry is different from theoretical chemistry in that it concerns solving

chemical problems, not directly developing new theoretical techniques. The development of theoretical methods allows new chemical problems to be studied, whereas calculations and insights obtained from computational chemistry can pinpoint the limitations of theory and suggest new areas for further theoretical development.

One of the practical considerations in computational chemistry is that any method employed to study a chemical system is constrained by a compromise between accuracy and cost. In general, the more accurate the methodology, or model chemistry, the more costly it is computationally, although highly parametrised low-cost methods can sometimes obtain this accuracy. A variety of computational methods are available for the study of a range of chemical systems of varying sizes to different degrees of desired accuracy. These methods can be broadly divided into quantum mechanical methods and classical mechanical methods. Quantum mechanical methods aim to understand the electronic structure of a chemical system and include *ab initio* methods based entirely on solving the governing equations in quantum mechanics, without any experimental data input; semi-empirical methods include additional parameters from empirical data for better speed/accuracy in the study of large systems. For even larger systems and where dynamical effects are important, classical mechanical methods based on numerically solving the Newton's equations of motion are employed. Examples of popular quantum mechanical methods include density functional theory (DFT) methods and examples of classical mechanical methods include molecular mechanics (MM) – a form of empirical potential governing the interactions between the atoms of a molecular system – used in molecular dynamics (MD) simulations.

1.2 Quantum Mechanics

As all endeavours in science, quantum mechanics (QM) developed when existing theory could not adequately explain the experimental observations. Classical mechanics provide the physical laws governing the motion and properties of macroscopic systems. However, a series of observations made in the 19th and 20th centuries concerning systems of atomic and subatomic scale could not be reconciled with classical laws. These observations, such as the discovery of cathode rays (Faraday, 1838), the black-body radiation problem (Kirchhoff, 1859) and the photoelectric effect (Hertz, 1887), called for new theoretical framework governing phenomena at the atomic scale. In 1900, in a radical proposal, Max Planck first suggested that the energies emitted by an atomic system come in discrete values, i.e., they are quantised. Then in 1905, in an attempt to explain the photoelectric effect, Einstein proposed, in consistency with Planck, that light is made up of discrete particles, later on termed photons, with quantised energy. As the development of QM progressed, it became clear that not only is light quantised, but also are electrons and atoms. Early contributions from de Broglie, Schrödinger, Heisenberg, Born and others underlie the foundations of theory for modern computational chemistry.

1.2.1 The Schrödinger equation

A chemical system can be described *exactly* by the time-dependent Schrödinger equation (TDSE):

$$\hat{H}\Psi(\mathbf{X},t) = i\hbar\frac{\partial}{\partial t}\Psi(\mathbf{X},t) \tag{1.1}$$

where $\hat{H}$ is the Hamiltonian operator, whose measurements yield the total energy of the system; $\Psi(\mathbf{X},t)$ is the time-dependent wavefunction of the system, whose squared modulus, $|\Psi(\mathbf{X},t)|^2 = \Psi^*(\mathbf{X},t)\Psi(\mathbf{X},t)$, gives the probability density of finding a particle

at position **X** (**X** is a collection of positions of electrons, at **r**, and nuclei, at **R**) at time *t*. For time-independent physical and chemical properties, the solution of the time-independent Schrödinger equation (TISE)

$$\hat{H}\Psi = E\Psi \tag{1.2}$$

is desired.

This is an eigenvalue problem where the eigenfunction is the wavefunction of the system, Ψ, and the eigenvalue is the energy of the system, *E*. The solution of the TISE cannot be obtained exactly except for the simplest, single-electron systems. For a multi-electronic system with *N* electrons, at position vectors $\mathbf{r}_i$'s, and *M* nuclei, at position vectors $\mathbf{R}_A$'s, the Hamiltonian of the system, in atomic units, is given by

$$\hat{H} = -\sum_{i=1}^{N}\frac{1}{2}\nabla_i^2 - \sum_{A=1}^{M}\frac{1}{2M_A}\nabla_A^2 - \sum_{i=1}^{N}\sum_{A=1}^{M}\frac{Z_A}{r_{iA}} + \sum_{i=1}^{N}\sum_{j>i}^{N}\frac{1}{r_{ij}} + \sum_{A=1}^{M}\sum_{B>A}^{M}\frac{Z_A Z_B}{R_{AB}} \tag{1.3}$$

where $r_{iA} = |\mathbf{r}_i - \mathbf{R}_A|$ is the distance between i^{th} electron and A^{th} nucleus, $r_{ij} = |\mathbf{r}_i - \mathbf{r}_j|$ is the distance between i^{th} electron and j^{th} electron, $R_{AB} = |\mathbf{R}_A - \mathbf{R}_B|$ is the distance between A^{th} nucleus and B^{th} nucleus; M_A and Z_A are the atomic mass and charge of nucleus *A*, respectively. The five terms in the total Hamiltonian represent, respectively, the kinetic energy of the electrons, the kinetic energy of the nuclei, the Coulomb attraction between the electrons and nuclei, the electron-electron repulsion and the nucleus-nucleus repulsion. Thus, the total Hamiltonian operator can be written as a sum of the operators for each of these separate contributions, viz.,

$$\hat{H} = \hat{T}_e + \hat{T}_n + \hat{V}_{ne} + \hat{V}_{ee} + \hat{V}_{nn} \tag{1.4}$$

1.2.2 The Born-Oppenheimer approximation

The full Hamiltonian for a molecular system given in Equation (1.3) makes the TISE in Equation (1.2) difficult to be solvable without a number of approximations; the presence of electron-nuclei interactions, $\hat{V}_{ne}$, makes the Hamiltonian inseparable into electronic and nuclear degrees of freedom. One of the most fundamental approximations employed is the Born-Oppenheimer (BO) approximation.[6] The validity of this approximation rests on the fact that the mass of a nuclei is much larger than the mass of an electron (1 a.m.u. = 1836 m_e), such that their motions can be separately treated. Within the BO approximation, the nuclei of the system are considered "clamped" in positions; the electrons move in this "clamped-nuclei" framework. By having the nuclei fixed, the nuclear kinetic energy (second term of Equation (1.3)) can be neglected ($\hat{T}_n = 0$); in addition, the nucleus-nucleus repulsion can be considered as a constant at fixed nuclear positions **R** ($\hat{V}_{nn} = V_{nn}(\mathbf{R})$). With these simplifications, the Hamiltonian in Equation (1.3) becomes

$$\hat{H} = -\sum_{i=1}^{N} \frac{1}{2}\nabla_i^2 - \sum_{i=1}^{N}\sum_{A=1}^{M} \frac{Z_A}{r_{iA}} + \sum_{i=1}^{N}\sum_{j>i}^{N} \frac{1}{r_{ij}} + V_{nn} \tag{1.5}$$

which is the Hamiltonian describing the motion of N electrons in the field of M fixed nuclear charges. The constant nucleus-nucleus repulsion, V_{nn}, is frequently neglected since it is just a constant within the BO approximation and that adding a constant to a quantum operator just shifts the eigenvalues and does not change the eigenfunctions, i.e., the representation of the system is unaffected. The electronic Hamiltonian is then given by

$$\hat{H}_{el} = -\sum_{i=1}^{N} \frac{1}{2}\nabla_i^2 - \sum_{i=1}^{N}\sum_{A=1}^{M} \frac{Z_A}{r_{iA}} + \sum_{i=1}^{N}\sum_{j>i}^{N} \frac{1}{r_{ij}} \tag{1.6}$$

such that the electronic Schrödinger equation is now

$$\hat{H}_{el}\Psi_{el}(\mathbf{r}, \mathbf{R}) = E_{el}(\mathbf{R})\Psi_{el}(\mathbf{r}, \mathbf{R}) \tag{1.7}$$

where the electronic wavefunction $\Psi_{el}(\mathbf{r}, \mathbf{R})$ depends on the positions of electrons and the fixed nuclear coordinates. The total energy of the full molecular system, at the fixed nuclear positions, **R**, includes the constant nuclear repulsion and is given by

$$E_{tot}(\mathbf{R}) = E_{el}(\mathbf{R}) + V_{nn}(\mathbf{R}) \tag{1.8}$$

By varying the nuclear positions and solving the electronic SE, we are able to arrive at the total energy of the system at different nuclear positions (Equation (1.8)). This total energy, with parametric dependence on the nuclear positions, provides a potential for the nuclear motion. This gives rise to the concept of **potential energy surface** (PES), which is the electronic energy of the system over the nuclear coordinates, $E_{el}(\mathbf{R})$. The nuclear motion can now be solved, with the nuclear Hamiltonian for the motion of nuclei in the field of the electrons given by

$$\hat{H}_{nuc} = -\sum_{A=1}^{M} \frac{1}{2M_A}\nabla_A^2 + E_{el}(\mathbf{R}) + V_{nn}(\mathbf{R}) = -\sum_{A=1}^{M} \frac{1}{2M_A}\nabla_A^2 + E_{tot}(\mathbf{R}) \tag{1.9}$$

and with the nuclear SE given by

$$\hat{H}_{nuc}\Psi_{nuc} = E\Psi_{nuc} \tag{1.10}$$

The BO approximated total energy is given by E from Equation (1.10). As a result of this separation, the total molecular wavefunction of the system, Ψ, can be written as a product of the electronic wavefunction and the nuclear wavefunction, as

$$\Psi = \Psi_{el}\Psi_{nuc} \tag{1.11}$$

We focus on solving the electronic TISE given in Equation (1.7).

1.2.3 Quantum mechanical measurements

For any physical observable Q, there is a corresponding Hermitian quantum operator $\hat{Q}$ giving the measurement of the observable. The Hermiticity of the operator ensures that the measured physical observable of a system, represented by the wavefunction Ψ, is real, as is necessary for being physically sound. The mean value of the observable Q in a series of measurements is given by the expectation value of the corresponding operator $\hat{Q}$, via the formula,

$$Q = \left\langle \hat{Q} \right\rangle = \frac{\langle \Psi | \hat{Q} | \Psi \rangle}{\langle \Psi | \Psi \rangle} \tag{1.12}$$

Therefore, if the quantum operator is the total Hamiltonian, then, the total energy of the system is the expectation value of the Hamiltonian, given by

$$E = \left\langle \hat{H} \right\rangle = \frac{\langle \Psi | \hat{H} | \Psi \rangle}{\langle \Psi | \Psi \rangle} \tag{1.13}$$

1.2.4 The variational principle

The exact solution of the TISE is possible only for a limited number of systems. In cases where the exact solutions are not available, we can find approximate wavefunctions to the system. In many cases, we are interested in the ground state of a system, represented

by the wavefunction ψ_0, with ground state energy E_0. The variational principle asserts that for an arbitrary trial wavefunction $\tilde{\psi}$ satisfying the boundary conditions for a system, the expectation value of its energy $\tilde{E}$ provides an upper bound to the lowest eigenvalue of the Hamiltonian, the true ground state energy E_0. That is, we have

$$\tilde{E} = \frac{\left\langle \tilde{\psi} \middle| \hat{H} \middle| \tilde{\psi} \right\rangle}{\left\langle \tilde{\psi} \middle| \tilde{\psi} \right\rangle} \geq E_0 = \frac{\langle \psi_0 | \hat{H} | \psi_0 \rangle}{\langle \psi_0 | \psi_0 \rangle} \tag{1.14}$$

In general, the flexibility of the trial wavefunction can be increased by including in it an adjustable parameter or parameters, so that the energy of the trial wavefunction can be further refined by minimising the trial energy with respect to those parameters. The variational principle (Equation (1.14)) implies that any approximate wavefunction to the true ground state wavefunction will yield an expectation energy that is higher than or equal to the true ground state energy; equality is satisfied when the trial wavefunction is exactly the same as the ground state wavefunction.

1.2.5 Linear variation method and the secular equations

Given that we do *not* have the eigenfunctions of the true Hamiltonian, we can write the trial wavefunction $\tilde{\psi}$ as a linear combination of N independent functions $\{\phi_i\}$ (often the atomic orbitals),

$$\tilde{\psi} = \sum_{i=1}^{N} c_i \phi_i \tag{1.15}$$

so that Equation (1.14) becomes

$$\tilde{E} = \frac{\left\langle \tilde{\psi} \middle| \hat{H} \middle| \tilde{\psi} \right\rangle}{\left\langle \tilde{\psi} \middle| \tilde{\psi} \right\rangle} = \frac{\sum_i^N \sum_j^N c_i^* c_j \left\langle \phi_i \right| \hat{H} \left| \phi_j \right\rangle}{\sum_i^N \sum_j^N \left\langle \phi_i | \phi_j \right\rangle} = \frac{\sum_{i,j} c_i^* c_j H_{ij}}{\sum_{i,j} c_i^* c_j S_{ij}} \tag{1.16}$$

which can be rearranged to

$$\tilde{E} \sum_{i,j} c_i^* c_j S_{ij} = \sum_{i,j} c_i^* c_j H_{ij} \tag{1.17}$$

.

To minimise the energy with respect to the coefficients c_i's, we take the partial derivative of Equation (1.17) with respect to the coefficient c_k and require that

$$\frac{\partial \tilde{E}}{\partial c_k} = 0 \tag{1.18}$$

so that we arrive at

$$\begin{aligned}
&\frac{\partial \tilde{E}}{\partial c_k} \sum_{i,j} c_i^* c_j S_{ij} + \tilde{E} \sum_{i,j} \left[c_j \frac{\partial c_i^*}{\partial c_k} + c_i^* \frac{\partial c_j}{\partial c_k} \right] S_{ij} = \sum_{i,j} \left[c_j \frac{\partial c_i^*}{\partial c_k} + c_i^* \frac{\partial c_j}{\partial c_k} \right] H_{ij} \\
&\qquad \Longrightarrow \; \tilde{E} \sum_{i,j} \left[c_j \delta_{ik} + c_i^* \delta_{jk} \right] S_{ij} = \sum_{i,j} \left[c_j \delta_{ik} + c_i^* \delta_{jk} \right] H_{ij} \\
&\qquad \Longrightarrow \; \tilde{E} \left[\sum_j c_j S_{kj} + \sum_i c_i^* S_{ik} \right] = \left[\sum_j c_j H_{kj} + \sum_i c_i^* H_{ik} \right] \\
&\qquad \Longrightarrow \; 2\tilde{E} \sum_j c_j S_{kj} = 2 \sum_j c_j H_{kj} \\
&\qquad \Longrightarrow \; \sum_j (H_{kj} - \tilde{E} S_{kj}) c_j = 0
\end{aligned} \tag{1.19}$$

where we have used $S_{ij} = S_{ji}$ and $H_{ij} = H_{ji}$ (due to Hermiticity of the Hamiltonian operator). Equation (1.19) are the secular equations of the system. In matrix form, this is

$$(\mathbf{H} - E\mathbf{S})\mathbf{c} = \mathbf{0} \tag{1.20}$$

1.2.6 Spin-statistics theorem and Pauli exclusion principle

Due to the indistinguishability of quantum particles, the exchange of labels on any two identical particles should preserve the probability density of the system. This observation is encapsulated by *spin-statistics theorem*, which states that, in exchanging two identical particles (both space and spin coordinates), the total wavefunction is antisymmetric (sign change) for fermions and symmetric (no sign change) for bosons.

Since electrons are fermions, the exchange of two identical electrons requires that the total wavefunction of the system changes sign, viz.,

$$\hat{P}\Psi(\mathbf{r}_1, \mathbf{r}_2) = \Psi(\mathbf{r}_2, \mathbf{r}_1) = -\Psi(\mathbf{r}_1, \mathbf{r}_2). \tag{1.21}$$

where $\hat{P}$ is the exchange/permutation operator. The probability density of the system is preserved since the probability of finding an electron is given by the square modulus of the total wavefunction and is thus not affected by the sign change, that is

$$|\Psi(\mathbf{r}_2, \mathbf{r}_1)|^2 = |-\Psi(\mathbf{r}_1, \mathbf{r}_2)|^2. \tag{1.22}$$

The **Pauli exclusion principle**, which states that no two or more identical fermions can occupy the same quantum state, follows immediately: if we have two fermions in the same state (same spatial and spin coordinates), then, $\mathbf{r}_2 = \mathbf{r}_1 = \mathbf{r}$, Equation (1.21) then becomes $\Psi(\mathbf{r}, \mathbf{r}) = -\Psi(\mathbf{r}, \mathbf{r}) \implies 2\Psi(\mathbf{r}, \mathbf{r}) = 0 \implies \Psi(\mathbf{r}, \mathbf{r}) = 0$, resulting in no such wavefunction.

1.2.7 Spin orbitals, Hartree product and Slater determinants

A spin orbital $\chi(\mathbf{X})$ is a wavefunction for an electron containing a spatial orbital $\psi(\mathbf{r})$, which is a function of the position vector of the electron at **r**, multiplied by the spin of the electron σ_{m_s}. The coordinate **X** is a collection of individual space coordinates **r** and

the associated spin coordinates. Mathematically, $\chi(\mathbf{X}) = \psi(\mathbf{r})\sigma_{m_s}$ where the electron spin takes either spin up (α) or spin down (β). Each spin orbital can accommodate one electron, since, no two electrons can have the same four quantum numbers, as a consequence of Pauli exclusion principle.

For a system with *N* electrons, we can construct a many-electron wavefunction called the *Hartree product* $\Psi^{\mathrm{HP}}(\mathbf{X})$, which is a product of individual particle wavefunctions, i.e., a product of spin orbitals. Mathematically,

$$\Psi^{\mathrm{HP}}(\mathbf{X}) = \Psi^{\mathrm{HP}}(\mathbf{x}_1, \mathbf{x}_2, \cdots, \mathbf{x}_N) = \chi_1(\mathbf{x}_1)\chi_2(\mathbf{x}_2)\cdots\chi_N(\mathbf{x}_N). \tag{1.23}$$

The Hartree product is a *mean-field* wavefunction where the individual electrons are assumed to be non-interacting; it is an uncorrelated wavefunction. The Hartree product suffers the deficiency that it does not conform to the antisymmetry of the overall wave-function under the exchange of electron labels, i.e., it violates the Pauli principle.

We can obtain the correct antisymmetric wavefunction of the *N*-electron system, called a *Slater determinant*, Ψ^{SD}, from the Hartree product, Ψ^{HP}, by applying an antisymmetriser operator, $\hat{A}$, to it. That is, we have

$$\Psi^{\mathrm{SD}} = \hat{A}\Psi^{\mathrm{HP}} = \hat{A}\left[\chi_1(\mathbf{x}_1)\chi_2(\mathbf{x}_2)\cdots\chi_N(\mathbf{x}_N)\right], \tag{1.24}$$

where the antisymmetriser operator is defined as

$$\hat{A} = \frac{1}{\sqrt{N!}}\sum_{u}^{N!}\sigma_u\hat{P}_u. \tag{1.25}$$

$\hat{P}_u$ is a permutation operator that permutes the coordinates in the Hartree product; σ_u is the sign of permutation that is even (+1)/odd (–1) if the number of single interchanges is

even/odd. Applying the antisymmetriser on the Hartree product leads us to the Slater determinant, viz.,

$$\Psi^{\mathrm{SD}} = \frac{1}{\sqrt{N!}} \begin{vmatrix} \chi_1(\mathbf{x}_1) & \chi_2(\mathbf{x}_1) & \cdots & \chi_N(\mathbf{x}_1) \\ \chi_1(\mathbf{x}_2) & \chi_2(\mathbf{x}_2) & \cdots & \chi_N(\mathbf{x}_2) \\ \vdots & \vdots & \ddots & \vdots \\ \chi_1(\mathbf{x}_N) & \chi_2(\mathbf{x}_N) & \cdots & \chi_N(\mathbf{x}_N) \end{vmatrix} \tag{1.26}$$

The Slater determinant is correctly antisymmetrised and satisfies the antisymmetry and Pauli exclusion principles since, for example, exchanging the electron labels for any two rows or columns results in sign change, and that having any two electron labels the same results in a vanishing determinant. It can be shown that[7] for a single Slater determinantal description of an *N*-electron system, the motion of electrons of parallel spins is correlated (electron exchange) but the motion of electrons of opposite spins is uncorrelated.

1.3 Basis sets

A basis set is a collection of known vectors/functions used to span a vector/Hilbert space. The simplest example of a basis set is the collection of unit vectors, $\{\hat{i}, \hat{j}, \hat{k}\}$, which spans the Euclidean 3D space. In other words, any vector in space can be represented as a linear combination of the unit vectors. Similarly, in quantum chemistry, a basis set is a collection of known functions, usually one-particle functions such as the atomic orbitals (AOs), used to represent the molecular orbitals (MOs) of a system of interest. The MOs can be written as a linear combination of AOs where their coefficients can be variationally determined. In almost all quantum chemical calculations, a finite set of basis functions is used. If the finite basis set is expanded toward completeness of an infinite basis set, then calculations using such an infinite basis set are said to approach the **basis set limit**.

1.3.1 Slater-type orbitals vs Gaussian-type orbitals

There are two types of basis functions in quantum chemistry. The **Slater-type orbitals** (STOs; named after John C. Slater) are similar to the eigenfunctions of the hydrogen atom and have the following functional form,

$$\chi_{\zeta,n,l,m}(r,\theta,\varphi) = NY_{l,m}(\theta,\phi)r^{n-1}e^{-\zeta r} \tag{1.27}$$

where N is a normalisation constant, $Y_{l,m}$ are the spherical harmonics; the radial part is given by r^{n-1}, with ζ the Slater exponent that controls the width of the orbital. Note the exponential dependence on r. Since the STOs have resemblance to the hydrogen atomic orbitals, they are naturally good for molecular orbitals. In addition, they have the correct behaviours at short ($R \to 0$) and long ($R \to \infty$) ranges. However, the evaluation of integrals using these STOs are difficult and computationally resource-consuming.

An alternative and much more popular type of basis set employed in quantum chemistry is the **Gaussian-type orbitals** (GTOs; first proposed by Francis Boys). The functional forms of the GTOs are given below,

$$\begin{aligned} &\chi_{\alpha,l_x,l_y,l_z}(x,y,z) = Nx^{l_x}y^{l_y}z^{l_z}e^{-\alpha r^2} \quad \text{(Cartesian)} \\ &\chi_{\alpha,n,l,m}(r,\theta,\phi) = NY_{l,m}(\theta,\phi)r^{n-1}e^{-\alpha r^2} \quad \text{(Spherical)} \end{aligned} \tag{1.28}$$

where α is the Gaussian orbital exponent that controls the width of the GTOs (the larger the value of α, the more contracted the GTO is) and l_x, l_y and l_z are non-negative integers. The sum of these numbers, $l = l_x + l_y + l_z$, is analogous to the angular momentum quantum number and gives an indication of the type of functions as *s*-type (l = 0), *p*-type (l = 1), *d*-type (l = 2) etc. The GTOs have the advantage that they are simpler to handle than STOs computationally since the calculation of multi-centre electron repulsion integrals

are easier using GTOs due to the Gaussian product theorem (the product of two Gaussians at different centres is another Gaussian at a new centre). The GTOs, however, have incorrect behaviours both at short ($R \to 0$; no nuclear cusp) and long ($R \to \infty$; too fast decay) ranges. To overcome these shortcomings, a number of GTOs (primitives) are commonly taken as a linear combination to create *contracted* Gaussian functions (CGFs) to resemble the STOs as much as possible:

$$\chi^{\mathrm{CGF}} = \sum_i a_i \chi_i^{\mathrm{GTO}} \tag{1.29}$$

The CGFs are variationally optimised with respect to the Hartree-Fock (HF) energy of free atoms to produce an optimal set of contraction coefficients and Gaussian exponents of the primitives, which are then fixed. The optimised CGFs are the used to construct Gaussian-type basis sets.

1.3.2 Single-ζ, multiple-ζ and split-valence basis sets

A minimal basis set, or **single-ζ** basis set**,** is one where a single basis function is used for each orbital in a Hartree-Fock (*vide infra*) calculation on the free atom. The most common example of minimal basis set is STO-*n*G, first proposed by John Pople, where *n* Gaussian primitives are used to approximate a single STO. For example, an STO-3G basis function is a linear combination of 3 primitive Gaussian functions with the coefficients determined via a least square fit to the single STO. Using this basis set, a carbon atom, for example, will have only one STO-3G orbital for each of 1s, 2s and three 2p orbitals. This minimal basis set is generally considered to be insufficient for accurate representation of orbitals in quantum chemistry.

To increase the accuracy of orbital descriptions by the basis sets, two or more functions can be used to describe each type of orbital, giving rise to **double-ζ (DZ)**, **triple-ζ (TZ)**, and **quadruple-ζ (QZ)** basis sets. For example, a carbon atom with DZ basis set will have two functions for each of 1s, 2s and three 2p orbitals (1s, 1s', 2s, 2s' and two sets of p-functions 2p and 2p').

In chemical bonding, the core orbitals are only weakly affected whereas the valence orbitals can change substantially. The majority of chemistry is governed by the movement of valence electrons. It is therefore more computationally efficient to implement basis set that allows for a greater flexibility in the valence orbitals rather than the core orbitals. The **split-valence (SV)** basis set introduced by Pople aims to achieve this balance of flexibility and cost. In a SV basis set, single-ζ basis functions are used for core orbitals and double- and higher-ζ basis functions for valence orbitals. These SV basis sets are represented as *n-ij*G or *n-ijk*G where *n* is the number of Gaussian primitives used for the core shells; the numbers *i, j, k* are the numbers of Gaussian primitives used for contractions in the *first, second* and *third* STO of the valence shells, respectively. The *ij* notation is used for basis set of valence double-ζ (VDZ) quality (two functions for the valence orbitals) while the *ijk* notation is used for basis set of valence triple-ζ (VTZ) quality (three functions for the valence orbitals). For example, the split-valence triple-ζ basis set 6-311G uses 6 Gaussian functions to describe the core orbital, and respectively 3, 1, 1 Gaussian function(s) for the first, second, third STO of the valence orbital.

1.3.3 Polarisation functions

The GTOs in the previous subsections are optimised by minimising the HF energy of the atoms. This gives the basis functions that have the same angular momentum *l* as those in atoms. However, during bonding in the formation of molecules, these atomic orbitals are

distorted. Under these situations, the s-orbital acquires p-character while the p-orbital acquires d-character and so on. These changes are not satisfactorily represented by the Gaussian AOs. To account for these orbital distortions upon molecular bonding, functions of higher angular momentum are usually added. These additional functions are called *polarisation functions* and when added to the basis set, is denoted by the letter "P". Thus, DZP means double-ζ basis set with polarisation functions added. In the Pople-type basis sets, the polarisation functions are denoted by the parenthesis behind the basis set names, for example, in 6-31G(d,p) basis set, the notation "(d,p)" denotes that a set of d-orbital functions are added to the heavy atoms and that a set of p-orbital functions are added to the H atoms.

The addition of polarisation functions removes the spherical symmetry of the AOs so that the basis set can give a better description of bonding environment. Polarisation functions introduce an additional node. For example, when polarisation is added to 1s AO of a hydrogen atom, a p-function is added; similarly, when polarisation is added to valence p-orbitals, d-type functions are added to the basis set. For heavy atoms, higher angular momentum polarisation functions (d, f, …) may be important. In all calculations where electron correlation is important, it is necessary to include polarisation functions.

1.3.4 Diffuse functions

For anionic systems or systems in excited states, the electrons are usually loosely bound. This necessitates an accurate description of the wavefunction towards the tail region. *Diffuse functions*, having very small exponents and decaying more slowly with distance from the nucleus, are included to provide improved description of the tail region. These Gaussian functions are usually of s- and p-type functions and their inclusion allow better description of anions, weak bonds (e.g. hydrogen bonds) and calculation of properties

such as dipole moments and polarizabilities etc. The addition of diffuse functions to a Pople-type basis set is indicated by "+" in *n-ij*+G or *n-ij*++G where a single "+" indicates that one diffuse s-type and p-type Gaussian functions are added on heavy atoms and a double "++" indicates that on top of the functions added on heavy atoms in "+" basis set, an additional diffuse s-type Gaussian function is added on hydrogen atoms.

1.3.5 Correlation-consistent (cc) basis sets

Correlation-consistent (cc) basis sets are widely used basis sets developed by Dunning and co-workers[8–16] for wavefunction-based calculations. They are primarily designed for correlated calculations and are optimised using correlated (CISD) wavefunctions. They are designed to converge systematically to the complete basis set (CBS) limit. These basis sets are denoted cc-pVXZ (X = D, T, Q, 5, 6, 7…) which means correlation-consistent, polarised valence, X-zeta basis. Additional set of tight functions with large exponents can be added to recover core-core and core-valence electron correlation, producing the cc-pCVXZ basis sets (where C stands for core). A prefix "aug" can be added to show that a set of diffuse functions has been included for every angular momentum present in the basis set, therefore, aug-cc-pVDZ for C atom for example, has diffuse s, p, d functions added.

1.3.6 Karlsruhe basis sets

The basis sets discussed previously are rather expensive computationally (non-linear dependence) and suffer from basis set incompleteness if a finite basis set is used. The Karlsruhe basis sets provide an attractive alternative as they are property-optimised balanced basis sets of quality for all elements up to radon (Z = 86). These basis sets show similar convergence for SV, DZ, TZ and QZ quality and are more computationally economical.[17]

Def2-basis sets are examples of segmented contracted basis sets.[18,19] These are designed for all the elements H-Rn for varying flexibility and accuracy. The basis sets are named def2-SV(P) to def2-QZVPP. They were tested for a set of *ca.* 300 molecules representing nearly all elements in nearly all common oxidation states and are designed to give similar errors for all the elements across the periodic table for a given basis set type. It is recommended that[18] for DFT calculations, one uses def2-SV(P) basis sets to obtain qualitative results and def2-TZVP basis sets to obtain results close to DFT basis set limit. For similar accuracies in HF and MP2 and other post-HF calculations, larger polarisation sets are required and that def2-SVP and def2-TZVPP bases are recommended, for the above purposes respectively. For first-order property calculations, such as bond energies, using DFT, def2-TZVPP bases are recommended to approach the DFT basis set limit.[18]

1.3.7 Effective core potentials

For systems involving heavier elements such as those from the third period and beyond of the periodic table, there is a large number of core electrons for these elements. To reach a proper description of the valence electrons, a large number of basis functions are first required to describe the core electrons, which are relatively less important in chemical reactions. The situation is complicated by the increasing importance of relativistic effects for heavy elements. To overcome these problems, effective core potentials (ECP), also called pseudopotentials, are introduced to represent the chemically inert core electrons and capture the dominant effects of relativity. This has the advantage that the size of the basis set needed for the molecular description can be significantly reduced. The ECPs from Hay and Wadt, also called Los Alamos National Laboratory (LANL) ECPs[20,21] (non-relativistic for the first-row transition metals), is an example of popular ECPs in modern use.

1.3.8 Basis set superposition error

Calculations of a molecular system using a finite (especially small) basis set are prone to *basis set superposition error* (BSSE).[22,23] The interaction energy between two monomers A and B is given by the energy difference between the complex AB and the sum of the individual energy of A and B. As the two monomers A and B approach each other in the complex formation, the complex AB can be artificially stabilised as monomer A utilises the basis functions from monomer B and vice versa. Each monomer is able to access the basis functions on the other monomer at short, but not long, intermolecular distance. This differential treatment of monomers at varying intermolecular distances is the source of BSSE. In the event that BSSE can be eliminated by treating the monomers with same number of basis functions at different intermolecular distances, the system can still be subject to basis set incompleteness errors (BSIEs) due to the finite size of the basis set used.

The Boys and Bernardi counterpoise correction (CP) is commonly used to remove BSSE.[24] Briefly, the BSSE is calculated by additional calculations using the dimer basis for all species and subtracting the energy difference between the monomer in dimer basis and the monomer in monomer basis.

1.3.9 Basis sets used in this thesis

We used GTOs throughout this thesis. For systems where small organic molecules are involved (Chapters 2 and 3), we used a small Pople-type basis set for geometry optimisation. For example, in Chapter 2, we study the radical cationic system involving small organic molecules, we used a small basis set 6-31G(d) for geometry optimisation. For Chapter 3, in the study of hydroxyphosphine bifunctional catalyst, where hydrogen bonding and proton movements are potentially important, we used 6-31+G(d,p) basis set

for geometry optimisation. Here we added in diffuse functions for a better description of hydrogen bonding and additional polarisation functions for the hydrogen atom for better bonding description of the formation and breaking of O–H and N–H bonds.

For the study of transition metal (TM) catalysed reactions (Chapters 4 to 7), the initial geometry optimisations were all performed with a small basis set of def2-SVP quality. The Karlsruhe basis set was chosen as it provides a balanced description of all elements, up to Rn, on the periodic table. The Pople basis sets were not used as these do not provide descriptions of elements beyond Kr (such as Pd, and Ir that we use in our catalytic system). For a finer geometry optimisation, we used a mixture of bases for the description of these organometallic systems. Typically, a larger basis set, such as def2-TZVPPD used for the TMs in this thesis, is needed to provide a sufficient description of the d-orbitals.[18] The diffused functions (indicated by the letter "D" in the basis name) are also included to better describe the second (e.g. Pd) and third row (e.g. Ir) TM p- and d-orbitals.[18]

For single-point (SP) calculations, we generally use a large basis set from the Karlsruhe basis set family, such as def2-QZVPP, which provides a good description for all elements and yields a good accuracy.

1.4 The Hartree-Fock or Self-Consistent Field Method

The Hartree-Fock (HF) method is central to quantum chemistry. HF commonly serves as a starting point for more sophisticated methods such as those accounting for the effects of electron correlation. The underlying idea of HF is that a single Slater determinantal wavefunction can be used to approximate a multi-electronic system where electron-electron interactions are treated in an average way.

1.4.1 Hartree-Fock equations

For an *N*-electron system, we can use a single Slater determinant of the form in Equation (1.26) to approximate the ground state wavefunction. We aim to minimise the electronic energy to find the best spin orbitals using the variational method. That is, we want to minimise

$$E_0 = \frac{\langle \Psi_{\mathrm{HF}} | \hat{H} | \Psi_{\mathrm{HF}} \rangle}{\langle \Psi_{\mathrm{HF}} | \Psi_{\mathrm{HF}} \rangle} = \langle \Psi_{\mathrm{HF}} | \hat{H} | \Psi_{\mathrm{HF}} \rangle \text{ if } \Psi_{\mathrm{HF}} \text{ is normalised} \tag{1.30}$$

by systematically varying the spin orbitals $\{\chi_i\}$, subject to the constraint that these spin orbitals remain orthonormal, $\langle \chi_i | \chi_j \rangle = \delta_{ij}$. Doing this formally leads to a set of one-electron Fock equations

$$\hat{f}_i \chi_i = \varepsilon_i \chi_i \tag{1.31}$$

where the Fock operator $\hat{f}_i$ gives the effective *one-particle* Hamiltonian:

$$\hat{f}_i = \hat{h}_i + \hat{V}_i^{\mathrm{HF}} = -\frac{1}{2}\nabla_i^2 - \sum_{A=1}^{M} \frac{Z_A}{r_{iA}} + \sum_j \left(\hat{J}_j(1) - \hat{K}_j(1) \right) . \tag{1.32}$$

The Fock operator is a sum of the core Hamiltonian operator $\hat{h}_i$,

$$\hat{h}_i = -\frac{1}{2}\nabla_i^2 - \sum_{A=1}^{M} \frac{Z_A}{r_{iA}}, \tag{1.33}$$

and the effective *one-electron* HF potential operator, $\hat{V}_i^{\mathrm{HF}}$,

$$\hat{V}_i^{\mathrm{HF}} = \sum_j \left(\hat{J}_j(1) - \hat{K}_j(1) \right) \tag{1.34}$$

where $\hat{J}_i$ and $\hat{K}_i$ are the Coulomb and exchange operators, respectively, defined as

$$\hat{J}_j(1)\,|\chi_i(1)\rangle = \left\langle \chi_j(2) \left| \frac{1}{r_{12}} \right| \chi_j(2) \right\rangle |\chi_i(1)\rangle$$
$$\hat{K}_j(1)\,|\chi_i(1)\rangle = \left\langle \chi_j(2) \left| \frac{1}{r_{12}} \right| \chi_i(2) \right\rangle |\chi_j(1)\rangle \tag{1.35}$$

The *Coulomb operator* $\hat{J}_i$ accounts for the Coulombic repulsion between electrons and is local in nature in the sense that it gives the averaged potential due to other electrons at a point in space and does not depend on other points in space. The *exchange operator* $\hat{K}_i$ is, on the other hand, non-local since there does not exist a simple potential that uniquely define the exchange at a local point in space. The exchange energy accounts for the effects of electron exchange interactions due to the indistinguishability of identical particles and results from the antisymmetry of the Slater determinantal wavefunction.

The HF equations are a set of non-linear coupled differential equations in that the Fock operator $\hat{f}_i$ for one electron depends on the spin orbitals of all other electrons and that each spin orbitals χ_i is obtained as a solution of the Fock equation. As a result, an iterative approach is needed to solve the HF equations. This is done by first proposing a set of guess orbitals, from which the average HF potential operator $\hat{V}_i^{\mathrm{HF}}$ is constructed. The Fock equations (Equation (1.31)) can then be solved to obtain a new set of orbitals. This procedure is iterated until the difference between the new orbitals and the input orbitals falls below a predefined threshold value. As a result, this method is known as the **self-consistent field** (SCF) method.

1.4.2 Restricted close-shell, restricted open-shell and unrestricted HF

The presence of electron spins gives rise to different energy expressions for the HF procedures. In a restricted close-shell HF (**RHF**), the electron spins are all paired up in orbitals. It can be shown the energy expression for the RHF single Slater determinantal wavefunction is given by

$$E^{RHF} = 2\sum_{i}^{n} h_{ii} + \sum_{ij}^{n}[2(ii|jj) - (ij|ij)] \tag{1.36}$$

where the spin of the system has been taken into account and factored out so that only spatial orbitals $\{\psi_i\}$ are used. In the expression,

$$h_{ii} = \langle \psi_i | \, \hat{h} \, | \psi_i \rangle \tag{1.37}$$

is the matrix element of the core Hamiltonian, Equation (1.33), representing the electronic energy of an electron in spatial orbital *i* in the combined electrostatic potential averaged over *all other* electrons;

$$(ii|jj) = \left\langle \psi_i(i)\psi_j(j) \left| \frac{1}{r_{ij}} \right| \psi_i(i)\psi_j(j) \right\rangle \tag{1.38}$$

is the Coulomb energy between electrons *i* and *j* (labels in parenthesis) in orbitals *i* and *j* (labels in subscripts of the wavefunctions); and that

$$(ij|ij) = \left\langle \psi_i(i)\psi_j(j) \left| \frac{1}{r_{ij}} \right| \psi_i(j)\psi_j(i) \right\rangle \tag{1.39}$$

is the exchange energy. Note that the direct Coulomb energy results from pairwise interactions between *all* electrons whereas the exchange energy results from the pairwise interactions between electrons of *parallel* spins only.

For openshell systems, two approaches are generally adopted. Using unrestricted HF (**UHF**), the lowest energy for the single Slater determinantal wavefunction is given by

$$E^{\mathrm{UHF}} = \sum_{i}^{\alpha+\beta} h_{ii} + \frac{1}{2}\sum_{ij}^{\alpha+\beta}(ii|jj) - \frac{1}{2}\sum_{ij}^{\alpha}(ij|ij) - \frac{1}{2}\sum_{ij}^{\beta}(ij|ij) \tag{1.40}$$

where the α and β orbitals have different spatial parts. The Slater determinant is an eigenfunction of $\hat{S}_z$ but not an eigenfunction of $\hat{S}^2$. Spin contamination, the artificial mixing of electronic states of different spins, can lead to inaccurate energies. Techniques exist, however, to eliminate spin contamination.[25–27] UHF is commonly used to study openshell systems due to its simplicity, computational efficiency and ease for post-Hartree Fock method implementation.

Another method for dealing with openshell system is restricted open-shell HF (**ROHF**). In this method, electrons are first paired up in doubly occupied spatial orbitals, leaving unpaired electrons in singly occupied orbitals. The energy expression for ROHF is given by

$$\begin{aligned} E = &\sum_i 2h_{ii} + \sum_{ij}[2(ii|jj) - (ij|ij)] \\ &+ \sum_m h_{mm} + \frac{1}{2}\sum_{mn}[(mm|nn) - (mn|mn)] \\ &+ \sum_{im}[2(mm|ii) - (im|im)] \end{aligned} \tag{1.41}$$

where *i*, *j*… denote doubly occupied orbitals and *m*, *n*… denote singly occupied α orbitals; the last term gives the mixing between doubly and singly occupied orbitals since they are chemically distinct. The ROHF picture is chemically accurate in that the wavefunction is an eigenfunction of the total spin operator $\hat{S}^2$. In other words, the ROHF wavefunction does not suffer from spin contamination. However, this method is much less frequently used than the UHF method in modern quantum chemistry due to its higher difficulty in implementation and higher computational cost. The ROHF method lacks a unique effective Fock operator,[28] such that the resulting orbitals and orbital energies are

different depending on the choice of Fock operators, making the physical interpretation somewhat difficult.

1.4.3 Roothaan-Hall equations

The direct solution of the Fock equations (Equation (1.31)) is non-trivial. In 1951-52, Roothaan[29] and Hall[30] independently proposed a method of converting the set of integro-differential equations into a set of algebraic equations by introducing basis functions (section 1.3). Taking electron spin out of consideration by adopting the appropriate HF method, we consider only the spatial orbitals. A set of of K known basis functions or AOs $\{\phi_\mu(\mathbf{r})\}$ is commonly employed, so that each MO ψ_i can be expressed as a linear combination of these AOs, viz.,

$$\psi_i = \sum_{\mu=1}^{K} c_{\mu i}\phi_\mu(\mathbf{r}) \tag{1.42}$$

Substituting the above expression into the Fock equations $\hat{f}_i\chi_i = \varepsilon_i\chi_i$, we have

$$\hat{f}_i \sum_{\mu=1}^{K} c_{\mu i}\phi_\mu(\mathbf{r}) = \varepsilon_i \sum_{\mu=1}^{K} c_{\mu i}\phi_\mu(\mathbf{r}) \tag{1.43}$$

which is equivalent to the following matrix equation for the expansion coefficients:

$$\mathbf{FC} = \mathbf{SC}\boldsymbol{\varepsilon} \tag{1.44}$$

These are the Roothaan-Hall equations. **F** is the Fock matrix with the matrix element $F_{\mu\nu} = \langle\phi_\mu|\,\hat{f}\,|\phi_\nu\rangle$; **S** is the overlap matrix with the $S_{\mu\nu} = \langle\phi_\mu|\phi_\nu\rangle$ giving the overlap between the basis functions; **C** is the coefficient matrix containing the expansion coefficients $c_{\mu i}$; $\boldsymbol{\varepsilon}$ is a diagonal matrix of orbital energies. All these matrices are $K \times K$ in

dimension. The integro-differential HF equations, using the Roothaan-Hall formalism, is thus converted to standard algebraic matrix equations.

If the set of basis functions used is complete, then the expansion Equation (1.42) would be exact, and we would be able to obtain the lowest possible variational energy, the **HF limit**, within the single Slater determinantal approximation. In practice, however, limited by computational resources, a *finite* set of K basis functions is used. For a system of N electrons, using a set of K basis functions gives a total of $2K$ spin orbitals, consisting of N occupied spin orbitals and $2K - N$ unoccupied, or virtual, orbitals. The single Slater determinantal wavefunction formed from the occupied spin orbitals is then the best approximation to the ground state of the system.

1.4.4 Electron correlation

Because the HF potential uses central field approximation, electron-electron interactions are not directly taken into account and are only treated in an averaged manner. As a result, there is a finite probability that, within the HF approximation, two electrons will occupy the same space, which is unphysical. The deficiency of HF theory is that the motion of an electron can be affected by the motion of other electrons and this *electron correlation* is not captured by HF theory. The correlation energy E_{corr} is defined as

$$E_{\text{corr}} = E_{\text{exact}} - E_{\text{HF}} \tag{1.45}$$

This correlation due to electron-electron interactions is sometimes called *dynamical* electron correlation as it results from the motion of these electrons. As the HF is single Slater determinantal, it also fails to account for *non-dynamical* correlation, arising from different determinants contributing similar weights to a system due to their near or exact degeneracy in frontier orbitals.

E_{corr} is always negative as the HF limit, E_{HF}, is an upper bound to the true ground state energy, as dictated by the variational principle. Although this correlation energy is normally only 1% of the total energy, its exclusion can lead to major errors in chemistry. This is particularly true for cases such as transition metal systems, where the neglect of electron correlation can result in huge errors. Therefore, methods accounting for electron correlation are required for high accuracy quantum chemistry.

1.5 Post-Hartree-Fock Methods

To account for electron correlation, it is essential to go beyond Hartree-Fock. Broadly speaking, two classes of methods can be distinguished – the variational and perturbative. Variational methods, such as configuration interaction (CI), uses a linear combination of discrete solution sets whereas perturbative methods, such as many-body perturbation theory (MBPT), separate the problem into an exactly solvable part and a difficult part with no general analytic solution as a small perturbation to that solvable part.

1.5.1 Configuration interaction

The configuration interaction (CI) wavefunction is constructed from a linear combination of Slater determinants called the *configuration state functions*, that is

$$\Psi_{\mathrm{CI}} = \sum_i c_i \left|\Psi_{\mathrm{i}}\right\rangle = c_0\Psi_{\mathrm{HF}} + \sum_{\mathrm{S}} c_{\mathrm{S}}\Psi_{\mathrm{S}} + \sum_{\mathrm{D}} c_{\mathrm{D}}\Psi_{\mathrm{D}} + \sum_{\mathrm{T}} c_{\mathrm{T}}\Psi_{\mathrm{T}} + \sum_{\mathrm{Q}} c_{\mathrm{Q}}\Psi_{\mathrm{Q}} + \cdots \quad (1.46)$$

where the Slater determinants are obtained by promoting electrons from the occupied orbitals to the virtual orbitals in the reference HF Slater determinant. The number of electrons promoted determines the nature of these configuration state functions: promotion of one electron generates the singly excited state functions Ψ_{S}, and two

electrons, doubly excited state functions Ψ_{D}, etc. The CI coefficients are obtained by variationally minimising the electronic energy for the ground state:

$$E_{\mathrm{CI}} = \min_{\Psi_{\mathrm{CI}}} \frac{\langle \Psi_{\mathrm{CI}} | \hat{H} | \Psi_{\mathrm{CI}} \rangle}{\langle \Psi_{\mathrm{CI}} | \Psi_{\mathrm{CI}} \rangle} \tag{1.47}$$

For a given basis set, a full CI (FCI) wavefunction can be constructed by considering all the configurations that can be generated from the reference Slater determinant and including them in the calculation. A full CI calculation is highly computationally expensive due to its poor scaling with the number of electrons and basis functions, it is thus only achievable for very small systems. For most cases, it is necessarily to truncate the CI expansion, Equation (1.46), so that only a subset of the determinants is included. In general, since lower-order excitations are more important than higher-order ones, *hierarchical truncation* is used. As an illustration, the CI singles-and-doubles (CISD) wavefunction recovers ~94.5% of the correlation energy while CISDT with triples recovers ~ 95.9%. This goes up to 99.9% at CISDTQ with quadruple excitations.

The method above of using a single HF Slater determinant as a reference state function is called *single-reference* CI. In systems where a single determinant is insufficient to represent the ground state due to (near-)degeneracy (source of non-dynamical electron correlation), a *multi-reference* CI (MRCI) wavefunction is necessary. A reference space consisting of more than one dominant determinant is constructed, from which excitation determinants are generated from each of the reference determinants.

1.5.2 Many-body perturbation theory

Another systematic approach to recover the electron correlation energy is the many-body perturbation theory (MBPT). This perturbative method treats electron correlation as a

small perturbation to the ground state wavefunction; this method is not variational but size-consistent. The simplest example is the Møller-Plesset (MP) theory[31] – an example of Rayleigh Schrödinger perturbation theory – denoted by MP*n* where *n* is the order at which the perturbation is truncated. The starting point for the MP theory are the eigensolutions of the Fock equations, $\hat{f}_i\chi_i = \varepsilon_i\chi_i$. Using MBPT, we wish to solve the eigenvalue problem for electronic state *n*:

$$\hat{H}\left|\Psi_n\right\rangle = (\hat{H}_0 + \hat{V})\left|\Psi_n\right\rangle = \mathrm{E_n}\left|\Psi_n\right\rangle \tag{1.48}$$

Expanding the wavefunction and energy as power series, we have

$$\left(\hat{H}^{(0)} + \lambda\hat{V}\right)\left(\sum_{i=0}\lambda^i\Psi_n^{(i)}\right) = \left(\sum_{i=0}\lambda^i E_n^{(i)}\right)\left(\sum_{i=0}\lambda^i\Psi_n^{(i)}\right) \quad \Longleftrightarrow$$
$$(\hat{H}_0 + \lambda\hat{V})\left|\Psi_n^{(0)} + \lambda\Psi_n^{(1)} + \ldots\right\rangle = (E_n^{(0)} + \lambda E_n^{(1)} + \lambda^2 E_n^{(2)} + \ldots)\left|\Psi_n^{(0)} + \lambda\Psi_n^{(1)} + \ldots\right\rangle \tag{1.49}$$

We choose the reference Hamiltonian to be the sum of the Fock operators,

$$\hat{H}_0 = \sum_i^N \hat{f}_i \quad , \tag{1.50}$$

such that the perturbation is defined as

$$\hat{V} = \hat{H} - \hat{H}_0 = \hat{H} - \sum_i^N \hat{f}_i \quad . \tag{1.51}$$

The zeroth order reference determinant is the HF Slater determinant $\Psi^{(0)} = \Psi_{\mathrm{HF}}$.

Equating the different power terms in λ in the series expansion of Equation (1.49), we find that the first-order change in the n^{th} state wavefunction is given by

$$\left|\Psi_n^{(1)}\right\rangle = \sum_{m\neq n} \frac{\left\langle \Psi_m^{(0)}|V|\Psi_n^{(0)}\right\rangle}{E_n^{(0)} - E_m^{(0)}} \left|\Psi_m^{(0)}\right\rangle \tag{1.52}$$

and has contributions from each of the eigenstates with $m \neq n$. The second order (MP2) perturbation energy is given by

$$E_n^{(2)} = \sum_{m\neq n} \frac{\left|\left\langle \Psi_m^{(0)}|V|\Psi_n^{(0)}\right\rangle\right|^2}{E_n^{(0)} - E_m^{(0)}} \tag{1.53}$$

which is proportional to the square of the matrix element of the perturbation that mixes the eigenstates *m* and *n* (the numerator), and inversely proportional to the energy difference between eigenstates *m* and *n*, showing that the contribution to the perturbation energy is the largest if the other eigenstates are close in energy to the state of interest.

Although higher order energy corrections can be calculated (MP3, MP4…), they are rarely used since the MP theory is non-variational and frequently the inclusion of higher orders, at additional computational cost, does not improve the calculated results.

1.5.3 Coupled-cluster theory

The coupled-cluster (CC) theory, originally proposed for problems in physics, is one of the most accurate methods that treat electron correlation for practical *ab initio* quantum chemistry. It has wide-ranging applications in the study of molecular structures and properties, excited states and spectroscopy. The basic equations for CC theory have a rather simple appearance. Instead of using a linear expansion of wavefunctions as in CI, CC uses an exponential ansatz for the wavefunction, viz.,

$$|\Psi\rangle = e^{\hat{T}}\,|\Phi_0\rangle = \left(1 + \hat{T} + \frac{1}{2}\hat{T}^2 + \frac{1}{3!}\hat{T}^3 + \cdots\right)|\Phi_0\rangle \tag{1.54}$$

where $|\Phi_0\rangle$ is the reference wavefunction, which is typically a Hartree-Fock determinant, but can also be other wavefunction arising from, for example, CI. The cluster operator $\hat{T}$ can be written as a sum of operators that, for an *N*-electron system, generate single ($\hat{T}_1$), double ($\hat{T}_2$) and triple ($\hat{T}_3$), …, up to *N*-tuple excitations ($\hat{T}_N$),

$$\hat{T} = \hat{T}_1 + \hat{T}_2 + \hat{T}_3 + \cdots + \hat{T}_N \tag{1.55}$$

in the reference wavefunction. The CC energy, which is not variational, is given by

$$E = \langle\Phi_0|\, e^{-\hat{T}} H e^{\hat{T}}\,|\Phi_0\rangle = \big\langle\Phi_0|\bar{H}|\Phi_0\big\rangle \tag{1.56}$$

where $\bar{H} = e^{-\hat{T}} H e^{\hat{T}}$ is the similarity-transformed (rotated) Hamiltonian of the system. The CC energy is a function of unknown amplitudes which can be obtained by solving the amplitude equation

$$\big\langle\Phi_{ij\ldots}^{ab\cdots}|\bar{H}|\Phi_0\big\rangle = 0 \tag{1.57}$$

The cluster operator is usually truncated to give different models. One of the most popular ones is the coupled cluster singles-and-doubles (**CCSD**)[32] where the cluster operator is taken as $\hat{T} = \hat{T}_1 + \hat{T}_2$. This CCSD method has the same number of parameters as CISD but has better approximations as it also accounts for higher order terms using the products of lower order terms – for example, substituting $\hat{T} = \hat{T}_1 + \hat{T}_2$ in the exponential wavefunction ansatz Equation (1.54) gives $\hat{T}_2^2$ and $\hat{T}_2^3$ terms (and others), which approximately accounts for quadruple and sextuple (and other) excitations, respectively. For coupled cluster singles-doubles-and-triples (CCSDT), we take $\hat{T} = \hat{T}_1 + \hat{T}_2 + \hat{T}_3$.

As CCSDT is rather expensive, a popular method for improving upon CCSD calculations is the **CCSD(T)** method,[33] which consists of full CCSD treatment with an estimate of the connected triples contribution by a non-iterative calculation of MBPT. This is frequently considered the "gold standard" in quantum chemistry.

1.6 Density Functional Theory

The *ab initio* wavefunction-based methods discussed earlier are rather expensive and are practical only for systems with a small number of atoms. Density functional theory (DFT) aims to provide an alternative framework within which the electronic structure problem is tackled. The central idea behind DFT is that it is not necessary to solve the Schrödinger equation for the wavefunction of the system (a *4N*-variable quantity – *3N* spatial and *N* spin coordinates – for an *N*-electron system) to compute the ground state energy, but rather it is sufficient to express the energy (and other properties) as a functional of the electron density, which is a 3-dimensional quantity.

1.6.1 Hohenberg-Kohn theorems

The foundations of modern DFT are grounded in two theorems developed by Hohenberg and Kohn (HK) in 1964.[34] The first theorem (HK1) states that the ground state electron density uniquely determines the external potential, thus the total energy, of a system. This means that the total energy is a unique functional of the ground state electron density. We know that the Hamiltonian of a system depends on the nuclear positions $\{R_A\}$ and atomic numbers $\{Z_A\}$ of the atoms and the total number of electrons, N (Equation (1.3)). It is quite easy to see that knowing the ground state electron density immediately gives us these *three* quantities since, 1) the integral of the density over all space gives the number of electrons N, viz.,

$$\int \rho(\mathbf{r}) d\tau = N; \tag{1.58}$$

2) the electron density maxima give the positions of the nuclei $\{R_A\}$; and 3) for any nucleus A at density maximum, the atomic number Z_A is given by

$$\left.\frac{\partial \bar{\rho}(r)}{\partial r}\right|_{r=0} = -2Z_A\,\rho\,(0) \tag{1.59}$$

where r is the radial distance from nucleus A, $\bar{\rho}\,(r)$ is the spherically averaged density. In words, this means that the radial derivative of the spherically averaged electron density, at the nuclear position, gives twice the density at the nucleus, $\rho\,(0)$, multiplied by the negative of the atomic number. At this stage, we see that given a known electron density, one can form the Hamiltonian for the system, solve the Schrödinger equation and thus determine the wavefunctions and energies of the system:

$$\rho(\mathbf{r}) \Rightarrow \{N, Z_A, R_A\} \Rightarrow \hat{H} \Rightarrow \Psi_0 \Rightarrow E_0 \text{ (and all other properties)} \tag{1.60}$$

The second theorem (HK2) guarantees that the ground state energy can be variationally found, provided that we can find an *exact* energy functional of the electron density $E[\rho]$; it states that any trial density satisfying the boundary conditions delivers an energy that is an upper bound to the true ground state energy and that the energy is exactly the same as the true ground state energy only if the trial density is exactly the true density, that is,

$$E_0 = E_0[\rho_0] \leq E[\tilde{\rho}] \tag{1.61}$$

These theorems prove the existence of the functional for finding the energies but they do not prescribe how one can find the functional!

1.6.2 The energy functional

The electronic Hamiltonian Equation (1.6) contains three terms: the kinetic energy of the electrons, the electron-electron interactions and electron-nucleus interactions and can be written as

$$\hat{H} = \hat{T} + \hat{V}_{ee} + \hat{V}_{Ne} \tag{1.62}$$

and that the energy functional is given by

$$E[\rho] = T[\rho] + V_{ee}[\rho] + V_{Ne}[\rho] = F[\rho] + \int \rho(\mathbf{r}) v(\mathbf{r}) d\mathbf{r} \tag{1.63}$$

where

$$v(\mathbf{r}) = -\sum_{A=1}^{M} \frac{Z_A}{r_A} \tag{1.64}$$

is the external potential that depends on the system. This term can be trivially evaluated once the system is specified, that is, once the potential $v(\mathbf{r})$ is known;

$$F[\rho] = T[\rho] + V_{ee}[\rho] = T[\rho] + (J[\rho] + E_{nc}[\rho]) \tag{1.65}$$

is the internal energy functional or the Hohenberg-Kohn functional that is *independent* of the external potential $v(\mathbf{r})$ and is thus universal for all systems (depends only on the total density). The electron-electron interaction energy functional $V_{ee}[\rho]$ can be further separated into the functional due to classical Coulomb interaction, $J[\rho]$, and *non-classical* contributions, $E_{nc}[\rho]$. If this functional $F[\rho]$ were known, we would have solved the SE for *all* systems. However, the explicit form of this functional is unknown and this is a major challenge for DFT development.

1.6.3 The Kohn-Sham approach

The quest for the universal functional $F[\rho]$ is not directly in sight. The method of Kohn and Sham[35] gives us one way to proceed with practical DFT. The essential idea behind the KS approach is the introduction of a fictitious system of non-interacting particles that generate the same density as the true system of interacting particles. In doing so, a special type of one-particle orbitals $\{\phi_i\}$ is reintroduced. The internal energy functional $F[\rho]$ can then be written as

$$F[\rho] = T[\rho] + J[\rho] + E_{nc}[\rho] = T_s[\rho] + J[\rho] + E_{xc}[\rho] \tag{1.66}$$

where the exchange-correlation functional $E_{xc}[\rho]$, given by

$$E_{xc}[\rho] = (T[\rho] - T_s[\rho]) + (V_{ee}[\rho] - J[\rho]), \tag{1.67}$$

is a collection of all portions of the total energy that are not exactly known.

In this approach, the bulk of the kinetic energy of the true system can be recovered using the kinetic energy of the fictitious non-interacting systems, $T_s[\rho]$, given by

$$T_s[\rho] = -\frac{1}{2}\sum_{i}^{N} \langle \phi_i \left| \nabla^2 \right| \phi_i \rangle \tag{1.68}$$

The electron density of the system is also exactly known in term of these orbitals,

$$\rho(\mathbf{r}) = \sum_{i}^{N} f_i \left| \phi_i \right|^2 \tag{1.69}$$

where f_i is the occupation number of i^{th} orbital.

To find the set of orbitals $\{\phi_i\}$ that minimises the energy functional, we apply the variational principle and take the functional derivative of the energy functional to arrive at the Kohn-Sham equations:

$$\left(-\frac{1}{2}\nabla^2 + v(\mathbf{r}) + v_J(\mathbf{r}) + v_{xc}(\mathbf{r})\right)\phi_i(\mathbf{r}) = \varepsilon_i\phi_i(\mathbf{r}) \quad . \tag{1.70}$$

The external potential due to the electron-nucleus interactions is given by $v(\mathbf{r})$ in Equation (1.64); the Coulomb potential $v_J(\mathbf{r})$ is given by

$$v_J(\mathbf{r}) = \int \frac{\rho(\mathbf{r}')}{|\mathbf{r} - \mathbf{r}'|} d\mathbf{r}' \tag{1.71}$$

and the exchange-correlation potential $v_{xc}(\mathbf{r})$ is given by the functional derivative of the exchange-correlation functional E_{xc}, viz.,

$$v_{xc}(\mathbf{r}) = \frac{\delta E_{xc}}{\delta \rho(\mathbf{r})} \tag{1.72}$$

The KS equations (1.70) is a set of coupled *one-particle* Schrödinger equations that can only be solved self-consistently, as the sum of the potential terms depends on the density, and thus the orbitals, of the system that we are trying to solve for.

1.6.4 Hartree-Fock vs DFT

The HF method is a single Slater-determinantal approximation to the true ground state wavefunction and that the HF equations are obtained by optimising the MOs of the trial wavefunction to get the best energy. DFT is formally exact. The KS formalism is one approach to DFT that tries to optimise the particle density that maps a non-interacting system to a physical, interacting system to get the best energy. Thus, to get a property from wavefunction-based methods, one needs to know the correct quantum operator

corresponding to that property, but to get the property from DFT, one only needs to know how that property depends on the density of the system.

The KS orbitals are introduced to reproduce the particle density of the true interacting systems and have no strict physical meanings, except for the HOMO, whose energy gives the negative of the ionisation energy.[36–39] In practice, however, these KS orbitals have similar shapes to the HF orbitals, allowing for qualitative analysis.

1.6.5 The exchange-correlation energy

The exchange-correlation energy is commonly separated into the exchange energy and the correlation energy. The exchange energy results from Pauli Exclusion principle and arises due to the antisymmetry requirement of the total electronic wavefunction of the system. It describes the non-classical effect (interactions not due to the electronic charges but electronic spins) that electrons of parallel spins avoid each other in space. This energy gives the lowering of total energy due to the presence of this "exchange hole".

The correlation energy is what remains of the true total energy after taking away the kinetic and exchange energies. Unlike the exchange energy, correlation energy is more pronounced for electrons with anti-parallel spins, as these have higher likelihood of occupying the same region in space. This energy lowering can be understood as the effect arising from quantum fluctuations of electrons of anti-parallel spins as they coordinate their movements to minimise their Coulomb energy. The energy difference between the true kinetic energy and the non-interacting kinetic energy is also a major contribution to the exchange energy in KS-DFT.

1.6.6 Density functional approximations

The exchange-correlation functional can be approximated to varying degrees of accuracy, generally at increasing computational cost. These density functional approximations (DFAs) can be described as rungs of the Jacob's ladder (Scheme 1.1).

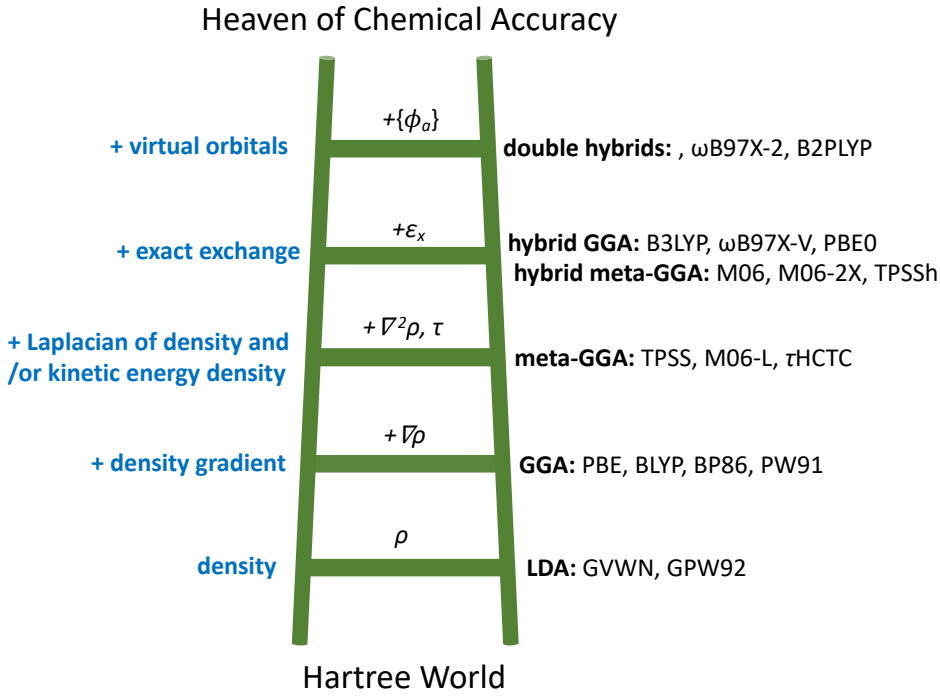

Scheme 1.1. Jacob's ladder of Density Functional Approximations (DFAs).

The crudest form of approximations is the local density approximation (**LDA**) which assumes that the electron density is the same at every position in space (the uniform electron gas (UEG)). The exchange energy (of the UEG) can be obtained exactly and is given by

$$E_{\mathrm{x}}^{\mathrm{LDA}}[\rho] = C \int \rho^{4/3}(\mathbf{r}) d\mathbf{r} \qquad (1.73)$$

The correlation energy from the LDA is generally obtained by fitting to the results of accurate numerical quantum Monte Carlo simulations of the UEG (e.g. the correlation

functional $E_{\mathrm{c}}^{\mathrm{VWN}}[\rho]$ due to Vosko, Wilk and Nusair[40]). LDA functionals are widely used in the study of solid-state systems but are considered inadequate for the study of molecular systems.

To account for the rapidly varying electron densities in molecules, generalised gradient approximation (**GGA**) functionals are developed. These functionals take into account the gradients of the density (thus "semi-local") and have the general form of

$$E_{\mathrm{xc}}^{\mathrm{GGA}}[\rho] = \int \rho(\mathbf{r})\varepsilon_{\mathrm{xc}}(\rho(\mathbf{r}), |\nabla\rho(\mathbf{r})|)d\mathbf{r} \quad (1.74)$$

Most GGA functionals are constructed as correction terms that are added to the LDA functionals. These GGA functionals reproduce the LDA functionals in the limit of zero density gradient. GGAs can give better results than LDAs in predicting geometries and ground state energies of molecules and solids and in the description of covalent bonds and systems with weak bonding. However, they are not necessarily accurate due to, for example in B88 exchange functional, incorrect asymptotic behaviour.

In **meta-GGA** functionals, the Laplacian/second derivative of the density $\nabla^2\rho(\mathbf{r})$ is included to improve accuracy. Additionally, the kinetic energy density τ is also included as it is numerically more stable and helps to reduce self-interaction error (SIE; *vide infra*) present in DFAs. Examples of meta-GGAs include TPSS[41] functional. These functionals have been shown in various cases to perform better than LDAs and GGAs in the study of molecular properties,[42–45] although hybrid GGAs (*vide infra*) can perform better than pure meta-GGAs for many applications.

Since LDA and GGA functionals overbind, whereas HF underbinds, another strategy is to mix in a portion of exact HF exchange to form the so-called **hybrid GGA** functionals.

When the same amount of HF is added for all molecular ranges, these are called *global* hybrid functionals. The most popular one is B3LYP.[40,46–48] This functional has 3 parameters (fitted to empirical data) that control the amount of HF exchange added. The exchange-correlation has the general form

$$E_{\mathrm{xc}} = E_{\mathrm{xc}}^{\mathrm{LDA}} + a_1 \left(E_{\mathrm{x}}^{\mathrm{HF}} - E_{\mathrm{x}}^{\mathrm{LDA}}\right) + a_2 \Delta E_{\mathrm{x}}^{\mathrm{GGA}} + a_3 \Delta E_{\mathrm{c}}^{\mathrm{GGA}}. \tag{1.75}$$

These hybrid functionals have been shown to be further improvements for molecular and solid-state properties over LDAs and GGAs.[44,45,49–51]

Range-separated functionals are a subclass of hybrid functionals. In these functionals, the inter-electron interaction is divided into a short-range (SR) and a long-range (LR) part:

$$\frac{1}{r_{12}} = \frac{1 - \left[\alpha + \beta\left(1 - \omega_{\mathrm{RSF}}\left(\gamma, r_{12}\right)\right)\right]}{r_{12}} + \frac{\alpha + \beta\left(1 - \omega_{\mathrm{RSF}}\left(\gamma, r_{12}\right)\right)}{r_{12}} \tag{1.76}$$

where the first term is the SR part described by exchange from (semi-)local functionals such as PBE and the second term is the LR part described by exchange from HF; α and β are the mixing parameters and ω is the range parameter that depend on the functional. The general form of the exchange-correlation is given by

$$E_{XC} = a E_X^{\text{SR-DFT}} + b E_X^{\text{LR-HF}} + c \Delta E_C^{\mathrm{DFT}} \tag{1.77}$$

Range-separated functionals include CAM-B3LYP and ωB97X-D and are popular for the study of excited states and other time-dependent phenomena.

In the next rung of the Jacob's ladder is the **double hybrid GGAs** which include the exchange energy from MP2 to improve the dispersion and exact exchange. Virtual orbitals are used. The exchange-correlation has the form

$$E_{XC} = aE_X^{DFT} + (1-a)E_X^{HF} + c\Delta E_C^{DFT} + (1-c)\Delta E_C^{PT}. \tag{1.78}$$

This class of functionals include B2PLYP and ωB97X-2. These functionals have much higher formal computational scaling than HF.

1.6.7 Dispersion

The failure to capture London dispersion interaction is a major inadequacy in accurately accounting for thermochemistry, kinetics and non-covalent interactions.[52–54] Most DFT functionals cannot reproduce the long-range London dispersion of the form $-C_6/R^6$, but instead fall off exponentially. Empirical dispersion correction of the form

$$E_{\text{disp}} = -\sum_{j>i} f_{\text{damp}}\left(R_{ij}\right) \frac{C_{6ij}}{R_{ij}^6} \tag{1.79}$$

which is in fact Grimme's D2 dispersion correction[55] used in functionals such as ωB97X-D[56], has been widely added to DFT functionals to improve calculations, especially in the study of systems with weak bonding. The interatomic coefficients C_{6ij} are obtained by fitting to accurate data and the damping function f_{damp} is required to ensure R^{-6} convergence at small internuclear separation. More recent developments in the dispersion correction include the so-called Grimme's D3 dispersion correction,[57] where in addition to the (unscaled) C_6 terms, additional C_8 terms are included.

1.6.8 Self-interaction error

The self-interaction is a spurious interaction arising from the approximate nature of DFAs.[58] In HF theory, the exchange energy is computed exactly, the correlation energy is absent and the self-interaction is exactly cancelled out. The Coulomb interaction results from the interaction of two different electrons and this is accurately captured by wavefunction theory. In KS-DFT, the energy is a functional of single-particle electron density; the two-electron Coulomb interaction cannot be distinguished from the self-interaction. The Coulomb energy in DFT results from the interactions of each electron with the entire electron density, including its own density, thus giving rise to SIEs. SIEs have been shown to cause inaccuracy in the study of numerous phenomena including orbital localisation,[58–61] ionisation,[62–65] charge transfer[66–68] and photoemission[36,69–71] processes. In DFT development, one generally includes the self-interaction and then tries to remove it from the Coulomb energy in the exchange-correlation functional.[58]

1.6.9 Density functionals used in this thesis

M06-2X.[72] M06-2X is a global hybrid meta-GGA exchange-correlation functional. It is a functional parametrised for non-metals only and has twice the amount of nonlocal exchange (2X) as compared to similar functional M06 (*vide infra*) which is parametrised for transition metal and non-metals. The parametrisation of M06-2X uses 314 data points, out of a total of 496 data points from bond lengths, vibrational frequencies, vibrational zero-point energies (ZPEs) and so on. This functional is recommended for applications involving main-group thermochemistry, kinetics and non-covalent interactions (NCIs).

This is the DFT functional we used for the study of radical cationic system in Chapter 2 of this thesis. M06-2X includes 54% of exact Hartree-Fock exchange (HFX), which was shown to be in the optimal range of 50%-60% HFX in successful spin density localisation

of a single hole in a cluster of 64 water molecules.[73] It has been shown to perform very well for describing neutral and anionic model system having dispersion and hydrogen-bonding interactions[74,75] and for ionisation energies and aqueous redox potentials of organic molecules.[76] (see subsection 2.3.1 for a detailed discussion on the choice of DFT functional).

***ω*B97X-D.**[56] *ω*B97X-D is a range-separated hybrid functional where the inter-electronic interactions are separated to short-range and long-range interactions controlled by a separation parameter ω. This functional, with the inclusion of Grimme's D2 dispersion correction, captures weak NCIs, such as the attractive London dispersion component of van der Waals interactions, which can influence the structures and energetics.[54] We applied this functional to study the phosphorus-containing system in Chapter 3, as this functional has been successfully employed in the study of similar phosphorus-containing catalytic reaction mechanisms.[77]

MN15.[78] MN15 is a recently developed global hybrid meta-NGA (non-separable gradient approximation; so called since the approximations to the exchange and the correlation of the energy functional are not separated) functional from Truhlar and co-workers. According to the developers of this functional, it has greater accuracy than any previously available ones for a broad range of applications. This functional uses a wide range of physical and chemical properties, including energies, thermochemistry, reaction barrier heights, NCIs, excited state energies, and molecular structures, for parametrisation. It has overall the best performance for both single-reference and multi-reference chemical systems amongst 83 functionals tested. This is the functional we used for the study of TM catalysis in this thesis. MN15 was used as it performs better than many others in predicting TM dimer bond lengths and bond energies (TMBE33 dataset[79–83]) and barrier

heights (TMBH21 dataset[84–86]) for reactions involving TMs.[78,87,88] Its accuracy for barrier heights are comparable to the popular M06 functional[72] employed for the study of TM catalysis.[89–96] MN15 also performs the best for TM coordination database (WCCR10[97]). In a recent study of tri-copper complex catalysed methane-to-methanol conversion,[98] MN15 came out the best amongst 31 functionals tested, including TPSS, M06, B2PLYP, ωB97X and ωB97X-D3. It has been employed in a number of theoretical study of TM catalysis[98–103] and spectroscopy[104], giving good quantitative experimental agreements. The combination of MN15 with ECP basis sets has been shown to perform well for bond lengths and dissociation energies for bimetallic diatomic molecules.[105]

1.7 Solvation Models

Two classes of solvation can be distinguished: the explicit solvation model includes the individual solvent molecules and considers their molecular detail together with the solute molecules; the implicit solvation model treats the solvent as a continuous medium within which the solute molecules are dissolved. Due to the large number of solvent molecules in a chemical reaction, in quantum chemical calculations, implicit solvation is almost always the choice of solvation model used.

In the implicit model, the free energy of solvation is given by

$$\Delta G_{\mathrm{solv}} = \Delta G_{\mathrm{cav}} + \Delta G_{\mathrm{disp}} + \Delta G_{\mathrm{elec}}\,(+\Delta G_{\mathrm{hb}}) \tag{1.80}$$

where ΔG_{cav} is the free energy required to create the solute cavity; ΔG_{disp} is the van der Waals interaction between the solute and solvent; ΔG_{elec} is the electrostatic component due to the charge redistribution and reorientation induced by the polarisation between solute and solvent; ΔG_{hb} accounts for hydrogen bonding interactions. The

implicit solvation models can differ in the descriptions of the cavity and the dielectric media and the cavity calculation methods.

Two major classes of implicit models can be distinguished: the conductor-like screening models and the continuum models. In the conductor-like screening models, the solvent is treated as a conductor of infinite permittivity.[106] Examples of this class include COSMO[107] and COSMO-RS[108,109]. In COSMO, the cavity is based on the solvent accessible surface and the electrostatic interactions are treated approximately. This model can be a good approximation for very polar solvents. In COSMO-RS, the "conductor-like screening model for real solvents", the COSMO results are additionally augmented with statistical thermodynamic treatment of the screening charge density on the surface of the solute.

In the continuum models, a parametrised dielectric medium is used to surround the solute cavity and represent the solvent polarisation caused by the solute.[106] Due to the mutual polarisation between solute molecules and the solvent medium, the screening of the solute's electrostatic field by the continuum is calculated iteratively. Examples of such models include polarizable continuum models (PCMs) such as IEF-PCM[110–112] and C-PCM[107,113,114] and the SM*x*[115,116] and SMD[117] models. In PCMs, the cavity is formed from the overlapping van der Waals spheres and the electrostatic interactions between the solute and the polarisation of solvent is obtained by solving the Poisson equation.

1.7.1 Solvation model used in this thesis

For this thesis, we have generally used the SMD model, from Truhlar and co-workers, to account for implicit solvation effect of the reaction solvents. This model is parametrised using a training set of 2821 solvation data including 2346 solvation free energies for 318

neutral solutes in 91 solvents and 143 transfer free energies for 93 neutral solutes between water and 15 organic solvents. The elements present in the solutes are H, C, N, O, F, Si, P, S, Cl, and Br. The SMD model employs a single set of optimised parameters (intrinsic atomic Coulomb radii and atomic surface tension coefficients). This model was found to be the most accurate in computational redox potential studies[118] and was thus used in Chapter 2. For other systems, this solvation model is favoured, especially when used in combination with DFT functionals from the Truhlar group (e.g., M06-2X and MN15), since the parametrisation of the SMD parameters are optimised using the functionals (M05-2X) from the same research group.[117]

1.8 Chemical Reactivity and Selectivity

1.8.1 Transition state theory

In chemical systems, the interesting transitions from the reactants to the products occur in a very small timescale. These transitions through the transition states (TSs), which are first-order saddle points on the PES, are rare events. We want to study the rates of reaction using results from, for example, conventional DFT calculations. Transition state theory (TST), also known as activated complex theory (ACT), is a method for calculating the thermal rates of change in such chemical reactions.[119–121] This theory assumes that there is a quasi-equilibrium between the reactant molecule and the activated complex at the transition state in that the redistribution of internal vibrational energies of the reacting solute and solvent species is much faster than the timescale for bond breaking/formation. As a result, kinetic theory using Maxwell-Boltzmann statistics can be applied at the activated complex to study the rates of the conversion of the activated complex to the products, without re-crossing. TST further assumes that the PES is adiabatic, that is Born-Oppenheimer separation of the electronic and nuclear motions applies. Within this

framework, the macroscopic rate constant for the formation of the product is given by the Eyring equation:

$$k = \frac{k_{\mathrm{B}}T}{h}\mathrm{e}^{-\Delta G^{\ddagger}/RT} \tag{1.81}$$

where $\Delta G^{\ddagger}$ is the activation free energy for the formation of the activated complex.

It is helpful to mention **Hammond's postulate** which states that the TS of a reaction resembles either one of the reactants or the products that is closer to it in energy. Thus, in an exergonic reaction, the TS is closer to the reactants in energy and thus resembles the reactants in structure, as usually the case in early-TS formation. Conversely, in an endergonic reaction, the TS is closer to the products in energy, and resembles the products, as in late-TS formation.

It is necessary to bear in mind that despite the successes of simple TST to account for the rates and selectivities of many thermal reactions, TST is only valid under the assumptions outlined before, and recently there have been studies showing examples where TST is insufficient to describe the chemical reactions due to the breakdown of the underlying assumptions.[122,123]

1.8.2 Kinetic vs thermodynamic control of reactions

In a chemical reaction where two products are possible from the same reactants, different sets of products can be formed under different reaction conditions, as first observed in the formation of both *endo*- and *exo*-diastereoisomers in the Diels-Alder reaction between 6,6-pentamethylenefulvene and maleic anhydride, first described by Woodward and Baer in 1944.[124] The exact outcomes for such reactions are determined by a balance between kinetic and thermodynamic influences.

A possible simplified PES for such a reaction is shown in Scheme 1.2. Under kinetic control, typically at low temperature, the reaction proceeds irreversibly such that the ratio between the two products, A and B, is solely determined by the difference in the activation barriers, $\Delta\Delta G^{\ddagger}$, for the rate-determining steps and is quantitatively given, using simple TST, as the ratio of the relative rates of formation, viz.,

$$\frac{[\mathrm{A}]}{[\mathrm{B}]} = \frac{k_1}{k_2} = \frac{(k_\mathrm{B}T/h)\mathrm{e}^{-\Delta G_A^{\ddagger}/RT}}{(k_\mathrm{B}T/h)\mathrm{e}^{-\Delta G_B^{\ddagger}/RT}} = \mathrm{e}^{-(\Delta G_A^{\ddagger} - \Delta G_B^{\ddagger})/RT} = \mathrm{e}^{-\Delta\Delta G^{\ddagger}/RT} \quad (1.82)$$

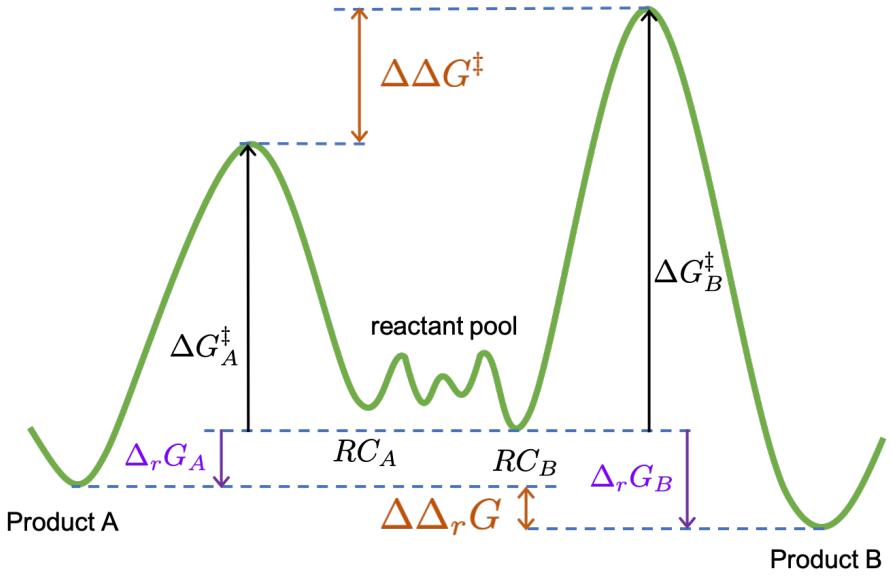

Scheme 1.2. Schematic potential free energy surface.

We here assume that the **Curtin-Hammett principle** applies: the reaction complexes in the reactant pool equilibrate amongst themselves very rapidly, at rates that are much faster than product formation, such that the lowest energy reaction complex (RC) is taken as the reference energy zero. In this framework, the activation barrier for the formation of product A is given by $\Delta G_A^{\ddagger}$, taken from the lowest energy RC (RC_B here) to the activated complex, in accordance with the energetic span model.[125]

Under thermodynamic control, typically at high reaction temperature and prolonged reaction time, the reaction becomes reversible and is under thermodynamic control. That is, both activation barriers for the product formations become thermally accessible, so that the product ratio is dictated by the difference in their thermodynamic stabilities, measured by their difference in the Gibbs energies of reaction, $\Delta\Delta_r G$, and is given quantitatively by

$$\frac{[\mathrm{A}]}{[\mathrm{B}]} = K_{\mathrm{eq}} = \frac{\mathrm{e}^{-\Delta_r G_A/RT}}{\mathrm{e}^{-\Delta_r G_B/RT}} = \mathrm{e}^{-(\Delta G_A - \Delta G_B)/RT} = \mathrm{e}^{-\Delta\Delta_r G/RT} \quad . \tag{1.83}$$

1.8.3 Conformational sampling and Boltzmann weighting

In many cases, different conformations of the TSs exist that lead to the same product at the given reaction temperature. In those cases, the ratio of product selectivity is dictated by all the thermally accessible TSs for the competing product formations. All the rate-limiting TS conformers are then used for Boltzmann weighting to give the selectivity ratio. Standard procedures for Boltzmann weighting can be found in, for example, Equation (2) of reference[126] and the SI of reference[127]. Specifically, the selectivity between two products A and B is calculated via

$$\frac{[\mathrm{A}]}{[\mathrm{B}]} = \frac{\sum_{i\,\in\,\text{all confs},A}^{N_A} \mathrm{e}^{-\Delta\Delta G^{\ddagger}_{0i,A}/RT}}{\sum_{j\,\in\,\text{all confs},B}^{N_B} \mathrm{e}^{-\Delta\Delta G^{\ddagger}_{0j,B}/RT}} \tag{1.84}$$

where $\Delta\Delta G^{\ddagger}_{0i,X} = \Delta G^{\ddagger}_{i,X} - \Delta G^{\ddagger}_{0}$ is the energy difference between the i^{th} conformer of product X ($X = A, B$) and the lowest energy conformer of all products, state 0, having the lowest activation barrier of $\Delta G^{\ddagger}_{0}$.

Time is all you have and you may find one day that you have less than you think.

— Randy Pausch, The Last Lecture

2

SET-catalysed Cyclobutanation

2.1 Introduction

The cyclobutyl ring is a ubiquitous structural motif in natural products and bioactive molecules.[128–130] Cyclobutanes can be considered useful synthons for 3-membered and 5-membered rings via regio- and/or stereoselective transformations by ring-contraction[131] or ring-expansion[131,132] reactions to form otherwise challenging products. The inherent ring strain in cyclobutane makes its selective cleavage to access both acyclic and cyclic systems highly amenable. Spurred by the broad synthetic applicability of cyclobutanes, the field of cyclobutane chemistry research has burgeoned over the past decades. Although the construction of such 4-membered rings via thermal [2+2] cycloaddition is symmetry-forbidden based on Woodward-Hoffmann rules, research into other methods to access this highly versatile motif, with precise chemo-, regio- and stereo-control, has advanced with unabated enthusiasm. Since the first report of photochemical [2+2]

cycloaddition to access this 4-membered carbocycle by Liebermann in 1877,[133] the construction of 4-membered cyclobutyl rings from photocycloaddition of alkenes have become arguably the most employed technique for cyclobutanation.[134–139]

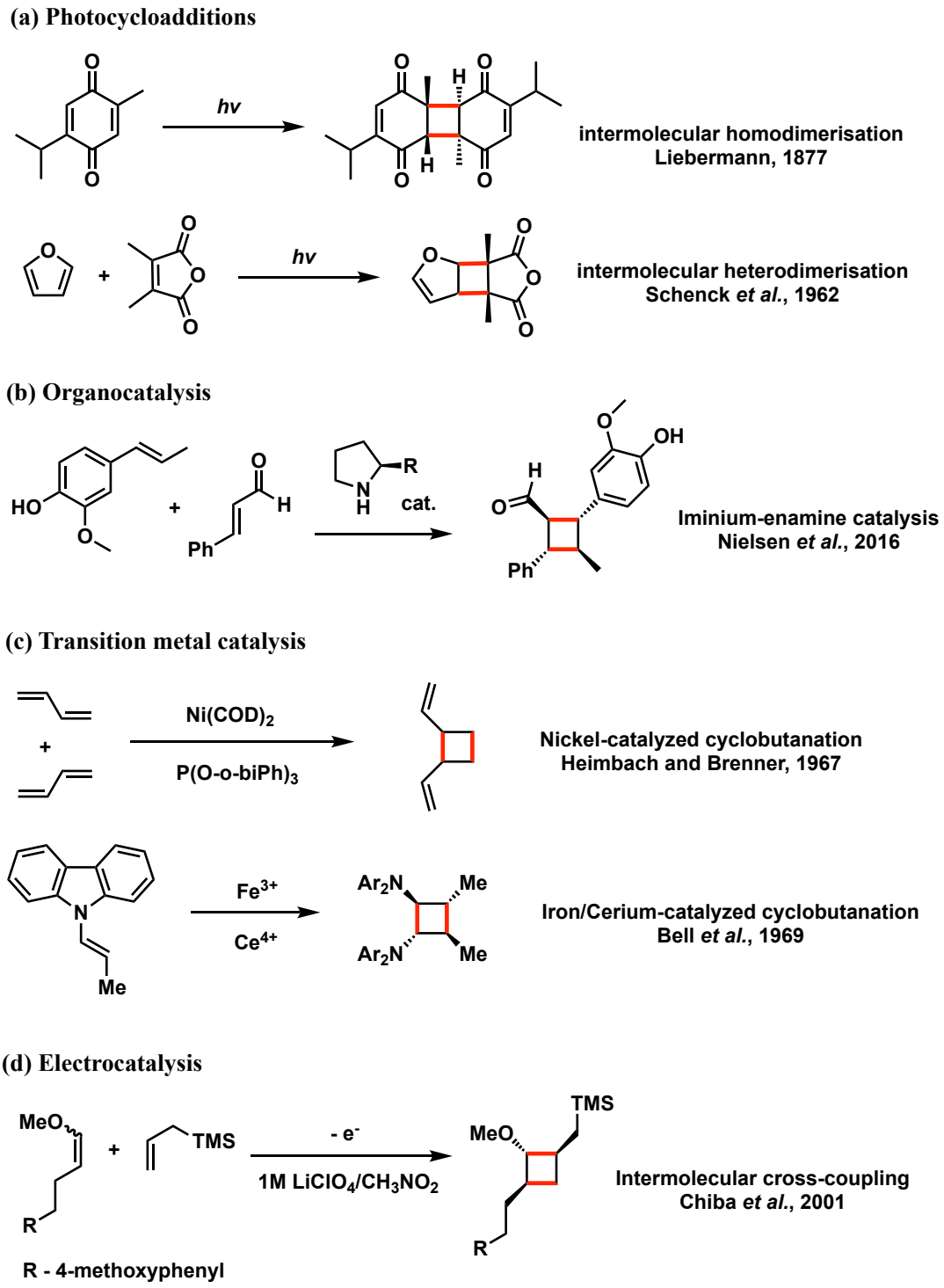

Scheme 2.1. Selected examples for [2+2] cyclobutanation.

Cyclobutanation can now also be readily achieved via organocatalysis,[140–142] organometallic catalysis[134,143–145] as well as electrocatalysis[146–149] (Scheme 2.1). Until recently when the synthesis of substituted cyclobutanes can be realised via selective C–H functionalisations of unsubstituted cyclobutanes,[150–153] formal [2+2] cycloaddition remains the main strategy for the synthesis of complex, tetra-substituted cyclobutyl rings.[154–157] For the latter strategy, the formation of an unsymmetrical, tetra-substituted cyclobutane can arise from intermolecular heterodimerisation of two substituted alkenes. This, however, remains a challenge as a varied mixture of products can result from the reaction of two alkenes due to a lack of control on homo- and hetero-[2+2]-dimerisation and the possibility of regiochemical (head-to-head vs head-to-tail) and stereochemical (*cis* vs *trans*) variations. Many examples of both head-to-head and head-to-tail coupled cyclobutanes exist in biologically active natural products (Scheme 2.2), however, to be synthetically useful, method development with precise selectivity is required.

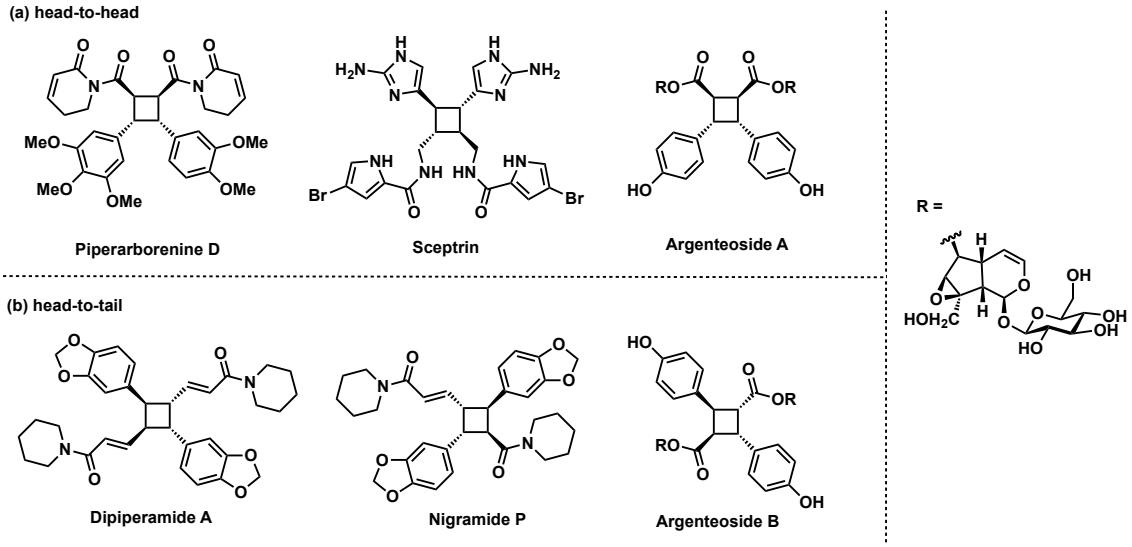

Scheme 2.2. Selected examples of cyclobutane-containing biologically active substances arising from head-to-head and head-to-tail coupling of alkenes.

Radical cations constitute an important class of intermediates for a variety of chemical syntheses due to its versatility in forging C–C and C–X bonds.[158–163] The formation of

radical cationic starting material is achieved via single-electron transfer (SET) where an electron is removed from a neutral substrate, creating a "hole" in the system. This process can be mediated using transition metals, either by itself[134,164–166] or coupled with organic[167] or organometallic[168–171] photoredox catalysts; it can also be mediated by oxidants, such as aminium radical cationic salts.[172] In this last approach, powerful oxidants are typically necessary, but these can easily decompose or induce undesirable side reactions;[173–175] they can also adversely impact the environment and human health. Due to these limitations, the use of oxidants for SET-initiation and catalysis of cyclobutanation is very much underexplored compared to photochemical means. To overcome some of these problems, Donohoe and co-workers reported an elegant study where a mild hypervalent iodine oxidant was employed to promote radical cationic cycloaddition of different alkenes to rapidly access unsymmetrical, tetra-substituted cyclobutyl rings.[140,176] The regio- and stereochemical outcomes of their reported mild oxidant-promoted, SET-catalysed heterodimerisation of two unsymmetrical alkenes present an interesting avenue for detailed mechanistic study (Scheme 2.3 (a)). In particular, we note that these stereochemical outcomes are rather similar to those obtained by Bauld and co-workers in their pioneering study of triarylamine radical cation catalysed cyclobutanation from the homocoupling of internal, unsymmetrical alkenes (Scheme 2.3 (b)). Note that in all these products, only the so-called "head-to-head" cyclobutanes are observed.

The detailed mechanism of intermolecular radical cation cycloaddition has been probed experimentally, where both stepwise[177–180] and concerted, asynchronous[172,181–183] pathways have been proposed. The prototypical SET-catalysed homodimerisation of electron-rich 4-methoxystyrene, a terminal alkene, has been computationally studied by

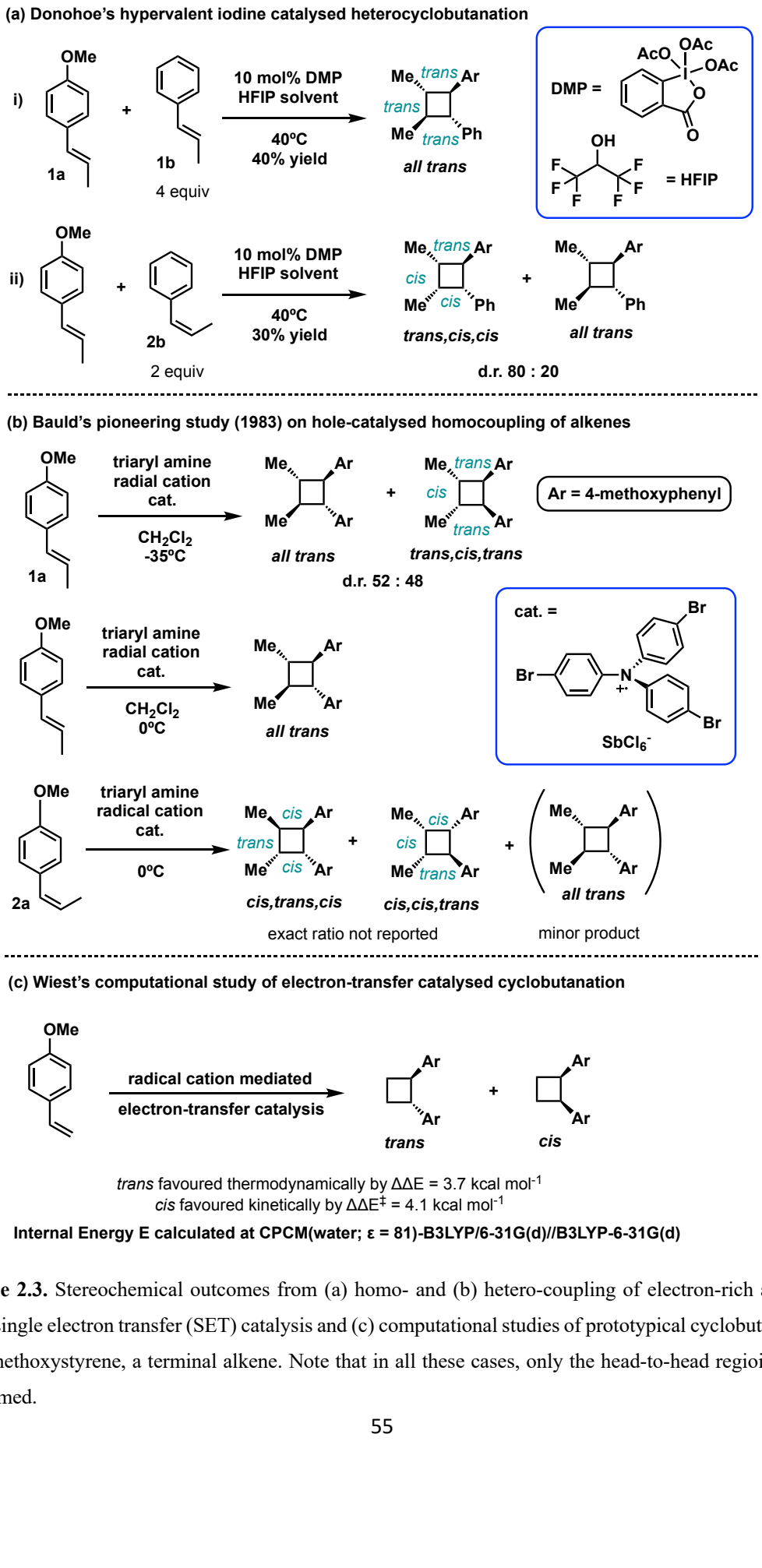

Scheme 2.3. Stereochemical outcomes from (a) homo- and (b) hetero-coupling of electron-rich alkenes under single electron transfer (SET) catalysis and (c) computational studies of prototypical cyclobutanation from methoxystyrene, a terminal alkene. Note that in all these cases, only the head-to-head regioisomers are formed.

Wiest and co-workers where a stepwise mechanism was suggested.[184] Following this study, Metzger and co-workers in 2008 detected a distonic (where charge and radical sites are separated) radical cationic intermediate via extractive electrospray ionisation mass spectrometry, lending direct support to the stepwise mechanism.[185] In Wiest's computational study, however, the employment of a terminal alkene as a model system gives a straightforward stereochemical outcome – using the exchange-correlation B3LYP functional, they reported that the *cis*-adduct is favoured kinetically by an activation barrier $\Delta\Delta E^{\ddagger}$ of 4.1 kcal mol^{-1} whereas the *trans*-adduct is favoured thermodynamically by a reaction energy $\Delta\Delta E$ of 3.7 kcal mol^{-1} (Scheme 2.3 (c)). Although the comparative thermodynamic stability agrees with Bauld's study of homodimerisation of *trans*-anethole at different temperature (Scheme 2.3 (b)), it is now well known that B3LYP can lead to poor results for thermochemistry, kinetics and non-covalent interactions due to its lack of dispersion description and the inherent presence of self-interaction error (SIE).[54,186–191] In addition, the molecular origins of the intriguing stereochemical outcomes in the homo- and hetero-[2+2] formation of tetra-substituted cyclobutanes are not immediately obvious from that study. We herein report a theoretical investigation into the origins governing the chemical reactivities and selectivities effecting the observed stereochemical outcomes in the heterodimerisation of two unsymmetrical, electron-rich alkenes under oxidant-promotion (Scheme 2.3 (a)).

2.2 Computational Methods

DFT calculations were performed with *Gaussian 09* rev. D.01.[192] Geometry optimisations were carried out using the hybrid meta-GGA functional M06-2X[72] within the unrestricted formalism using the Unrestricted Kohn-Sham (UKS) theory, with the Pople-type double-ζ split-valence basis set 6-31G(d).[193] For the hypervalent iodine oxidant, a mixed basis

set of LANL2DZ[20] for the Iodine atom and the 6-31G(d) basis set for all other atoms was used. Minima and transition structures on the potential energy surface (PES) were confirmed as such by harmonic frequency analysis at the same level of theory. Intrinsic reaction coordinate (IRC)[194,195] analyses were carried out to connect the proposed TS structures to correct minima. The eigenvalues of the spin operator $\mathbf{S^2}$ after annihilation of spin contamination were found to range from 0.750 to 0.751 for all radical cationic structures, in agreement with the expected value of *S(S+1)* = 0.75 for a doublet wavefunction, indicating that spin contamination is not a problem for the present methodology. Single point corrections were carried out with M06-2X functional using the Karlsruhe-family polarised triple-ζ def2-TZVPP basis set.[18,196,197] The SMD continuum solvation model[117] was included to account for the effect of implicit solvents acetonitrile (MeCN) and hexafluoroisopropanol (HFIP) on the computed Gibbs energy profile. HFIP is a versatile solvent in organic synthesis, especially in its role in stabilising radical cations[176,198,199] and promoting single electron oxidation when combined with hypervalent iodine reagents[140,176], making its computational parametrisation within the SMD model important for general use. Since HIFP solvent is not available in the list of default/pre-defined solvents in *Gaussian 09* software, it is herein parametrised using a set of seven parameters.[117] These include the static dielectric constant of the solvent at 25ºC (*Eps* = 16.7);[199–201] dynamic dielectric constant – the square of the refractive index value of 1.275 at 20ºC was used[202] (*EpsInf = 1.625625*); hydrogen bond acidity (*HBondAcidity = 1.96*) and basicity (*HBondBasicity = 0.00*),[199] which are Abraham's *A* and *B* values respectively; the surface tension of the solvent at interface (*SurfaceTensionAtInterface = 23.23*);[203,204] carbon aromaticity – the fraction of aromatic carbons (*CarbonAromaticity = 0.00*) and electronegative halogenicity – the fraction of halogens (*Electronegative Halogenicity = 0.60*). These parameters were specified using the keyword "SCRF =

(SMD, Solvent= Generic, Read)" in *Gaussian 09*. All Gibbs energies were evaluated at 313.15K and were corrected for zero-point vibrational energies at the same level of theory. These values were further corrected by applying the quasi-rigid rotor harmonic oscillator (quasi-RRHO) for the vibrational entropies, as described by Grimme,[205] using a free-rotor approximation for anharmonic vibrational modes below 100 cm^{-1} and a rigid rotor harmonic oscillator approximation above this wavenumber.[206] The free energies were further corrected using a standard concentration of 1 mol L^{-1}, which was used in solvation calculations. The solvent-corrected SMD(HFIP)-UM06-2X/def2-TZVPP// UM06-2X/6-31G(d) values are used for discussion. Molecular structures, non-covalent interaction plots and spin density plots were visualised using PyMol software.[207] *Unless otherwise stated, all energy values are quoted in kcal* mol^{-1} *and bond distances in Å.*

Geometries of all optimised structures (in *.xyz* format with their associated energy in Hartrees) and an associated README file have been deposited online and made freely available (DOI: 10.5281/zenodo.3370470). All Python scripts used for data analysis have been made available - https://github.com/bobbypaton - under a creative commons CC-BY license.

2.3 Results and Discussions

2.3.1 Choice of DFT functional and solvation model: initial considerations

The Becke-3-parameter hybrid generalized gradient (GGA) with Lee-Yang-Parr (LYP) exchange-correlation functional (B3LYP) has been used on several occasions for the computational study of cycloaddition reactions of radical cationic systems.[208,209] However, the shortcomings of B3LYP are well documented, and qualitative failures have been reported in the descriptions of organic mechanisms[186] and geometry optimisation and enthalpies of formation of alkanes.[187,188] The lack of medium- and long-range

electron correlation in B3LYP and other (semi-)local functionals results in the failure to capture London dispersion interactions, and this is a major inadequacy in accurately accounting for thermochemistry, kinetics and non-covalent interactions.[54] Perhaps more critically for the present study, the well-known self-interaction error (SIE) inherent in B3LYP leads to excessive hole (positive charge) delocalisation, as shown in single-electron oxidised DNA bases,[189–191] rendering the results for SET-catalysed radical cationic systems obtained using this functional some degree of uncertainty. The aromatic rings in our system suggest that non-covalent interactions (NCIs) could be important in understanding the reaction mechanism.

It is therefore important to use a functional that reduces SIE and at the same time accounting for non-covalent interactions. The M06-2X functional from the Truhlar group can achieve both outcomes. Its functional form contains many free parameters that are empirically fit to broad sets of experimental data including non-covalent interactions. Additionally, the inclusion of 54% of exact Hartree-Fock exchange (HFX) in M06-2X has been shown to be within the optimal range of 50%-60% HFX in successful spin density localisation of a single hole in a cluster of 64 water molecules.[73] Importantly, M06-2X has been shown to perform better than B3LYP functional for describing neutral and anionic model system having dispersion and hydrogen-bonding interactions[74,75] and for ionisation energies and aqueous redox potentials of organic molecules.[76] More recently, M06-2X has been successfully applied to study cyclisation and cyclobutane formations.[210–212] We later on showed that M06-2X gives the best estimation of redox potentials of our starting materials *trans*-anethole, **1a**, and *trans*-β-methylstyrene, **1b**, amongst various functionals considered (see subsection 2.3.3).

The understanding of experimental oxidation potentials of neutral organic compounds is extremely telling of the feasibility of an oxidation reaction in a single electron transfer process. Quantum chemical benchmarking of measured redox potentials have been extensively carried out for neutral and ionic organic compounds using various implicit solvation models.[213–222] These studies identify the principal source of error as the solvation free energy of the oxidised radical cations.[213,222,223] A judicious choice of solvation model not only can accurately estimate the oxidation potentials of our starting molecules, but also lend confidence to our energy profile for our reaction mechanism in various solvent systems. Of several popular implicit solvation models (SM8,[116] SMD,[218] C-PCM,[107,113,114] IEF-PCM,[110–112] and COSMO-RS[108,109]), Guerard and Arey[118] found that SMD model is the most accurate in comparing against experimental solvation free energies and oxidation potentials for a group of organic compounds including phenol, anisole, aniline, indole and their derivatives. As anethole is an anisole derivative, our usage of SMD model for implicit solvation is appropriate.

2.3.2 Conformational considerations

Two possible conformers were found for the starting material *trans*-anethole, **1a** (Scheme 2.4). Conformer 2 is 0.5 kcal mol^{-1} lower in Gibbs energy than conformer 1 in its neutral form, whereas conformer 1 is 0.5 kcal mol^{-1} lower in Gibbs energy than conformer 2 in its radical cationic form. For all subsequent calculations, including the calculation of redox potentials, the lowest form of each was used.

conformer 1 **conformer 2**

Scheme 2.4. Conformational considerations for *trans*-anethole.

2.3.3 Computational electrochemical potentials: benchmarking

The feasibility of radical cation generation in the initiation step and the reduction of the radical cation product in the termination step is strongly dependent on the electrochemical potentials of these reacting species. For a reaction between two different alkenes, their electrochemical potentials directly determine their role selectivity as *caticogen* (one that readily forms radical cation under oxidation/SET conditions) or *caticophile* (one/neutral species that attacks the radical cation). The calculation of reduction potentials provides a direct measure of the thermodynamic feasibility of these steps.

Ab initio computations of reduction potentials of various systems have been widely explored.[224,225,234,226–233] In general, two methods for such calculations exist. For reaction potential of radical cationic substrate shown in Scheme 2.5, to calculate the overall Gibbs energy of reaction in solvent, ΔG^o_{rxn}, one can either a) directly calculate the reaction energies within continuum solvation models, i.e., direct geometry optimisations of both neutral and radical cationic species in the solution phase, or b) construct a thermodynamic cycle by separate gas phase geometry optimisations with single point solvation energy of each species.

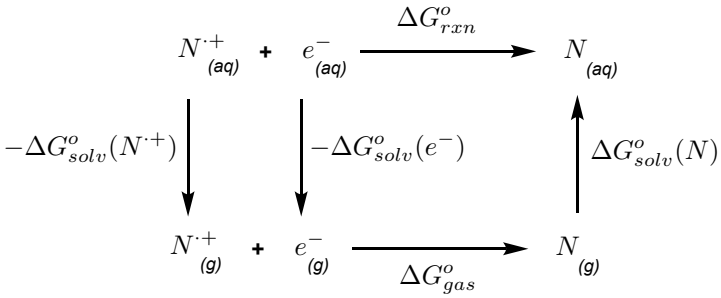

Scheme 2.5. Computation of redox potential for the reduction of a radical cation to its neutral form.

We use a thermodynamic cycle here to express ΔG^o_{rxn} in terms of the free energy of reaction in gas phase, ΔG^o_{gas}, and the free energies of solvation, ΔG^o_{solv}, of the reacting

species as shown.[222,235] Since the differences in the redox potentials obtained from both direct and thermodynamic cycle methods are very small when solvent-induced geometry changes are small (for example, no change in protonation state upon solvation),[222] we adopt the thermodynamic cycle approach here.

In our calculations, the gas phase energy change, ΔG^{o}_{gas}, is further refined by calculating the single point energy in gas-phase at a larger basis set (def2-TZVPP) for improved accuracy.[222] The reduction potentials calculated here are *adiabatic* reduction potentials (ARP) since the energy is taken from each optimised species, i.e.,

ARP = E(optimised neutral) – E(optimised radical cation). (2.1)

We then have

$$\Delta G^{o}_{rxn} = -\Delta G^{o}_{solv}(N^{\bullet+}) - \Delta G^{o}_{solv}(e^{-}) + \Delta G^{o}_{gas}(N^{\bullet+}) + \Delta G^{o}_{solv}(N) \quad (2.2)$$

The reduction potential of the reaction is then given by

$$E_{cell} = -\frac{\Delta G^{o}_{rxn}}{nF} - E_{SHE} \quad (2.3)$$

We need not consider the free energy of solvation of the electron as their contribution cancels out when we consider the full reaction against experimentally measured values.[235]

To decide on the best functional for the present study, we did a benchmarking study on the reduction potential of our substrates *trans*-anethole **1a** and *trans*-β-methylstyrene **1b** in MeCN solvent using a number of functionals. The results are given in Table 2.1, which shows that M06-2X functional gives the best agreement (smallest mean unsigned error) with the experimental redox potential values amongst 8 functionals tested. This is in

agreement with a study of both experimental and computational electrochemical potentials for over 180 organic substrates where M06-2X functional gives an R^2 value of 0.97 for the correlation between the experimental and calculated redox potentials.[236] We used M06-2X for all subsequent DFT calculations.

	Expt[a]	B3LYP	B3LYP-D3	B97D	CAM-B3LYP	M06-2X	revPBE	TPSS-D3	ωB97X-D
1a	1.484	1.184	1.183	0.975	1.289	1.388	1.162	1.006	1.203
1b	1.984	1.621	1.587	1.430	1.709	1.815	1.604	1.461	1.635

[a] Values are taken from ref.[236] where potentials are reported against standard calomel electrode in MeCN solvent (1.24V for **1a** and 1.74V for **1b**). These values are converted to be relative to SHE using conversion constants (+0.244V) in ref.[237] and then reported herein. For computational studies, a value of E_{SHE} = 4.28V in SMD model is used.[222,235,238]

Table 2.1 Computed reduction potentials of *trans*-anethole **1a** and *trans*-β-methylstyrene **1b** in MeCN solvent using a variety of functionals. All values are in V.

2.3.4 Computational electrochemical potentials: role selectivity and solvent effects

The redox potential of the hypervalent iodine oxidant, Dess-Martin Periodinane (DMP, chemical structure in Scheme 2.3 (a)), was computed at SMD(solvent)-M06-2X/def2-TZVPP//M06-2X/GenECP(LanL2DZ for I atom and 6-31G(d) for other atoms) where each of MeCN and HFIP solvents was separately calculated. The results, together with the redox potentials for our starting materials, are given in Table 2.2. From the table, we can see that in both solvents, *trans*-anethole **1a** can be oxidised more easily than *trans*-β-methylstyrene **1b** to their respective radical cation. For example, in MeCN, the oxidation of **1a** to $[\mathbf{1a}]^{\bullet+}$ by DMP has E_{cell} of -0.122 – 1.388 = -1.510 V and the oxidation of **1b** to $[\mathbf{1b}]^{\bullet+}$ has E_{cell} of -0.122 – 1.815 = -1.937 V, the latter being much less favourable thermodynamically (by about 10 kcal mol^{-1}). Thus, **1a** will act as a *caticogen* where it is

oxidised to its radical cationic form whereas the neutral **1b** will act as a *caticophile*, attacking the radical cationic [**1a**]$^{\bullet+}$ in the subsequent cyclobutanation steps.

	1a	1b	2a	2b	DMP	DMP-HFIP
Expt[a]	1.484	1.984	–	–	–	–
MeCN	1.388	1.815	1.506	1.917	-0.122	-0.125
HFIP	1.467	1.879	1.596	1.988	0.083	0.147

[a] Values in MeCN solvent and are are taken from ref.[236] as in Table 2.1.

Table 2.2. Computed reduction potentials of substrates *trans*-anethole **1a**, *trans*-β-methylstyrene **1b**, *cis*-anethole **2a**, *cis*-β-methylstyrene **2b** and hypervalent iodine oxidant DMP and DMP-HFIP complex in MeCN and HFIP solvents using M06-2X functional.

The (implicit) effect of solvent seems to have a greater influence on the redox potential of the iodinated oxidant DMP, whose reduction potential becomes less negative (by 205 mV) in HFIP solvent than in MeCN, indicating its greater oxidising strength in the fluorinated solvent, in agreement with an electrochemical study on the enhanced oxidising power of phenyliodine(III) diacetate (PIDA) oxidant in HFIP (by 850 mV) than in MeCN.[176] The molecular origin of that enhanced reactivity was traced to the formation of a strong hydrogen-bonded PIDA-HFIP complex, as revealed by NMR and HRMS studies.[176] By including one molecule of HFIP explicitly in our (re-)calculation of redox potentials of DMP, we found that the computed redox potential of DMP becomes even more positive, being now 64 mV more favoured than without an explicit molecule of HFIP for hydrogen-bonding (272 mV more favoured in HFIP than in MeCN solvent). The DMP-HFIP complex in MeCN solvent has a quite negative redox potential (much the same as the redox potential of DMP without HFIP additive in MeCN solvent), indicating that the DMP-HFIP complex is a poor oxidising reagent in MeCN solvent, consistent with the experimental finding that using HFIP as an additive to the hypervalent

iodine oxidant (PIDA) in MeCN solvent does not lead to significant cyclobutanation product formation (< 5% yield).[176]

We can now see that the formation of radical cationic [**1a**]$^{\bullet+}$ can be more easily achieved in HFIP solvent (with an overall E_{cell} of 0.147 – 1.467 = -1.320 V) than in MeCN solvent (overall E_{cell} of -0.122 – 1.388 = -1.510 V), by ~ 4.4 kcal mol^{-1}, suggesting a potential influence of the fluorinated solvent on the initiation step (SET) of the cyclobutanation reaction (for example, HFIP could help in the stabilisation of the resultant radical cation[176,198,199]). This SET step is expected to be endergonic, as reflected by the overall negative electrochemical cell potential; the weakly oxidising iodinated reagent is employed to ensure that only a small amount of radical cation is produced *in situ* to avoid dimerisation and any further oxidation to dications.[176,239,240]

2.3.5 Reactivity and selectivity between *trans*-anethole and *trans*-β-methylstyrene (P1)

For the reaction between *trans*-anethole **1a** and *trans*-β-methylstyrene **1b** (reaction P1) as shown in Scheme 2.3 (a) i), we know that **1a** will be preferentially oxidised by DMP via SET to give radical cation [**1a**]$^{\bullet+}$ which then adds to the neutral alkene partner **1b**. The concerted mechanism is ruled out as no productive TS was found. For the stepwise mechanism, both head-to-head and head-to-tail cyclobutanes are possible. In addition, *syn*- and *anti*-adducts could be formed depending on the orientation of the reacting alkenes when they approach each other. The Gibbs energy profile corrected at the reaction temperature of 40ºC is given in Figure 2.1. All possible conformations of the rate-determining TSs were considered (Figure 2.3) and the lowest energy conformers were used. We can see from Figure 2.1 that the head-to-head TSs (**ts1** and **ts1'**) have lower activation barrier than head-to-tail TSs (**ts1-g1** and **ts1-g2**), by at least 4.7 kcal mol^{-1} (1

in 410, using simple TST), although the radical cationic and neutral cyclobutyl rings are very close in energy. This suggests that the reaction is under kinetic control, where the head-to-tail addition is hugely disfavoured. In comparing the head-to-head *syn*- vs *anti*-adducts, we note that the *anti*-adduct **int3n** is both kinetically and thermodynamically favoured than the *syn*-adduct **int3'n**. For the last step of reduction of radical cationic cyclobutyl rings to their neutral forms, although the oxidation of the hypervalent iodine catalyst ($DMP^{\bullet-}$) is much easier than that of the neutral *trans*-anethole, the alkene is present in a large excess so that the radical cationic products would be reduced by neutral alkene rather than the catalyst. With this in mind, we use neutral *trans*-anethole as our source of reductant in the catalytic cycle.

Since the radical reactivity is dominated by the bond strength of the reacting/broken bonds and the stability of the resulting radical intermediate, we plot the spin density of the TSs (Figure 2.2) to help us understand this regioselectivity. The distonic radical cation $[\mathbf{1a}]^{\bullet+}$ has the unpaired electron localised on the α-carbon next to the methyl group (Figure 2.1 box), as expected by the resonance structure where the lone pair from oxygen atom of the methoxy-group of anethole delocalises onto the β-carbon. The attack from the radical site (α-carbon) to the neutral *trans*-β-methylstyrene in a head-to-head fashion leaves the radical on the carbon adjacent to the phenyl ring (**ts1** and **ts1'**, Figure 2.2) whereas that in a head-to-tail fashion leaves the radical on carbon adjacent to the methyl group (**ts1-g1** and **ts1-g2**, Figure 2.2). The phenyl ring in the head-to-head TSs helps to stabilise the unpaired electron whereas it is destabilised by the electron-releasing methyl group in the head-to-tail TSs. Thus, the head-to-head TSs have much lower activation barriers. From the experimental results showing that only the all *trans*-product is formed, we believe that the regioselectivity (head-to-head vs head-to-tail) is kinetically controlled

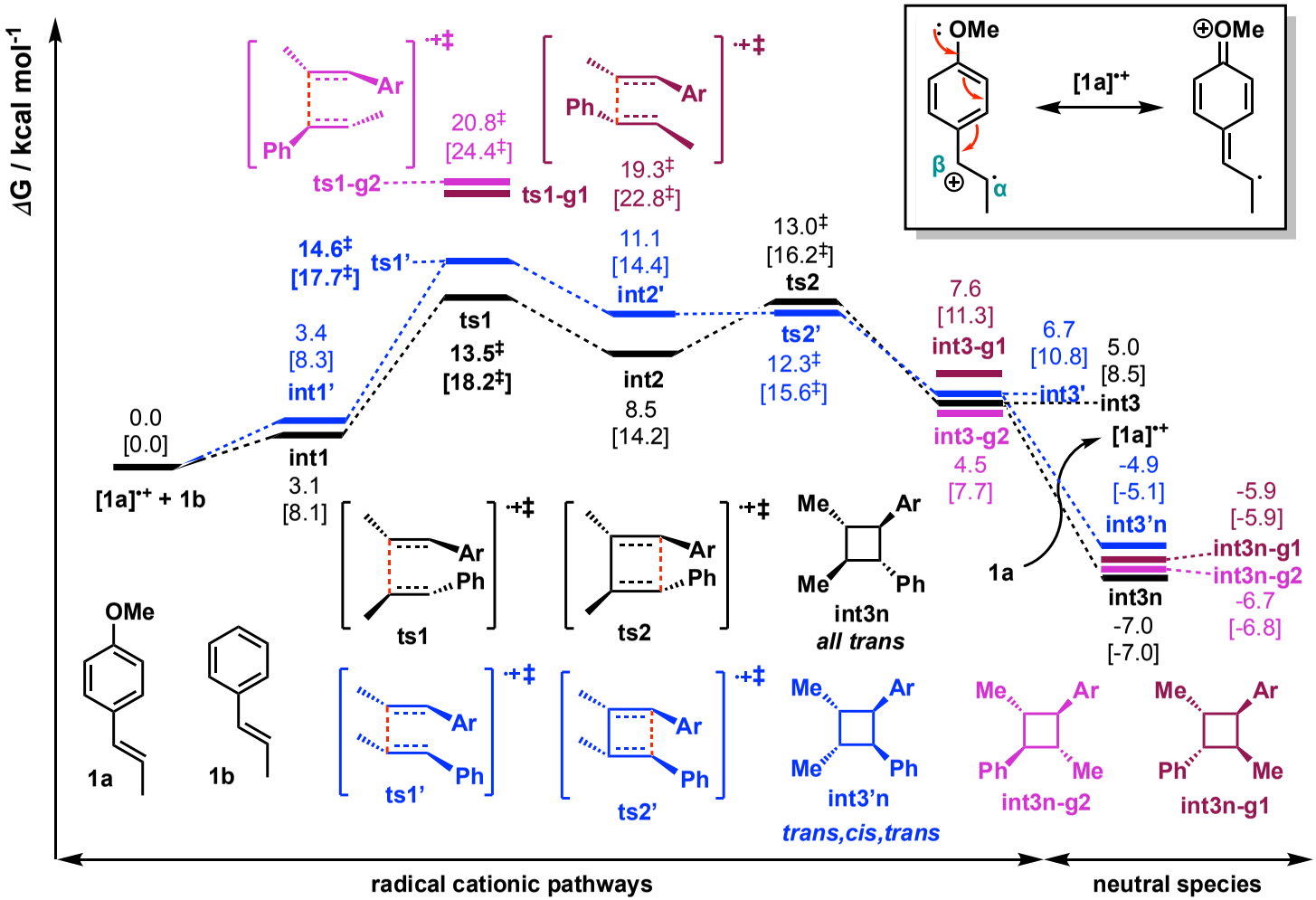

Figure 2.1. Gibbs energy profile for reaction between *trans*-anethole and *trans*-β-methylstyrene. The values in HFIP are given together with values in MeCN in square brackets.

[1a]$^{\bullet+}$	ts1	ts1'
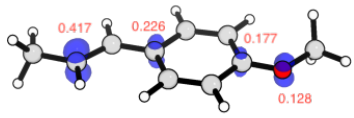	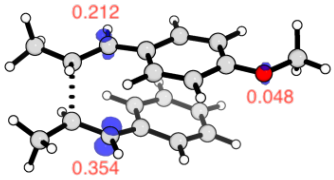	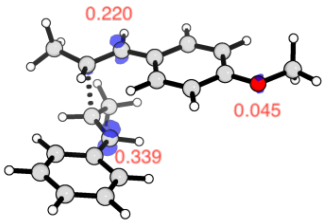
ts1-g1	**ts1-g2**	
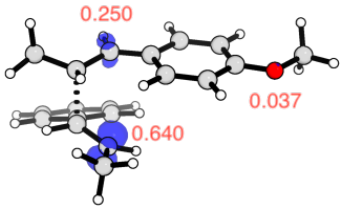	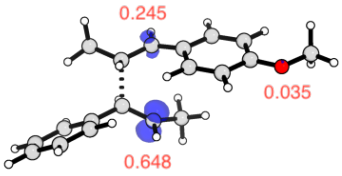	

Figure 2.2. Spin density plots (at an isovalue of 0.02) and the Mulliken spin density values of radical cationic *trans*-anethole and relevant TSs.

since the head-to-tail products **int3n-g1** and **int3n-g2** are close in energy to **int3n** but not observed. The electron transfer barrier for the reduction of the radical cationic products to their neutral form can be estimated using Marcus-Hush theory and it was found that the barriers are much smaller than any bond-forming barriers in the PES (*vide infra*, subsection 2.3.8).

To further understand the steric and electronic factors influencing the head-to-head vs head-to-tail regioselectivity, we applied the activation strain model[241–244] or equivalently, the distortion-interaction model[244,245] to the TSs for the formation of first C–C bond for the present reaction (Figure 2.4). As we can see, the energetic penalty to distort the reacting molecules as they come together in the TSs, i.e., the activation strain or the distortion energy (in blue), for all 4 TSs are similar; the head-to-tail TSs are disfavoured due to their less favourable interaction energies (in green) than the head-to-head TSs, although this is less obvious in the non-covalent interaction (NCI) plots in these TSs (Figure 2.5).

ts1	ts1-c2	ts1-c3
13.5‡ (18.2‡)	15.7‡ (18.4‡)	15.7‡ (21.2‡)
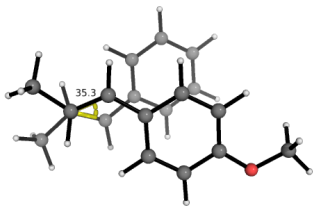	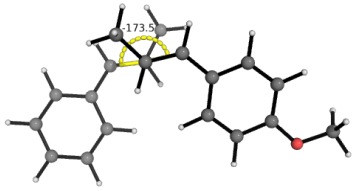	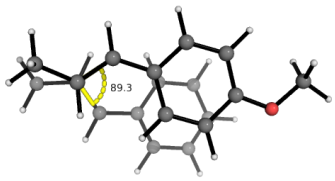
r = 2.09 Å	r = 2.15 Å	r = 2.04 Å
ts1-c4	**ts2**	**ts1'**
18.3‡ (21.4‡)	13.0‡ (16.2‡)	14.6‡ (17.6‡)
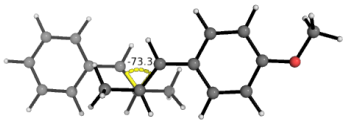	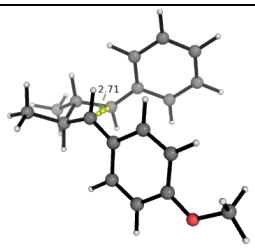	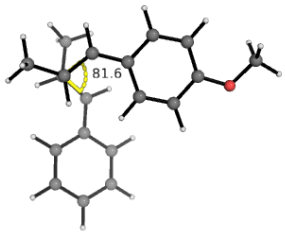
r = 2.01 Å	r = 1.57 Å	r = 2.18 Å
ts1'-c2	**ts1'-c3**	**ts2'**
14.6‡ (18.0‡)	17.6‡ (20.8‡)	12.3‡ (15.7‡)
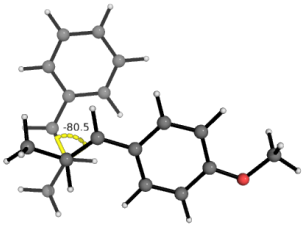	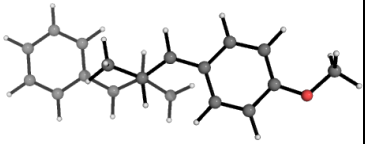	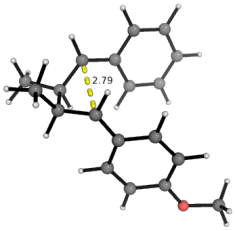
r = 2.10 Å	r = 2.12 Å	r = 1.59 Å
ts2'-c2	**ts1-g1**	**ts1-g1-c2**
12.5‡ (16.3‡)	19.3‡ (22.8‡)	22.1‡ (24.8‡)
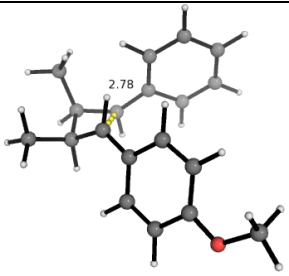	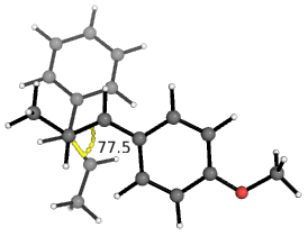	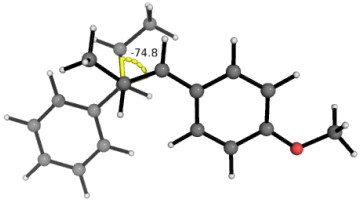
r = 1.56 Å	r = 1.96 Å	r = 1.81 Å

ts1-g2	ts1-g2-c2	
20.8‡ (24.4‡)	20.9‡ (25.6‡)	
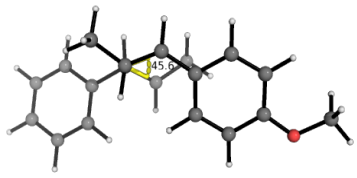	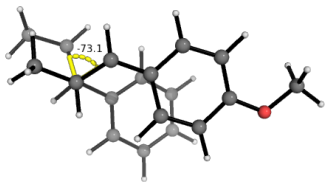	
r = 1.93 Å	r = 1.82 Å	

Figure 2.3. Conformations of all TSs for the reaction between *trans*-anethole and *trans*-β-methylstyrene. Distances of the first C–C bond formation (r) is given.

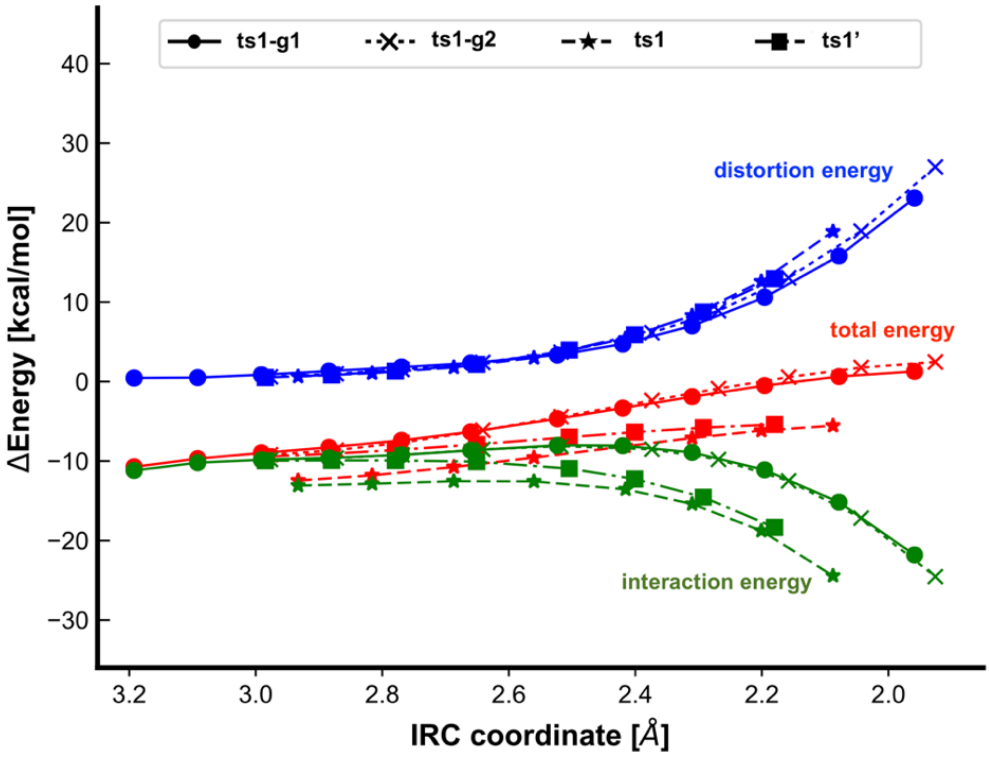

Figure 2.4. The activation strain or distortion-interaction analyses applied to transition structures for both head-to-head (**ts1** and **ts1'**) and head-to-tail (**ts1-g1** and **ts1-g2**) first C–C bond formation TSs. All energies are calculated at UM062X/def2TZVPP//UM062X/6-31G(d) and used without any further corrections.

It is worth noting that the Gibbs energies for all radical cationic species in the reaction are much lower in HFIP than in MeCN solvent (by 3.2 to 5.7 kcal mol^{-1}), indicating the former solvent's ability in stabilising the radical cationic species, which is well-known[176,198,199]; the energies for the neutral species (**int3n**, **int3'n**, **int3n-g1** and **int3n-**

g2), on the other hand, do not significantly differ in either solvent system (within 0.2 kcal mol^{-1}). In other words, only radical cations, and not the neutral species, are preferentially stabilised in HFIP solvent than in MeCN solvent.

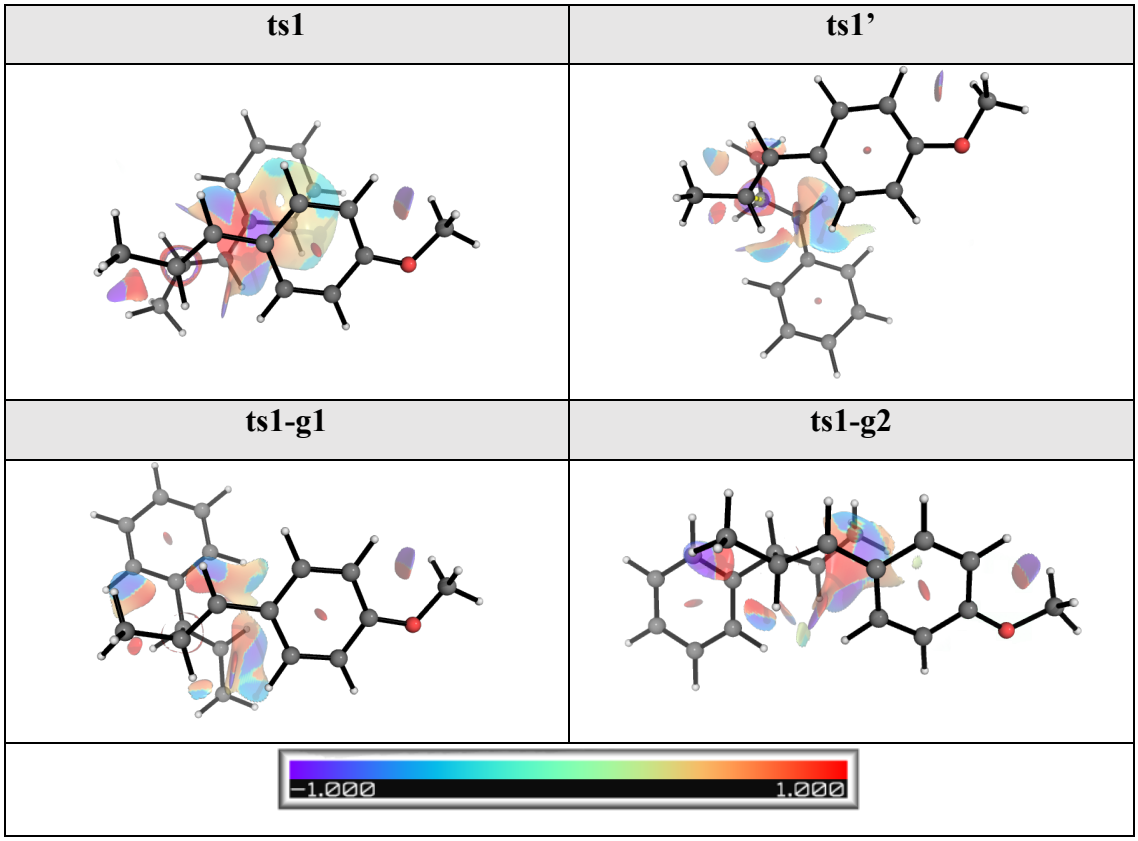

Figure 2.5. NCI plots for head-to-head and head-to-tail first C–C bond formations TSs.

Formal [4+2] side reaction

For the reaction between *trans*-anethole **1a** and *trans*-β-methylstyrene **1b** (P1), after the formation of the first C–C bond, the intermediate could undergo different cyclisation to give competing products. Formal [2+2]-addition gives cyclobutanes discussed earlier. In addition, formal [4+2]-addition is possible, yielding Diels-Alder adducts. The Gibbs energy profile for this periselectivity is given in Figure 2.6. For the *anti*-addition (black pathways), the stepwise Diels-Alder cycloaddition attacking the *ortho*-carbon on the anethole ring (**ts2-an**) is slightly lower (by 0.4 kcal mol^{-1}) than that attacking the *ortho*-

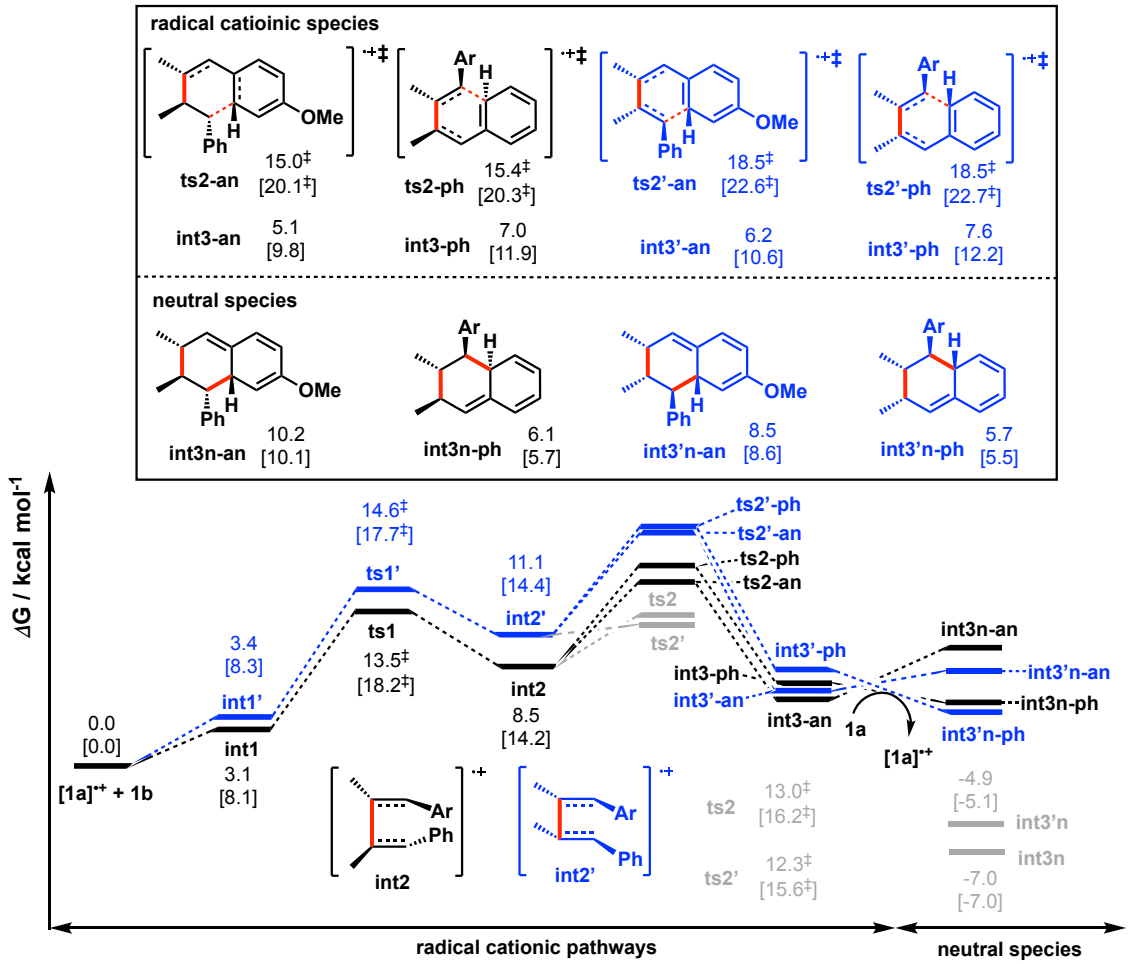

Figure 2.6. Gibbs energy profile for formally [4+2] Diels-Alder reaction between *trans*-anethole and *trans*-β-methylstyrene. The values in HFIP are given together with values in MeCN in square brackets.

carbon on the phenyl ring (**ts2-ph**). Both these TSs are, however, higher in activation barrier (by 2.0 and 2.4 kcal mol^{-1} respectively) than the formal [2+2]-cycloaddition (**ts2**), which occurs at 13.0 kcal mol^{-1} in HFIP solvent. Similarly, for the *syn*-addition (blue pathways), the Diels-Alder addition TSs (**ts2'-an** and **ts2'-ph**) are (much) higher than the cyclobutanation TS (**ts2**), by 6.2 kcal mol^{-1}. These results indicate that Diels-Alder product formations are much less favoured kinetically than the cyclobutyl product formations, potentially resulting from the breaking of the ring aromaticity in forming Diels-Alder adducts. In addition, we note that although the radical cationic ring products (**int3x**) are rather close for Diels-Alder addition and cyclobutanation, the reduction of

Diels-Alder radical cations to their neutral forms are endergonic, with respect to the starting materials, whereas the reduction of cyclobutyl radical cations to their neutral forms (**int3n** and **int3'n**) are exergonic and thus thermodynamically favourable. Note that once again, the radical cationic species are much favoured in HFIP than in MeCN solvent, whereas this HFIP stabilisation is not seen for neutral products (as evidenced by their rather close energies in both solvents).

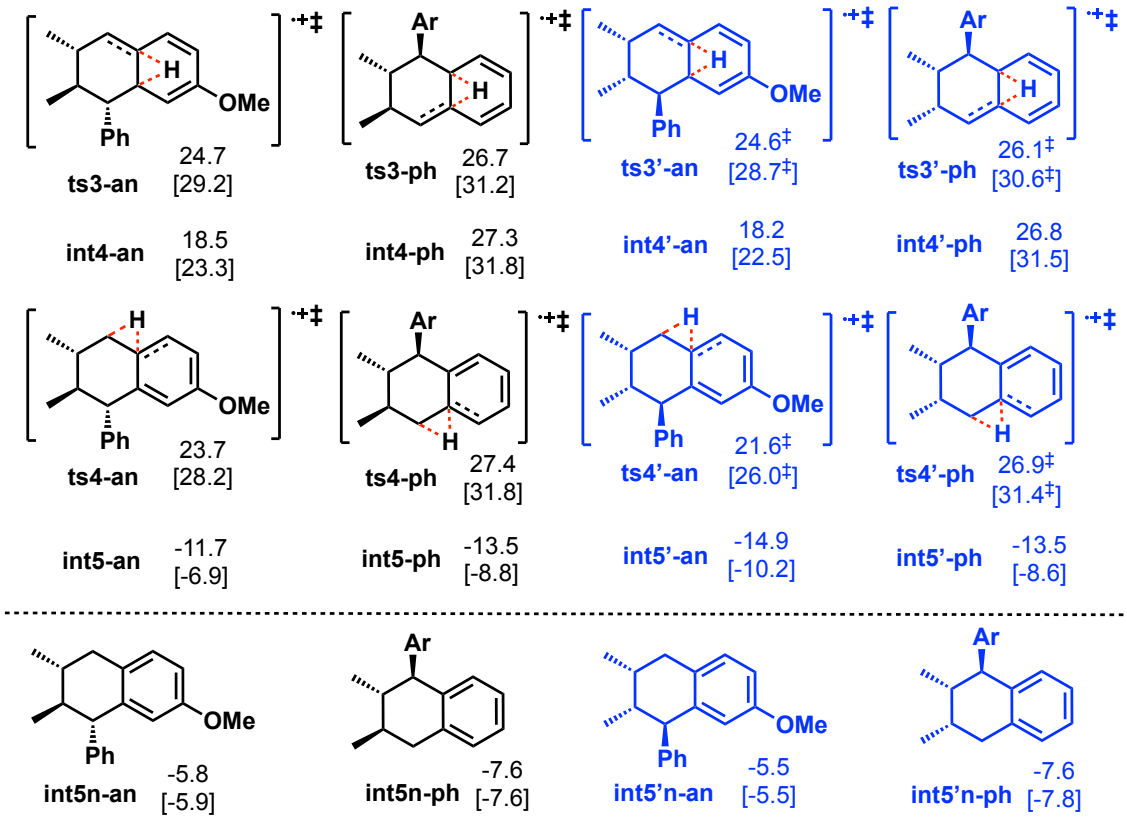

Figure 2.7. Gibbs energies for the successive 1,2-H shifts to regain aromaticity of the rings in the Diels-Alder products. The values in HFIP are given together with values in MeCN in square brackets.

The radical cationic Diels-Alder products formed from [4+2]-cycloaddition can further undergo two successive 1,2-H shifts to regain aromaticity. The Gibbs energies are given in Figure 2.7 for completeness. The TSs for 1,2-H shifts are all very high, ranging from 21.6 to 27.4 kcal mol^{-1} and are thus kinetically disfavoured. Thermodynamically, the final products regain ring aromaticity and are exergonic, although the reduction of the radical

cationic forms to their neutral species are all uphill; these Diels-Alder side products can be favoured under thermodynamic control at high reaction temperatures and prolonged reaction time.

2.3.6 Reactivity and selectivity between *trans*-anethole and *cis*-β-methylstyrene (P2)

We herein similarly investigated the SET hole-catalysed reaction between *trans*-anethole **1a** and *cis*-β-methylstyrene **2b** (reaction P2) as shown in Scheme 2.3 (a) ii). From the calculated redox potentials for these substrates in Table 2.2, we know that *trans*-anethole **1a** will be oxidised preferentially to *cis*-β-methylstyrene **2b** by the hypervalent iodine reagent in the fluorinated solvent. The Gibbs energy profile for both head-to-head and head-to-tail cyclobutanation is shown in Figure 2.8 (conformations were considered and the results shown in Figure 2.9). The *syn*-addition (blue pathway) has the lowest activation barrier, at 15.1 kcal mol^{-1}, with **ts7'** (second C–C bond formation) as the overall turnover-frequency determining transition state (TDTS)[125]. The *anti*-addition (black pathway) has **ts6** (first C–C bond formation) as the overall TDTS, at 17.1 kcal mol^{-1}. The head-to-tail additions are again higher in activation barriers than the head-to-head barriers due to the unfavourable radical stabilisation in the head-to-tail TSs (Figure 2.10). Energy decomposition of the first C–C bond formation TSs shows again that the interaction energy is more favourable in head-to-head isomers than in head-to-tail isomers whereas the distortion energies are similar in all cases (Figure 2.11). We note that only the *trans,cis,cis* product **int8'n** (no *trans,trans,cis* product **int8n**) is observed experimentally. Product **int8'n** is kinetically favoured by 2.0 kcal mol^{-1} and thermodynamically favoured by 1.2 kcal mol^{-1} than product **int8n**.

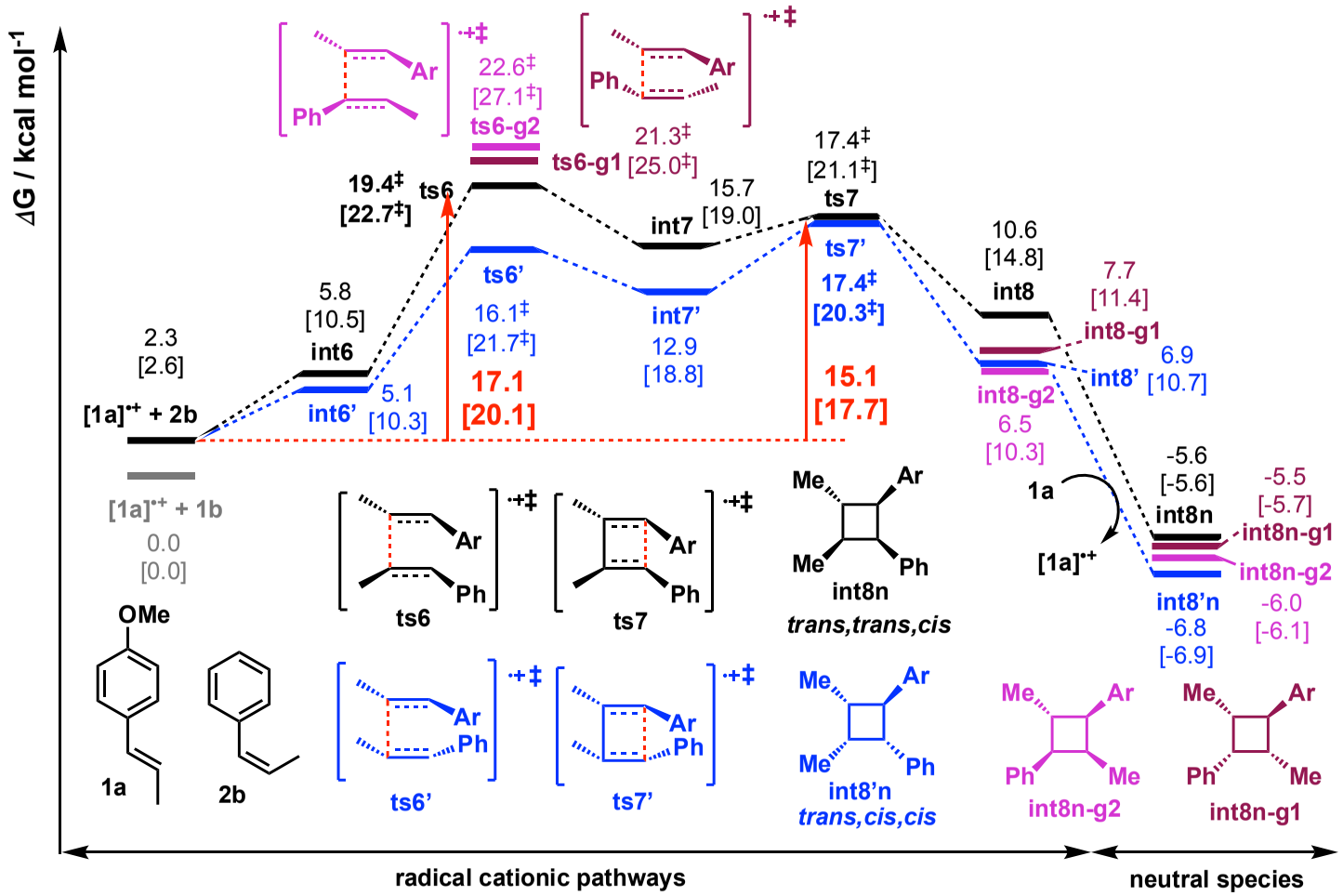

Figure 2.8. Gibbs energy profile for reaction between *trans*-anethole and *cis*-β-methylstyrene. Same energy zero is used as previously. The values in HFIP are given together with values in MeCN in square brackets.

ts6	ts6-c2	ts7
19.3‡ (22.7‡)	21.2‡ (24.6‡)	17.4‡ (21.1‡)
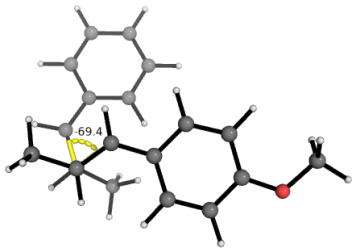	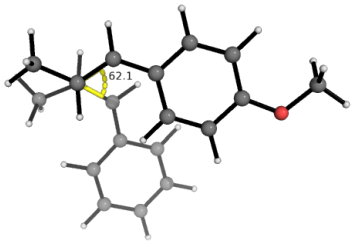	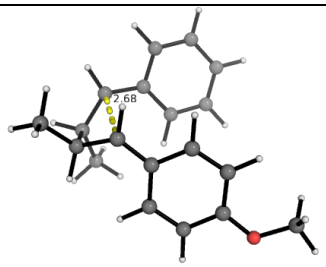
r = 2.09 Å	r = 2.12 Å	r = 1.58 Å
ts6'	**ts6'-c2**	**ts7'**
16.1‡ (21.7‡)	21.1‡ (23.6‡)	17.4‡ (20.3‡)
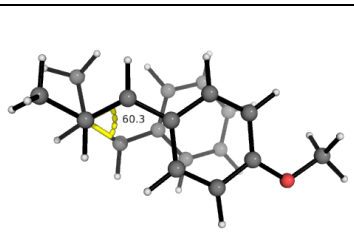	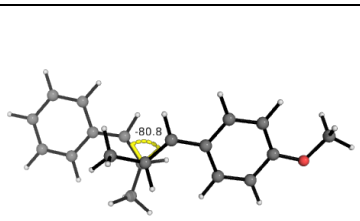	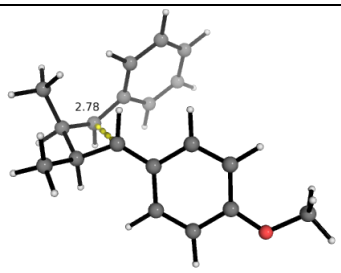
r = 2.07 Å	r = 1.97 Å	r = 1.58 Å
ts6-g1	**ts6-g1-c2**	**ts6-g2**
21.3‡ (25.0‡)	26.5‡ (29.9‡)	22.6‡ (27.1‡)
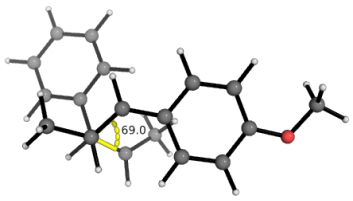	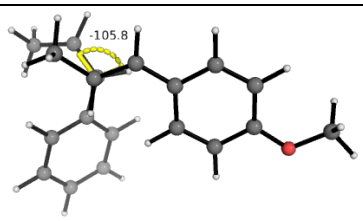	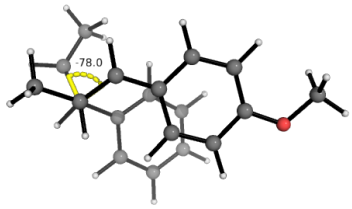
r = 1.94 Å	r = 1.81 Å	r = 1.82 Å
ts6-g2-c2		
23.6‡ (26.9‡)		
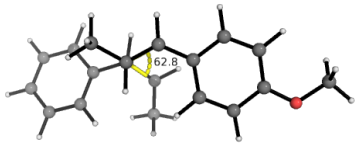		
r = 1.94 Å		

Figure 2.9. Conformations of all TSs for the reaction between *trans*-anethole and *cis*-β-methylstyrene. Distances of the first C–C bond formation (r) is given.

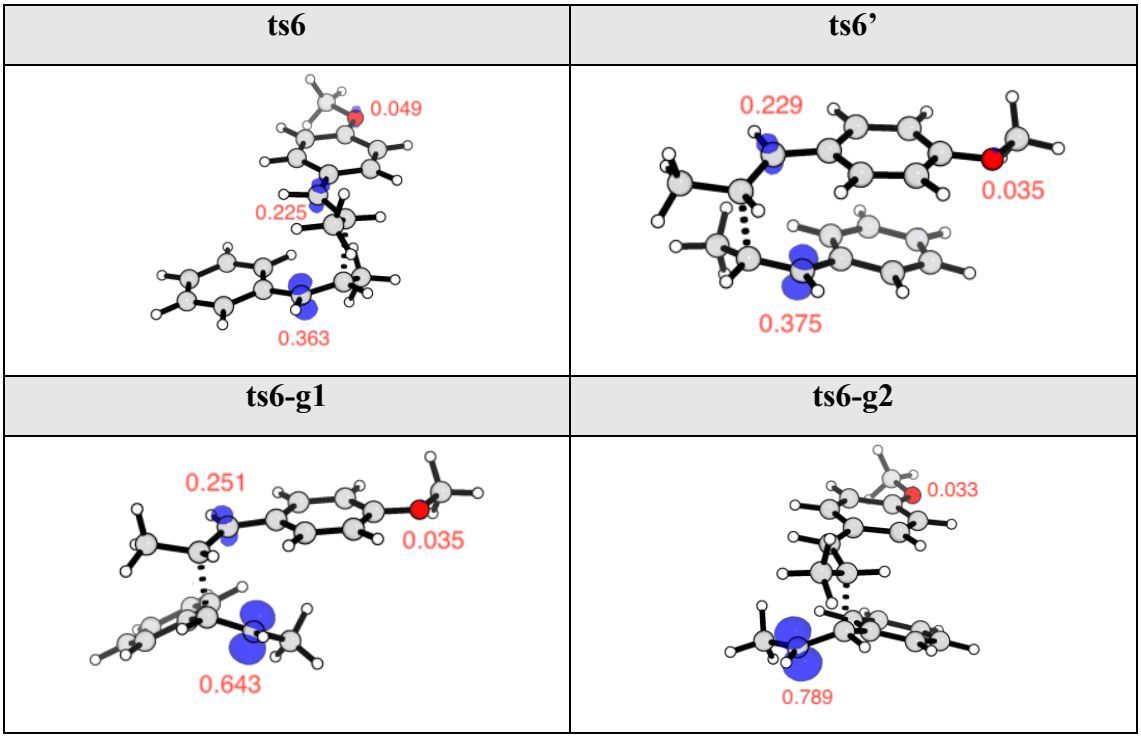

Figure 2.10. Spin density plots (at an isovalue of 0.02) and the Mulliken spin density values of radical cationic TSs for the reaction between *trans*-anethole and *cis*-β-methylstyrene.

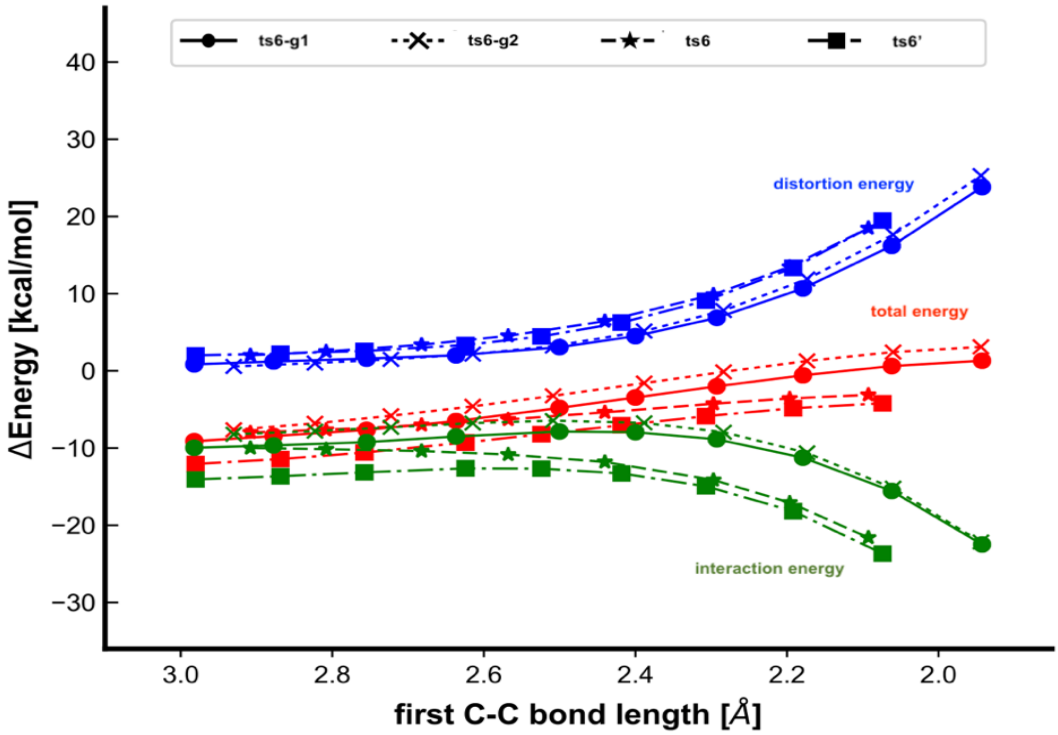

Figure 2.11. The activation strain or distortion-interaction analyses applied to transition structures for both head-to-head (**ts6** and **ts6'**) and head-to-tail (**ts6-g1** and **ts6-g2**) first C–C bond formation TSs. All energies are calculated at UM062X/def2TZVPP//UM062X/6-31G(d) and used without any further corrections.

The Gibbs energy profile in Figure 2.8 explains the selectivity in favour of the formation of *trans,cis,cis* cyclobutane **int8'n**. Experimentally, however, in addition to this product, the *all trans* cyclobutane **int3n** is also formed in the present reaction. The diastereomeric ratio of **int8'n** : **int3n** is 4 : 1 (Scheme 2.3 (a) ii)). The cycloadduct **int3n** cannot be formed directly from the starting materials in the present transformation; two possibilities could occur to yield **int3n**: either *cis*-β-methylstyrene undergoes isomerisation to give *trans*-β-methylstyrene before formal [2+2] cycloaddition, or the intermediates after first C–C bond formation undergo a competitive rotation before the second C–C bond formation/cyclisation to give product **int3n**. The isomerisation of neutral *cis*-β-methyl-styrene to its *trans*-form cannot be achieved thermally at the reaction temperature as it involves breaking a π-bond, which requires an average value of *ca.* 60 kcal mol^{-1}.[246,247] Alternatively, the isomerisation via hole-catalysed rotation can be achieved more readily than in the neutral counterpart,[248] however, the higher redox potential of *cis*-β-methylstyrene than *trans*-anethole (Table 2.2) implies the latter would form radical cation first, which subsequently attacks the neutral *cis*-β-methylstyrene. Thus, the possibility in the isomerisation of *cis*-β-methylstyrene is ruled out.

The free rotations along C–C single bonds for radical cationic systems are known to be facile and play important roles in reactions as demonstrated by previous studies;[184,208] the bond rotations can be more easily achieved in radical cationic species than in their neutral counterparts.[248] Figure 2.12 shows the energy profiles for the reactions between *trans*-anethole **1a** and either *trans*-β-methylstyrene **1b** (P1) or *cis*-β-methylstyrene **2b** (P2). These two reactions are interconvertible via a rotation about C1–C2 bond in the intermediate after the first C–C bond formation. In the reaction between [**1a**]$^{\bullet+}$ and **1b** for example (P1), at the intermediate **int2** after the first C–C bond formation, direct second

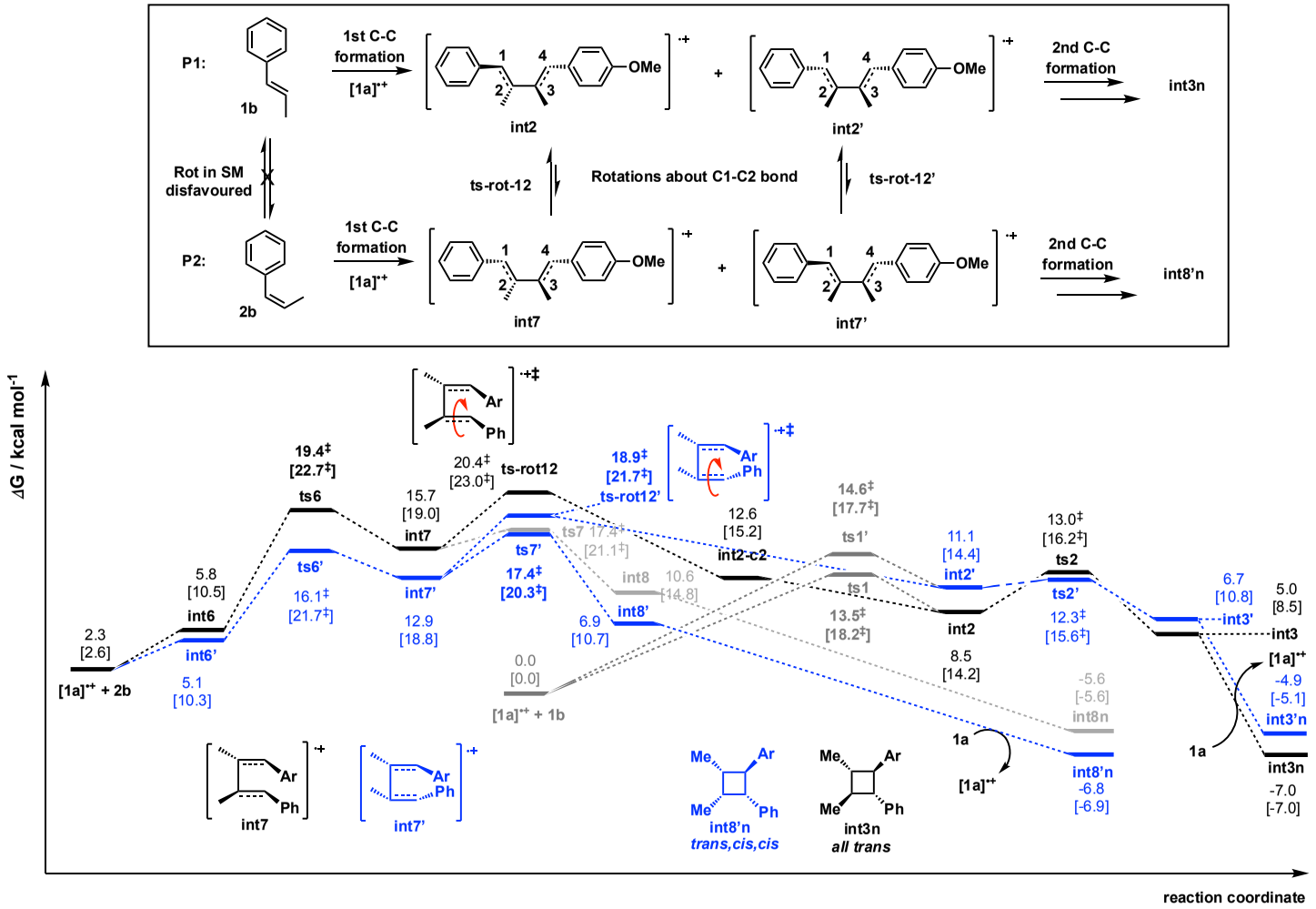

Figure 2.12. Gibbs energy profile for reaction between *trans*-anethole and *cis*-β-methylstyrene with rotational barriers that connect this transformation to the reaction between *trans*-anethole and *trans*-β-methylstyrene. The values in HFIP are given together with values in MeCN in square brackets.

C–C bond formation (**ts2**, 13.0 kcal mol^{-1}) has a much lower activation barrier than the rotational barrier to access pathways P2 (**ts-rot-12**, 20.4 kcal mol^{-1}), such that only **int3n** is formed as the sole product. In the reaction between [**1a**]$^{\bullet+}$ and **2b** (P2), after the first C–C bond formation, the intermediate **int7** can undergo either a direct second C–C bond formation (**ts7'**, 17.4 kcal mol^{-1}) or a competitive rotational barrier (**ts-rot-12'**, 18.9 kcal mol^{-1}) to give **int2'**, allowing the reaction to access pathways P1. This intermediate can cyclorevert to give [**1a**]$^{\bullet+}$ and **1b**, which subsequently forms **int3n** as the thermodynamic product. Note that structures **int3n** and **int8'n** are almost isoenergetic and are favoured both kinetically (by 1.6 – 2.0 kcal mol^{-1}) and thermodynamically (by 1.2 – 2.1 kcal mol^{-1}) over **int3'n** and **int8n**.

The activation barrier difference of $\Delta\Delta G^{\ddagger}$ of 1.5 kcal mol^{-1} between second C–C bond formation/cyclisation and rotation gives a selectivity ratio of 6.8 : 1 under kinetic control; this is close to the experimentally observed ratio of 4:1. The exact ratio is likely influenced by dynamical effects in such radical cationic intermediates, shown in a meta-dynamics study of radical cationic Diels-Alder cycloaddition.[249]

Formal [4+2] side reaction

For completeness, the periselectivity for this reaction between *trans*-anethole **1a** and *cis*-β-methylstyrene **2b** was similarly studied. As previously, formal [4+2]-cycloadditions giving the Diels-Alder adducts are less favourable than formal [2+2]-cycloaddition. The comparative Gibbs energy profile for this periselectivity is given in Figure 2.13. The results are the same as for the reaction between *trans*-anethole **1a** and *trans*-β-methylstyrene **1b** (P1) – the [4+2]-cycloadditions (**ts7-ph** and **ts7'-ph**) are much less favourable, by at least 3.4 kcal mol^{-1}, than the [2+2]-cycloadditions (**ts7** and **ts7'**). The TSs for the successive 1,2-H shifts (**ts8-x** and **ts9-x**) are all rather high in activation

barriers (25.3 – 27.9 kcal mol^{-1}) and are expected to be less favourable kinetically, although the final products **int10-x** can regain aromaticity and be thermodynamically favoured, as in reaction P1.

2.3.7 Reactivity and selectivity between *cis*-anethole and *trans*-β-methylstyrene (P3)

The reaction between *cis*-anethole (**2a**) and *trans*-β-methylstyrene (**1b**) (reaction P3) is connected to the reaction between *trans*-anethole (**1a**) and **1b** (reaction P1) via a rotation in the C3–C4 bond in the intermediates after the first C–C bond formation (Figure 2.14), much in the same way that reaction P2 is related to P1 (Figure 2.12). The calculated redox potential of **2a** is lower than that of **1b** (Table 2.2) such that **2a** acts as a caticogen and **1b** caticophile. The Gibbs energy profile for reaction P3 is shown in Figure 2.14, together with the rotational barriers about C3–C4 bond in the intermediates after first C–C bond formation. Conformations of TSs were studied and the optimised structures are given in Figure 2.15. The energy pathways are very similar, in terms of energetics, to those obtained for the reaction between *trans*-anethole and *cis*-β-methylstyrene (P2). The *anti*-addition has the first C–C bond formation (**ts11**, 19.4 kcal mol^{-1}) as the TDTS, whereas the *syn*-addition has the second C–C bond formation (**ts12'**, 17.7 kcal mol^{-1}) as the TDTS (Figure 2.14). Again, head-to-head formations are kinetically favoured, by more than 4.7 kcal mol^{-1} than head-to-tail formations. The formation of *syn*-cyclobutyl ring **int13'n** is both kinetically (by 1.7 kcal mol^{-1} in HFIP) and thermodynamically (by 3.1 kcal mol^{-1} in HFIP) more favoured than the *anti*-cyclobutyl ring **int13n**.

The rotational barrier in the *syn*-addition intermediate after the first C–C bond formation (**ts-rot34'**, 18.4 kcal mol^{-1}) is comparable (0.7 kcal mol^{-1} difference) to direct second C–C bond formation in the cyclisation step (**ts12'**, 17.7 kcal mol^{-1}), such that rotation about

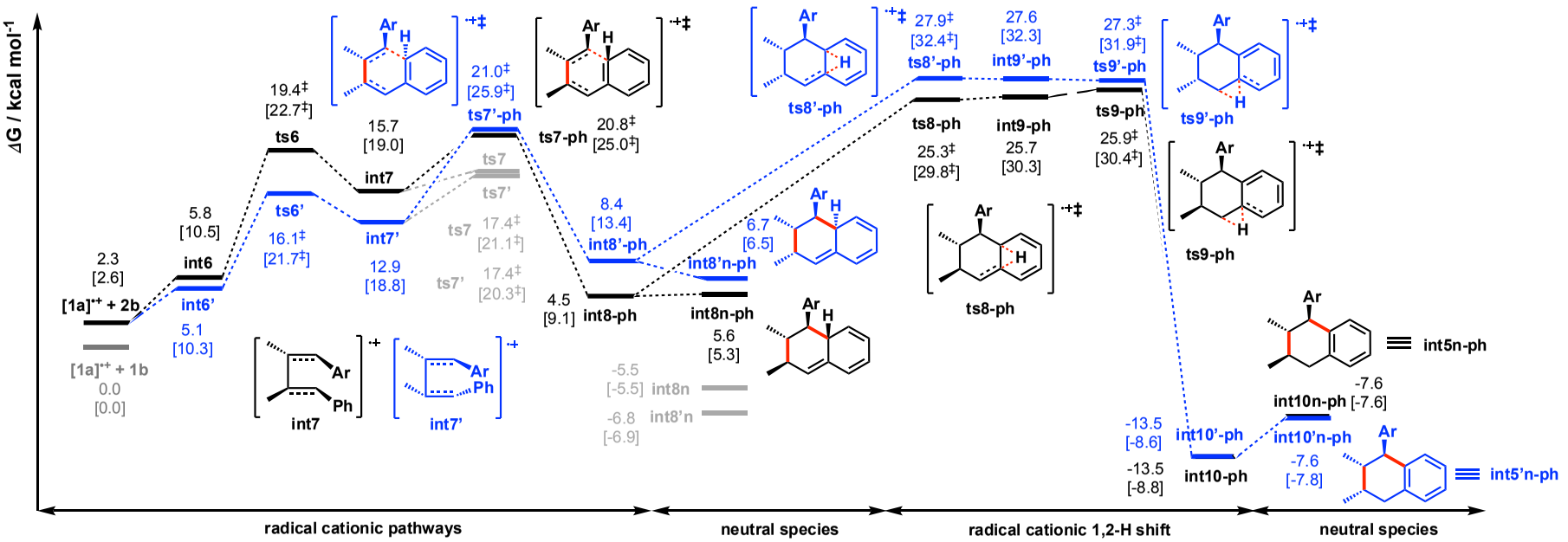

Figure 2.13. Gibbs energy profile for formally [4+2] Diels-Alder reaction between *trans*-anethole and *cis*-β-methylstyrene and successive 1,2-H shifts to regain aromaticity of the rings in the Diels-Alder products. The values in HFIP are given together with values in MeCN in square brackets.

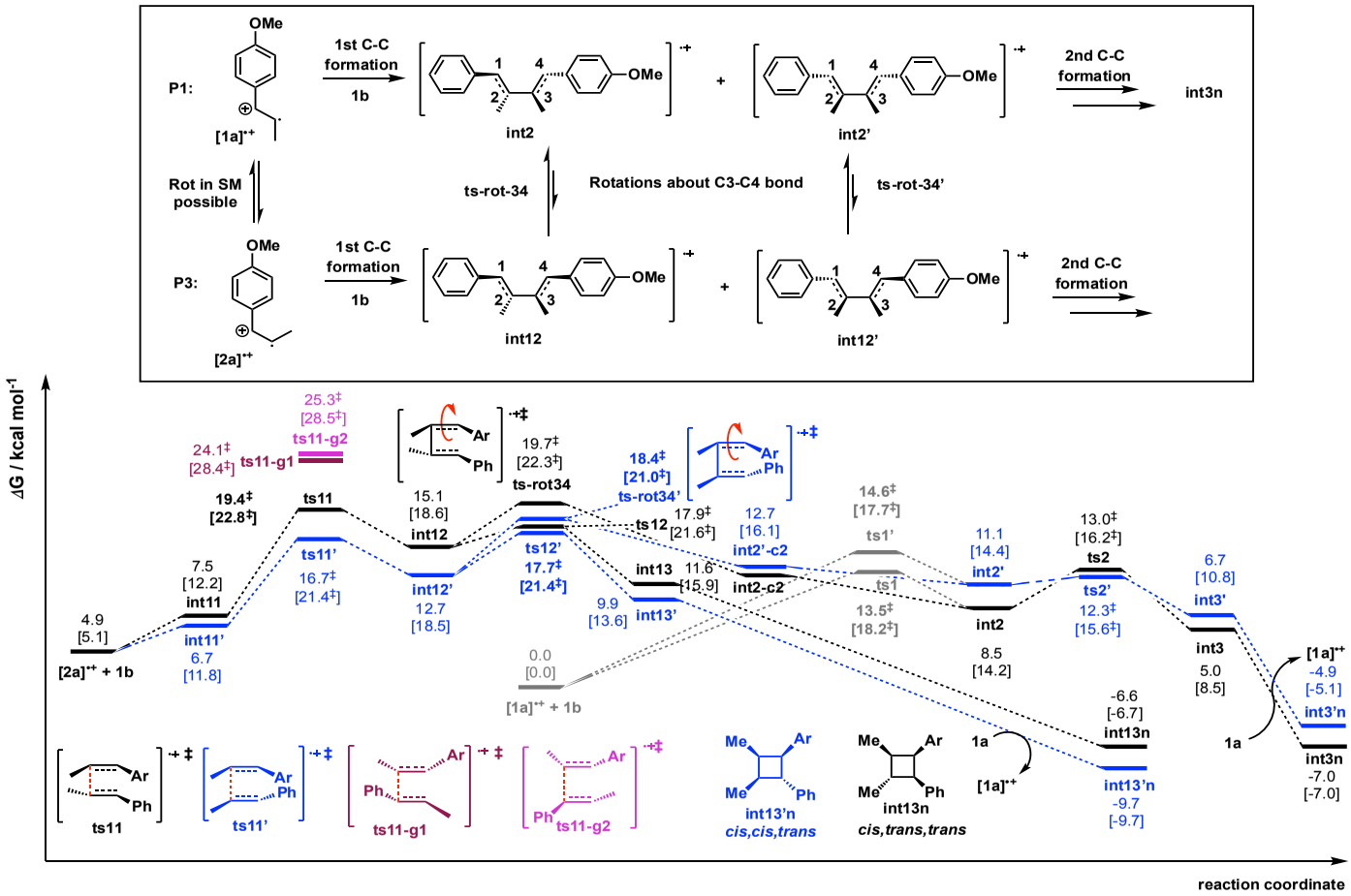

Figure 2.14. Gibbs energy profile for reaction between *cis*-anethole and *trans*-β-methylstyrene with rotational barriers that connect this transformation (P3) to the reaction between *trans*-anethole and *trans*-β-methylstyrene (P1). The values in HFIP are given together with values in MeCN in square brackets.

C3–C4 bond in **int12'** to access the reaction P1 becomes possible. For the *anti*-addition intermediate **int12**, rotational barrier **ts-rot34** is 1.8 kcal mol^{-1} higher than the direct second C–C bond formation in the cyclisation step. In similar reaction conditions, the reaction between *cis*-anethole and *trans*-β-methylstyrene is predicted to yield a mixture of cyclobutanes, with **int13'n** being present as the major product and **int13n** and **int3n** as minor products. These product outcomes are probable and are similar to the product outcomes observed in the homodimerisation of *trans*-anethole using triaryl amine radical cation catalyst pioneered by Bauld and co-workers (Scheme 2.3 (b)).

ts11	**ts11-c2**	**ts12**
19.4‡ (22.8‡)	21.3‡ (24.9‡)	17.9‡ (21.6‡)
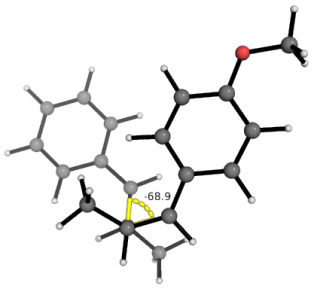	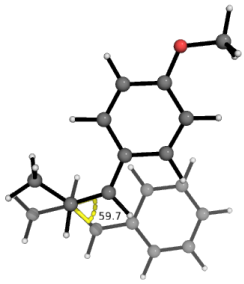	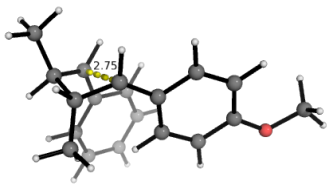
r = 2.12 Å	r = 2.10 Å	r = 1.59 Å
ts12-c2	**ts11'**	**ts11'-c2**
15.4‡ (19.0‡)	16.7‡ (21.5‡)	20.4‡ (22.9‡)
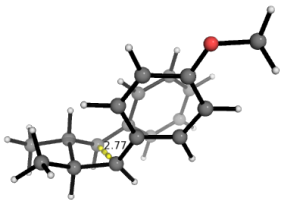	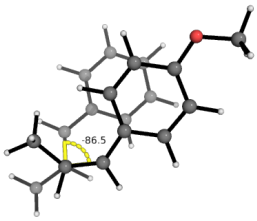	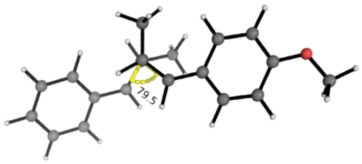
r = 1.59 Å	r = 2.00 Å	r = 2.05 Å
ts12'		
17.7‡ (21.4‡)		

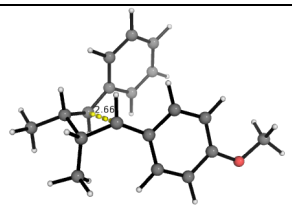		
r = 1.59 Å		

Figure 2.15. Conformations of all TSs for the reaction between *cis*-anethole and *trans*-β-methylstyrene. Distances of the first C–C bond formation (r) is given.

Formal [4+2] side reaction

The periselecitivity for this reaction between *cis*-anethole **2a** and *trans*-β-methylstyrene **1b** was similarly studied. As previously, formal [4+2]-cycloadditions giving the Diels-Alder adducts are less favourable kinetically than formal [2+2]-cycloaddition. The comparative Gibbs energy profile for this periselectivity is given in Figure 2.16. The TSs for the successive 1,2-H shifts (**ts13x** and **ts14x**) have activation barriers (20.1 – 23.6 kcal mol^{-1}) that are lower than those in Figure 2.13 where the [4+2]-cycloaddition forms C–C bond to the phenyl ring, although they are still much higher than the cyclobutanation TDTS. The final products **int15x** can again be thermodynamically favoured upon regaining ring aromaticity.

2.3.8 Estimation of electron transfer barriers

In the Marcus-Hush[250–253] framework, parabolic energy curves are used to represent the states of reactant and products. Within the diabatic representation (where the coupling between the two potential energy surfaces is due to electronic terms), the TS for the electron transfer (ET) occurs at where the two parabolas cross. It is further assumed that the two parabolas have the same curvature. With these, the activation energy of the ET, $\Delta G^{\ddagger}$, is given by

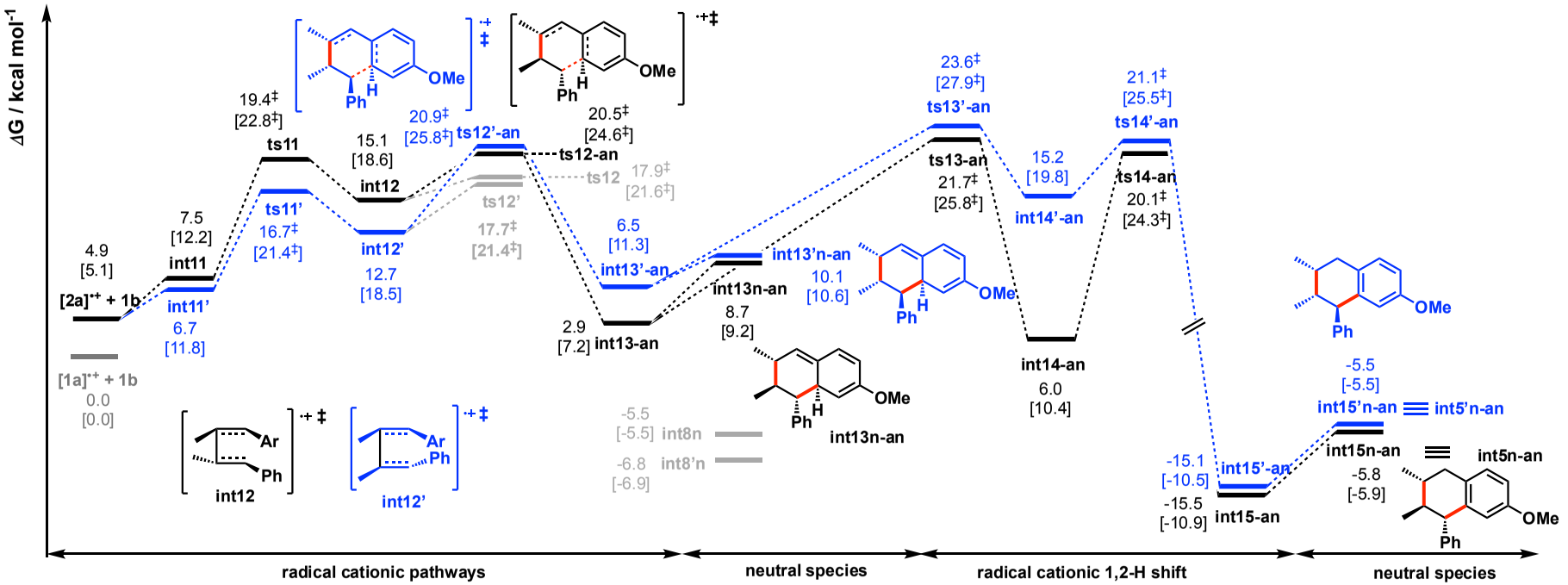

Figure 2.16. Gibbs energy profile for formally [4+2] Diels-Alder reaction between *cis*-anethole and *trans*-β-methylstyrene and successive 1,2-H shifts to regain aromaticity of the rings in the Diels-Alder products.

$$\Delta G_{ET}^{\ddagger} = \frac{\lambda}{4}\left(1 + \frac{\Delta G_r}{\lambda}\right) \tag{2.4}$$

where ΔG_r is the free energy change of the reaction and λ is the reorganisation energy.

The reorganisation energy is composed of two parts, the internal reorganisation energy, λ_i, and external polarisation, λ_o, i.e., $\lambda = \lambda_i + \lambda_o$. The former term λ_i describes the energy associated with geometry changes when going from the reactant to the product state; the latter term λ_o describes the energy change due to the polarisation in the surrounding (solvent) molecules due to the ET process.

In our estimation of the ET barriers, we assume that the geometry change upon electron transfer is small such that we can ignore the internal reorganisation energy ($\lambda_i = 0$). Thus, $\lambda = \lambda_o$. Using Marcus equation, the solvent polarisation energy is given by

$$\lambda_o = (322 \text{ kcal mol}^{-1})\left[\frac{1}{2a_1} + \frac{1}{2a_2} - \frac{1}{R}\right] \cdot \left[\frac{1}{\epsilon_{op}} - \frac{1}{\epsilon}\right] \tag{2.5}$$

where a_1 and a_2 are the radii of the molecules involved, $R = a_1 + a_2$ is the sum of these radii, ϵ_{op} is the optical dielectric constant ($\epsilon_{op} = 2.05$) and ϵ is the static dielectric constant of the solvent. Hence, by calculating the molecular radii of the molecules (using *Gaussian* "volume" keyword) involved in an electron transfer process, we are able to estimate the barrier of such a process using the Marcus-Hush theory outlined above.

For our SET-mediated cycloaddition, we focus on the termination steps. Studies of both organic[254–256] and inorganic[257–259] systems in the gas phase revealed fast electron transfer rates close to diffusion limit. The reaction barriers are thus much smaller than that for the chemical transformations. It was also shown that the rate of electron transfer in gas phase is more than 10^4 times faster than in solvents.[259] We found that the ET barriers are very

small (0.62–1.84 kcal mol^{-1} in MeCN and 0.46–1.65 kcal mol^{-1} in HFIP) for the reduction of radical cationic products to their neutral forms for the exergonic reactions. These calculations show that ET processes occur much faster than bond-forming events.

2.4 Conclusions

We herein employed DFT to study the hypervalent iodine oxidant-promoted single electron transfer catalysed cyclobutanation via radical cationic intermediates. The product stereochemical outcomes for the reactions between anethole and β-methylstyrene were studied. The computed redox potentials of these substrates allow us to predict the chemoselective oxidation by the iodine oxidant DMP in the heterodimerisation reaction. The formation of head-to-head regioisomers are more favourable than head-to-tail regioisomers due to more favourable interaction energies and radical stabilisation whereas distortion are similar in these TSs.

The stereochemical outcomes for the reaction between two unsymmetrical *trans*-alkenes are relatively simple, with no competitive diastereomeric product formations, apart from the major isomer, due to the highly unfavourable rotational barriers in the intermediates after first C–C bond formation, so that diastereomeric pathways are not accessible. On the other hand, in the reaction between a *trans*-alkene and a *cis*-alkene, the rotational barriers in the intermediates after first C–C bond formation are comparable in energy to direct second C–C bond formation in the subsequent cyclisation step, allowing the formation of products that are normally formed from the reaction of two alkenes of *trans*-geometry. In addition, *anti*-addition (giving *trans*-geometry across the first C–C bond formation) is favoured when the reacting alkenes are both of *trans*-geometry whereas *syn*-addition (*cis*-geometry across the first C–C bond formation) is favoured when one of

the reacting alkenes is of *cis*-geometry due to comparable rotational barriers to second C–C bond cyclisation. These calculations agree well with experimental observations.

We have herein shown that the radical cation-mediated cycloaddition is predominantly influenced by electronic factors and is under both kinetic and thermodynamic controls. The regioselectivity for head-to-head over head-to-tail isomer formations is likely under kinetic control, as both these neutral 4-membered rings have rather close energies. For the head-to-head isomers (*syn*- vs *anti*-adducts), although the major isomer is favoured both kinetically and thermodynamically, the product selectivity is likely controlled by thermodynamics of the neutral products since the experimentally observed product distribution agrees better with the thermodynamic energetic differences rather than the kinetic activation barrier differences. The understanding of this mechanism opens up some possibilities of experimentally controlling the chemoselectivity, periselectivity, regioselectivity and stereoselectivity in oxidant-promoted SET-catalysed, radical cation-mediated heterodimerisation of electron-rich alkenes in accessing complex, tetra-substituted cyclobutyl rings. Using computational calculations of redox potentials of different alkenes and understanding their inherent steric and electronic properties, we envisioned that intermolecular heterodimerisation of different alkenes can be efficiently controlled, with precise chemical selectivity, to efficiently access cyclobutanes.

Everywhere is walking distance if you have the time.

— Steven Wright

3

Hydroxyphosphine-catalysed Staudinger Reduction

3.1 Introduction

"*Ohne Phosphor, Kein Gedanke."* Indeed, phosphorus chemistry is of central importance in a wide range of organic and biochemical processes. Phosphorus-based compounds, such as phosphine and its derivatives, have played important roles in transformations such as Appel,[260] Mitsunobu,[261,262] Wittig,[263,264] aza-Wittig[265,266] and Staudinger[265,266] reactions. In particular, the Staudinger reduction is one of the most important and widely used methods to convert organic azides into primary amines.[267] In a classical Staudinger reduction (Scheme 3.1 (a)), an organic phosphine, typically a triarylphosphine, reacts with an azide to give an iminophosphorane, or phosphazene, with a concomitant evolution of dinitrogen gas. The P(V) iminophosphorane intermediate can later be hydrolysed using water to yield the primary amine and the highly stable phosphine oxide

with a very strong P=O bond (the P–O single bond strength is about 142.4 kcal mol^{-1} in the gas phase[268] and the P=O double bond is expected to be much higher). This method has the disadvantage that a stoichiometric amount of phosphine reagent is required for the amine generation and the highly stable phosphine oxide, whose regeneration is not always easy, is obtained as a by-product. In addition, the separation of the amine product from this mixture is not always easy.[269,270]

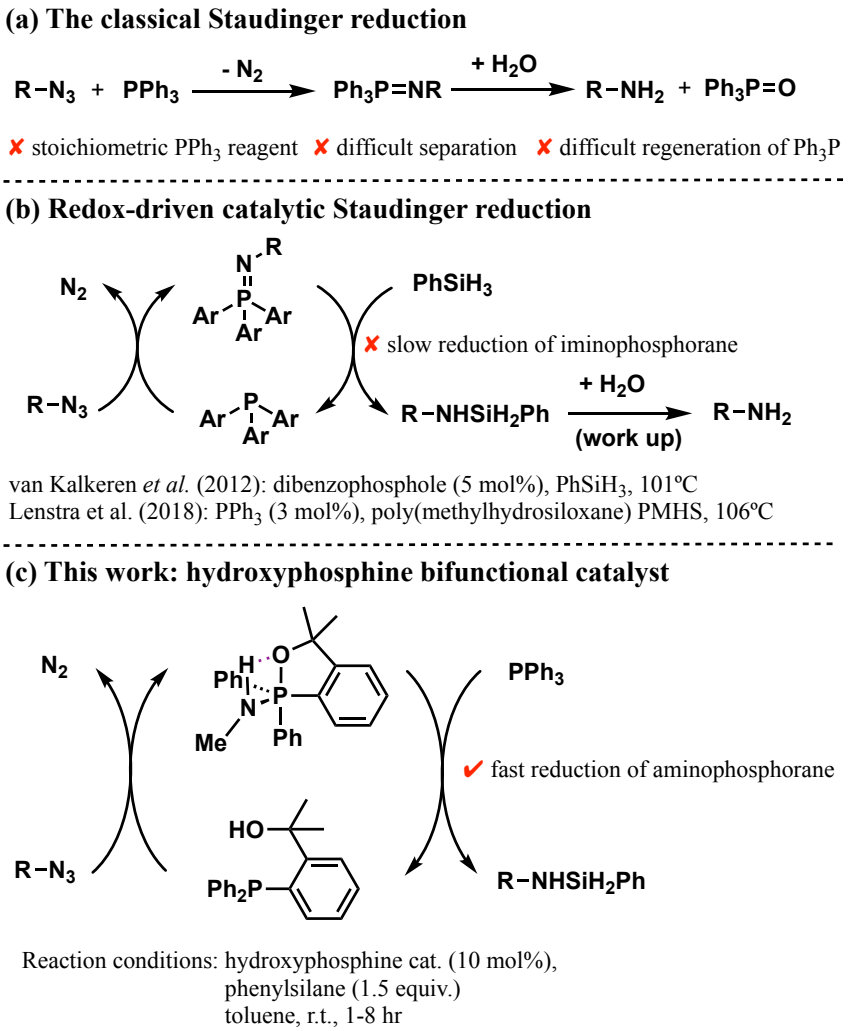

Scheme 3.1. Various methods for performing Staudinger reductions.

To reduce the amount of stoichiometric phosphine oxide waste and to provide an atom- and step-economical way to access the primary amines from organic azides, van Kalkeren and co-workers in 2012 first reported a catalytic Staudinger reduction, where a phenyl-

silane was used as a reductant to reduce the iminophosphorane intermediate generated *in situ*, thereby sustaining the catalytic P(III)/P(V) cycle (Scheme 3.1 (b)).[271] The direct reduction of iminophosphorane by silane forms Si–N bond, which is highly sensitive to water[272,273] and can thus be reduced easily in subsequent aqueous work-up to yield primary amines. In this way, there is no need for *in situ* water, which is incompatible with most reductants. Without any water present in the reaction, the formation of phosphine oxide is negated so that facile product separation can be achieved. In addition, this method was shown to give excellent yields and high functional group tolerance. However, the silane reduction of the P=N bond in the iminophosphorane was shown to be the rate-determining step and could be rather slow,[271] as evidenced by the relatively high reaction temperature (101ºC) required.

Following this report, various methods have been developed for the catalytic Staudinger reduction. These have focused on the *in situ* reduction of either the phosphine oxide[274–276] or the iminophosphorane intermediate[277] formed. To overcome the unfavourable reduction of stable iminophosphorane and/or phosphine oxide, our experimental collaborators (the Denton Research Group at the University of Nottingham) envisioned a σ^5-P(V) intermediate that can be formed from the σ^3-P(V) iminophosphorane intermediate by the action of a bifunctional phosphine catalyst having a tertiary hydroxyl group (Scheme 3.1 (c)). It was reasoned that the reduction of the aminophosphorane P–N bond by the phenylsilane would be easier than the corresponding reduction of the iminophosphorane intermediate P=N bond. This would then open up a new σ^3-P/σ^5-P catalytic cycle,[278] thereby giving rise to a faster and potentially more efficient catalytic Staudinger reduction. We herein performed computational investigations to understand the mechanisms involving this novel bifunctional hydroxyphosphine catalyst.

All experimental work was performed by our experimental collaborators and all computational work was performed by the present author under the supervision of Prof. Robert Paton.

3.2 Computational Methods

3.2.1 Density functional theory (DFT)

DFT calculations were performed with *Gaussian 09* rev. D.01.[192] Geometry optimisations were carried out using the range-separated double-hybrid functional ωB97X-D[56] with the Pople type split-valence Gaussian AO basis set 6-31+G(d,p).[193] Minima and transition structures on the potential energy surface (PES) were confirmed as such by harmonic frequency analysis at the same level of theory. Intrinsic reaction coordinate (IRC)[194,195] analyses were performed to connect reacting species at both ends of any transition state. Single point corrections were performed with a polarized triple-ζ def2-TZVPP basis set[18,196,197] using either ωB97X-D or the global hybrid functional M06-2X[72]. The SMD continuum solvation model[117] was used to include the effect of toluene on the computed Gibbs energy profile. Gibbs energies were evaluated at 298.15 K, using a quasi-RRHO treatment of vibrational entropies[205,206] and corrected at 1 mol L^{-1} as in Chapter 2. The computed SMD(toluene)-ωB97X-D/def2-TZVPP//ωB97X-D/6-31+G(d,p) values are given together with the SMD(toluene)-M06-2X/def2-TZVPP// ωB97X-D/6-31+G(d,p) values in square brackets. These two sets of values agree very well and unless otherwise stated, the former set of values is used for discussion. *Unless otherwise stated, all energy values are quoted in kcal* mol^{-1} *and bond distances in Å.*

Chemical shielding tensor calculations were carried out to confirm the experimental assignment of reaction intermediates by comparing against experimental ^{13}C, ^{1}H and ^{31}P chemical shifts (CSs).[279] These are performed using the Gauge-Including Atomic Orbitals

(GIAOs)[280] method with the Gaussian keyword "nmr = (GIAO,Mixed)" in either gas or solvent phase. Linear scaling parameters were applied to relate the computed isotropic tensor to the experimental CS. See subsection 3.3.11 for a detailed discussion.

Non-covalent interactions (NCIs) were analysed using NCIPLOT[281] calculations. The *.wfn* files for NCIPLOT were generated at the same level of theory as geometry optimisation. NCI indices calculated with NCIPLOT were visualised at gradient isosurface value of $s = 0.5$ au. These are coloured according to the sign of $(\lambda_2)\rho$ over the range of –0.1 (blue = attractive) to +0.1 (red = repulsive). All molecular structures and molecular orbitals (MOs) were visualized using *PyMOL* software.[207] *Unless otherwise state, all MOs were plot at an isovalue of 0.05.*

Geometries of all optimised structures have been deposited online and made freely available (DOI: 10.5281/zenodo.3560475).

3.2.2 Molecular dynamics (MD)

Conformational sampling of the hydroxyphosphine catalyst (in **1a-eq** and **1a-ax** forms) was performed using GROMACS molecular dynamics package (version 5.1.4)[282–287] with optimised potential for liquid simulations (OPLS-AA 2005) forcefield[288,289]. Forcefield parameters were generated using Schrodinger Maestro software (*ffld_server* utility, version 14).[290] The atomic charges required for evaluating non-bonded electrostatic energies were calculated using restrained electrostatic potential (RESP) scheme.[291,292] RESP charges were fitted to HF/6-31G(d) electrostatic potential using Ambertools18.[293] Simulations were performed in explicit toluene solvent whose topology was obtained from virtualchemistry.org.[294,295] Protocols used are similar to those in references[2,296]. Briefly, the catalyst was first centred in a cubic box having 3D periodic

boundary conditions (PBC) with a species-boundary distance of 15 Å. A 1 nm cut-off was used for both Van der Waals interactions and the particle mesh Ewald method.[297] Linear constraint solver algorithm (LINCS)[298] was used for simulations. System temperature was kept constant using the velocity rescaling method,[299] with a time constant of 100 fs. Pressure was kept constant (NPT ensemble) at a value of 1 bar and compressibility of 4.5 x 10^{-5} bar^{-1}, using Parrinello-Rahman barostat,[300,301] with time constant of 2 ps. The system was first minimised by steepest-descents method for 5000 steps. Initial random velocities were drawn from the Maxwell-Boltzmann distribution at 173K. The system was equilibrated at constant volume (NVT), with 1 fs timestep and heavy atom position restraints for 200 ps. The system temperature was raised gradually (173K, 223K, 298.15K) to that required for the NPT production run (room temperature). The system was then equilibrated for a further 400 ps under constant pressure (NPT) with 2 fs timestep. At this stage, the temperature, pressure and volume of the system were verified to have stabilized. NPT production run was then carried out for 100 ns, with a time step of 2 fs. Trajectories from the NPT production run were used for analysis by calculating the RMSD between frames (*gmx rms*) and clustering (*gmx cluster*) using a cutoff of 1.5 Å with the GROMOS algorithm[302] in GROMACS program. The centre structure of each cluster was taken as possible conformers of the catalyst.

3.3 Results and Discussions

3.3.1 Conformational considerations

Two major conformers for the bifunctional catalyst (**1a-eq** and **1a-ax**) were found using DFT. These are shown in Figure 3.1 Top, together with their computed phosphorus NMR shifts (see subsection 2.3.8). The TS for the interconversion between the conformations

of hydroxyphosphine catalyst **1a-eq** and **1a-ax** could not be found by DFT, we suspect these conformers can interconvert but it involves a composite of small rotational barriers.

DFT Structures			
1a-eq		**1a-ax**	
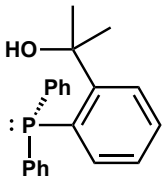	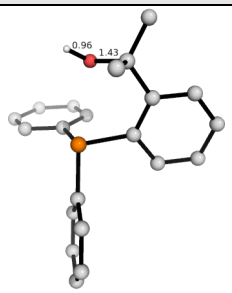	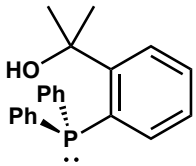	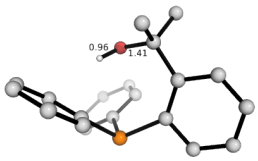
δ_P = -15.1 ppm		δ_P = 22.9 ppm	
$\Delta\Delta G$ = 0.0 [0.0] kcal mol^{-1}		$\Delta\Delta G$ = 6.4 [7.1] kcal mol^{-1}	
Clusters from MD simulation using 1-ax as a starting point			
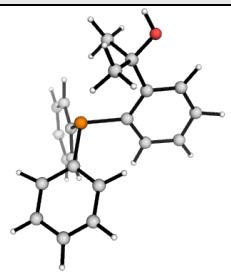	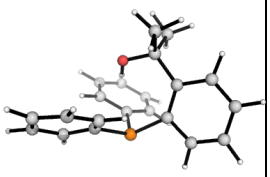	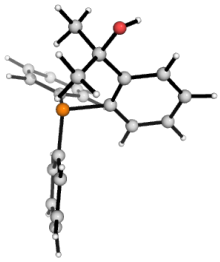	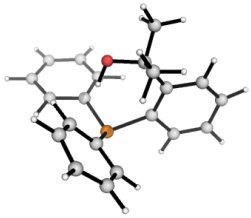
93.4%	**5.1%**	**1.5%**	**<1%**
Clusters from MD simulation using 1-eq as a starting point			
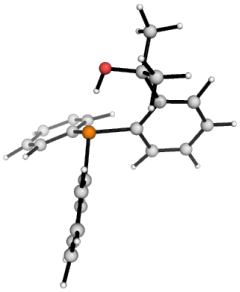	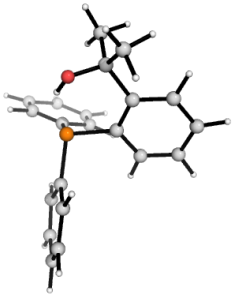	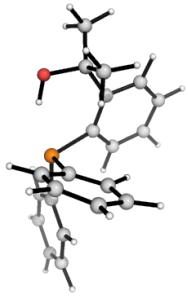	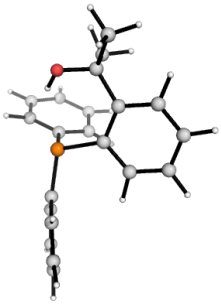
90.7%	**9.2%**	**< 1%**	**< 1%**

Figure 3.1. Top: Two forms of hydroxyphosphine catalyst, their optimised structure and relative energies. **Bottom**: Middle structures from each cluster in MD simulations of hydroxyphosphine catalyst and their weight percent.

We thus performed a quick MD simulation, with explicit solvation, at room temperature to show that this interconversion is possible (Figure 3.1 Bottom). From the MD analysis, we can imagine successive facile rotations about single bonds that allow interconversion between **1a-ax** and **1a-eq**. The structures from the MD results were further optimised using DFT to yield structures for NMR computations, with Boltzmann weighting. The more thermodynamically stable conformer **1a-eq** dominates. The reaction of the lower energy conformer **1a-eq** is discussed. See subsections 3.3.6 – 3.3.7 for a discussion of the reaction of the higher energy conformer of the catalyst **1a-ax** for completeness.

3.3.2 Main reaction energy profile involving equatorial catalyst 1a-eq

The overall Gibbs energy profile is given in Figure 3.2. The lowest conformer of the bifunctional phosphine catalyst (**1a-eq**) is used as a reference. The computed reaction mechanism proceeds via the formation of P–N bond at the azide terminal nitrogen atom (**ts1-eq**, Figure 3.3). This addition step is promoted by the presence of a stabilising hydrogen bond between the catalyst hydroxyl group and the incoming azide. The formation of a hydrogen bond at the N3-position makes the terminal N-atom more electrophilic (as electron density is pulled away from this site) and thus more susceptible to the attack by the nucleophilic P-atom of the catalyst (see later for comparison to the methoxylated version of the catalyst and the classical triphenylphosphine PPh_3 catalyst, which do not have any assistive hydrogen bonding for this step).

The azide approaches the phosphine P-atom in a *cis*-geometry, consistent with earlier theoretical studies.[303–305] The subsequent loss of N_2 gas occurs with concerted cleavage of N–N and N–P bonds (**ts3-eq**, Figure 3.3**)** with an activation barrier of 24.8 kcal mol^{-1}. This is the rate-limiting step for the iminophosphorane formation, broadly consistent with room temperature reactivity (rapid evolution of N_2 gas in under 1h, *ca.* 22.0 kcal mol^{-1}

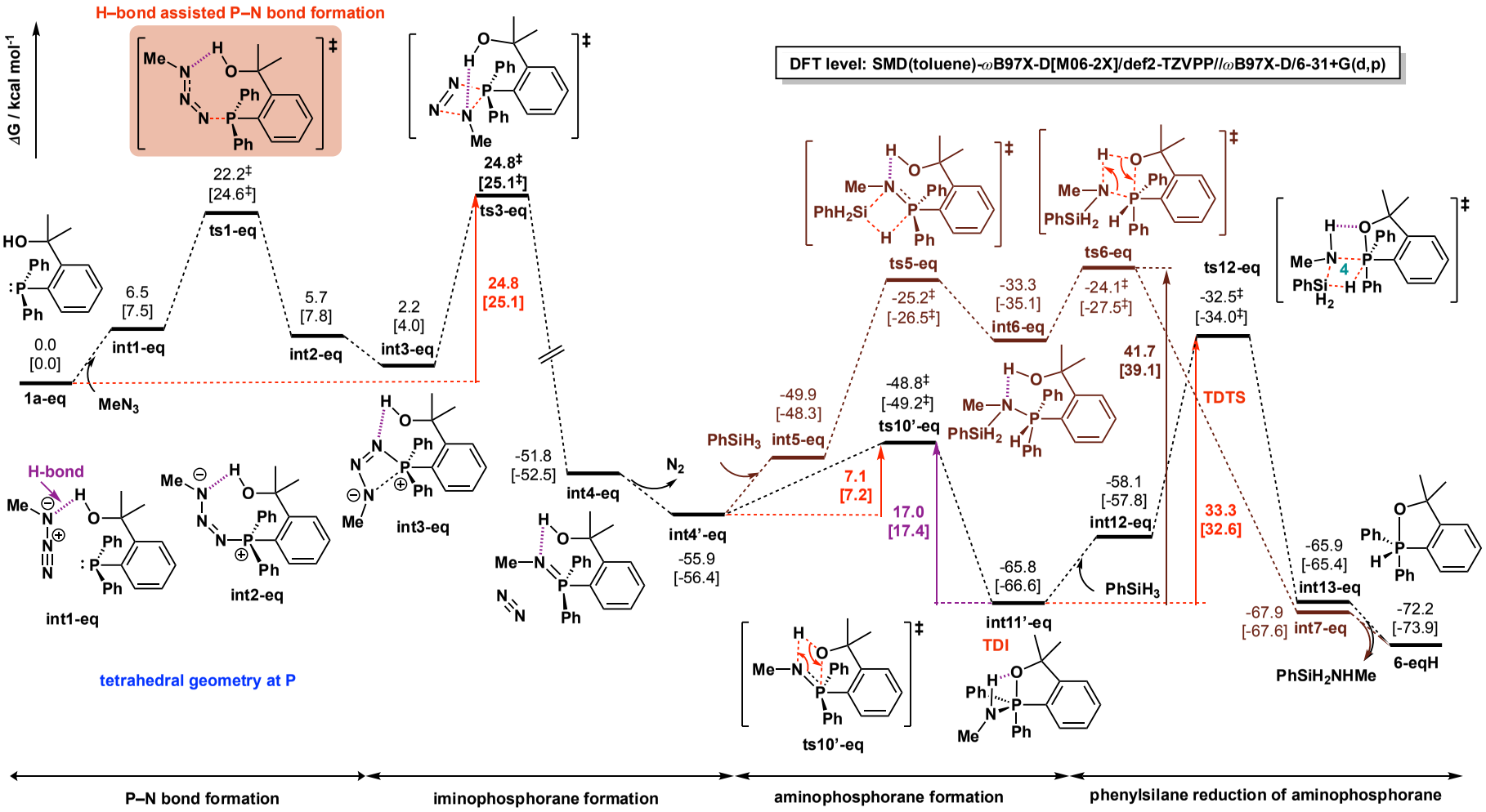

Figure 3.2. Gibbs energy profiles (corrected at 25ºC and 1 mol L^{-1}) for the overall reaction at SMD(toluene)-ωB97X-D[M06-2X]/def2-TZVPP//ωB97X-D/6-31+G(d,p) level of theory.

experimental barrier). The formation of iminophosphorane **int4-eq** is highly exergonic and therefore irreversible, driven by the entropically favourable loss of dinitrogen gas.

In a classical Staudinger reaction, the presence of water reduces the iminophosphorane to give an amine and phosphine oxide. To be catalytic, the phosphine species has to be regenerated from the phosphine oxide, where a strong P=O bond has to be reduced, usually by an external reductant. Phenylsilane has been employed in such fashions to reduce phosphine oxide to phosphine, thus sustaining the redox-driven P(III)/P(V) catalytic manifold.[270,274–276,306–310]

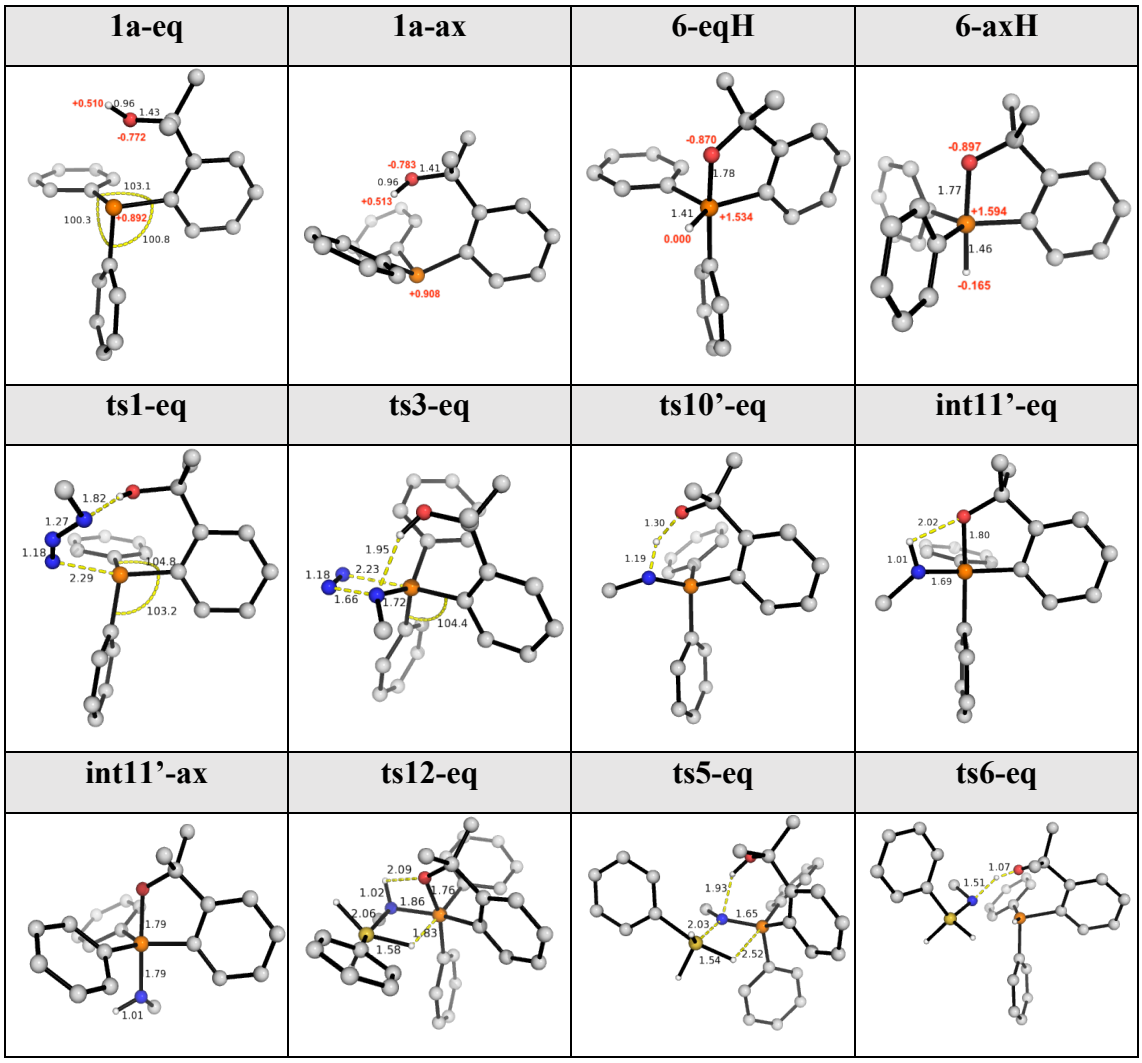

Figure 3.3. Selected optimised structures with their key geometry parameters. Bond distances are given in black in Å, angles are given in °. Where appropriate, NBO charges are given in red (first row).

Our bifunctional catalyst with a hydroxyl group in the close vicinity of the iminium N-atom presents interesting possibilities. Without phenylsilane, the iminium N-atom can easily deprotonate the hydroxyl proton (**ts10'-eq**, with a low activation barrier of 7.1 kcal mol^{-1}), as the resulting alkoxide attacks into the P=N double bond, giving a σ^5-P aminophosphorane (**int11'-eq**, Figure 3.3), which is exergonically downhill. Amino-phosphorane **int11'-eq** is 1.4 kcal mol^{-1} lower in energy than the corresponding **int11'-ax** that has the electronegative amine group axial at the P-centre (Figures 3.3 and 3.13), despite the apicophilicity of the N-atom, due to favourable hydrogen bonding present in **int11'-eq** (see subsection 3.3.4 for the pseudorotational TS connecting these two configurational isomers and their respective reduction by phenylsilane reductant).

In the presence of phenylsilane, the P–N bond of this σ^5-P aminophosphorane could be reduced to yield the silylamine product. Different mechanistic possibilities for this step were considered (Scheme 3.2). The concerted reduction of the P–N bond in the amino-phosphorane intermediate (Scheme 3.2 (b)), via hydride transfer either to the phosphorus centre (**ts12-eq** via a 4-membered TS, or **ts12'-eq** via a 6-membered TS with the help of one additional amine molecule) or to the N-atom in an umpolung fashion (**ts12u-eq**) all occur with relatively high reaction barriers (Figure 3.4) with **ts12-eq**, having a barrier of 33.3 kcal mol^{-1}, being the most likely TS by which the reduction of aminophosphorane P–N bond by the phenylsilane occurs (*vide infra*).

The stepwise reduction of the P–N bond was also considered (Scheme 3.2 (c)). Although the TS structure for the stepwise phenylsilane reduction of aminophosphorane could not be found, the charge-separated phosphonium silanehydride ion-pair is 34.0 kcal mol^{-1} higher than the turnover frequency-determining intermediate (TDI) **int11'-eq** so that the formation of stepwise reduction intermediate would require a barrier at least this high,

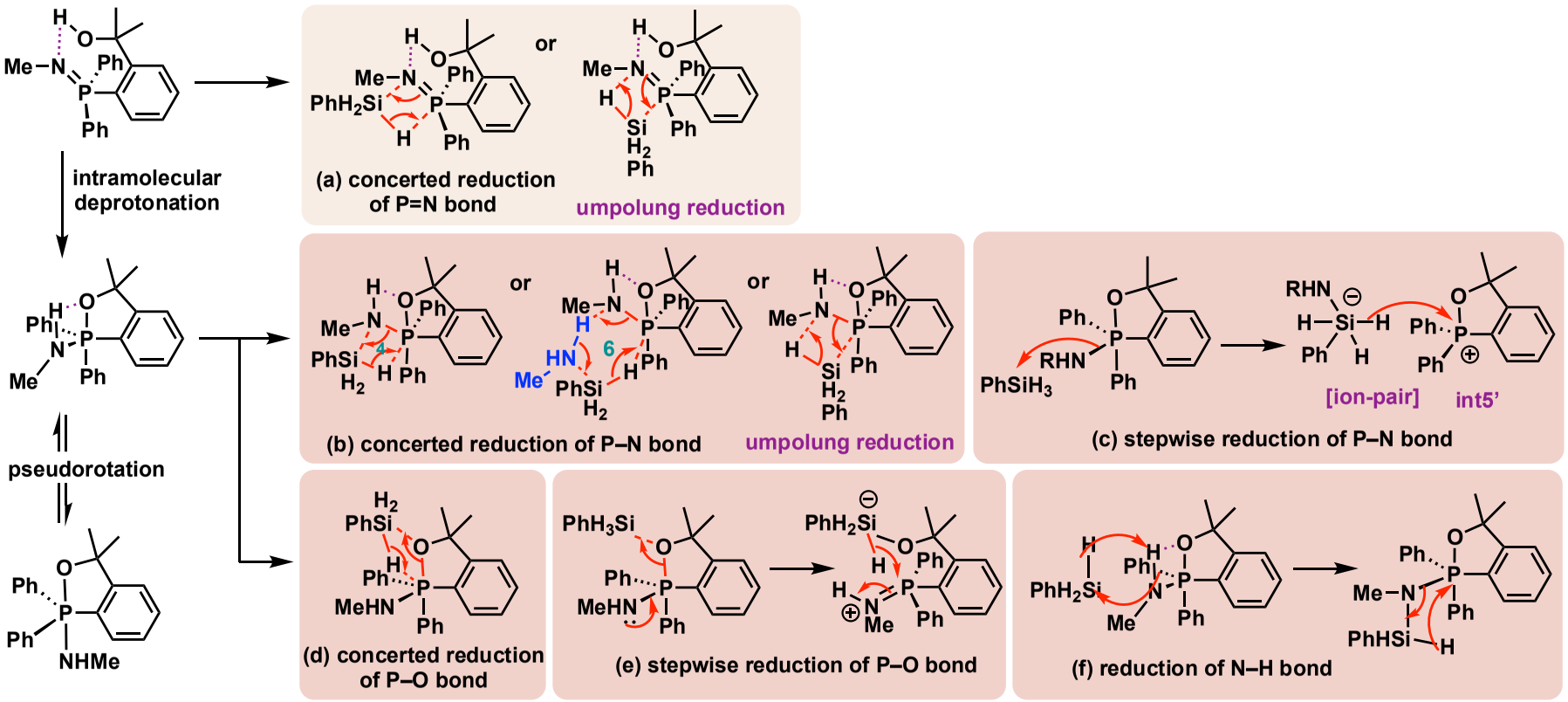

Scheme 3.2. Mechanistic possibilities for the phenylsilane reduction of iminophosphorane (a) and of aminophosphorane (b-f).

making this stepwise mechanism less competitive as compared to the concerted reduction of P–N bond in the equatorial aminophosphorane **ts12-eq**, although the subsequent hydride transfer to the phosphonium anion was found to be almost barrierless.

ts12-eq	**ts12-eq-c2**	**ts12-eq-c3**
$\Delta G^{\ddagger}$ = **-32.5‡ [-34.0‡]**	-30.1‡ [-31.9‡]	-30.0‡ [-31.1‡]
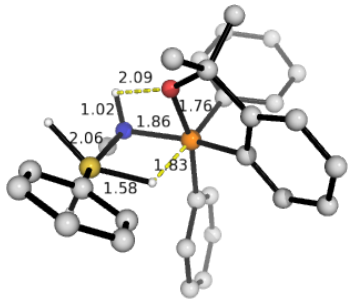	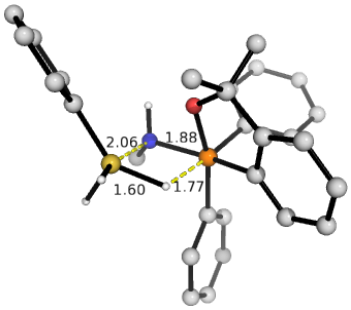	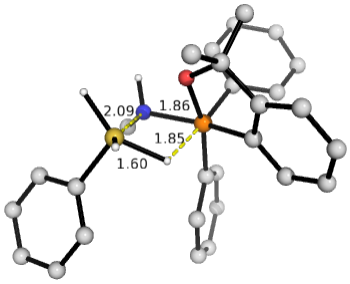
ts12i-eq-c1	**ts12i-eq-c2**	**ts12i-eq-c3**
-21.5‡ [-23.2‡]	-21.3‡ [-22.9‡]	-19.5‡ [-21.0‡]
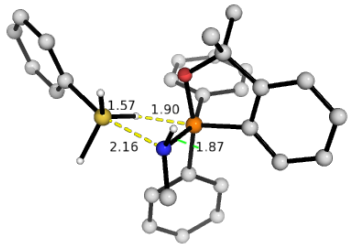	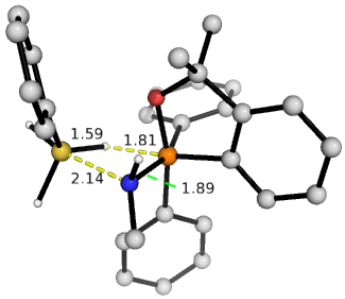	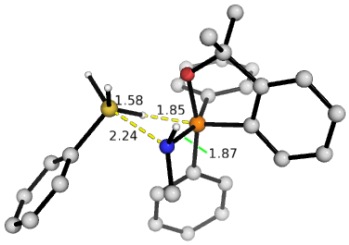
ts12n-eq	**ts12n-eq-c2**	**ts12n-eq-c3**
-21.2‡ [-22.9‡]	-11.6‡ [-12.2‡]	-16.3‡ [-18.1‡]
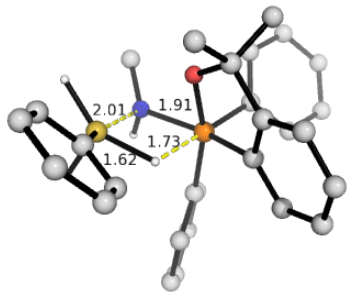	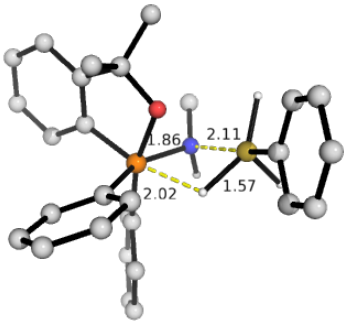	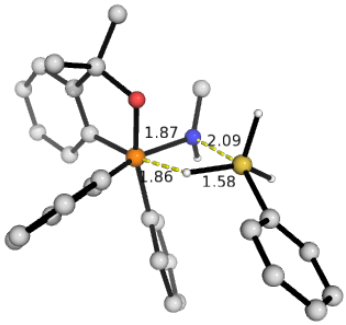
ts12'-eq	**ts12u-eq**	**ts12z-eq**
-21.2‡ [-22.9‡]	-11.6‡ [-12.2‡]	-16.3‡ [-18.1‡]

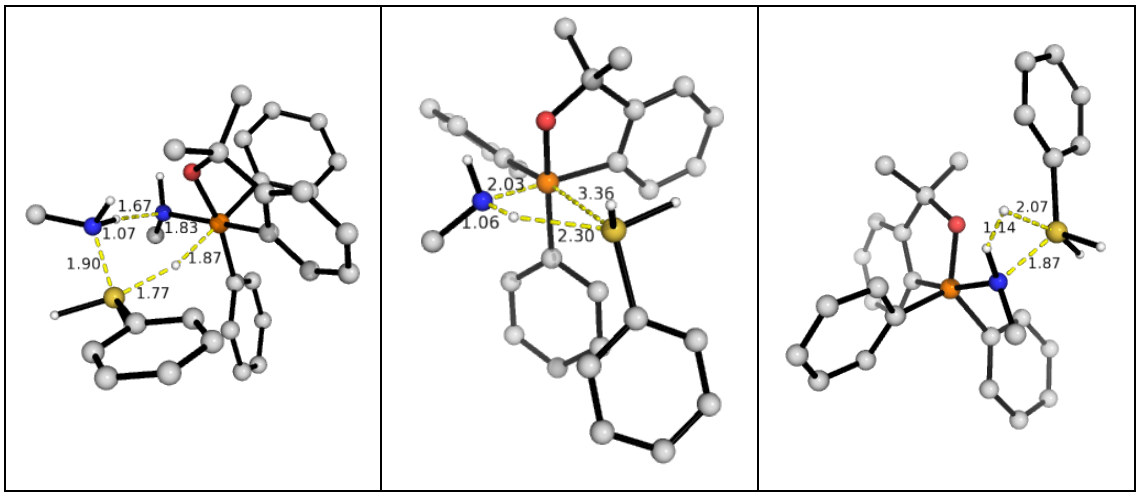

Figure 3.4. TS structures for the reduction of the equatorial aminophosphorane P–N bond. Conformers of TSs are labelled with a suffix of c1, c2, …, etc in order of increasing Gibbs energy. **ts12i** are the TSs with a different configuration at the N-centre. All $\Delta G^{\ddagger}$ values are given in kcal mol^{-1}.

The alternative reduction of the P–O bond of the aminophosphorane (Scheme 3.2 (d) and (e)) was considered to see if this would give any TS with lower activation barrier than **ts12-eq** (at -32.5‡ [-34.0‡] kcal mol^{-1}). No lower TSs were found after computational sampling of all possible TSs (Figure 3.5); these TSs are at least 5.4 kcal mol^{-1} higher in barriers than **ts12-eq**. In some of these TSs (**ts12o-eq-c1/c2/c3**), the reduction of the P–O bond seems to occur in a stepwise fashion by first forming a Si–O bond followed by hydride delivery to the P-centre (Scheme 3.2 (e)), rather than those TSs in a concerted manner (**ts12o-eq-c4/c5**) as shown in Scheme3.2 (d).

The possibility of reducing the N–H bond with the evolution of hydrogen gas followed by the reduction of the P–N bond in the resulting intermediate (Scheme 3.2 (f)) was considered. The TS for the reduction of N–H bond (**ts12z-eq**, at -16.3 kcal mol^{-1}, Figure 3.4) is 16.2 kcal mol^{-1} higher than **ts12-eq**. Therefore, this pathway is not kinetically favourable.

ts12o-eq-c1	ts12o-eq-c2	ts12o-eq-c3
$\Delta G^{\ddagger}$ = -27.1‡ [-28.0‡]	-24.5‡ [-26.3‡]	-21.5‡ [-24.0‡]
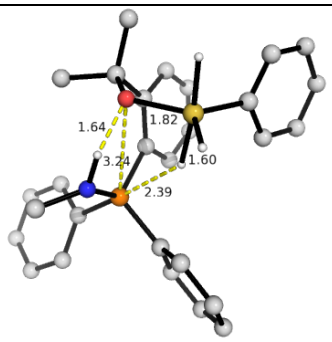	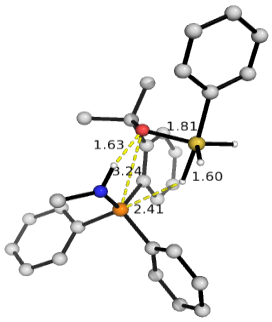	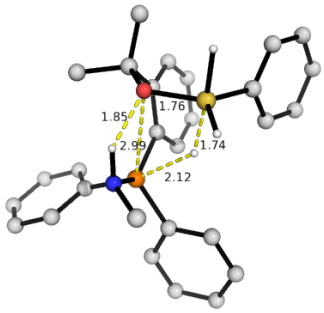
ts12o-eq-c4	**ts12o-eq-c5**	
-19.7‡ [-22.3‡]	-19.1‡ [-21.8‡]	
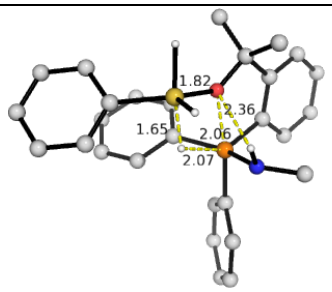	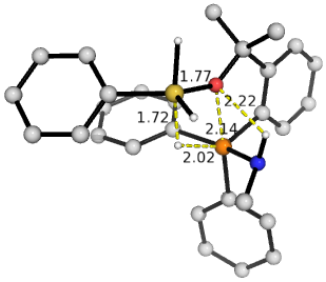	

Figure 3.5. TS structures for the reduction of the equatorial aminophosphorane P–O bond. Conformers and geometric isomers (inversion about N-atom) of TSs are labelled with a suffix of **c1**, **c2**, …, etc in order of increasing Gibbs energy. All $\Delta G^{\ddagger}$ values are given in kcal mol^{-1}.

The pseudorotation between different configurational isomers of the aminophosphorane and their respective reduction by phenylsilane were considered but no lower TSs were found (see subsection 3.3.4). The lowest barrier TS for the reduction of the amino-phosphorane is **ts12-eq** with a barrier of 33.3 kcal mol^{-1}; the negatively charged N atom (NBO charge = -1.049, Figure 3.6) attacks the positively charged Si (NBO charge = +0.931) on phenylsilane as the hydride (NBO charge = -0.165) is transferred to the positively charged P-centre (NBO charge = +1.971). This is consistent with the HOMO(aminophosphorane)–LUMO (phenylsilane) gap (0.34692 au) and the HOMO of the reduction TS showing such electron movements (Figure 3.6).

	Phenylsilane (PS)	Iminophosphorane	Aminophosphorane
NBO charges	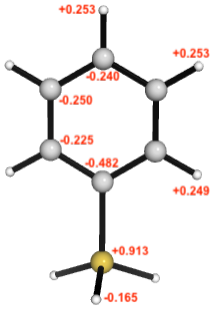	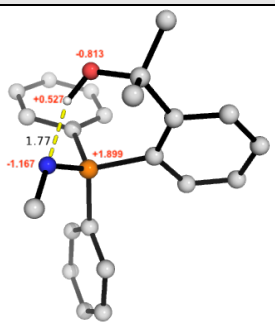	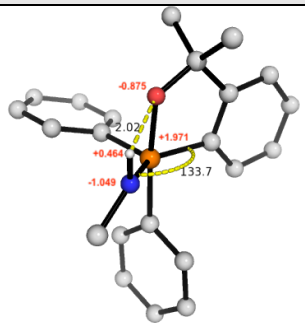
HOMO with energy / au	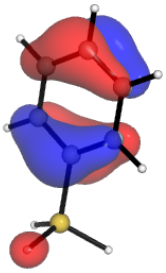	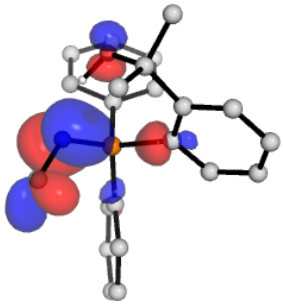	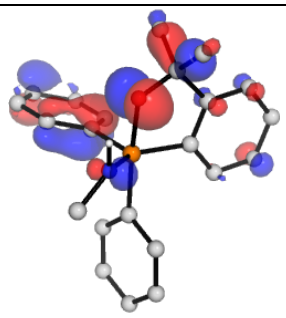
	-0.33380	-0.28363	-0.30891
LUMO with energy / au	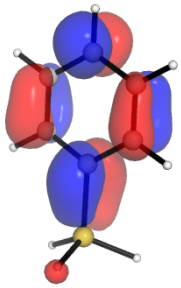	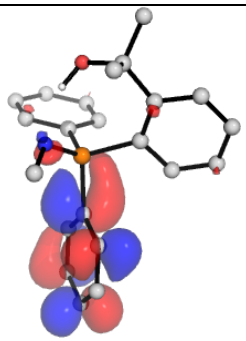	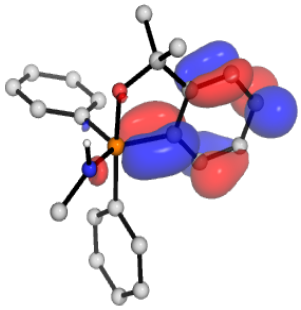
HOMO(PS)-LUMO gap/ au		0.36136	0.3696
HOMO-LUMO(PS) gap/ au		0.32164	0.34692

Reduction of iminophosphorane	Reduction of aminophosphorane
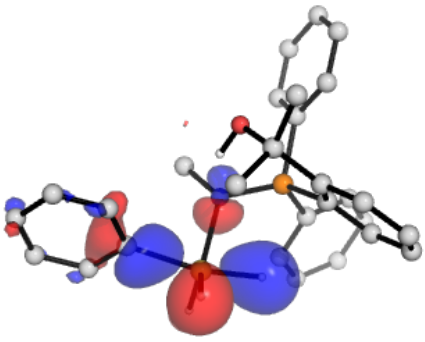	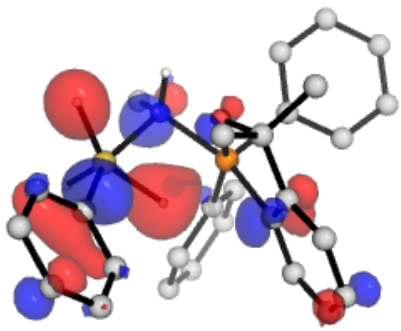

Figure 3.6. Top: Optimised structure, NBO charges and FMOs of phenylsilane, iminophosphorane and aminophosphorane and relevant HOMO-LUMO gaps. **Bottom**: HOMO of reductions by phenylsilane.

The other possibility is the direct reduction of the P=N bond of σ^3-P iminophosphorane **int4'-eq** by phenylsilane (Scheme 3.2 (a) and the brown energy pathway, Figure 3.2). As per reduction of aminophosphorane, the reduction of the iminophosphorane occurs as its N-atom (NBO charge = -1.167, Figure 3.6) attacks the Si-centre on the reductant while the hydride is transferred to the P-centre (NBO charge = +1.899). This is again consistent with the HOMO (iminophosphorane)–LUMO (phenylsilane) gap (0.32164 au) and the reduction TS HOMO (Figure 3.6). The umpolung reduction by the transfer of hydride from phenylsilane to the nucleophilic N-atom of iminophosphorane is impossible based on NBO charges and MO analysis. Indeed, this TS (**ts5u-eq**) has a much higher barrier (by 13.4 kcal mol^{-1}) than **ts5-eq** (Figure 3.7).

ts5-eq	**ts5u-eq**	**ts6-eq**
$\Delta G^{\ddagger}$ = -25.2‡ [-26.5‡]	-11.8‡ [-11.8‡]	-24.1‡ [-27.5‡]
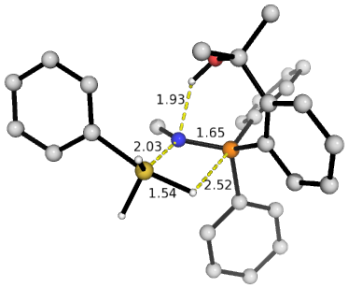	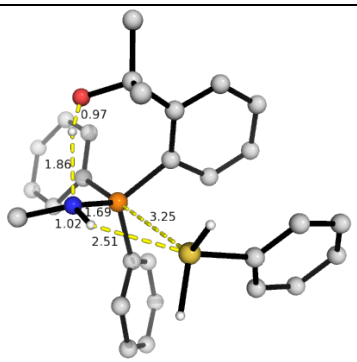	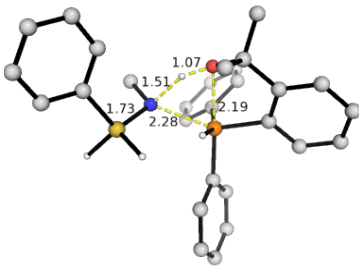

Figure 3.7. TS structures for the reduction of the equatorial iminophosphorane P=N bond. All $\Delta G^{\ddagger}$ values are given in kcal mol^{-1}.

The σ^3-P iminophosphorane intermediate can either be first reduced by phenylsilane (**ts5-eq**) followed by the deprotonation of the intermediate (**ts6-eq**) or first deprotonate to form the σ^5-P aminophosphorane followed by phenylsilane reduction. Although the apparent activation barrier for the reduction of the iminophosphorane P=N bond (from **int4'-eq** to **ts6-eq**, at 31.8 kcal mol^{-1}) is lower than the reduction of aminophosphorane (**ts12-eq**, at

33.3 kcal mol^{-1}) (within less than 2 kcal mol^{-1}), the low barrier of aminophosphorane formation (**ts10-eq**, at 7.1 kcal mol^{-1}) implicates that the formation of the amino-phosphorane from the iminophosphorane is facile, such that the aminophosphorane **int11'-eq** will be the TOF-determining intermediate (TDI). Thus, according to the energetic span model,[125] the true activation barrier for the reduction of the imino-phosphorane is the energetic span from **int11'-eq** to **ts6-eq**, giving a barrier of 41.7 kcal mol^{-1} (Figure 3.2). This indicates that the reduction of the iminophosphorane P=N bond is more difficult than the corresponding reduction of the aminophosphorane P–N bond for the present case. In fact, the reduction of the iminophosphorane P=N bond (**ts6-eq**, at -24.1 kcal mol^{-1}) is 8.4 kcal mol^{-1} kinetically *less* favourable than the reduction of the aminophosphorane P–N bond (**ts12-eq**, at -32.5 kcal mol^{-1}).

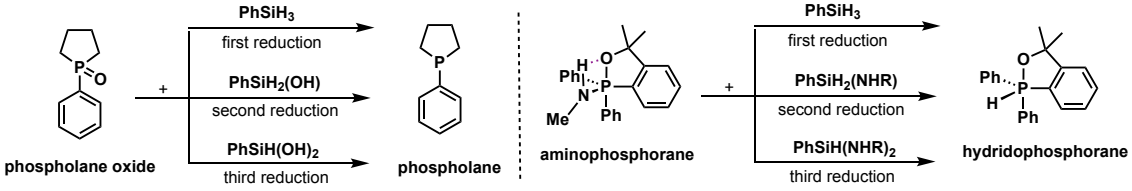

Scheme 3.3. Sequential reduction by phenylsilane and its reduction product.

We wonder if the silylamine product $PhSiH_2NHR$ from the reaction can better reduce the aminophosphorane intermediate than phenylsilane $PhSiH_3$, in a similar fashion where the silanol by-product from the phenylsilane reduction of phospholane oxide (containing a P=O bond) can further reduce phospholane oxide substrate[311] (Scheme 3.3). The energy profile for the sequential reduction of the aminophosphorane intermediate is shown in Figure 3.8. We see that the second reduction of aminophosphorane by silylamine $PhSiH_2(NHR)$ (**ts12b-eq**) has a barrier of 25.1 kcal mol^{-1} that is quite a lot lower (by 8.2 kcal mol^{-1}) than the first reduction of aminophosphorane by phenylsilane $PhSiH_3$ (**ts12-eq**; 33.3 kcal mol^{-1}). This is the same as the reactivity trend observed in reference[311]

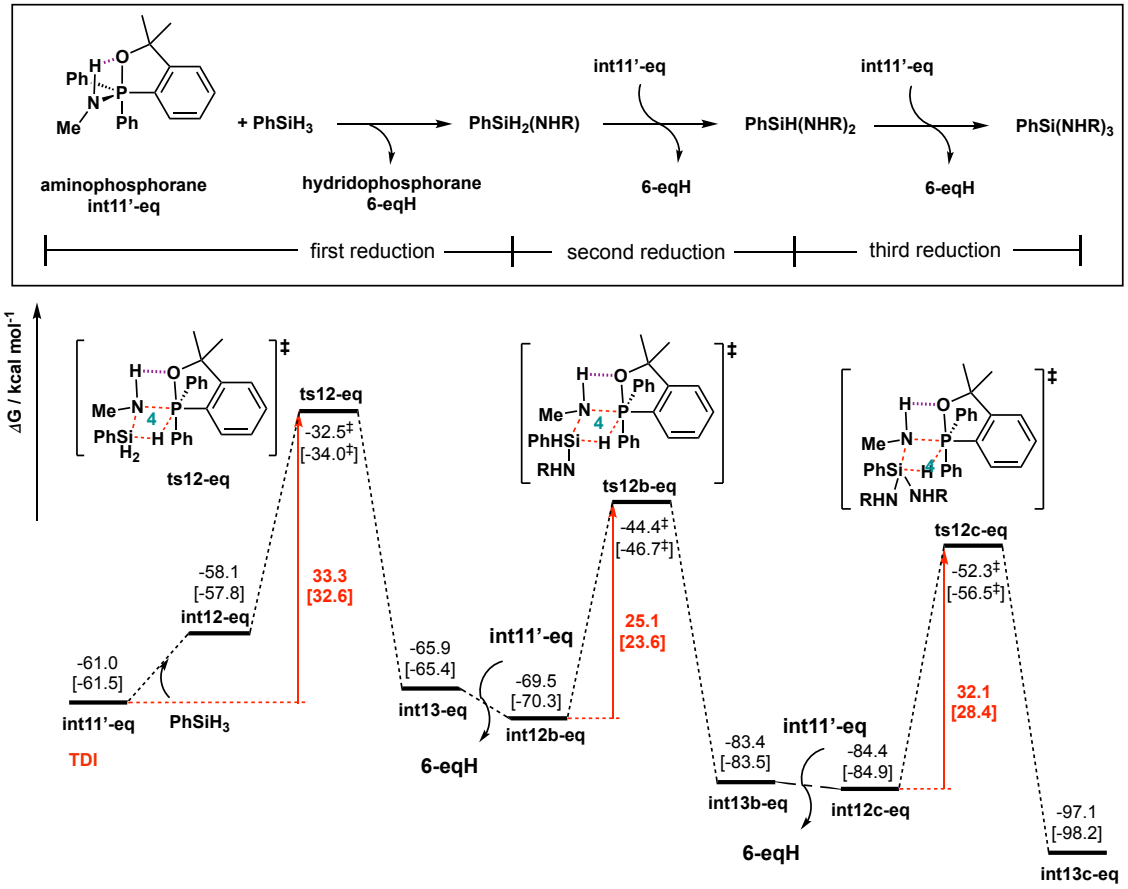

Figure 3.8. Gibbs energy profile for the reduction of aminophosphorane intermediate sequentially by phenylsilane and its silylamine and silyldiamine variants.

(Scheme 3.3) where the silanol reduction of P=O bond (second reduction, with a barrier of 25.2 kcal mol^{-1}) is easier (by 4.3 kcal mol^{-1}) than the phenylsilane reduction of the P=O bond (first reduction, with a barrier of 29.5 kcal mol^{-1}).

After considering all these possibilities, we propose that the reaction proceeds via the reduction of the P–N bond of aminophosphorane with a Gibbs energy barrier of 33.3 kcal mol^{-1} (**ts12-eq**). The silylamine formed can further be used to reduce the P–N bond of aminophosphorane with a much lower barrier of 25.1 kcal mol^{-1} (**ts12b-eq**), broadly consistent with room temperature reactivity. Using simple TST, a reaction that occurs at room temperature under 1 hour has an activation barrier of about 22.0 kcal mol^{-1}. The deviation of about 3 to 10 kcal mol^{-1} in this case potentially result from the inadequacies

in the computational model in describing such class of reactions. For example, the prototypical Staudinger reduction of PH_3 and N_3H studied computationally using the standard model chemistry B3LYP/6-31G(d) reported an overall activation barrier of *ca.* 40 kcal mol^{-1}.[305] We know that B3LYP exchange-correlation functional, lacking dispersion, overpredicts activation barrier due to its lack of ability to describe attractive van der Waals interactions. Although our use of dispersion-corrected ωB97X-D functional corrects some of these errors, other sources of error such as inaccurate description of the solvation free energy,[312] could result in this discrepancy between computation and experiment.

We recomputed the reaction energy profile using the relative enthalpies and energies, with solvent and zero-point energy (ZPE) correction, at the SMD(toluene)-ωB97X-D/def2-TZVPP//ωB97X-D/def2-SVP level (Figure 3.9). We first observe that both the relative enthalpies and the energies agree very well with each other (within 1 kcal mol^{-1}). Additionally, the reaction profile is not particularly different from the Gibbs energy profile in Figure 3.2, except that the reaction barriers are now more compatible with the reaction temperature. We can see from Figure 3.9 that the activation barrier, measured in relative enthalpy (energy), for the loss of N_2 gas in the iminophosphorane formation (**ts3-eq**, 21.9 (22.0) kcal mol^{-1}) is very close to that for the phenylsilane reduction of the aminophosphorane (**ts12-eq**, 21.7 (23.2) kcal mol^{-1}), which are consistent with room temperature reactivity. We see that the activation barriers for **ts3-eq** are similar using Gibbs energy (24.8 kcal mol^{-1}, Figure 3.2), enthalpies and energy, but quite different for **ts12-eq** (33.3 kcal mol^{-1}), when the dinitrogen gas was "taken out" of the reaction profile. It is worth emphasising that when the dinitrogen gas is not involved in the energy profile,

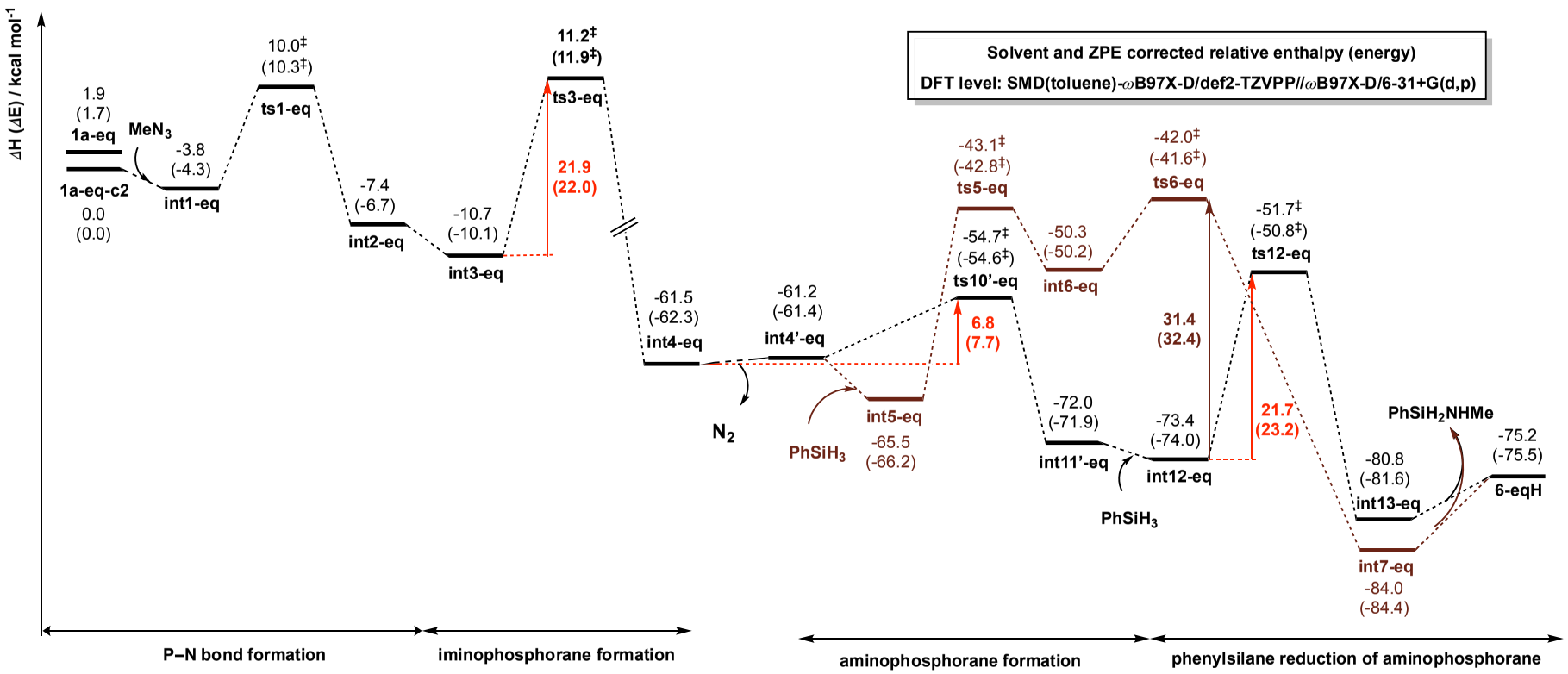

Figure 3.9. Enthalpies and energy profiles for the overall reaction at SMD(toluene)-ωB97X-D/def2-TZVPP//ωB97X-D/6-31+G(d,p) level of theory, with solvent and ZPE correction.

as in the catalyst regeneration (subsection 3.3.3, Figure 3.11), the relative Gibbs energy, enthalpy and energy profiles all agree with one another, suggesting that the Gibbs energy profile might be artificially affected by the dinitrogen gas moving in and out of the energy profile.

3.3.3 Regeneration of catalyst

Following this pathway, we note that only the equatorial form of the hydridophosphorane **6-eqH** is formed. However, this species was not observed experimentally; instead only the axial form **6-axH** was observed via experimental NMR. Computations suggest greater thermodynamic stability for **6-axH** (by $\Delta\Delta G = 5.1$ kcal mol^{-1}), potentially due to its better sterics (the substituents on P-atom in **6-axH** are more spaced out, although it is difficult to see from the NCI plots, Figure 3.10). If interconversions were relatively fast at room temperature, then **6-axH** would be the sole species observed by experimental NMR.

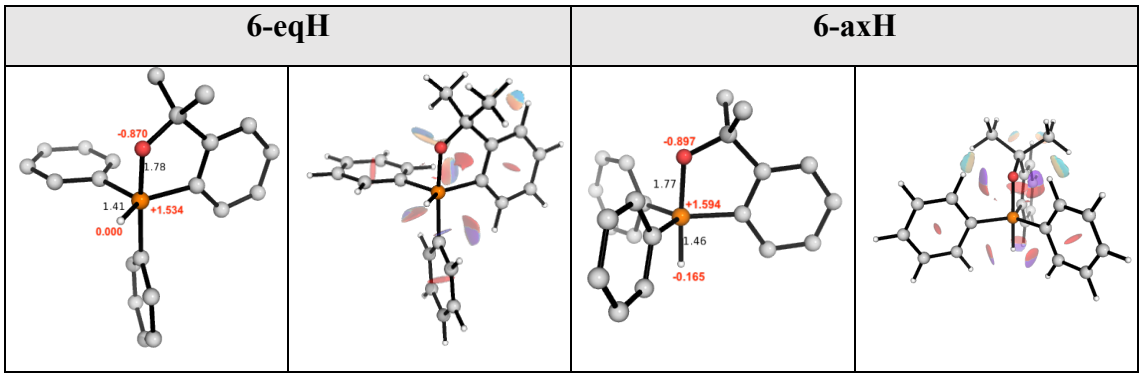

Figure 3.10. Optimised structures of hydridophosphoranes with key bond distances given in black and NBO charges given in red. NCI plots are also shown.

We investigated all possible pathways leading from **6-eqH** (Figure 3.11). First, we note that the relative Gibbs energy, enthalpy and energy profiles agree with each other very well; all relevant activation barriers have similar magnitudes. Gibbs energy values are used for discussion. We found that **6-eqH** can undergo a facile pseudorotation to give **6-axH**, with a barrier of 24.6 kcal mol^{-1} which is close to its intramolecular reductive elimi-

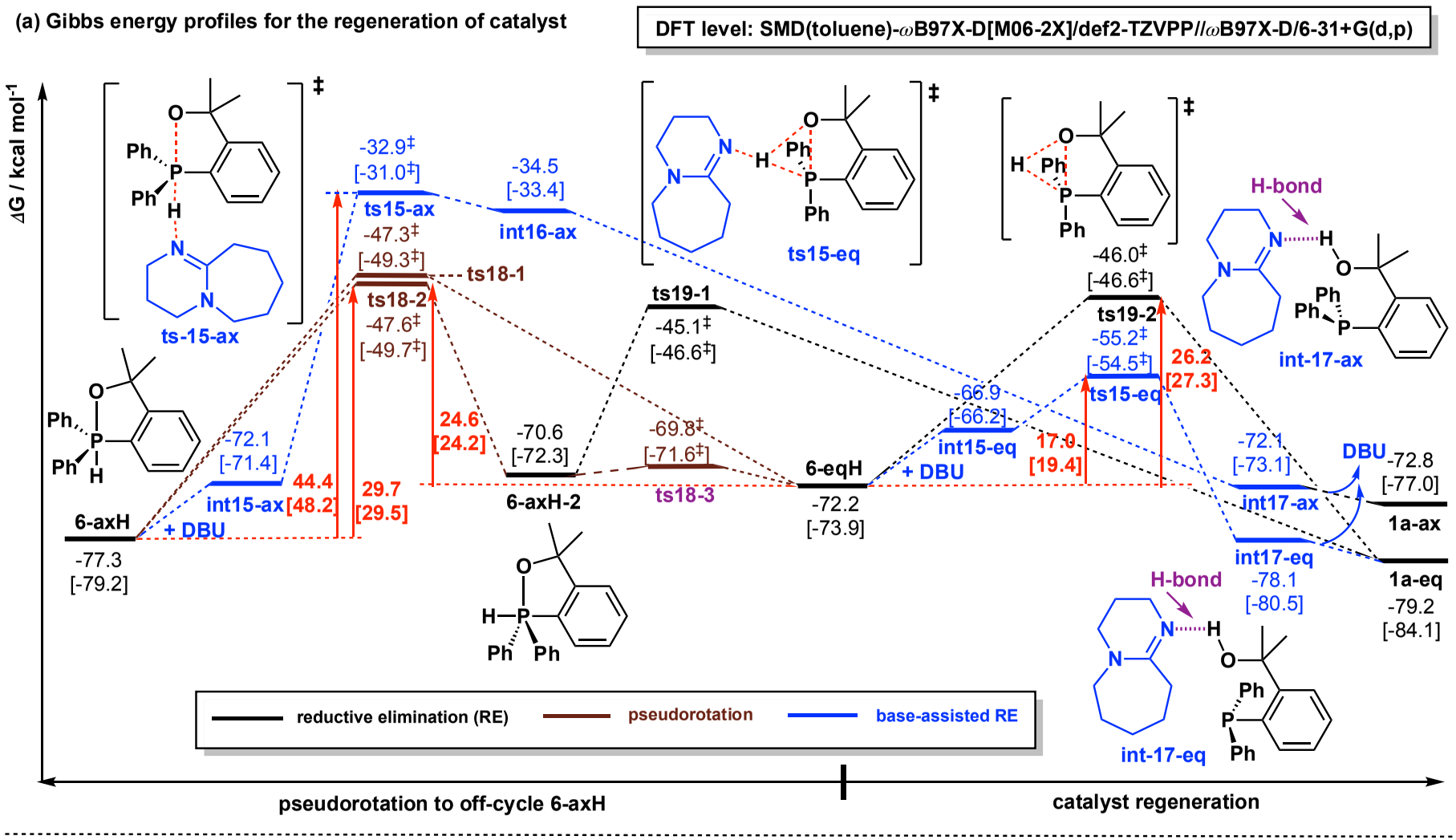
(a) Gibbs energy profiles for the regeneration of catalyst
DFT level: SMD(toluene)-ωB97X-D[M06-2X]/def2-TZVPP//ωB97X-D/6-31+G(d,p)
ΔG / kcal mol-1
ts-15-ax
6-axH
-77.3
[-79.2]
-72.1
[-71.4]
int15-ax
+ DBU
44.4
[48.2]
-32.9‡
[-31.0‡]
ts15-ax
-47.3‡
[-49.3‡]
ts18-1
ts18-2
-47.6‡
[-49.7‡]
29.7
[29.5]
24.6
[24.2]
-34.5
[-33.4]
int16-ax
-70.6
[-72.3]
6-axH-2
ts19-1
-45.1‡
[-46.6‡]
-69.8‡
[-71.6‡]
ts18-3
ts15-eq
6-eqH
-72.2
[-73.9]
-66.9
[-66.2]
int15-eq
+ DBU
17.0
[19.4]
-46.0‡
[-46.6‡]
ts19-2
-55.2‡
[-54.5‡]
ts15-eq
26.2
[27.3]
H-bond
int-17-ax
-72.1
[-73.1]
int17-ax
DBU
-72.8
[-77.0]
1a-ax
int17-eq
-78.1
[-80.5]
H-bond
1a-eq
-79.2
[-84.1]
int-17-eq
reductive elimination (RE)
pseudorotation
base-assisted RE
pseudorotation to off-cycle 6-axH
catalyst regeneration

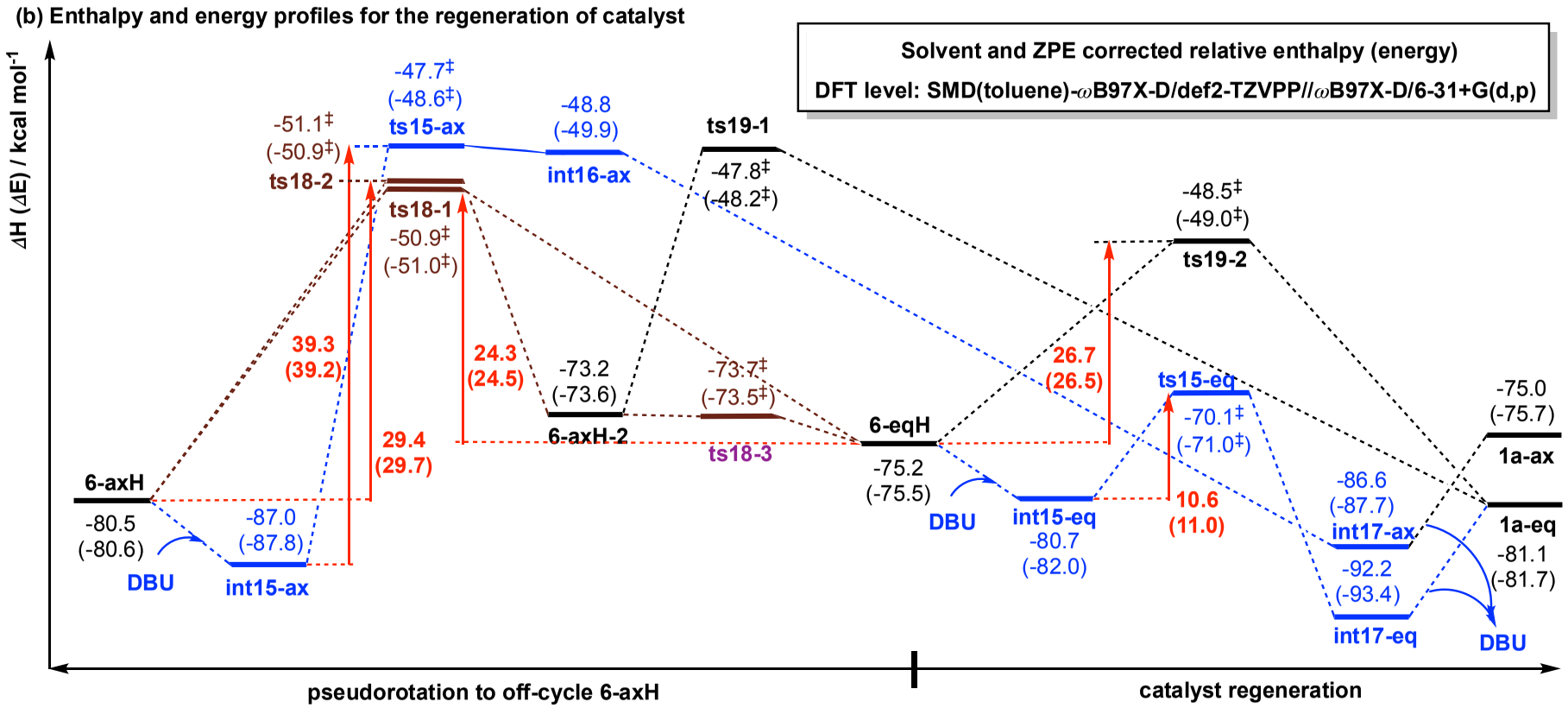

Figure 3.11. (a) Gibbs energy profile (corrected at 25ºC and 1 mol L^{-1}) at SMD(toluene) -ωB97X-D[M06-2X]/def2-TZVPP//ωB97X-D/6-31+G(d,p) level of theory, and (b) enthalpy and energy profiles (solvent and ZPE corrected) for the regeneration of hydroxyphosphine catalyst from the hydridophosphoranes at SMD(toluene)-ωB97X-D/def2-TZVPP//ωB97X-D/6-31+G(d,p) level of theory.

nation (**ts19-2**, barrier of 26.2 kcal mol^{-1}) for catalyst regeneration. The closeness of these barriers implicates that the formation of axial hydridophosphorane **6-axH** directly competes with the regeneration of the catalyst **1a-eq**.

The pseudorotational barrier from **6-axH** to **6-eqH** is about 29.7 kcal mol^{-1} ($\Delta H^{‡}$ = 29.4 kcal mol^{-1}; $\Delta E^{‡}$ = 29.7 kcal mol^{-1}), making this thermally less accessible at room temperature. The intramolecular reductive elimination of the axial hydridophosphorane **6-axH** was considered. Although the axial-axial reductive coupling is symmetry-allowed according to Woodward-Hoffmann rules,[313] a TS was not found, possibly because the oxygen atom forms part of the rigid oxyphosphorane ring and could not be brought close to P–H for conducive orbital overlap since doing so would incur hugely unfavourable sterics due to geometrical distortion; the reductive elimination of **6-axH** would have to pass through the equatorial form before it could occur.

Driven by the experimental observation that the addition of an exogenous base can accelerate the reaction, we explored the role of base DBU on the mechanism of catalyst regeneration from the hydridophosphorane **6-eqH**. To our delight, we found that the barrier for hydroxyphosphine catalyst regeneration, via a base-assisted reductive elimination (**ts15-eq**), is lowered to 17.0 kcal mol^{-1}, so that the regeneration of the catalyst outcompetes the formation of **6-axH**. The reprotonation of the deprotonated **6-eqH** follows almost immediately (barrierless, IRC analysis) to give **int17-eq**, in agreement with previous observation that intermediate ion-pair is short-lived, especially in non-polar solvent (toluene here), with a very small barrier (< 4 kcal mol^{-1}) for reprotonation.[296] Base-assisted deprotonation of **6-axH**, on the other hand, is much more difficult (**ts15-ax**, 44.4 kcal mol^{-1}). The differences in the reactivities of the hydridophosphoranes with DBU can be traced to their different electronic structures (Figure 3.12) and the differences

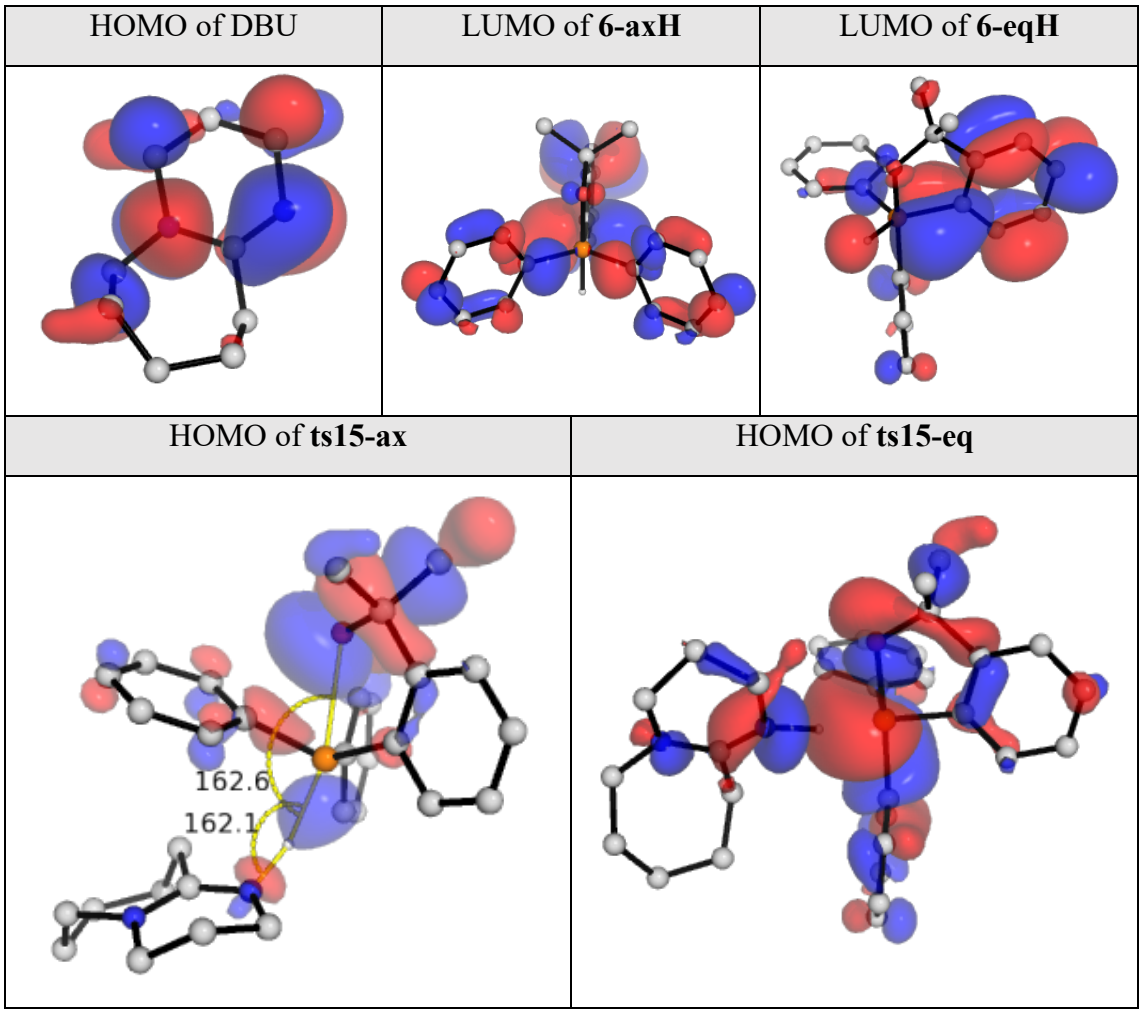

Figure 3.12. FMO diagrams of the relevant structures in the DBU-assisted regeneration of the hydroxy-phosphine catalyst from the hydridophosphoranes. Isosurface value of 0.025 is used.

in the acidities of the protons on these hydridophosphoranes (NBO charges, Figure 3.10). The poor overlap between the LUMO of **6-axH** and the HOMO of DBU (shown by the HOMO of **ts15-ax**, Figure 3.12) results in the high TS barrier. On the other hand, there is a maximal overlap between the LUMO of **6-eqH** and the HOMO of DBU (shown by the HOMO of **ts15-eq**), allowing effective deprotonation to occur. Inspection of the MO energies indicated that the LUMO of **6-axH** is 0.6 kcal mol^{-1} higher than that of **6-eqH**, giving a slightly worse, albeit negligible energy mismatch with the HOMO of DBU. The predominant FMO symmetry mismatch in **6-axH** contributes to the increased difficulty in its deprotonation. In addition, the proton in **6-eqH** is more acidic (NBO charge = 0.000)

than that in **6-axH** (NBO charge = -0.165), making the former more susceptible to base deprotonation.

Thus, we have shown that the pseudorotation from **6-axH** to **6-eqH** is difficult and that the reductive elimination of **6-axH** to regenerate the hydroxyphosphine is unlikely. In addition, its deprotonation (**6-axH**) by an exogenous base involves a high activation barrier. From these observations, it is likely that **6-axH** is formed from the pseudorotation of **6-eqH** after the latter is formed in the phenylsilane reduction of aminophosphorane and thence becomes off-cycle.

3.3.4 Reduction of configurational isomers of aminophosphoranes

The intermediate formed after the loss of dinitrogen, **int4'-eq**, is an iminophosphorane. As discussed, this iminophosphorane can be easily converted to the corresponding aminophosphorane, which can be further reduced (**ts12-eq**, $\Delta G^{\ddagger}$ = 33.3 kcal mol^{-1} and **ts12b-eq**, $\Delta G^{\ddagger}$ = 25.1 kcal mol^{-1}, Figure 3.8) to give hydridophosphorane and silylamine / silyldiamine. To check if this aminophosphorane, with the amino-group equatorial to the P(V) centre, undergoes facile pseudorotations to give any configurational isomer that can be more easily reduced by phenylsilane, we explored all the interconversions between these possible isomers and their subsequent reduction by phenylsilane (Figure 3.13). Although apicophilicity at P(V) centre predicts that the more electron-withdrawing amino-group would occupy the axial position,[314] making the configurational isomer **int11'-ax** more thermodynamically stable than **int11'-eq**, the latter is actually more stable, by 1.4 kcal mol^{-1}, due to its ability to form productive hydrogen bonding between the oxyphosphorane-O atom and the amino-H atom (Figure 3.13), which can stabilise the structure more than apicophilicity or any unfavourable sterics.

(a)			
int11'-eq (1)	**int11'-ax (2)**	**int11'-ax2 (3)**	**int11'-eq2 (4)**
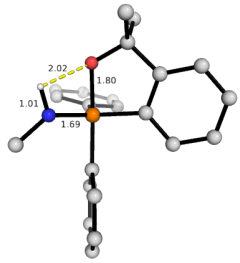	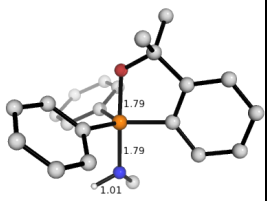	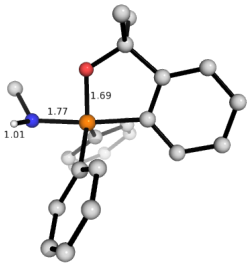	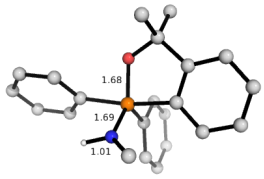
ΔΔG = 0.0 [0.0]	1.4 [0.2]	5.3 [5.1]	2.1 [2.4]
(b)			
ts-rot-13	**ts-rot-24**	**ts-rot-23**	**ts-rot-14**
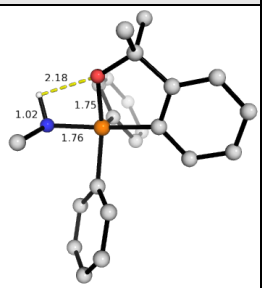	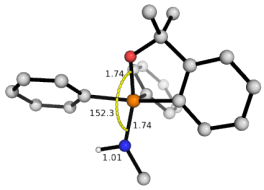	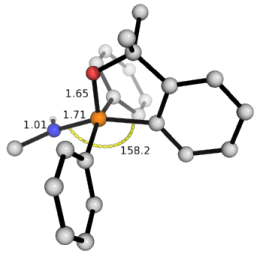	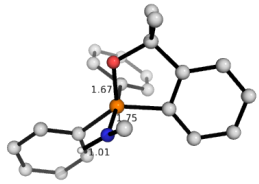
$\Delta G^{\ddagger}$ = 20.8 [20.9]	13.2 [12.7]	21.3 [20.8]	27.5 [26.5]
(c)			
ts12-eq	**ts12-ax**	**ts12-ax2**	**ts12-eq2**
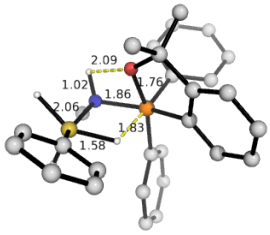	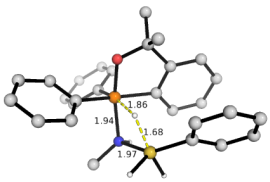	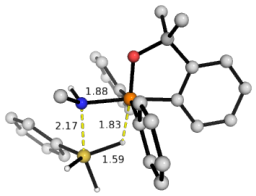	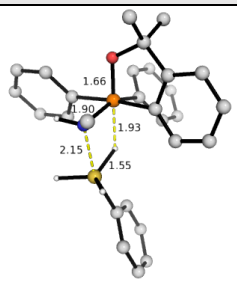
$\Delta G^{\ddagger}$ = 33.3 [32.6]	40.1 [41.0]	44.9 [43.8]	40.7 [39.2]

Figure 3.13. PyMol structures of **(a)** optimised configurational isomers of aminophosphoranes, **(b)** pseudorotational TSs for the interconversions of aminophosphoranes, relative to **int11'-eq** and **(c)** TSs of phenylsilane reduction of each configurational isomer. Non-polar protons are ignored for clarity. All values are given in kcal mol^{-1}.

We can see that the pseudorotations between the configurational isomers can be facile but have a large range of barriers (13.2 – 27.5 kcal mol^{-1}). The phenylsilane reduction of any other configurational aminophosphorane (Figure 3.13 (c)) has higher activation barriers than the reduction of the equatorial form of the aminophosphorane (**ts12-eq**, 33.3 kcal mol^{-1}).

3.3.5 Alternative possible mechanism for 1a-eq

For the pathways discussed in subsection 3.3.2, the overall energetic span for the overall transformation is ΔG = 33.3 kcal mol^{-1} (**ts12-eq**) or ΔH = 21.9 kcal mol^{-1} (**ts3-eq**) or ΔE = 23.2 kcal mol^{-1} (**ts12-eq**). We found an alternative pathway with an overall activation barrier of ΔG = 26.2 kcal mol^{-1}, where a stepwise reduction of phosphazide intermediate was implicated (Figure 3.14).

After the first P–N bond formation, the phosphazide intermediate **int2-eq**, facilitated by hydrogen bonding, could easily deprotonate the hydroxyl moiety of the bifunctional catalyst (**ts20-eq** at 12.0 kcal mol^{-1}), giving **int21-eq** stabilised by hydrogen bonding. In the presence of phenylsilane reductant, *stepwise* reduction of the phosphazie intermediate **int21-eq** gives a phosphonium silanehydride ion-pair **int23-eq** which further undergoes facile hydride transfer to give a mixture of axial and equatorial hydridophosphoranes **6-eqH** and **6-axH** (LUMO of phosphonium cation has roughly equal coefficients axial and equatorial to phosphorus atom, Figure 3.15). This step (**ts22-eq**) is driven by the loss of N_2 gas which is highly entropically favoured. The intermediate **int23-eq** immediately after stepwise reduction has the silanehydride Si–H in equatorial plane of phosphonium P-atom, which, given the very low barrier for the subsequent hydride transfer (1.8 kcal mol^{-1}, **ts23-eq**), readily forms equatorial hydridophosphorane **6-eqH**.

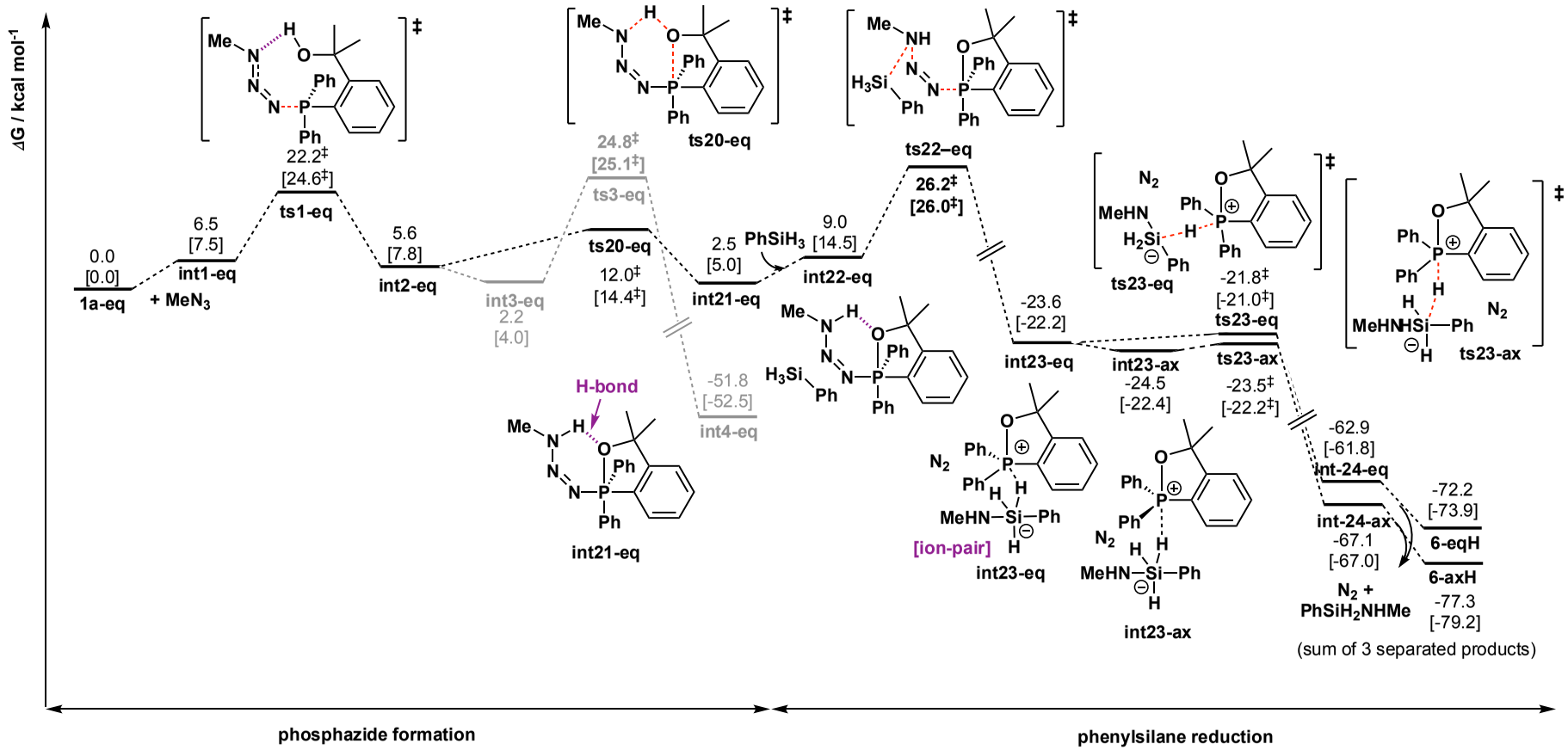

Figure 3.14. Gibbs energy profile (corrected at 25ºC and 1 mol L^{-1}) for the stepwise phenylsilane reduction of phosphazide intermediate formed from **1a-eq**, computed at SMD(toluene)-ωB97X-D[M06-2X]/def2-TZVPP//ωB97X-D/6-31+G(d,p) level of theory.

The ion pair could also readily equilibrate due to non-directional interactions in contact ion-pairs in non-polar solvents such as toluene,[296] interconverting between **int23-eq** and **int23-ax**. In **int23-ax**, silanehydride Si–H is axial to phosphonium P-atom, such that following a small barrier (1.0 kcal mol^{-1}), axial hydridophosphorane **6-axH** could be formed. If this mechanism is true, then, it implicates direct access to both axial and equatorial forms of hydridophosphoranes **6-eqH** and **6-axH**. Since the hydride transfer is highly exergonic and irreversible, the exact ratio of **6-eqH : 6-axH** formed would be dictated by the difference between the activation barrier of **ts23-eq** and the barrier of the conversion from **int23-eq** to **int23-ax**.

LUMO of phosphonium cation	HOMO of silanehydride anion
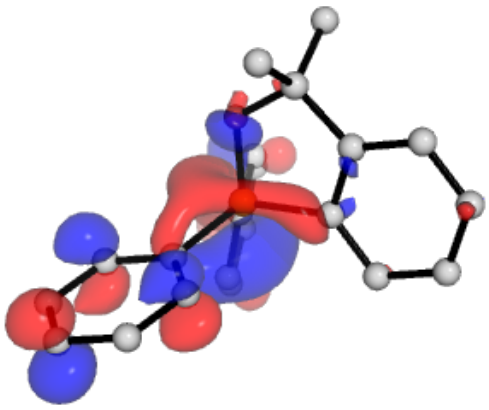	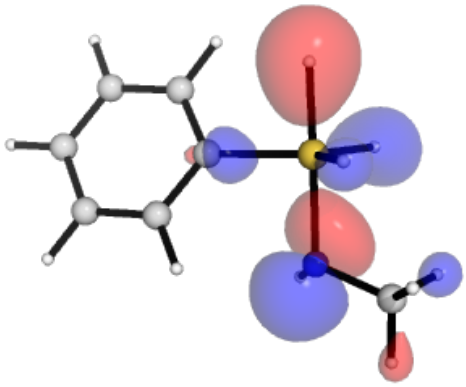

Figure 3.15. MO diagrams of the phosphonium cation and silanehydride anion. The optimisations of phosphonium species resulting from axial and equatorial hydridophosphorane give the same structure.

Although the overall barrier here is lower than the overall barrier of the pathways discussed in subsection 3.3.2, the direct loss of N_2 in the iminophosphorane formation (**ts3-eq**) is highly exergonic and irreversible and has a lower barrier (24.8 kcal mol^{-1}) than the stepwise reduction of the phosphazide intermediate (**ts22-eq**, 26.2 kcal mol^{-1}), and is thus more likely, despite the formal [2+2] cycloreversion being symmetry-disallowed.[315]

3.3.6 Reaction pathways for axial hydroxyphosphine catalyst 1a-ax

The reaction of conformer **1a-ax** (6.4 kcal mol^{-1} higher than **1a-eq**, translating to 1 in ~7000) was investigated for completeness. The reaction pathway for **1a-ax** is very similar to that for **1a-eq**. The energy profile is shown in Figure 3.16. In this case, the TDTS for the iminophosphorane formation is the concerted loss of N_2, **ts3-ax**, at 33.2 kcal mol^{-1}, relative to the lowest energy conformer of the hydroxyphosphine catalyst, **1a-eq**. The subsequent phenylsilane reduction of the iminophosphorane intermediate (**ts5-ax** and **ts6-ax**) has higher energetic span than the reduction of aminophosphorane intermediate, since **int11'-ax** is taken as the common TDI. This is the same as observed in the reaction of the equatorial form of the hydroxyphosphine catalyst, **1a-eq** (Figure 3.2).

3.3.7 Alternative possible mechanism for 1a-ax

For **1a-ax**, the competing pathway of stepwise phenylsilane reduction of phosphazide intermediate is shown in Figure 3.17. It is interesting to note that, in this case, the stepwise reduction of phosphazide (**ts22-ax**, at 27.1 kcal mol^{-1}) has a lower barrier, by 6.1 kcal mol^{-1}, than the concerted loss of N_2 (**ts3-ax**, at 33.2 kcal mol^{-1}), such that the first step of P–N bond formation (**ts1-ax**, 30.4 kcal mol^{-1}) in the reaction is the overall TDTS for this mechanism. This stepwise reduction of phosphazide intermediate converges to give the phosphonium silanehydride ion-pair that would be formed in a similar fashion by **1a-eq** (Figure 3.14).

3.3.8 Comparative study using methylated catalyst, methoxyphosphine 1b

Experimentally, to elucidate the role of the hydroxyl group in the hydroxyphosphine bifunctional catalyst, the methylated phosphine **1b**, where a methoxy group replaces the hydroxyl group, was used in comparative experiments (performed by our experimental collaborators; Scheme 3.4). It was found that the formation of iminophosphorane with

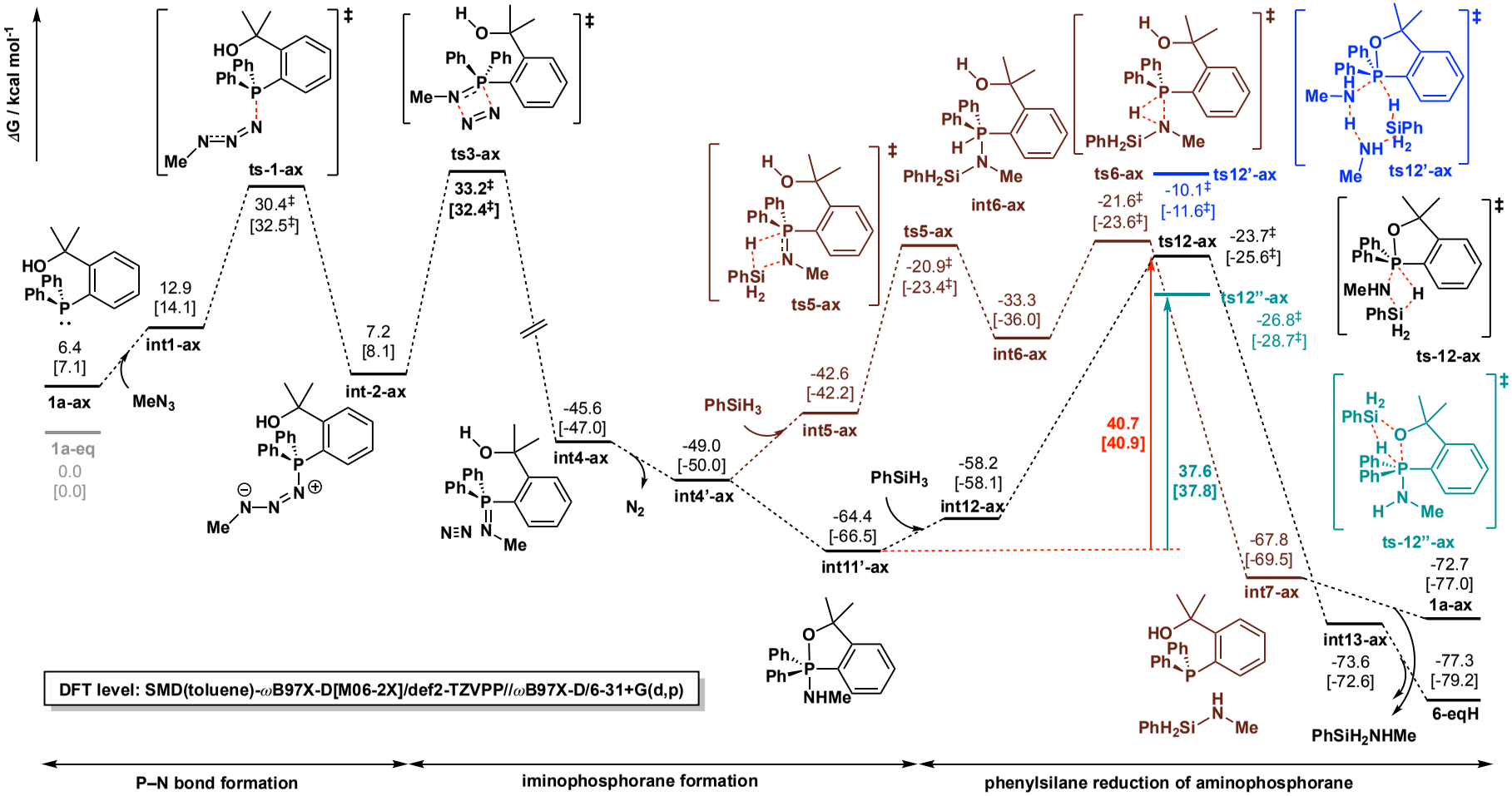

Figure 3.16. Gibbs energy profile (corrected at 25ºC and 1 mol L-1) for the reaction from axial form of the hydroxyphosphine catalyst **1a-ax**, computed at SMD(toluene)-ωB97X-D[M06-2X]/def2-TZVPP//ωB97X-D/6-31+G(d,p) level of theory.

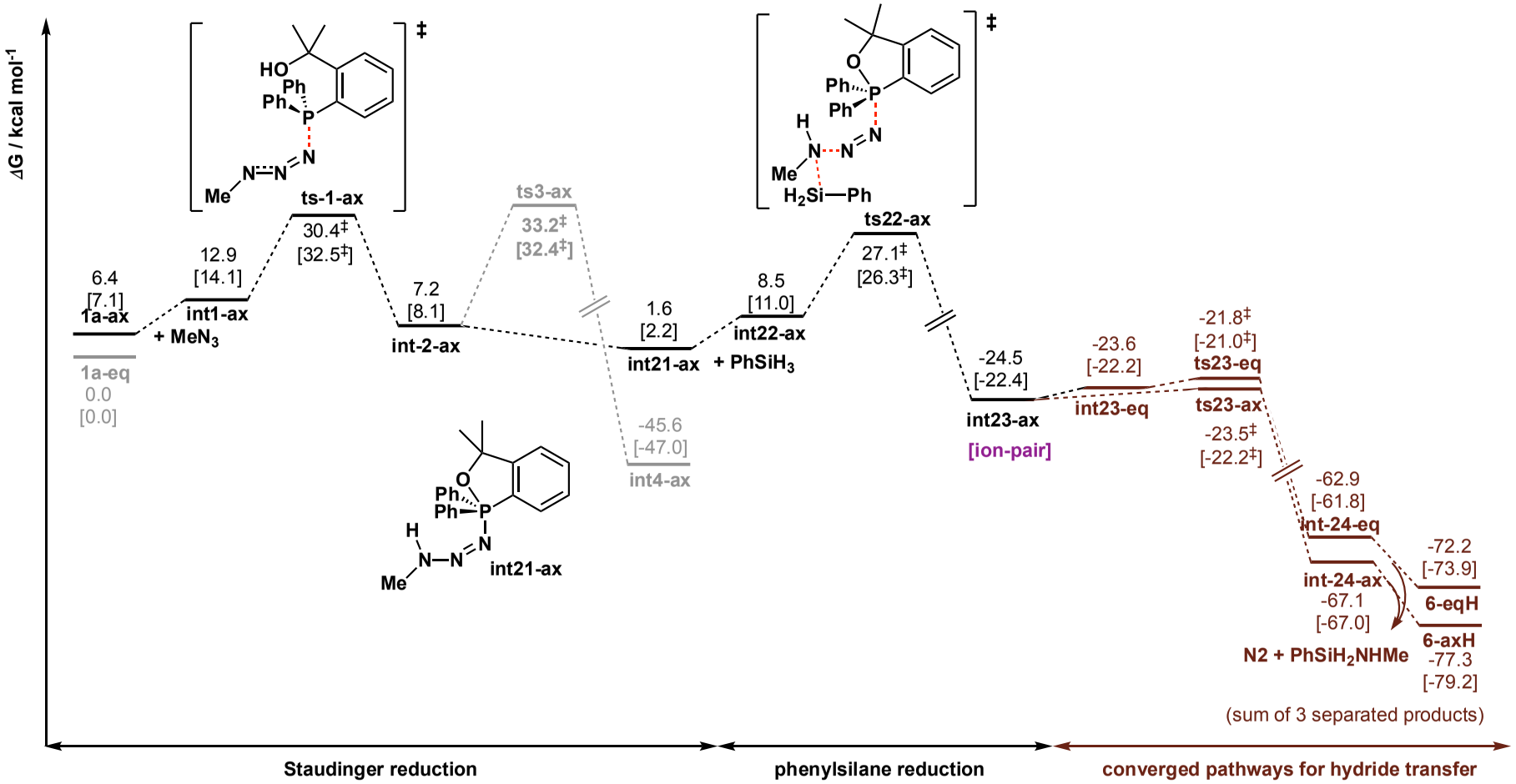

Figure 3.17. Gibbs energy profile (corrected at 25ºC and 1 mol L-1) for the stepwise phenylsilane reduction of phosphazide intermediate formed from **1a-ax**, computed at SMD(toluene)-ωB97X-D[M06-2X]/def2-TZVPP//ωB97X-D/6-31+G(d,p) level of theory.

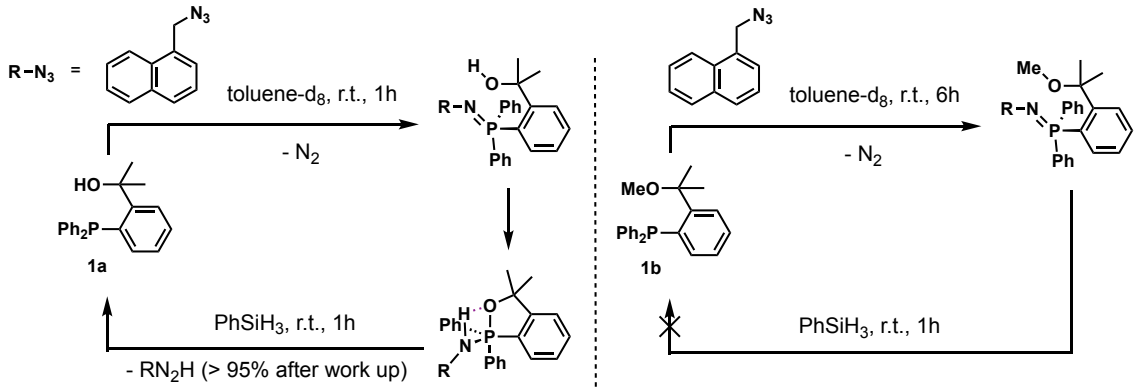

Scheme 3.4. Comparative study for the reduction of azide using hydroxyphosphine catalyst **1a** and its methoxylated analogue **1b**. Experimental work is performed by our experimental collaborators.

the loss of N_2 took 6 hr at r.t. using **1b**, compared to 1h at r.t. when hydroxyphosphine **1a** was used.

The overall energy profile for this reaction is shown in Figure 3.18; selected key optimised structures are given in Figure 3.19. The formation of P–N bond in the first step is the overall TDTS, at 27.8 kcal mol^{-1}, which is 3.0 kcal mol^{-1} higher than the corresponding TS in the formation of iminophosphorane using the hydroxyphosphine catalyst **1a-eq** (**ts3-eq**, 24.8 kcal mol^{-1}, Figure 3.2). The hydroxyl group present in catalyst **1a** could assist in the formation of P–N bond by productive hydrogen bonding interactions (**ts1-eq**, Figure 3.3), thus lowering the activation barrier for P–N bond formation. The higher activation barrier and thus longer reaction time taken for the methoxylated catalyst **1b** in the iminophosphorane formation step results from this lack of hydrogen bonding in the TS for P–N bond formation.

Computations suggest that the reduction of the iminophosphorane intermediate by phenylsilane in the present transformation using catalyst **1b** (**ts5-MeO** and **ts7-MeO**, activation barrier of *circa.* 27.5 kcal mol^{-1}) has comparable barriers to the iminophosphorane formation, although the P=N bond reduction intermediate **int6-MeO**

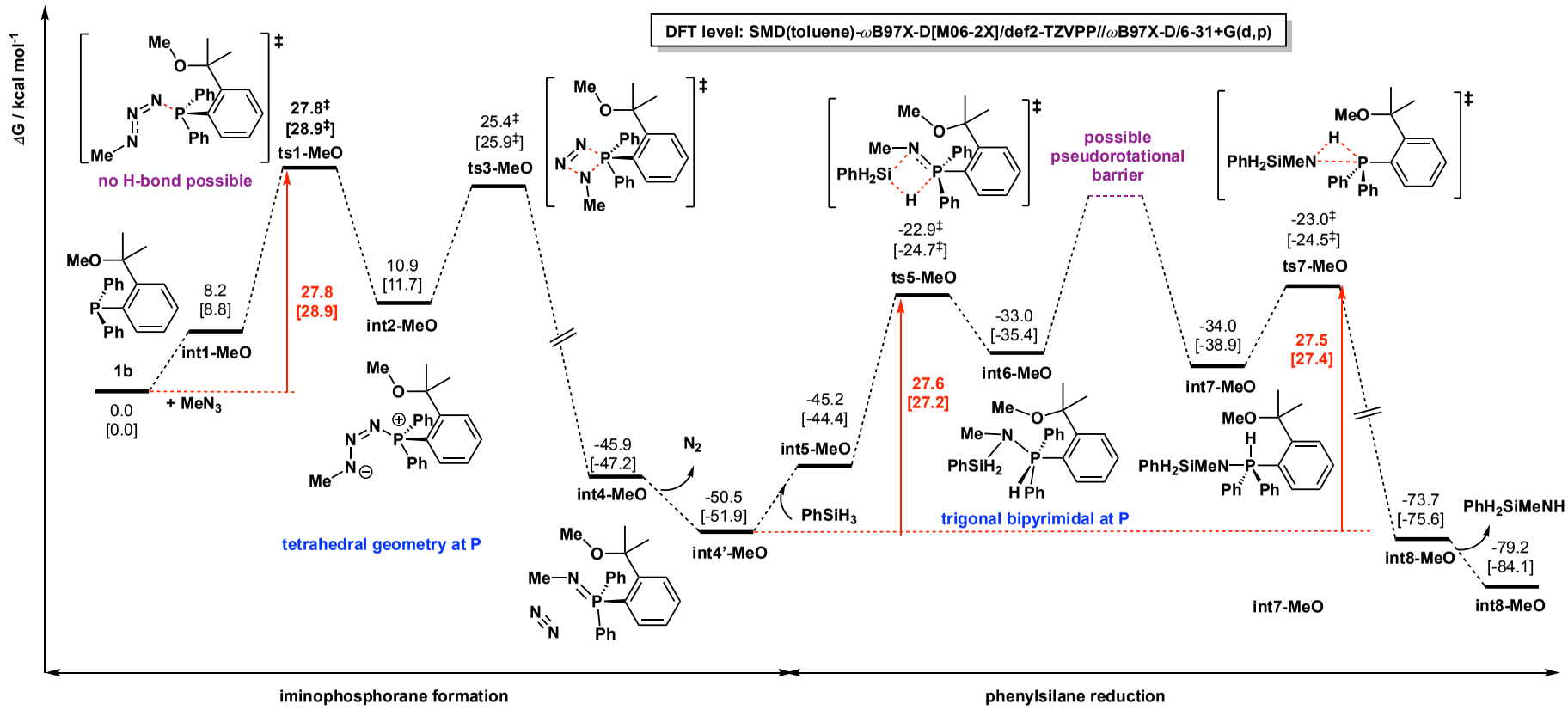

Figure 3.18. Gibbs energy profile (corrected at 25°C and 1 mol L^{-1}) for the present transformation using methylated phosphine catalyst, **1b**, computed at SMD(toluene)-ωB97X-D[M06-2X]/def2-TZVPP//ωB97X-D/6-31+G(d,p) level of theory.

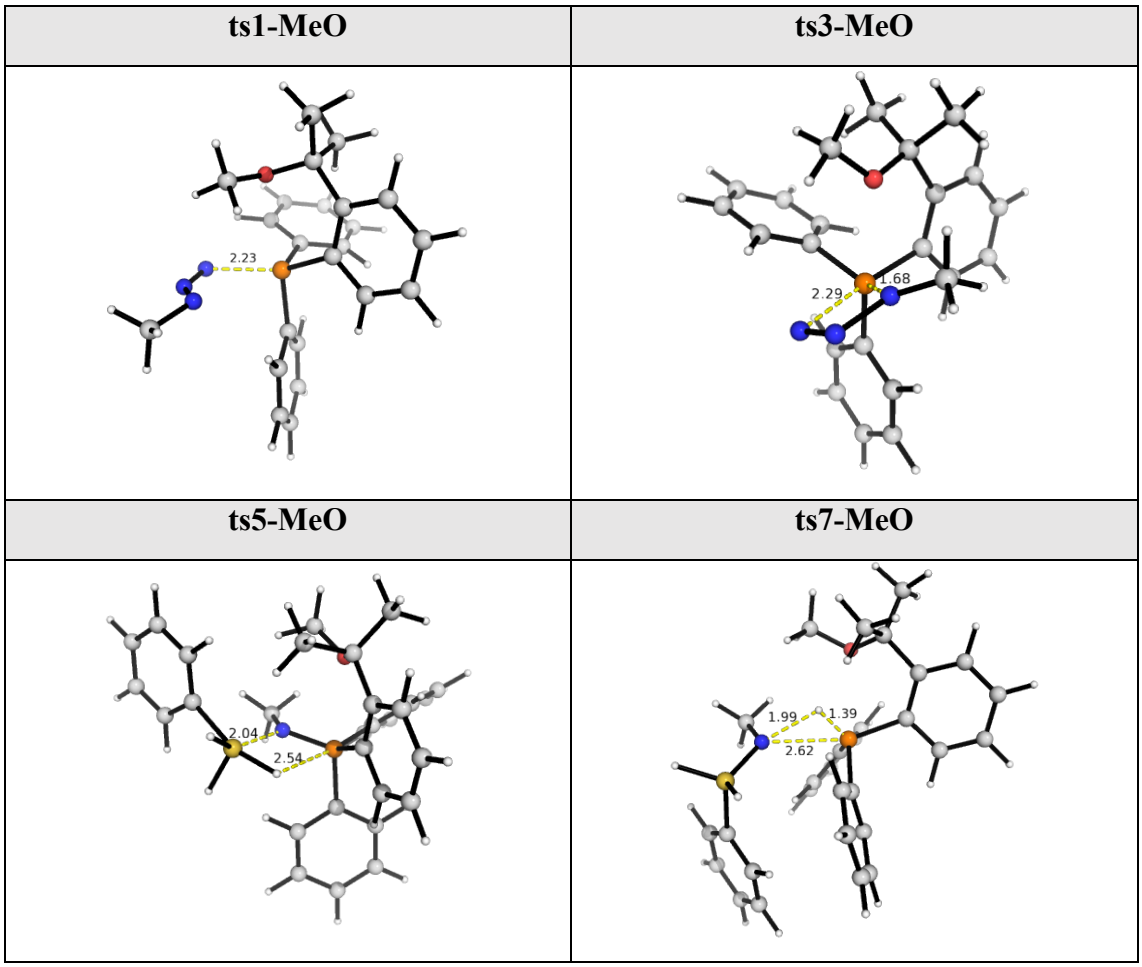

Figure 3.19. Optimised TS structures for the methoxyphosphine **1b** catalysed transformation.

is uphill by 17.5 kcal mol^{-1}. It is not difficult to see that a pseudorotation is required to bring **int6-MeO**, where the H-atom attached to the P-centre is in axial position, to **int7-MeO**, where the H-atom is in equatorial position, in a similar fashion for the pseudorotation of the hydridophosphoranes discussed in subsection 3.3.3 (Figure 3.11). Although this pseudorotational barrier could not be found, we suspect that it falls in a similar activation barrier range as the pseudorotation for the hydridophosphoranes (25 – 30 kcal mol^{-1}). This would make the phenylsilane reduction of the iminophosphorane difficult as a high pseudorotational barrier needs to be overcome. This could explain the experimental observation that the phenylsilane reduction of iminophosphorane formed from the methoxylated catalyst **1b** is difficult to achieve in 1 hr at r.t. (Scheme 3.4)

We can compare this to the classical Staudinger reduction using PPh_3 catalyst (subsection 3.3.9), which shows that the reduction of the iminophosphorane intermediate formed by phenylsilane can be difficult, although the hydrolysis of the iminophosphorane can be quite easily achieved to give phosphine oxide, whose reduction by phenylsilane can be kinetically difficult (*vide infra*).

3.3.9 Comparative study using triphenylphosphine, PPh_3

We study the classical Staudinger reduction using triphenylphosphine catalyst, PPh_3, to compare the iminophosphorane formation without any hydrogen bonding (Figure 3.20) and to show the competing pathways for the reduction vs hydrolysis of the iminophosphorane intermediate (Figure 3.21).

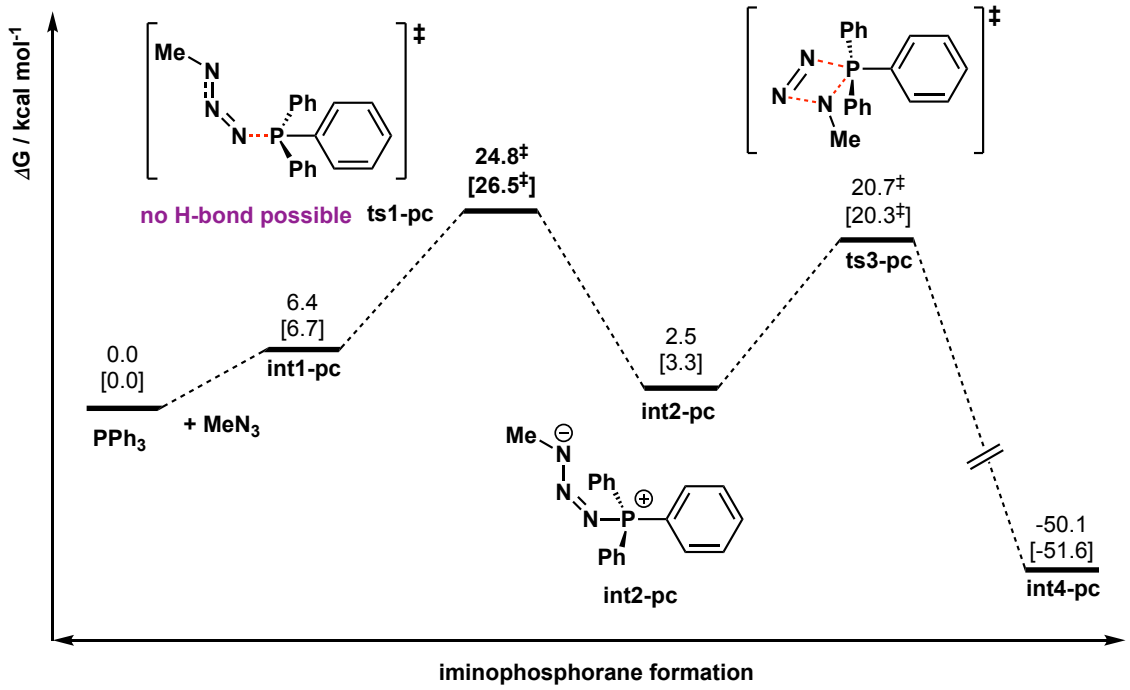

Figure 3.20. Gibbs energy profile (corrected at 25ºC and 1 mol L^{-1}) for the formation of iminophosphorane using triphenylphosphine catalyst, PPh_3.

For the iminophosphorane formation, when compared to our hydroxyphosphine bifunctional catalyst (Figure 3.2), we can see that the P–N bond formation **ts1-pc** has a

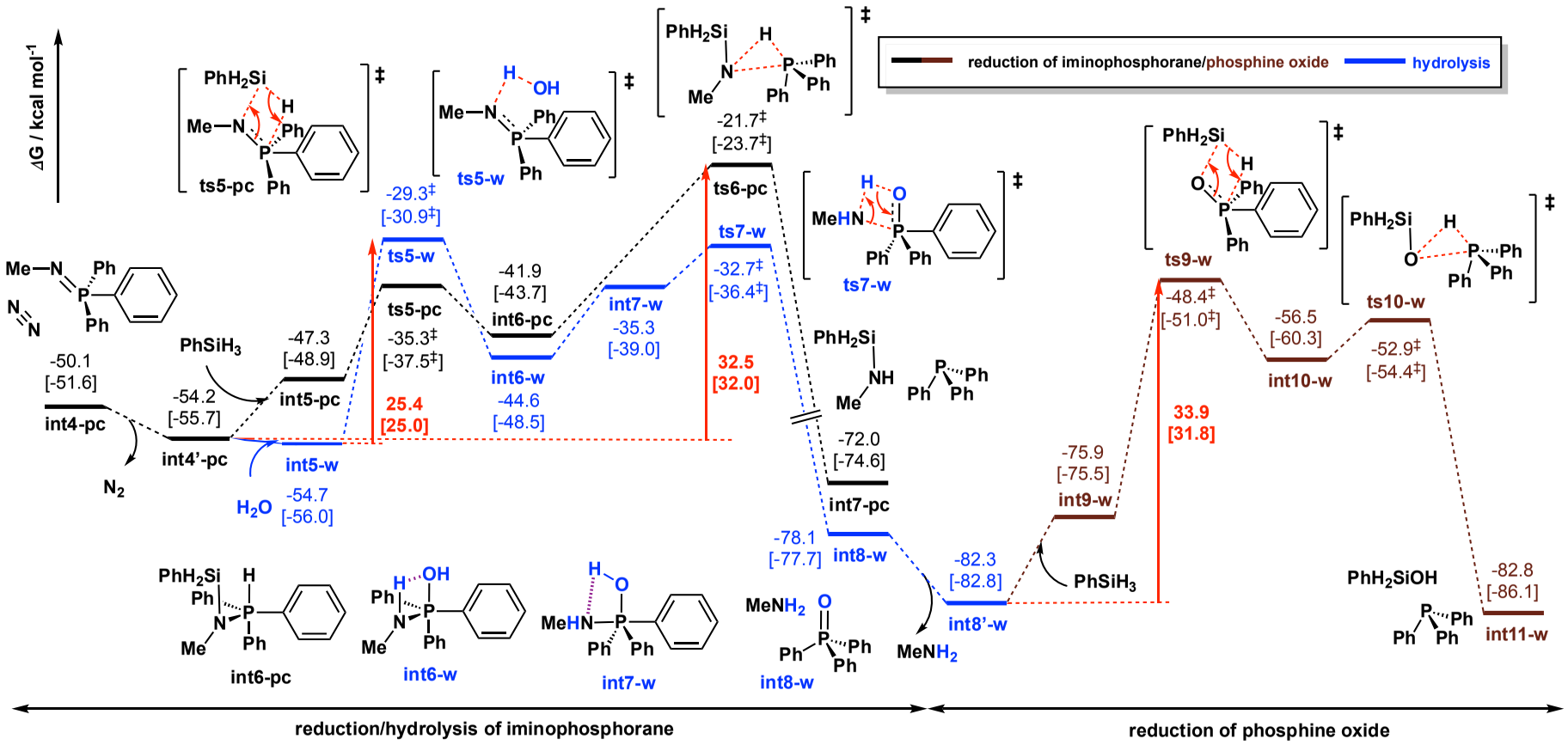

Figure 3.21. Gibbs energy profile (corrected at 25ºC and 1 mol L^{-1}) for classical Staudinger reduction using triphenylphosphine catalyst, PPh_3, computed at SMD(toluene)-ωB97X-D[M06-2X]/def2-TZVPP//ωB97X-D/6-31+G(d,p) level of theory.

higher barrier, by 2.6 kcal mol^{-1}, than **ts1-eq** (22.2 kcal mol^{-1}) due to the absence of assistive H-bonding in the former. On the other hand, for the concerted loss of dinitrogen gas, the presence of H-bonding, as seen in **ts3-eq** (24.8 kcal mol^{-1}) gives a higher barrier, by 4.1 kcal mol^{-1}, than **ts3-pc**. In this case, the formation of H-bonding in **ts3-eq** is disfavouring the loss of N_2, as the electron on the N-atom becomes less available to attack the P-centre after forming H-bonding with the hydroxyl group on the hydroxyphosphine.

Comparing the reduction and hydrolysis of the iminophosphorane intermediate (Figure 3.21), we can see that the reduction of the iminophosphorane by the phenylsilane (**ts6-pc**, barrier of 32.5 kcal mol^{-1}) is thermally more difficult than the corresponding hydrolysis of the iminophosphorane (**ts5-w**, barrier of 25.4 kcal mol^{-1}) to give highly stable phosphine oxide. The subsequent reduction of the phosphine oxide can have a high barrier of 33.9 kcal mol^{-1}, making this rather difficult at room temperature.

The presence of a hydroxyl group in our bifunctional hydroxyphosphine catalyst **1a** can thus negate the formation of this highly stable phosphine oxide (no water is used in the present transformation) by forming the corresponding aminophosphorane whose reduction by phenylsilane can be achieved in a milder condition, as demonstrated experimentally.

Based on these comparative studies, we can identify the roles of the hydroxyl group in our bifunctional hydroxyphosphine catalyst **1a**: 1) it lowers the activation barriers of the P–N bond formation in the first step as the P-atom of the catalyst attacks the terminal N-atom of the incoming azide, by providing favourable hydrogen bonding interactions; 2) it negates the formation of the highly stable phosphine oxide by a facile formation of an aminophosphorane from the corresponding iminophosphorane intermediate. The

aminophosphorane intermediate can be further reduced by phenylsilane to give a silylamine, whose Si–N bond can be easily hydrolysed in subsequent aqueous work-up,[272,273] and a hydridophosphorane, which can be converted back to the hydroxyphosphine catalyst under base-promotion (subsection 3.3.3).

3.3.10 Proposed catalytic cycle

Based on our calculations, we proposed that the reaction occurs via the mechanism shown in Scheme 3.5. First, the more stable form of the hydroxyphosphine catalyst **1a-eq** attacks the terminal N-atom of the azide in a *cis*-geometry, forming the P–N bond. This step is assisted by productive hydrogen bonding interactions made possible by the hydroxyl group present in the catalyst, thus lowering the activation barrier. This is followed by the

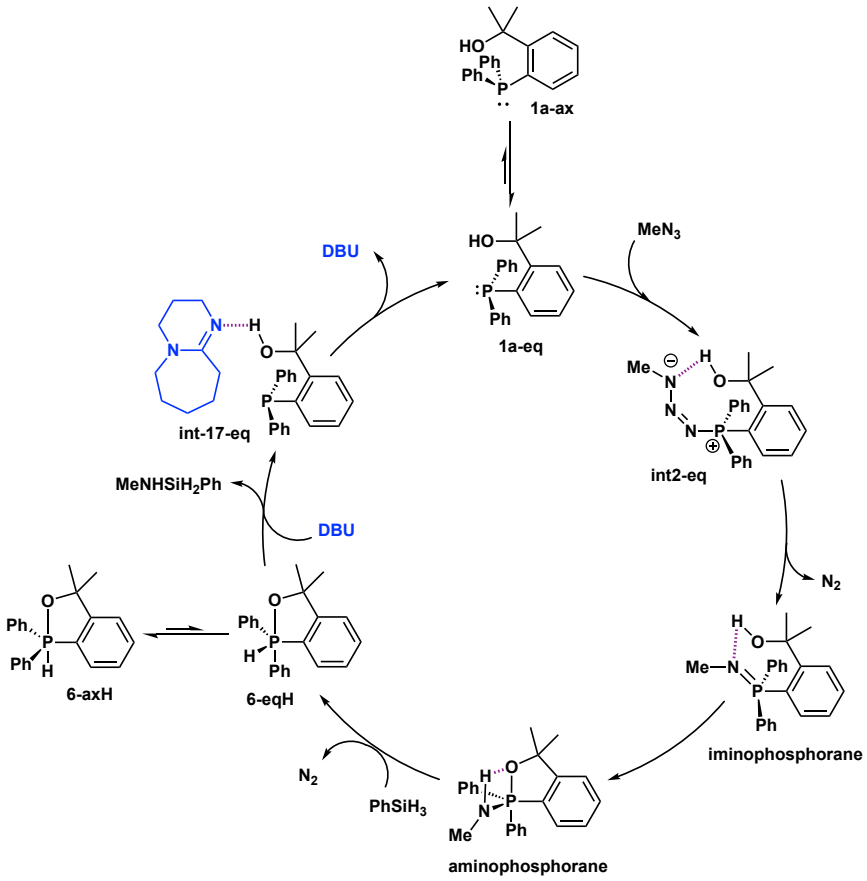

Scheme 3.5. Proposed catalytic cycle involving the bifunctional hydroxyphosphine catalyst **1a** .

subsequent highly exergonic loss of N_2 gas. The resulting iminophosphorane intermediate, with a tethered hydroxyl group in close proximity, readily forms a σ^5-P(V) aminophosphorane, which is energetically downhill. This aminophosphorane can then be reduced by phenylsilane to give the equatorial form of the hydridophosphorane, from which the hydroxyphosphine catalyst can be regenerated with the help of an exogenous base, such as DBU. Base-assistance lowers the barrier of the catalyst regeneration by acting as an intermolecular proton-shuttle between P and O atoms of the catalyst.

3.3.11 Computational ^{31}P NMR

^{31}P NMR is an attractive method for probing the structures of phosphorus-containing compounds due to the 100% natural abundance of ^{31}P element which is nuclear spin-active. It is also sensitive as a small change in structure can result in a big change in chemical shift (CS) due to the strong dependence of the CS on the structure. The computational prediction of ^{31}P NMR CS, however, is faced with a number of challenges. For one, the experimental reference for ^{31}P NMR is 85% H_3PO_4 in H_2O, which is difficult to assign an absolute reference shielding tensor computationally. The other challenge is that computational ^{31}P NMR shielding tensors are normally calculated in the gas phase, it is not entirely clear how this calculated shielding tensor in vacuum state relates to the shielding tensor in the solution phase. Although we can compute the shielding tensor in the solution phase, a lot of times, there are not enough accurate ^{31}P NMR CS data for a set of phosphorus-containing molecules in synthetically relevant solvents for the scaling factors to be obtained.

Initially, we performed the ^{31}P NMR calculations at the mPW1PW91/6-311+G(2d,p) level of theory,[316] including an SMD description of toluene solvation taking the structures from previous optimisations at ωB97X-D/6-31+G(d,p) level of theory. Linear scaling

parameters are applied to relate the computational isotropic shielding tensor (IST) σ to the experimental CS δ via[317]

$$\delta = \frac{\text{intercept} - \sigma}{-\text{slope}} \tag{3.1}$$

For ^{13}C and ^{1}H NMR calculations, the linear scaling parameters are taken from reference[318] (calculated at CPCM(chloroform)-GIAO-mPW1PW91/6-311G(d,p)// ωB97X-D/6-31G(d) level); these scaling factors are ^{13}C NMR: slope = -1.04194 and intercept = 187.35633 (R^2 = 0.999, based on 91 chemical shifts); ^{1}H NMR: slope = -1.07411 and intercept = 31.99466 (R^2 = 0.992, based on 77 chemical shifts). These scaling factors compare better (i.e., give closer agreement with experimental NMR shifts) than using the scaling factors from Tantillo's CHESHIRE databases (Table #5 – Toluene)[317]: ^{1}H NMR (slope = -1.0543, intercept = 31.4262, R^2 = 0.992); ^{13}C NMR (slope = -1.0411, intercept = 186.1331, R^2 = 0.999), which used same level of theory for NMR calculations (mPW1PW91/6-311+G(2d,p)) but a different level of theory for geometry optimisation (B3LYP/6-31+G(d,p)). For ^{13}C and ^{1}H NMR CS predictions, we use the calculated IST values from this method (SMD(toluene)-GIAO-mPW1PW91/6-311G(d,p)//ωB97X-D/6-31+G(d,p)).

Since the scaling factors for phosphorus ^{31}P are not available, we attempt to establish the linear scaling parameters. In the initial attempt (Method 1), we used a set of *eight* small phosphorus-containing molecules (PH_3, PMe_3, PEt_2H, OPF_3, PF_3, PCl_2Me, PCl_3, H_3PO_4), whose ^{31}P NMR values in the gas phase were experimentally accurately measured,[319] to compute the scaling factor for ^{31}P at the same level of theory as before for ^{13}C and ^{1}H NMR CSs. We obtain ^{31}P slope = -1.1275, intercept = 292.74, R^2 = 0.99449 to relate the computed IST to the experimental CS values via Equation (3.1). Although the computed

^{13}C and ^{1}H NMR CSs at this level of theory give good agreement with the experimental results, the computed ^{31}P CSs (RMSD = 43.6 ppm) do not agree very well.

We adopt the second approach (Method 2)[320] where the a wide range of 32 P-containing molecules are optimised at the PBE1PBE[321–324]/6-31+G(d) DFT level and the NMR ISTs computed at PBE1PBE/6-311G(2d,2p). In this method, the computed IST values (σ_{calc}) are first adjusted relative to the gas phase IST value for the reference molecule H_3PO_4 (σ_{iso} = 298.7776) to get the unscaled chemical shift, $\delta_{unscaled}$, via,

$$\delta_{\text{unscaled}} = \sigma_{\text{iso}} - \sigma_{\text{calc}} \tag{3.2}$$

This is then further scaled using the scaling factors (slope = 1.073; intercept = -14.4) obtained from a fit to experimental data to obtain better CS values, δ_{scaled}, via,

$$\delta_{\text{scaled}} = \frac{\delta_{\text{unscaled}} - \text{intercept}}{\text{slope}} \tag{3.3}$$

This method has an RMSD value of 10.9 ppm.

Structure	Calc. (Method 1)	Calc. (Method 2)	Expt values
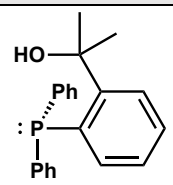 **1a-eq**	δ_P = -23.1 ppm	δ_P = -15.1 ppm	δ_P = -12.2 ppm
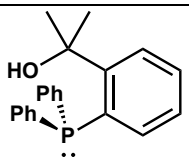 **1a-ax**	δ_P = 4.3 ppm	δ_P = 22.9 ppm	–

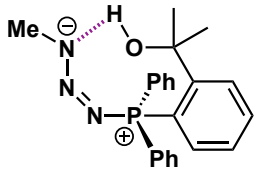 **int2-eq**	δ_P = -25.1 ppm	δ_P = -7.7 ppm	–
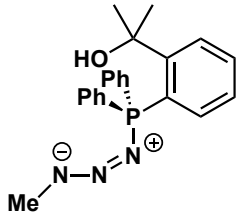 **int2-ax**	δ_P = 0.6 ppm	δ_P = 5.7 ppm	–
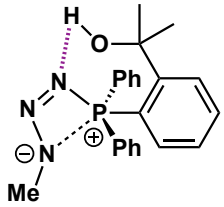 **int3-eq**	δ_P = 1.9 ppm	δ_P = 18.3 ppm	–
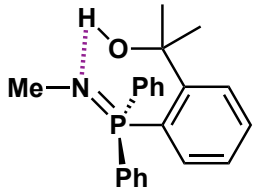 **int4'-eq**	δ_P = 4.4 ppm	δ_P = 21.6 ppm	δ_P = 13.5 ppm †
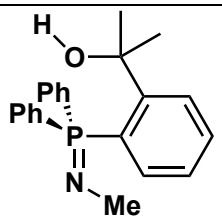 **int4'-ax**	δ_P = -11.3 ppm	δ_P = 3.5 ppm	
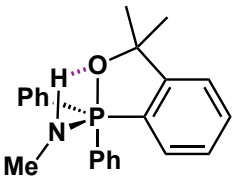 **int11'-eq**	δ_P = -61.5 ppm J_{PH} = 6.7 Hz	δ_P = -45.9 ppm J_{PH} = 7.2 Hz	δ_P = -58.3 ppm †

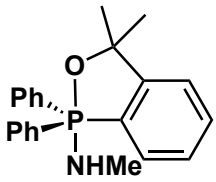 **int11'-ax**	δ_P = -67.0ppm J_{PH} = 5.0 Hz	δ_P = -54.7 ppm J_{PH} = 4.4 Hz	
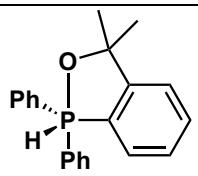 **6-eqH**	δ_P = -73.2 ppm J_{PH} = 667.5 Hz	δ_P = -55.9 ppm J_{PH} = 646.3 Hz	–
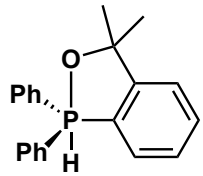 **6-axH**	δ_P = -69.9 ppm J_{PH} = 248.4 Hz	δ_P = -51.7 ppm J_{PH} = 237.3 Hz	δ_P = - 61.1 ppm J_{PH} = 262.1 Hz (assigned based on coupling constant)
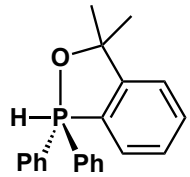 **6-axH-2**	δ_P = -67.4 ppm J_{PH} = 549.7 Hz	$\delta_P = \delta_P$ = -50.6 ppm J_{PH} = 547.1 Hz	–

†The azide used experimentally is naththyl azide instead of methyl azide and this is likely to give different ^{31}P chemical shift values.

Table 3.1. Computational vs experimental ^{31}P NMR chemical shifts and coupling constants.

The comparison of the computed ^{31}P NMR CS and relevant P–H coupling constants using both methods 1 and 2 vs experimental values are given in Table 3.1. There seems to be no one method that is better for all the structures in terms of ^{31}P NMR prediction. For example, the experimental ^{31}P NMR CS for the hydroxyphosphine catalyst is –12.2 ppm; the calculated CS using the first method (SMD(toluene)-mPW1PW91/6-311+G(2d,p)// ωB97X-D/6-31+G(d,p)) gives –23.1 ppm (for **1a-eq**) whereas the second method (PBE1PBE/6-311G(2d,2p)//PBE1PBE/6-31+G(d)) gives –15.1 ppm, with Boltzmann weighting of relevant conformers. For the assignment of hydridophosphorane, **6-axH**, the experimental value of δ_P = –61.1 ppm agrees better with the CS value computed using

Method 1, δ_P = –69.9 ppm, with an error of 8.8 ppm. The computed coupling constants from both methods, on the other hand, agree quite well with the experimental value of J_{PH} = 262.1 Hz (Table 3.1). We assigned the structure of the hydridophosphorane experimentally measured by NMR to structure **6-axH**, instead of **6-eqH**, based on this J_{PH} coupling constant, which seems to be much more reliable than the chemical shifts computed with either method.

3.4 Conclusions

In this chapter, we have conducted a detailed survey of the mechanisms underlying the novel bifunctional hydroxyphosphine catalysed Staudinger reduction developed by our experimental collaborators at the University of Nottingham (the Denton group). The key intermediate involved is a σ^5-P(V) aminophosphorane whose reduction by phenylsilane is demonstrated for the first time experimentally and has been studied in great computational detail. We found that the reduction of the P–O bond is uncompetitive compare to the P–N bond. The stepwise reduction of the P–N bond is also ruled out. The reduction of the corresponding iminophosphorane P=N bond is shown to be more difficult than that of the aminophosphorane P–N bond. More importantly, the formation of a difficult-to-reduce phosphine oxide is circumvented in the present catalytic system as no water is used and in its place, the hydroxyl group on the same catalyst allows the formation of a σ^5-P(V) aminophosphorane, which is reductively labile. Our additional computational studies of the related methoxylated phosphine and the triphenylphosphine catalysts allow us to probe the specific roles of the hydroxyl group of the bifunctional catalyst, establishing its roles in lowering the iminophosphorane formation steps and assisting in the formation of the aminophosphorane intermediate from

iminophosphorane. Our computational studies provide an augmented understanding of the catalytic mechanism of the present transformation.

Alles Gescheite ist schon gedacht worden, man muß nur versuchen, es noch einmal zu denken.

— Johann Wolfgang von Goethe

4

Pd-catalysed δ-C(sp^3)–H arylation[***]

4.1 Introduction

The direct functionalisation of C–H bonds in molecules presents many opportunities for organic synthesis.[325] The use of transition metals (TMs) to selectively functionalise C–H bonds is particularly attractive as it provides atom economical ways to access C–X (where X = B, C, O, N, S, halogens) functional groups, either converting small alkanes to higher valued, functionalised molecules or directly manipulating complex molecules with other functional groups present.[326] Over the past decades, the functionalisation of C(sp^2)–H has been extensively studied and achieved with impressive applications.[327–336] The activation of C(sp^3)–H bond of alkyl groups is, however, more challenging, potentially due to the lack of π-system that assists in productive interactions with transition metal centre for further activation and the greater flexibility in the alkyl backbone. A common

[***] This work has been published in *Angew. Chem. Int. Ed.* **2019**, *58*, 5633. DOI:10.1002/anie.201900479. Permission has been granted by the publisher to re-use part of the material for this thesis.

strategy for site-selective C–H activation is employing removable directing groups (DGs) that favourably bind metal catalyst and strategically position the target site in close proximity to the metal centre for activation.[337–339] DGs are frequently used for directed C–H activations in both C(sp^2)–H and C(sp^3)–H activations.

Aliphatic amines and α-amino acids (αAAs) are ubiquitous structural motifs in biologically active molecules and pharmaceuticals.[340–342] Due to their widespread popularity and importance, method developments for efficient and straightforward synthesis and derivatisation of these compounds have been an area of active research. Transition metal catalysis[343,344,353,345–352] has emerged as a complementary approach for aliphatic amines and αAA functionalisation in addition to nature's enzymatic[354] approach. While several methods exist for the direct C(sp^3)–H functionalisation of secondary and tertiary aliphatic amines at α-,[355–360] β-,[361] and γ-position,[361,362] examples of site-selective functionalisation of primary amines are less common and usually up to γ-C(sp^3)−H position (Scheme 4.1 (a)).[362–371] The functionalisation of αAAs and their derivatives can be similarly achieved at these positions: α-functionalisation occurs mostly via single electron transfer (SET)/visible light mediation[372] or α-oxidation[373,374] (Scheme 4.1 (b)), whereas the functionalisation at the primary or secondary β- and γ-C(sp^3)−H positions usually capitalises on the formation of a cyclometallated intermediate between a transient DG and the transition metal catalyst (Scheme 4.1 (b)).[351,374,383–392,375,393,376–382] The functionalisation at δ-C(sp^3)−H positions of αAAs and its primary aliphatic amine counterparts are rare[394–399] due to the required formation of a six-membered metallacycle intermediate which is kinetically less favoured than a five-membered metallacycle (which would lead to γ-activation). Here, our experimental collaborators (the Maiti Research Group at the Indian Institute of Technology, Bombay) reported a directed δ-

C(sp^3)−H of αAAs and their amine analogues using a transient DG based on picolinic acid (Scheme 4.1 (c)).

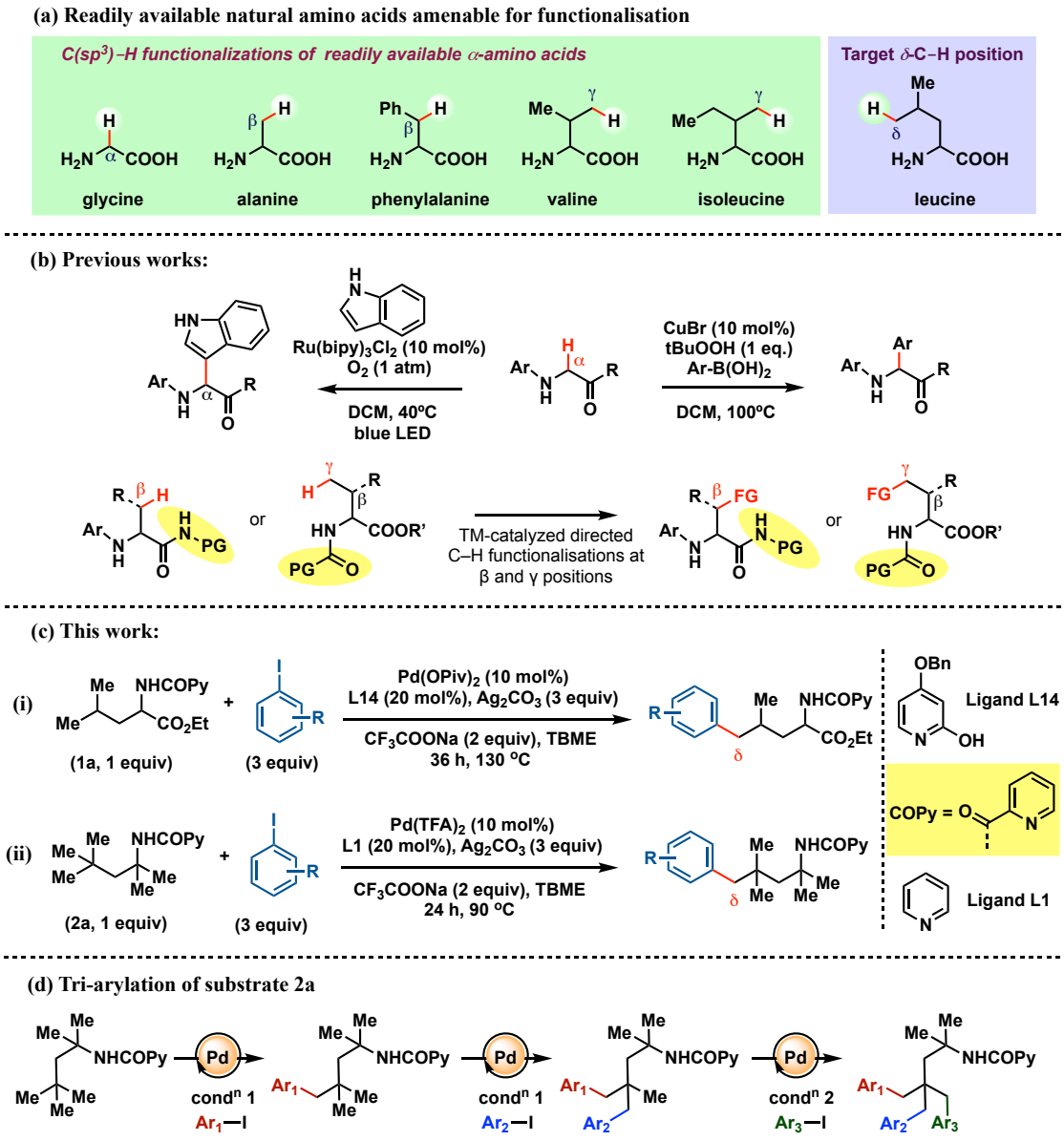

Scheme 4.1. Functionalisation of α-amino acids and amine derivatives at various positions.

Experimentally, it was found that two different substrates (ethyl ester of leucine, **1a** and 2,4,4-trimethylpentan-2-amine **2a**) required different ligands (**L14** and **L1** respectively) for optimal yield and reactivity. In addition, substrate **2a** can undergo iterative arylation, giving tri-arylated product (Scheme 4.1 (d)) in the absence of ligands; the addition of

pyridine ligand favours mono-arylation. Computational studies were performed to understand the energetics and mechanisms of these reactions. All experimental work was performed by our collaborators and all calculations were performed by the present author.

4.2 Computational Methods

Density functional theory (DFT) calculations were performed with Gaussian 16 *rev.* A.03 software.[400] Geometry optimisations were carried out using global hybrid meta-NGA MN15 functional[78] initially with the Karlsruhe-family basis set def2-SVP[18,19] for all atoms. The resulting optimised geometries were further refined at a large basis set using a mix of triple-ζ valence def2-TZVPPD (where 'D' indicates diffuse basis functions) for Pd,[17,401] Ag[17,401] and I[402] atoms and def2-SVP for all other atoms, denoted GenECP in *Gaussian 16* (BS1). This functional was chosen as it performs much better than many other functionals in predicting transition metal reaction barrier heights.[78] Previously, Pd(II)-catalysed C–C bond formations have been studied using other functionals including meta-GGA TPSS and range-separated ωB97X-D functionals.[403,404] MN15 has been shown to give better agreement in geometry predictions of both transition metal complex and organic molecules[78] and in reproducing the energetic profile of trinuclear Cu-catalysed methane-to-methanol catalytic conversion[98] than many other functionals including ωB97X-D and TPSS. Minima and transition structures on the PES were confirmed as such by harmonic frequency analyses, showing respectively zero and one imaginary frequency, at the same level of theory.

Single point (SP) corrections were performed with MN15 functional and the same basis set as before except where def2-SVP was replaced by def2-TZVPP basis set (BS2). The SMD continuum solvation model[117] was included to account for the implicit solvation effect of *tert*-butyl methyl ether (TBME) solvent on the computed Gibbs energy profile.

TBME is not found in the list of pre-defined solvents and thus needs to be parametrized. This SMD parametrisation was done using a set of *seven* solvent parameters.[117] These include 1) static dielectric constant (ε) of the solvent at 25ºC (Eps=2.6);[405] 2) dynamic dielectric constant (n^2) – the square of the refractive index value of 1.3664 at 20ºC was used[406] (EpsInf=1.867); 3) hydrogen bond acidity (α) (HBondAcidity=0.00) and 4) basicity (β) (HBondBasicity=0.54),[407] which are Abraham's A and B values respectively; 5) surface tension at interface (γ) (SurfaceTensionAtInterface=15.717);[408] 6) carbon aromaticity (φ) – fraction of aromatic carbons (CarbonAromaticity=0.00) and 7) electronegative halogenicity (ψ) – fraction of halogens in the molecule (ElectronegativeHalogenicity=0.00). The first two parameters (1-2) are used for manually defining a PCM solvent while the last five parameters (3-7) are SMD-specific keywords. These parameters are specified using the keyword "*SCRF=(SMD, Solvent=Generic, Read)*" in *Gaussian 16*. Gibbs energies were evaluated at 363.15 K, using a quasi-RRHO treatment of vibrational entropies.[205,206] Vibrational entropies of frequencies below 100 cm^{-1} were obtained according to a free rotor description, using a smooth damping function to interpolate between the two limiting descriptions.[205] The free energies were further corrected using a standard concentration of 1 mol L^{-1}, which was used in solvation calculations. *Unless otherwise stated, all Gibbs energy values in the text and figures are quoted in kcal mol^{-1} and all bond distances are given in Å throughout.*

Stereoelectronic properties, including donor-acceptor interactions and steric effects, were analysed using NBO3[409] and NCIPLOT[281] calculations, respectively. The *.wfn* files for NCIPLOT were generated at MN15/DGDZVP[410,411] level of theory. NCI indices calculated with NCIPLOT were visualised at a gradient isosurface value of s = 0.5 au.

These are coloured according to the sign of (λ_2) over the range of -0.1 (blue = attractive) to +0.1 (red = repulsive). All molecular structures and molecular orbitals were visualized using PyMOL software.[207] *Unless otherwise stated, isosurface value of 0.05 is used throughout for the visualisation of molecular orbitals.*

Geometries of all structures (in *.xyz* format with their associated energy in Hartrees) have been deposited online and made freely available (DOI: 10.5281/zenodo.2611814).

4.3 Results and Discussions

4.3.1 Nature of the Pd(II)-catalyst

Palladium(II) acetate and its variants are known to exist in polynuclear forms in both the solid state as well as in solution.[412–414] Palladium(II) trifluoroacetate has been shown to exist in trimeric form $[Pd(TFA)_2]_3$ in solid phase. Factors such as solvent identity and ligand effects influencing the trimeric/monomeric equilibrium have been extensively explored.[415–418] Our calculations showed that the formation of the dimeric complex is exergonic by -26.4 kcal mol^{-1} and that of the trimeric complex is exergonic by -56.7 kcal mol^{-1} in TBME solvent relative to the monomeric complex. These values are in good agreement with both experimental and theoretical values for the palladium acetate system (-34.9 kcal mol^{-1} for dimer and -59.3 kcal mol^{-1} for trimer).[413,418] We found that each Pd(II) atom is in a square planar environment and altogether the trimer exists in a cyclic form (Figure 2.1 (c)), with interactions between its paddlewheel ligands and between Pd–Pd metal centres. The most stable starting complex of palladium trifluoroacetate catalyst used in this reaction thus exists in trinuclear form. The use of mononuclear species in the Gibbs energy calculations artificially lowers the activation barriers of such catalytic systems since the mononuclear species is higher in energy than the most stable trinuclear species. For energy calculations, 1/3 of $Pd_3(TFA)_6$ trimer is used.

(a)	(b)	(c)
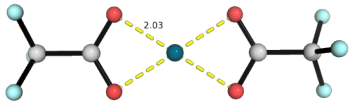	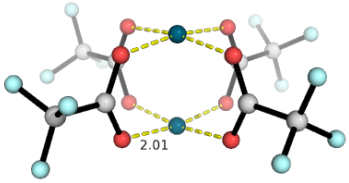	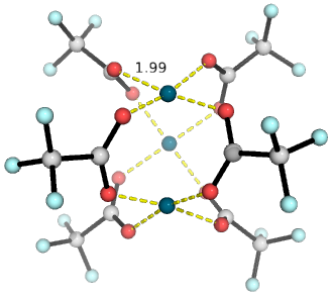

Figure 4.1. Optimised structures of (a) monomeric, (b) dimeric and (c) trimeric palladium trifluoroacetate.

4.3.2 Substrate 2a: mononuclear pathway for Pd(II) catalysis

We first consider the reaction pathway involving the mononuclear Pd(II)-catalyst for substrate **2a**. For modelling purposes, 4-iodoanisol (81% yield) was used as the aryliodide coupling partner. The solvent-corrected free energy profile for the mononuclear pathways is shown in Figure 4.2. The palladacycle formation occurs with two successive concerted metalation-deprotonation (CMD) steps. The initial coordination of the picolinamide molecule to monomeric $Pd(TFA)_2$ is assisted by the formation of hydrogen bonding between amide-H atom and oxygen atom on one of the trifluoroacetate (TFA) ligands. The amide N–H proton is easily deprotonated by the coordinating TFA ligand while Pd interacts with the breaking N–H nitrogen (**ts-1**). This CMD step, albeit facile, is reversible. The immediate loss of a trifluoroacetic acid (HTFA) molecule makes this step exergonic, giving **int-3** at 1.1 kcal mol^{-1}. In the absence of pyridine ligand, one of the coordination sites on Pd gets displaced by C–H bond, which coordinates to the Pd metal by agostic interaction. The non-coordinating O-atom of the TFA ligand then carries out a second CMD (**ts-4**), forming Pd–C bond in intermediate **int-5**. This CMD step is reversible with the subsequent steps having higher activation barriers. The TSs for oxidative addition (OA) (**ts-6**) of aryliodide and reductive elimination (RE) (**ts-7**) of C–C bond formation have comparable Gibbs energies of activation. Conformational effects

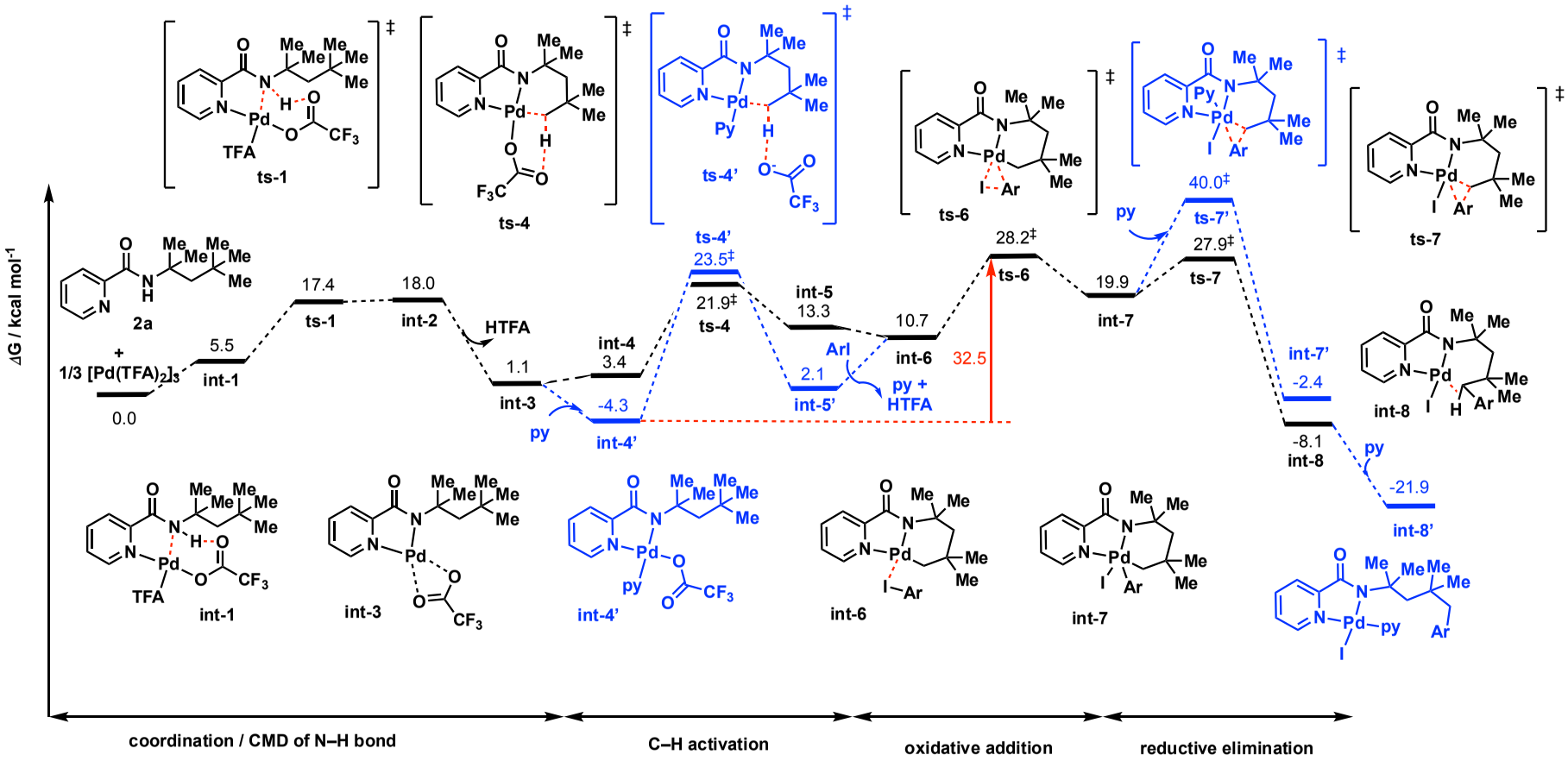

Figure 4.2. Gibbs free energy profile for first arylation in the absence (black) and presence (blue) of pyridine ligand **L1** with mononuclear palladium catalyst as a starting material for substrate **2a**.

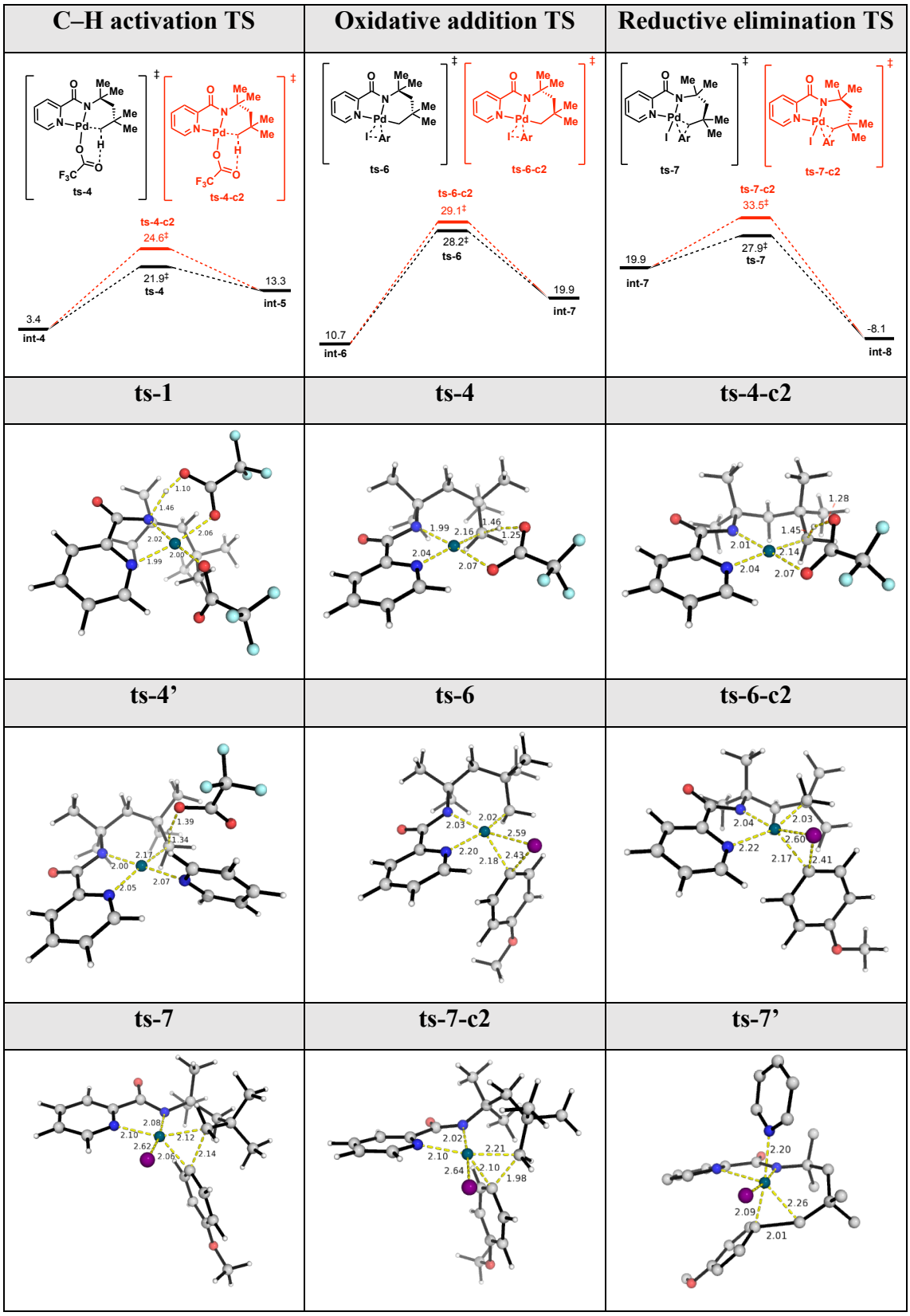

Figure 4.3. **Top:** Free energies for C–H activation, oxidative addition and reductive elimination TSs with different conformations of the 6-membered palladacycle. **Bottom:** Selected TS structures for the energy profile in Figure 4.2.

of each TS were considered; in particular, we found that the 6-membered palladacycle adopts two conformations (Figure 4.3), with the ring puckered in opposite orientations. The lowest energy conformations were taken for discussion, assuming that these conformers can interconvert easily and rapidly. The first arylation product, **int-8**, at -8.1 kcal mol^{-1}, is thermodynamically stable with respect to the starting material or any prior intermediates, making the reaction favourable under thermodynamic control.

In the presence of pyridine, we found no TSs that are lowered in activation barrier by direct pyridine participation (Figure 4.4). In particular, pyridine molecule could not coordinate to Pd metal during the OA of aryliodide. The displacement of pyridyl group on the picolinamide by pyridine is also unfavourable. For RE, although pyridine could coordinate to Pd, this TS (**ts-7'**, 40.0 kcal mol^{-1}, Figure 4.3) however, has a much higher activation barrier (by 12.1 kcal mol^{-1}) than that without pyridine ligand (**ts-7**, 27.9 kcal mol^{-1}). A RE step with non-coordinating pyridine, **ts-7'-c1**, at 34.8 kcal mol^{-1} (Figure 4.4), however, is found to be lower in activation barrier than **ts-7'**, but still higher than without any pyridine ligand **ts-7**. This is due to the unfavourable loss of entropy as one additional molecule of pyridine is brought close to the TS. Considering all possible geometric isomers by swapping the positions of the coordinating I–/Ar–/pyridine groups on Pd metal, we did not find any TS with lower activation barrier than that without pyridine ligand (Figure 4.4). This is consistent with the observation that complexes with even number of coordination undergo RE less readily than those with odd number of coordination.[419–421] Ligand exchange of I^- by CF_3COO^- for reductive elimination (**ts-7'-c11** and **ts-7'-c12**) also has higher activation barriers than **ts-7**. Our thorough TS searches conclude that pyridine ligand does not participate directly in the reaction TDTS for our present system.

ts-7'-c1	ts-7'-c2	ts-7'-c3
$\Delta\Delta G^{\ddagger} = 6.9$	$\Delta\Delta G^{\ddagger} = 7.3$	$\Delta\Delta G^{\ddagger} = 12.1$
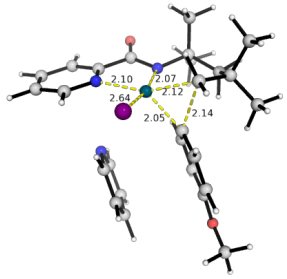	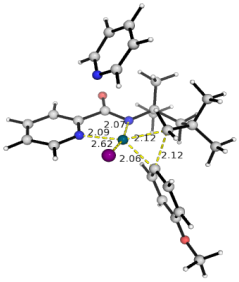	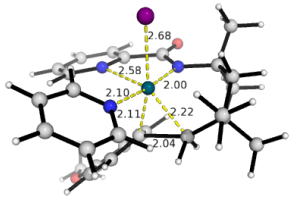
ts-7'-c4	**ts-7'-c5**	**ts-7'-c6**
$\Delta\Delta G^{\ddagger} = 13.0$	$\Delta\Delta G^{\ddagger} = 14.2$	$\Delta\Delta G^{\ddagger} = 14.7$
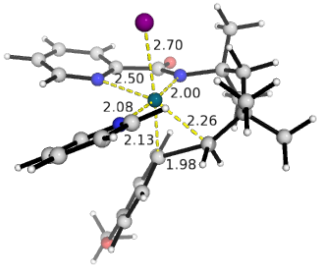	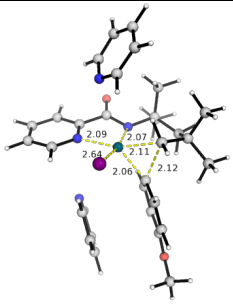	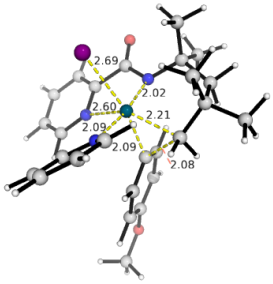
ts-7'-c7	**ts-7'-c8**	**ts-7'-c9**
$\Delta\Delta G^{\ddagger} = 20.8$	$\Delta\Delta G^{\ddagger} = 28.4$	$\Delta\Delta G^{\ddagger} = 31.0$
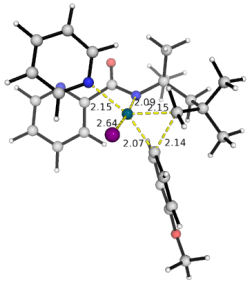	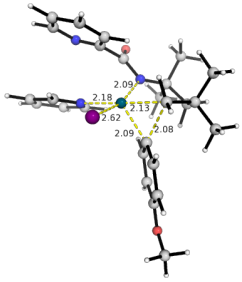	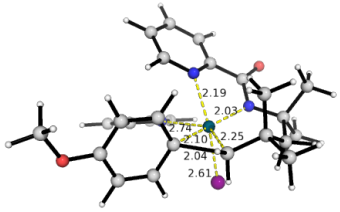
ts-7'-c10	**ts-7'-c11**	**ts-7'-c12**
$\Delta\Delta G^{\ddagger} = 31.6$	$\Delta\Delta G^{\ddagger} = 20.9$	$\Delta\Delta G^{\ddagger} = 21.4$
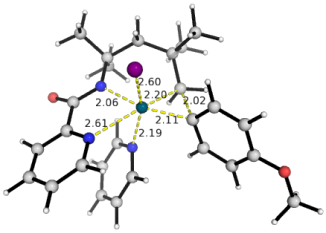	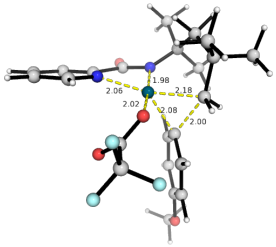	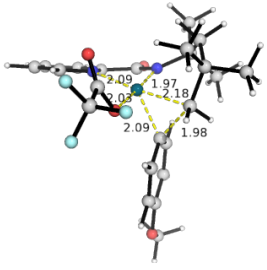

Figure 4.4. TSs considered for reductive elimination step in the presence of pyridine ligand. Gibbs free energies of activation relative to the lowest TS **ts-7** ($\Delta\Delta G^{\ddagger}$) are given in kcal mol^{-1}.

4.3.3 Substrate 2a: trinuclear pathway for Pd(II) catalysis – first arylation

Mononuclear Pd-catalyst gives an overall activation barrier of 28.2 kcal mol^{-1} in the absence of pyridine ligand, with the oxidative addition being overall rate-determining; this barrier increases to 32.5 kcal mol^{-1} with pyridine coordination (Figure 4.2). This is inconsistent with the experimental observation that the reaction proceeds faster with a higher yield in pyridine ligand. The consideration of a potentially polynuclear Pd-catalyst is therefore necessary; the trinuclear catalyst is thermodynamically the most stable (section 4.3.1). More directly, the synthesis of a C–H activated trinuclear complex, coupled with computational studies, by Yu and Houk *et. al* provides unequivocal evidence for the involvement of a trinuclear catalytic species in such reactions.[422] We began our computational exploration of such a possibility by considering a similar trinuclear Pd(II)-complex as an active catalyst. The overall Gibbs free energy profile for the reaction starting from trimeric Pd-catalyst is shown in Figure 4.5. With pyridine, the dissociation of the trimeric complex is favourable. The interactions between Pd-centre and nitrogen atoms of pyridine ligand **L1** molecules compensate for the enthalpic loss of paddlewheel interactions between ligands and the Pd–Pd interactions when the trinuclear complex **A** dissociates to its mononuclear form; this dissociation is driven by the exergonic formation of $Pd(TFA)_2(\mathbf{L1})_2$ complex.[423] The OA/RE steps are both catalysed by the monomeric form of palladium catalyst, since Pd(II) metal is tetra-coordinating and there needs to be a vacant coordination site on the metal for the incoming aryl iodide to be added. As we can see from the energy profile, the activation barrier in the absence of pyridine ligand is 41.4 kcal mol^{-1} whereas this decreases to 30.5 kcal mol^{-1} in the presence of pyridine ligand **L1**. This corroborates well with the experimental observation that the reaction yield improves in the presence of pyridine ligand, albeit the reaction can also occur in its absence.

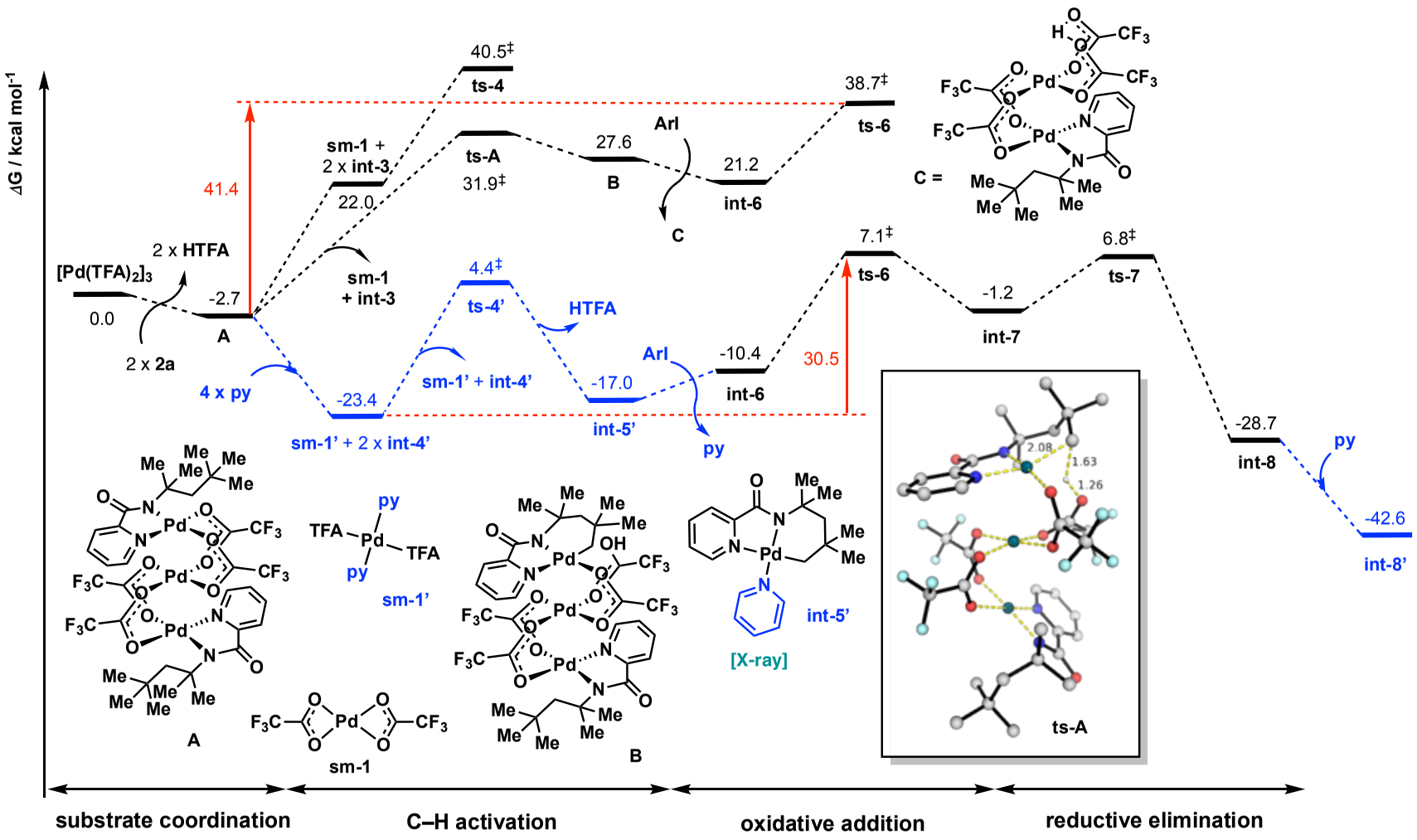

Figure 4.5. Gibbs free energy profile for first arylation in the absence (black) and presence (blue) of pyridine ligand **L1** with trinuclear palladium catalyst as starting material for substrate **2a**.

The C–H activation step is reversible both in the presence and absence of pyridine ligand, as the subsequent OA of aryl iodide (**ts-6**) has a higher activation barrier than the reverse step of C–H activation. This is in excellent agreement with experimental evidence using kinetic isotope effect (KIE) and H/D exchange studies. Our calculations support the lack of primary KIE and the ease of deuterium incorporation (40% at reaction condition with D_4-AcOH solvent and up to 85% at 130ºC) observed experimentally, showing that C–H activation step is unlikely rate-determining. Much like the mononuclear pathway, the subsequent OA and RE occur in the absence of pyridine ligand: the aryl iodide inserts oxidatively to form a pentavalent Pd(IV) intermediate **int-7** that is highly endergonic which further undergoes RE, reverting the metal from Pd(IV) to Pd(II) in the arylated product. It is worth noting that the OA and RE steps have comparable activation barriers (within 0.5 kcal mol^{-1}), making it difficult to pinpoint exactly which of these steps is rate-determining; RE step, in fact, becomes rate-determining for second and third arylation (section 4.3.4).

The overall first arylation is reversible without pyridine ligand but irreversible with pyridine ligand, since structure **int-8** can be further stabilised by pyridine coordinating to the Pd(II) metal to give **int-8'**, thereby stabilising the end product. With pyridine coordination to the end product, the first arylation is thus thermodynamically favoured.

4.3.4 Substrate 2a: trinuclear pathway for Pd(II) catalysis – second and third arylation

The steps for second arylation are similar to those of first arylation except now that two diastereomers are possible; these conformations were thoroughly explored (Figure 4.7). The overall Gibbs free energy profile for diastereomer 1 is shown in Figure 4.6 (the energy profile for diastereomer 2 is similar). In contrast to first arylation, the RE step has

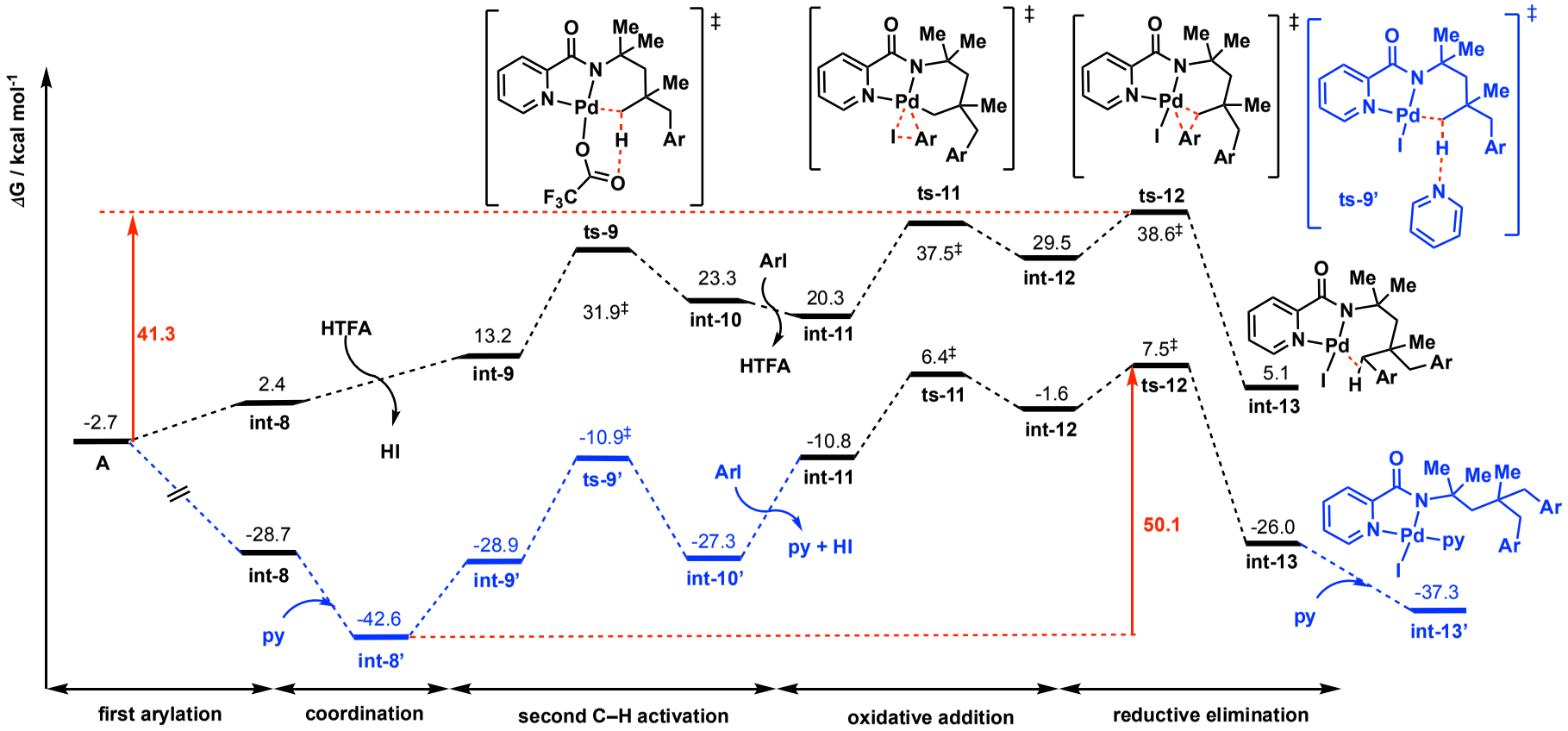

Figure 4.6. Gibbs free energy profile for second arylation in the absence (black) and presence (blue) of pyridine ligand **L1** with trinuclear palladium catalyst as starting material for substrate **2a**. Note that only one stereoisomer (site of arylation) is shown, the other stereoisomer was calculated and found to have similar results.

(a) Second C–H activation TSs	
ts-9	**ts-9-c2**
$\Delta\Delta G^{\ddagger} = 0.0$	$\Delta\Delta G^{\ddagger} = 5.4$
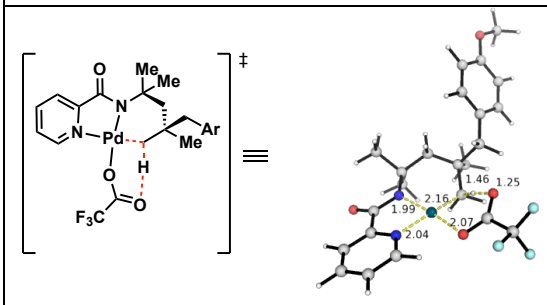	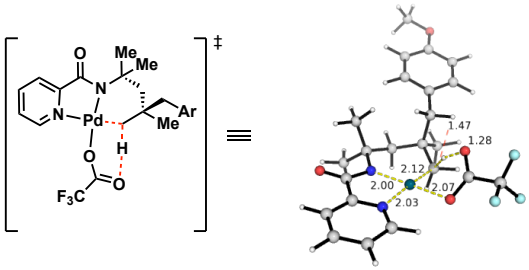
ts-9-c3	**ts-9a**
$\Delta\Delta G^{\ddagger} = 0.0$	$\Delta\Delta G^{\ddagger} = 3.9$
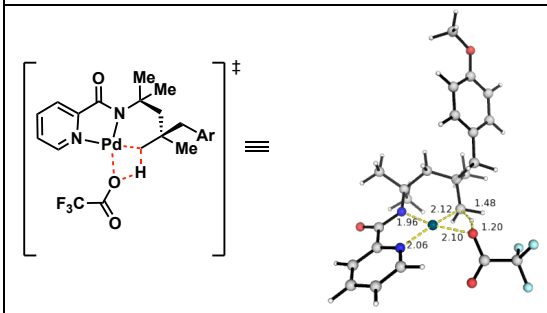	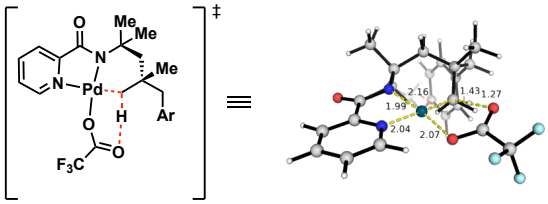
ts-9a-c2	**ts-9a-c3**
$\Delta\Delta G^{\ddagger} = 2.2$	$\Delta\Delta G^{\ddagger} = 13.7$
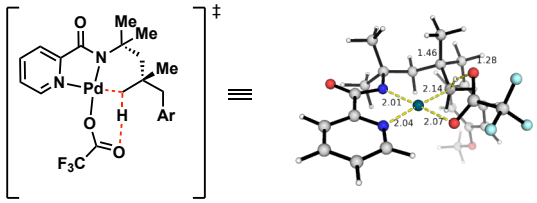	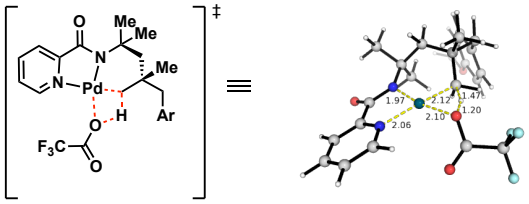
(b) Oxidative insertion TSs	
ts-11	**ts-11-c2**
$\Delta\Delta G^{\ddagger} = 0.0$	$\Delta\Delta G^{\ddagger} = 1.0$
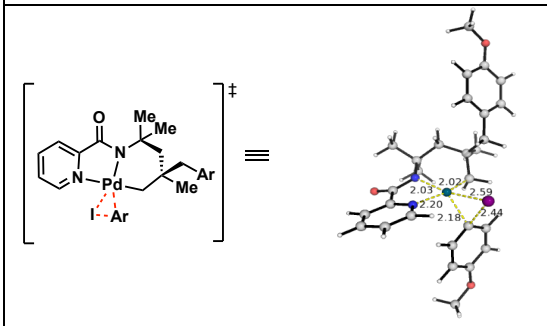	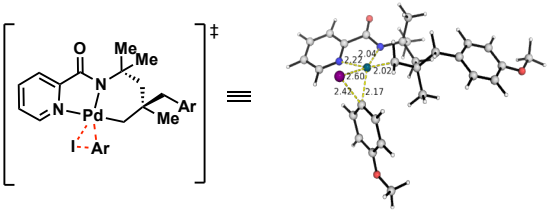

ts-11a	ts-11a-c2
$\Delta\Delta G^{\ddagger} = 0.3$	$\Delta\Delta G^{\ddagger} = 1.0$
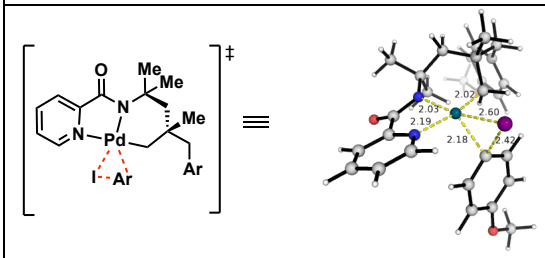	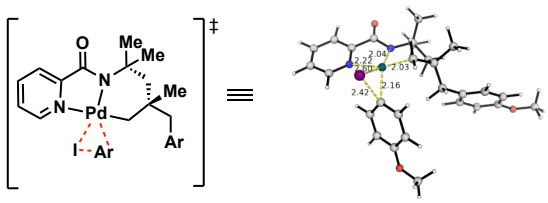
(c) Reductive elimination TSs	
ts-12	**ts-12-c2**
$\Delta\Delta G^{\ddagger} = 0.0$	$\Delta\Delta G^{\ddagger} = 4.8$
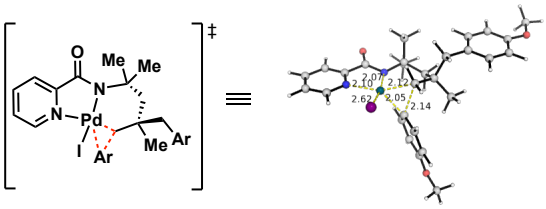	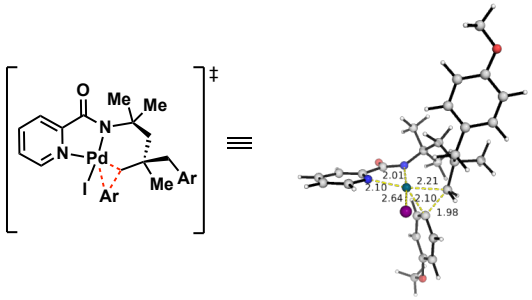
ts-12a	**ts-12a-c2**
$\Delta\Delta G^{\ddagger} = 2.7$	$\Delta\Delta G^{\ddagger} = 4.1$
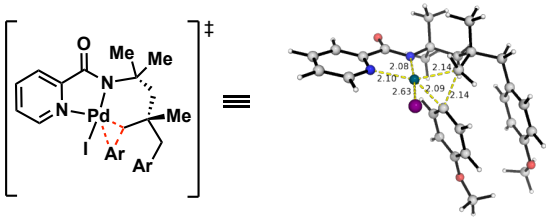	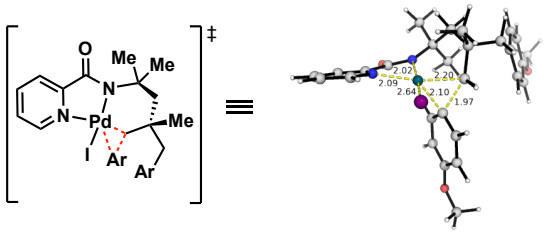

Figure 4.7. Relative activation energies and optimised structures for TS conformers of (a) C–H activation, (b) oxidative addition and (c) reductive elimination for second arylation.

slightly higher activation barrier than OA (by 1.1 kcal mol^{-1} here for second arylation), suggesting that these two steps are indeed very close in activation barriers. Without pyridine, the energy span for second arylation is 41.3 kcal mol^{-1} (between structures **A** and **ts-12**), which is within 0.5 kcal mol^{-1} of the energy span for first arylation (at 41.4 kcal mol^{-1}). This closeness in the activation barrier spans, coupled with the fact that both

first and second arylation in the absence of pyridine ligand are reversible, resulted in the experimentally observed small mono- vs di-arylation selectivity. With pyridine, the end product of first arylation gets coordinated by pyridine ligand to give much more stabilised **int-8'** with much lowered energy. This stabilisation of the first arylated product by pyridine coordination increases the energy barrier span for second arylation to 50.1 kcal mol^{-1}, making it thermally unfeasible. This explains the experimental observation that the use of pyridine ligand favours mono-arylation over di-arylation product.

The steps for third arylation, where possible TSs with palladacycle in different puckered conformations, was similarly analysed (Figure 4.9); the Gibbs free energy profile for the lowest-energy pathway is shown in Figure 4.8. Here the RE step is 3.1 kcal mol^{-1} higher than the OA step (c.f. first arylation: OA 0.3 kcal mol^{-1} higher than RE; second arylation: RE 1.1 kcal mol^{-1} higher than OA). Additional TS conformer searches (**ts-17-c3/c4/c5**) did not yield any lower RE TS, indicating that the RE step here is most likely the rate-determining TS.

The energy span for third arylation without pyridine ligand is 43.9 kcal mol^{-1} (between structures **A** and **ts-17**), whereas this increases to 47.8 kcal mol^{-1} in the presence of pyridine, due to its stabilising coordination to the second arylation product (**int-13'**). Without pyridine ligand **L1**, the energy spans for all three arylations are really close (41.3, 41.4 and 43.9 kcal mol^{-1} respectively) and all the arylation products are endergonic with respect to the starting complex, suggesting possible tri-arylation (Figure 4.1(d)). The slightly higher activation barrier for third arylation (by ~2.5 kcal mol^{-1} than first and second arylation), suggests that third arylation would be more difficult to occur. This is indeed what was observed: the reaction temperature had to be increased from 90ºC to 130ºC for tri-arylated product to be formed.

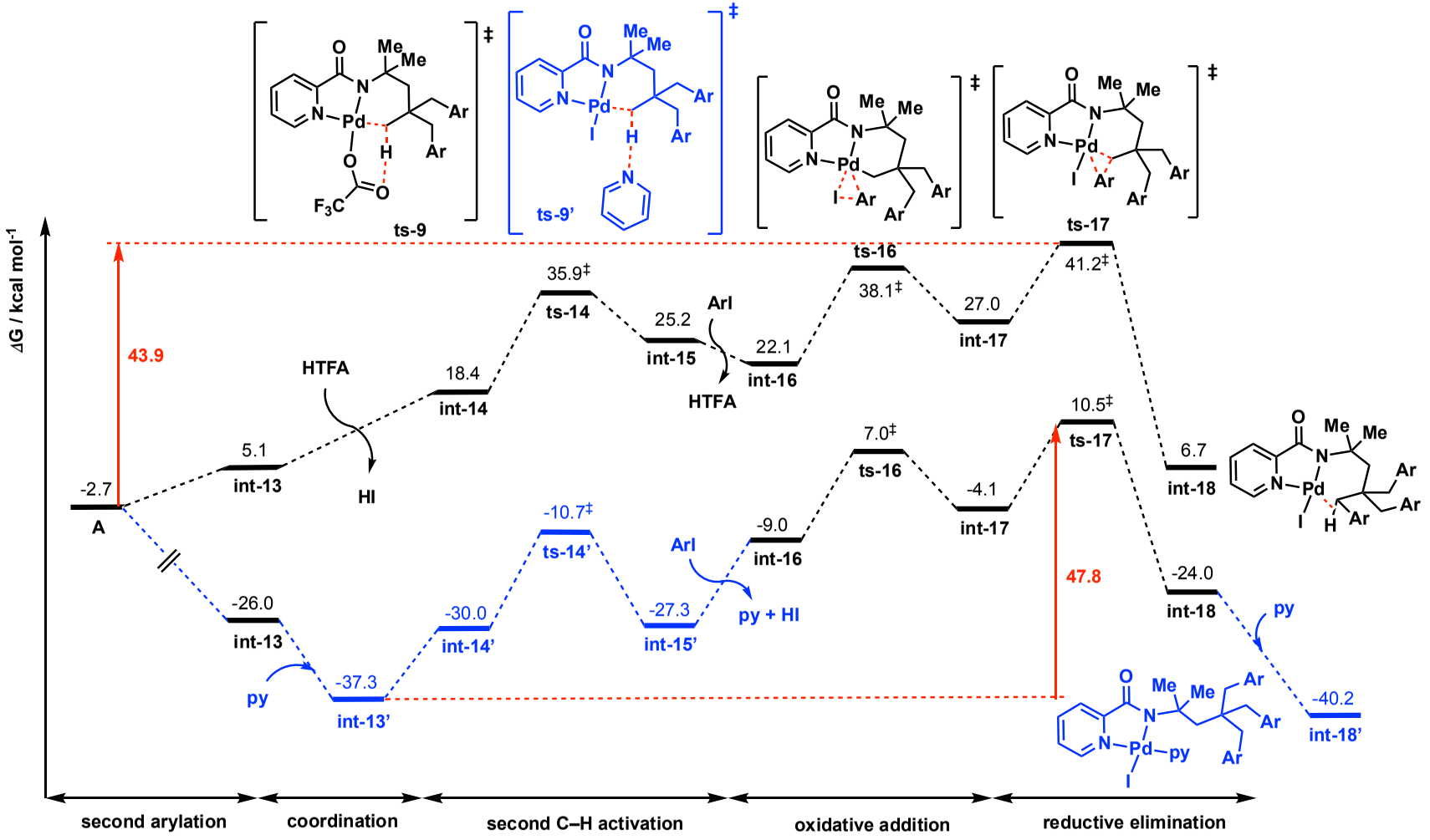

Figure 4.8. Gibbs free energy profile for third arylation in the absence (black) and presence (blue) of pyridine ligand **L1** with trinuclear palladium catalyst as starting material for substrate **2a**.

(a) Third C–H activation TSs	
ts-14	**ts-14-c2**
$\Delta\Delta G^{\ddagger} = 0.0$	$\Delta\Delta G^{\ddagger} = 1.5$
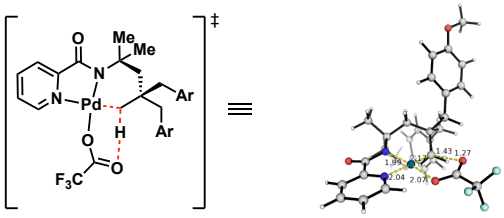	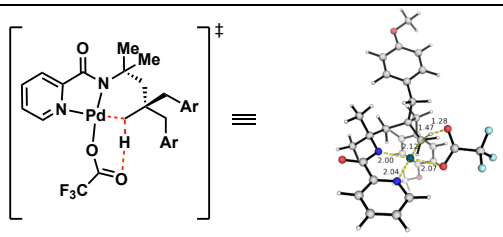
(b) Oxidative insertion TSs	
ts-16	**ts-16-c2**
$\Delta\Delta G^{\ddagger} = 0.0$	$\Delta\Delta G^{\ddagger} = 5.0$
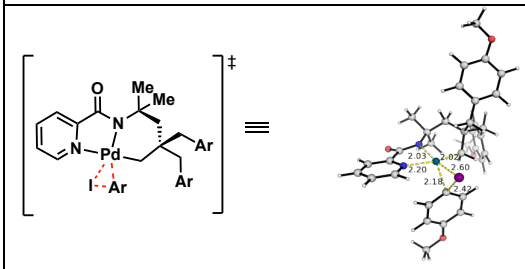	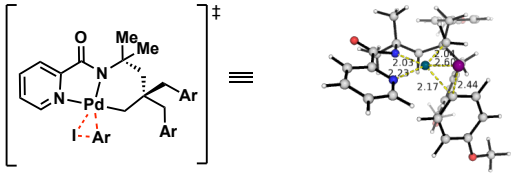
(c) Reductive elimination TSs	
ts-17	**ts-17-c2**
$\Delta\Delta G^{\ddagger} = 0.0$	$\Delta\Delta G^{\ddagger} = 2.7$
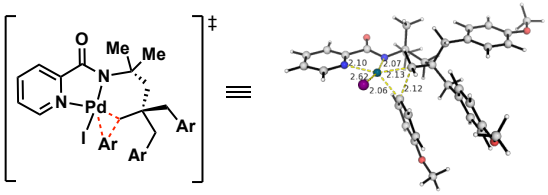	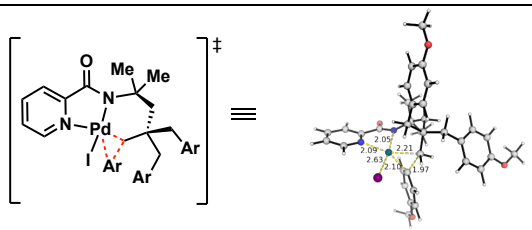
ts-17-c3 / $\Delta\Delta G^{\ddagger} = 1.9$	**ts-17-c4** / $\Delta\Delta G^{\ddagger} = 4.4$
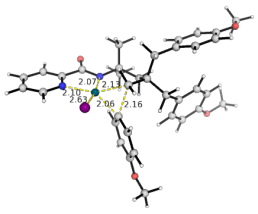	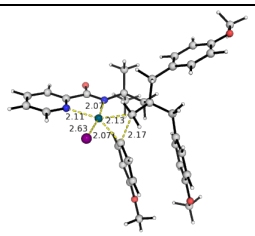
ts-17-c5 / $\Delta\Delta G^{\ddagger} = 10.0$	
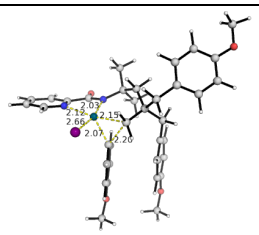	

Figure 4.9. Relative activation energies and optimised structures for TS conformers of (a) C–H activation, (b) oxidative addition and (c) reductive elimination for third arylation.

Our calculations suggest that tri-arylations can be achieved more easily in the absence, rather than the presence, of the pyridine ligand. This is indeed what was observed experimentally.

4.3.5 Effects of directing groups

The initial experimental screening for the best directing group (DG) for the arylation reaction showed that the picolinic acid-based DG (**DG1**, Table 4.1) worked the best for this reaction. The list of DGs includes adding substituents *ortho* (**DG2**, **DG3**, **DG8**) and *meta* (**DG4**, **DG8**) to the pyridyl ring of **DG1**, where **DG2** and **DG3** have different electronic demands (in **DG2**, the inductive electron-withdrawing effect slightly dominate over resonance electron-donating effect while in **DG3**, the electron-donation dominates over electron withdrawal). **DG5** and **DG6** are respectively the pyrimidine and pyrazine analogues of picolinamide **DG1**. All of these DGs form [5,6]-fused carbopalladated intermediate upon C–H activation except **DG7**, which forms a [6,6]-carbopalladated intermediate.

Computational studies were performed to understand how the different steric and electronic effects of these DGs impact on the yield of the reaction outcome. The reaction barriers for C–H activation, OA and RE steps were explored and the results are given in Table 4.1. The overall rate-determining transition state (RDTS) for each DG is highlighted in bold. We note that either the OA or RE step can be rate-determining depending on the substrate structure. This is in agreement with our observation that in first arylation, OA and RE have rather close activation barriers. From Table 4.1, the order of increasing energy span is **DG1** (30.5) ~ **DG5** (30.9) < **DG6** (32.0) ~ **DG4** (32.3) < **DG2** (36.1) ~ **DG3** = **DG8** (36.4) << **DG7** (46.1) where the overall energy span for activation given in the parentheses are quoted in kcal mol^{-1}. Structures **DG1** and **DG5**

have the lowest activation barriers and are thus predicted to be the best directing groups for arylation. Experimentally, **DG5/DG6** give much lower yield than **DG1** and **DG4**. This could be because the extra N atom in the heteroaromatic rings in **DG5/DG6** interact with other molecules (such as solvent) to impede the OA and RE steps. The strong coordinating ability of the extra N-atom could also outcompete substrate binding sites and deactivate catalytic activity. Structures **DG2/DG3/DG8**, with substituents at the *ortho*-position relative to the N-atom in the pyridine ring, all have higher activation barriers (~ 6 kcal mol^{-1}) than **DG1**, indeed, these give very poor yields.

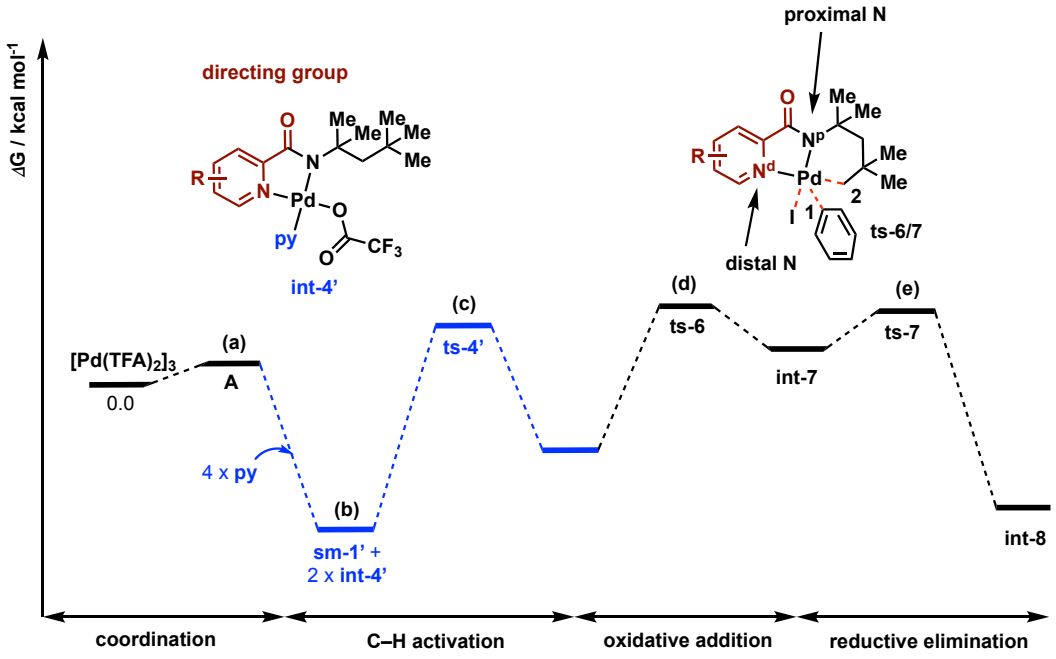

DGs	Expt Yield	(a)	(b)	(c)	(d)	(e)	Overall barrier
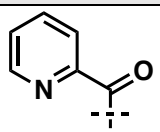 **DG1**	77%	-2.7	-23.4	4.4	**7.1**	6.8	30.5
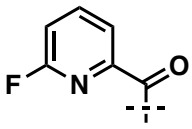 **DG2**	0%	11.5	-14.3	14.3	17.7	**21.8**	36.1

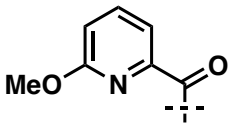 **DG3**	0%	2.9	-20.2	9.5	13.5	**16.2**	36.4
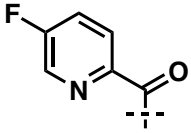 **DG4**	75%	1.1	-20.9	7.1	11.2	**11.4**	32.3
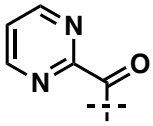 **DG5**	7%	2.1	-20.7	7.7	**10.2**	9.9	30.9
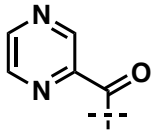 **DG6**	25%	4.0	-19.6	8.5	12.0	**12.4**	32.0
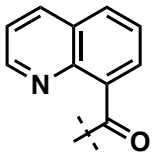 **DG7**	0%	3.5	-17.8	21.5	15.9	**28.3**	46.1
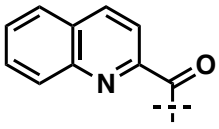 **DG8**	10%	1.3	-21.0	11.4	12.9	**15.4**	36.4

Table 4.1. The reaction barriers for different directing groups used in the arylation reaction. The rate-determining TS step for each is given in bold.

With these comparative energy profiles, detailed stereoelectronic influences of these DGs on the activation barriers (and thus yield) were analysed. Analysis of the HOMO of the TSs for both OA and RE steps for all DGs indicates that the electron distributions are rather similar (Figures 4.10). The key geometrical parameters in these TSs show that the RE TSs have very similar geometries (Table 4.2); the OA TSs have varying Pd-N^d bond

distances, implicating a different degree of electron donation from the lone pair on the directing groups to the electrophilic Pd metal centre.

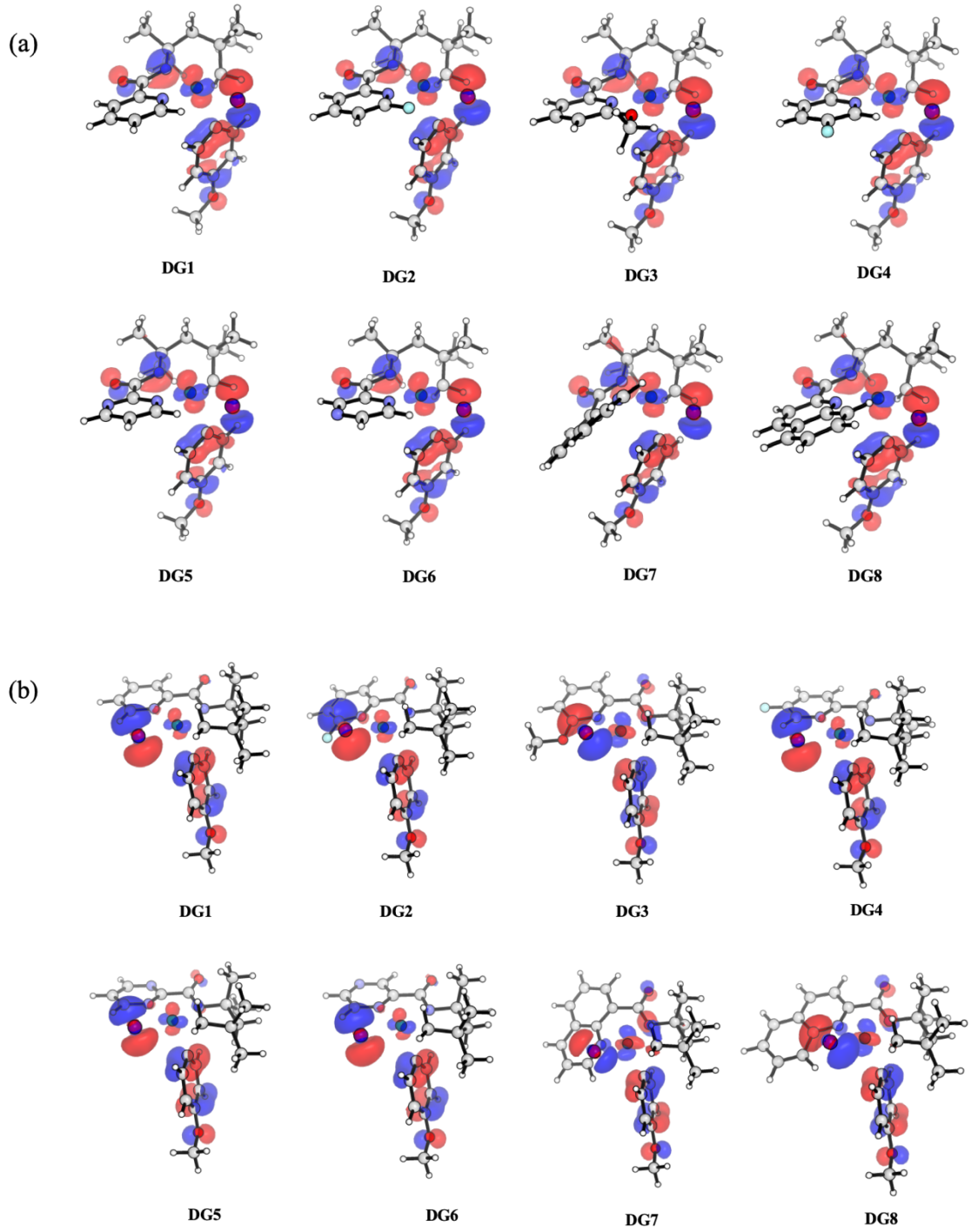

Figure 4.10. HOMO of TSs for (a) oxidative addition and (b) reductive elimination at a surface isovalue of 0.05.

Oxidative addition TSs								
	Bond distances / Å					Bond angles / °		
DGs	**Pd-N^p**	**Pd-N^d**	**Pd-I**	**Pd-C1**	**Pd-C2**	**N^p-Pd-I**	**C2-Pd-N^d**	**I-Pd-C1**
DG1	2.03	2.20	2.59	2.18	2.02	163.2	168.2	60.4
DG2	2.04	2.26	2.59	2.14	2.02	161.1	165.3	63.1
DG3	2.04	2.25	2.60	2.14	2.03	162.4	164.9	62.3
DG4	2.03	2.21	2.59	2.18	2.02	162.8	168.2	60.7
DG5	2.02	2.20	2.60	2.18	2.02	162.4	168.0	60.6
DG6	2.03	2.21	2.59	2.17	2.02	162.6	168.1	61.2
DG7	2.03	2.22	2.59	2.15	2.03	173.2	171.0	62.8
DG8	2.03	2.28	2.60	2.15	2.03	166.6	163.8	61.6
Reductive elimination TSs								
	Bond distances / Å					**Bond angles / °**		
DGs	**Pd-N^p**	**Pd-N^d**	**Pd-I**	**Pd-C1**	**Pd-C2**	**N^p-Pd-I**	**C2-Pd-N^d**	**C2-Pd-C1**
DG1	2.08	2.10	2.62	2.06	2.12	166.7	157.2	61.5
DG2	2.08	2.11	2.62	2.06	2.12	160.5	162.7	60.8
DG3	2.08	2.10	2.63	2.05	2.12	159.0	162.4	60.9
DG4	2.08	2.10	2.62	2.06	2.12	167.1	156.8	61.5
DG5	2.07	2.10	2.62	2.06	2.12	167.0	158.1	61.6
DG6	2.08	2.10	2.62	2.06	2.12	167.2	156.6	61.8
DG7	2.06	2.09	2.63	2.07	2.12	158.6	175.1	60.1
DG8	2.07	2.10	2.63	2.05	2.12	157.7	164.1	60.9

Table 4.2. Key geometrical parameters for the TSs in the oxidative addition and reductive elimination steps.

Oxidative addition TSs								
	NBO charge *q/e*						Largest E_2 / kcal mol^{-1}	
DGs	**Pd**	**N^p**	**N^d**	**I**	**C1**	**C2**	**N^p**	**N^d**
DG1	0.208	-0.586	-0.417	0.187	-0.044	-0.433	-38.50	-38.02
DG2	0.201	-0.595	-0.446	0.173	-0.030	-0.406	-4.56	-37.10
DG3	0.216	-0.595	-0.442	0.167	-0.031	-0.417	-4.39	-37.11
DG4	0.204	-0.588	-0.397	0.189	-0.045	-0.427	-38.41	-37.95
DG5	0.201	-0.589	-0.443	0.186	-0.049	-0.433	-4.65	-40.64
DG6	0.202	-0.588	-0.385	0.184	-0.041	-0.423	-38.14	-38.18
DG7	0.213	-0.598	-0.428	0.141	0.001	-0.424	-5.57	-35.91
DG8	0.215	-0.591	-0.407	0.160	-0.030	-0.413	-4.53	-33.03
Reductive elimination TSs								
	NBO charge *q/e*						Largest E_2 / kcal mol^{-1}	
DGs	**Pd**	**N^p**	**N^d**	**I**	**C1**	**C2**	**N^p**	**N^d**
DG1	0.227	-0.567	-0.395	-0.202	0.034	-0.322	-5.74	-47.13
DG2	0.213	-0.567	-0.432	-0.169	0.043	-0.345	-7.67	-44.48
DG3	0.236	-0.566	-0.426	-0.205	0.045	-0.352	-6.46	-46.96
DG4	0.222	-0.568	-0.378	-0.194	0.033	-0.319	-5.53	-45.07
DG5	0.221	-0.569	-0.425	-0.209	0.034	-0.322	-83.25	-47.63
DG6	0.217	-0.568	-0.367	-0.191	0.033	-0.316	-80.40	-45.23
DG7	0.245	-0.572	-0.398	-0.171	0.062	-0.398	-77.96	-43.75
DG8	0.228	-0.562	-0.381	-0.189	0.046	-0.357	-70.58	-45.11

Table 4.3. NBO charges and the largest perturbative stabilisation energy (E_2) due to the lone pair (LP) donation from N to Pd LP* orbital.

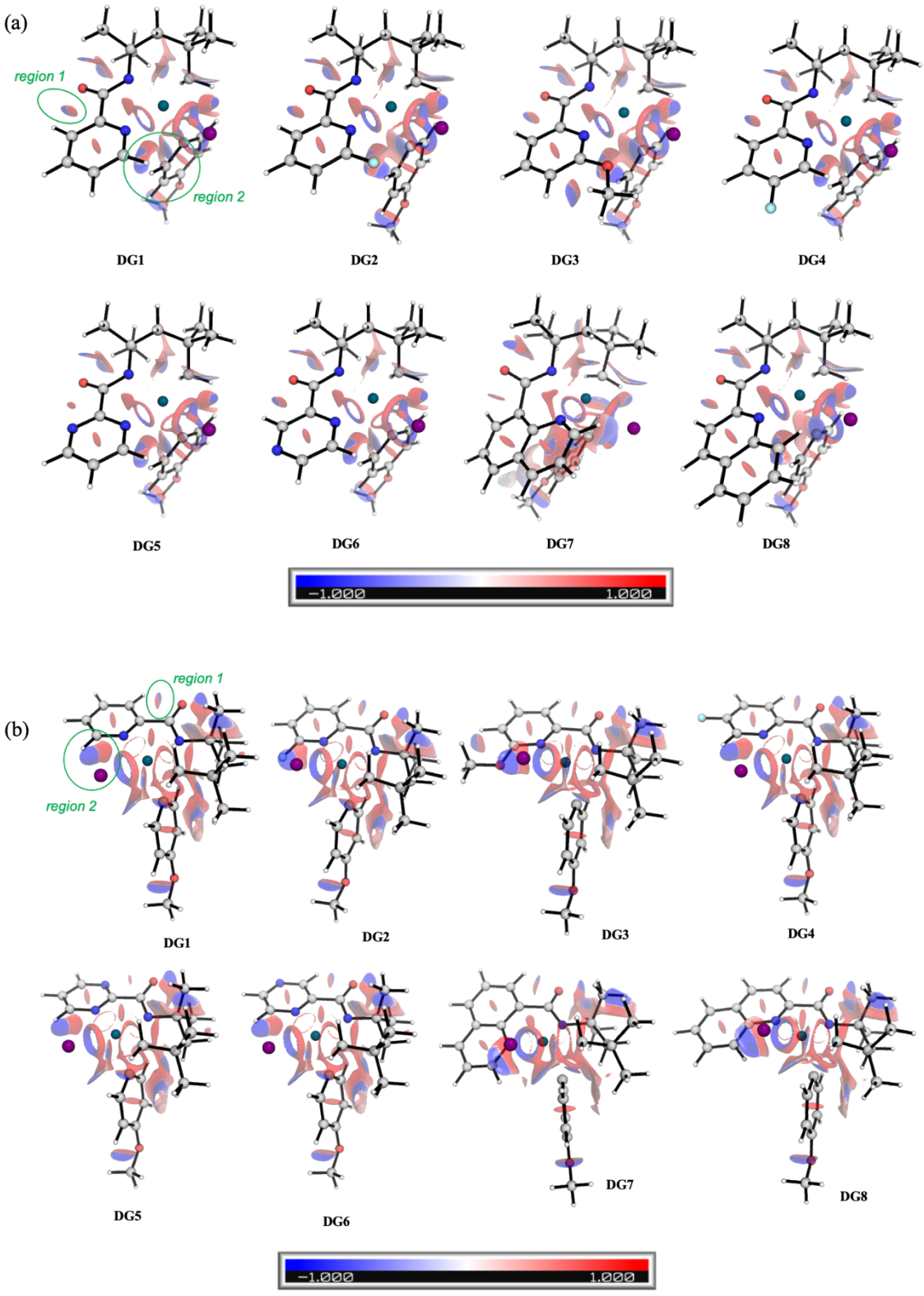

Figure 4.11. NCI plots of TSs for (a) oxidative addition and (b) reductive elimination at an isosurface value of 0.05.

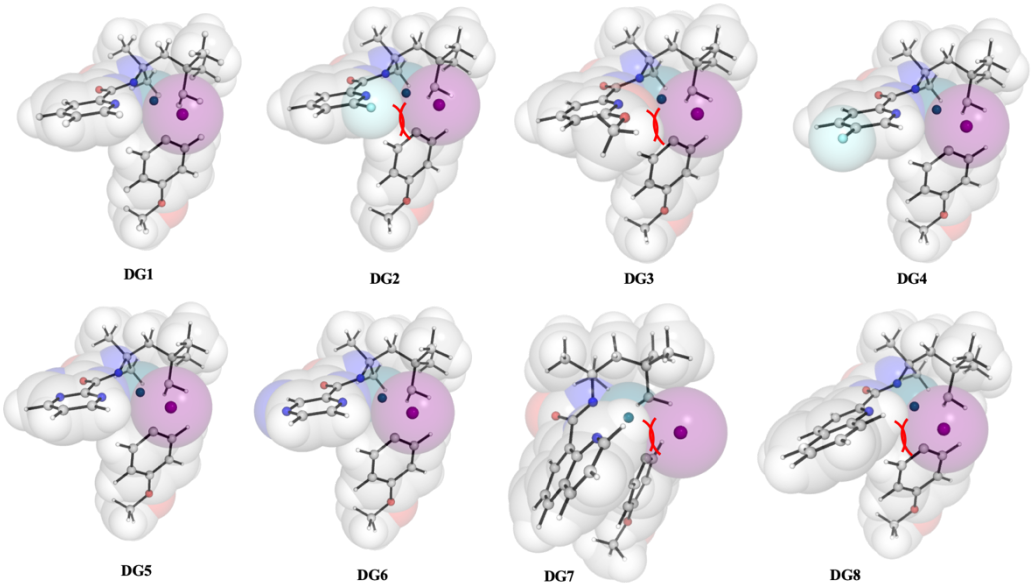

Figure 4.12. van der Waals surfaces visualisation of oxidative addition TSs. Steric clashes between the substituents *ortho*- to pyridyl ring and the incoming aryliodide (**DG2/3/8**) can clearly be seen.

DG2, DG3 and **DG8** (overall barrier 36.1 to 36.4 kcal mol^{-1}) all have longer Pd-N^d bond distances (2.25–2.28 Å) than that in **DG1** (2.20Å), suggesting smaller degrees of electron donation. Quantitative NBO analysis using second-order perturbative stabilisation energy (E_2) is consistent with this observation and indicates that these TSs are stabilised to a lesser extent than **DG1** (Table 4.3). Steric factors play an important role in the OA step. The incoming Ar–I groups increase steric crowding, therefore, any steric bulk hindering the incoming aryl iodide will disfavour this step. The substituents at the *ortho*-position relative to N-atom of the pyridyl ring in these DGs give rise to unfavourable steric hinderance to the 4-iodoanisol that is being oxidatively added. These steric clashes between the *ortho*-substituents and the incoming coupling partner is evident in the NCI plots as well as van der Waals surface plots in the OA transition structures (Figures 4.11 and 4.12); these unfavourable repulsions heighten the barrier heights. Therefore, both

steric and electronic factors dictate that these DGs (**DG2/DG3/DG8**) would perform less well than **DG1**, in agreement with experimental observations.

For **DG4, DG5** and **DG6** (overall barrier 30.9 to 32.3 kcal mol^{-1}), both NBO analyses and NCI plots indicate similar electronic and steric interactions to those in **DG1**, implicating similar yields possible. **DG5** and **DG6** are analogous to **DG1** and have similar sterics as **DG1**; they differ in the position of the extra N-atom in the six-membered ring. The lone pair on the heterocyclic N-atom in **DG5** had unfavourable repulsive interaction with the amide oxygen atom (NCI plot, Figures 4.11, region 1), therefore destabilising the TS more than in **DG6**, giving lower experimental yield. **DG5** and **DG6**, although satisfying the stereoelectronic constraints on the rate-determining OA step, performed badly experimentally, possibly due to the above-mentioned coordinating ability of the heterocycles to outcompete substrate binding and deactivate catalytic activity or to bind to extra molecules (other ligand/solvent molecules) that impede OA/RE steps in ways that are not captured in the present considerations. **DG4** has F atom *meta* to the directing N-atom, thereby, out of steric clashes with the incoming iodoanisol that is being oxidatively added. In addition, the perturbative stabilisation energy (E_2) from pyridyl N-atom donation to Pd is similar to that in **DG1** (within 1 kcal mol^{-1}, Table 4.3). This electronic stabilisation greatly favoured oxidative addition as the Pd-metal cycled from Pd(II) to Pd(IV) in the OA TS. This similarity in the steric and electronic factors for **DG1** and **DG4** explained their similar yield obtained experimentally (77% and 75% respectively, Table 4.1).

For **DG7**, the OA TS forms a [6,6]-palladacycle, which, although has similar electron distributions and bond distances in the TS as that for **DG1** (Figure 4.10 and Table 4.2), introduces very unfavourable ring twisting, thus giving augmented repulsive interactions

(Figures 4.11 and 4.12). The [6,6]-palladacycle is hugely disfavoured due to the steric constraints and this observation is consistent with various studies of similar catalytic systems.[366,368,377,379,381,396,424,425]

To sum up, for DGs that chelate to Pd metal forming a [5,6]-fused carbopalladated intermediate, the presence of a substituent at the *ortho*-position relative to the ring N-atom, regardless of its electronics (electron-withdrawing –F group in **DG2** and electron-donating –OMe group in **DG3**, and benzene ring as part of quinoline in **DG8**), renders the DG ineffective. For DGs that chelate to Pd metal forming a [6,6]-fused intermediate, hugely disfavoured geometrical distortion occurs and introduces massive ring strain that renders the transition structure rather high in energy, giving low product yield.

4.3.6 Substrate 3a: mononuclear pathway for Pd(II) catalysis

Experimentally, when substrate **1a** was used for δ-C(sp^3)–H arylation, it was found that the reaction required harsher conditions (higher temperature and longer time) than for substrate **2a**; pyridine ligand **L1** was found to be incompetent in effecting arylation while a different ligand, pyridone ligand **L14** (Scheme 4.1(c)), was required. In addition, kinetic isotope effect studies and order determinations suggest an irreversible C–H activation step as overall rate-determining for substrate **1a**, in contrast to substrate **2a**.

For computational modelling, substrate **3a**, where the ethoxycarbonyl group (–COOEt) on the α-Carbon of substrate **1a** is replaced by a methyl group (–Me), was employed. This substrate (**3a**) worked well for δ-arylation and it only differs from substrate **2a** in the two extra methyl groups on α- and γ-positions (useful for comparisons later). An additional simplification in modelling was replacing the benzyl protecting group (–Bn) on the pyridone ligand **L14** by a methyl group (–Me). The mononuclear pathways (Figure 4.13)

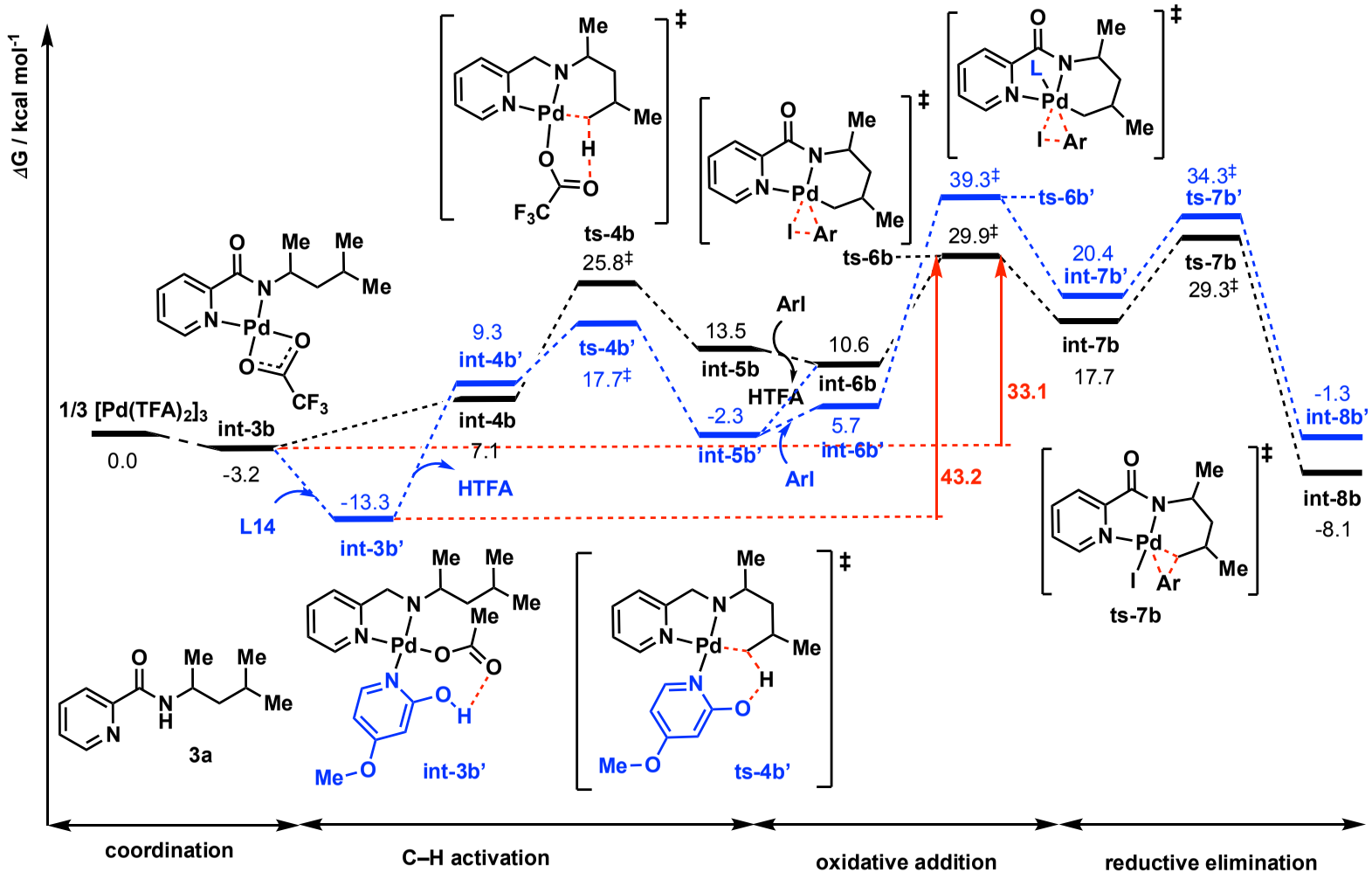

Figure 4.13. Gibbs free energy profile for first arylation in the absence (black) and presence (blue) of pyridone ligand **L14** with mononuclear palladium catalyst as a starting material for substrate **3a**.

are similar to those for substrate **2a** in Figure 4.2: the overall barrier in the absence of ligand is 33.1 kcal mol^{-1} whereas this is 43.2 kcal mol^{-1} with ligand. This is inconsistent with experimental observations that this reaction required the presence of ligand to occur; the absence of ligand or the use of pyridine ligand (**L1**) did not work. As for substrate **2a**, the ligand was not found to participate in either OA or RE step as the inclusion of the ligand in the TSs (**ts-6b'** and **ts-7b'**, Figure 4.14) increases the barrier for these steps (in **ts-7b'**, the ligand could not coordinate to the Pd-centre as RE took place). We proceed to look at the trinuclear pathway as previously (*vide infra*).

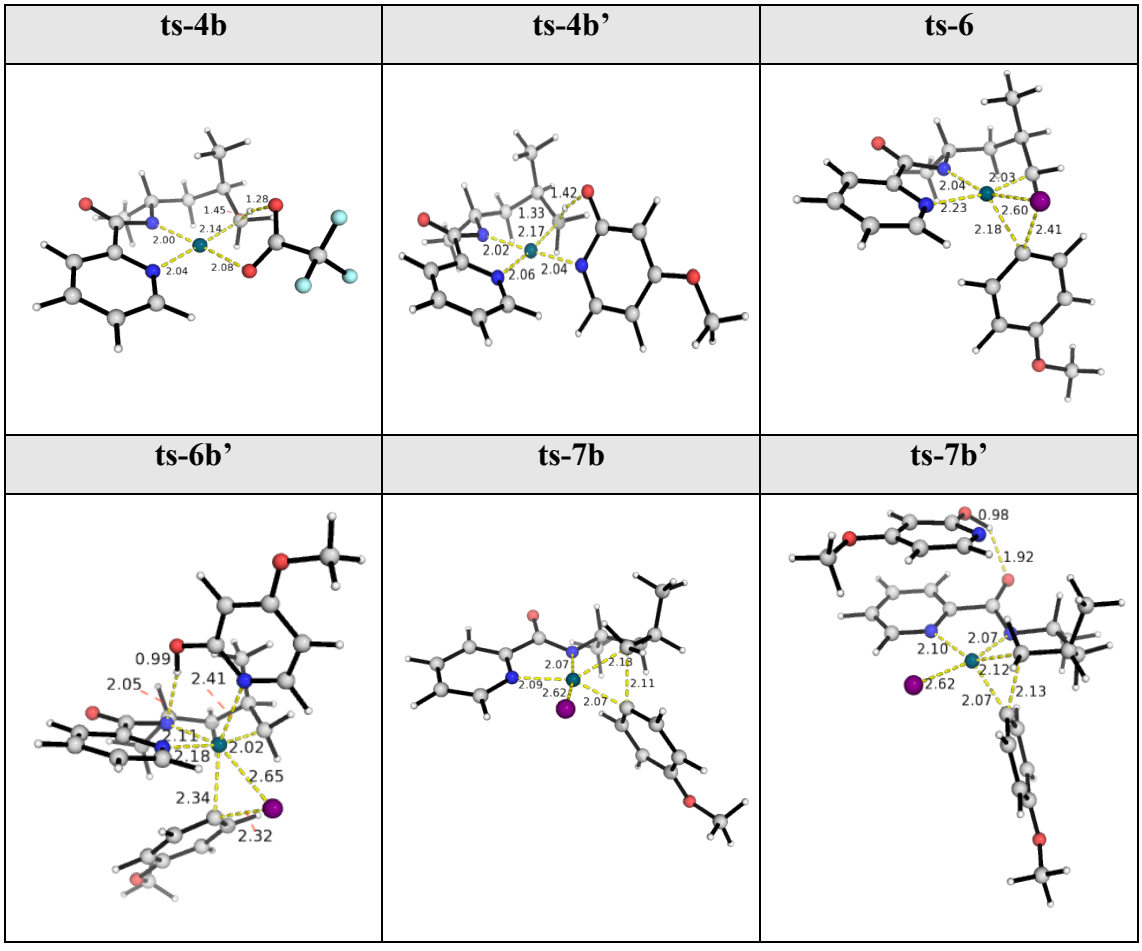

Figure 4.14. Selected TS structures for the energy profile in Figure 4.13.

4.3.7 Substrate 3a: trinuclear pathway for Pd(II) catalysis

The trinuclear pathways for substrate **3a** in Figure 4.15 present a similar picture to that for substrate **2a** (Figure 4.5). In the absence of any ligand (the black pathways on top), the dissociation of trimeric $Pd_3(TFA)_6$ catalyst complex to its monomeric form that further undergoes OA/RE is thermally rather inaccessible, requiring energy to overcome a very high reaction barrier of 50.9 kcal mol^{-1}. The direct C–H activation via CMD of the trimeric complex **Ab** is more favourable than its dissociation, giving an overall activation barrier of 42.5 kcal mol^{-1}. With pyridone ligand **L14**, the trimeric complex **Ab** favourably dissociates into its monomeric forms **sm-1b'** and **int-3b'**. This is followed by a ligand-assisted C–H activation **ts-4b'**. The subsequent OA and RE steps are higher than the C–H activation step and very close in activation barriers (within 1 kcal mol^{-1}), giving an overall barrier of 43.2 kcal mol^{-1}, which is slightly higher than that without pyridone ligand via C–H activation of the trinuclear complex **Ab**. The pyridone ligand **L14** was not found to directly participate in either OA/RE steps as these (**ts-6b'** and **ts-7b'**) have higher activation barriers than the steps without pyridone ligand (**ts-6b** and **ts-7b**). These pathways both point to the OA step as the overall rate-determining, as in substrate **2a**. It conflicts the experimental finding that the C–H activation step is the rate-limiting step for this pyridone-assisted arylation of substrate **3a**.

4.3.8 Role of silver carbonate as a co-ligand

We wonder if the silver additive or the cationic sodium counterion, in concert with the pyridone ligand **L14**, plays any role in lowering the OA step in substrate **3a**, such that the overall rate-determining TS becomes the C–H activation step. We then considered the possible pathways involving cationic intermediates in the OA step to see if this provides an alternative pathway.[404,426] The introduction of either Ag^+ or Na^+ cation in the presence

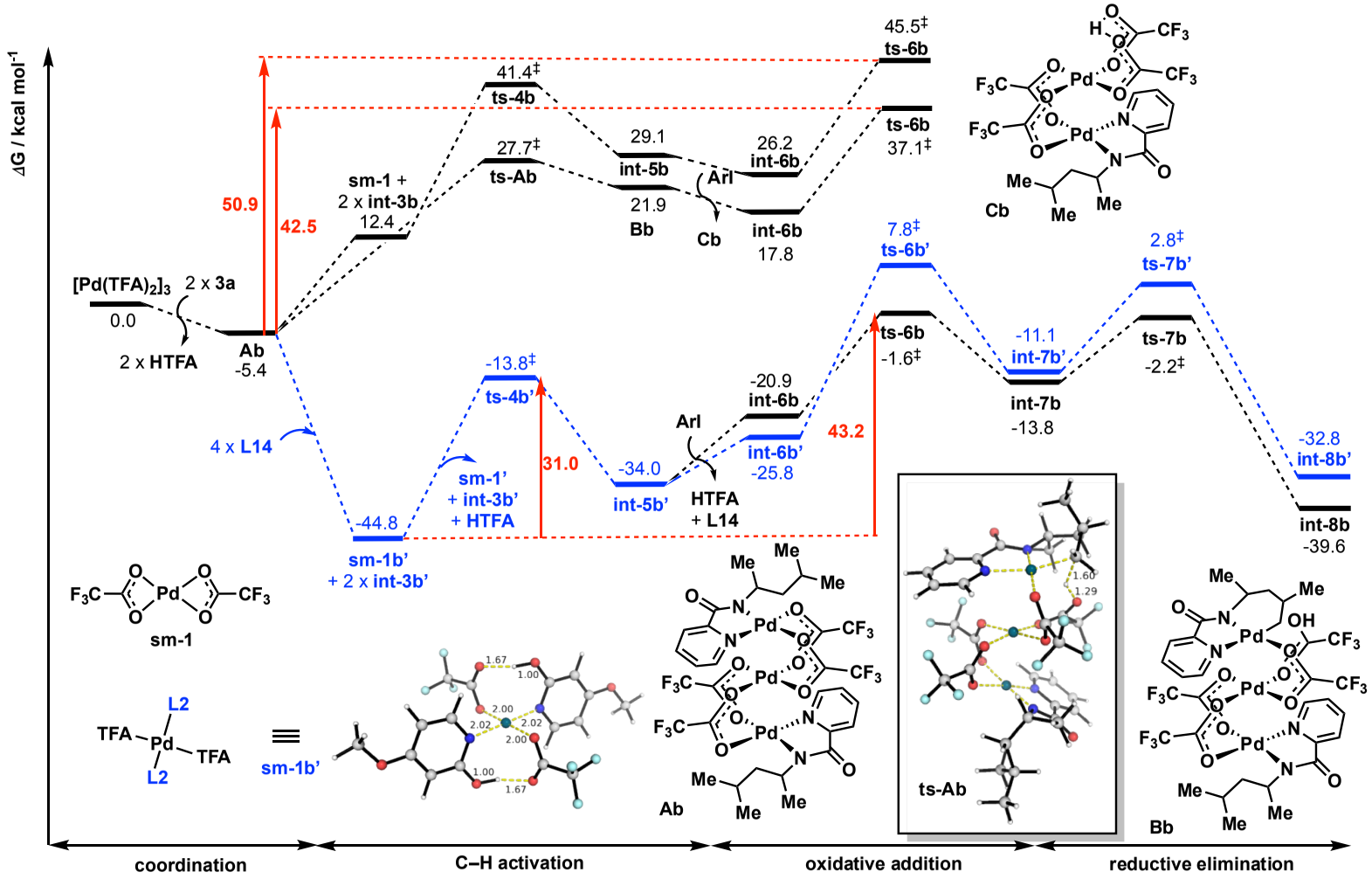

Figure 4.15. Gibbs free energy profile for first arylation in the absence (black) and presence (blue) of pyridone ligand **L14** with trinuclear palladium catalyst as a starting material for substrate **3a**.

of ligand **L14** was separately explored. We found that the activation barrier for OA is 30.3 kcal mol^{-1} with Na^+ cation and 20.1 kcal mol^{-1} with Ag^+ cation, relative to the cationic intermediates, implicating possible Ag^+ cation participation (Figure 4.16). Since it is difficult to compare species with different overall charges due to huge differences in the solvation energies involved,[427,428] we considered a heterodimeric catalytic species involving silver cation for the OA/RE steps in neutral pathways, in a fashion similar to the heterodimeric Pd–Ag catalytic species considered for C–H activation step by Houk and Schaefer.[429,430] A similar Pd–Ag heterobimetallic TS structure was also implicated in the β-bromide elimination step in the Pd-catalysed C(sp^2)–H alkynylation via inverse Sonogashira coupling using bromoethynytrimethylsilane (see subsection 6.3.4).

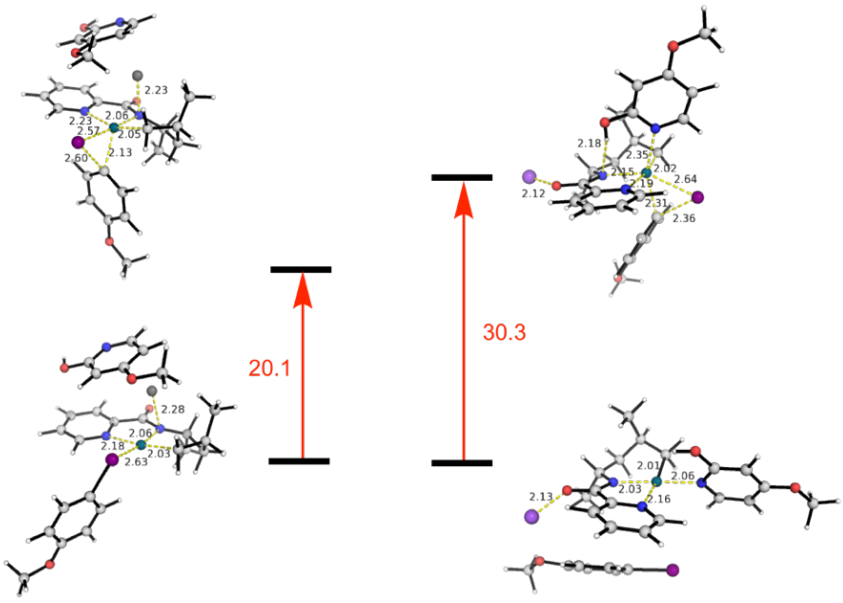

Figure 4.16. Optimised structures involving cationic species. Left: with silver cation; right: with sodium cation.

The overall Gibbs energy profile with silver carbonate participation is shown in Figure 4.17. The addition of Ag_2CO_3 to intermediate **int-5b'** yields structure **int-9b** that is highly stabilised. The carbonate anion first deprotonates the hydroxyl proton on pyridone ligand **L14**, without any barrier – although the pKa of bicarbonate, at ~10.3, is much lower

(carbonate a weaker conjugate base) than that of pyridone (~11.7 for 2-pyridone), the O–H bond on the pyridone ligand is likely to be weakened significantly as the pyridyl-N donates electron to the electrophilic Pd-centre. The N-atom on the pyridyl group of the DG gets displaced as it coordinates to a silver ion; this silver ion is also held in place by the deprotonated hydroxyl-O on pyridone **L14** (**int9b**, Figure 4.17). A second silver ion coordinates to the O atoms of the picolinamide DG and the TFA ligand and is held in close proximity to iodine, facilitating the subsequent highly exergonic formation of insoluble AgI as the reaction proceeds.

The overall stabilising non-covalent interactions (NCIs) in the highly organised transition structure **ts-9b** (Figure 4.18), together with the enthalpically favourable electrostatic interactions between Ag^{+} and I^{-} ions, greatly lower the activation barrier of the OA step to 28.3 kcal mol^{-1}. With this cooperative pyridone/silver carbonate binding, the C–H activation step, with a barrier of 31.0 kcal mol^{-1}, becomes overall rate-determining.

We note that the pyridone ligand **L14** is necessary as the deprotonated hydroxyl-oxygen played a crucial role in giving a highly ordered transition structure; replacing it with pyridine ligand **L1** resulted in the loss of this organisation, indicating that this could be a plausible reason why pyridine ligand did not work very well experimentally (*vide infra*). The final product, **int-11b**, is highly exergonic, assisted by the favourable formation of insoluble AgI salt and thus thermodynamically favoured.

For the second C–H activation, the TS **ts-9b'** occurs at a very high energy barrier relative to the first arylation product **int-11b**, which is highly stabilised. The activation barrier of 60.6 kcal mol^{-1} for second arylation was insurmountable so that the second arylation for substrate **3a** was not observed experimentally.

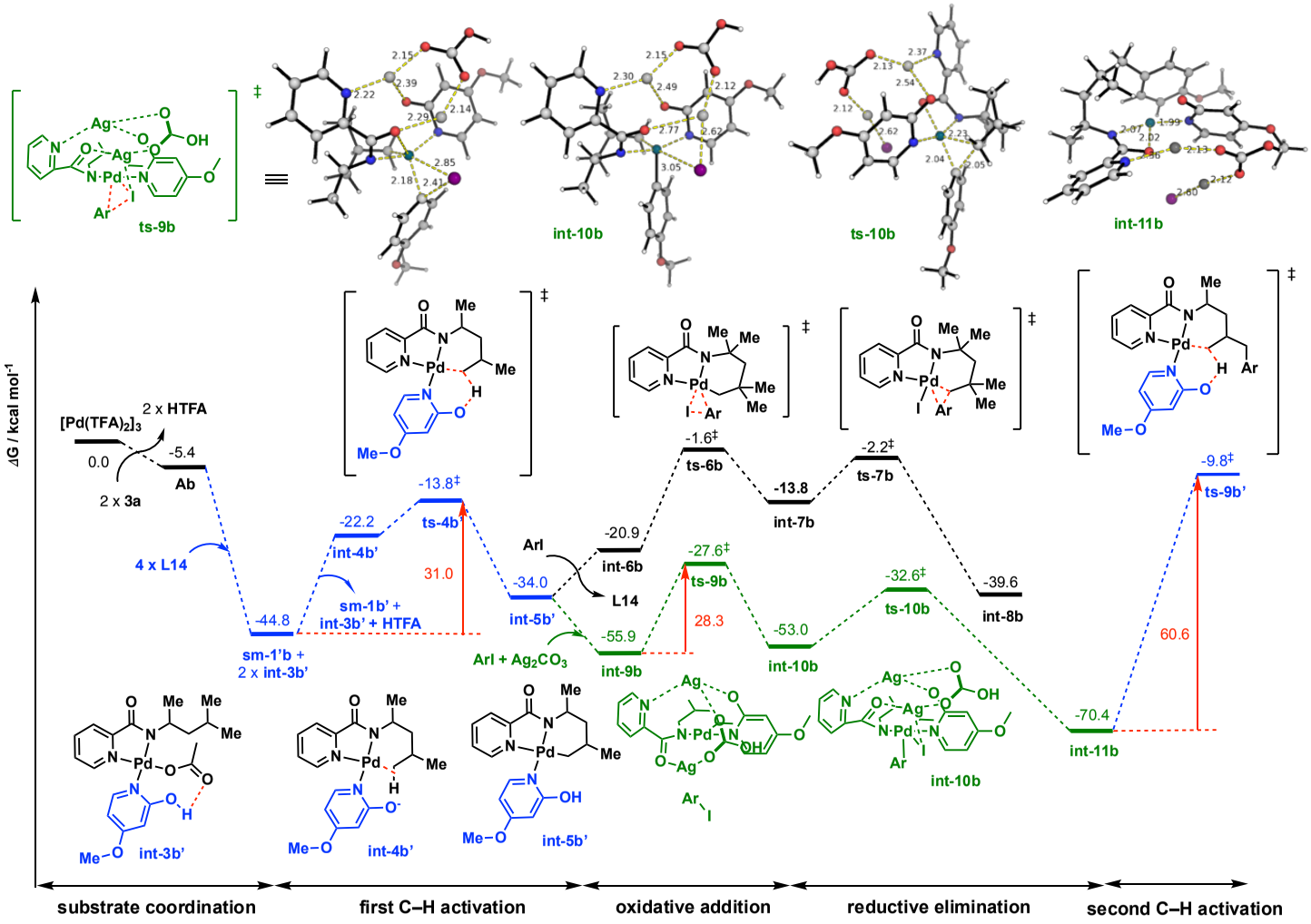

Figure 4.17. Gibbs free energy profile for first arylation in the presence of pyridone ligand **L14** and silver carbonate (green) with trinuclear palladium catalyst as a starting material for substrate **3a**.

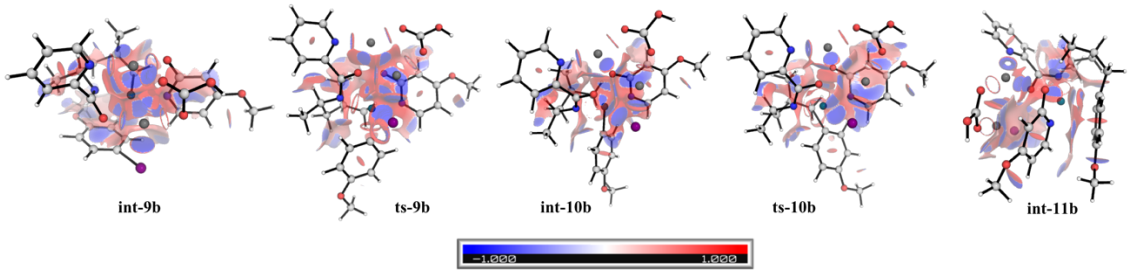

Figure 4.18. NCI plots of heterodimeric Pd–Ag catalytic structures at an isosurface value of 0.05 for substrate **3a** in the presence of pyridone ligand **L14**.

To see if silver carbonate has any similar effect on substrate **2a** in the presence of pyridine ligand **L1**, we performed a similar TS search on the parent system in the presence of silver carbonate. Most TS searches failed to yield the expected structure due to the increased degree of freedom in the silver carbonate positions as pyridine could not hold silver ion in position after its N-atom coordinates to the Pd metal. The TS we found for this OA step, **ts-9c** (at 11.0 kcal mol^{-1}), is higher in activation barrier than **ts-6** without the involvement of either pyridine or silver carbonate (at 7.1 kcal mol^{-1}); the overall barrier for arylation increases from 30.5 kcal mol^{-1} without Ag_2CO_3 to 38.8 kcal mol^{-1} with Ag_2CO_3 participation (Figure 4.19). In **ts-9c**, the pyridine ligand could not hold silver ion in a highly organised fashion as compared to **ts-9b** (Figure 4.17), resulting in poorer interactions and higher activation barriers.

4.3.9 Substrate 3a: C–H activation step and diastereoselectivity

A high degree of diastereoselectivity in the products was observed experimentally when the *L*-isomer of leucine and its derivatives were subjected to the present transformation (Scheme 4.2). Experimental characterisation using NMR could only establish the ratio of relative stereochemistry of the diastereomeric mixture of products. We thus recourse to computational investigations to assign the absolute stereochemistry and predict the diastereoselectivity ratio (*d.r.*) of the mixture of diastereomeric products. Indeed, our

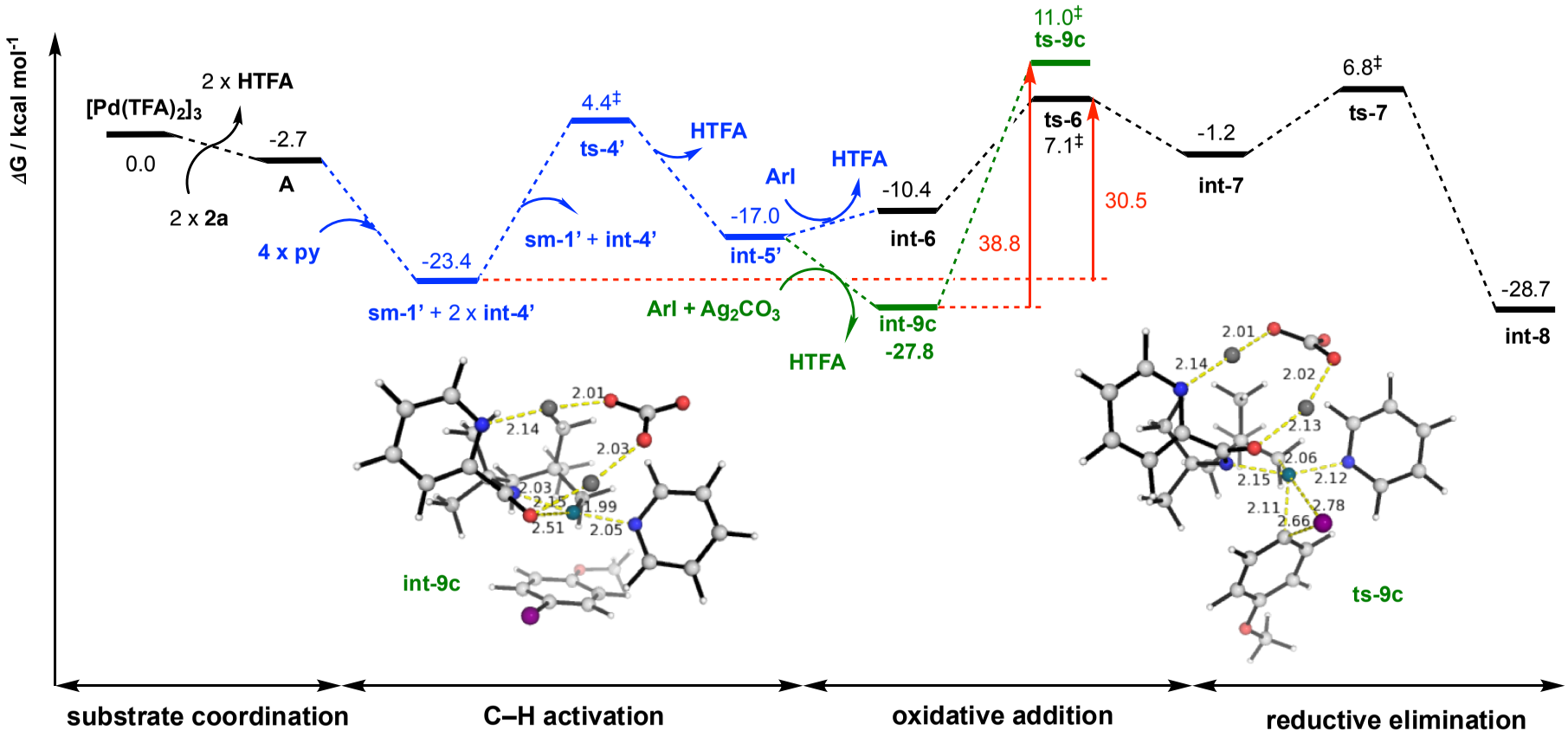

Figure 4.19. Gibbs free energy profile for first arylation in the presence of pyridine ligand **L1** and silver carbonate (green) with trinuclear palladium catalyst as a starting material for substrate **2a**.

computational assignments agreed very well with previously reported experimental results.[396]

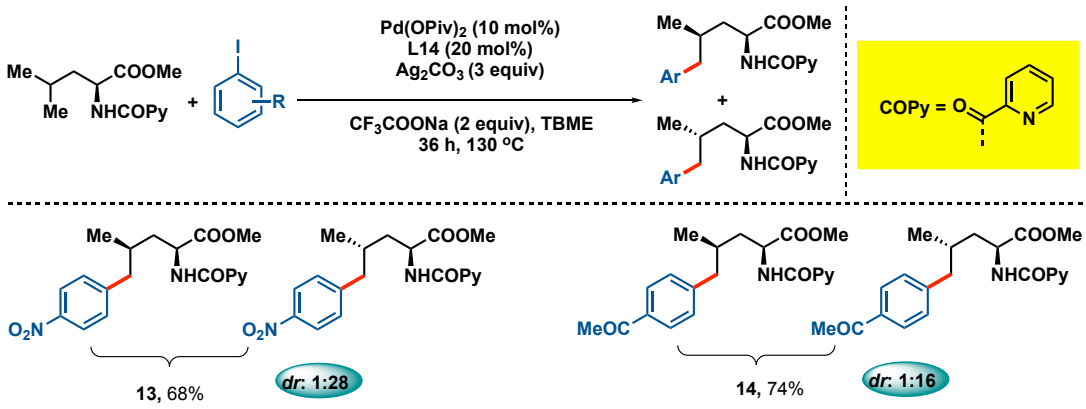

Scheme 4.2. Diastereoselective δ-mono-arylation of L-leucine.

The C–H activation step was found, both experimentally and computationally, to be overall rate-determining for substrate **3a** (subsections 4.3.7 and 4.3.8), an *L*-leucine derivative. A detailed investigation of this step would warrant a good understanding of the origin of the diastereoselectivity and was thus carefully performed. The different possibilities for the C–H activation step were considered with their relative activation barriers given (Figure 4.20). The lowest-barrier TS from each scenario is used for discussion.

Without any ligand participation (Figure 4.20 (b)), the C–H activation step (**ts-4b**) is 3.4 kcal mol^{-1} higher in barrier than the lowest TS (**ts-4b'** via pyridone **L14**). Using pyridine in place of pyridone ligand **L14**, the C–H activation step is 3.1–5.1 kcal mol^{-1} higher depending on whether pyridine acts as a ligand (**ts-4b'-py**) or as a base (**ts-4b''-py**). In all cases, these are not as efficient as using pyridone ligand **L14**. The absence of Thorpe-Ingold effect in substrate **3a** (subsection 4.3.10) renders the rate-determining C–H activation step via CMD more difficult. Using pyridine in addition to a separate TFA ion as a base is not as good in bringing the C–H bond into position for activation as using

pyridone ligand **L14** which can bring the C–H bond close to Pd(II) metal by N-coordination to the metal while carrying out the CMD step in a well-coordinated transition structure (**ts-4b'**).

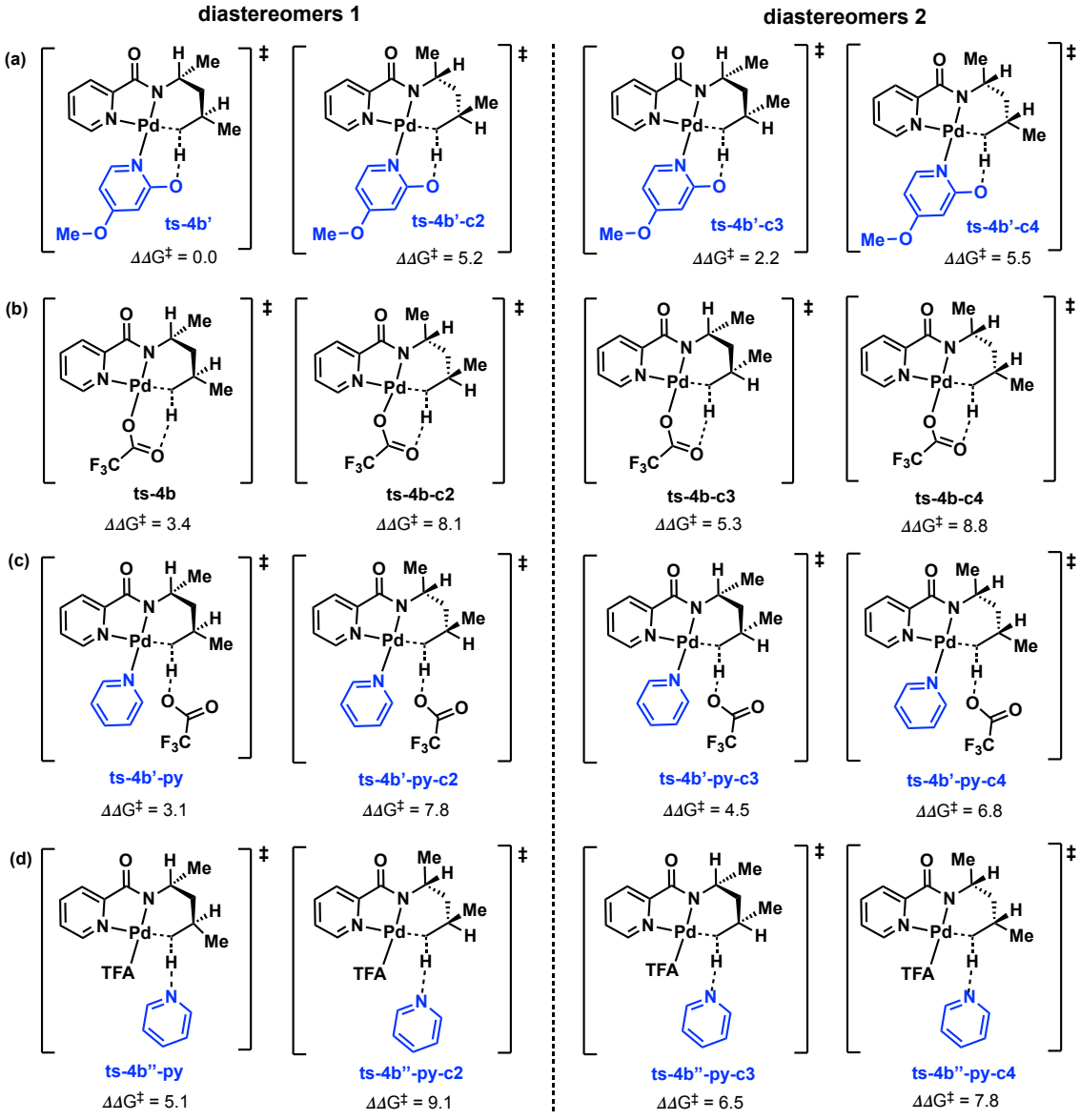

Figure 4.20. Different conformations considered for C–H activation step using (a) pyridone **L14** (b) TFA ion (c) TFA ion with pyridine **L1** as ligand (d) pyridine **L1**. All $\Delta\Delta G^{\ddagger}$ values are taken relative to the lowest activation barrier **ts-4b'** and are quoted in kcal mol^{-1}.

More importantly, our calculations give the differences in the C–H activation barriers ($\Delta\Delta G^{\ddagger}$) between the two diastereomers (**ts-4b'** and **ts-4b'-c3**, Figure 4.20) as 2.2 kcal

mol^{-1}. This corresponds to a diastereoselectivity of 21:1, in good agreement with experimentally observed ratio of 28:1. While the absolute configurations for the observed *d.r.* could not be determined by experimental means, computations allow us to establish the absolute stereochemistry of the arylated products with confidence.

4.3.10 Comparing substrates 2a and 3a: Thorpe-Ingold effect

The differences in the C–H activation barriers for substrates **2a** and **3a** can be demonstrated by comparing the relative heats of enthalpies for the formations of their respective C–H activated complexes (Scheme 4.3). We considered the case where each activated intermediate has pyridine ligand coordinated to it. Conformations of the activated complexes where the 6-membered palladacycle puckered in different orientations were considered. For the second reaction (Scheme 4.3 (ii)), these include the activated complexes formed in Figure 4.20 (c) after losing an HTFA molecule. The lowest energy conformer for each reaction is used for comparison. The differences in the enthalpies, $\Delta\Delta H = \Delta H_1 - \Delta H_2$, gives the relative ease of formation of each activated complex. Computations show that the enthalpic formation of the C–H-activated complex for **3a** is 1.2 kcal mol^{-1} higher than for **2a**, in agreement with our prediction that the lack of Thorpe-Ingold effect in the C–H activation TS for **3a** makes it more difficult than C–H activation for **2a**.

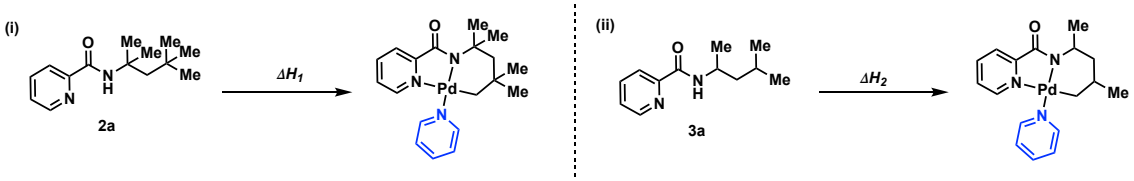

Scheme 4.3 Relative heats of enthalpies for the formation of C–H activated complexes for substrates **2a** and **3a**

4.3.11 Regioselectivity studies for a variety of substrates

Experimentally, good regioselectivity for different aliphatic amine derivatives were obtained in the final product despite the presence of multiple inequivalent C–H sites for activation (Scheme 4.4). For substrate **4a**, it was found that arylation occurred selectively at the primary methyl C–H over the secondary methylene C–H. For substrates **5a**, **6a** and **7a**, highly δ-selective mono-arylated products were obtained, keeping other accessible δ- and γ-sites intact. Computational studies were performed to elucidate the origins of such regioselectivity.

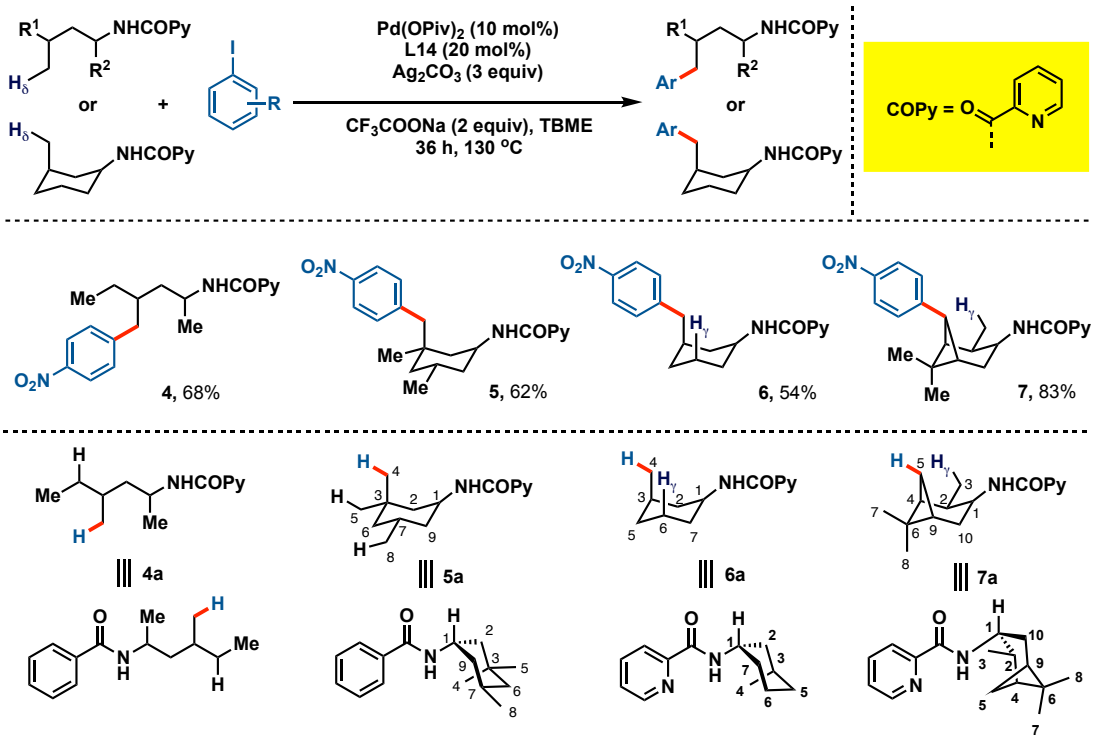

Scheme 4.4. Regioselectivity study for different aliphatic amines.

Substrate **4a** presents two inequivalent δ-C(sp^3)–H positions for arylation. To rationalise the observed regioselectivity, we calculated the relative energy differences ($\Delta\Delta G^{\ddagger}$) between the TSs for C–H activation step which was shown to be the rate-limiting step for this reaction. The primary methyl C–H bond (**4a-1**) is selectively activated over secondary methylene C–H bond (two conformations **4a-2-c1** and **4a-2-c2**); this is

favoured by 2.3 kcal mol^{-1}, corresponding to a 24:1 selectivity for the primary C–H activation using simple transition state theory. NCI plots and van der Waals surfaces suggest that the unfavourable steric clashes between the ε-methyl group and the heterocyclic ring of **L14** and adjacent methyl groups account for the relative activation barriers observed experimentally (Figure 4.21). In TS **4a-2-c2**, there is only steric clashes between ε-methyl group and the heterocyclic ring of **L14**, whereas in TS **4a-2-c1**, in addition to the steric clashes between ε-methyl group and the heterocyclic ring of **L14**, there is additional steric clashes between ε-methyl group and the methyl group on α-carbon, such that TS **4a-2-c1** has higher activation barrier than TS **4a-2-c2**.

4a-1	**4a-2-c1**	**4a-2-c2**
$\Delta\Delta G^{\ddagger} = 0.0$	3.7	2.3
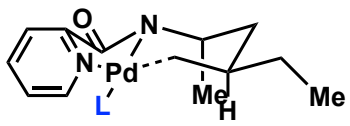	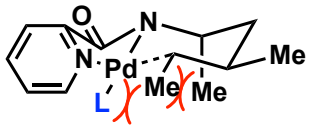	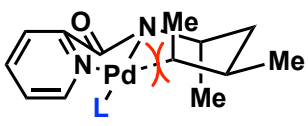
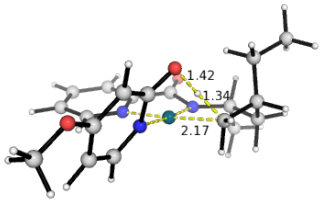	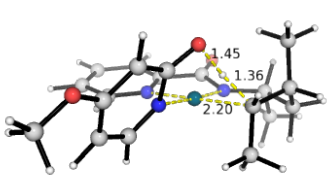	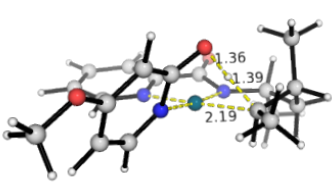
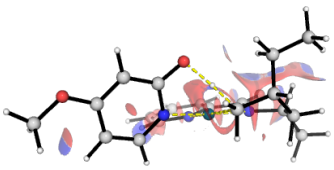	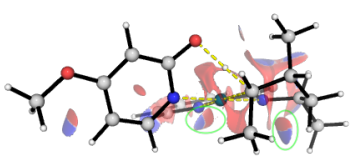	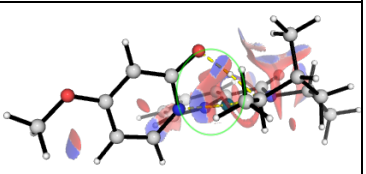
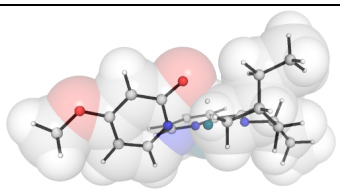	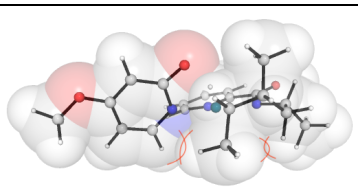	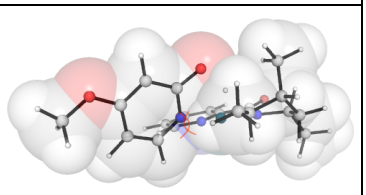

Figure 4.21. Optimised structures, NCI plots and van der Waals surfaces for C–H activation TSs of substrate **4a** by pyridone ligand **L14**.

Substrate **5a** presents multiple inequivalent δ-C(sp^3)–H and γ-C(sp^3)–H positions for arylation. Four TSs were found for the C–H activation step (Figure 4.22). TS structure **5a-2** has a high activation barrier due to the distortion of the γ-H-atom while C–H activation occurred, giving rise to unfavourable interactions as shown in the NCI plots in Figure 4.22. Similarly, TS structures **5a-3** and **5a-4** distort unfavourably, giving rise to elevated activation barriers. These are not competitive to TS **5a-1** that gives observed product. TS structures **5a-5** and **5a-6** were not computationally found (Scheme 4.5); the activation of these C–H bonds would require placing a Me–/H–group inside the palladacycle ring, giving rise to immensely repulsive interactions and were thus not experimentally observed.

5a-1	**5a-2**	**5a-3**	**5a-4**
$\Delta\Delta G^{\ddagger} = 0.0$	34.9	10.8	10.3
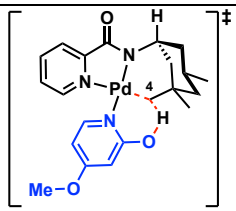	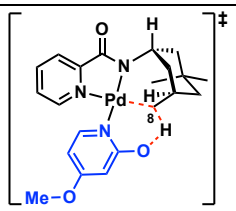	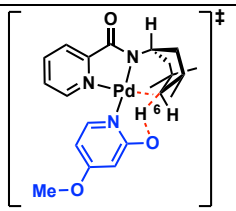	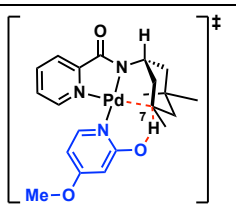
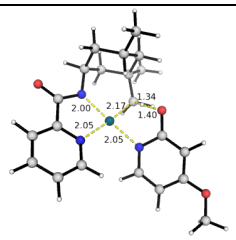	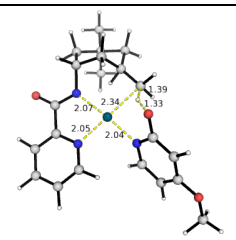	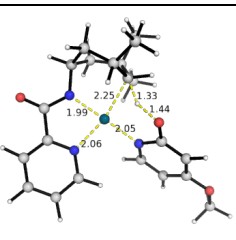	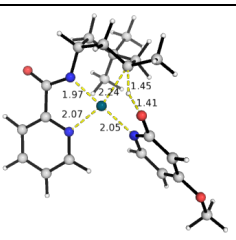
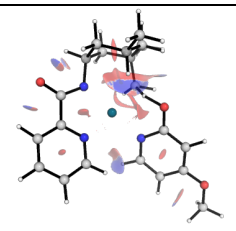	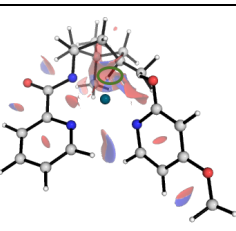	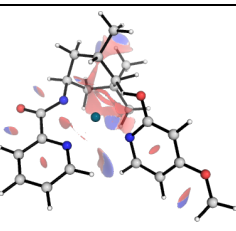	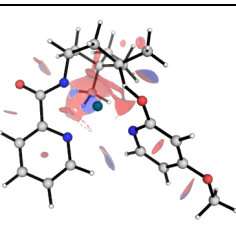

Figure 4.22. Optimised structures, NCI plots and van der Waals surfaces for C–H activation TSs of substrate **5a** by pyridone ligand **L14**.

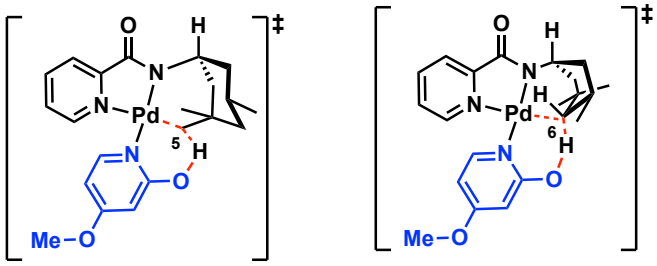

Scheme 4.5 Highly geometrically strained TSs for substrate **5a** that were not found.

6a-1	**6a-2**
$\Delta\Delta G^{\ddagger} = 0.0$	4.2
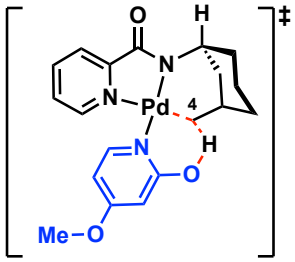	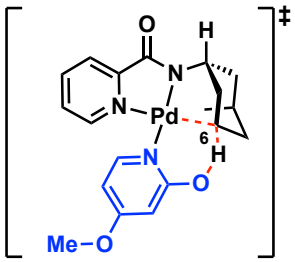
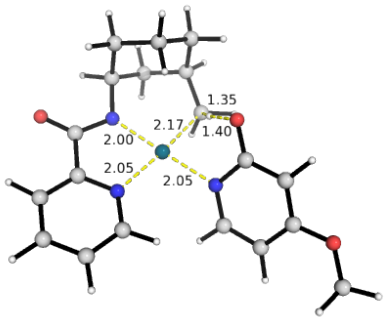	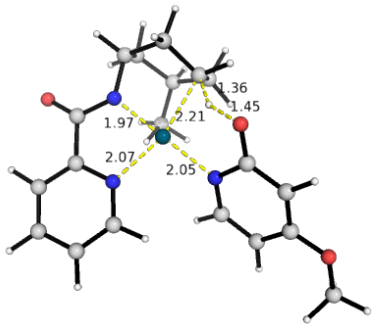
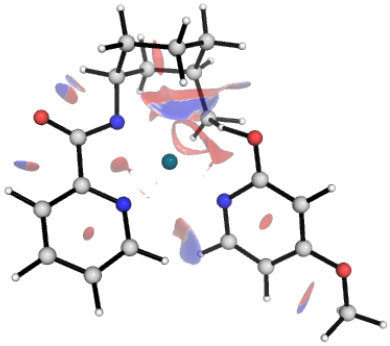	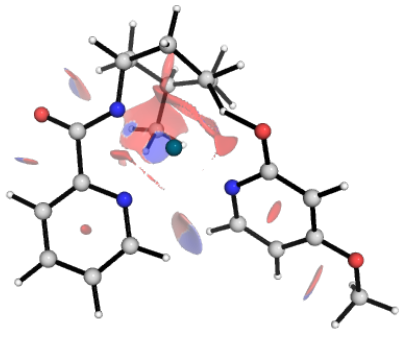

Figure 4.23. Optimised structures, NCI plots and van der Waals surfaces for C–H activation TSs of substrate **6a** by pyridone ligand **L14**.

Substrate **6a** is structurally similar to substrate **5a** (Scheme 4.4). The activation at γ-C(sp^3)–H position (**5a-4**) would give less steric crowding than before, due to fewer methyl groups present. Therefore, we recalculated this possibility. The relative energy difference ($\Delta\Delta G^{\ddagger}$) between the TSs for C–H activation step at δ-C(sp^3)–H (**6a-1**) and γ-C(sp^3)–H position (**6a-2**) is 4.2 kcal mol^{-1}, corresponding to a 337:1 selectivity for the δ-C(sp^3)–H position. The selectivity is again traced to non-covalent interactions present in these TSs (NCI plots, Figure 4.23).

For substrate **7a**, we considered the regioselectivity between the secondary δ-C(sp^3)–H and the primary γ-C(sp^3)–H. Calculation predict that the primary γ-C(sp^3)–H would be favoured by a factor of 56:1 over secondary γ-C(sp^3)–H provided that the C–H activation is the TDTS for this reaction ($\Delta\Delta G^{\ddagger}$ = 2.9 kcal mol^{-1}). We note that C–H activation step is unlikely to be rate-determining if there is steric crowding in the substrate, as in the case of substrate **2a**. Thus, we calculated the oxidative addition step for each activated complex and found that OA is the TDTS for this reaction, with methylene δ-C(sp^3)–H functionalisation being 7.0 kcal mol^{-1} lower than for γ-C(sp^3)–H activation, thus only methylene δ-C(sp^3)–H functionalisation was observed, in agreement with the experiment.

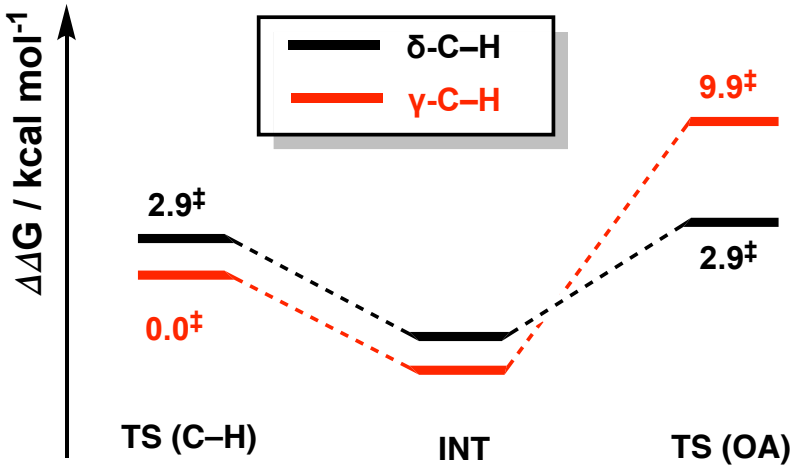

7a-1 (C–H)	7a-1 (OA)	7a-2 (C–H)	7a-2 (OA)
$\Delta\Delta G^{\ddagger} = 2.9$	2.9	0.0	9.9
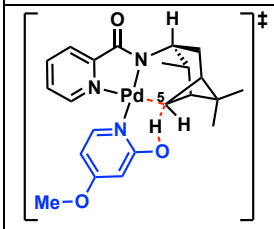	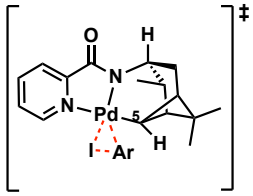	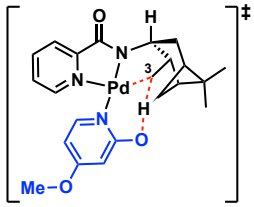	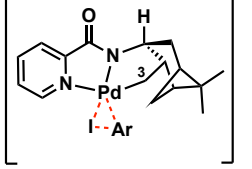
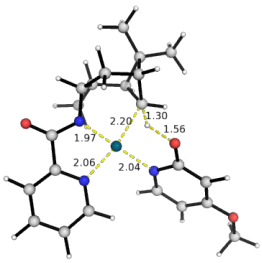	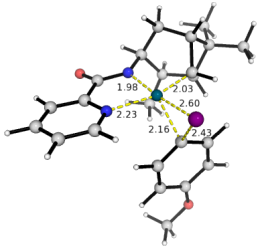	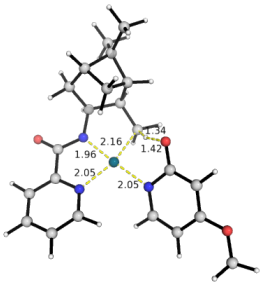	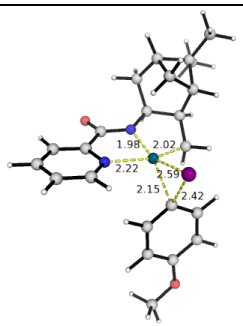
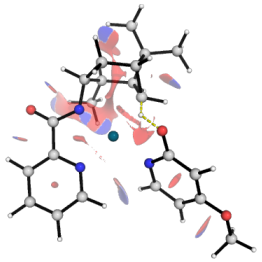	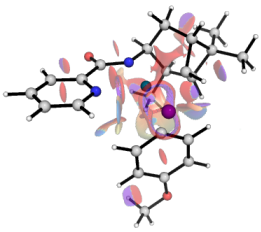	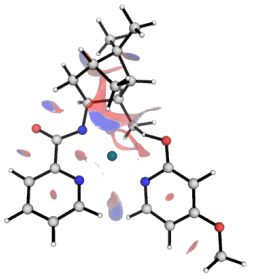	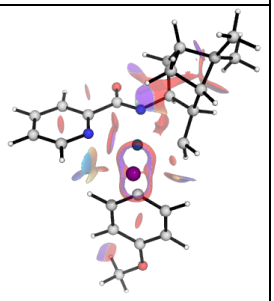

Figure 4.24. Optimised structures, NCI plots and van der Waals surfaces for C–H activation TSs of substrate **7a** by pyridone ligand **L14**.

4.3.12 Proposed catalytic cycles

Based on our calculations, together with experimental evidence from reversibility study, kinetic measurements and order determination, we observe that substrates having a quaternary γ-centre undergo a reversible C–H activation with OA/RE as the TDTS whereas substrates without a quaternary γ-centre undergo an irreversible rate-determining C–H activation. We propose that the reaction for substrate **2a** (with a quaternary γ-centre) proceeds via first coordination to the catalytic Pd(II)-trimer, followed by pyridine ligand-assisted dissociation (pathway II, Scheme 4.6) and subsequent reversible C–H activation

to give the catalytically active palladacycle, **int-5'**. Subsequent oxidative addition and reductive elimination through the Pd(II)/Pd(IV) manifold give the final arylated product. The reaction mechanism is slightly different in substrate **3a** (without a quaternary γ-centre): cooperative silver carbonate/pyridone ligand binding gives highly organised TSs that lower the OA and subsequent RE steps so that C–H activation becomes overall rate-determining (Figure 4.17). Stabilisation of the first arylated product in a Pd–Ag heterometallic complex makes subsequent second arylation thermally inaccessible.

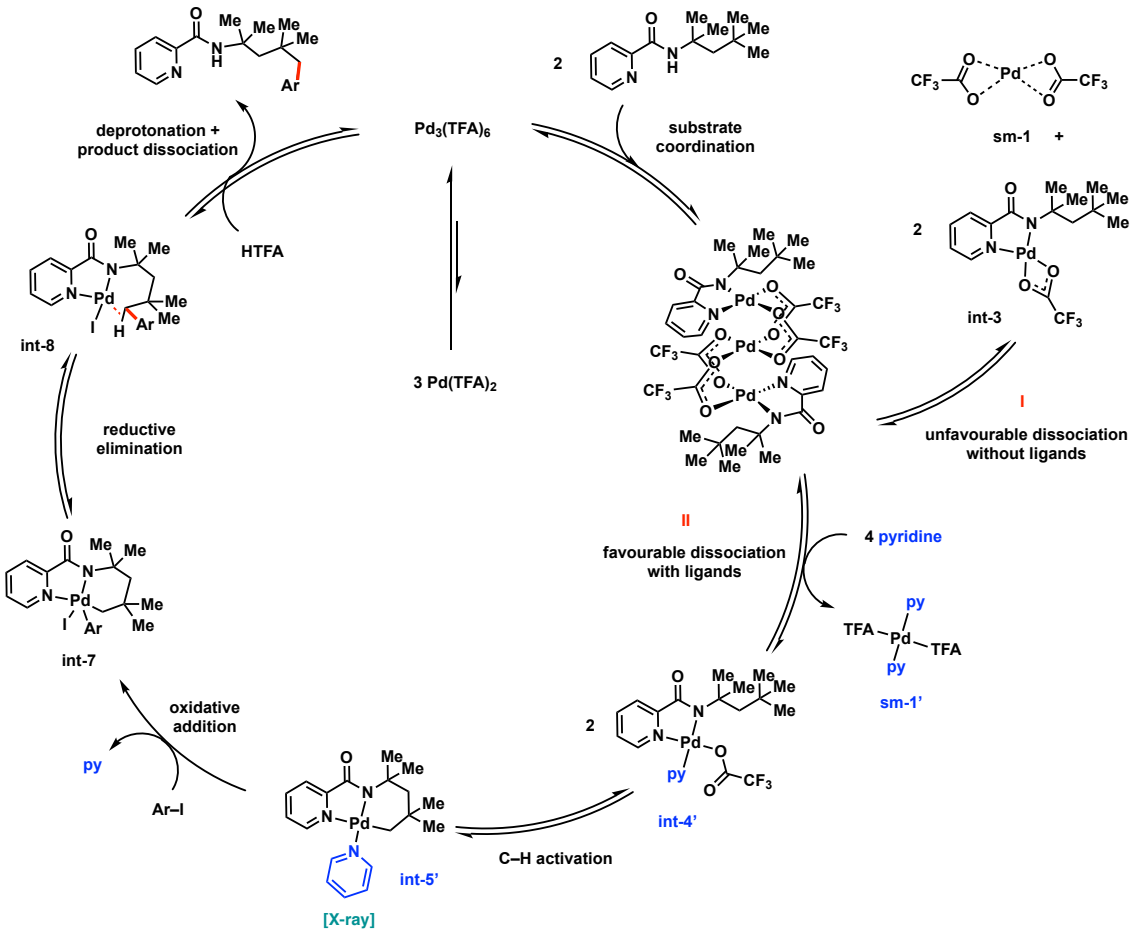

Scheme 4.6. Proposed mechanistic cycle for substrate **2a**.

4.4 Conclusions

Our computational investigations on the reaction mechanisms of structurally varying substrates for δ-arylation shed light on the origins of differences in the observed reactivity

(the relative ease of C–H activation and the differing rate-determining steps). A trinuclear coordination complex was implicated in both reactions. For substrates with a quaternary γ-centre, C–H activation can be more easily achieved due to Thorpe-Ingold effect, making it non-rate determining. For substrates without a quaternary γ-centre, C–H activation is more difficult and requires a pyridone ligand which helps in a tighter TS for C–H activation. In addition, the pyridone ligand can bind to silver additive cooperatively, giving a heterobimetallic Pd–Ag transition structure that lowers steps subsequent to C–H activation. Detailed steric and electronic factors influencing the performance of different directing groups were analysed, lending justifications to the experimentally observed yields for different directing groups. Experimentally observed regioselectivity for a variety of substrates were carefully studied computationally, allowing us to probe the stereoelectronic origins of such regioselectivity and offering an augmented understanding of the molecular picture of the experimentally observed selectivity outcomes.

"I could have done it in a much more complicated way," said the Red Queen, immensely proud.

— Lewis Carroll, Alice in Wonderland

5

Pd-catalysed C(sp^2)–H allylation[***]

5.1 Introduction

Transition metal (TM) catalysed, directing group-assisted selective functionalisation of C–H bonds in molecules has revolutionised the fields of organic and natural products syntheses as well as material science.[325,431–433] One of the earliest examples of TM-catalysed C–H activation involves the functionalisation of C(sp^2)–H of an arene.[434] Since then, the field of C(sp^2)–H functionalisation has burgeoned, finding diverse applications ranging from pharmaceutical and agrochemical industry to organic electronics and materials design,[332,432,433] helped by the ubiquity of the aromatic rings in those molecules. To be useful, the inherent inertness of the C–H bonds and the site selectivity for activation have to be addressed. Transient directing groups (DGs) are frequently employed to

[***] This work has been published in *Angew. Chem. Int. Ed.* **2019**, 58, 10353. DOI: 10.1002/anie.201904608. Permission has been granted by the publisher to re-use part of the material for this thesis.

achieve proximal *ortho*-C(sp^2)–H activation,[435–438] whereas distal *meta*- and *para*-C–H bond activations are relatively underexplored.[439–444] The *meta*-position is arguably the most challenging site for activation due to the fine balance between the mesomeric and inductive effects of the substituents on arenes.

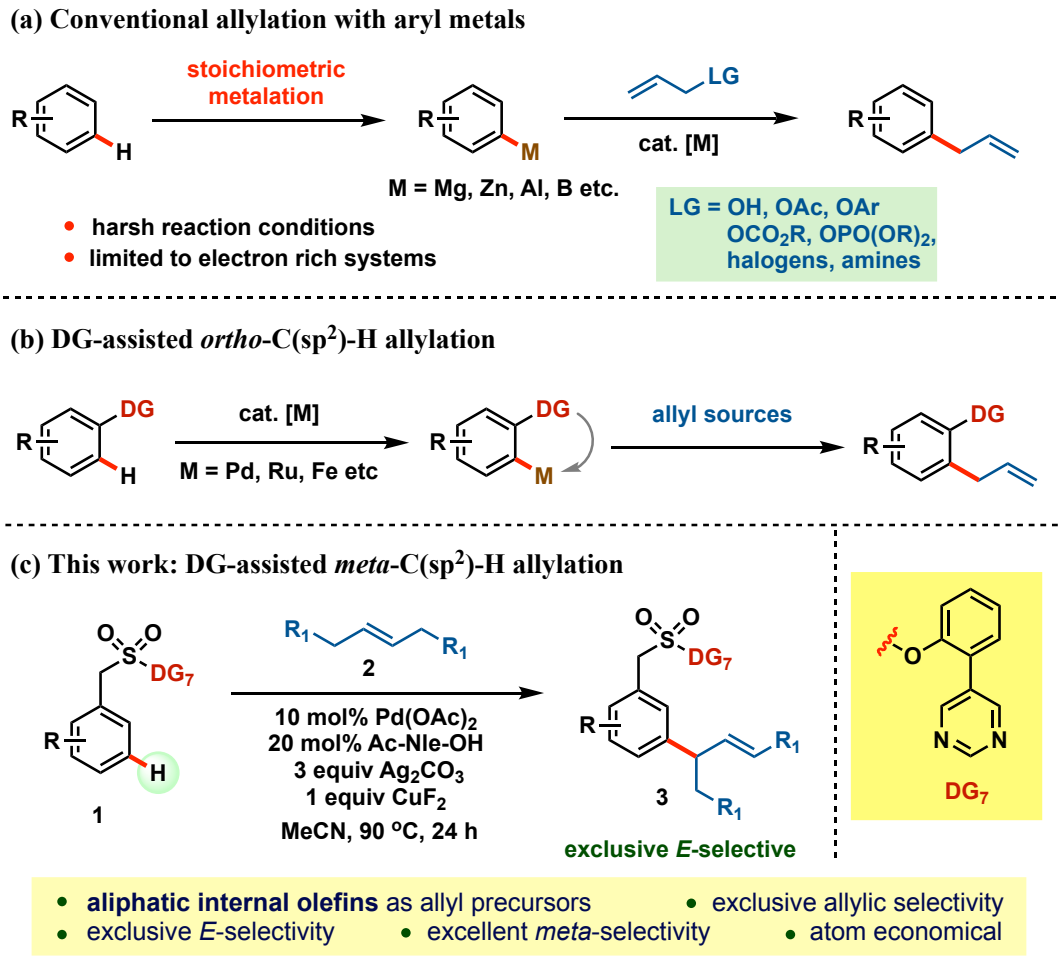

Scheme 5.1. Methods for C(sp^2)–H allylation reactions.

The allylarene functional group is of central importance in many natural products and bioactive molecules; compounds containing the allyl moiety are also amenable to downstream modifications, providing a versatile building block for constructing complex molecules.[445,446] Direct C–H allylation is an important method in view of atom and/or step economy and synthetic utility. Aryl metal compounds (such as magnesium, aluminium, zinc) and boron reagents have conventionally been utilized for transition

metal catalysed allylation with allylic electrophiles (Scheme 5.1(a)).[447–455] Despite their excellent site-selectivity, these protocols suffer from requisite preactivation of the arenes or halogenated arenes, thus requiring a stoichiometric amount of metals for metalation and resulting in substantial salts waste. With progressive research and development in the field of C–H functionalisation methods, direct C–H allylation via TM catalysis has sought to overcome such problems. Various metals (such as Cu,[456,457] Ni,[458] Pd,[459,460] Ru,[461] Re,[462] Ir[463] and Rh[464–469]) have successfully been employed in catalytic amounts for such transformations. The versatility of direct allylation is greatly expanded by using a number of possible allylic surrogates including allylic halides,[470–472] allylic alcohols,[473–476] allylic amines,[477–482] their derivatives (such as allylic acetates[461,483,484] and carbonates[464,483,485,486]), allenes[463,468,469,487–489] and dienes[489].

Very few reports on utilizing unactivated allylic coupling partners have been reported in the literature.[490–492] Compared to the extensive studies on C–H alkenylation reactions with activated olefins, unactivated olefins have not been extensively employed, presumably due to their inertness to undergo migratory insertion.[437,493] Recently, our experimental collaborators, the Maiti Research Group at the Indian Institute of Technology, Bombay (IITB), demonstrated the utilisation of unactivated olefins for dehydrogenative heck reactions at the *ortho*-position with Pd and high-valent Co-catalyst.[437,490,491] To reach out to the distal *meta*-C–H bond, the Maiti Group adopted a Pd-catalysed *meta*-C–H allylation of arenes utilising readily available unactivated internal olefins as allyl surrogates. Instead of using the nitrile DG[494] for *meta*-C–H allylation, whose weak coordination and side-on binding restrict the transformations to the introduction of less reactive coupling partners, a stronger coordinating pyrimidine-based DG[495–497] was employed (Scheme 5.1 (c)). It was found that this method proceeds

with broad substrate scope, wide functional group tolerance and good to excellent yields; late-stage functionalisations of complex pharmaceuticals can also be achieved. In particular, the reaction proceeds with exclusive *meta*-selective *E*-allyl over *Z*-allyl or styrenyl product formations in the presence of a catalytic amount of $Pd(OAc)_2$ and mono-protected amino acid (MPAA), *N*-acetyl nor-leucine ligand.

We carried out computational studies to understand the reaction mechanism and elucidate the molecular origins of these observed selectivities. For computational modelling of the reaction shown in Scheme 5.1(c), arene **1a** (structure **1** with R = *m*-Me) and *trans*-hex-3-ene (structure **2** with R_1 = Me) were used for calculations. All experimental work was performed by our experimental collaborators (Tapas Achar, Rahul Mondal, *et. al*, IITB) and all computational work was performed by the present author.

5.2 Computational Methods

Computational methods employed for the present study is similar to that employed for the study on Pd-catalysed δ-C(sp^3)–H arylation carried out in Chapter 4 using DFT as implemented in Gaussian 16 *rev.* A.03 software.[400] Following the success of the previous studies, MN15 functional[78] is employed here as well – MN15/def2-SVP[18,19] initially optimised geometries were further refined using GenECP (def2-TZVPPD for Pd[17,401] and def2-SVP for all other atoms) basis set. This larger basis set is denoted BS1. Minima and transition structures on the PES were verified as previously. Here, single point (SP) corrections were performed separately with either MN15 or ωB97X-D[56] functional and def2-QZVPP[4] basis set for all atoms. This modification from the methods in Chapter 4 is so that no separate specifications of basis sets for different atom types are required for SP calculations. Herein, two functionals are included for SP calculations to verify that they agree well with each other. The SMD continuum solvation model[117] was used to include

the implicit solvation effect of acetonitrile (MeCN) solvent on the computed Gibbs energy profile. Gibbs energies were evaluated at 363.15 K, using a quasi-RRHO treatment of vibrational entropies.[205,206] As before, vibrational entropies of frequencies below 100 cm^{-1} were obtained according to a free rotor description, using a smooth damping function to interpolate between the two limiting descriptions. The free energies were further corrected using standard concentration of 1 mol L^{-1}. SMD(MeCN)-ωB97X-D/def2-QZVPP//MN15/BS1 Gibbs energies are given with SMD(MeCN)-MN15/def2-QZVPP//MN15/BS1 Gibbs energies in parenthesis throughout. *Unless otherwise stated, all Gibbs energy values in the text and figures are quoted in* kcal mol^{-1} *and all bond distances are given in* Å *throughout.*

The *.wfn* files for NCIPLOT were generated at MN15/DGDZVP[410,411] level of theory. Noncovalent interactions (NCIs) were computed and visualised using NCIPLOT[281] and *PyMOL*[207] software respectively, with same settings as in Chapter 4. Dihedral angle scans were performed in gas phase using MN15/def2-SVP and the energies were taken without further corrections. Geometries of all optimised structures (in *.xyz* format with their associated energy in Hartrees) and an associated README file have been deposited online and made freely available (DOI: 10.5281/zenodo.2775841).

5.3 Results and Discussions

5.3.1 Conformational considerations for starting materials

The starting materials for computational modelling, sulfonyl arene, **1a**, and *trans*-hex-3-ene, were first conformationally sampled. The possible rotamers for arene **1a** were generated by systematically varying a combination of key dihedral angles shown in red (Scheme 5.2) and optimising the resulting structures. The crystal structure of *trans*-hex-3-ene was obtained as a starting point for structure optimisation; additional rotamers were

generated by varying the given dihedral angle in red (Scheme 5.2) and doing structural optimisations. The lowest energy conformer for each starting material was used for subsequent calculations.

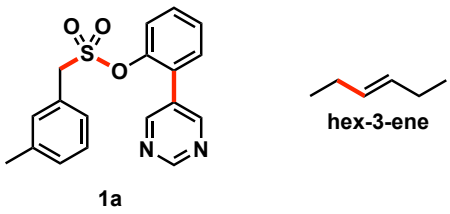

Scheme 5.2. Generation of rotamers by varying the dihedral angles in red for conformational sampling.

5.3.2 Overall reaction energy profile for *trans*-hex-3-ene

The overall Gibbs energy profile for the C(sp^2)–H allylation reaction between arene **1a** and *trans*-hex-3-ene is shown in Figure 5.1. The reaction proceeds with MPAA ligand-promoted C–H activation, followed by 1,2-migratory insertion of alkene and the subsequent selective β-hydride elimination to yield the final product.

In the absence of ligand, the C–H activation step (**ts-1**, 26.7‡ kcal mol^{-1}, Figure 5.2) is the overall turnover frequency-determining transition state (TDTS)[125] and unfavourable. The coordination of amino acid ligand, *N*-acetyl norleucine (Ac-Nle-OH), with displacement of two acetic acid molecules, is entropically favoured. Transition structure **ts-1'** (at 20.0‡ kcal mol^{-1}) has the characteristic [5,6]-palladacycle conducive for C–H activation (Figure 5.2).[498–501] The formation of a 5-membered palladacycle by the ligand strategically positions the amide oxygen atom for facile C–H activation via concerted metalation deprotonation (CMD). Other possible arrangements/coordination modes of the MPAA Ac-Nle-OH ligand were considered (Scheme 5.3), but they all have higher barriers than **ts-1'**, where a [5,6]-palladacyclic ring is involved.

Although the overall TDTS of the reaction is 1,2-migratory insertion in the presence of

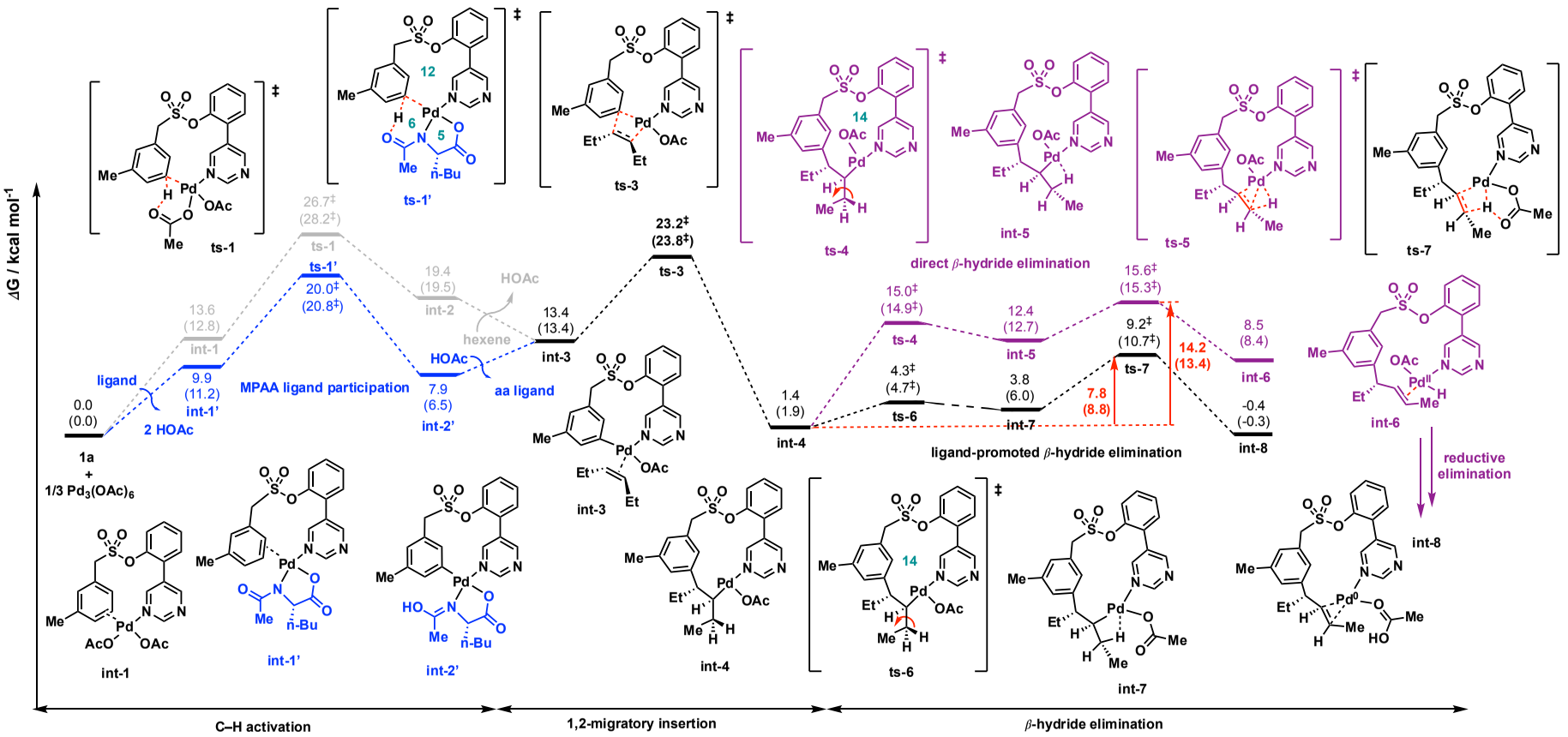

Figure 5.1. Gibbs energy profile for *meta*-selective C(sp^2)–H allylation using *trans*-hex-3-ene.

ts-1	ts-1'	ts-3
26.7‡ (28.2‡)	20.0‡ (20.8‡)	23.2‡ (23.8‡)
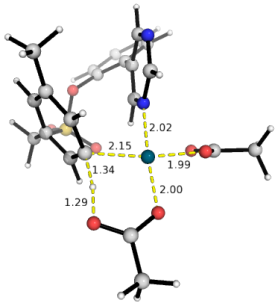	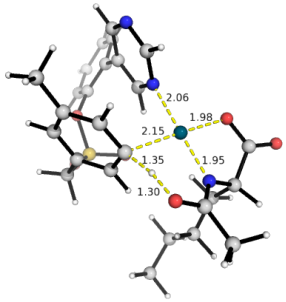	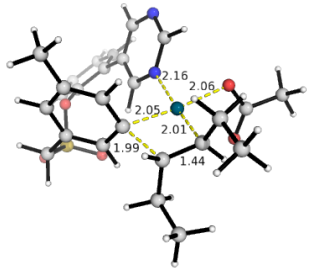
ts-5	**ts-7**	**ts-7'**
15.6‡ (15.3‡)	9.2‡ (10.7‡)	27.4‡ (27.1‡)
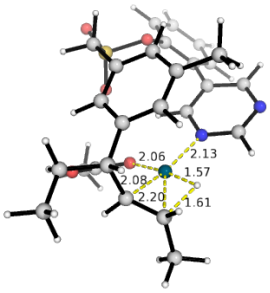	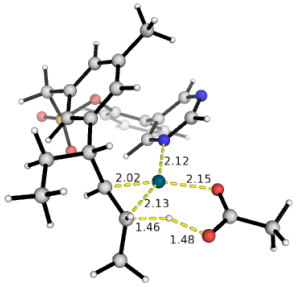	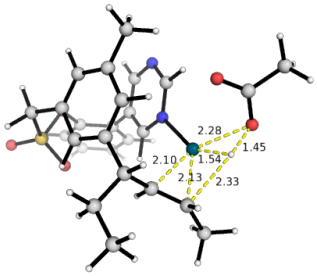

Figure 5.2. Selected optimised structures for C(sp2)–H meta-allylation using trans-hex-3-ene.

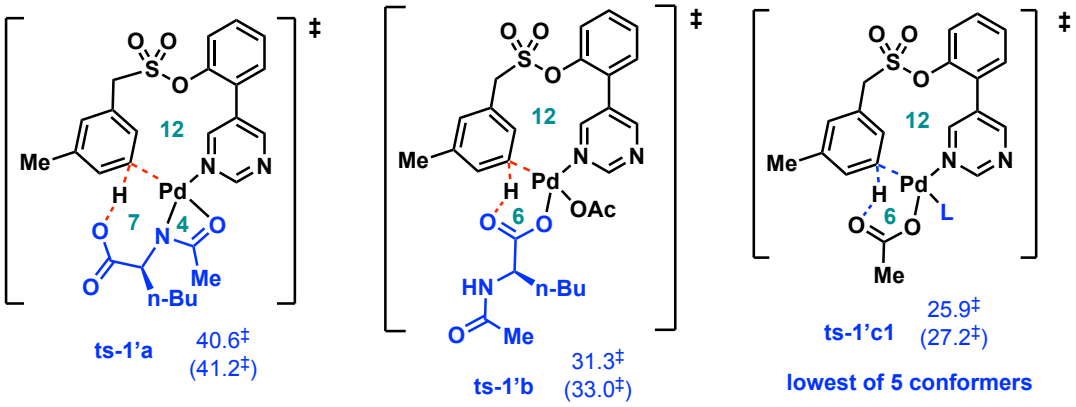

Scheme 5.3. Other possible ligand coordination modes for the C–H activation step.

the MPAA ligand, the regio-(allyl/styrenyl) and stereo-(*E/Z*) selectivities are determined by the subsequent β-hydride elimination step. Direct β-hydride elimination requires positioning the ligand in close proximity to the palladacycle ring, giving unfavourable sterics in **int-5**, which subsequently proceeds via **ts-5** (15.6 kcal mol^{-1}, Figures 5.1 and

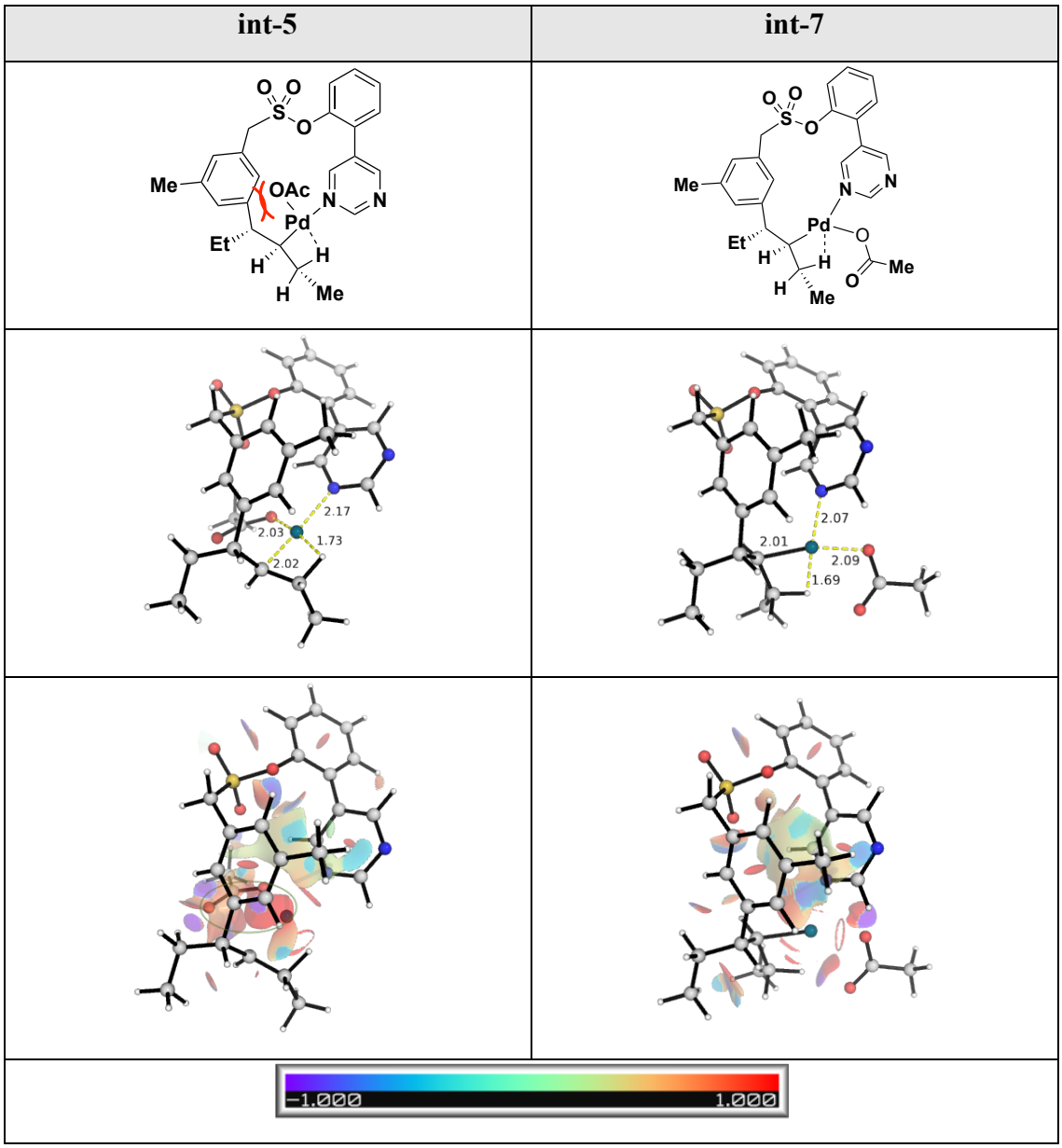

Figure 5.3. Relative stabilities of **int-5** and **int-7** and their NCI plots.

5.2) to give the desired product (verified via IRC analyses). This leaves palladium in a formal +2 oxidation state forming a metal-bonded Pd(II) hydride, **int-6**, that can further undergo reductive elimination between the acetate ligand and H to generate Pd(0) catalyst. More favourably, a facile rotation in the C–C bond (**ts-6**) strategically positions the free O-atom of the acetate ligand for ligand-assisted β-hydride elimination (**ts-7**, 9.2 kcal mol^{-1}, Figures 5.1 and 5.2), giving final product **int-8** directly

and regenerating Pd(0). This product **int-8** is exergonic (-0.4 kcal mol^{-1}) and irreversible, such that **ts-7** is overall regio- and stereo-determining.

Note that for ligand-assisted β-hydride elimination, the TS via 3-membered ring formed by the acetate ligand coordinating O-atom carrying out the CMD (**ts-7'**, 27.4 kcal mol^{-1}, Figure 5.2) is much less favoured than **ts-7**, where the non-coordinating O-atom of acetate carries out the CMD step via a 5-membered ring TS.

We further note that although **int-7** and **int-5** have similar structures (they differ in the positions of the acetate ligand), **int-7** (at 3.8 kcal mol^{-1}) is much more stable than **int-5** (at 12.4 kcal mol^{-1}) since in the latter, the acetate group is near the 14-membered palladacycle ring, giving rise to unfavourable steric interactions with the arene, as shown in the NCI plot (circled in green) in Figure 5.3; this unfavourable sterics is not present in **int-7**.

5.3.3 Exact identity of the ligand in 1,2-migratory insertion TDTS

The intermediate after MPAA ligand-assisted C–H activation (**int-2'**) has the resulting ligand in imidic acid form. The subsequent 1,2-migratory insertion TS leading from here (**ts-3'a**, 41.7 kcal mol^{-1}, Scheme 5.4) has a much higher barrier than its tautomeric amide form (**ts-3'b**, 27.1 kcal mol^{-1}). The coordination by acetate (**ts-3**, 23.2 kcal mol^{-1}), on the other hand, has the lowest barrier amongst these three possibilities.

We anticipate that **ts-3** and **ts-3'b** would be rather close in energy, since they both coordinate to Pd-centre in a monodentate fashion (Scheme 5.4), where the Pd–N interactions would dominate over other possible non-covalent interactions (NCIs) in the side chains. Although the amino acid side chain could provide better NCIs than the methyl group in acetate, it could also give rise to potentially more steric hinderance.

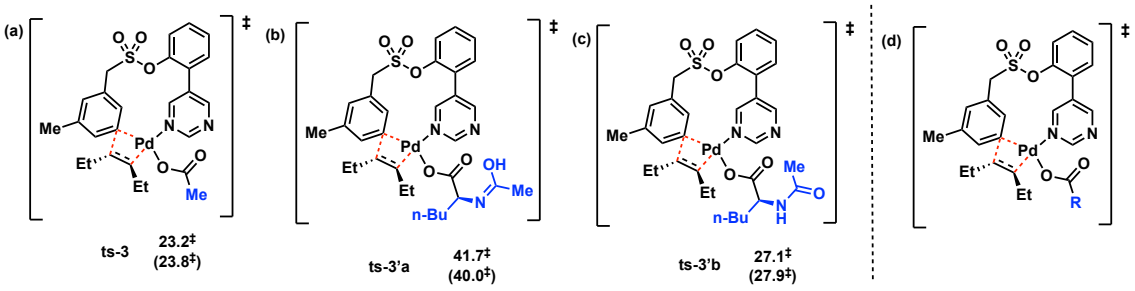

Scheme 5.4. 1,2-migratory insertion rate-determining step with either acetate (a) or MPAA in tautomeric forms (b and c) as monodentate ligand. These can be thought of having the general structure in (d) where the R–group varies.

In the computational studies of similar systems where amino acid ligands were used for the C–H activation step, the amino acid (a.a.) was retained as a monodentate ligand for all subsequent steps.[502,503] We envisioned that the acetate ligand and the a.a. ligand would have similar effects in 1,2-migratory insertion step and replacing the a.a. ligand with acetate would not affect the energy profile too much (Note that the main role of the a.a. ligand is in the C–H activation step).

Conformational searches were thus performed for the 1,2-migratory insertion step with either acetate or MPAA as the monodentate coordinating ligand. Altogether, 6 TSs for the acetate ligand and 12 TSs for the a.a. ligand were found (Figure 5.4). All these TSs have higher Gibbs energy barriers than the C–H activation step, as expected, since the 1,2-migratory insertion step is overall turnover frequency-determining and C–H activation is reversible as measured by kinetic isotopic effect experimentally.

As expected, the MPAA ligand binds in a monodentate fashion via one of the carboxylate O-atom and that the side chains do not directly participate in the TS organisation around the Pd-centre (Figure 5.4). Although the lowest barrier TSs are those with the MPAA ligand, these are within ~1.5 kcal mol^{-1} of the lowest TS with the acetate ligand. For modelling purposes, it is thus sufficient to use acetate instead of the full MPAA ligand.

1,2-migratory insertion TSs with acetate ligand		
ts-3-Ac-c1 (ts-3)	**ts-3-Ac-c2**	**ts-3-Ac-c3**
23.2‡ (23.8‡)	23.4‡ (23.9‡)	24.0‡ (24.7‡)
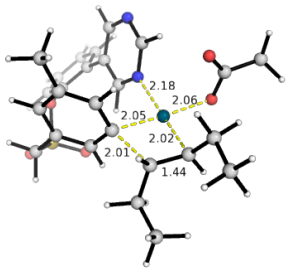	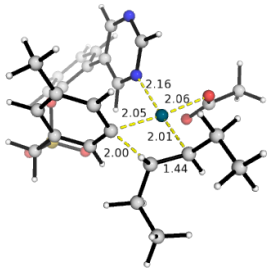	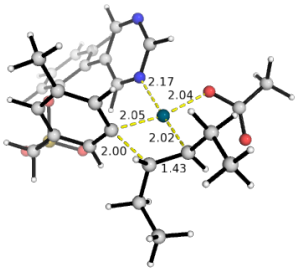
ts-3-Ac-c4	**ts-3-Ac-c5**	**ts-3-Ac-c6**
24.3‡ (24.5‡)	25.2‡ (26.1‡)	27.6‡ (27.9‡)
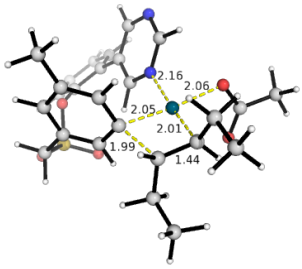	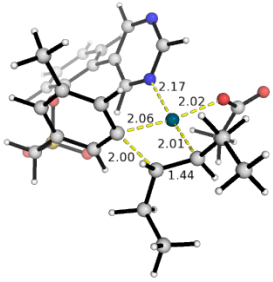	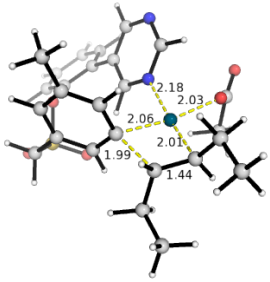
1,2-migratory insertion TSs with MPAA ligand		
ts3'b-aa-c1	**ts3'b-aa-c2**	**ts3'b-aa-c3**
21.8‡ (21.9‡)	22.3‡ (22.6‡)	22.0‡ (23.2‡)
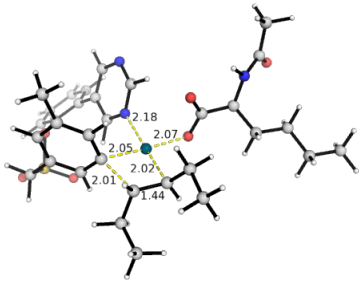	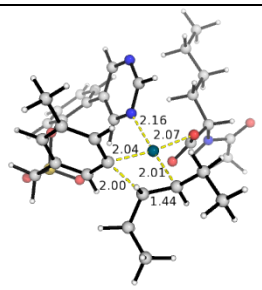	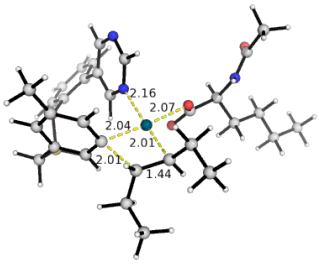
ts3'b-aa-c4	**ts3'b-aa-c5**	**ts3'b-aa-c6**
22.1‡ (23.2‡)	22.8‡ (23.6‡)	23.8‡ (24.2‡)
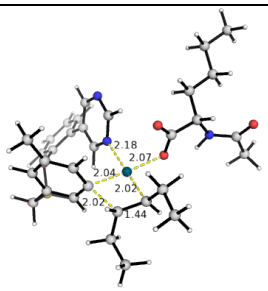	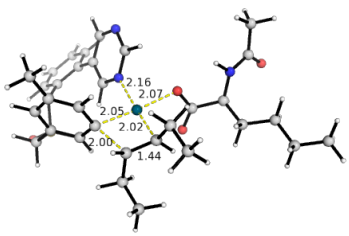	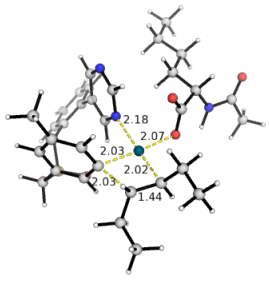

ts3'b-aa-c7	ts3'b-aa-c8	ts3'b-aa-c9
23.5‡ (24.9‡)	25.1‡ (24.9‡)	25.9‡ (26.5‡)
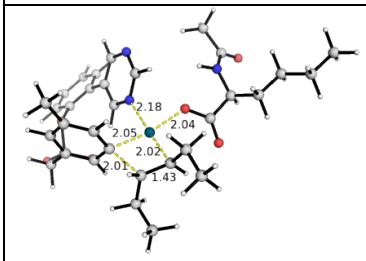	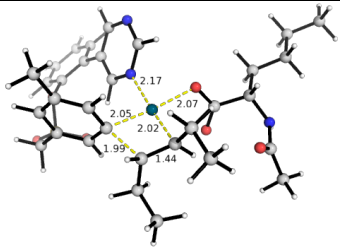	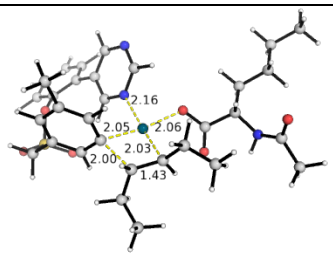
ts3'b-aa-c10	**ts3'b-aa-c11**	**ts3'b-aa-c12**
25.9‡ (27.0‡)	27.8‡ (27.4‡)	27.1‡ (27.9‡)
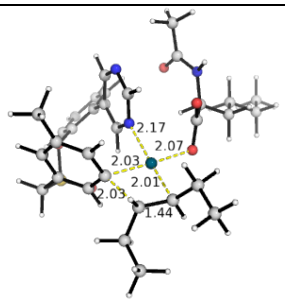	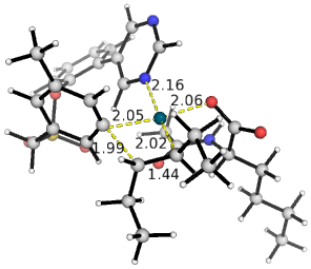	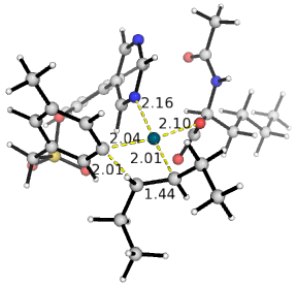

Figure 5.4. 1,2-migratory insertion TSs with either acetate or MPAA ligand.

5.3.4 Arene site-selectivity studies

Experimentally, it was found that the reaction is exclusively *meta*-selective. The site selectivity of C–H activation on the arene (*ortho*- vs *meta*- vs *para*-position) was studied computationally. We studied both C–H activation and 1,2-migratory insertion steps. The comparative Gibbs energies for these steps are given in Table 5.1. In all cases, without the MPAA ligand, the C–H activation has a higher barrier than 1,2-migratory insertion; the presence of the MPAA ligand lowers the barrier of the C–H activation step so that the turnover frequency determining step becomes the 1,2-migratory insertion step. As expected, *meta*-insertion (**ts-3**, 23.2 kcal mol^{-1}) has the lowest activation barrier whereas *para*-insertion (**ts-3p**, 28.2 kcal mol^{-1}) is 3.9 kcal mol^{-1} higher, translating to 1 in 222 selectivity using simple transition state theory (TST); *ortho*-insertion (**ts-3o**, 37.0 kcal mol^{-1}) is 12.7 kcal mol^{-1} higher than **ts-3**, making *ortho*-insertion uncompetitive (1 in 40

million). These agree very well with the experimentally observed selectivities (*ortho*- and *para*-products have too low experimental yields for quantitative comparison with *meta*-product).

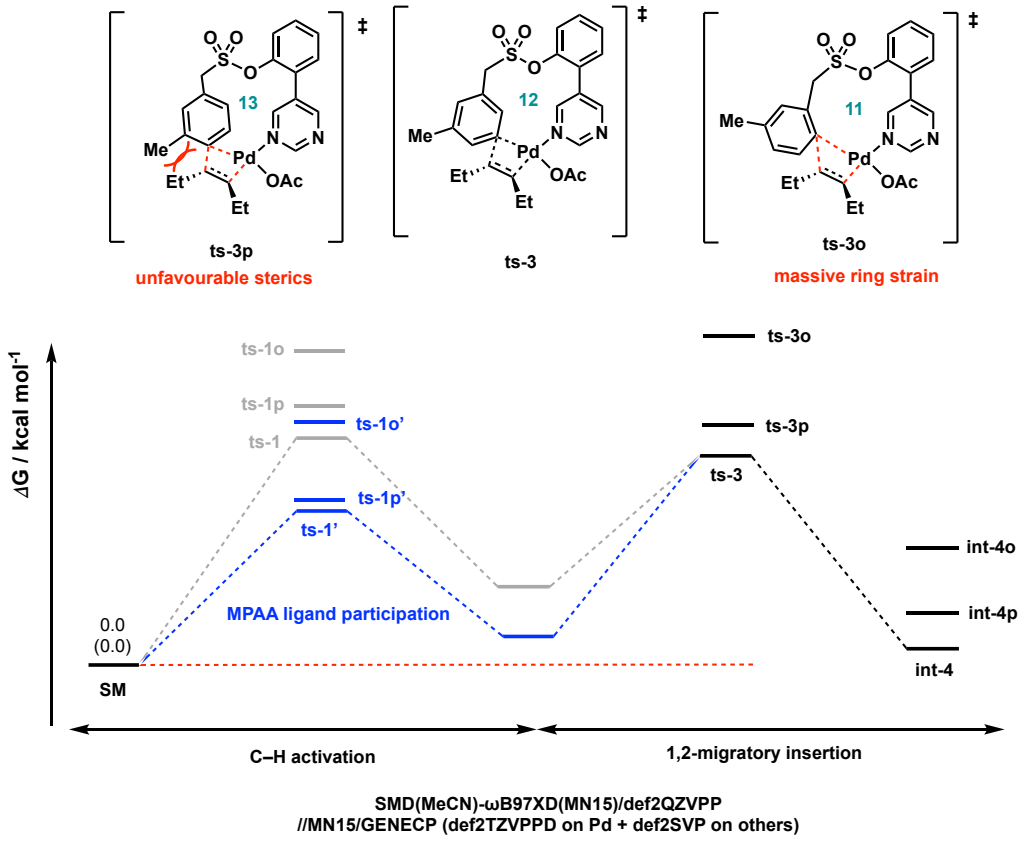

Allylation site	ts-1x	ts-1x'	ts-3x	int-4x
meta- (**x = nil**)	26.7‡ (28.2‡)	20.0‡ (20.8‡)	**23.2‡ (23.8‡)**	1.4 (1.9)
ortho- (**x = o**)	35.8‡ (34.9‡)	28.7‡ (29.2‡)	**37.0‡ (35.5‡)**	19.2 (18.2)
para- (**x = p**)	28.6‡ (28.6‡)	20.5‡ (20.0‡)	**28.2‡ (26.7‡)**	8.4 (8.2)

Table 5.1. Arene site-selectivity studies for allylation. MPAA ligand lowers C–H activation in all cases such that 1,2- migratory insertion (**ts-3x**) becomes the TDTS. The overall barrier for each case is given in bold.

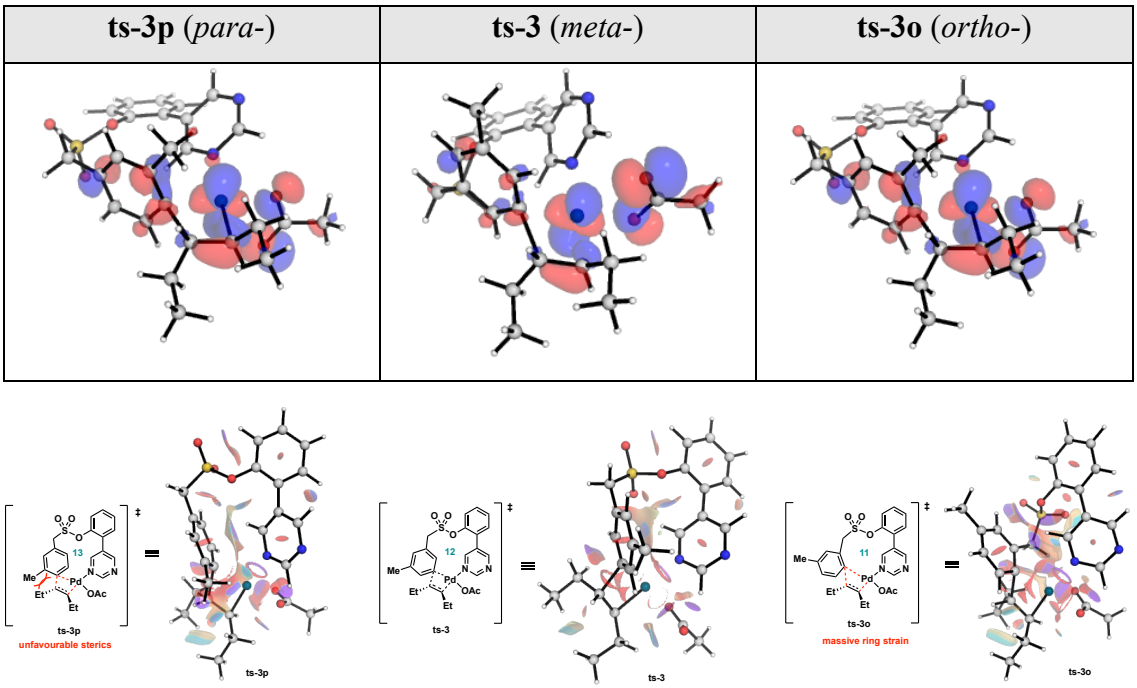

Figure 5.5. 1,2-migratory insertion TSs from *para*-, *meta*- and *ortho*-activated complexes. **Top:** HOMOs at an isosurface value of 0.04. **Bottom:** NCI plots.

The HOMOs for the rate-determining 1,2-migratory insertion TSs for *meta*-/*ortho*-/*para*-activation are plotted in Figure 5.5 Top. These show similar electron distributions, suggesting that electronic factors are less important in the site-selectivity of arene C–H activation. NCI plots (Figure 5.5 Bottom) show that for *para*-activation, **ts-3p** is sterically disfavoured as the methyl-group on the ring comes close to the alkene being added whereas for *ortho*-activation in **ts-3o**, the excessive ring strain makes this TS highly strained (the directing group got twisted out of shape), giving rise to unfavourably high activation barrier. The possibility of addition to the other *ortho*-site would bring the methyl-group into close proximity of the alkene being added, further increasing the activation strain and was thus not considered.

In addition to the stereoelectronic effects associated with arene site selectivity, the ring strain energies in these TSs were calculated from the reaction enthalpy of the isodesmic reaction[504,505] (Scheme 5.5). Specifically, a hypothetical pyridine ligand was used for TS

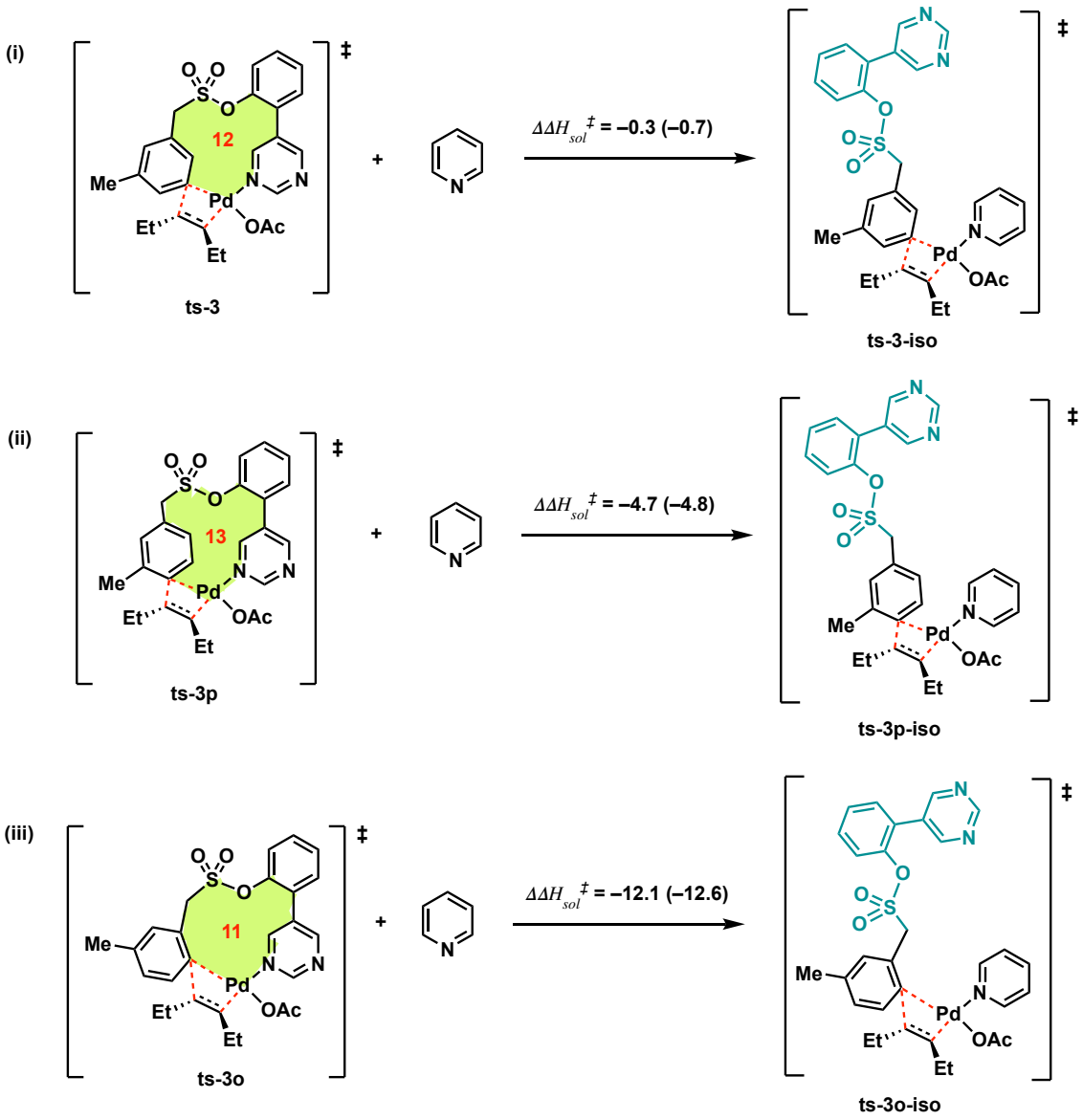

Scheme 5.5. Computed ring strain energies by study of isodesmic reaction where a hypothetical pyridine ligand is involved. Enthalpies quoted are corrected with solvent effect and in kcal mol^{-1}.

searches to release the ring strain where the directing group (DG) got uncoordinated. Note that in an isodesmic reaction, the total number and type of all bonds in the reactants and the products are preserved.

The starting conformation for the DG (in green, Scheme 5.5) in all 3 cases was made the same in a linear form for subsequent TS searches. The enthalpies of the reactions were further corrected with SMD solvation model:

$$\Delta\Delta H^{\ddagger}_{\mathrm{sol}} = \Delta\Delta H^{\ddagger}_{\mathrm{gas}} - \Delta\Delta E^{\ddagger}_{\mathrm{gas}} + \Delta\Delta E^{\ddagger}_{\mathrm{sol}} \quad (5.1)$$

where $\Delta H^{\ddagger}_{gas}$ is the enthalpy change of the reaction in the gas phase at low level of theory for computation, $\Delta E^{\ddagger}_{gas}$ is the energy change of the reaction in the gas phase at low level of theory for computation and $\Delta E^{\ddagger}_{sol}$ is the energy change of the reaction in the solvent phase at high level of theory for computation.

The calculations showed that the *meta*-insertion TDTS, a 12-membered palladacyclic ring, has the lowest ring strain at 0.3 kcal mol^{-1}, followed by *para*-insertion TDTS (13-membered), with 4.7 kcal mol^{-1}; *ortho*-insertion TDTS (11-membered) has the largest ring strain at 12.1 kcal mol^{-1} (Scheme 5.5). These values are in excellent quantitative agreement with the selectivity studies in Table 5.1, where the *para*-TDTS is about 4 kcal mol^{-1} and the *ortho*-TDTS is about 12 kcal mol^{-1} higher than the *meta*-TDTS.

5.3.5 Product selectivity studies for *trans*-hex-3-ene substrate

To study the product regio-selectivity (allyl vs styrenyl) and stereo-selectivity (*E*-allyl vs *Z*-allyl) for the present system, both direct and ligand-assisted β-hydride elimination steps were considered (Table 5.2). The formations of both *E*- and *Z*-allylated products proceed via ligand-assisted β-hydride elimination (**ts-7x**); styrenylation proceeds via direct β-hydride elimination (**ts-5x**) due to its unfavourable arrangement of the acetate ligand for ligand-assisted β-hydride elimination. Styrenylation involves unfavourable palladacycle ring strain such that its direct β-hydride elimination proceeds via the displacement of the directing group pyrimidinyl-N atom by the acetate ligand that subsequently binds in bidentate mode (**ts-5b**, 19.2 kcal mol^{-1}) rather than via the intact palladacycle with the directing group bound in a monodentate fashion (**ts-5b-c2**, 21.1 kcal mol^{-1}); **ts-5b** is

more favourable than **ts-5b-c2** due to the release of the palladacyclic ring strain as styrenylation occurs (Figure 5.6).

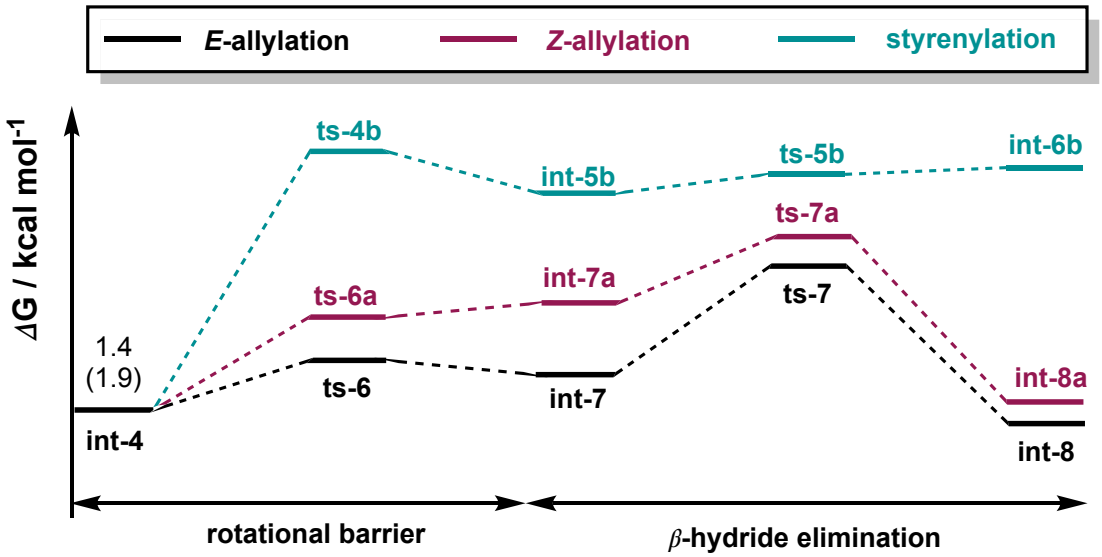

Final prd	direct β-H elimination				ligand-promoted β-H elimination				Overall barrier [a]
	ts-4x	int-5x	ts-5x	int-6x	ts-6x	int-7x	ts-7x	int-8x	
E-allyl **x = nil**	15.0‡ (14.9‡)	12.4 (12.7)	15.6‡ (15.3‡)	8.5 (8.4)	4.3‡ (4.7‡)	3.8 (6.0)	**9.2‡ (10.7‡)**	-0.4 (-0.3)	**7.8 (8.8)**
Z-allyl **x = a**	16.8‡ (16.5‡)	14.7 (15.1)	17.6‡ (17.6‡)	9.6 (10.0)	5.9‡ (6.4‡)	7.0 (8.9)	**11.3‡ (12.7‡)**	0.7 0.6	**9.9 (10.8)**
Styrenyl **x = b**	**21.0‡, [b] (21.8‡)**	17.9 (18.7)	19.2‡, [c] (19.2‡)	20.4 (18.3)	**21.0‡, [b] (21.8‡)**	3.9 (4.7)	48.5‡ (48.3‡)	10.5 (8.3)	**19.6 (19.9)**

[a] We take the lowest value of the two. Both *E*- and *Z*-allylation prefer acetate-promoted β-hydride elimination, whereas styrenylation prefers direct β-hydride elimination via Pd(II) hydride complex.

[b] Rotational TS for styrenylation are the same regardless of whether β-hydride elimination occurs directly or via ligand involvement. The prerequisite is to bring the H_s atom to interact agostically with Pd(II)-centre.

[c] The TS where the directing group got displaced (**ts-5b**) has a lower activation barrier than the one where it remains coordinated (**ts-5b-c2**) since the former released the unfavourable strain in the palladacycle.

Table 5.2. Gibbs energies for product selectivity studies for *trans*-hex-3-ene substrate. TDTS values are given in bold.

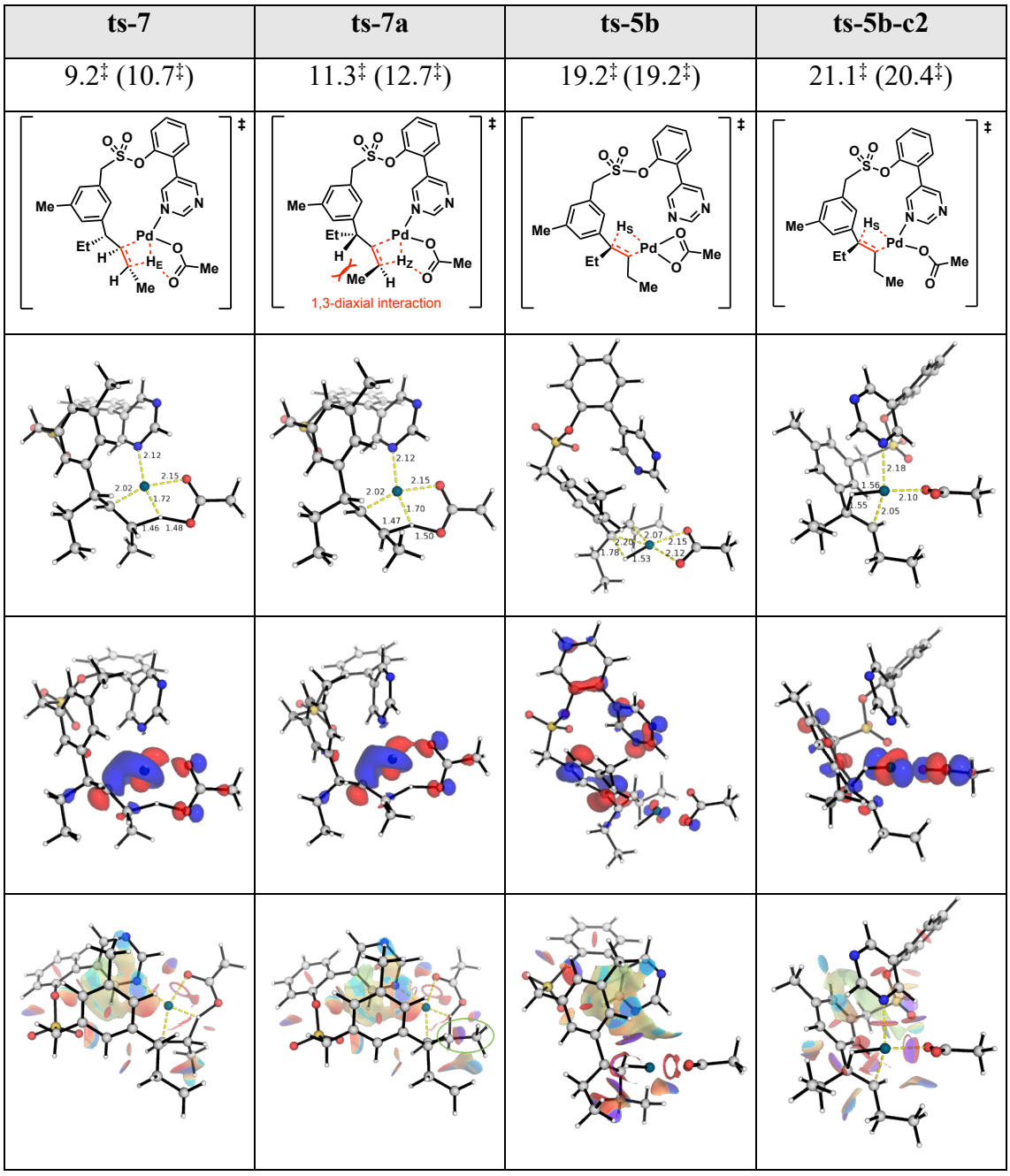

Figure 5.6. Product selectivity studies for *trans*-hex-3-ene substrate. The β-hydride elimination TSs for each product formation is given, with their HOMOs and NCI plots.

Due to the massively unfavourable ring strain as styrenylation occurs, the rotational barrier to bring the requisite H_S-atom to interact with Pd-centre agostically becomes the overall rate-determining step for styrenylation; this requires a very high barrier as the palladacycle experiences huge strain when H_s is brought to interact agostically with Pd(II)

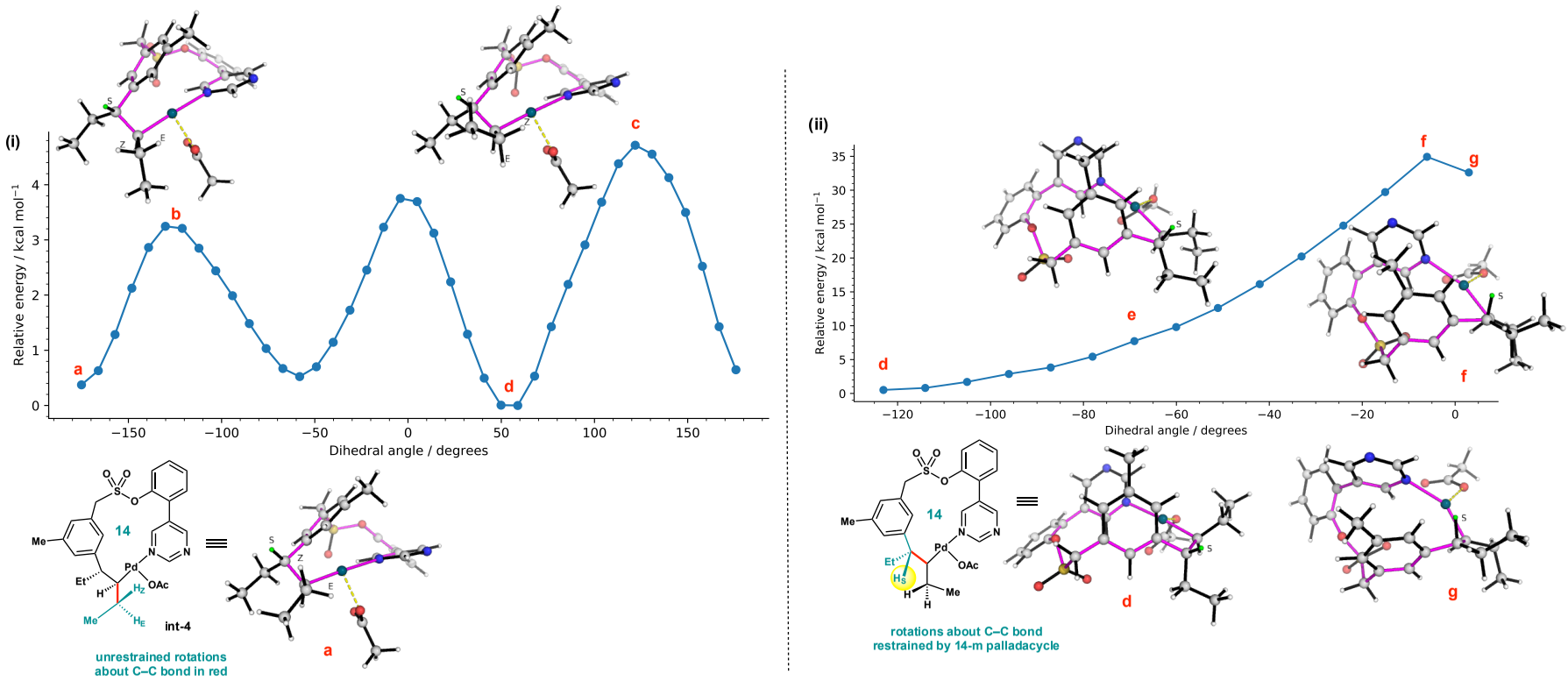

Figure 5.7. Dihedral angle scans (about C–C bonds in red) for rotational barrier for the formation of (i) *E*-/*Z*-allylated products and (ii) styrenyl product for *trans*-hex-3-ene substrate. Note the different energy scales used. In (ii), note the position of styrenyl proton (H_s, labelled *S* in green), which is restrained in a position away from Pd(II)-centre by the conformationally rigid ring (outlined in purple).

centre. In order to see the ring strain incurred for styrenylation and ligand-assisted β-hydride elimination, we performed a dihedral angle scan about the C–C bonds in red shown in Figure 5.7. The dihedral angle scans allow us to compare the rotational barriers required to form allyl- vs styrenyl-product since the rotational barrier for the latter is regio-determining. We can see that styrenylation has a hugely disfavoured ring strain when the requisite H atom (H_s in Figure 5.7(ii)) is brought to interact agostically with Pd(II) centre – a prerequisite for the subsequent β-hydride elimination. On the other hand, both *E*- and *Z*-allylation involve steps that do not impose any strain on the 14-membered palladacycle since both rotation and β-hydride elimination occur outside the ring (Figure 5.7(i)) whereas styrenylation severely distorts the palladacycle, giving rise to hugely unfavourable ring strains.

5.3.6 Reactivity and selectivity for *cis*-hex-3-ene substrate

Experimentally, *cis*-olefin was found to be slightly less reactive than *trans*-olefin (Figure 5.8), we modelled the TDTS (1,2-migratory insertion) of *cis*-olefin and compared this to *trans*-olefin. Since there are expected to be numerous conformers close in energy (within 5 kcal mol^{-1}), conformational samplings of the TDTSs for both *cis*- and *trans*-olefins were performed and the resulting TSs Boltzmann weighted for comparison (see subsection 5.3.8 for the TS conformers).

We can do this comparison since the reaction mechanism is the same for both olefin substrates and the lowest resting states are the separated reactants. A ratio of 1.2 : 1 (*trans*-hex-3-ene vs *cis*-hex-3-ene) for the relative rates is obtained using ωB97X-D functional for SP correction whereas this ratio reverses and becomes 1 : 1.3 using MN15 functional. This suggests that the reactivity for either olefin would be rather comparable, mirroring the similar experimental rates observation in Figure

5.8. The similar rates obtained for both *trans*- and *cis*-hex-3-ene are perhaps unsurprising: both electronic and steric factors seem to be similar in both TSs (Figure 5.9), implicating similar chemical reactivity.

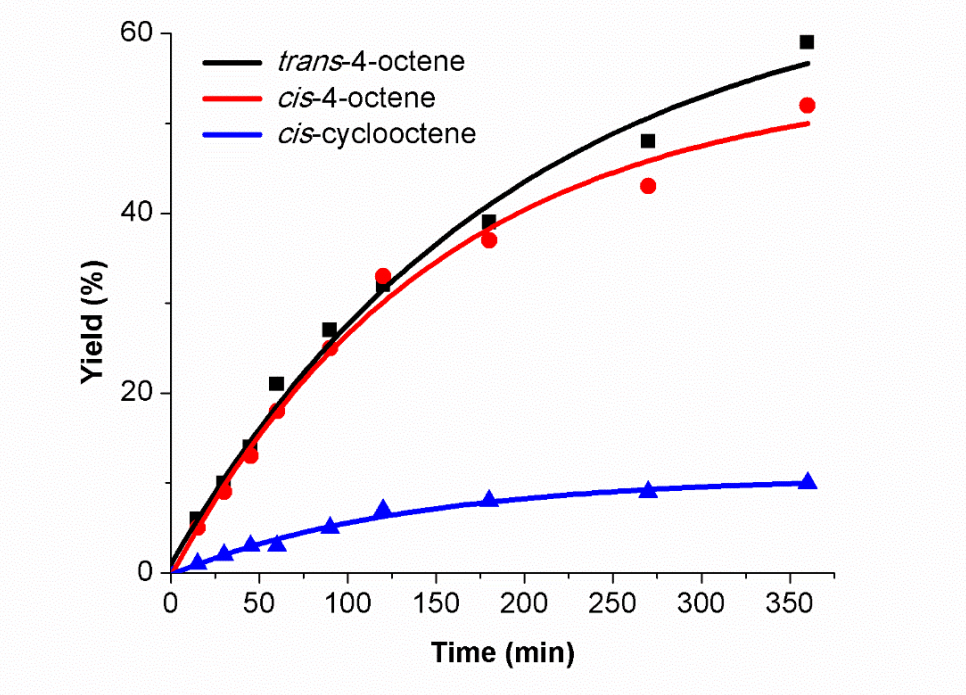

Figure 5.8. Kinetic comparison of different aliphatic internal olefins. This result is from the experimental work carried out by our experimental collaborators. Figure is used here without further modifications.

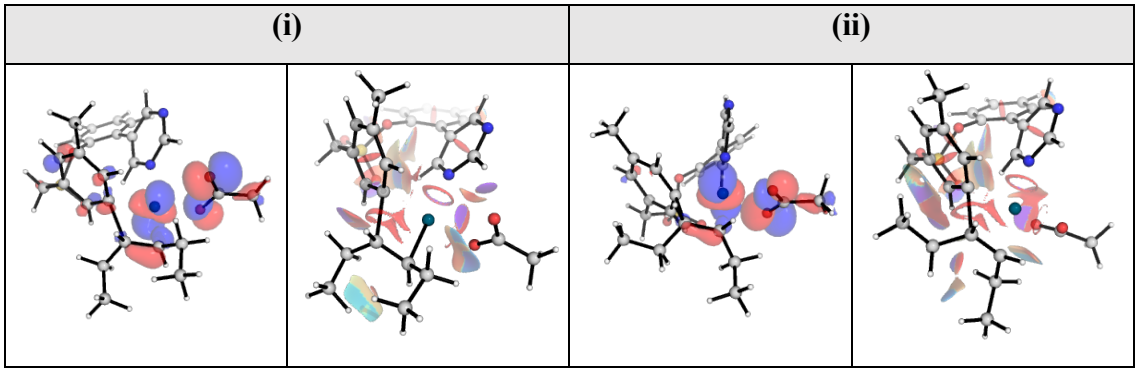

Figure 5.9. HOMO (isosurface value of 0.04) and NCI plots for the 1,2-migratory insertion TDTS using the lowest barrier conformer for (i) *trans*-hexene and (ii) *cis*-hexene.

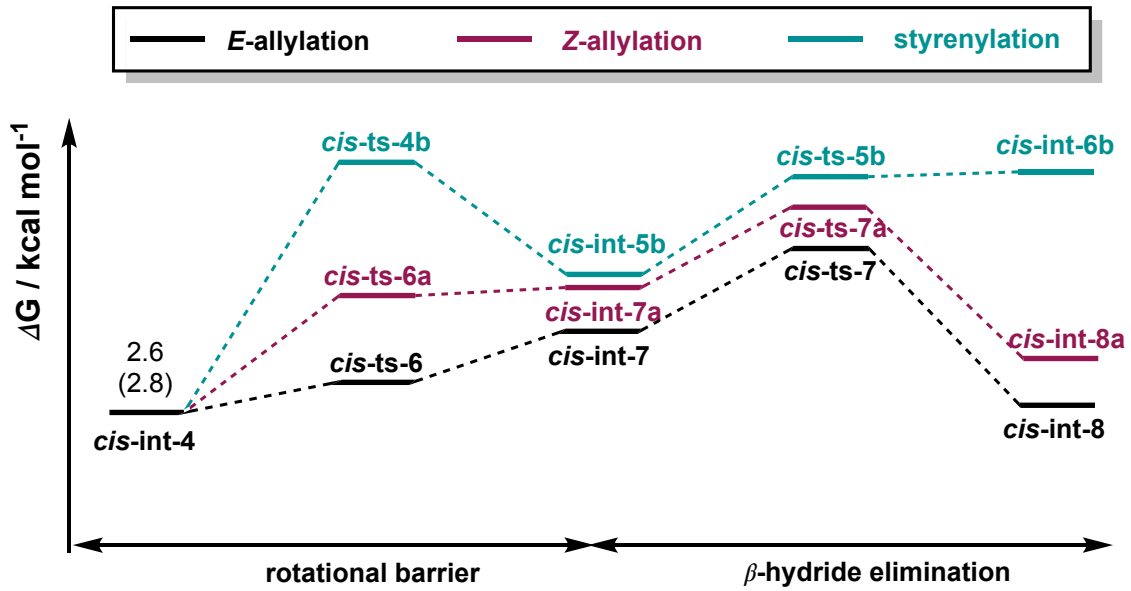

Final prd	direct β-H elimination				ligand-promoted β-H elimination				Overall barrier [a]
	cis-ts-4x	*cis*-int-5x	*cis*-ts-5x	*cis*-int-6x	*cis*-ts-6x	*cis*-int-7x	*cis*-ts-7x	*cis*-int-8x	
E-allyl **x = nil**	–	–	–	–	4.9‡ (5.1‡)	10.8 (10.5)	**13.8‡ (14.9‡)**	3.5 (3.0)	**11.2 (12.1)**
Z-allyl **x = a**	–	–	–	–	10.7‡ (11.4‡)	11.7 (13.3)	**17.4‡ (18.6‡)**	7.1 (6.4)	**14.8 (15.8)**
Styrenyl **x = b**	**20.8‡ (22.2‡)**	11.7 (12.3)	16.1‡ (15.3‡)	17.1 (14.8)	–	–	–	–	**18.2 (19.4)**

Table 5.3 Gibbs energies for product selectivity studies for *cis*-hex-3-ene substrate. TDTS values are given in bold.

The product selectivity for *cis*-hex-3-ene was similarly studied. The lowest pathways (ligand-assisted vs direct β-hydride elimination) for *cis*-hex-3-ene product formations were studied (Table 5.3): for *E-/Z*-allylation, the ligand-assisted β-hydride elimination is the lowest barrier pathway whereas for styrenylation, direct β-hydride elimination is the lowest pathway. The key optimised TS structures are shown in Figure 5.10.

cis-int-4	cis-ts-6	cis-int-7
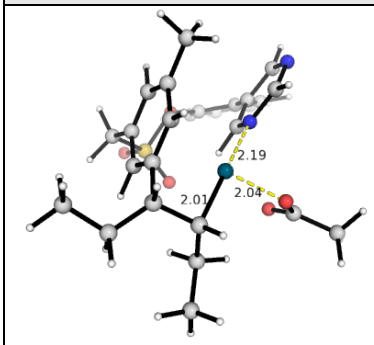	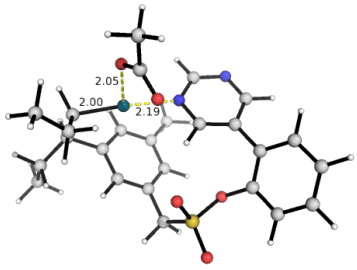	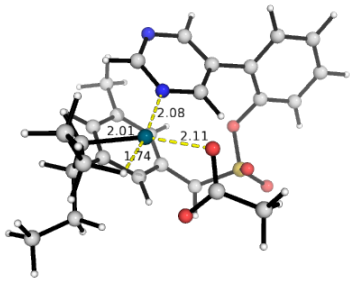
cis-ts-7	**cis-int-8**	**cis-ts-6a**
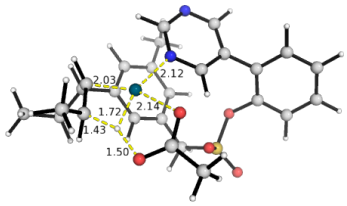	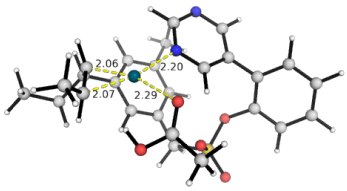	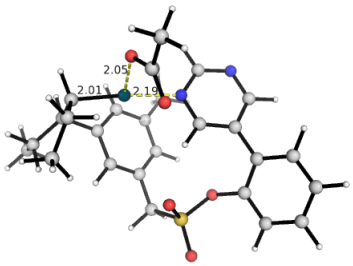
cis-int-7a	**cis-ts-7a**	**cis-int-8a**
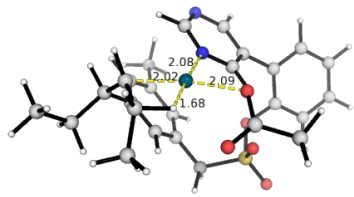	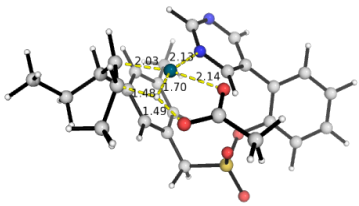	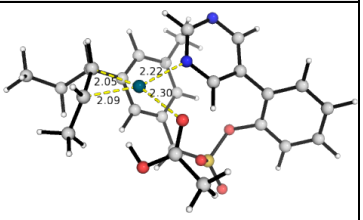
cis-ts-4b	**cis-ts-5b-c2**	**cis-int-5b**
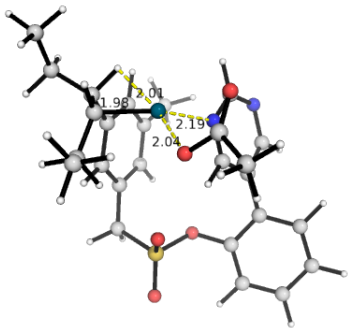	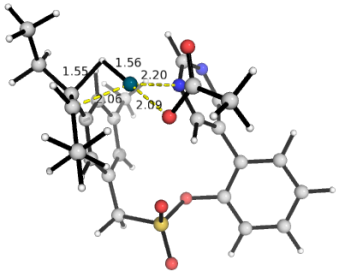	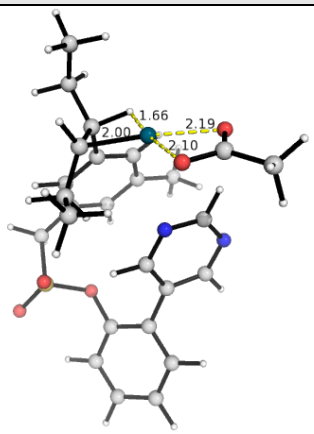

cis-ts-5b	cis-int-6b	
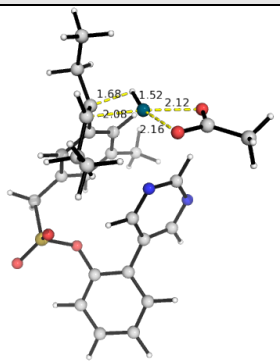	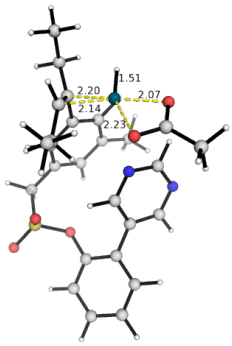	

Figure 5.10. Optimised TS structures for selectivity studies using *cis*-hex-3-ene substrate.

As before, *E*-allylation (***cis*-ts-7**) has the lowest barrier, at 13.8 kcal mol^{-1}. The barrier for *Z*-allylation (***cis*-ts-7a**) is 3.6 kcal mol^{-1} higher (1 in 147) and can be traced to the steric clashes (less favourable 1,3-diaxial interactions in *Z*-allylation) as evidenced by the NCI plots (Figure 5.11) where the Z-allylation TS has slightly less favourable NCIs. The HOMOs for ligand-assisted β-H elimination for both allylation using *cis*-hex-3-ene substrate (Figure 5.11) are similar to each other and similar to those for *trans*-hex-3-ene (Figure 5.6), where a σ^*_{CH} bond is broken and a π_{CC} bond is formed as the deprotonation occurs. Styrenylation is once again uncompetitive, as for *trans*-hex-3-ene, due to the unfavourable ring strains experienced by the palladacycle when the styrenyl proton H_S is brought to interact agostically with the Pd(II)-centre (Figure 5.12(ii)).

***cis*-ts-7 (*E*-allylation)**		***cis*-ts-7a (*Z*-allylation)**	
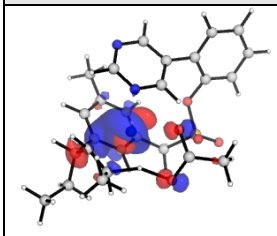	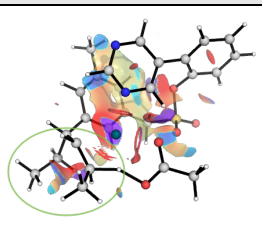	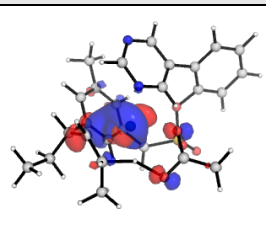	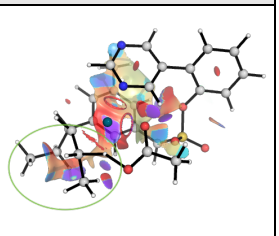

Figure 5.11. HOMOs and NCI plots for *E*- vs *Z*-allylated product selectivity for *cis*-hex-3-ene substrate.

Here again, for styrenylation, the TS where the DG got displaced (***cis*-ts-5b** at 16.1‡ kcal mol^{-1}) has a lower activation barrier than the one where it remained coordinated (***cis*-ts-5b-c2** at 23.1‡ kcal mol^{-1}) since the former released the unfavourable ring strain in the palladacycle as the styrenyl H atom is brought into agostic interaction with the Pd(II)-centre.

It is important to realise that allylation has β-H elimination occurring outside the rigid palladacyle ring in the insertion intermediate whereas styrenylation has β-H elimination incurring unfavourable distortions of the palladacyle; this is once again evident from the dihedral angle scans about key C–C bonds (Figure 5.12).

5.3.7 Reactivity and selectivity for cyclohexene substrate

Experimentally, cyclic olefin was found to be much less reactive than *trans*-olefin, with significantly poorer yield (Figure 5.8). The rate-determining 1,2-migratory insertion step of cyclohexene substrate was compared to that of *trans*-olefin. Boltzmann weighting of the TS conformers (subsection 5.3.8) gives a ratio of 1 : 44–56 (cyclohexene vs *trans*-hexene) for their relative rates.

The product selectivity for cyclohexene substrate was also studied. Initial dihedral angle scans were performed about the key C–C bonds to locate rotational barriers bringing the H atom (for subsequent β-H elimination) to interact agostically with Pd(II)-centre (Figure 5.13). Only rotational barriers for *Z*-allylation could be located with a barrier of 13.1 kcal mol^{-1} (**cy-ts-7a**); both *E*-allylation and styrenylation had rotational barriers that are about 30 kcal mol^{-1} higher than for *Z*-allylation. The cyclohexene ring fused to the rigid palladacycle in the bicyclic insertion intermediate severely restricts the degree of rotational freedom: both the H_E and H_S atoms could not be brought to interact agostically

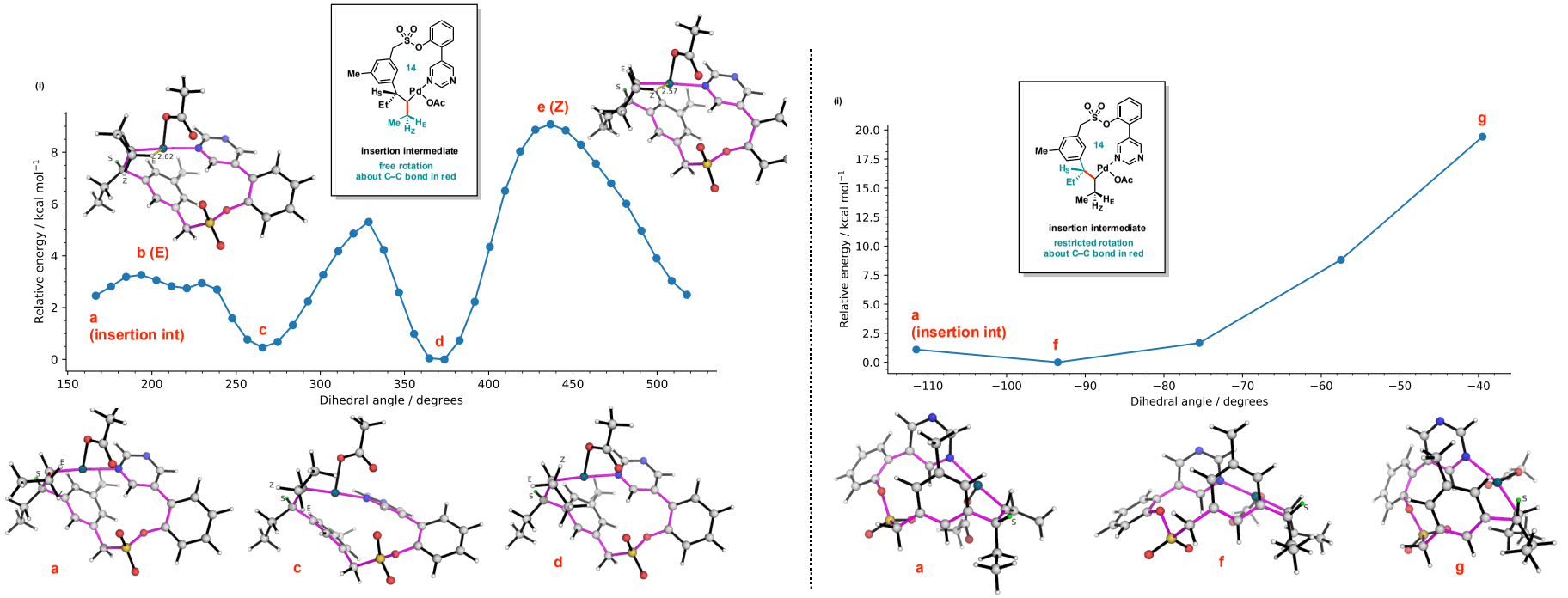

Figure 5.12. Dihedral angle scan (about C–C bond in red) for rotational barrier for the formation of (i) *E*-/*Z*-allylated products and (ii) styrenyl product for *cis*-hex-3-ene substrate. Note the different energy scales used. In (ii), the position of styrenyl proton (H_s, labelled *S* in green) is restrained away from Pd(II)-centre by the conformationally rigid ring (outlined in purple).

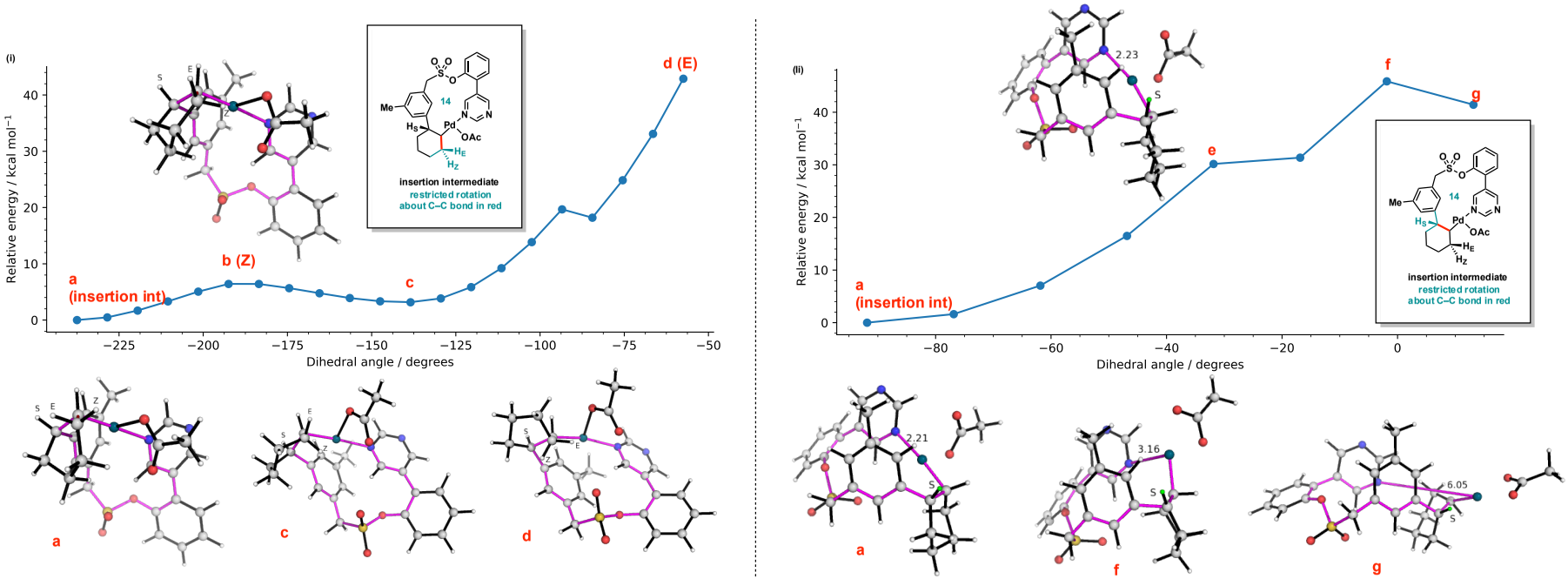

Figure 5.13. Dihedral angle scan (about C–C bond in red) for rotational barrier for the formation of (i) *E*-/*Z*-allylated products and (ii) styrenyl product for cyclohexene substrate.

with the Pd(II) centre without incurring unduly strains due to geometric constraints and unfavourable ring distortions (Figure 5.13).

The overall Gibbs energy profile for cyclohexene substrate is shown in Figure 5.14. Given that the subsequent ligand-assisted β-H elimination for *Z*-allylation (**cy-ts-7a**) is 6.3 kcal mol^{-1} higher than the rotational barrier (**cy-ts-6a**), we estimate that the barriers for both *E*-allylation and styrenylation are at least ~20 kcal mol^{-1} higher than *Z*-allylation (**cy-ts-7a**), thus being disfavoured by 1 in a trillion. Thus, if at all, the allylation product would adopt *Z*-geometry that formed part of the cyclohexene ring. The formation of Z-allylated product **cy-int-8a** is endergonic with respect to the insertion intermediate **cy-int-4**, making this product formation thermodynamically reversible, thus explaining its poor yield obtained experimentally.

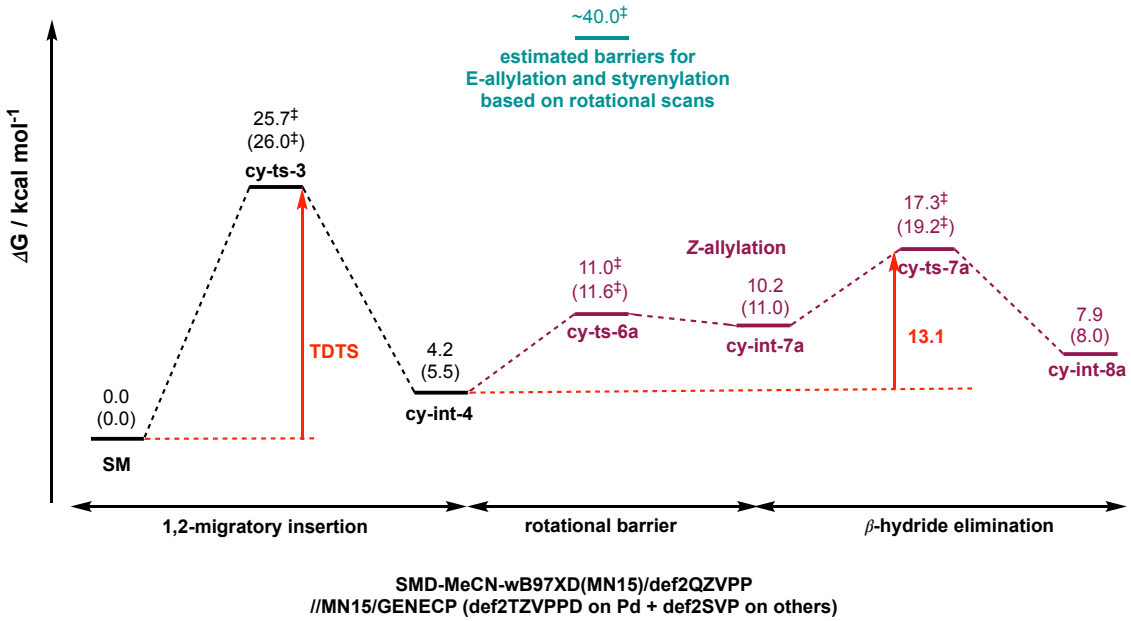

Figure 5.14. Gibbs free energy profile for *Z*-allylation using cyclohexene substrate.

5.3.8 General conformational sampling

Once a TS was found, the structure was used as starting guesses for searching other TS conformers. The palladacycle ring was frozen and the rotamers via rotations along C–C bonds in red (Scheme 5.6) were generated for subsequent TS conformational searches. For cyclohexene substrate, the buckling of the half-chair in different orientations were considered. Altogether, 9 TSs were found for each orientation of alkene (18 TSs for each of *trans*-hex-3-ene and *cis*-hex-3-ene) and 4 TSs were found for each orientation of cyclohexene (8 TSs altogether). The optimised TS structures and their relative energy barriers with respect to the lowest barrier TS for *trans*-hex-3-ene substrate ($\Delta\Delta G^{\ddagger}$) are shown in Figure 5.15.

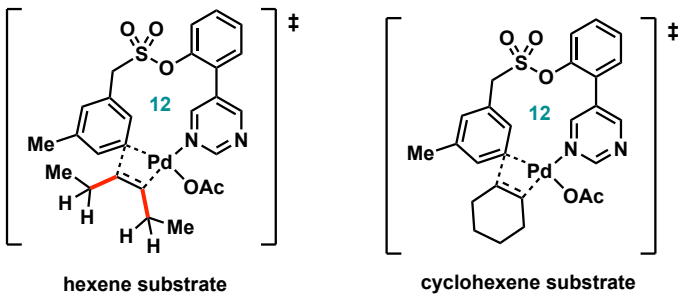

Scheme 5.6. Generation of rotamers in the conformational sampling of the 1,2-migratory insertion TDTSs for *trans*- and *cis*-hex-3-ene substrates and cyclohexene.

Boltzmann weighting of the conformers were performed using Equation (1.84) as described in Chapter 1 subsection 1.8.3.

***trans*-d1-c1**	***trans*-d1-c2**	***trans*-d1-c3**
$\Delta\Delta G^{\ddagger}$ = 1.2 (1.3)	$\Delta\Delta G^{\ddagger}$ = 1.3 (1.1)	$\Delta\Delta G^{\ddagger}$ = 2.4 (1.7)
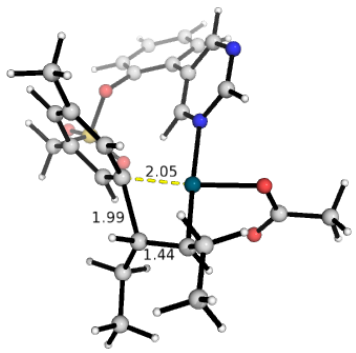	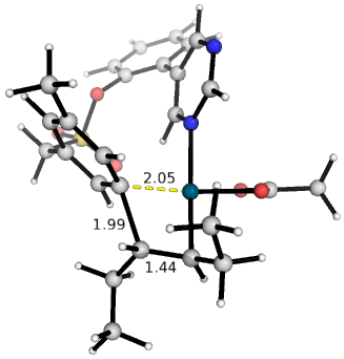	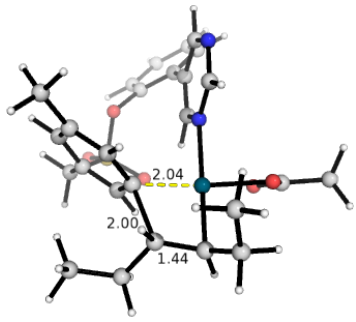
***trans*-d1-c4**	***trans*-d1-c5**	***trans*-d1-c6**
$\Delta\Delta G^{\ddagger}$ = 2.6 (2.6)	$\Delta\Delta G^{\ddagger}$ = 2.9 (2.5)	$\Delta\Delta G^{\ddagger}$ = 2.9 (3.5)
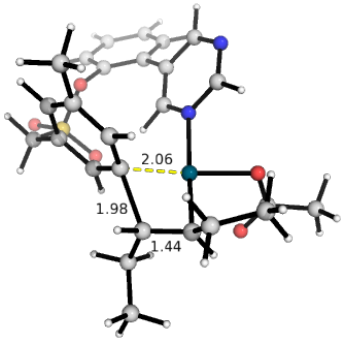	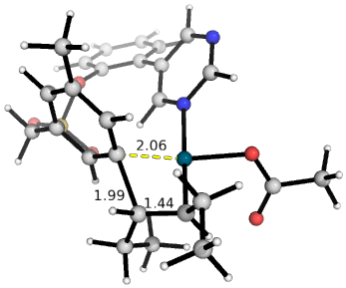	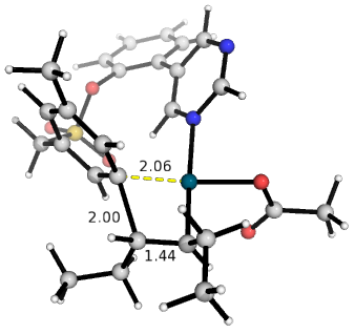
***trans*-d1-c7**	***trans*-d1-c8**	***trans*-d1-c9**
$\Delta\Delta G^{\ddagger}$ = 3.3 (2.4)	$\Delta\Delta G^{\ddagger}$ = 3.7 (3.0)	$\Delta\Delta G^{\ddagger}$ = 5.2 (4.6)
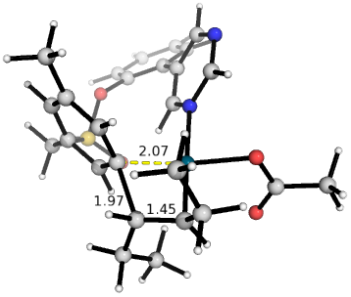	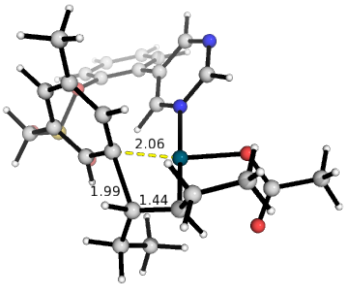	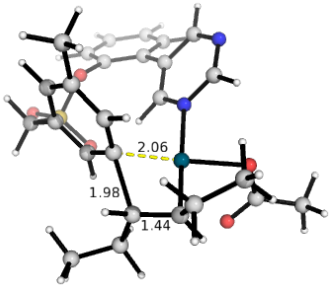

(a) Conformers for 1,2-migratory insertion TDTS for diastereomer 1 (d1) formation from *trans*-hex-3-ene.

***trans*-d2-c1**	***trans*-d2-c2**	***trans*-d2-c3**
$\Delta\Delta G^{\ddagger}$ = 0.0 (0.0)	$\Delta\Delta G^{\ddagger}$ = 0.6 (0.4)	$\Delta\Delta G^{\ddagger}$ = 1.2 (0.9)
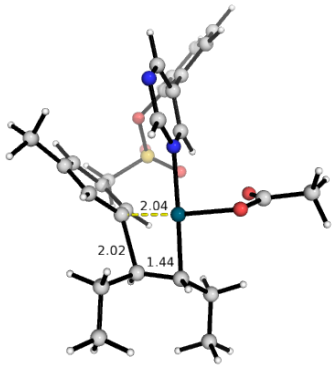	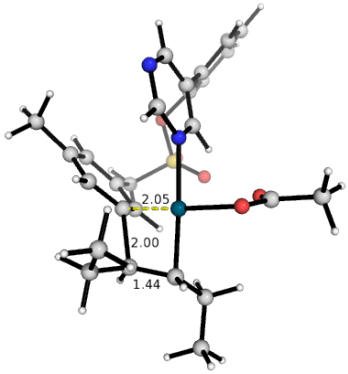	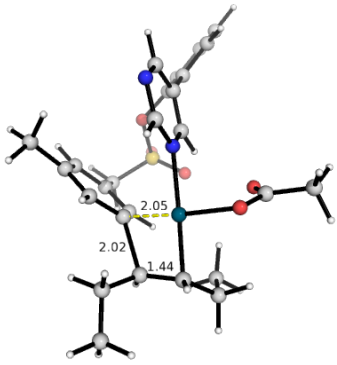
***trans*-d2-c4**	***trans*-d2-c5**	***trans*-d2-c6**
$\Delta\Delta G^{\ddagger}$ = 2.0 (1.3)	$\Delta\Delta G^{\ddagger}$ = 2.2 (2.4)	$\Delta\Delta G^{\ddagger}$ = 2.4 (2.1)
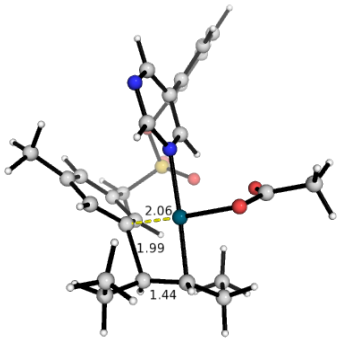	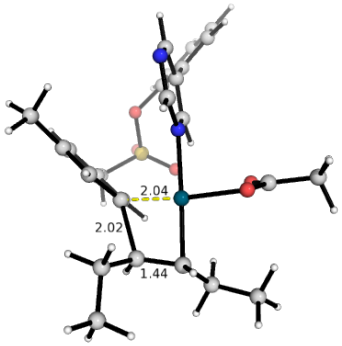	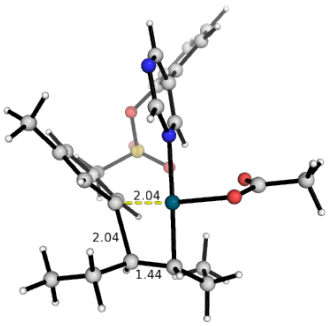
***trans*-d2-c7**	***trans*-d2-c8**	***trans*-d2-c9**
$\Delta\Delta G^{\ddagger}$ = 2.6 (2.1)	$\Delta\Delta G^{\ddagger}$ = 2.6 (1.9)	$\Delta\Delta G^{\ddagger}$ = 4.5 (4.0)
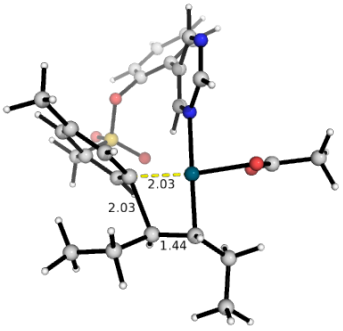	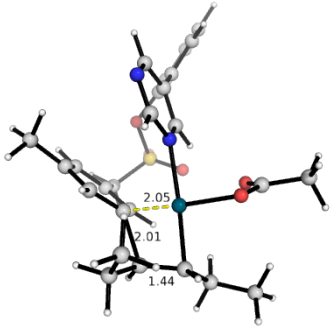	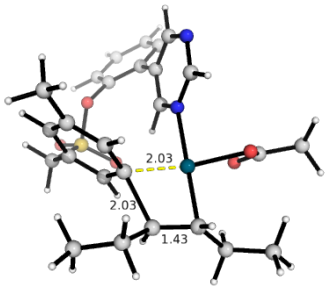

(b) Conformers for 1,2-migratory insertion TDTS for diastereomer 2 (d2) formation from *trans*-hex-3-ene.

***cis*-d1-c1**	***cis*-d1-c2**	***cis*-d1-c3**
$\Delta\Delta G^{\ddagger}$ = 0.3 (-0.2)	$\Delta\Delta G^{\ddagger}$ = 1.0 (0.6)	$\Delta\Delta G^{\ddagger}$ = 1.2 (1.0)
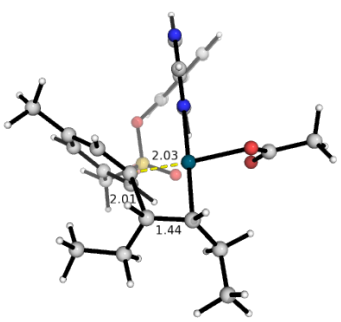	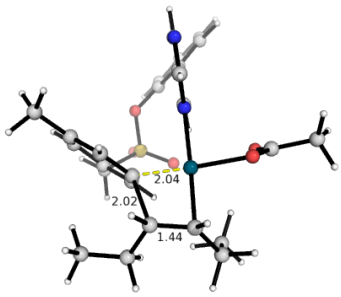	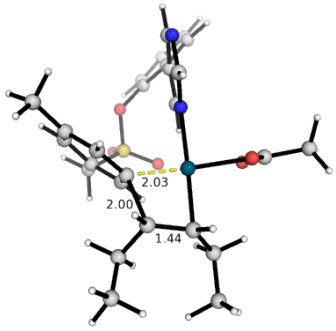
***cis*-d1-c4**	***cis*-d1-c5**	***cis*-d1-c6**
$\Delta\Delta G^{\ddagger}$ = 1.2 (1.2)	$\Delta\Delta G^{\ddagger}$ = 1.7 (0.8)	$\Delta\Delta G^{\ddagger}$ = 2.5 (2.1)
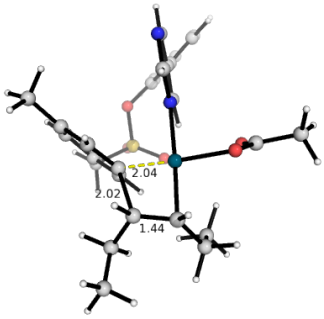	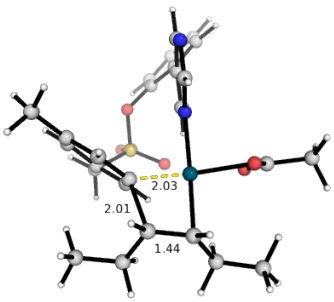	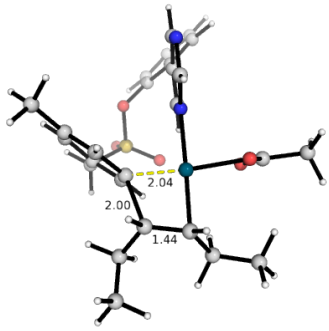
***cis*-d1-c7**	***cis*-d1-c8**	***cis*-d1-c9**
$\Delta\Delta G^{\ddagger}$ = 5.8 (4.5)	$\Delta\Delta G^{\ddagger}$ = 5.8 (4.8)	$\Delta\Delta G^{\ddagger}$ = 10.9 (9.7)
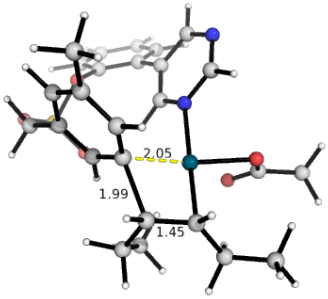	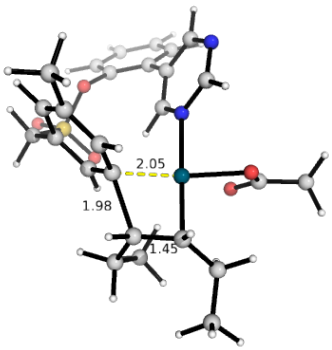	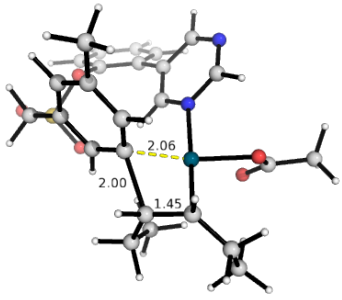

(c) Conformers for 1,2-migratory insertion TDTS for diastereomer 1 (d1) formation from *cis*-hex-3-ene.

***cis*-d2-c1**	***cis*-d2-c2**	***cis*-d2-c3**
$\Delta\Delta G^{\ddagger}$ = 1.6 (1.0)	$\Delta\Delta G^{\ddagger}$ = 1.7 (1.4)	$\Delta\Delta G^{\ddagger}$ = 1.8 (1.1)
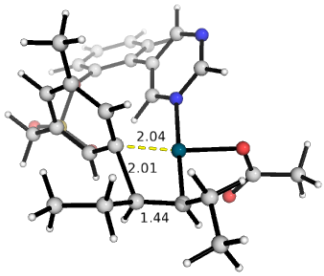	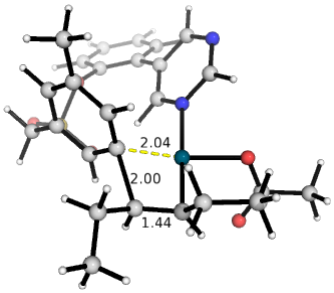	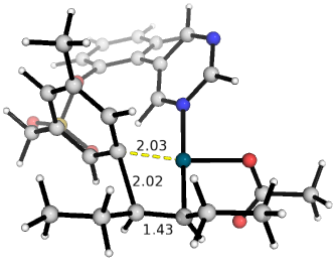
***cis*-d2-c4**	***cis*-d2-c5**	***cis*-d2-c6**
$\Delta\Delta G^{\ddagger}$ = 2.2 (0.9)	$\Delta\Delta G^{\ddagger}$ = 2.5 (1.5)	$\Delta\Delta G^{\ddagger}$ = 2.6 (2.3)
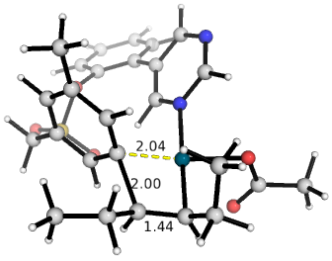	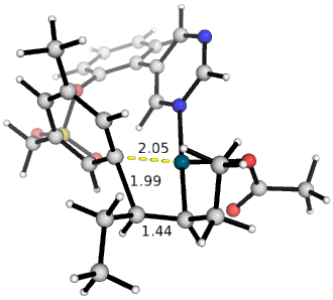	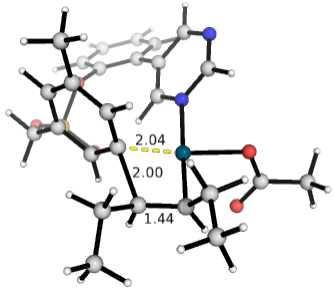
***cis*-d2-c7**	***cis*-d2-c8**	***cis*-d2-c9**
$\Delta\Delta G^{\ddagger}$ = 4.2 (4.1)	$\Delta\Delta G^{\ddagger}$ = 6.4 (6.8)	$\Delta\Delta G^{\ddagger}$ = 7.4 (7.1)
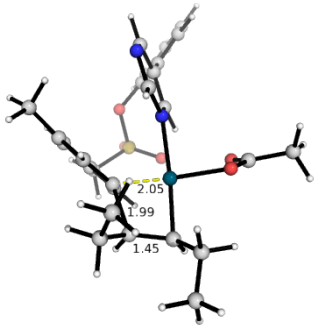	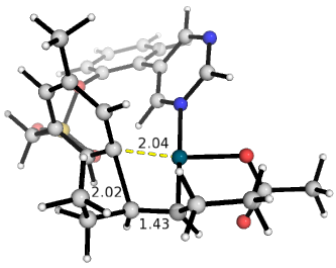	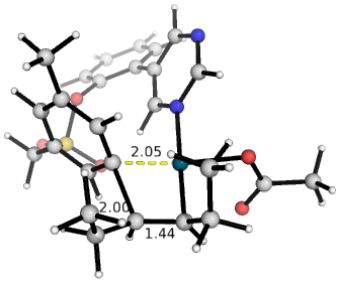

(d) Conformers for 1,2-migratory insertion TDTS for diastereomer 2 (d2) formation from *cis*-hex-3-ene.

cy-d1-c1	cy-d1-c2	cy-d1-c3
$\Delta\Delta G^{\ddagger}$ = 2.7 (2.8)	$\Delta\Delta G^{\ddagger}$ = 3.3 (3.6)	$\Delta\Delta G^{\ddagger}$ = 4.5 (3.7)
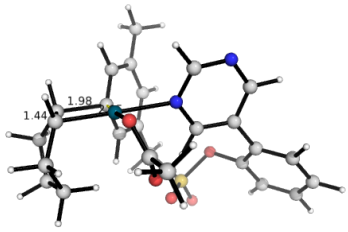	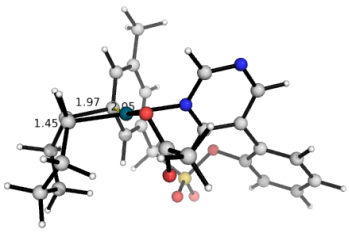	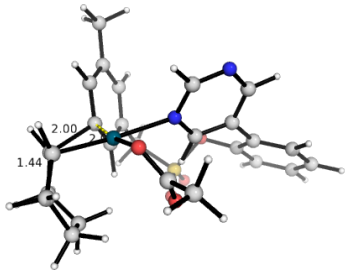
cy-d1-c4		
$\Delta\Delta G^{\ddagger}$ = 5.2 (5.0)		
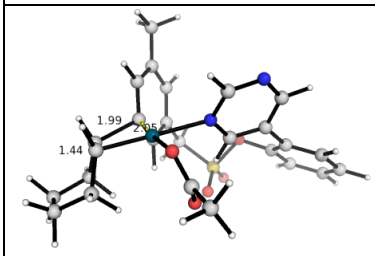		

(e) Conformers for 1,2-migratory insertion TDTS for diastereomer 1 (d1) formation from cyclohex-3-ene (cy).

cy-d2-c1	cy-d2-c2	cy-d2-c3
$\Delta\Delta G^{\ddagger}$ = 3.7 (4.0)	$\Delta\Delta G^{\ddagger}$ = 4.3 (3.3)	$\Delta\Delta G^{\ddagger}$ = 4.4 (4.6)
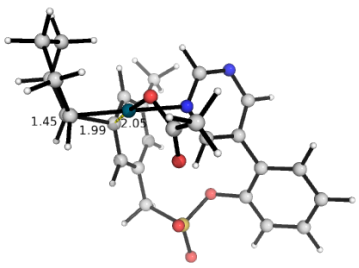	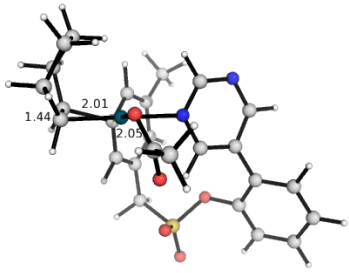	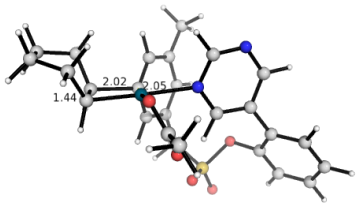

cy-d2-c4		
$\Delta\Delta G^{\ddagger}$ = 4.4 (4.8)		
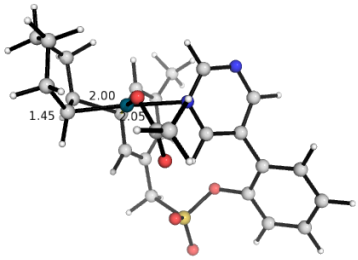		

(f) Conformers for 1,2-migratory insertion TDTS for diastereomer 2 (d2) formation from cyclohex-3-ene (cy).

Figure 5.15. Optimised TS geometries for 1,2-migratory insertion TDTS step for *trans*-hexne (**a** and **b**), *cis*-hex-3-ene (**c** and **d**) and cyclohex-3-ene (**e** and **f**). All TSs were taken relative to the same minima (***trans*-d2-c1**). Relative $\Delta\Delta G^{\ddagger}$ values are in kcal mol^{-1}. Bond lengths are given in Angstroms.

5.3.9 Proposed catalytic cycle

Based on our computational mechanistic studies, together with experimental evidence from H/D exchange, order determination and kinetic studies, we propose a catalytic cycle for the *meta*-selective C(sp^2)–H allylation reaction using internal olefin as an allyl surrogate (Scheme 5.7). We believe that arene **1a** coordinates to the palladium catalyst via the heteroaromatic ring on the directing group. Subsequent MPAA-assisted *meta*-hydrogen abstraction from the arene via concerted metalation deprotonation leads to C–H activated intermediate **int-2'**. Coordination of electronically unbiased internal olefins and the subsequent rate-determining migratory insertion afford a cyclophane-like 14-membered metallacycle **int-4** which further undergoes selective β-H elimination to deliver the allylated product. Stability and conformational restraints of intermediate **int-4** play a crucial role for both regio- and stereo-selective outcomes of this reaction: the rotational TSs for allylation and the subsequent ligand-assisted β-H elimination occur outside the conformationally rigid metallacycle whereas the rotational TS for

styrenylation incurs huge ring strains in the metallacycle which has to be twisted in order to bring the requisite H atom to interact with Pd(II)-centre agostically before subsequent β-H elimination could occur.

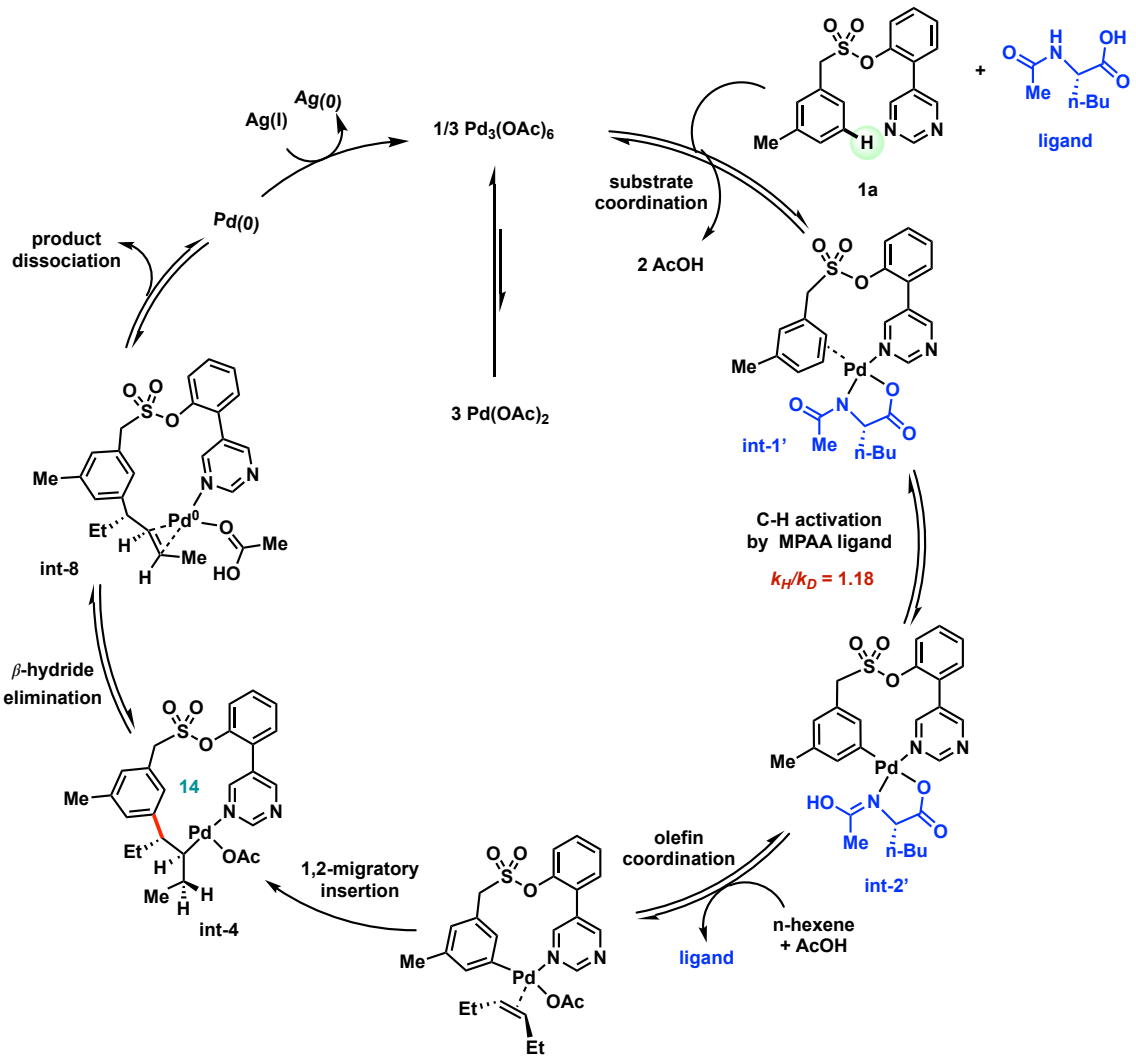

Scheme 5.7. Proposed catalytic cycle.

5.4 Conclusions

Our computational investigations on the reaction mechanisms of using aliphatic internal olefins as allyl surrogates give us great mechanistic insights into the *meta*-selective C(sp^2)–H allylation of directing group linked arenes. We found 1,2-migratory insertion of the incoming olefin to be the overall turnover frequency determining step while the

subsequent β-hydride elimination is the regio- and stereo-selective step in determining the product selectivity. Steric factors play an essential role in such these transformations. Primarily, the *meta*-selectivity of arene C–H activation is dictated by the ring strain in the formation of the cyclophane-like intermediate. The product selectivities are dictated by the steric influences of the alkyl groups in the close vicinity of the C=C bond and the conformational rigidity afforded by the palladacycle intermediate in β-H elimination step. Allylation is more favoured over styrenylation since for the former, both bond rotation to bring the requisite H atom for agostic interaction with Pd-centre and its subsequent elimination do not distorted the palladacycle, whereas for the latter, bond rotation to bring the requisite H atom for agostic interaction with Pd-centre greatly distorts the palladacycle, giving rise to unduly high ring strains such that its rotational TS becomes thermally much less accessible. For allylation, *E*-allylated product is favoured over *Z*-allylated product due to more favourable sterics of the alkyl groups in the close vicinity of the C=C bond in the former case.

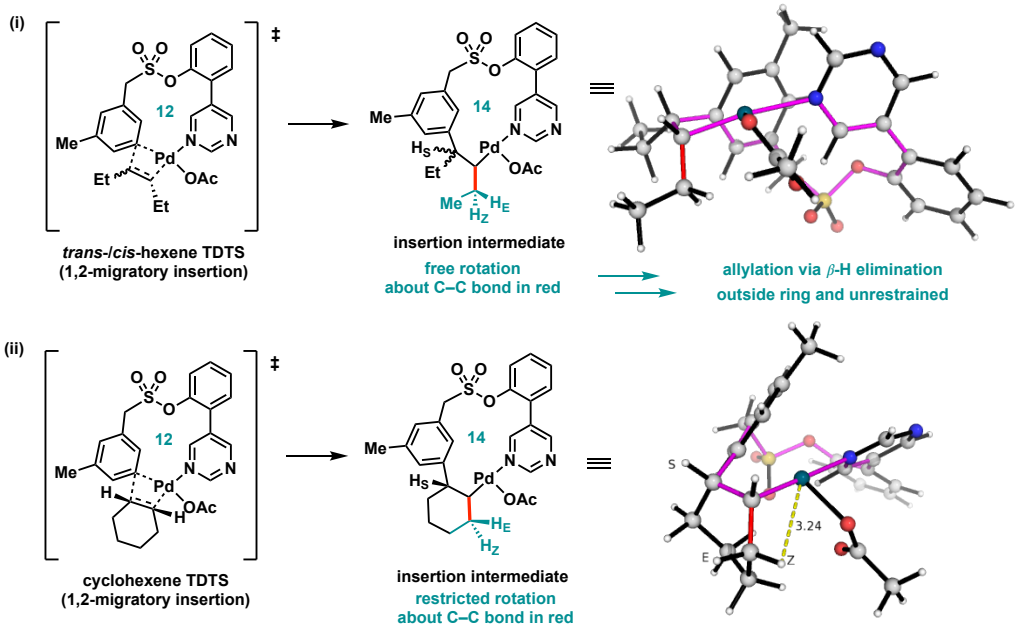

Scheme 5.8. Steric influences of the olefin substrates on chemical reactivity.

In terms of the influence of substrate structure on the reactivity, we note that acyclic aliphatic internal olefins (*trans*- and *cis*-hex-3-ene) react more favourably than alicyclic olefins (cyclohexene). The molecular origins for these differences in the reactivity can be traced to the key product determining step: after 1,2-migratory insertion step forming the 14-membered palladacyclic intermediate, rotations in the monocyclic insertion intermediate from acyclic olefin are unrestricted and do not impose unfavourable ring strains on the palladacycle (Scheme 5.8 (i)) whereas the rotations in the bicyclic insertion intermediate from alicyclic olefin introduces massive ring strain (Scheme 5.8 (ii)). Our computations provide us an augmented understanding of the mechanism and selectivity of the present transformation.

One cannot stumble on an idea unless one is running.

— Vladimir K. Zworykin

6

Pd-catalysed C(sp^2)–H alkynylation[***]

6.1 Introduction

In Chapter 5, we looked at Pd(II)-catalysed C(sp^2)–H allylation using pyrimidine-based directing group (DG).[103] The pyrimidine-based DG is a popular DG frequently employed for its efficacy in binding to TMs due to its strong binding affinity and thus effecting directed C–H functionalisations. Herein we report the computational study of using this highly versatile DG for Pd(II)-catalysed C(sp^2)–H alkynylation of a variety of arenes.

Aromatic rings are a common structural motif in many natural products, bioactive molecules and polymer chemistry.[332,432,433] The introduction of acetylenic functional group to arenes greatly expands the synthetic utility of such molecules due to the

[***] This work has been deposited as a preprint on *ChemRxiv* with DOI: **10.26434/chemrxiv.9846083.v1**. This work has also been submitted to a journal and is currently under review.

versatility of acetylene for further modifications.[506,507] Amongst the existing methods, Sonogashira coupling between aryl halides and terminal alkynes is perhaps the most popular to access the arylalkynes via C(sp^2)–C(sp) coupling (Scheme 6.1 (a)). This method, however, requires the pre-functionalisation of the aryl coupling partner. To overcome this problem, the alternative direct C(sp^2)–H activation of arenes utilising an "inverse Sonogashira coupling"[351,508] of unreactive C–H bonds with readily available alkynyl halides is often employed (Scheme 6.1 (b)). Such transformations, frequently catalysed by transition metals (such as Ni,[509] Cu,[510,511] Pd,[512–515] Au,[516,517] and Ir[518]), prove to be particularly attractive as they circumvent the need for the pre-functionalisation of the aromatic coupling partner. To be widely applicable, the regioselectivity of such activation has to be precisely controllable. To this end, transient directing groups are commonly employed for site-selective C(sp^2)–H activation. Alkynylation at *ortho*-position has been well studied and achieved with an impressive range of catalytic systems.[377,513,518–522] Examples of *para*-alkynylations can also be found.[517,523] The *meta*-position can be challenging for C–H activation due to the fine balance between the mesomeric and inductive effects of the substituents on arenes. As a result, *meta*-alkynylation is relatively underexplored.[524]

Our experimental collaborators (the Maiti Research Group at the Indian Institute of Technology, Bombay) have recently developed an experimental procedure for chelation-assisted *meta*-selective C(sp^2)–H alkynylation, which was shown to be efficacious with broad substrate scope, wide functional group tolerance and good to excellent yields (Scheme 6.1 (c)). Experimentally it was found that when the substrate bromoethynyl-trimethylsilane **1b** (hereafter bromoalkyne) was used, the reaction proceeded with high efficiency with good conversion and yield of the products. However, when the substrate

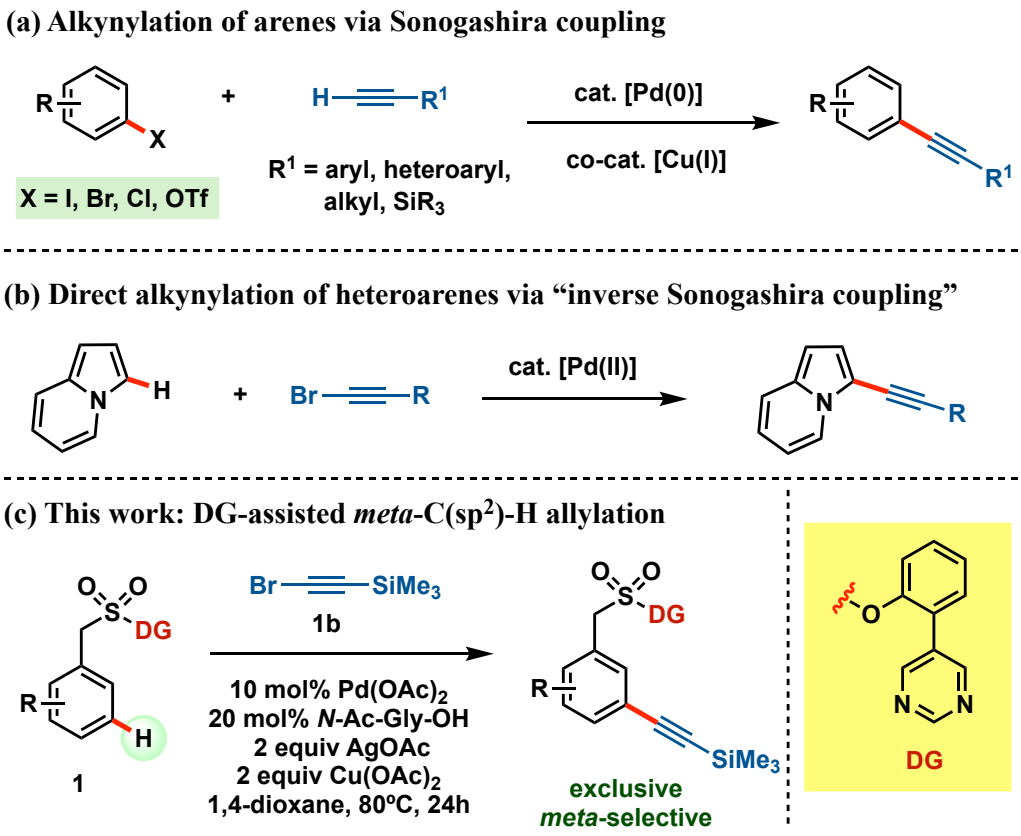

Scheme 6.1. Methods to access arylalkynes.

ethynyltrimethylsilane **1c** (hereafter TMS-alkyne) was used, the reaction did not work well at all. Similarly, when the substrate bromoethynylbenzene **1d** was used, the reaction did not work well too – the majority of the substrate was recovered. Our computational studies shed light on the reaction mechanism, implicating a 1,2-migratory insertion rate-determining step and a Pd–Ag heterobimetallic TS in effecting the transformation. In addition, we found that substrate TMS-alkyne **1c** was incompetent due to unfavourable β-H elimination in the migratory insertion product and that substrate bromoethynyl-benzene **1d** is incompetent possibly due to its enhanced coordination to the catalytic metals, thus inactivating the TM for catalysis. For our computational modelling of the reaction shown in Scheme 6.1 (c), arene **1a** (structure **1** with R = *m*-Me) was used. All experimental work was performed by our experimental collaborators (Sandip Porey *et. al*) at IITB and all computational work was performed by the present author.

6.2 Computational Methods

Computational methods employed for the present transformation are the same as those employed in the study of Pd(II)-catalysed C(sp^2)–H allylation in Chapter 5. Geometry optimisations were performed with MN15/GenECP (def2-TZVPPD for Br[17], Pd[17,401] and Ag[17,401] atoms and def2-SVP[18,19] for all other atoms, collectively denoted BS1). Gibbs energy corrections were performed at the experimental temperature of 80ºC. SMD(1,4-dioxane)-ωB97X-D/def2-QZVPP//MN15/BS1 Gibbs energies are given with SMD(1,4-dioxane)-MN15/def2-QZVPP//MN15/BS1 Gibbs energies given in brackets throughout. Unless otherwise stated, the former set of Gibbs energy values are used for discussion. *All Gibbs energy values in the text and figures are quoted in kcal mol^{-1} throughout.*

Geometries of all optimised and an associated README file have been deposited online and made freely available (DOI:10.5281/zenodo.3376707).

6.3 Results and Discussions

6.3.1 Conformational considerations for starting materials

Conformational samplings of the starting material sulfonyl arene, **1a**, was performed as in subsection 5.3.1. The lowest energy conformer for the starting material was used for subsequent calculations.

6.3.2 Frontier molecular orbitals (FMOs) of starting materials

Figure 6.1 shows the FMOs for the starting materials bromoalkyne **1b** and TMS-alkyne **1c**. In **1b**, the HOMO arises predominantly from the π-electrons from the alkyne triple bond. This electron-rich π-bond can be donated to a vacant d-orbital on the electrophilic Pd(II) centre, giving rise to π-complexes with the transition metal before further transformations. Interestingly, the LUMO of **1b** is σ^*_{CBr} instead of π^*_{CC}. These have

implications on the reactivity of bromoalkyne **1b**, suggesting that oxidative insertion of **1b** breaking the C–Br bond could be possible. FMOs for TMS-alkyne **1c** are also shown in Figure 6.1. The HOMO is π_{CC} and the LUMO is π^*_{CC}. These are rather different from the FMOs in **1b**, implicating different reactivity (see subsection 6.3.8 for a discussion of the reactivity with **1c** as a substrate).

HOMO of 1b	**LUMO of 1b**
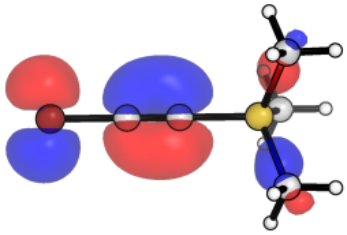	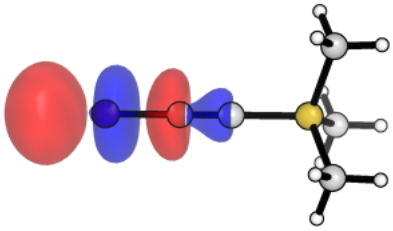
HOMO of 1c	**LUMO of 1c**
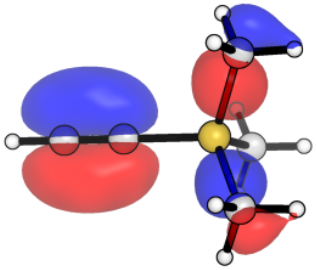	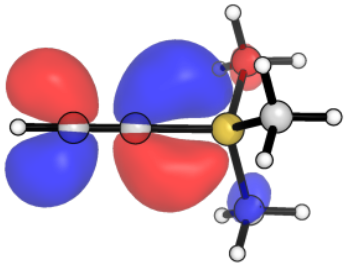

Figure 6.1. FMOs for bromoethynyltrimethylsilane **1b** and ethynyltrimethylsilane **1c** at an isosurface value of 0.05.

6.3.3 Overall reaction energy profile for substrate bromoethynyltrimethylsilane 1b

The overall Gibbs energy profile for the C(sp^2)–H alkynylation reaction between arene **1a** and bromoethynyltrimethylsilane **1b** is shown in Figure 6.2. As previously in C(sp^2)–H allylation in Chapter 5, the formation of C–H activated complex is assisted by an MPAA ligand, herein *N*-acetylglycine, which lowers the C–H activation from a barrier of 28.0 kcal mol^{-1} in its absence (**ts-1**) to 19.7 kcal mol^{-1} in its presence (**ts-1'**). The displacement of two acetate ligands by the MPAA ligand is entropically favoured.

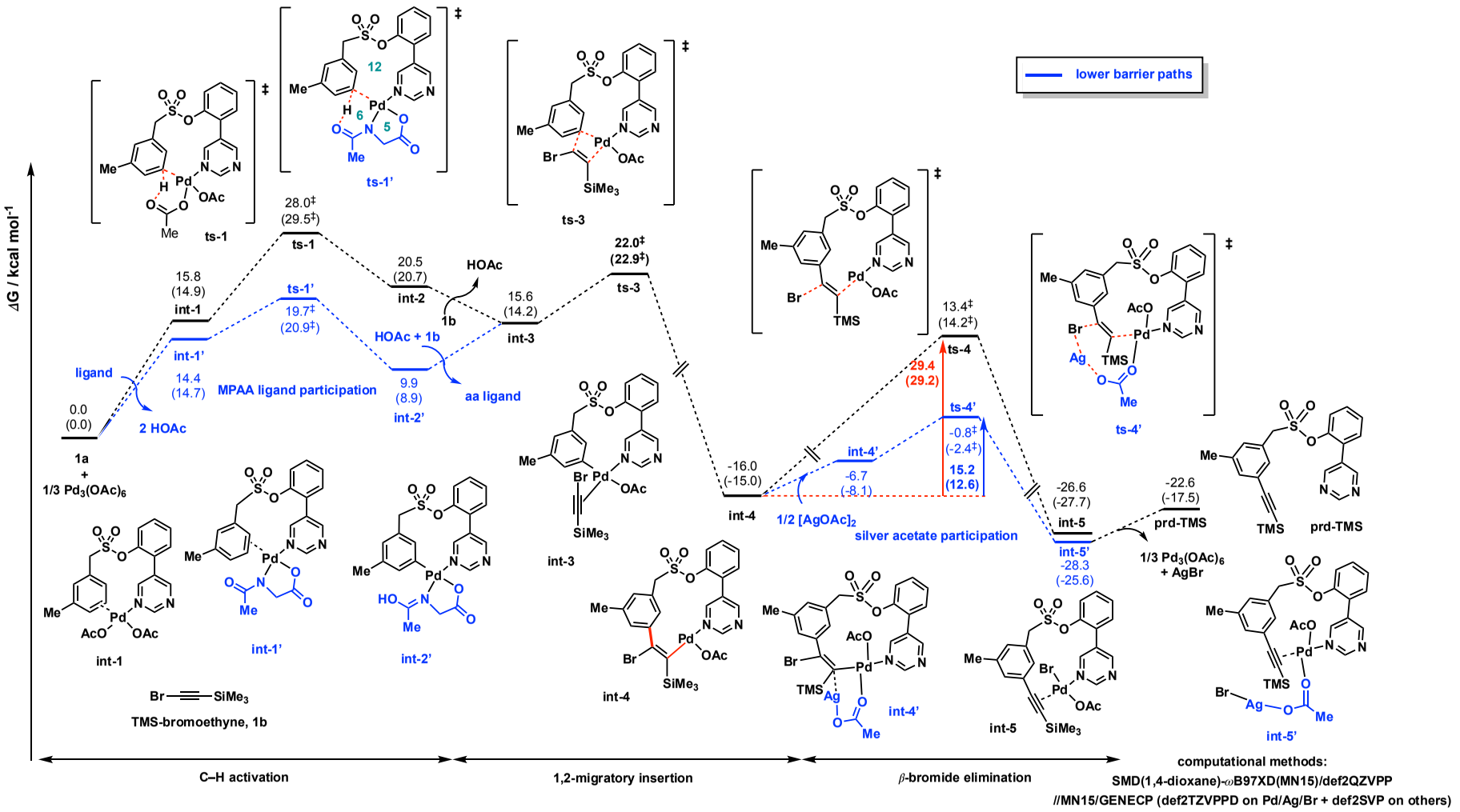

Figure 6.2. Gibbs energy profile for *meta*-selective C(sp^2)–H alkynylation using substrate **1b**.

ts-1	ts-1’	ts-3
28.0‡ (29.5‡)	19.7‡ (20.9‡)	22.0‡ (22.9‡)
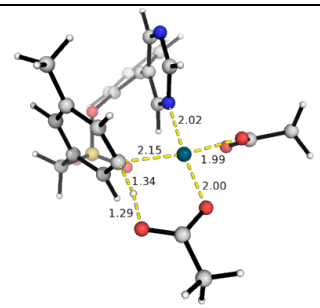	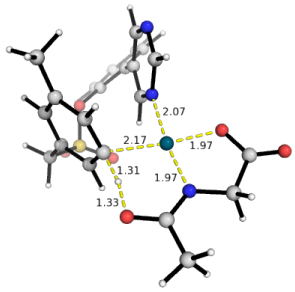	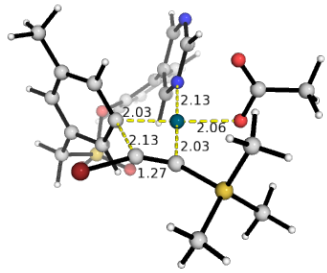
ts-3-c2	**ts-4**	**ts-4-c2**
22.1‡ (23.1‡)	13.4‡ (14.2‡)	-0.8‡ (-2.4‡)
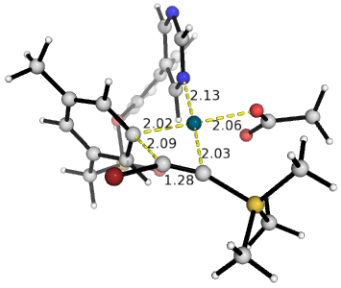	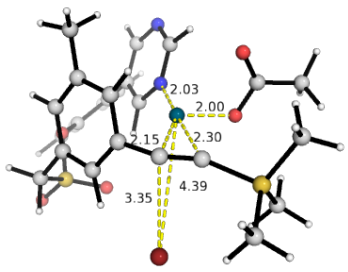	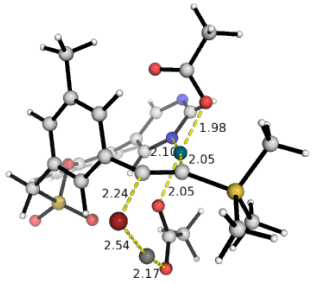
ts-4’		
-0.8‡ (-2.4‡)		
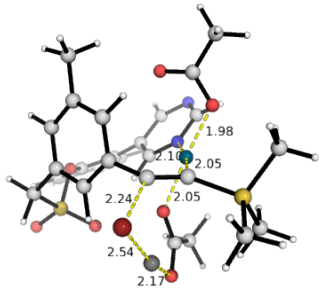		

Figure 6.3. Selected optimised structures for C(sp^2)–H *meta*-alkynylation using bromoalkyne **1b**.

Transition structure **ts-1’** has the characteristic [5,6]-palladacycle which strategically positions the amide oxygen atom for facile C–H activation via concerted metalation deprotonation (CMD) (Figure 6.3).[498–501] As in Chapter 5, other possible coordination modes of the MPAA ligand were considered (Scheme 6.2), but they all have higher barriers than **ts-1’**, where a [5,6]-palladacyclic ring is involved.

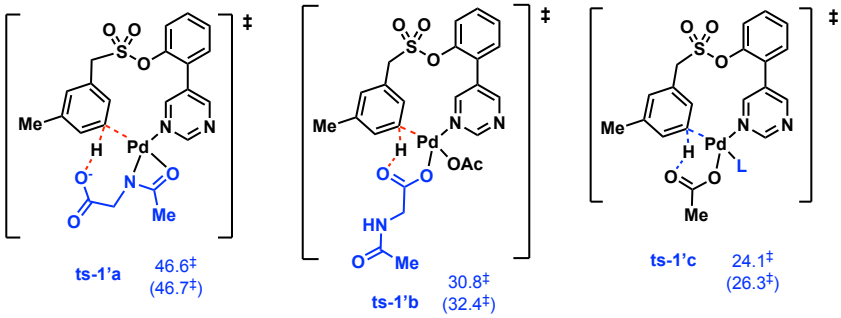

Scheme 6.2. Possible ligand coordination modes for the C–H activation step.

After the formation of the C–H activated complex, the bromoalkyne **1b** undergoes 1,2-migratory insertion, rather than oxidative addition (*vide infra*, Figure 6.4). This is followed by subsequent β-bromide elimination to yield the final product. Conformers for these steps were considered and the TSs are given in Figure 6.3. The conformers for these TSs were found to be very close in energy, indicating that the conformational flexibility in the ligand does not affect the TS energies very much. As previously in Chapter 5, the MPAA ligand in these steps was replaced by the acetate ligand to simplify the calculations in the modelling; this simplification is acceptable due to their close energetics (Scheme 6.3).

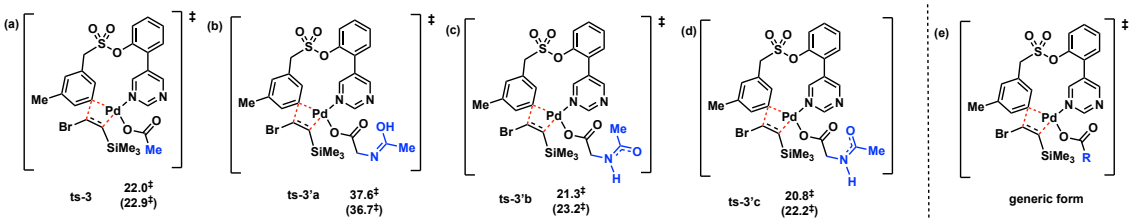

Scheme 6.3. 1,2-migratory insertion rate-determining step with either acetate (a) or MPAA in tautomeric forms (b, c and d) as monodentate ligand. These can be thought of having the general structure in (e) where the R–group varies.

In the presence of the MPAA ligand *N*-acetylglycine, the C–H activation step becomes reversible; the subsequent 1,2-migratory insertion of **1b** is the overall turnover frequency-determining transition state (TDTS)[125] with a higher barrier of 22.0 kcal mol^{-1}. The alternative mechanism of oxidative addition of **1b** breaking the C(sp^3)–Br σ-bond (Figure

6.4) was uncompetitive at > 40 kcal mol^{-1} (breaking a σ-bond is presumably less easy than breaking a π_{CC} bond via migratory insertion). The formation of the migratory insertion product was highly exergonic, giving highly stabilised **int-4** at -16.0 kcal mol^{-1} (a σ_{CC} bond is formed while a π_{CC} bond is broken). The subsequent β-bromide elimination, in the absence of silver acetate additive, had a rather high activation barrier of 29.4 kcal mol^{-1}; this was lowered to 15.2 kcal mol^{-1} in its presence, via a Pd–Ag heterometallic TS,[100,429,430] assisted by the enthalpically favourable formation of insoluble AgBr salt (see subsection 6.3.4 for a detailed discussion of the role of the silver

ts-3-oa-c1	**ts-3-oa-c2**
42.5‡ (41.8‡)	45.5‡ (44.9‡)
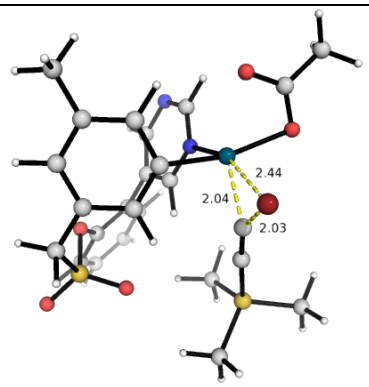	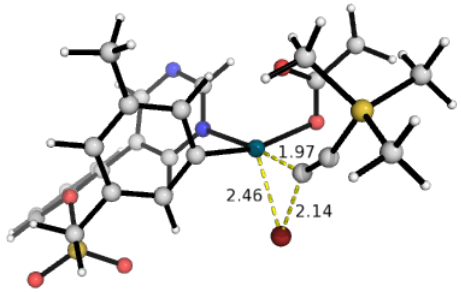
ts-3-oa-c3	**ts-3-oa-c4**
46.6‡ (45.5‡)	48.1‡ (47.5‡)
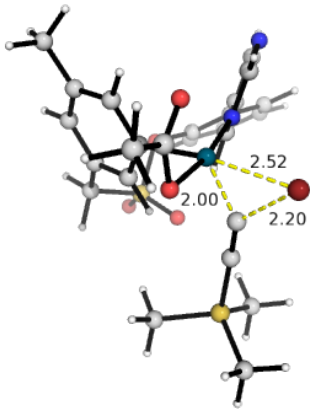	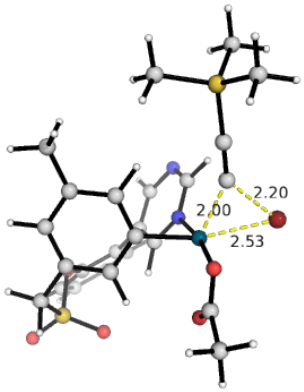

Figure 6.4. Oxidative addition of bromoethynyltrimethylsilane **1b**.

acetate additive). The final product was exergonic, at -28.3 kcal mol^{-1} with respect to the starting materials, thus favouring the product formation. Product dissociation then followed, regenerating Pd(II) catalyst for the next catalytic cycle. It is noteworthy that the palladium species remained in formal +2 oxidation state throughout the catalytic cycle, as opposed to the more common cycling through the Pd(II)/Pd(IV) manifold.

6.3.4 Role of silver acetate additive

Silver carboxylate salts are commonly employed as additives in Pd-catalysed C–H activation.[343,350,525–527] In many systems, silver salt plays an essential role in enhancing the reaction rate and/or yields. Various roles of silver carboxylate AgCOOR salts in such reactions have been proposed: (1) they serve as a source of carboxylate for the Pd(II) metal-centre, participating in carboxylate-assisted concerted metalation deprotonation (CMD) in the C–H activation step;[367,528–530] (2) they act as a terminal oxidant to regenerate Pd(II) catalyst;[332,531,532] (3) they form heterometallic Pd−Ag complexes that facilitate C−H activation;[430,531,533] (4) they directly activate C−H bond forming Ag–C intermediate;[534,535] (5) they act as halide scavengers in PdX (X = halide) complex after the reductive elimination step.[536] The experimental work to establish the exact role of these silver additives are rare and an understanding of their exact roles in the mechanistic picture is rather incomplete.

Silver carboxylates are known to exist in dimeric form.[537–539] We computed the energy differences in the thermodynamic stabilities of both the monomeric and dimeric form of silver acetate and found that the dimeric form $[AgOAc]_2$ is more stable; the formation of $[AgOAc]_2$ from AgOAc monomers is -16.7 (-19.9) kcal mol^{-1} downhill. This enhanced stability in the dimer has been attributed to Ag–Ag interactions.[527,538] The more stable dimer (or in fact, ½ $[AgOAc]_2$) is used in the Gibbs energy calculations of silver additive

ts-4	ts-4’	ts-4’z	ts-3’z
$\Delta G^{\ddagger}$ = 13.4‡ (14.2‡)	-0.8‡ (-2.4‡)	40.7‡ (41.7‡)	40.0‡ (41.9‡)
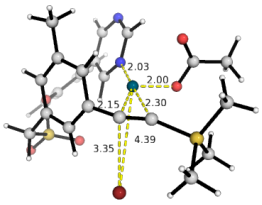	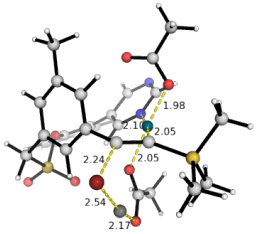	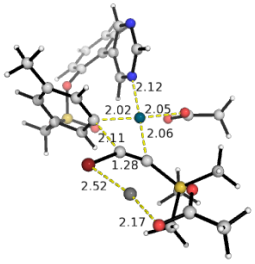	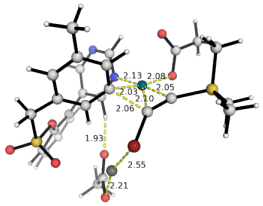
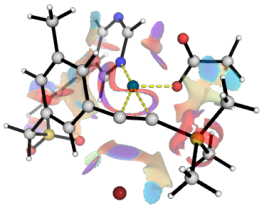	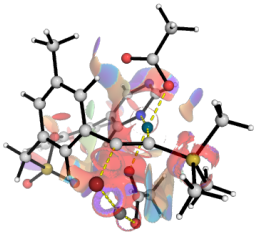	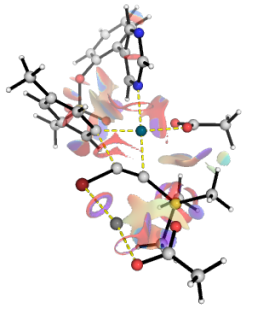	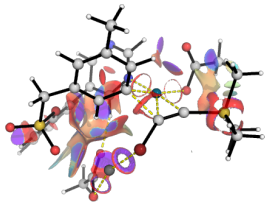
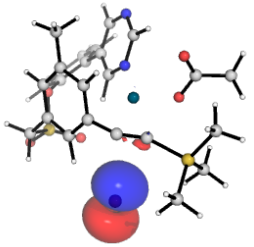	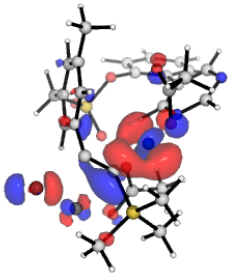	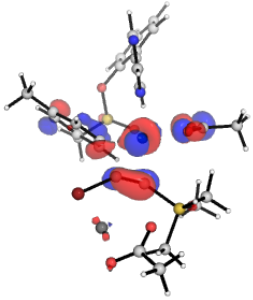	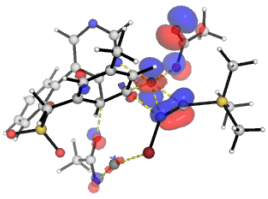

Figure 6.5. Optimised structures, NCI plots and HOMOs for β-bromide elimination without (**ts-4**) and with (**ts-4’** and **ts-4’z**) silver acetate co-ligand and for 1,2-migratory insertion with silver acetate co-ligand (**ts-3’z**).

participation throughout (the use of AgOAc monomer would artificially lower the activation barrier of **ts-4’** since AgOAc monomer is already high in energy).

In the present transformation, silver cation plays a role in assisting β-bromide elimination step by forming silver bromide salt as a by-product. An initial TS search placing the silver cation adjacent to the leaving bromide as the former pulls off the latter yielded a TS that is higher in activation barrier acetate (**ts-4’z**, at 40.7 kcal mol^{-1}, Figure 6.5) than one without silver; only in **ts-4’** (at -0.8 kcal mol^{-1}, Figure 6.5) where not only Ag^{+} interacts

with the leaving Br^- but also the acetate coordinates to Pd(II) is the transition state lower in activation barrier. In the presence of silver acetate, the HOMO of the Pd–Ag heterobimetallic TS **ts-4'** shows that there is predominant electron donation from bromoalkyne π-electrons to the vacant d-orbital on Pd(II) centre, this enhanced interaction is favourable for product formation as the bromide ion leaves (Figure 6.5). Although there seems to be more steric strain due to non-covalent interactions (NCIs) in **ts-4'**, the formation of Ag–Br bond is enthalpically favoured and likely more dominant over NCIs, thus lowering the activation barrier of this transition state.

For completeness, we went further to ascertain the role, if any, of silver acetate in affecting the 1,2-migratory insertion step. We found that, introducing AgOAc (**ts-3'z**) increased the activation barrier to 40.0 kcal mol^{-1}, which is much higher than **ts-3** without any AgOAc participation, at 22.0 kcal mol^{-1}. The acetate ligand from silver could not coordinate to Pd-centre (despite the initial geometry guess) in the optimised structure as Pd(II) is tetra-coordinating and all coordination sites have been occupied (Figure 6.5).

6.3.5 Arene site selectivity studies

The site-selectivity of arene activation was investigated, following a similar approach in Chapter 5 subsection 5.3.4. The rate-limiting 1,2-migratory insertion step was studied. The *ortho*-/*para*-positions on the arene for potential activation were compared to *meta*-activation (Table 6.1). The C–H activation and the 1,2-migratory insertion steps were studied. 1,2-migratory insertion was the TDTS for *meta*- and *para*-activation, whereas C–H activation was the TDTS for *ortho*-activation. Application of simple transition state theory (TST) suggests that the *para*-alkynylated product would be disfavoured by 1 in 41, and that the *ortho*-alkynylated product 1 in ~8000.

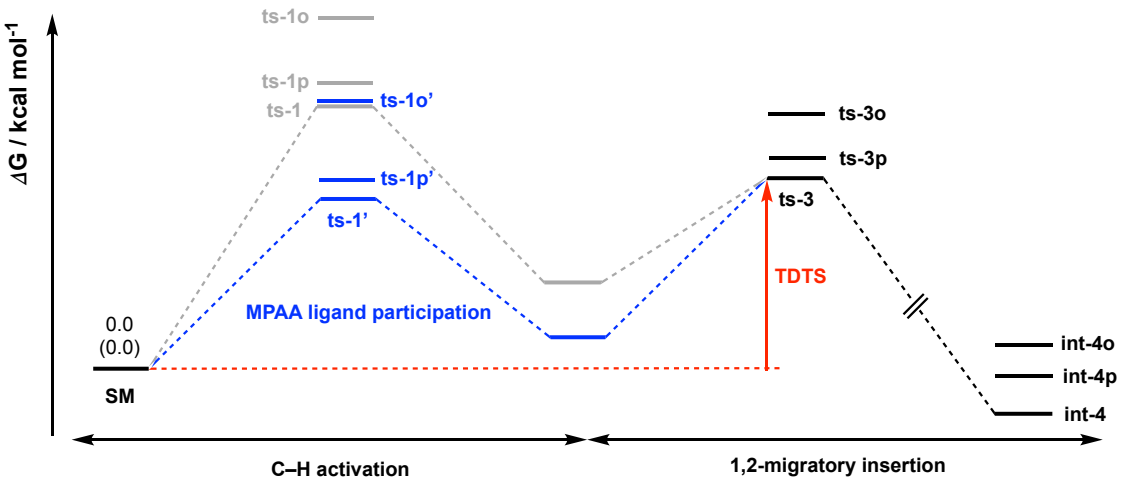

activation site	ts-1x	ts-1x'	ts-3x	int-4x
meta- (**x = nil**)	28.0‡ (29.5‡)	19.7‡ (20.9‡)	**22.0‡ (22.9‡)**	-16.0 (-15.0)
para- (**x = p**)	29.4‡ (29.4‡)	22.2‡ (21.6‡)	**24.6‡ (23.3‡)**	-9.9 (-10.1)
ortho- (**x = o**)	36.2‡ (35.2‡)	**28.3‡ (28.8‡)**	26.8‡ (26.1‡)	-4.5 (-4.4)

Table 6.1. Arene site-selectivity studies for alkynylation. MPAA ligand lowers C–H activation in both *meta*- and *ortho*-activation such that 1,2- migratory insertion (**ts-3x**) becomes the TDTS; for *para*-activation, C–H activation step is the TDTS. The overall barrier for each case is given in bold.

The optimised structures, HOMOs and NCI plots for 1,2-migratory insertion are given in Figure 6.6. We observe that the NCIs are rather similar in all 3 TSs. In an earlier studies of a similar system (Chapter 5),[103] the ring strain in *ortho*-selective TS is much higher than either *meta*- or *para*-activation. Herein, the *ortho*-selective TS **ts-3o** seemed to undergo a relatively early TS forming C–C bond and thereby relieving the ring strain, as the C–C bond distance is much shorter, at 1.99Å, than either *meta*- or *para*-selective TS, at 2.13Å and 2.15Å, respectively. This results in the C–H activation step as rate-limiting in *ortho*-activation.

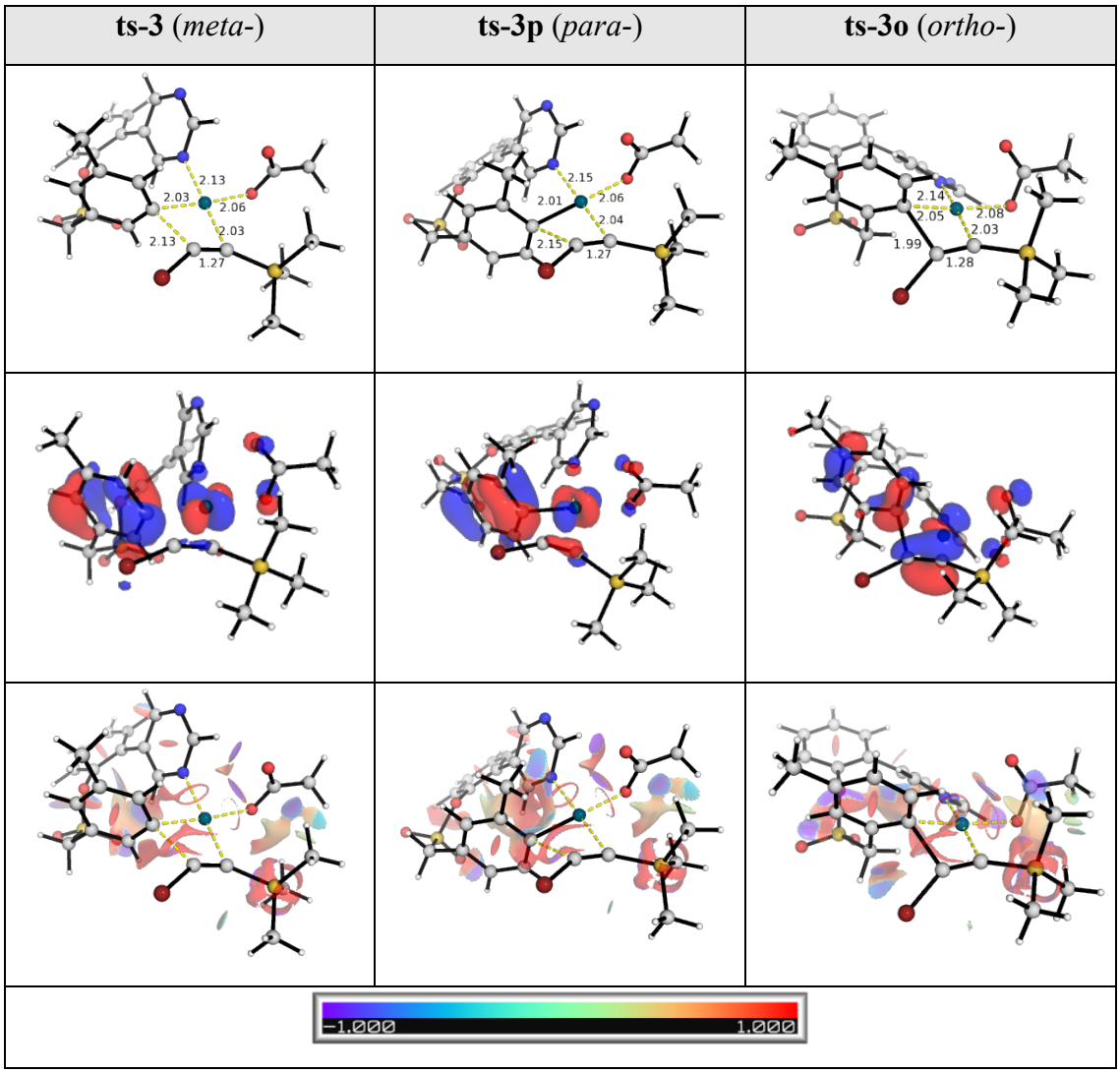

Figure 6.6. Optimised structures, HOMOs and NCI plots for 1,2-migratory insertion step in arene site-selectivity studies.

The differences in the ring strains in these 3 TSs were further verified using isodesmic studies,[504,505] as those discussed in Chapter 5 subsection 5.3.4, to compare the ring strains by computing the relative enthalpic changes of each reaction, where the number and type of bonds in the reactants and the products are preserved (see also references[103,391] for examples). The ring strain is measured by the relative change in the enthalpy as defined by Equation (5.1). These computations supported this conclusion (Scheme 6.4). From the enthalpic changes, we can see that there is 4.2 kcal mol^{-1} ring strain in **ts-3** as compared to 7.5 kcal mol^{-1} in **ts-3p** and 9.9 kcal mol^{-1} in **ts-3o**. Their ring strain energy differences

are similar to the differences in their activation barriers for this step, as shown in Table 6.1. As in Chapter 5, the 12-membered *meta*-selective TOF-determining palladacycle (**ts-3**) has the least strain, followed by 13-membered *para*-selective palladacycle (**ts-3p**) and then by 11-membered *ortho*-selective palladacycle (**ts-3o**).

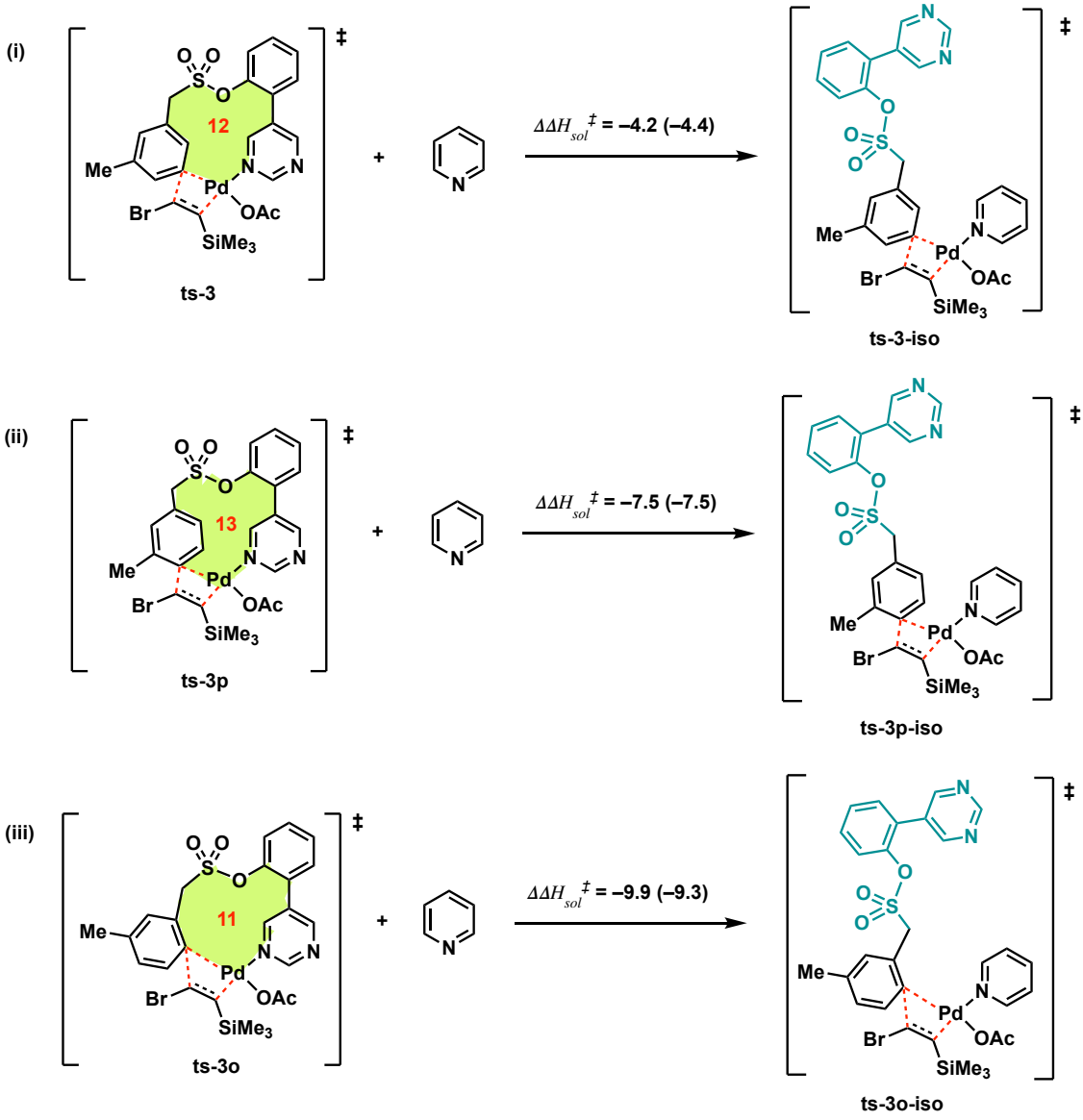

Scheme 6.4. Computed ring strain energies by study of isodesmic reaction where a hypothetical pyridine ligand is involved in the 1,2-migratory insertion TDTS.

6.3.6 Regioselectivity in 1,2-migratory insertion of bromoethynyltrimethylsilane 1b

The regioselectivity of the 1,2-migratory insertion step of the substrate bromoethynyl-trimethylsilane **1b** was investigated to check the efficiency of the present transformation. The full Gibbs energy profile is shown in Figure 6.7; key TSs with HOMOs are given in Figure 6.8. It was found that the regioisomeric 1,2-migratory insertions of **1b** (**ts-3** and **ts-3r**, Figure 6.7) have almost identical barrier, at 22.0 kcal mol^{-1}, suggesting unselective 1,2-migatory insertion.

Both insertion products are highly exergonic and irreversible. In the latter case, the regioisomeric insertion of **1b** affords a highly stabilized intermediate **int-4r** (at -14.1 kcal mol^{-1}) that further undergoes stepwise loss of bromide (**ts-4r'**) and 1,2-silyl shift (**ts-5r'**) to give regiospecifically the observed alkynylated product. 1,2-silyl shift occurs as the bromide leaves, gaining negative charge (NBO charge (Figure 6.7, numbers in red) from +0.106 in **int-4r** and +0.045 in **int-4r'** to -0.312 in **ts-4r'** and -0.501 in **int-5r'** and -0.601 in **ts-5r'**), while the carbon atom that it is attached gains carbocationic character (NBO charge at this site that is -0.157 in **int-4r** and -0.151 in **int-4r'** that goes to +0.025 in **ts-4r'** and +0.097 in **int-5r'**. Similar cationic 1,2-trialkylsilyl migrations have been observed in Ti,[540] Rh,[541] and Au[542,543] catalysis. Analogous anionic 1,*n*-silyl migration has also been reported in some organocopper-catalysed chemical systems.[544–546]

The rate-limiting step after the insertion product is 1,2-silyl migration **ts-5r'** at 19.7 kcal mol^{-1}, which, although is higher than the barrier of **ts-4'** at 15.2 kcal mol^{-1}, can still occur thermodynamically at the reaction temperature of 80ºC, especially given that the overall TDTS of this regioisomeric pathway is the 1,2-migratory insertion step **ts-3r** at 22.0 kcal mol^{-1}.

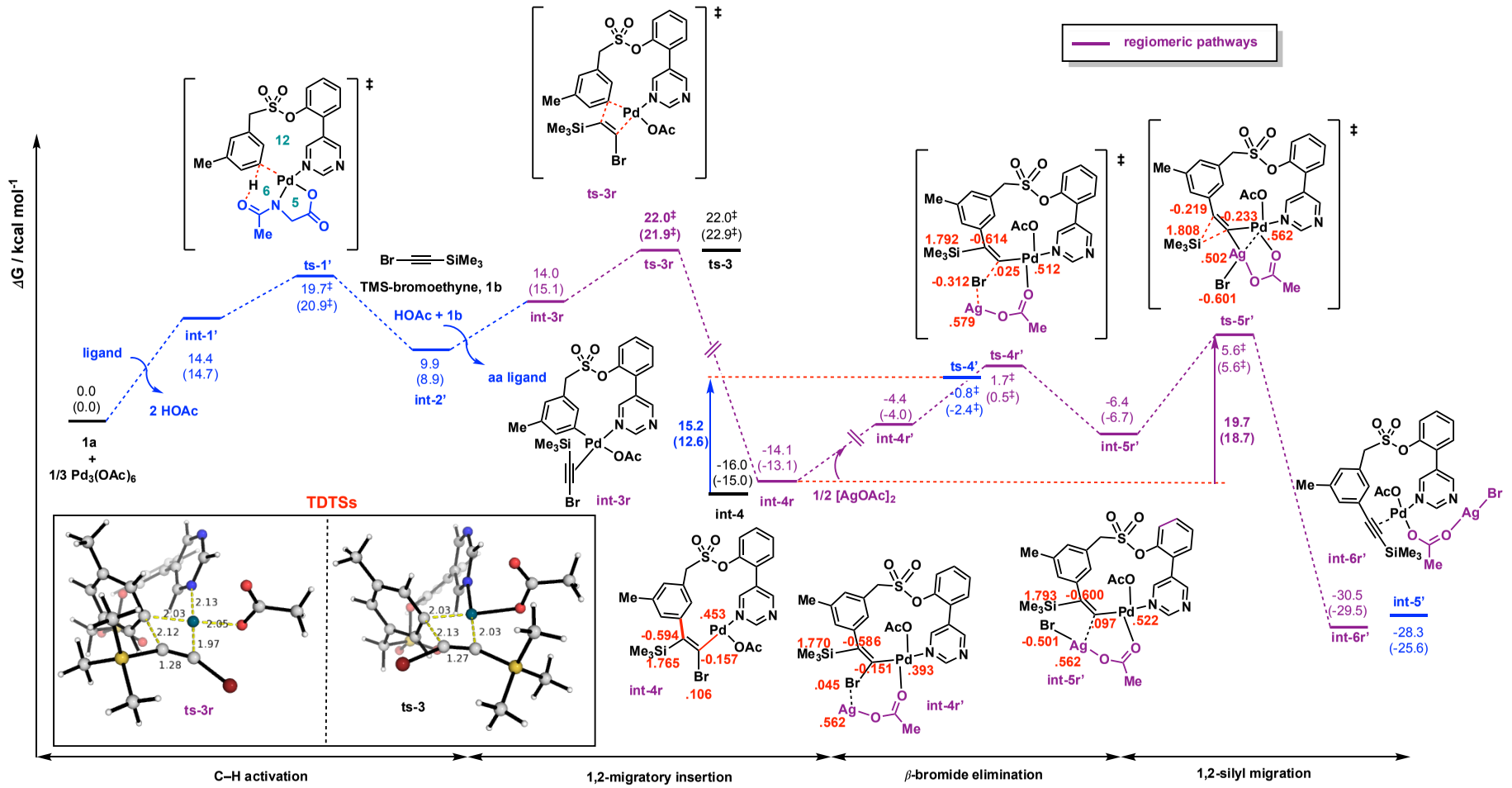

Figure 6.7. Gibbs energy profile for the regioisomeric insertion of bromoalkyne **1b** and its subsequent β-Br elimination and 1,2-silyl migration to regioconverge on the alkynylated product. Gibbs energies for the key structures from Figure 6.2 are included for comparison. NBO charges are given in red.

ts-3r	ts-4r’	ts-5r’
22.0‡ (21.9‡)	1.7‡ (0.5‡)	5.6‡ (5.6‡)
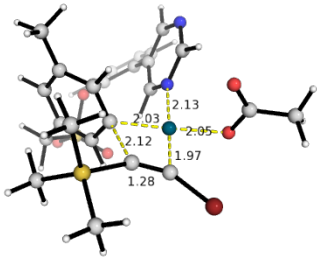	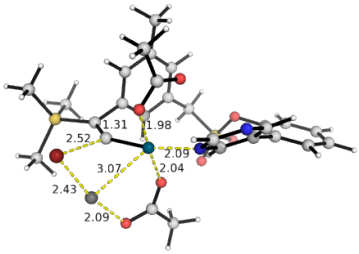	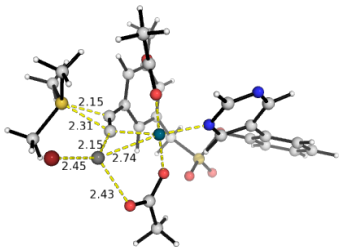
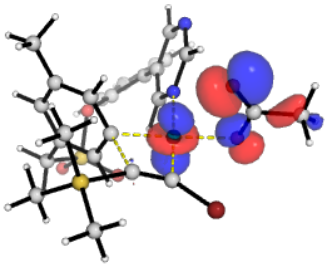	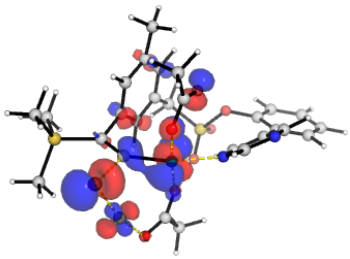	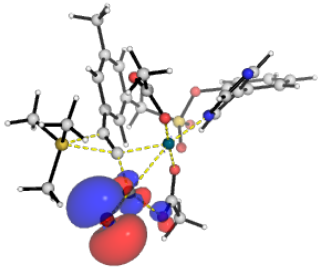

Figure 6.8. Selected optimised structures and HOMOs for TSs in Figure 6.7.

6.3.7 Possible role of copper according to computational studies

Experimentally, it was shown that the yield of the reaction is augmented by the addition of copper(II) acetate salt. The role of this copper additive was explored computationally. The most stable form of $Cu(OAc)_2$ is in triplet spin state (Figure 6.9 (a)), thus, we take ½ of triplet copper(II) acetate dimer as the reference species. Normally, any copper additive is assumed to play a role as a co-oxidant to regenerate the main catalyst or as a source of acetate ions; computational studies of these reactions do not normally consider its explicit role in the catalytic cycle and its exact roles in the catalytic cycle are poorly understood.[547–549] The explicit role of $Cu(OAc)_2$ salt was demonstrated in one study by Funes-Ardoiz and Maseras, who show that copper additive can act as a cooperative catalyst in the reductive coupling of a C–O bond in isocoumarin formation through a Rh–Cu heterobimetallic TS.[550] We wonder if $Cu(OAc)_2$ plays a similar role as AgOAc in the

present reaction in forming a heterometallic complex in the β-bromide elimination step, potentially forming $CuBr_2$ as a side product.

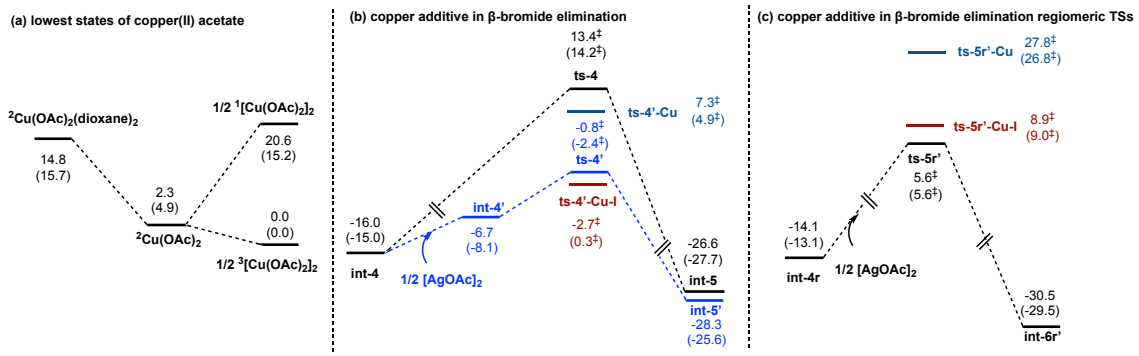

Figure 6.9. (a) Stability of mononuclear and dinuclear (singlet vs triplet) copper(II) acetate species. (b) TSs with copper additive in β-bromide elimination step, and (c) TSs with copper additive in β-bromide elimination step for the regioisomeric reaction.

We found that the Pd–Cu(II) heterobimetallic TS (**ts-4'-Cu**, 7.3 kcal mol^{-1}, Figure 6.10) gives an overall barrier of 23.3 kcal mol^{-1}; this is 8.1 kcal mol^{-1} higher than the Pd–Ag heterobimetallic TS (**ts-4'**, -0.8 kcal mol^{-1}), although it is 6.1 kcal mol^{-1} lower in activation barrier than the β-bromide elimination TS without any metal additive (**ts-4**, 13.4 kcal mol^{-1}) (Figure 6.9 (b)). The Pd–Cu(II) heterobimetallic TS for the regioisomeric rate-determining 1,2-silyl group migration (**ts-5r'-Cu**, 27.9 kcal mol^{-1}, Figure 6.10) also has a higher barrier than the Pd–Ag heterobimetallic TSs (**ts-5r'**, 5.6 kcal mol^{-1}) (Figure 6.9 (c)).

As the Cu(II) additive also acts as an oxidant, we considered if the reduced form Cu(I) had any effect on the activation barriers for the β-bromide elimination step. We found that the use of CuOAc gives a Pd–Cu(I) heterobimetallic TS for the β-bromide elimination step (**ts-4'-Cu-I**, -2.7 kcal mol^{-1}, Figure 6.10) with a lower activation barrier than the use of AgOAc (**ts-4'**, -0.8 kcal mol^{-1}). For the regioisomeric pathway, the use of AgOAc has lower activation barrier (**ts-5r'**, 5.6 kcal mol^{-1}, Figure 6.10) than CuOAc (**ts-**

Pd–Cu(II) heterobimetallic TSs	
ts-4'-Cu	**ts-5r'-Cu**
7.3‡ (4.9‡)	27.9‡ (26.8‡)
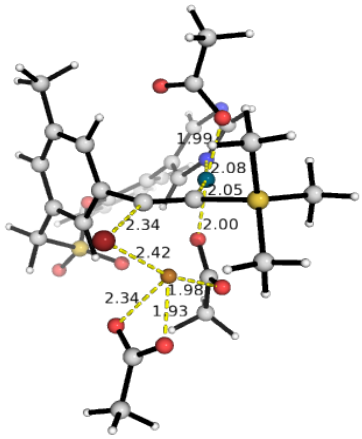	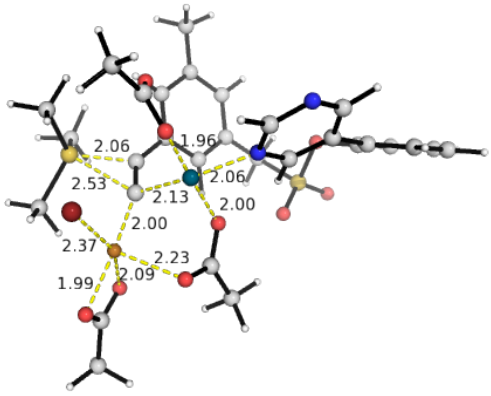
Pd–Cu(I) heterobimetallic TSs	
ts-4'-Cu-I	**ts-5r'-Cu-I**
-2.7‡ (0.3‡)	8.9‡ (9.0‡)
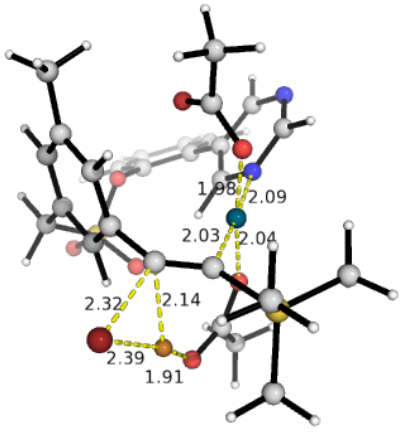	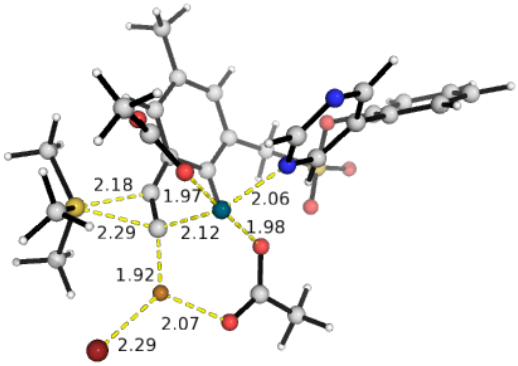

Figure 6.10. Optimised structures for Pd–Cu(II) and Pd–Cu(I) heterobimetallic TSs using $Cu(OAc)_2$ and CuOAc additive respectively.

5r'-Cu-I, 8.9 kcal mol^{-1}). Cu(I) additive give lower barriers than Cu(II) additive for both heterobimetallic TSs. We wondered if $Cu(OAc)_2$ helps to regenerate the silver salt. This is unlikely as 2 equivalents each of $Cu(OAc)_2$ and AgOAc were used in the reaction. We calculated the thermodynamics of the following reaction:

$$^{1}[AgBr]_2 + 1/2\ ^{3}[Cu(OAc)_2]_2 \longrightarrow {}^{1}[AgOAc]_2 + 1/2\ ^{3}[CuBr_2]_2$$

and found that this reaction has an uphill Gibbs energy of reaction of 16.4 (17.1) kcal mol^{-1}, thus ruling out this possibility.

Next, we checked if the copper salt helps in the release of palladium catalyst from its coordination to the alkynylated product, so that it can undergo the next catalytic cycle. Coordination of ½ $[Cu(OAc)_2]_2$ to the product releases the palladium catalyst for the next cycle. This transmetallation is more thermodynamically favourable than the direct release of product from **int-5'** (Figure 6.11), suggesting that it could possibly increase the yield by making palladium catalyst more available after each catalytic cycle.

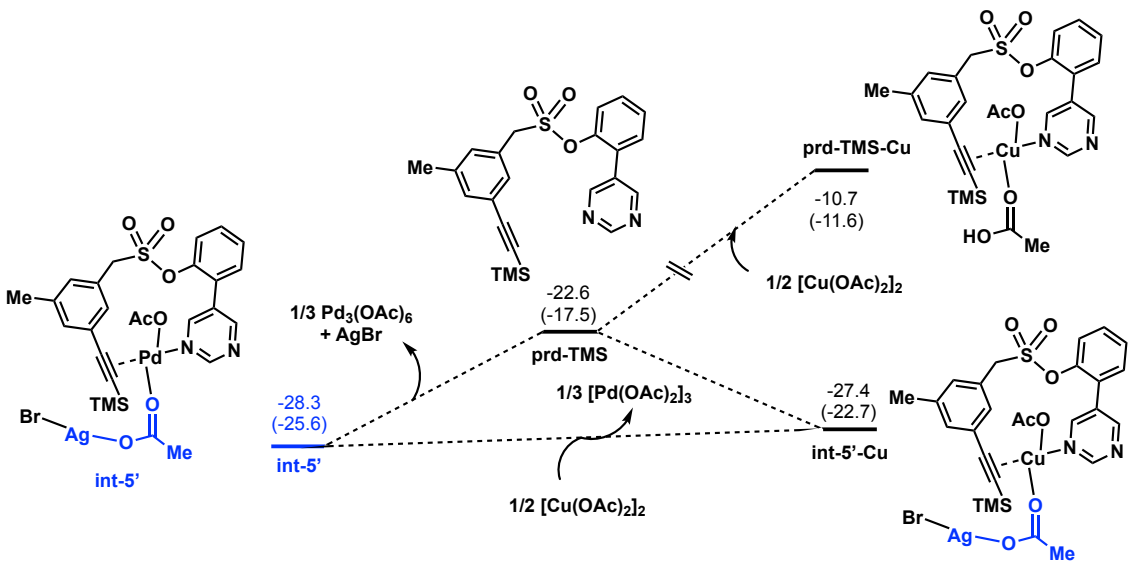

Figure 6.11. Transmetallation in the product release to free up palladium catalyst.

6.3.8 Reactivity for substrate ethynyltrimethylsilane 1c

Experimentally, when the reaction was carried out using ethynyltrimethylsilane **1c** instead of **1b**, the reaction did not occur; the substrate was recovered. Detailed TS searches showed that silver could not participate in the beta-H elimination step, perhaps unsurprising since silver cation cannot interact with a leaving hydride. The full Gibbs energy profile in Figure 6.12 suggests that, as a result, beta-H elimination giving a Pd–H (**ts-4H**, Figure 6.13) and the subsequent reductive elimination of acetic acid to generate

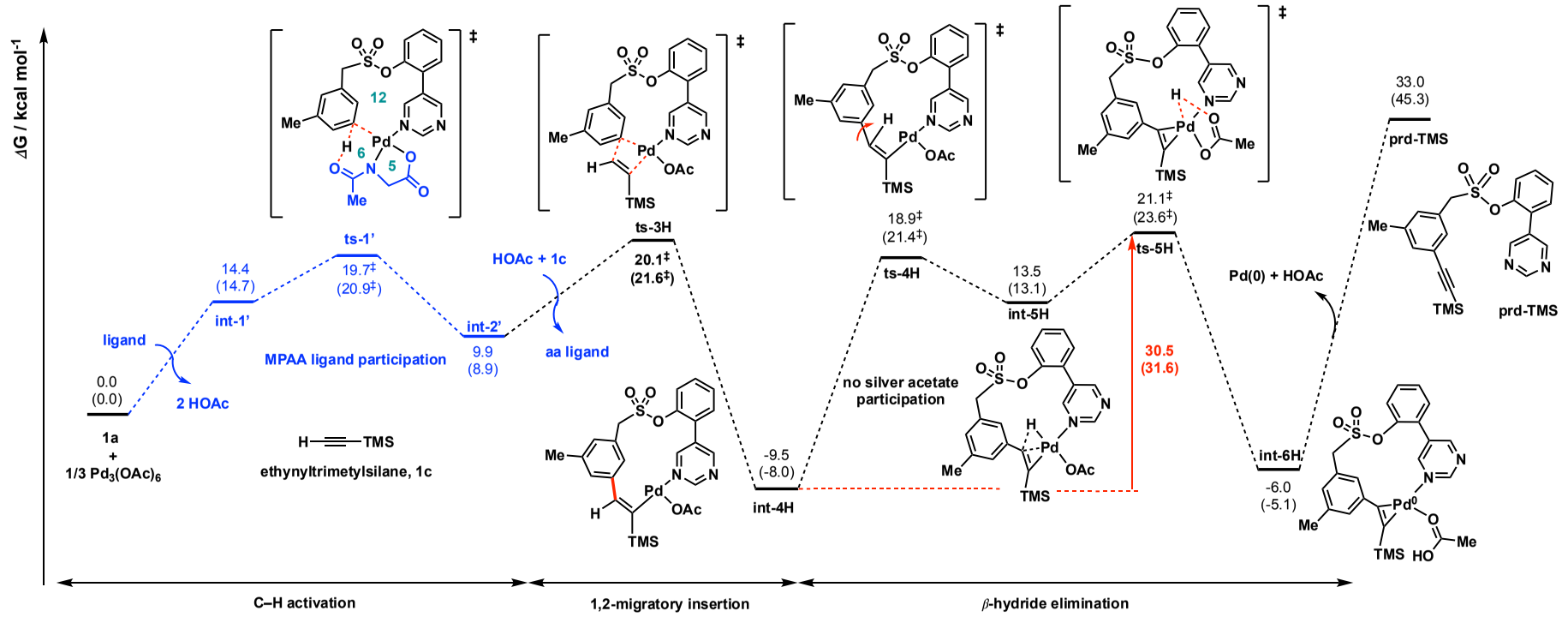

Figure 6.12. Gibbs energy profile for the reaction involving ethynyltrimethylsilane **1c**.

Pd(0) (**ts-5H**, Figure 6.13, overall barrier of 30.5 kcal mol^{-1}) are high in energy barrier, thus being kinetically unfavourable. In addition, the overall reaction gives endergonic intermediates relative to the 1,2-migratory insertion intermediate **int-4H**, making this reaction thermodynamically unfavourable. The potentially poor orbital overlap between the σ_{CH} of the beta-hydride and the d-orbital of Pd in **ts-4H** and that between lone pair orbital of acetate and $\sigma^*_{Pd–H}$ of the metal-hydride in **ts-5H** could be the reason for this unfavourability; the ring strains in the palladacycle (distorted geometries) potentially contribute to the high activation barriers too (Figure 6.13). In addition, the release of product **prd-TMS** from the end Pd(0) species is highly unfavourable thermodynamically. Therefore, both steric and electronic factors disfavour the reaction of substrate **1c** in this alkynylation reaction. In fact, the TDI for the reaction is **int-4H**, making the overall barrier for subsequent catalytic cycles to be > 50.0 kcal mol^{-1}, thus not thermally accessible at the reaction temperature.

ts-3H	**ts-4H**	**ts-5H**
20.1‡ (21.6‡)	18.9‡ (21.4‡)	21.1‡ (23.6‡)
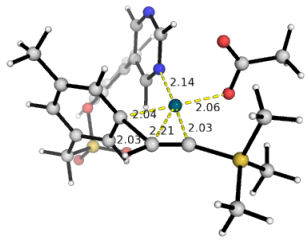	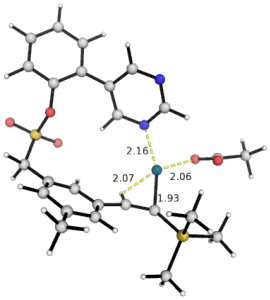	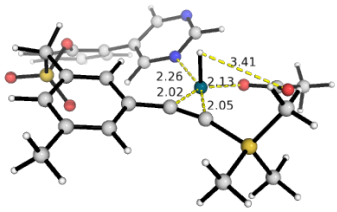
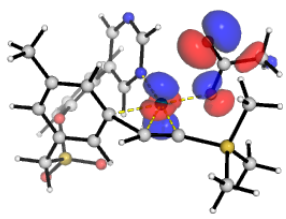	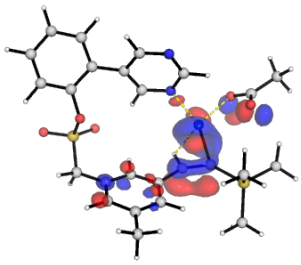	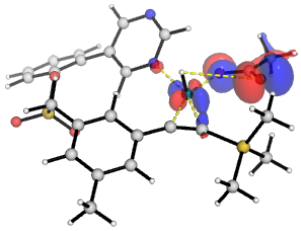

Figure 6.13. Optimised structures and HOMOs for TSs in Figure 6.12.

Experimentally, it is also possible that homocoupling of terminal alkynes occurs due to the presence of copper additives,[551–556] rendering this substrate incompetent.

6.3.9 Reactivity for substrate bromoethynylbenzene 1d

When bromoethynylbenzene **1d** was used experimentally, the reaction has a poor yield; the majority of the substrate was recovered unreacted. The full Gibbs energy profiles for the reaction using substrate bromoethynylbenzene **1d** are shown in Figure 6.14. These energy profiles indicate that the irreversible 1,2-migratory insertion steps occurred indiscriminately (**ts-3P** and **ts-3rP** have the same activation barrier, at 24.5 kcal mol^{-1}), where either carbon of the acetylene functional group of the substrate can form C–C bond with the activated arene. This is similar to the reaction using silylated alkynylbromide **1b** (**ts-3** and **ts-3r**, Figure 6.7). However, for the regioisomeric insertion, the subsequent 1,2-phenyl shift (**ts-5r'P**, at 28.3 kcal mol^{-1}) for regioconvergent product formation had a much higher barrier than 1,2-silyl shift (**ts-5r'**, Figures 6.7 and 6.8) using substrate **1b**. It can be rationalised that the 1,2-silyl migration on carbon atoms can occur much more readily than 1,2-aryl migration on carbon atoms. Similar 1,2-silyl migration reactions have been previously reported.[557,558]

Nevertheless, computations seem to suggest that the reaction is at least kinetically and thermodynamically feasible as that using substrate **1b**, though the selectivity/ regioconvergency of the product formation might not be as good (barrier of 28.3 kcal mol^{-1}, Figure 6.14) as using substrate **1b** (barrier of 19.7 kcal mol^{-1}, Figure 6.7), perhaps unsurprising as the phenyl group has a higher difficulty than the trialkylsilyl group in carrying out 1,2-migration.

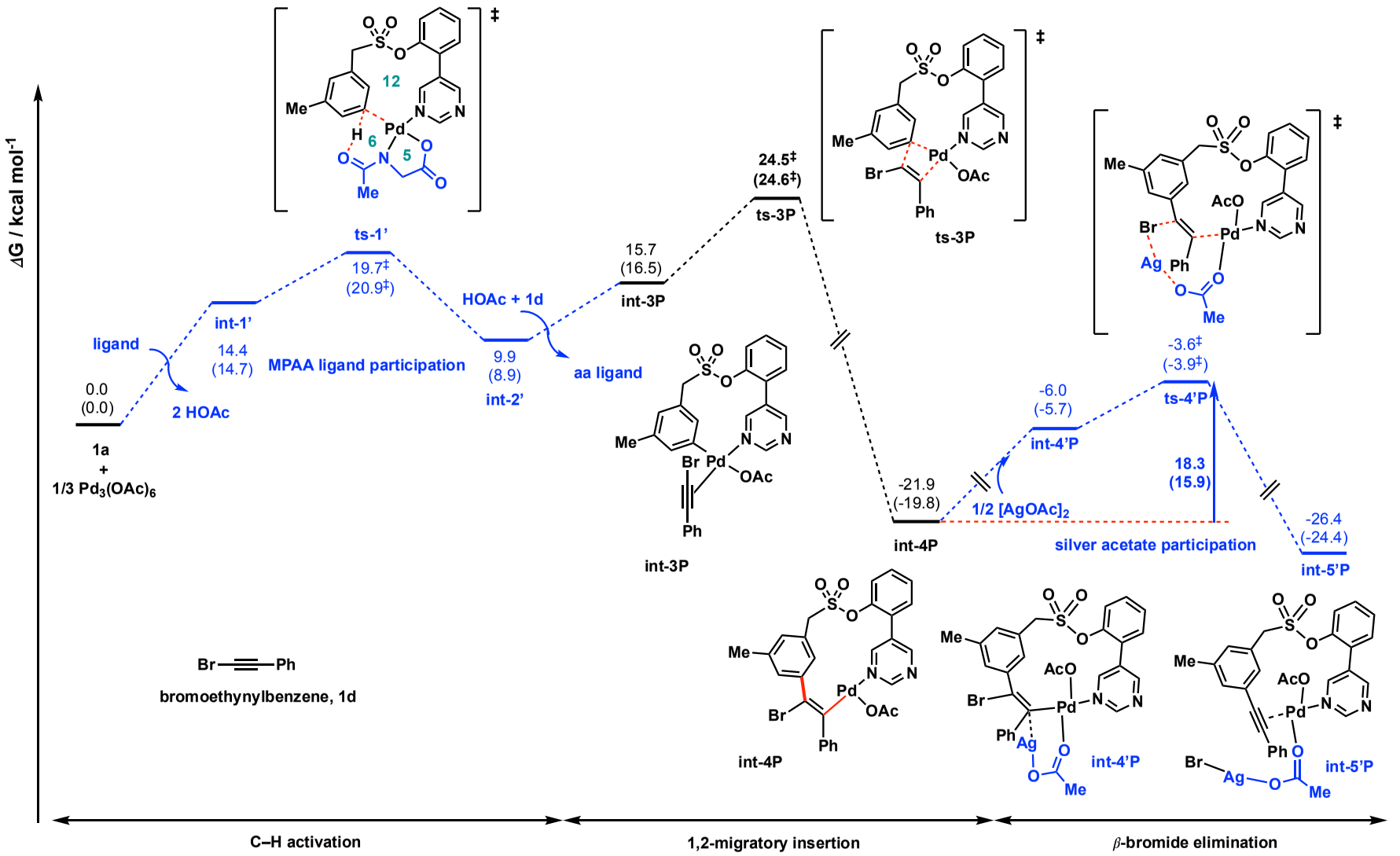
ΔG / kcal mol-1
ligand
0.0
(0.0)
1a
+
1/3 Pd3(OAc)6
2 HOAc
ts-1'
19.7‡
(20.9‡)
int-1'
14.4
(14.7)
MPAA ligand participation
9.9
(8.9)
int-2'
HOAc + 1d
aa ligand
15.7
(16.5)
int-3P
24.5‡
(24.6‡)
ts-3P
-21.9
(-19.8)
int-4P
-6.0
(-5.7)
int-4'P
-3.6‡
(-3.9‡)
ts-4'P
18.3
(15.9)
1/2 [AgOAc]2
silver acetate participation
-26.4
(-24.4)
int-5'P
Br—Ph
bromoethynylbenzene, 1d
C–H activation
1,2-migratory insertion
β-bromide elimination

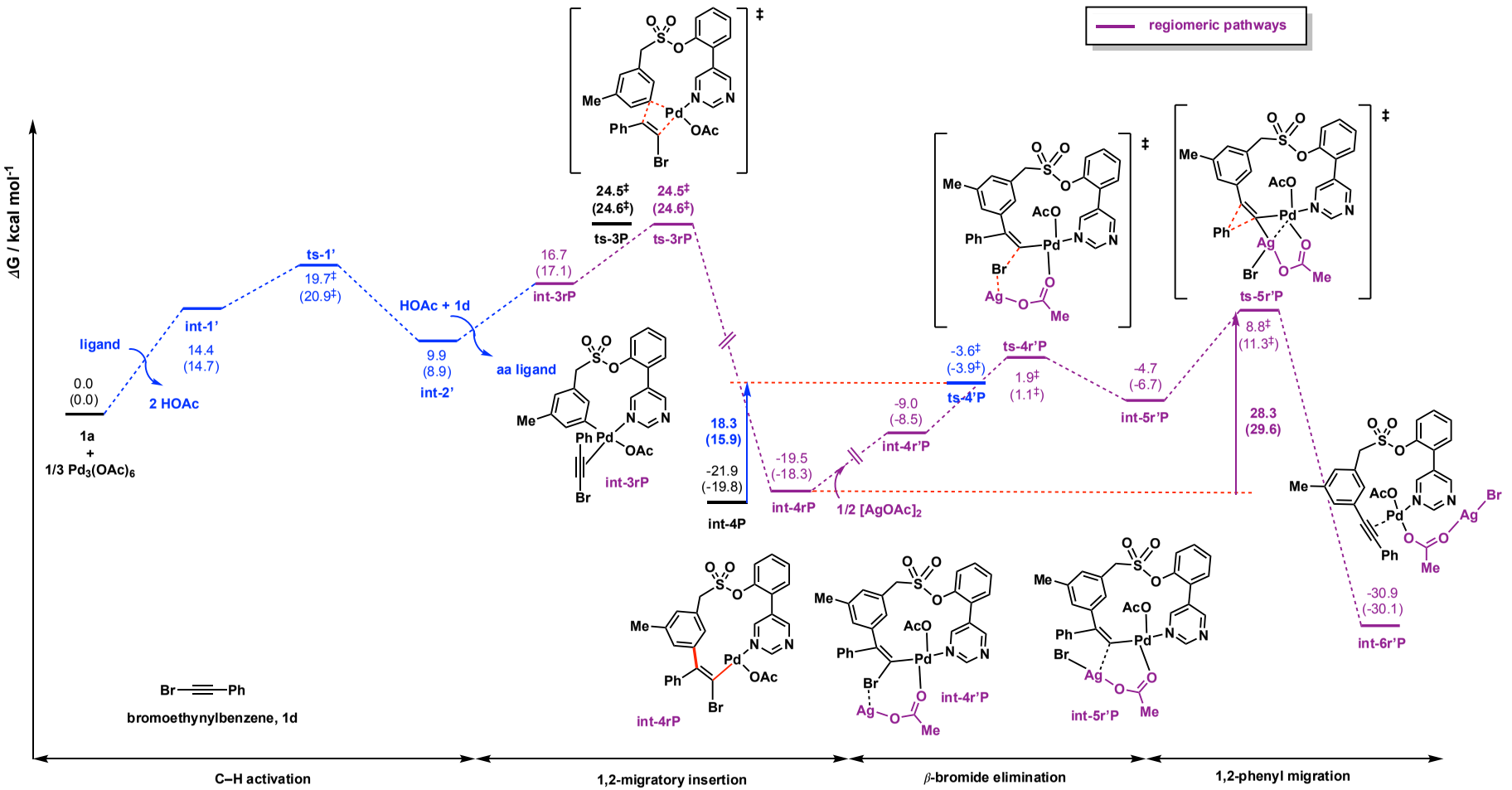

Figure 6.14. Gibbs energy profile for the reaction involving bromoethynylbenzene **1d**.

We hypothesised that the reactivity could potentially be hindered due to the propensity of bromoethynyl-benzene **1d** to form favourable π-π stacking[559–561] within themselves and with arene starting material; it can also form cation-π interactions[561,562] with Pd(II), making them less available for reaction. This is possible as the relative comparison of $[Pd(substrate)_2]^{2+}$ complexes showed that Pd(II) coordination with two bromoethynylbenzene **1d** molecules $[Pd(\mathbf{1d})_2]^{2+}$ is 11.9 (15.3) kcal mol^{-1} more stabilised than with two bromoethynyl-trimethylsilane **1b** molecules $[Pd(\mathbf{1b})_2]^{2+}$ (Figure 6.15).

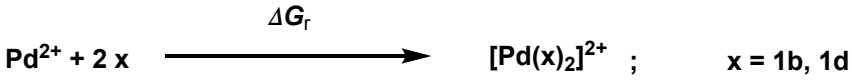

Pd-1d2-c1	Pd-1d2-c2	Pd-1b2-c1	Pd-1b2-c2
-188.7 (-203.8)	-179.0 (-198.6)	-176.8 (-186.8)	-171.1 (-184.9)
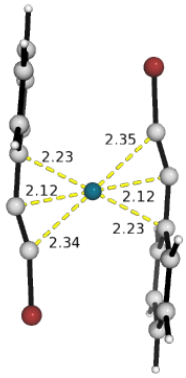	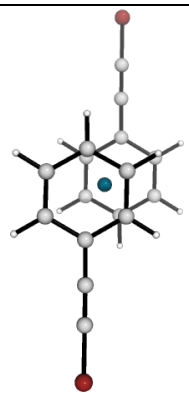	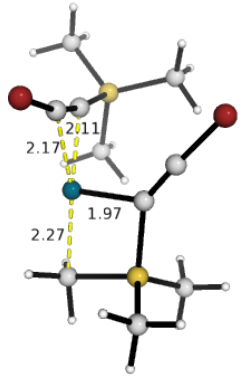	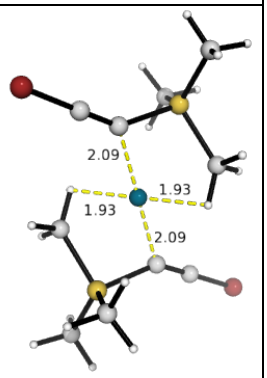

Figure 6.15. Gibbs energy of reaction (ΔG_r, in kcal mol^{-1}) for the coordination complexes of substrates **1b** and **1d** with Pd(II) cation.

This could perhaps be one of the possibilities, although other side reactions (such as dehalogentative homocoupling of terminal alkynyl bromide) that were not considered in the present computational studies could also be possible.

6.3.10 Proposed catalytic cycle

Based on our computational mechanistic studies, together with experimental evidence, we propose that the reaction proceeds via an MPAA-ligand directed, reversible C–H

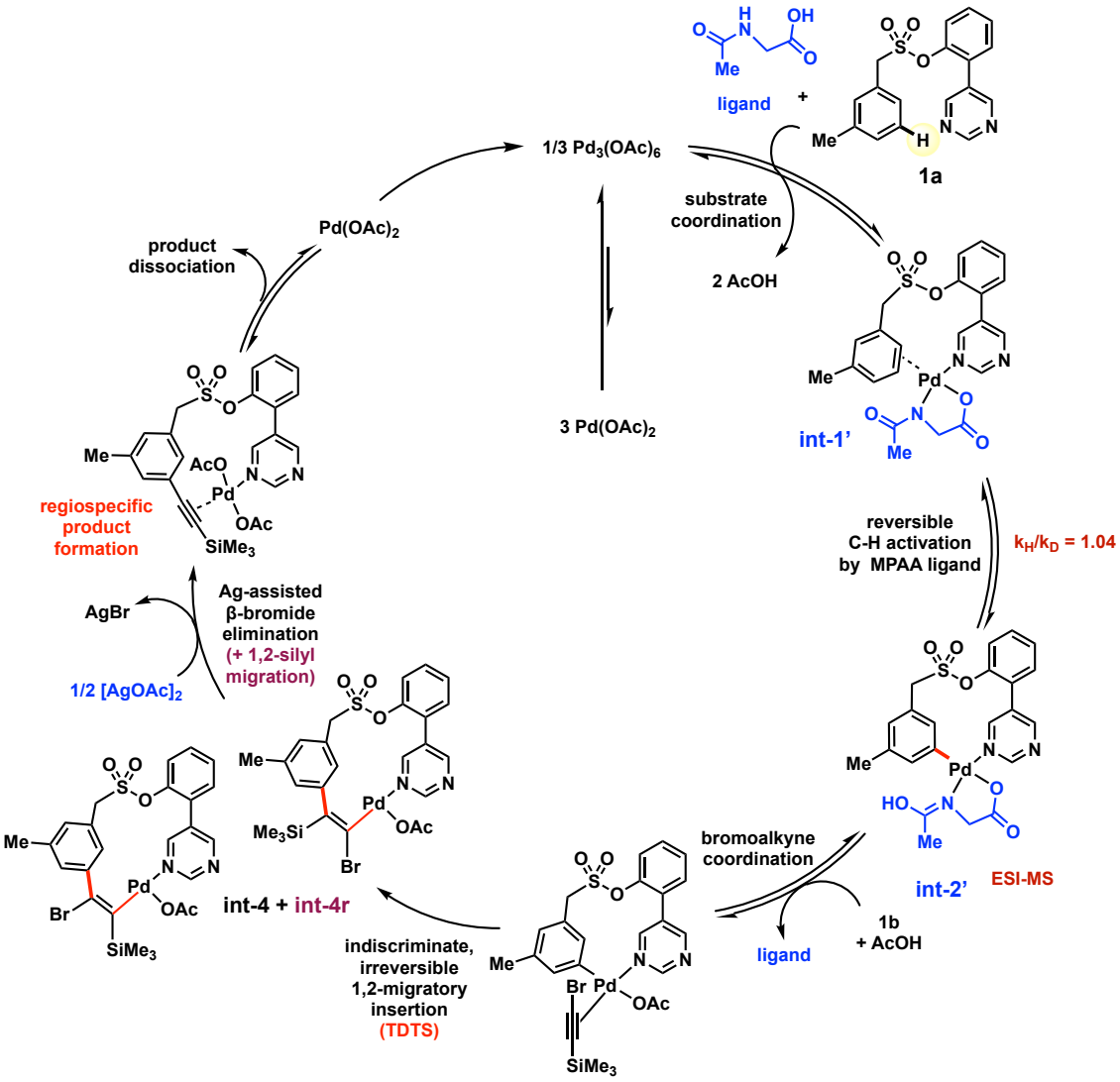

Scheme 6.5. Proposed catalytic cycle.

activation, followed by a rate-determining 1,2-migratory insertion of substrate to give a highly exergonic palladacyclic intermediate. Subsequent silver cation-assisted β-bromide elimination gives the final product (Scheme 6.5). Despite the indiscriminate 1,2-migratory insertion step, the reaction is found to regioconverge on the same alkynylated final product. This explains the high efficiency of the reaction observed experimentally. The bromine atom of the substrate was found to be essential for the formation of product via β-elimnation. The substrate ethynyltrimethylsilane **1c**, lacking bromine, did not work well, since β-hydride elimination cannot occur as easily. By comparing to substrate

bromoethynylbenzene **1d**, we hypothesized that the trialkylsilyl group is essential in the regioconvergency of the product formation.

6.4 Conclusions

Our detailed computational mechanistic investigations suggest that the present Pd-catalysed *meta*-selective C(sp^2)–H alkynylation proceeds via 1,2-migratory insertion, followed by β-elimination (where Pd-catalyst remains in formal +2 oxidation state throughout the catalytic cycle), rather than the commonly observed oxidative addition followed by reductive elimination (Pd(II)/Pd(IV) cycle). The 1,2-migratory insertion step is the overall rate-determining step. We found that despite 1,2-migratory insertion being irreversible and unselective towards the two possible regioisomers, convergence to the final, experimentally observed alkynylation product occurs via trialkylsilyl 1,2-migration following β-bromide elimination in one of the regioisomers. The role of silver additive is explicitly implicated in a heterobimetallic Pd–Ag TS that assists in β-bromide elimination, making it non-turnover frequency determining. The role of copper(II) acetate was similarly explored: Cu(II) could assist in product release, making Pd(II)-catalyst more available for the next cycle; its reduced form Cu(I) can potentially reduce the activation barrier for the β-bromide elimination step. Our computations provide us an augmented understanding of the mechanism and selectivity of the present transformation.

This mechanism opens up possible avenues for future exploration. The formation of aryl-alkynes herein via inverse Sonogashira coupling depends on the ability of the alkynyl bromide to undergo Ag-salt assisted β-elimination after 1,2-migratory insertion. The trialkylsilyl group, known to undergo 1,2-shift, is essential for the regiospecificity of the final product, despite unselective 1,2-migratory insertion of the acetylenic functional group.

For future explorations, we could potentially look at other halides (such as iodinated reagents[563,564]) attached to acetylenic coupling partners. By comparing the reactivities of bromo- vs iodo-alkynes, we might be able to perform sequential C–H functionalisations using 1-bromo-2-iodoethyne as a coupling partner. The unselective, TOF-determining 1,2-migratory insertion of the alkyne coupling partner calls for functional groups equivalent to trialkysily groups that are good at 1,2-shifts such as trialkyltin to be used to ensure the regioconvergency of the reaction pathways. Another possibility for future exploration is the employment of transition metal catalysts to effect difficult 1,2-migatory insertions in substrates that are able to form carbometallated intermediates.

When life itself seems lunatic, who knows where madness lies? Perhaps to be too practical is madness. To surrender dreams — this may be madness. Too much sanity may be madness — and maddest of all: to see life as it is, and not as it should be!

— Miguel de Cervantes Saavedra,
Don Quixote

7

Catalyst-controlled Regiodivergent Arylation of Isoquinolones

7.1 Introduction

The 2-pyridone and isoquinolone scaffolds are privileged structural motifs that occur in many natural products, bioactive molecules and functional materials.[565–571] Due to their ubiquity in a variety of molecules, the derivatisations and modifications of 2-pyridone- and isoquinolone-containing building blocks are an area of active research.[431,565,572,573] Owing to the highly similar steric and electronic properties of multiple C–H bonds present in these molecules, multiple outcomes are possible under similar reaction conditions. The selective functionalisation at desired positions is instrumental in yielding

target structures exclusively. This precise site selectivity, via chemo-, regio- and/or stereo-control, forms the cornerstone of modern chemical syntheses.[325,326,347,432,574]

Transition metals are frequently employed for the direct selective functionalisation of C–H bonds present in 2-pyridone[566,572,582,583,573,575–581] and isoquinolone[573,575,581,584–586] molecule. A common strategy for site-selective C–H functionalisation is using suitable directing groups (DGs) as seen in Chapters 4–6. Indeed, DG-assisted catalytic C–H activation at C3 position of isoquinolones, or equivalently, C6 positions of 2-pyridone has been achieved.[575,576,581,587] To overcome the installation and removal of DGs, thus simplifying such functionalisation by two steps, DG-free reaction conditions using catalyst and/or ligand control are highly desirable. Palladium-catalysed site-selective C–H functional-isation of heterocycles via substrate control, without any DG, has been previously reported.[588] DG-free reaction conditions usually take advantage of the electronic biases inherent in the substrate molecules. For 2-pyridone, C5 and C3 positions are relatively more electron-rich and react toward electrophiles more readily than other positions; similarly, C4, C7 and C5 positions of isoquinolones are the electron-rich sites that can undergo electrophilic attack on TM catalysts (Scheme 7.1 (a)). On the other hand, C4 and C6 positions of 2-pyridone as well as C3, C6 and C8 positions can be considered nucleophilic sites as incoming nucleophiles can add in a conjugate addition fashion. C4-selective arylation of isoquinolones via catalyst control, where electrophilic metalation was implicated mechanistically, was first pioneered by Hong and co-workers.[585] A similar reactivity is seen in 2-pyridone, where C5-selective arylation can be achieved via electrophilic palladation (Scheme 7.1 (b)).[582,583] Guided by these reasonings on the electronics of the substrate, in another study on catalyst controlled regiodivergent functionalisation of isoquinolones, Patil and co-workers reported gold-catalysed alkynyl-

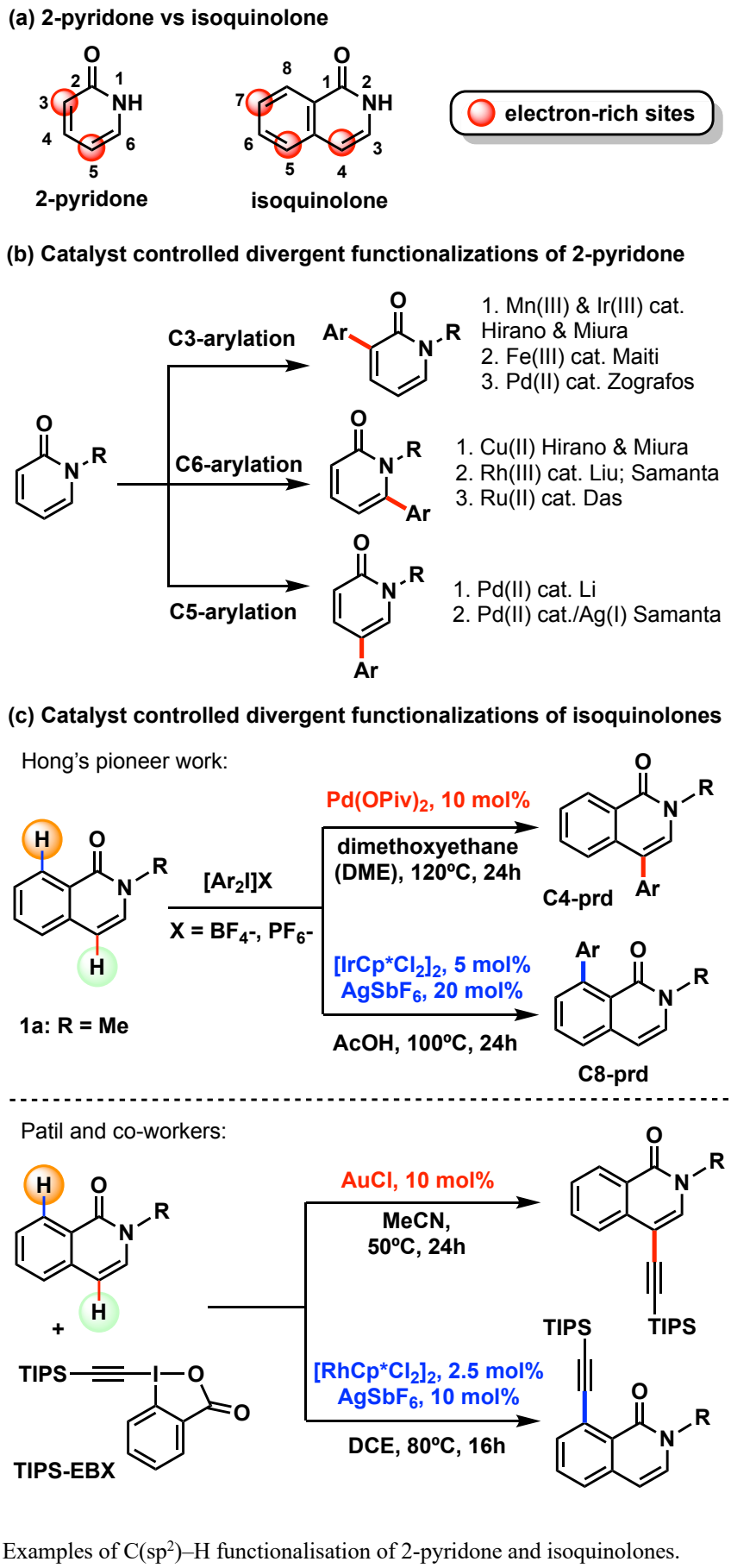

Scheme 7.1. Examples of C(sp^2)–H functionalisation of 2-pyridone and isoquinolones.

ation at C4-position, taking advantage of the electrophilicity of the TM catalyst (Scheme 7.1 (c)).[586] In both studies, C8-selective functionalisations can be achieved using different TM catalysts (Ir for arylation in Hong's work and Rh for alkynylation in Patil's work, Scheme 7.1 (c)) that presumably favour directed functionalisation by an energetically favourable coordination of the metal to the carbonyl group of the isoquinolone, thus functionalising the C(sp^2)–H bond in its proximity. This similar reactivity is seen in C3-selective arylation of 2-pyridone, where Mn(III),[589] Ir(III),[590] Fe(III)[591] and Pd(II)[592] have all been successfully employed. Due to this very general reactivity pattern in 2-pyridone and isoquinolone functionalisations, a detailed understanding of the catalytic mechanism and the factors influencing site selectivity is of broad interest and applicability.

The mechanism was first studied experimentally using H/D scrambling and kinetic isotopic effects (KIEs) experiments, providing evidence for the C–H activation step (*vide infra*). All experimental work described in this project was performed by our experimental collaborators (the Hong group, Korea Advanced Institute of Science and Technology (KAIST)). The complete picture of the energy landscape, in particular the overall turnover-frequency (TOF)-determining steps (TDTS) for each catalyst controlled C–H functionalisation, remains to be elucidated; in addition, the molecular origins influencing the site-selectivity are not well understood.[585] Due to the transient nature of the transition states, experimental tools for their direct observations are limited. Experimental techniques such as linear free energy relationships (LFERs), KIEs and spectroscopic characterisation of reactive intermediates provide indirect evidence for the reaction mechanism. To complement the understanding of the reaction mechanisms, in addition to the aforementioned experimental techniques employed, we embarked on a

theoretical study of the mechanisms by directly accessing the putative transition structures involved in these reactions.

Herein we performed detailed computational studies of the mechanisms involved in the regioselective C4- vs C8-functionalisation of isoquinolone pioneered by Hong and co-workers (Scheme 7.1 (c)) as a case study of the general reactivity pattern observed for both 2-pyridone and isoquinolone functionalisations. We consider only the C3-, C4- and C8-positions of isoquinolone for C(sp^2)–H functionalisation as these are the only positions observed experimentally. Our combined experimental and computational explorations reveal different mechanisms, with differing TDTSs[125] for each catalytic system.

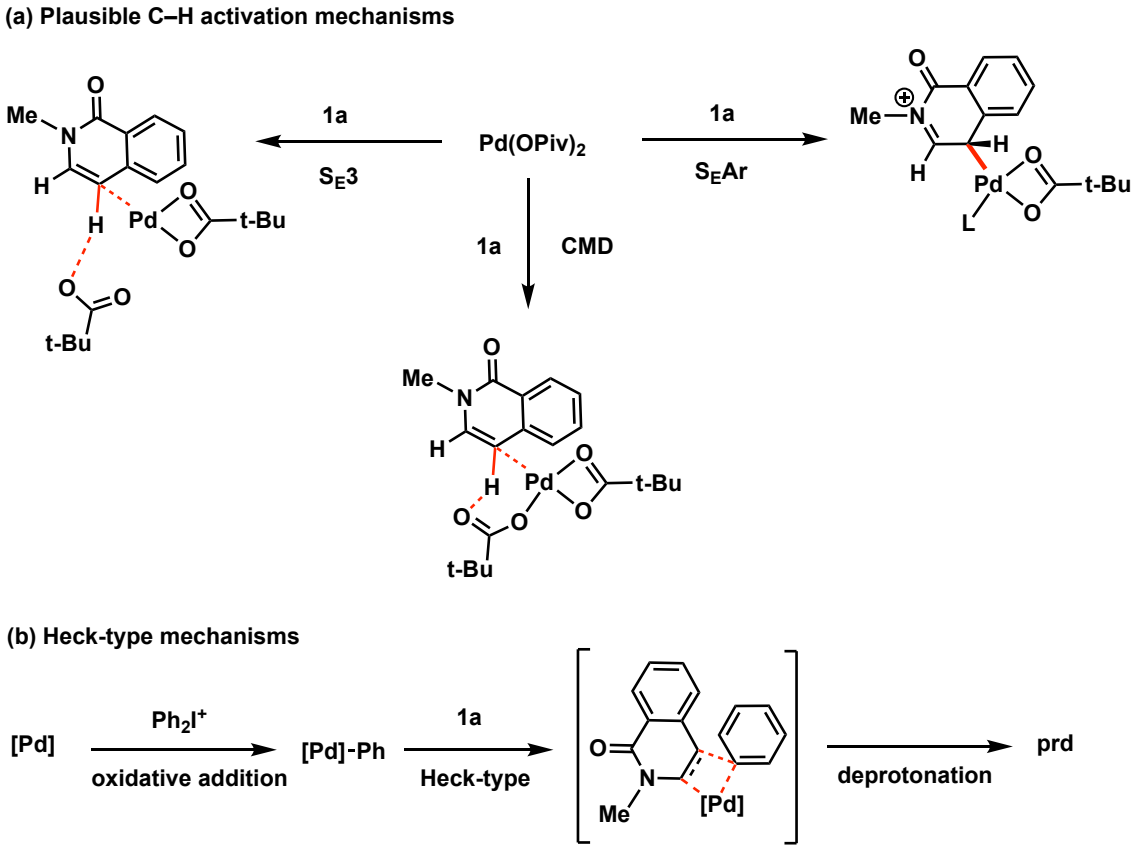

Scheme 7.2. Plausible mechanisms for Pd-catalysis.

A series of plausible mechanisms for the Pd-catalysis can be envisioned (Scheme 7.2). The first type of mechanism involves site-selective C–H activation of the isoquinolone by the palladium catalyst. This C–H activation step can be achieved in several ways (Scheme 7.2 (a)), either via concerted metalation-deprotonation (CMD),[100,103,404,429,593,594] electrophilic aromatic substitution (S_EAr),[595–597] or termolecular electrophilic substitution (S_E3),[598] where an outer coordination sphere base/ligand carries out the C–H activation step. The C–H activated carbopalladated complex could then undergo oxidative addition (OA) of diaryliodonium salt followed by C–C reductive elimination (RE) to give the final product. The reaction can also proceed via a Heck-type mechanism[438,599] (Scheme 7.2 (b)), where the OA of the diaryliodonium salt gives a carbopalladated intermediate that subsequently forms C–C reductive coupling with the isoquinolone before a β-hydride elimination yields the final product (*vide infra*).

For this project, some initial TSs of the C–H activation step (the neutral pathway for Pd-catalysis in subsection 7.3.3.1 and the cationic pathway for Ir-catalysis in subsection 7.3.7.1) were obtained by Dr. Peng Qian using ωB97X-D[56]/def2-TZVP[18] optimisation level, which was found to be very computationally expensive. These TSs were re-optimised using MN15[78] functional with smaller basis sets (section 7.2); all other computational work (some additional C–H activation TSs, OA and RE steps and Heck-type mechanistic investigations for both catalytic systems) and all results analysis and discussion were performed by the present author under the supervision of Prof. Robert Paton.

7.2 Computational Methods

Computational methods employed for the present transformation are the same as those employed in the study of Pd-catalysed C(sp^2)–H allylation/alkynylation in Chapter 5/6.

Gibbs energies were computed at SMD[117](solvent)-MN15(ωB97X)/def2-QZVPP[18]// MN15/GenECP (def2-TZVPPD for Pd,[17,401] Ir[17,401] and I[402] atoms and def2-SVP[18,19] for all other atoms (BS1)) level of theory. The solvents used are 1,2-dimethoxyethane (DME) for Pd-catalysis and acetic acid (AcOH) solvent for Ir-catalysis. Solvent DME was parametrised with the following parameters: the static dielectric constant of the solvent (*Eps*=7.3);[405] dynamic dielectric constant – the square of the refractive index value of 1.377 was used[406] (*EpsInf=1.896*); hydrogen bond acidity (*HBondAcidity=0.00*) and basicity (*HBondBasicity=0.68*);[407] *SurfaceTensionAtInterface=15.2*[600] (at 100ºC instead of reaction temperature of 120ºC as it is not available at higher temperatures); *CarbonAromaticity=0.00* and *ElectronegativeHalogenicity=0.00*. Gibbs energies were evaluated at their respective reaction temperatures (393.15K for Pd-catalysis and 373.15K for Ir-catalysis). SMD(solvent)-MN15(ωB97X)/def2-QZVPP//MN15/BS1 Gibbs energies are given. Unless otherwise stated, the first set of Gibbs energy values are used for discussion. *All Gibbs energy values in the text and figures are quoted in kcal mol^{-1} throughout.*

Geometries of all optimised structures (in *.xyz* format with their associated energy in Hartrees) and an associated README file have been deposited online and made freely available (DOI:10.5281/zenodo.3386599).

7.3 Results and Discussions

7.3.1 Bond dissociation enthalpies and frontier molecular orbitals of isoquinolone

The bond dissociation enthalpies (BDEs) of the substrate, isoquinolone, was computed in the gas phase at MN15/def2-SVP level of theory. The corresponding radicals where a hydrogen atom is removed were optimised, using unrestricted KS-DFT formalism, in addition to a hydrogen atom. The BDE is calculated as

$$\mathrm{BDE(R–H)} = H_{\mathrm{R}\cdot} + H_{\mathrm{H}\cdot} - H_{\mathrm{R–H}} \tag{7.1}$$

The BDE values at different C–H sites, superimposed on an electrostatic potential (ESP) surface, with the NBO charges of the carbon atoms are shown in Figure 7.1 Top. We can see that the C4–H bond is the strongest while C6–H bond is the weakest; the C–H bond strengths are very close in BDEs and that the largest difference is 3.8 kcal mol^{-1}, making selective functionalisation based solely on C–H bond strength challenging.

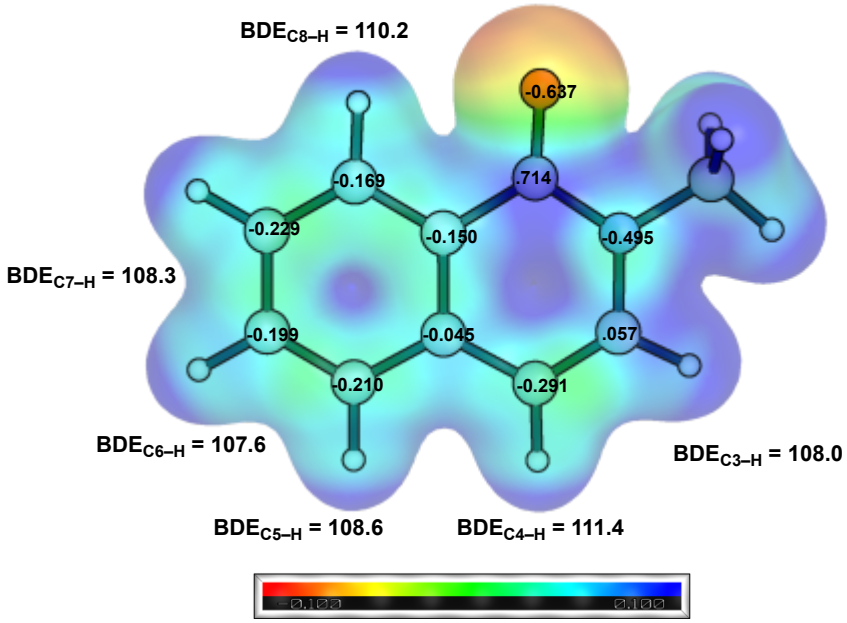

HOMO of isoquinolone	LUMO of isoquinolone
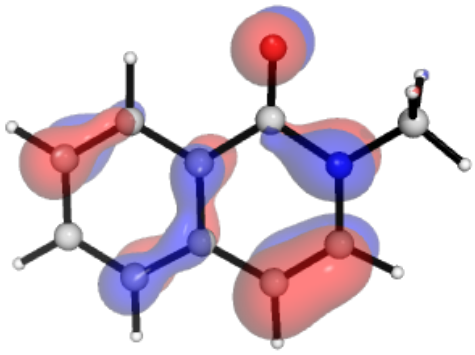	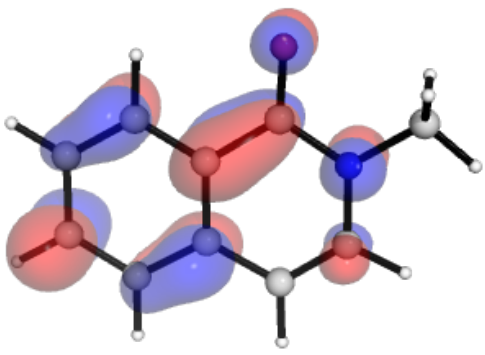

Figure 7.1. Top: Bond dissociation enthalpies (BDE) of various C–H bonds in kcal mol^{-1}, superimposed on an electrostatic potential (ESP) surface at an isovalue of 0.02. Bottom: HOMO and LUMO of isoquinolone.

Based on the ESP and NBO charges, we note that C4-position has the largest negative charge (-0.291) amongst carbon atoms. This implies that C4 is electron-rich which can participate in electrophilic attack on TM metal catalyst, as shown later. C3 is the only positively charged carbon (+0.057) other than the carbonyl carbon (+0.714). In addition, the frontier molecular orbitals (FMOs) of the isoquinolone are shown (Figure 7.1 Bottom). We can see that the dominant orbital coefficient of the HOMO is on the C4- and C3-position and that the LUMO has some orbital coefficient at the C3 position.

7.3.2 Isotopic labelling experiments

All work discussed in this subsection was performed by our experimental collaborators as stated previously. Deuterium labelling experiments were performed to understand the reversibility of the C–H activation step. The results are shown in Scheme 7.3. For the palladium catalysis (Scheme 7.3 (a)), it was found that H/D exchange can occur at C4-position, with 32% deuterium exchange in the presence of Pd-catalyst and 20 equivalents of D_2O. In addition, there was no primary kinetic isotope effect (KIE) when the C4-deuterated isoquinolone reacted under the reaction condition and compared to the unlabelled isoquinolone (intermolecular competition studies); the measured $k_H/k_D = 1.01$ indicates that the C–H activation step is not turnover-frequency (TOF)-determining. Taken together, we expect a facile, reversible C–H activation for the Pd-catalysed reaction.

For the iridium catalysis, four separate experiments were carried out (Scheme 7.3 (b)). Under the standard arylation conditions with deuterated acetic acid as solvent, we observed high levels of deuterium incorporation after 24h at both C4 (89% D) and C8 (94% D) positions; with hexane as solvent and 10 eq. of AcOD, noticeably higher level of deuteration occurs at C8 (67% D) than C4 (6% D) position after 3h. This suggests that

deuteration at C8 is reversible. Subsequently, we established that deuteration at C4 occurs in AcOD in the absence of catalyst (9% D after 32h) or with a silver salt (51% after 16h); no deuteration of C8 occurs without the Ir-catalyst. Thus, while the CMD mechanism is operative at C8, it is also likely that electrophilic pathway can occur at C4, with reversible deprotonation/protonation, allowing for reversible H/D exchange at this position.

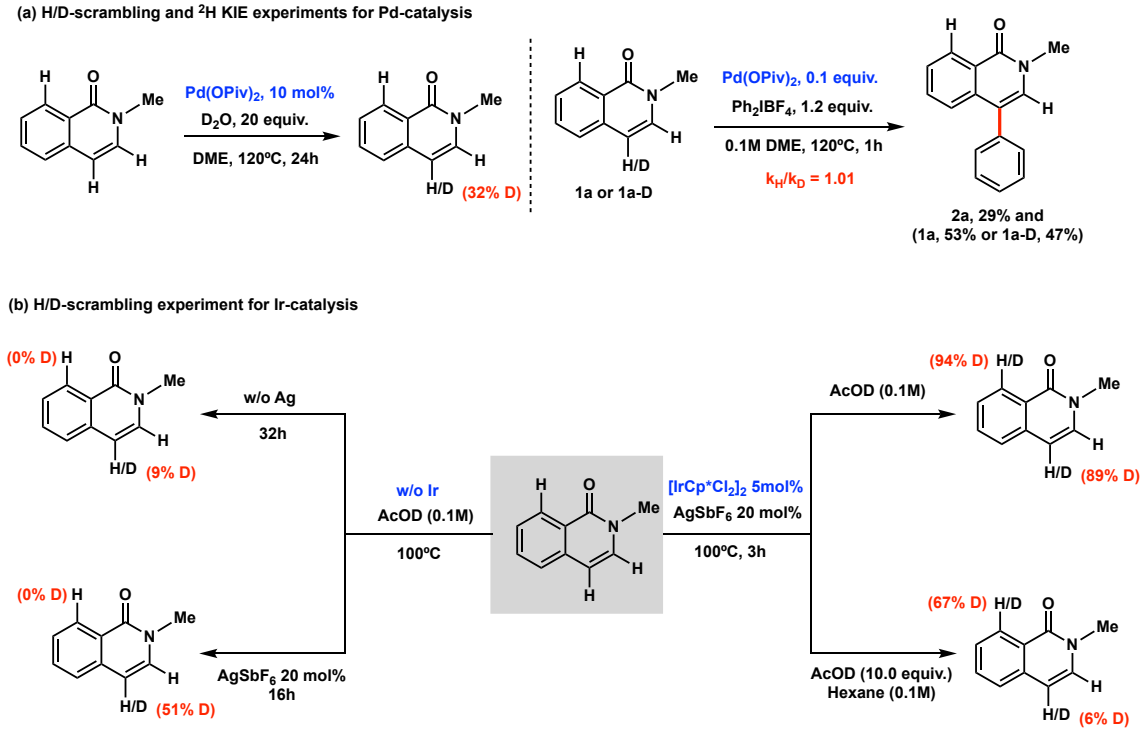

Scheme 7.3. Experimental deuterium labelling experiments. All results are from our experimental collaborators.

Palladium Catalysis

7.3.3 Pd(II)/Pd(IV) cycle: C–H activation, oxidative addition followed by reductive elimination

Although $Pd(OPiv)_2$ can exist as a trinuclear species,[412–414] we consider the mononuclear form to be the active catalyst in the present transformation. We considered the first possibility here: the reaction could proceed via a neutral pathway (a cationic pathway was also considered, *vide infra*), firstly a C–H activation, followed by oxidative addition (OA)

and reductive elimination (RE) as the palladium catalyst cycled through the Pd(II)/Pd(IV) manifold.[100,423] According to this energy profile (Figure 7.2), the isoquinolone molecule first undergoes a ligand-assisted C–H activation via concerted metalation deprotonation (CMD) (**C4-ts1**, at 26.1 kcal mol^{-1}), forming a carbopalladated complex, **C4-int2**, which is endergonic at 15.7 kcal mol^{-1}. The displacement of a neutral acid molecule by the diaryliodonium and pivalate ions is highly exergonic, giving **C4-int3** at -5.0 kcal mol^{-1}. This is followed by OA of diaryliodonium (**C4-ts3**, with a barrier of 17.9 kcal mol^{-1}), giving a Pd(IV) intermediate which further undergoes RE (**C4-ts4**, with a barrier of 12.8 kcal mol^{-1}) to give the final arylated product.

The S_EAr mechanism (electrophilic palladation) for the C–H activation step (Scheme 7.2 (a)) is ruled out as no stable structures corresponding to the formal Wheland intermediate could be located, in agreement with previous computational studies.[429,588] In addition, any attempts to find the TS for the S_E3 mechanism eventually yielded the CMD TSs.

For the OA of the diaryliodonium salt, we considered the effect of using different counter anions ($PivO^-$ vs BF_4^-) on the activation barrier of the TSs; in addition, we also consider the geometric isomers of the TSs arising from the different arrangements of the groups being added (subsection 7.3.3.2). We found that in general, the use of the more strongly coordinating pivalate ion in the inner coordination shell of the OA TS is more favoured than tetrafluoroborate ion, which is weakly coordinating. The formation of Pd–F bond is rather weak and does not give favourable stabilising interactions to the TS to lower its activation barrier.

This energy profile predicts that the C–H activation is not only turnover frequency-determining (TDTS), but also regio-determining. Although the site-selectivity predicted

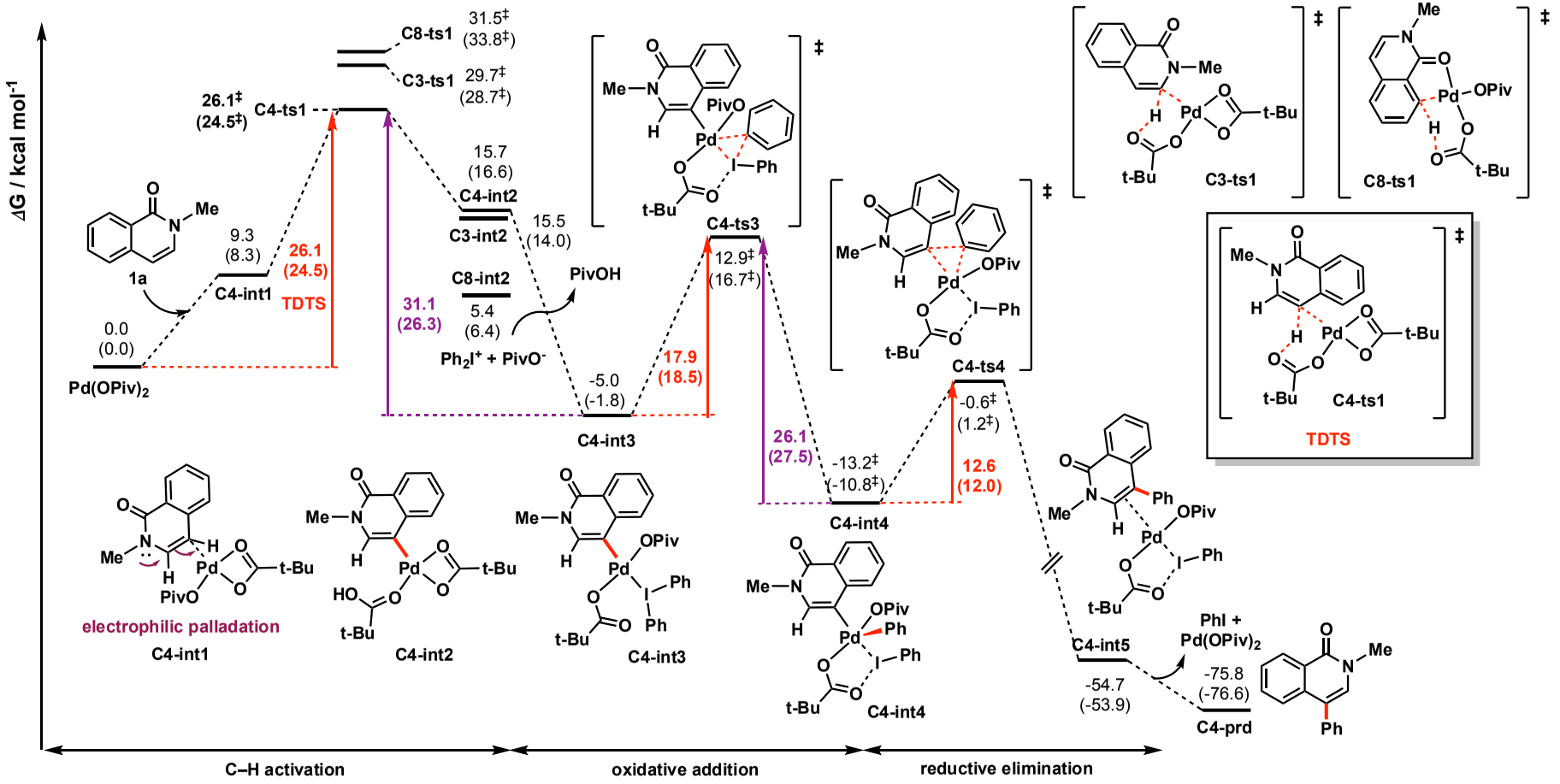

Figure 7.2. Gibbs energy profile for Pd(II)-catalysis via CMD followed by OA and RE.

by this mechanism agrees well with the observed experimental results (subsection 7.3.3.1): the TDTS is the C4-selective C–H activation (**C4-ts1**, 26.1 kcal mol^{-1}), due to the most productive orbital interactions and the least steric hindrance in this TS (Figure 7.4) than **C3-ts1** (29.7 kcal mol^{-1}; 1 in 100) and **C8-ts1** (31.5 kcal mol^{-1}; 1 in 1000), the experimental H/D scrambling and the lack of ^{2}H primary KIE suggest that, despite rightly predicting site-selectivity, this mechanistic picture is inconsistent with the experimental kinetic studies and thus unlikely to be correct.

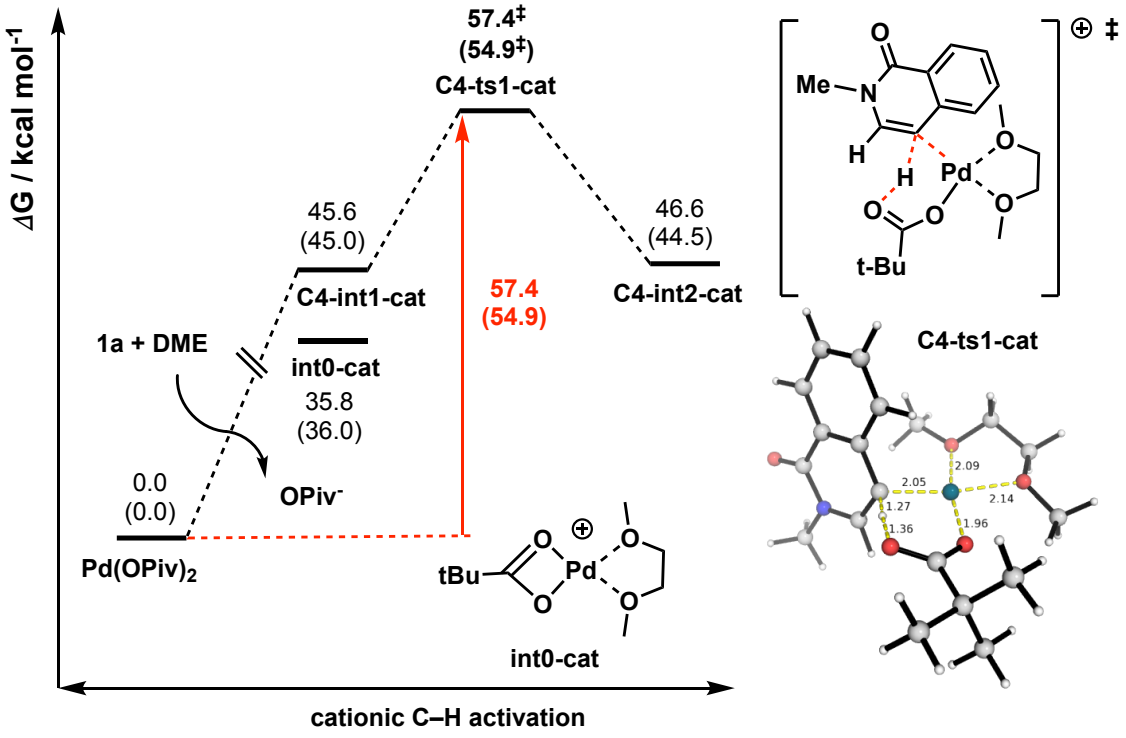

Figure 7.3. Gibbs energy profile for Pd(II)-catalysis via cationic CMD. Optimised TS structure is shown; key bond distances are given in Å.

For the corresponding cationic mechanism (Figure 7.3), we found that this is less favourable than the neutral pathway discussed above. We can see that the displacement of a pivalate anion from the inner coordination sphere of the catalyst by a solvent molecule, and thus creating an overall charged species, is very endergonic (by 35.8 kcal mol^{-1}, **int0-cat**), consistent with the fact that non-polar solvent used in this transformation

(dimethoxyethane) disfavours ionic mechanism as the cationic CMD TS (**C4-ts1-cat**) cannot be stabilised well by the solvent system.

7.3.3.1 Pd(II)/Pd(IV) cycle: site selectivity of C–H activation

In this subsection, we discuss how the C(sp^2)–H activation step for the Pd(II)-catalysed arylation of isoquinolone as described above was studied in some detail. For this first mechanistic possibility, the C–H activation was the overall TDTS and gives the correct regioselective outcomes. Although we know, from the experimental KIE and H/D scrambling experiments, that the C–H functionalisation lacks primary ^{2}H KIE so that the C–H activation step is not the TDTS, we include this discussion for completeness.[1]

As we can see in Figure 7.1 (BDEs), despite the fact that C4–H bond is the strongest, C4–H activation (**C4-ts1**) has the lowest activation barrier at 26.1 kcal mol^{-1}. We can see that the C–Pd bond distance is the shortest (2.06Å) in **C4-ts1** (Figure 7.4), indicating significant electron donation from the C=C bond into Pd(II)-centre, which is electrophilic. This productive orbital interaction facilitates the proton abstraction by the pivalate ligand (HOMO plot, Figure 7.4). In addition, the NCI plots indicate that there are the least steric crashes in **C4-ts1** amongst all three C–H activation sites (Figure 7.4).

When calculating C8–H activation barriers, we tried out all possible arrangements of the isoquinolone substrate and the ligands (Figure 7.4). **C8-ts1** was found to be lowest in activation barrier due to favourable coordination of O-atom of isoquinolone to Pd-centre, forming a [5,6]-palladacycle conducive for CMD. The alternative ligand arrangement in **C8-ts1-c4** where one pivalate coordinates in a bidentate fashion while another outer

[1] We initially thought this was the correct mechanism without the experimental evidence to the contrary and included this discussion here to see the steric and electronic factors that could potentially contribute to the site-selectivity. This CMD step was found to be operative in a later mechanistic possibility and the factors influencing the selectivity are similar; see subsection 7.3.5 for a discussion.

sphere non-coordinating pivalate ion carries out CMD is highly unfavourable. The tetra-coordinating nature of Pd(II) mandates that the latter pivalate ligand cannot coordinate to the Pd-centre, giving a rather loose [5,6]-member ring in the TS (long C–Pd bond distance of 2.42Å, Figure 7.4). In addition, this far arrangement of ligand gives rise to a lack of overlap between the HOMO of this pivalate ligand (the in-plane oxygen lone pair that is predominantly localized on O-atom) and the d-orbital of Pd-centre (Figure 7.4), thus **C8-ts1-c4** is 5.1 kcal mol^{-1} higher than **C8-ts1** (although their NCIs seem to be similar). **C8-ts1-c2** is 1.3 kcal mol^{-1} higher than **C8-ts1**. Although we expect the loss of coordination interaction between isoquinolone O-atom and Pd-centre in **C8-ts1-c2** to be compensated by a similar interaction between pivalate O-atom and Pd-centre, the NCI interactions are less sterically favourable in **C8-ts1-c2** due to the repulsion between the isoquinolone O-atom and the coordinating pivalate O-atom (Figure 7.4, NCI plot of **C8-ts1-c2**, circled in green). **C8-ts1-c3** is 1.4 kcal mol^{-1} higher than and differs from **C8-ts1** in the non-participating pivalate ligand which points in the opposite direction of the tetra-coordination plane, potential due to the unfavourable through-space interactions of the orbitals (Figure 7.4).

Note that in comparing C4 vs C8 activation, the isoquinolone carbonyl group directed C8(sp^2)–H activation (**C8-ts1**) is less favoured (by 5.4 kcal mol^{-1}) than the non-directed C4(sp^2)–H activation (**C4-ts1**). We have seen similar directing group-assisted C(sp^2)–H activation in Chapters 5 and 6, where the directing group coordinates to the Pd(II)-centre as the CMD step is carried out. We note that the difference here is that for those TSs (**ts-1'**, Figure 5.2 and Figure 6.3), the C(sp^2)–H bond to be activated and the base/ligand O-atom carrying out the CMD all lie on the same plane as the Pd-catalyst with its tetra-coordination and more importantly, *the aryl ring for activation is perpendicular to this*

C4-ts1	C3-ts1	C8-ts1
26.1‡ (24.5‡)	29.7‡ (28.7‡)	31.5‡ (33.8‡)
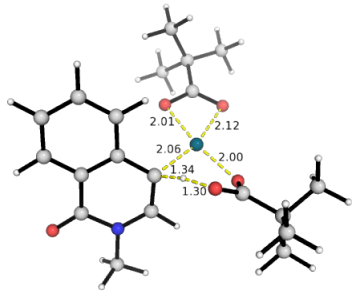	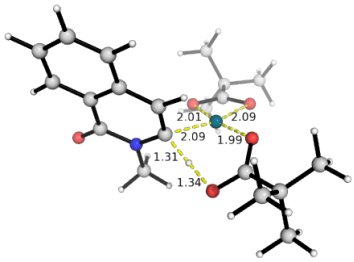	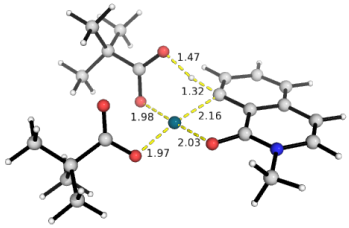
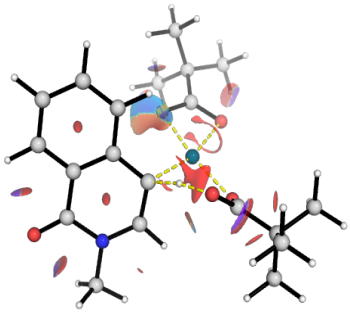	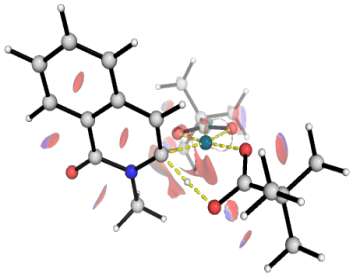	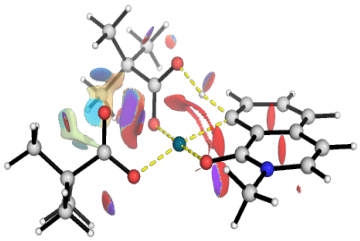
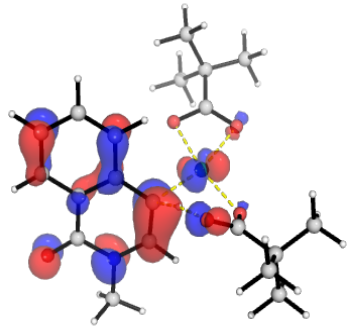	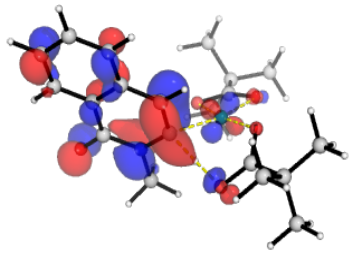	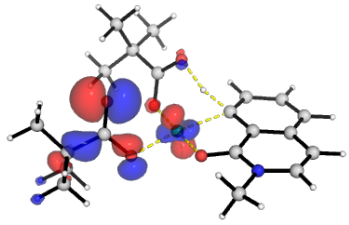
C8-ts1-c2	**C8-ts1-c3**	**C8-ts1-c4**
32.8‡ (32.3‡)	32.9‡ (34.7‡)	46.6‡ (47.8‡)
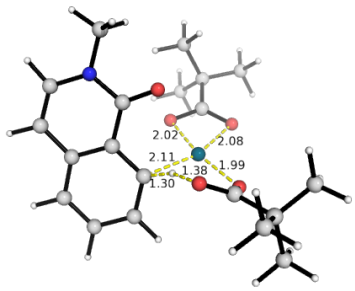	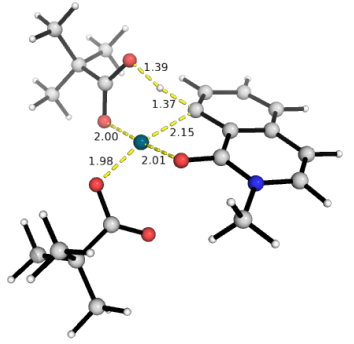	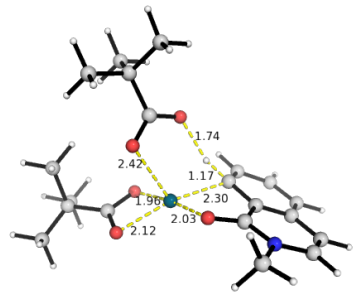

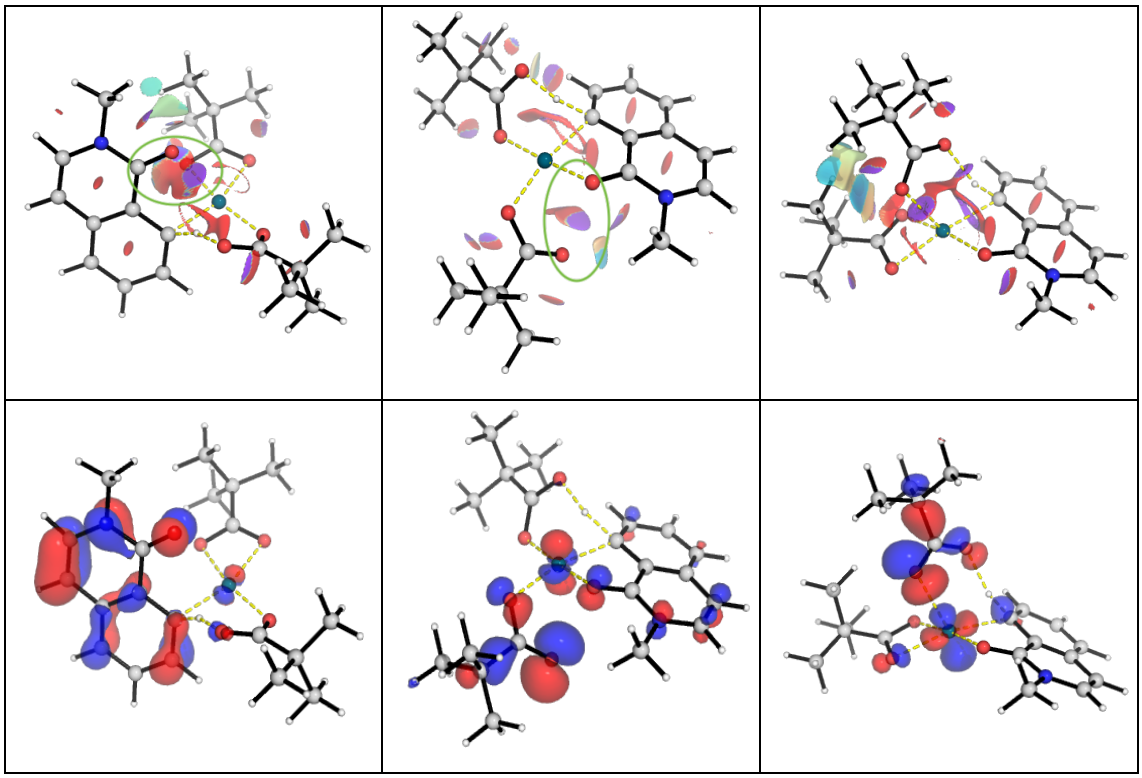

Figure 7.4. Optimised structures, NCI plots and HOMOs of TSs of C–H activation via CMD at different sites by neutral palladium catalysis.

plane whereas in **C8-ts1** the ligand O-atom carrying out the CMD is distorted out of the plane at an angle, due to the geometric constraint imposed by the coordinating carbonyl group and that the aryl ring for activation is on the same plane as the Pd-catalyst and its four coordinating groups (**C8-ts1**, Figure 7.4), making the TS sterically disfavoured. In fact, TS structure **C4-ts1** has closer resemblance to the TS structures for the CMD steps in Figures 5.2 and 6.3, in that the aryl ring for activation is perpendicular to the Pd in its coordination plane.

Thus, for this particular C–H activation of isoquinolone substrate via CMD involving a Pd-catalyst, C4-position is favoured over other positions due to favourable orbital interactions and least steric hindrance, despite the C4–H bond being the strongest amongst all.

7.3.3.2 Pd(II)/Pd(IV) cycle: OA and RE steps

For the OA of diaryliodonium salt, we considered the effect of different counter anions ($PivO^-$ vs BF_4^-) on the activation barrier of the TSs.[2] In addition, we also considered the geometric isomers of the TSs arising from the different arrangements of the groups being added (Figure 7.5). We found that in general, using pivalate ion (strong π-donor ligand) in the inner coordination shell of the OA TS is more favoured than tetrafluoroborate ion (BF_4^-), which is weakly or non-coordinating. This is in agreement with the fact that OA is favoured by strong donor ligands which enhance electron density on the metal and thus stabilise the higher oxidation state of the metal. In contrast, the formation of the Pd–F bond is rather weak and does not give favourable stabilising interactions to the TS to lower its activation barrier. Thus, for all subsequent mechanistic investigations involving the OA and RE steps where the diaryliodonium salt is involved, we used the appropriate ligands instead of the non-coordinating ions (BF_4^- and PF_6^-) in the TS searches.

For TSs with $PivO^-$ counteranion, the TS having I-atom coordinated axial to the activated C4–Pd bond of the isoquinolone (**C4-ts3**) gives the lowest activation barrier, at 12.9 kcal mol^{-1}. Although the coordination mode in **C4-ts3d** is similar, there seems to be more favourable non-covalent interactions (NCIs) in **C4-ts3** between the I-atom of diaryl-iodonium and the O-atom of pivalate, as evidenced by the its shorter I–O bond (2.54Å) than in **C4-ts3d** (3.28Å). This O–I NCIs occur prevalently, also in the Ir-catalysed system (*vide infra*). The TSs having I-atom adjacent to the activated C4–Pd bond of the isoquinolone (**C4-ts3b** and **C4-ts3c**) both have higher barriers than **C4-ts3** and are thus less favourable. Note that in the OA step, the octahedral coordination geometry is disfavoured as the TS search with the pivalate coordination via bidentate mode returned

[2] This consideration of different counterions in the OA and RE steps is essential as it applies to other mechanisms involving OA and/or RE steps such as the Heck-type mechanism discussed below.

C4-ts3 instead, which is penta-coordinate. This is the same as the observation made in Chapter 4, where the OA and RE steps occur more readily with odd, rather than even, number of coordination.[419–421]

OA with pivalate counteranion		
C4-ts3	**C4-ts3b**	**C4-ts3c**
12.9‡ (16.7‡)	18.2‡ (21.9‡)	18.8‡ (23.4‡)
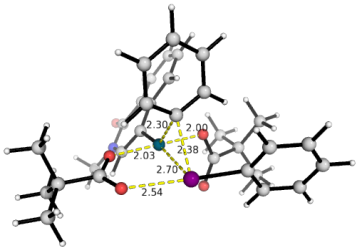	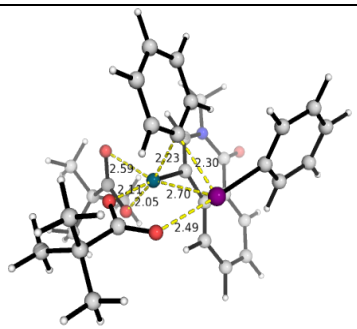	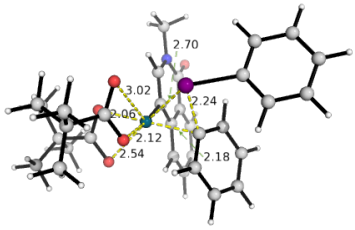
C4-ts3d		
21.0‡ (24.9‡)		
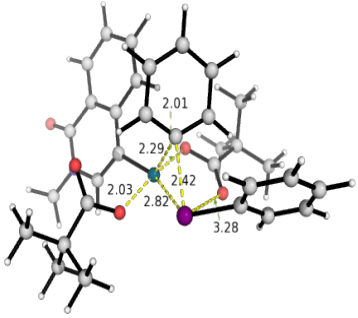		
OA with tetrafluoroborate counteranion		
C4-ts3'a	**C4-ts3'b**	**C4-ts3'c**
47.3‡ (52.2‡)	49.1‡ (52.3‡)	50.1‡ (55.0‡)
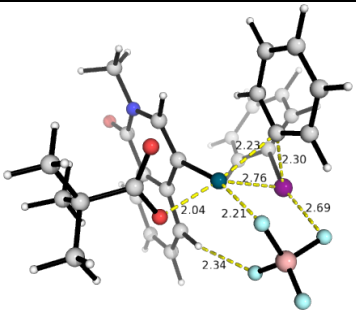	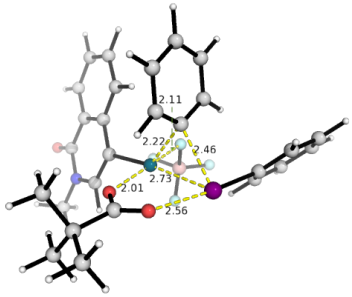	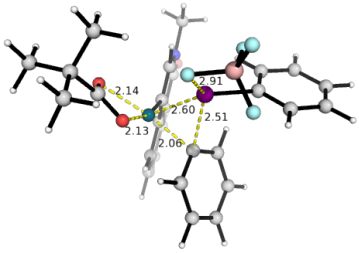

RE with pivalate or tetrafluoroborate counteranion		
C4-ts4	**C4-ts4b**	**C4-ts4'**
-0.6‡ (1.2‡)	1.4‡ (3.8‡)	43.8‡ (46.8‡)
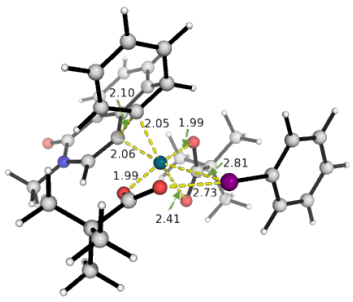	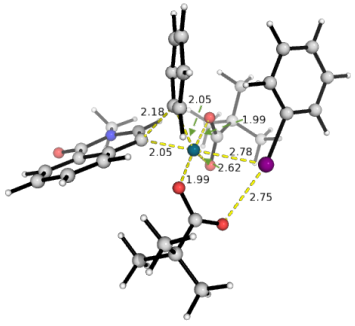	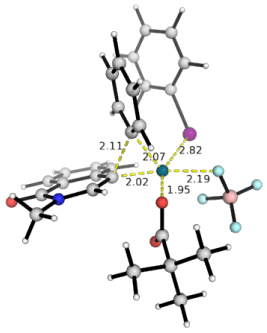

Figure 7.5. Optimised geometries for oxidative addition step using diaryliodonium salt with either pivalate anion or tetrafluoroborate anion (top) and reductive elimination step (bottom).

The RE TS for C–C bond formation, **C4-ts4**, has the lowest activation barrier; the other conformation of the TS (**C4-ts4b**) where the orientation of the isoquinolone moiety is rotated, is higher in barrier by 2.0 kcal mol^{-1} and thus disfavoured (Figure 7.5).

7.3.4 Pd(II)/Pd(IV) cycle: Heck-type mechanism

In this subsection, we consider the Heck-type mechanism shown in Scheme 7.2 (b). We first consider the Pd(II)/Pd(IV) cycle in a neutral pathway,[601–606] although the classical Heck reaction mechanism proceeds via a Pd(0)/Pd(II) cycle[607] (which we consider later on). The Gibbs energy profile is given in Figure 7.6; TS structures, with conformational sampling, by varying the conformations of the coordinating ligands, are given in Figure 7.7. This reaction mechanism proceeds with the OA of diaryliodonium (**H-ts1**, barrier of 21.3 kcal mol^{-1}) forming a Pd(IV)-aryl complex, **H-int2**, which is slightly uphill, by 3.0 kcal mol^{-1}. This OA step is reversible as the subsequent carbopalladation step has a higher activation barrier. For the OA step, the more strongly coordinating pivalate counterion is used in the inner coordination sphere, rather than the non-coordinating BF_4^- ion as discussed in subsection 7.3.3.2.

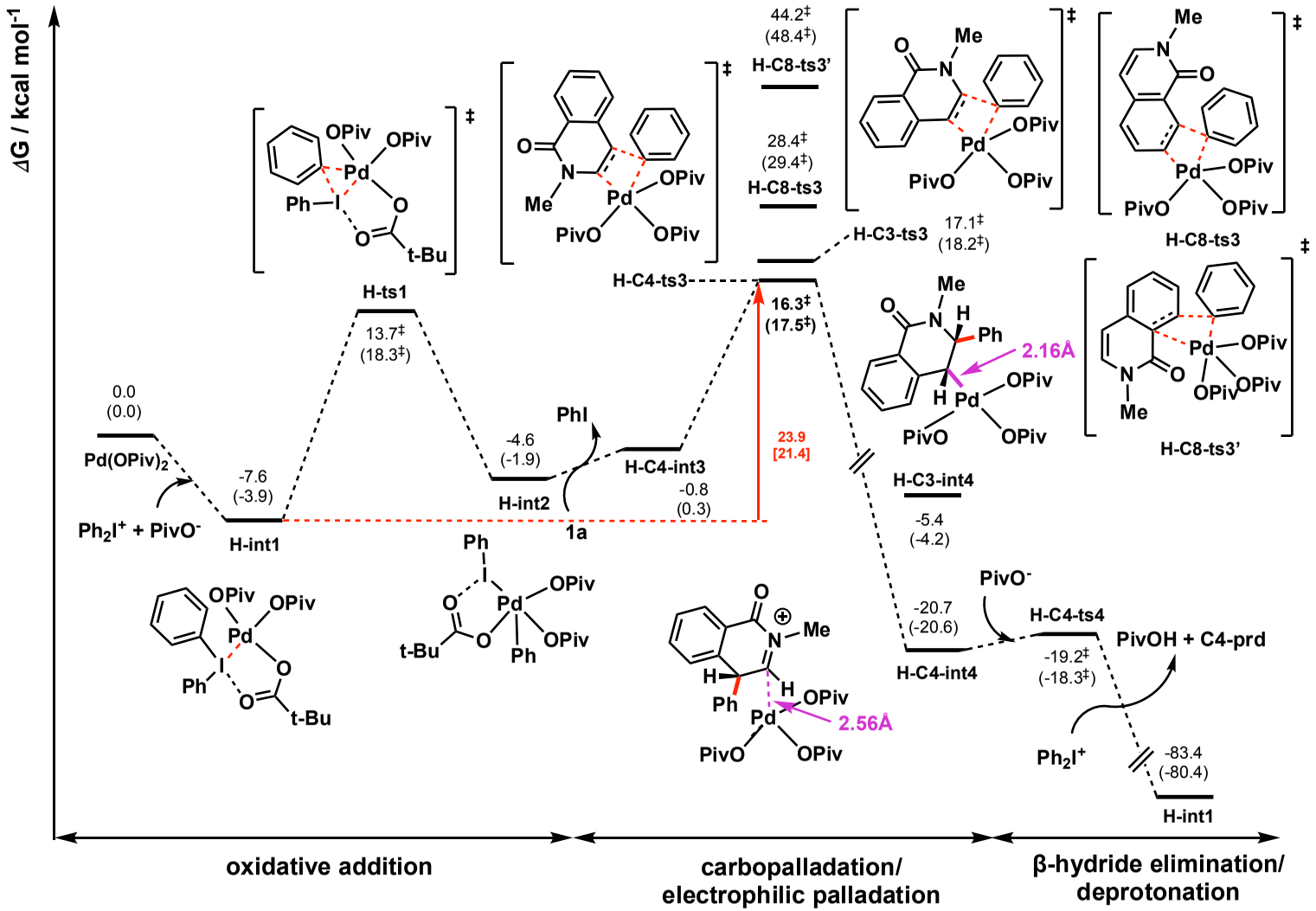

Figure 7.6. Gibbs energy profile for Pd(II)-catalysis via neutral Heck-type mechanism.

H-C4-ts3	H-C4-ts3-c2	H-C4-ts3-c3
16.3‡ (17.5‡)	16.3‡ (19.2‡)	16.8‡ (20.4‡)
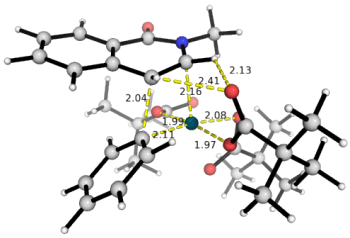	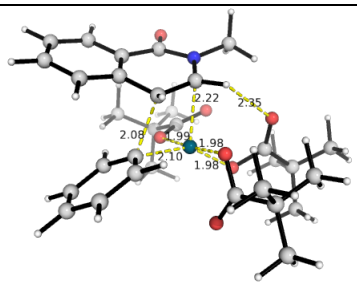	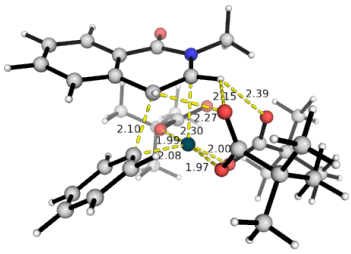
H-C4-ts3-c4	**H-C4-ts3-c5**	**H-C4-ts3-c6**
17.1‡ (17.2‡)	19.0‡ (21.2‡)	19.3‡ (20.9‡)
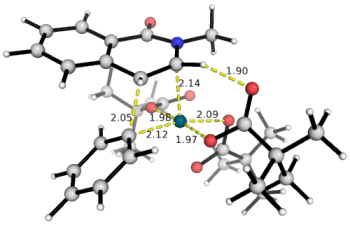	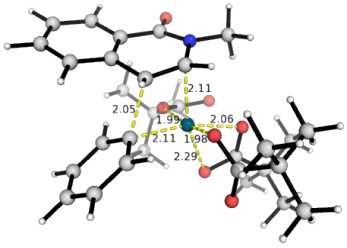	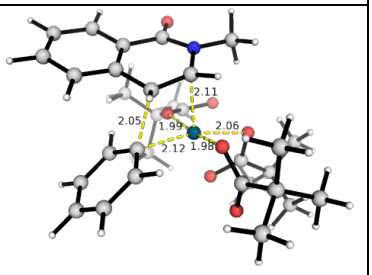
H-C3-ts3	**H-C3-ts3-c2**	**H-C3-ts3-c3**
17.1‡ (18.2‡)	17.2‡ (17.7‡)	17.6‡ (17.6‡)
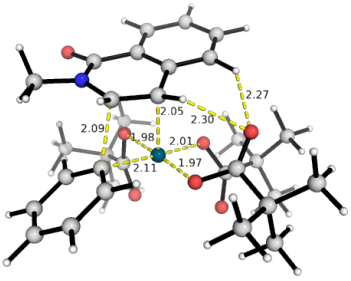	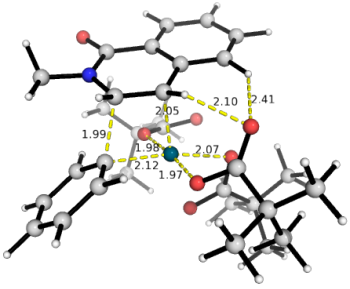	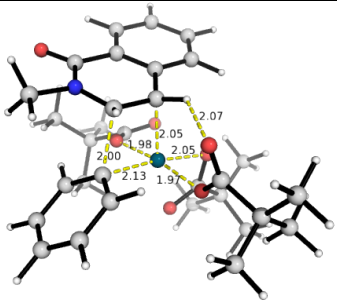
H-C3-ts3-c4	**H-C3-ts3-c5**	**H-C3-ts3-c6**
18.7‡ (18.9‡)	19.0‡ (19.7‡)	23.3‡ (21.8‡)
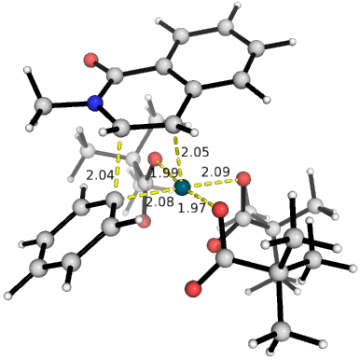	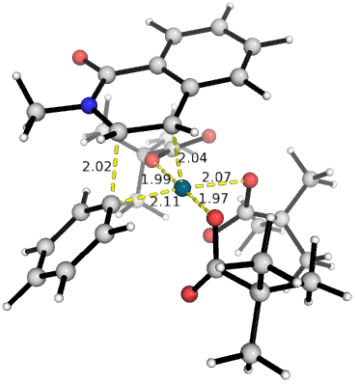	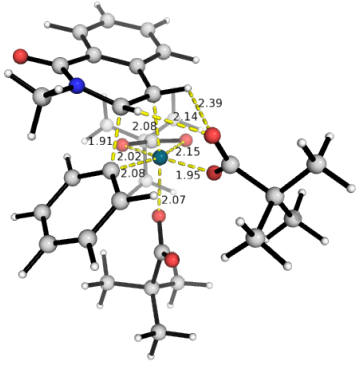

H-C8-ts3	H-C8-ts3'	H-C4-ts4
28.4‡ (29.4‡)	44.2‡ (48.4‡)	-19.2‡ (-18.3‡)
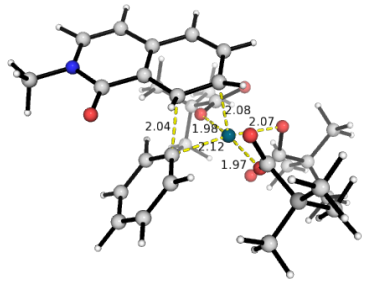	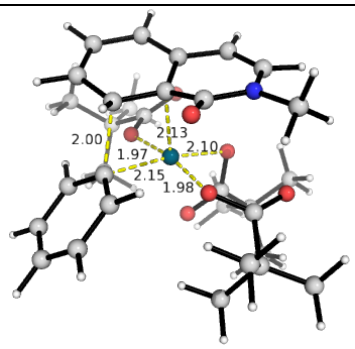	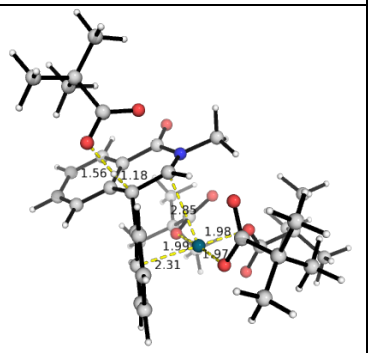

H-C4-int4	H-C3-int4
-20.7 (-20.6)	
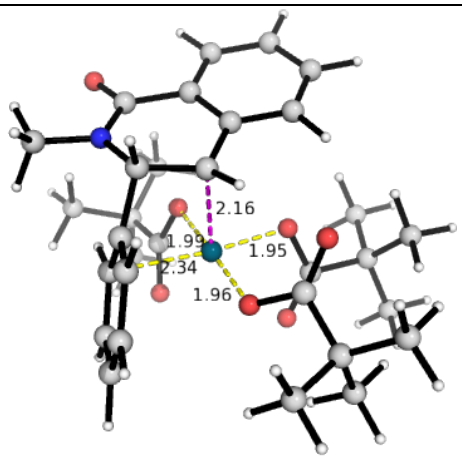	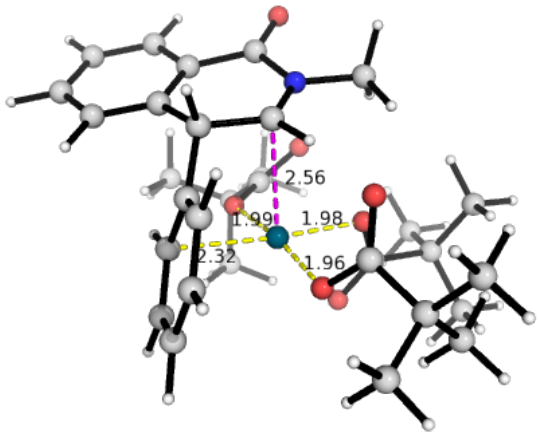

Figure 7.7. TS structures and two key intermediates for the carbopalladation/electrophilic palladation step.

The C–C bond formation step, for this mechanistic possibility, is both TOF-determining and regio-determining. The C–C coupling at C4, **H-C4-ts3**, has a lowest activation barrier, at 23.9 kcal mol^{-1}, whereas the C3 counterpart, **H-C3-ts3**, is 0.8 kcal mol^{-1} higher. This small difference in the energy barriers makes it difficult to distinguish the chemical selectivity between these two sites. This translates to roughly 3:1 regioselectivity using simple TST, although, the experimentally observed C4:C3 arylated product is 78:1. We can see from Figure 7.7 that the Pd–C bond in C4-selective TSs all have longer bond length (ranging from 2.11Å to 2.27Å) than the Pd–C bond in C3-selective TSs (from 2.04Å to 2.08Å). This is because in C3 TSs, there is electron donation from the N-atom

of the isoquinolone to the electrophilic Pd-centre, giving rise to a significant Pd–C4 bond formation as the C3-carbon undergoes C–C bond formation. This is a typical electrophilic palladation step as electron density flows from the N atom of the substrate to form the C4–Pd bond. For C4-selective TSs, less electron density is donated from C3-position of isoquinolone to Pd-centre, as an electrophilic C–C bond formatoin occurs at the C4-position due to the high electron density at this position. The resulting positive charge in the substrate is stabilised on the N-atom of the isoquinolone heterocycle. This has implications for the subsequent step for product formation. The C4-selective intermediate after the C–C bond formation, **H-C4-int4**, which has non-covalent Pd–C bond (2.56Å), can undergo a facile outer-sphere deprotonation by a ligand molecule (**H-C4-ts4**, Figures 7.6 and 7.7) to give the final arylated isoquinolone product. This low-barrier deprotonation step (1.5 kcal mol^{-1}) occurs after the TDTS and is thus consistent with the absence of ^{2}H primary KIE at C4-proton experimentally (Scheme 7.3 (a)).

On the other hand, the C3-selective intermediate, **H-C3-int4**, formed after carbo-palladation, has a formed Pd–C bond (2.16Å) which needs to undergo β-hydride elimination to form the arylated product (TS searches for deprotonation step failed to yield any result). As seen in Chapter 5, in such systems, the requisite C–H bond has to be brought to interact agostically with the Pd-centre before β-hydride elimination can occur. In this case, the C3-product is disfavoured, as the requisite H-atom cannot be brought to interact with the Pd-centre agostically without unduly strain and is very unfavourable.

The TSs for carbopalladation at C8-position, **H-C8-ts3** and **H-C8-ts3'** are at least 12.0 kcal mol^{-1} higher, making these much less favourable. For C8-functionalisation, the TS for the carbopalladation step with the carbonyl group coordinating to the Pd-centre could not be found.

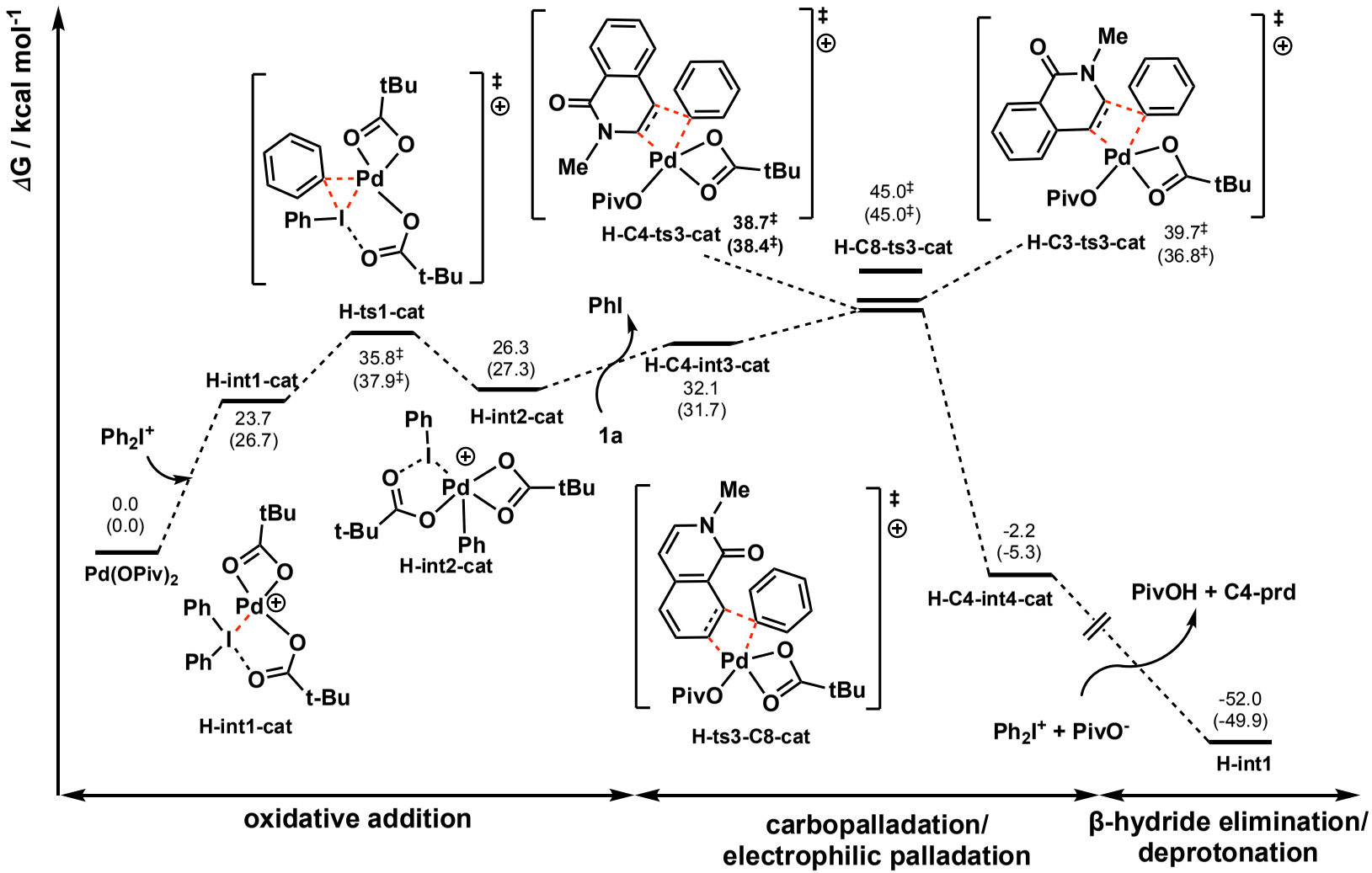

Figure 7.8. Gibbs energy profile for Pd(II)-catalysis via cationic Heck-type mechanism.

The overall energetic span of 23.9 kcal mol^{-1} for the present mechanistic possibility is lower than the CMD–OA–RE mechanism (Figure 7.2) with a span of 26.1 kcal mol^{-1} and is kinetically more feasible.

We further checked that the Pd(II)/Pd(IV) cationic pathway (Figures 7.8 and 7.9), with an energetic span of 38.7 kcal mol^{-1}, is not competitive, again as the overall cationic character of the intermediates/TSs is destabilised in the present non-polar solvent system and is thus kinetically disfavoured. The C–C bond formation step is the same as those for the neutral pathway: **H-C4-ts3-cat** proceeds via electrophilic C–C bond formation, with a Pd–C3 bond length of 2.28 Å whereas **H-C3-ts3-cat** proceeds via electrophilic palladation at C4 and C3–C_{Ph} bond formation, with a Pd–C4 bond length of 2.12 Å.

H-ts1-cat	**H-C4-ts3-cat**	**H-C3-ts3-cat**
35.8‡ (37.9‡)	38.7‡ (38.4‡)	39.7‡ (36.8‡)
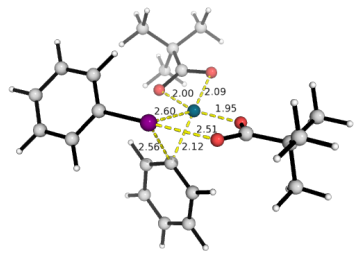	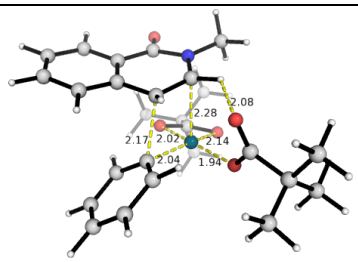	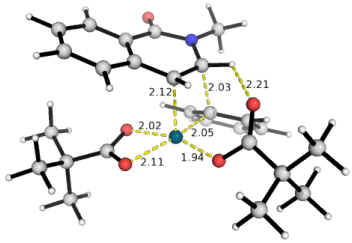
H-C8-ts3-cat	**H-C8-ts3'-cat**	**H-C8-ts3''-cat**
45.0‡ (45.0‡)	54.9‡ (55.9‡)	52.8‡ (56.8‡)
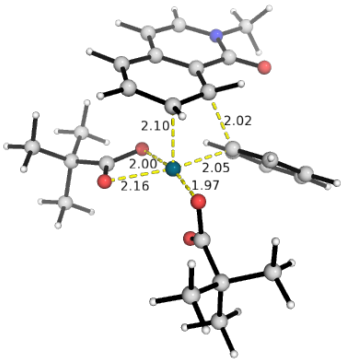	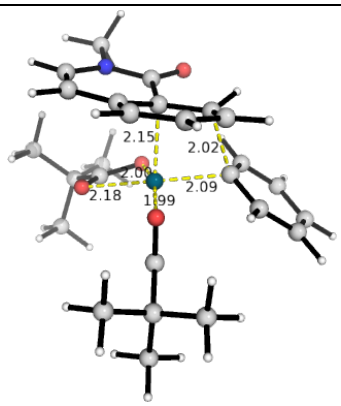	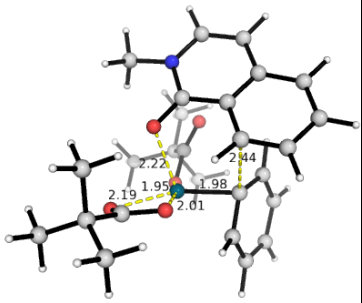

Figure 7.9. Optimised geometries for key TSs in via cationic Heck-type mechanism.

7.3.5 Pd(II)/Pd(IV) cycle: Oxidative addition, C–H activation followed by reductive elimination

Here we consider the Pd(II)/Pd(IV) mechanistic cycle in which the reaction proceeds with firstly OA, followed by ligand-assisted C–H activation via CMD and finally RE. The OA step is the same as those discussed in subsection 7.3.4. The neutral pathway is considered, as the cationic OA step is much less favoured, as shown previously (Figure 7.8). The Gibbs energy profile for this mechanistic possibility is given in Figure 7.10 with the key TS structures given in Figure 7.11. For this mechanism, the OA step is the overall TDTS, giving an energetic span of 21.3 kcal mol^{-1}; this is lower than the other two possibilities discussed above (subsection 7.3.3, CMD–OA–RE at 26.1 kcal mol^{-1} and subsection 7.3.4, OA–electrophilic palladation/carbopalladation–deprotonation/β-H elimination at 23.9 kcal mol^{-1}). The regio-determining step, however, is the subsequent C–H activation step via CMD. As the C–H activation step is not the TDTS (and occurs after it), there is an absence of primary ^{2}H KIE, in agreement with experimental measurements (Scheme 7.3 (a)). The low percentage of H/D exchange/scrambling (32%, Scheme 7.3 (b)) in the absence of diaryliodonium salt observed experimentally can arise from C4-selective C–H activation via electrophilic palladation followed by deprotonation as discussed earlier.

The C–H activation at C4-position has the lowest barrier (16.3 kcal mol^{-1}, from **H-int2** to **HC-C4-ts3**, since the reverse from **H-int2** to **H-int1** has a higher barrier of 18.3 kcal mol^{-1}), whereas the C3–H activation TS (**HC-C4-ts3**), has a barrier that is 7.1 kcal mol^{-1} higher. In TS **HC-C4-ts3**, the C–H activation proceeds via electrophilic CMD[608,609] where some electron flows from the electron rich N-atom of the isoquinolone to the electrophilic Pd-centre, as evident from the shorter Pd–C4 bond in **HC-C4-ts3** (2.12 Å) than in **HC-C3-ts3** (2.20 Å) (Figure 7.11).

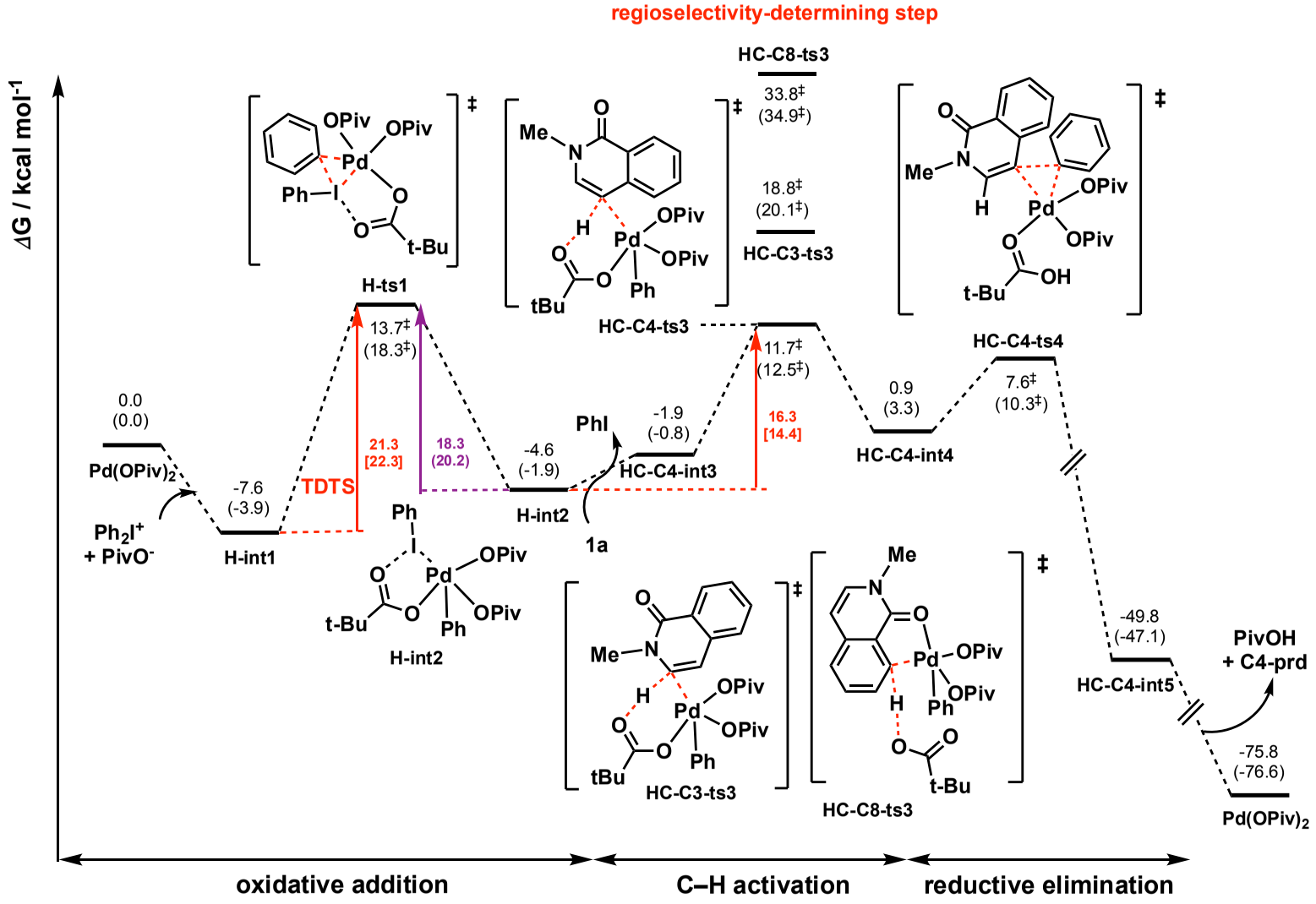

Figure 7.10. Gibbs energy profile for Pd(II)-catalysis via OA, followed by CMD and RE in a neutral pathway.

HC-C4-ts3	HC-C4-ts4	HC-C3-ts3
11.7‡ (12.5‡)	7.6‡ (10.3‡)	18.8‡ (20.1‡)
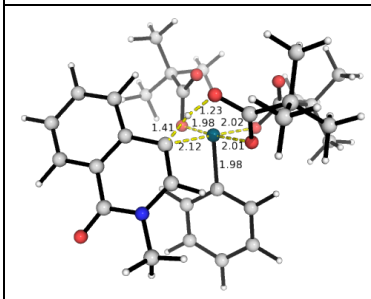	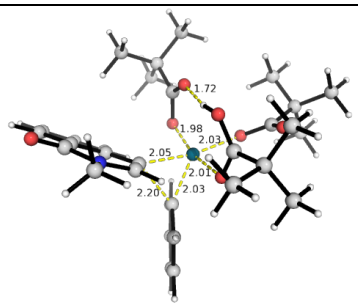	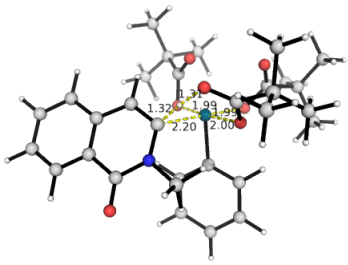
HC-C8-ts3	**HC-C8-ts3-c2**	**HC-C8-ts3-cat**
33.8‡ (34.9‡)	35.0‡ (37.4‡)	39.7‡ (40.5‡)
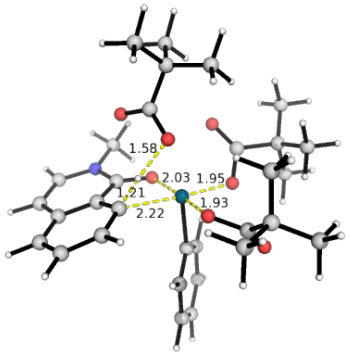	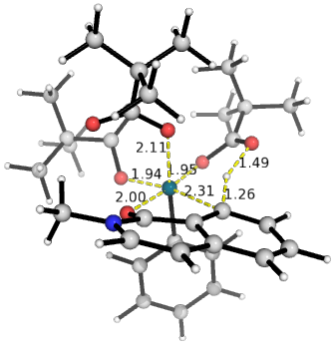	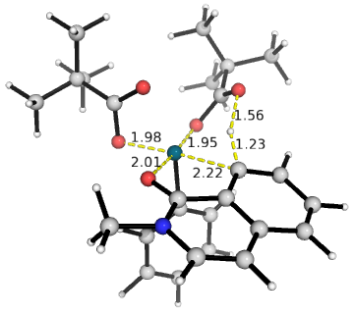

Figure 7.11. Optimised geometries for key TSs in via neutral OA– CMD–RE mechanism.

The C8–H activation is again unfavourable; both the TSs via CMD carried out by a coordinating (**HC-C8-ts3-c2**) and non-coordinating (**HC-C8-ts3**) pivalate ligand and the TS via a cationic pathway (**HC-C8-ts3-cat**) have higher activation barriers (Figure 7.11). The steric and electronic factors influencing these regioselectivies are likely the same as those discussed in subsection 7.3.3.1. That is, C4-position is favoured due to better orbital interaction and least steric hindrance, despite C4–H bond being the strongest amongst all.

7.3.6 Pd(0)/Pd(II) cycle: Heck-type mechanism

In the light of potential Pd(0) involvement in similar Heck-type mechanism using Pd(II) precatalyst,[438] we performed DFT calculations to investigate these pathways, both neutral and cationic, although we note that the reaction conditions here are not reducing as in

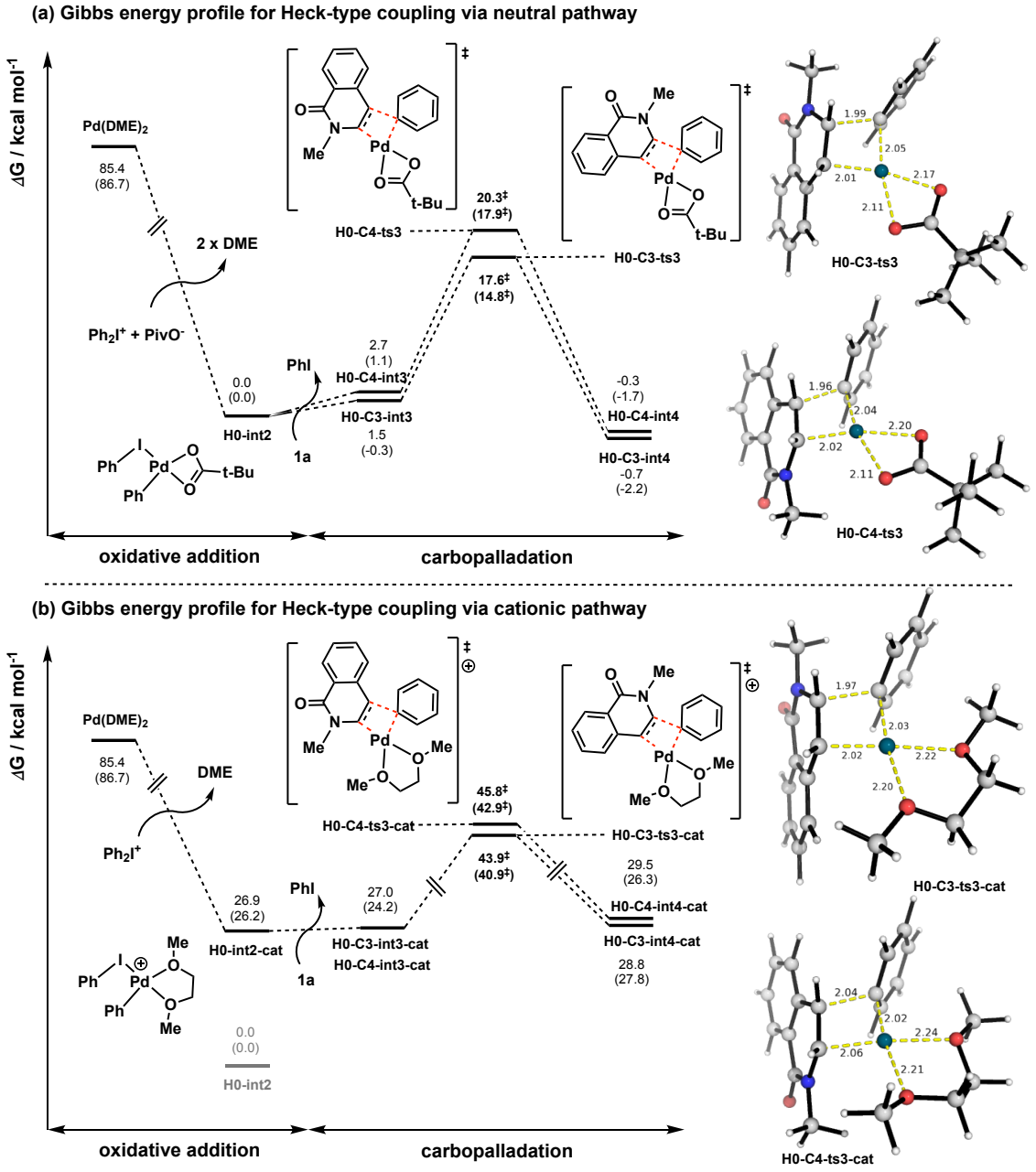

Figure 7.12. Gibbs energy profiles for the Heck-type C–C coupling using Pd(0) as active catalyst. (a) Neutral pathway (b) Cationic pathway. A common energy zero **H0-int2** is used for both pathways.

those needed to typically generate the active Pd(0) species from the *in situ* reduction of Pd(II) salts by, for example, the action of phosphines,[610–612] amines,[613] hydride sources,[614,615] or other additives.[616–620] We found that a Heck-type mechanism involving an active Pd(0) catalyst gives rise to C3-selective (over C4) arylated isoquinolone for

both neutral and cationic pathways (Figure 7.12).[3] Both TSs have similar Pd–C bond lengths (2.01 to 2.02 Å), indicating that both occur via carbopalladation, i.e., not electrophilic palladation followed by C–C bond coupling. This is perhaps due to the fact that Pd(0) is already electron-rich such that electrophilic attack on the metal from the N-atom of the substrate is much less likely. The cationic pathway, when compared to the neutral pathway, is much less thermodynamically favourable, as the formation of cationic TSs and intermediates are not stabilised by the non-polar dimethoxyethane solvent.

Iridium Catalysis

7.3.7 Ir(III)/Ir(V): C–H activation, oxidative addition followed by reductive elimination

The mechanism for C8-selective arylation of isoquinolone using Ir was investigated. We consider herein the Ir(III)/Ir(V) catalytic cycle, which has been shown,[608,621–625] both experimentally and computationally, to be operative in Ir-catalysed reactions. The neutral mechanistic pathway was first considered; the reaction profile is given in Figure 7.13. This neutral pathway involving a charge-balanced inner coordination sphere of Ir(III) complex was found to be C4-selective, with a C–H activation barrier of 27.0 kcal mol^{-1} (**C4-ts20**). This TS has one of the coordinating acetate ligands carrying out the CMD step via a 6-membered ring transition structure (Figure 7.14). The alternative TS where the acetate anion having O-atom both coordinating to Ir and carrying out CMD at the same time, via a 4-membered ring, is much less favoured (**C4-ts20b**, 38.9 kcal mol^{-1}), as seen previously in the Pd-catalysed system. This is commonly the case in many systems[608] (also in those observed in chapter 4).

[3] The TS for the OA step was not found – an optimisation of diaryliodonium in the presence of Pd(0)–OPiv gives the insertion product **H0-int2** directly. The OA step is facile likely because OA into electron-rich Pd(0) is easy.

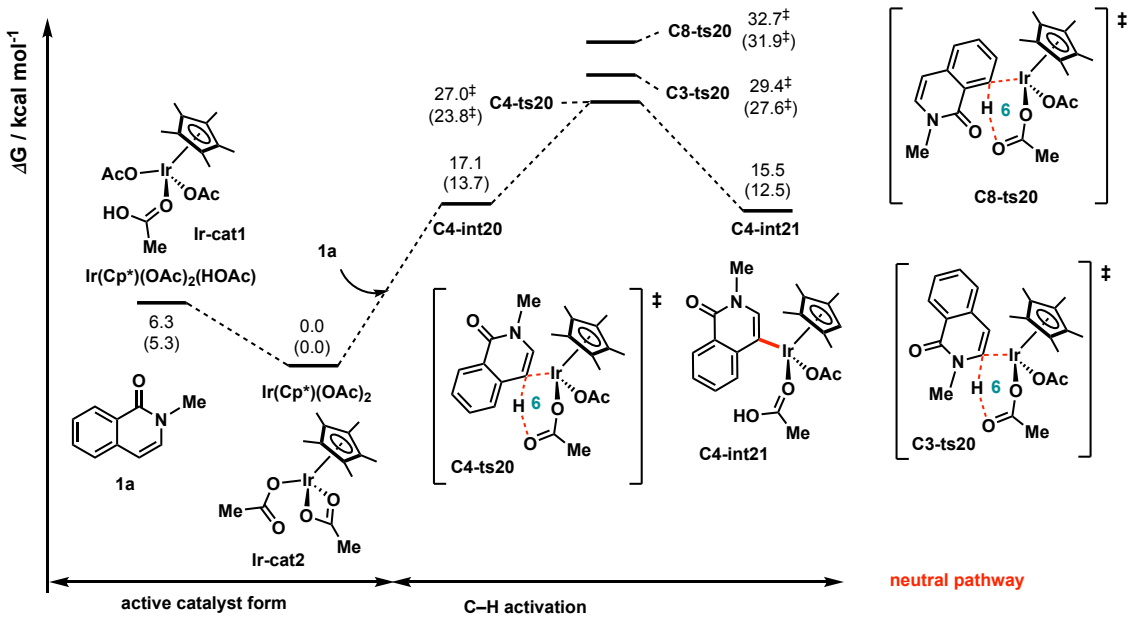

Figure 7.13. Gibbs energy profile for Ir-catalysed C–H activation via neutral pathway.

C4-ts20	C4-ts20b	C3-ts20
27.0‡ (23.8‡)	38.9‡ (36.5‡)	29.4‡ (27.6‡)
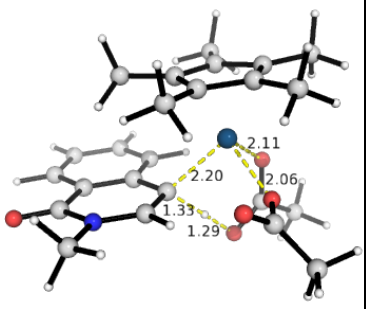	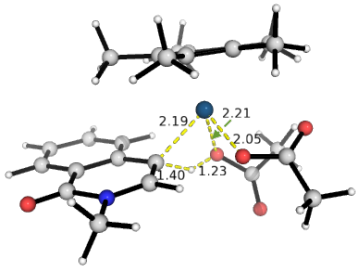	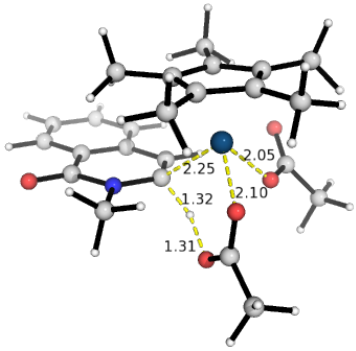
C8-ts20	**C8-ts20b**	**C8-ts20c**
32.7‡ (31.9‡)	44.0‡ (42.0‡)	44.7‡ (42.3‡)
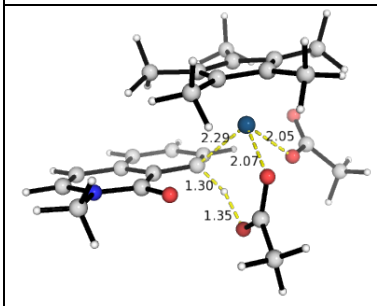	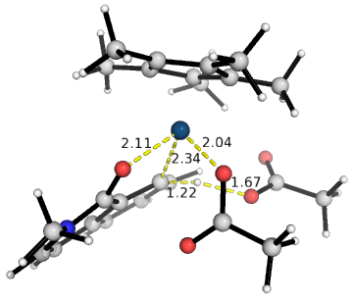	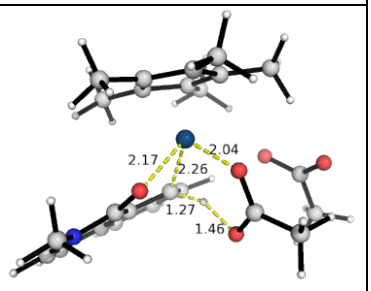

Figure 7.14. Optimised geometries for key TSs in via neutral OA– CMD–RE mechanism.

For C8–H activation, the TS with the same ligand coordination mode as **C4-ts20** has the lowest barrier, (**C8-ts20**, 32.7 kcal mol^{-1}); in this TS, the isoquinolone carbonyl-O atom does not coordinate to the Ir-centre. In cases where the carbonyl-O is coordinated to the Ir-centre (**C8-ts20b** and **C8-ts20c**), the activation barriers are much higher and less favoured (Figure 7.14). **C8-ts20c** is disfavoured likely because one of the acetate anions does not participate in the inner coordination sphere of the catalytic complex, so that there is no enthalpic gain for its inclusion, which occurs at an unfavourable entropic cost. This neutral pathway is less likely as the regioselectivity does not agree with the experimentally observed product.

Mounting evidence for Ir(III)-catalysed systems suggests the involvement of a cationic Ir-species in such transformations.[608,626–632] Indeed, we found the cationic pathway to be in agreement with the experimentally observed regioselectivity (Figure 7.15). In this mechanism, the reaction proceeds via ligand-assisted C–H activation, followed by OA and subsequent RE. We consider the catalyst **Ir-cat**$^{+}$ as the active form (one of the coordinating ligands is likely acetic acid, as this is the solvent used for the present transformation). The C–H activation is not the TDTS as the reaction barrier for OA following the CH activated complex (**C8-ts12-g1**, 32.2 kcal mol^{-1}) is much higher than the reverse barrier going back to unactivated complex **C8-int10** (24.7 kcal mol^{-1}); it is however, regio-determining (see subsection 7.3.7.1 for a detailed discussion). This, coupled with the relatively low barrier for C–H activation (**C8-ts10**, 22.6 kcal mol^{-1}), implicates that the C–H activation step is reversible with relative ease, consistent with experimentally observed reversible and fast C–H cleavage (> 98% H/D exchange in 10 mins at 100ºC).

The OA step (**C8-ts12-g1**) is the overall TDTS of this reaction, with a barrier of 32.2 kcal mol^{-1} (see subsection 7.3.7.2 for the consideration of all geometric and conformational isomers of this TS). The loss of PhI from the OA product is entropically favoured. Two possible geometric isomers arising from ligands occupying different coordination sites of the Ir-centre can be distinguished: one has the phenyl group and the C8 of isoquinolone not on adjacent coordination sites (denoted **g1**) and the other has these two on adjacent coordination sites (denoted **g2**) (Figures 7.15 and 7.17). Despite the oxidative addition products **C8-int14-g1** and **C8-int14-g2** differing in the coordination modes of the ligands, they both yield RE TSs (**C8-ts14-g1** and **C8-ts14-g2**) having the phenyl group and C8-atom of isoquinolone occupying adjacent coordination sites[4] (see Figure 7.18 for the optimised structures). The RE step forming the C–C bond is both kinetically and thermodynamically favourable: the activation barrier for this step is 9.0–11.3 kcal mol^{-1} and that the formation of the C8-arylated product is highly exergonic (**C8-int15-g1**, at -61.5 kcal mol^{-1} and **C8-int15-g2**, at -58.1 kcal mol^{-1}) (Figure 7.15).

Thus, for the present transformation by Ir-catalysis, our computational studies implicate a cationic pathway where the oxidative addition step is the TDTS, with a relatively facile reductive elimination step; the regio-determining C–H activation step is reversible and gives rise to the absence of ^{2}H primary KIE consistent with experimental findings.

[4] The TS structure **C8-ts14-g1** is correctly connected to **C8-int14-g1** and **C8-int15-g1** via IRC analyses. The initial TS search at MN15/def2-SVP level of theory for **C8-ts14-g1** shows how the phenyl group displaces the acetate ligand as the latter moves away from its original coordination site so that the phenyl group can occupy the adjacent coordination site to the C8-atom of isoquinolone, for subsequent reductive coupling (see *Gaussian 16* output file *C8-int14-ts-def2svp.log*). It is therefore reasonable to assume that the two geometric isomers arising from different coordination modes (**C8-int14-g1 and C8-int14-g2**) can easily interconvert, as the acetate ligand displaces the phenyl group and moves it to the adjacent coordination site.

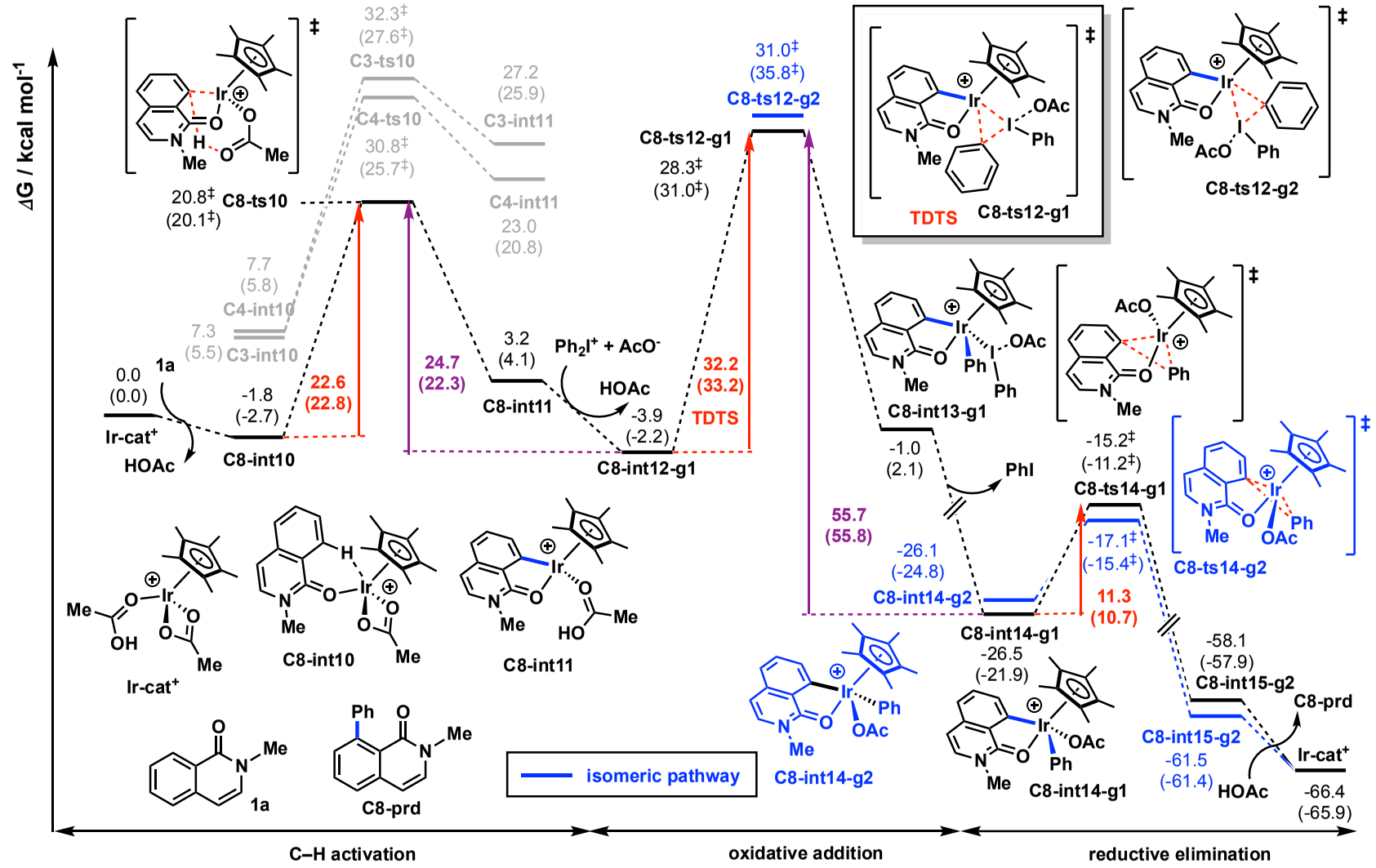

Figure 7.15. Gibbs energy profile for Ir(III)-catalysis via the cationic pathway.

7.3.7.1 Ir(III)/Ir(V): Cationic pathway C–H activation

Different coordination modes for the C–H activation step were considered. The results are given in Figure 7.16. For C–H activation at all sites, the presence of an extra molecule of acetic acid in the coordination sphere of these TSs (**Cx-ts10b, x=3,4,8**) increases the activation barrier as compared to the ones without (**Cx-ts10, x=3,4,8**), potentially due to entropic penalty associated with the introduction of an extra ligand. **C8-ts10** has the lowest activation barrier while **C4-ts10** and **C3-ts10** are, respectively, 10.0 and 11.5 kcal mol^{-1} higher and disfavoured; the coordination of isoquinolone carbonyl-O atom to Ir-centre in **C8-ts10** helps in lowering its activation barrier without the need of an extra acetic acid ligand to complete the coordination sphere of the metal (Figure 7.16). Additionally, the C–H activated intermediates for C3- (**C3-int11**,27.2 kcal mol^{-1}) and C4-selective (**C4-int11**, 23.0 kcal mol^{-1}) activation are thermodynamically unfavourable than for C8-selective activation (**C8-int11**, 3.2 kcal mol^{-1}, Figure 7.15).

The C8-selective activation is "directed" in this case where the isoquinolone carbonyl-O atom coordinates to the Ir-centre, as the CMD TS has the correct geometry for C–H activation: the acetate ligand carrying out the CMD step is perpendicular to the isoquinolone ring plane (**C8-ts10**, Figure 7.16), making it conducive for CMD to be carried out without unduly ring strain. This resembles **C4-ts1** in the Pd-catalysed C–H activation (Figure 7.4) and the TS structures for ligand-assisted CMD in Chapters 5 and 6 (**ts-1'**, Figures 5.2 and 6.3). This is in contrast to the unfavourable "directed" path in Pd-catalysis observed earlier (**C8-ts1**, Figure 7.4), where the tetra-coordinating Pd(II) requires that the inner sphere Pd-coordinating ligand carrying out the CMD and the isoquinolone ring lie on the same plane, making it geometrically unfavourable for C–H

activation. Thus, one of the reasons for the different regioselectivies observed using these two different catalysts arises from the different coordination modes of these metals.

C8-ts10	**C8-ts10b**	**C4-ts10**
20.8‡ (20.1‡)	37.3‡ (36.3‡)	30.8‡ (25.7‡)
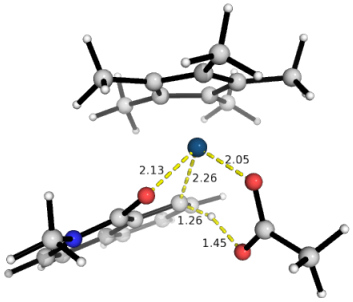	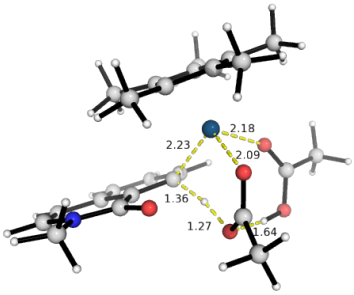	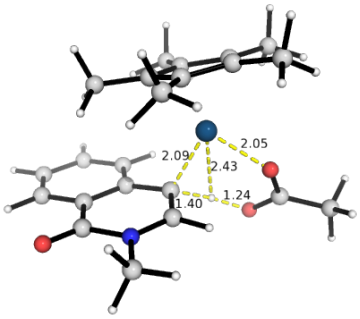
C4-ts10b	**C3-ts10**	**C3-ts10b**
34.7‡ (31.5‡)	32.3‡ (27.6‡)	37.6‡ (33.5‡)
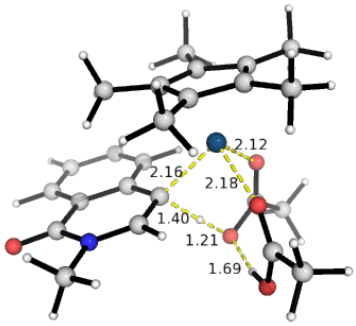	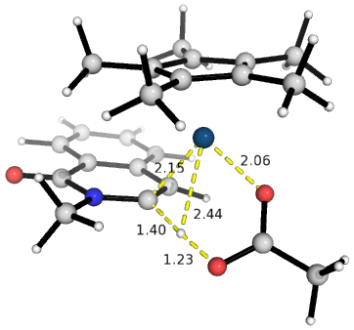	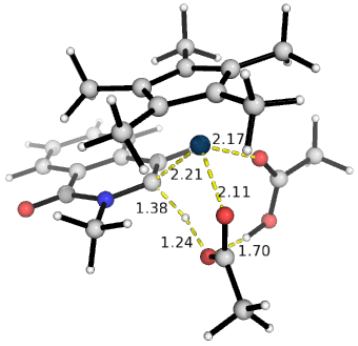

Figure 7.16. Optimised structures of TSs of C–H activation at different sites by cationic iridium catalysis.

Comparing the C–H activation TS at C4-position (**C4-ts10**) with those at C3- (**C3-ts10**) and C8-position (**C8-ts10**), we once again see that the Pd–C_{ipso} bond in **C4-ts10** is the shortest (2.09 Å) when compared to **C3-ts10** (2.15 Å) and **C8-ts10** (2.26 Å) due to some electrophilic C–H activation as the electron density flows from the electron-rich N-atom of isoquinolone to the electrophilic Ir-centre. This is the same as the electrophilic CMD[608,609] with electron-rich substrate observed earlier for the Pd-catalyst (subsection 7.3.5).

7.3.7.2 Ir(III)/Ir(V): Cationic pathway OA and RE steps

Different coordination geometries for the OA step were carefully considered (Figure 7.17). The ligand used for computations was the strong-coordinating acetate anion since acetic acid is the solvent used experimentally; chloride or the weakly coordinating BF_4^- anion as ligand for Ir-metal are not considered. Two geometric isomers arising from ligands occupying different coordination sites are possible, as discussed previously. For geometric isomer **g1**, **C8-ts12-g1** and **C8-ts12-g1-c2** are really similar in structure; they differ in the orientation of the Cp* ligand and a minor difference in the acetate ligand coordination. The non-covalent interaction between the O-atom of the acetate ligand and the H-atom of the hydrocarbon backbone, as seen by the shorter bond length (2.17Å), in **C8-ts12-g1** favours this TS slightly. Geometric isomers **g2** are slightly less favoured; the lowest such structure (**C8-ts12-g2**; 30.8 kcal mol^{-1}) is 2.5 kcal mol^{-1} higher than **C8-ts12-g1** at 28.3 kcal mol^{-1}.

The activation barriers for all these TSs are rather high, and we tried to investigate if any haptotropic shift from η^5 to η^3 to η^1 coordination mode of the Cp* ligand allowing octahedral geometry of Ir(III) complex (d^6 electronic configuration) would lower the activation barriers; such ring slippage reactions have been observed in various Ir-based systems.[633–636] In our investigations, however, all these ring-slipped η^1-coordinated Cp*Ir(III) complexes (**C8-ts12a** to **C8-ts12e**) all have higher activation barriers (Figure 7.17), perhaps unsurprising as these haptotropic shifts causes the Cp* ligand to lose ring aromaticity. The η^3-coordinated Cp*Ir(III) complexes were not found, in accordance with the observation that for d^6 complexes, η^5 to η^3 haptotropic shift is mostly disfavoured.[636]

For both geometric isomers arising from different coordination modes, a facile RE TS that is both kinetically and thermodynamically favourable can be found (Figure 7.15).

C8-ts12-g1	C8-ts12-g1-c2	C8-ts12-g1-c3
28.3‡ (31.0‡)	29.3‡ (32.3‡)	29.5‡ (32.6‡)
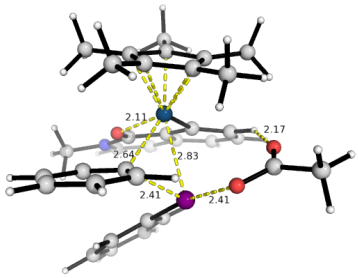	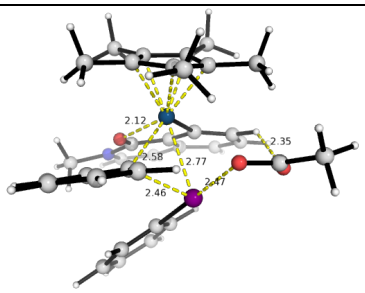	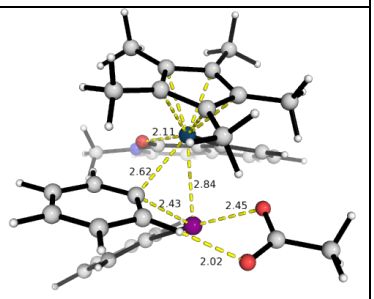
C8-ts12-g1-c4		**C8-ts12-g2**
32.4‡ (38.9‡)		30.8‡ (37.0‡)
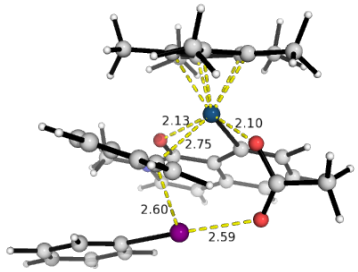		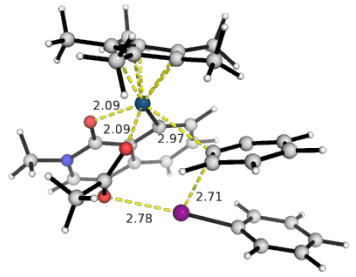
C8-ts12-g2-c2	**C8-ts12-g2-c3**	**C8-ts12-g2-c4**
31.0‡ (35.8‡)	31.1‡ (37.6‡)	43.5‡ (44.6‡)
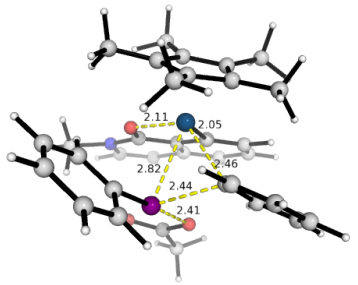	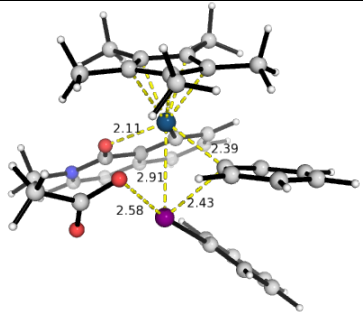	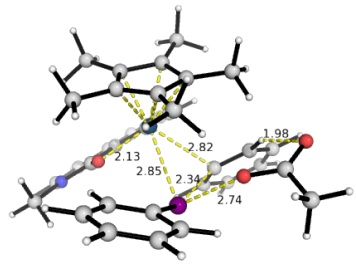
	C8-ts12a	**C8-ts12b**
	65.9‡ (71.8‡)	68.0‡ (73.7‡)
	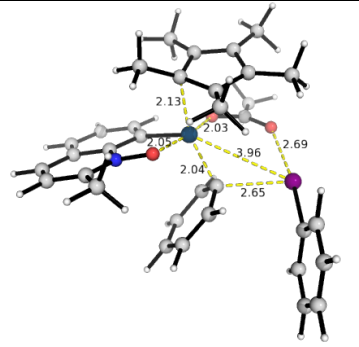	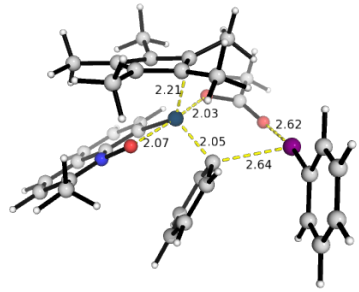

C8-ts12c	C8-ts12d	C8-ts12e
69.4‡ (75.4‡)	69.9‡ (74.8‡)	86.4‡ (92.0‡)
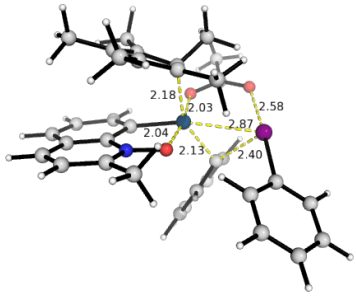	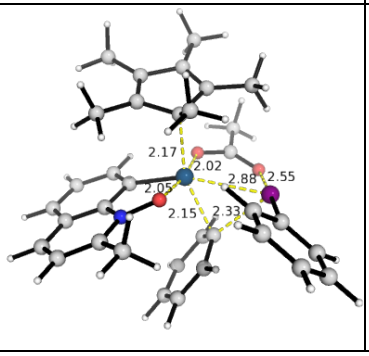	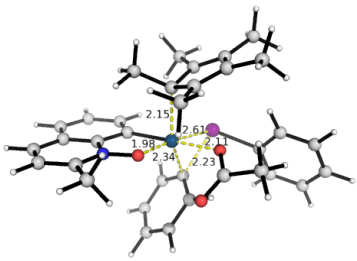

Figure 7.17. Optimised structures of geometric and conformational isomers of TSs of OA step by cationic iridium catalysis.

C8-int14-g1	C8-ts14-g1	C8-int15-g1
-26.5 (-21.9‡)	-15.2‡ (-11.2‡)	-58.1 (-57.9)
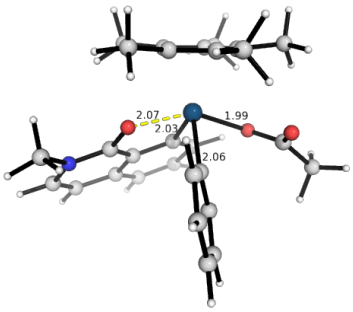	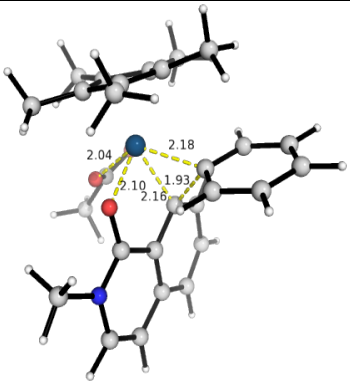	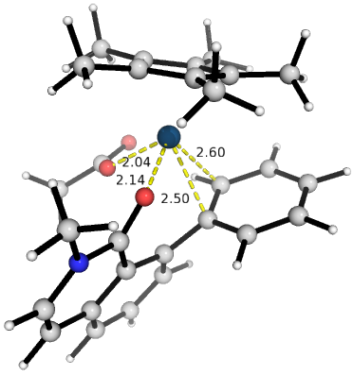
C8-int14-g2	**C8-ts14-g2**	**C8-int15-g2**
-26.1 (-24.8)	-17.1‡ (-15.4‡)	-61.5 (-61.5)
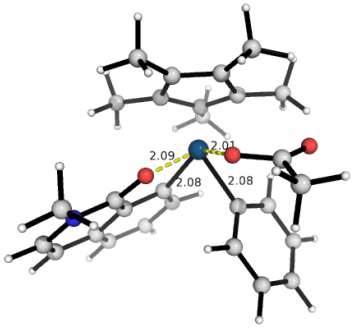	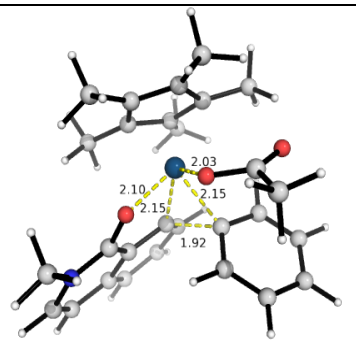	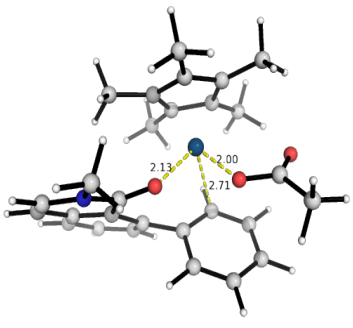

Figure 7.18. Optimised structures of geometric isomers from the OA and RE by cationic iridium catalysis.

These RE TSs (**C8-ts14-g1** and **C8-ts14-g2**) have a low barrier of 9.0 – 11.3 kcal mol^{-1}. The optimised structures are given in Figure 7.18. The RE products are highly thermodynamically stable and its release from the Ir-centre is exergonically downhill and thermodynamically favourable (Figure 7.15).

7.3.8 Ir(III)/Ir(V): oxidative addition before C–H activation

To see if a similar reaction mechanism of OA followed by C–H activation and then RE or followed by Heck-type carbometallation is operative for the present transformation, we explored the cationic OA step as the first step of reaction. We found that these give an activation barrier that is at least 37.0 kcal mol^{-1} (Figure 7.19), which is much higher than the energetic span as seen in Figure 7.15 (32.2 kcal mol^{-1}). Thus, this mechanism is less feasible than the one discussed previously.

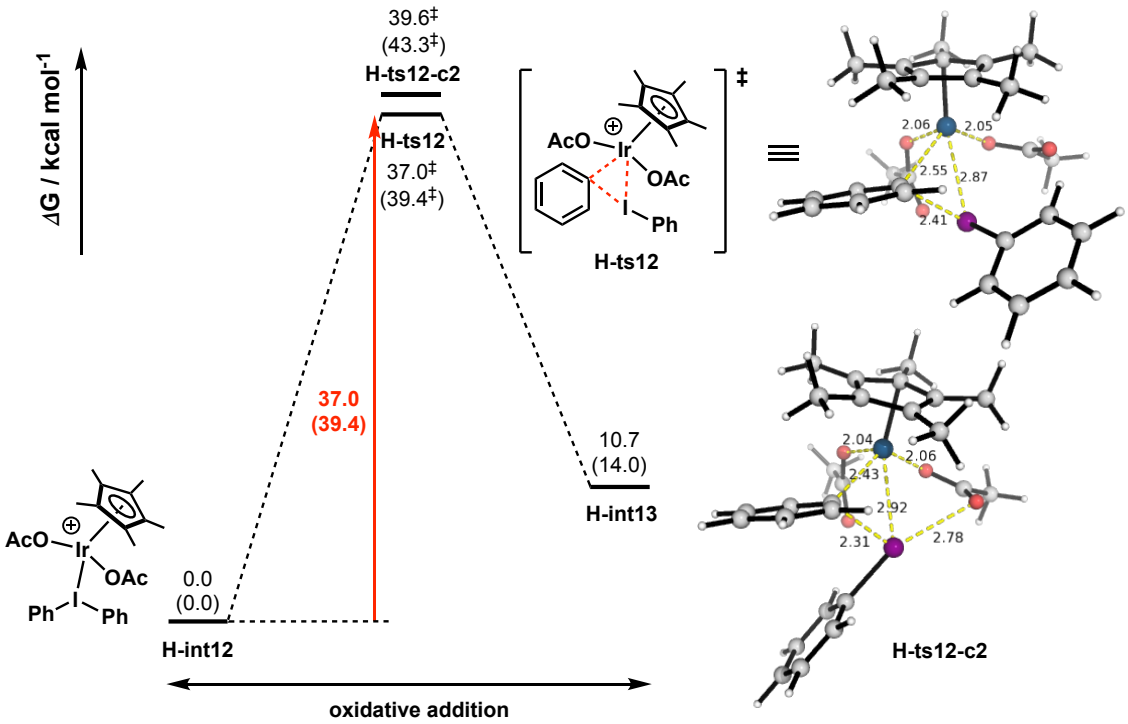

Figure 7.19. Oxidative addition as the first step of cationic iridium catalysis.

7.3.9 Proposed catalytic cycles

Based on our combined experimental and computational investigations, we propose the following mechanistic cycles for catalyst-controlled C4/C8-arylation of isoquinolone (Scheme 7.4). The Pd-catalysis occurs via a neutral pathway where first a TOF-determining oxidative addition of diaryliodonium salt occurs. This is followed by regioselective C4–H activation via a CMD mechanism, forming Pd–C bond. Reductive elimination then follows, giving the C4-arylated isoquinolone. As the C–H activation step occurs after the TDTS, there is no primary ^{2}H KIE observed in the experimental intermolecular competition studies using separated deuterated and non-deuterated isoquinolones (k_H/k_D = 1.01, Scheme 7.3 (a)). The low percentage of H/D exchange/ scrambling (32%, Scheme 7.3 (b)) in the absence of diaryliodonium salt possibly result from C4-selective C–H activation via electrophilic palladation followed by deprotonation as discussed in subsection 7.3.3. The end product is thermodynamically stabilised as a strong C–C σ-bond is formed. This neutral pathway is favoured in non-polar solvents such as 1,2-dimethoxyethane used in the reaction.

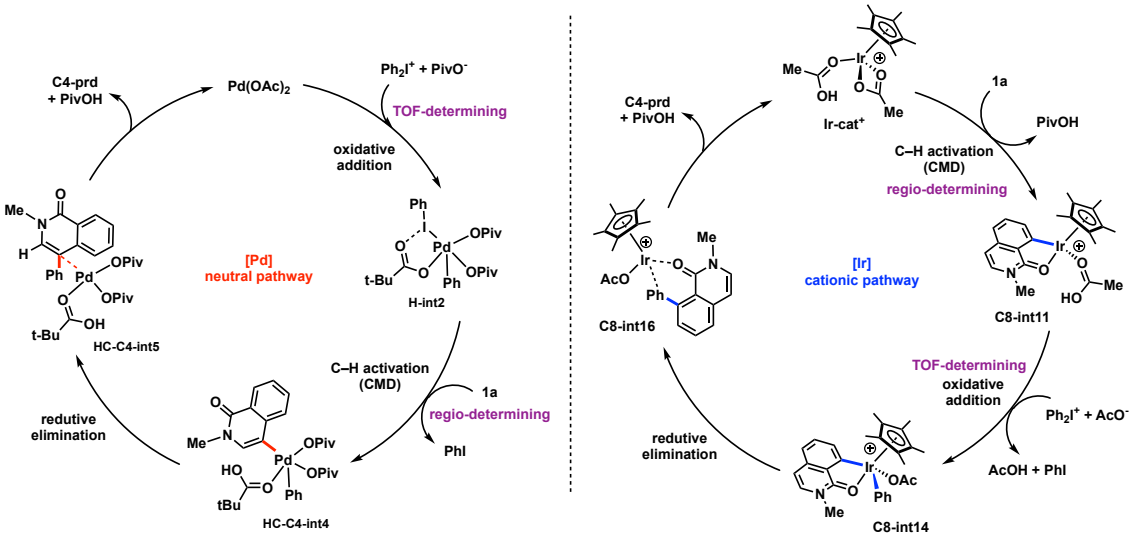

Scheme 7.4. Proposed mechanistic cycles for regioselective arylation of isoquinolone using **Left:** Pd-catalysis, and **Right:** Ir-catalysis.

For Ir-catalysis, the cationic pathway was found to be operative; this reaction is more favoured in polar solvent (acetic acid) where the cationic TSs and intermediates can be stabilised. C–H activation is fast and reversible whereas the OA step is the overall TDTS. A facile reductive elimination follows to give thermodynamically stabilised C8-arylated product due to the formation of a strong C–C σ-bond.

7.4 Conclusions

We herein employed DFT calculations to study the catalyst-controlled regiodivergent arylation of isoquinolone at C4- vs C8-position. Two different mechanisms are proposed. C4-selective arylation is promoted by Pd(II)-catalyst following a sequence of oxidative addition of diaryliodonium and then C–H activation and finally reductive elimination. C8-selective arylation is promoted by Ir(III)-catalyst undergoing a cationic pathway where the oxidative addition is the overall rate-determining step; the cationic C(sp^2)–H activation is the regio-determining step although it is fast and reversible. The mechanistic insights gained from the present studies shed light on the factors controlling regio-selectivity in different TM catalytic systems. The tetra-coordinating nature of Pd(II) dictates that the C8–H activation via CMD and simultaneous carbonyl oxygen atom coordination to Pd-centre is unfavourable, due to unfavourable geometric constraints; the "directed" pathway in the present C8-arylation is thus unfavourable. For Ir-catalysis, the carbonyl oxygen atom directed C8–H activation is favourable, since this has the right geometry as the coordinating ligand can carry out CMD at right angle to the plane of isoquinolone ring, as a result of the tetrahedral coordination mode of Ir-centre. The present findings are likely translatable to similar systems such as those work by Patil and co-workers on Au vs Rh regiodivergent alkynylation of isoquinolone (Scheme 7.1 (c)). Similar mechanisms are expected to be operative in 2-pyridone functionalisations due to

similar steric and electronic influences as in isoquinolone. This broadly applicable understanding of catalyst-controlled regiodivergent functionalisation of a class of similar substrates will spur further development and applications of these transformations in chemical syntheses and materials design.

7.5 Future Work

7.5.1 Future experimental work

Further experimental work can be performed to validate the mechanistic picture presented in Figure 7.10 and Scheme 7.4 using ^{13}C KIE experiments. Specifically, the ^{13}C primary KIE using the $^{13}C/^{12}C$ natural abundance method by quantitative ^{13}C NMR developed by Singleton and co-workers[637,638] can be employed. This method relies on the fact that the starting material will become more enriched in ^{13}C at the positions with positive ^{13}C primary KIE during the course of reaction, such that an increase in the ratio of $^{13}C/^{12}C$ between the recovered material and the original starting material will result. The KIE can then be worked out from this ratio (R/R_0) and the fractional conversion of reagents (F) via

$$R/R_0 = (1-F)^{(1/\mathrm{KIE})-1} \tag{7.1}$$

$$\mathrm{KIE} = \frac{\log(1-F)}{\log\left[(1-F)R/R_0\right]} \tag{7.2}$$

This method has been successfully employed in a variety of catalytic mechanistic investigations.[599,639–647] For our proposed mechanism, we expect to see the presence of primary ^{13}C KIE at the *ipso*-Carbon of the phenyl group of the diphenyliodonium cation undergoing oxidative addition.

7.5.2 Future computational work

Although experimentally only C3-, C4- and C8-functionalisation of isoquinolone have been achieved, for completeness and to gain further insights into the factors determining regioselectivity, it will be useful, for our future work, to study the regioselectivity-determining step for each catalytic system at all carbon sites (additionally C5-, C6- and C7-site). Additionally, we expect the C3- vs C6- vs C5-functionalisation of 2-pyridone, as introduced in Scheme 7.1 (b) to undergo similar reaction mechanisms, it will therefore be interesting to verify this computationally using both Pd and Ir catalysts.

"Either this is madness or it is Hell." "It is neither," calmly replied the voice of the Sphere, "it is Knowledge; it is Three Dimensions: open your eye once again and try to look steadily."

— Edwin A. Abbott, Flatland: A Romance of Many Dimensions

8

Concluding Remarks

Computational chemistry has far-ranging applications, such as in enzyme catalysis,[210,648–652] protein structure predictions and designs,[653–655] and materials science.[42,656] It has evolved over the years to become a mature branch of chemistry and an indispensable tool in rationalising experimental observations and elucidating reaction mechanisms. In this thesis, we have presented a number of case studies on how one particular tool in computational chemistry, the application of density functional theory (DFT), can be applied to study both organic and organometallic catalysis. In Chapters 2, we presented the DFT study of a small molecular system involving oxidant-promoted, SET-catalysed cyclobutanation. In Chapter 3, we looked at the application of DFT to the study of the catalytic mechanism of a novel hydroxyphosphine catalyst, designed by our experimental

collaborators, which has higher molecular complexity than the organic system present in Chapter 2. We then progress in molecular complexity to show how modern DFT functionals can be used to study sophisticated transition-metal catalysed systems in Chapters 4 to 7, focusing on the area of C–H functionalisations. In all these systems, chemical selectivities are explored and molecular origins contributing to the selective experimental outcomes are rationalised, with tools such as NBO, NCI and FMO analyses.

One of the challenges for the study of catalytic systems, especially for complex organometallic ones, as demonstrated in this thesis, is the complete/thorough conformational sampling of the TSs. The difficulty arises due to the difficult parametrisation of metals to give accurate force fields for dynamical conformational sampling. We have largely done this "by hand" and some chemical intuition, however, recent development in computational methodology, such as Stefan Grimme's xtb binding code,[657,658] which is a semi-empirical tight-binding method for efficient sampling of molecular geometries containing all spd-block elements (Z = 1–86), can be applied to molecular systems with more than 1000 atoms, a feat unachievable with DFT at current technological level.

Another challenge in computational modelling of homogeneous catalysis is the accurate translation of computed thermodynamics (Gibbs free energies) to predictive kinetic model for reaction selectivity. At present, we have considered how simple transition state theory (TST) can be used to estimate the relative rates and selectivity. However, as mentioned in Chapter 1, TST is an approximate theory that is only valid under certain assumptions. The predictions from simple TST can differ from experimental results due to a variety of non-classical influences such as quantum mechanical tunnelling and re-crossing, wavepacket "diffraction" and nonthermal energy distributions for reactive

intermediates. In many chemical systems, dynamic effects are implicated to play an important role in affecting product distribution.[659–666]

The present thesis only surveys predominantly DFT as an electronic structure method for exploring chemical reactivity and selectivity. There exist many computational methods, such as the empirical valence bond,[667,668] the hybrid quantum mechanics/classical mechanics (QM/MM),[669–673] and the wavefunction-in-DFT (WT-in-DFT) embedding,[674,675] for the study of complex systems. In this thesis, we have presented a few examples of how density functional theory (DFT), a popular technique, can be applied to study both organic and organometallic catalysis. The use of DFT in catalysis is, however, not without problems, as a plethora of functionals employing a variety of approximations exists; this thus requires practitioners of DFT calculations to make judicious choice of functional for their systems of interest. With continued DFT developments, deficiencies of earlier functionals, such as self-interaction error[54,186–191] and the lack of dispersion, have been partially fixed by, for example self-interaction correction[58,676] and addition of empirical dispersion.[53,205,677,678] On the theoretical and methodology development side, despite the fact that DFT cannot be systematically improved, modern DFT functional development continues to progress at an exciting pace. On the application side, the majority of computational studies has an explanatory character rather than predictive power. The elimination of expert influence in mechanistic elucidation and the need for predictive models in chemistry call for the development of automated reaction network discovery. To these purposes, machine learning (ML) has become increasingly popular as a tool for rapid exploration of chemical space.[679–683] The high quality experimental and *ab initio* data provide a shoulder upon which modern

development of data-driven techniques rest. The application of ML in chemistry is expected to accelerate reaction discovery and better catalyst design.

References:

(1) Straker, R. N.; Peng, Q.; Mekareeya, A.; Paton, R. S.; Anderson, E. A. Computational Ligand Design in Enantio- and Diastereoselective Ynamide [5+2] Cycloisomerization. *Nat. Commun.* **2016**, *7* (1), 10109.

(2) Pupo, G.; Ibba, F.; Ascough, D. M. H.; Vicini, A. C.; Ricci, P.; Christensen, K. E.; Pfeifer, L.; Morphy, J. R.; Brown, J. M.; Paton, R. S.; et al. Asymmetric Nucleophilic Fluorination under Hydrogen Bonding Phase-Transfer Catalysis. *Science* **2018**, *360* (6389), 638–642.

(3) Poree, C.; Schoenebeck, F. A Holy Grail in Chemistry: Computational Catalyst Design: Feasible or Fiction? *Acc. Chem. Res.* **2017**, *50* (3), 605–608.

(4) Thiel, W. Computational Catalysis-Past, Present, and Future. *Angew. Chem. Int. Ed.* **2014**, *53* (33), 8605–8613.

(5) Jover, J.; Fey, N. The Computational Road to Better Catalysts. *Chem.: Asian J.* **2014**, *9* (7), 1714–1723.

(6) Born, M.; Oppenheimer, R. Zur Quantentheorie Der Molekeln. *Ann. Phys.* **1927**, *389* (20), 457–484.

(7) Szabo, A.; Ostlund, N. S. Modern Quantum Chemistry: Introduction to Advanced Electronic Structure Theory; Dover Publications, Inc.: Mineola, 1996; pp 51–53.

(8) Dunning, T. H.; Jr., T. H. D. Gaussian Basis Sets for Use in Correlated Molecular Calculations. I. The Atoms Boron through Neon and Hydrogen. *J.*

Chem. Phys. **1989**, *90* (2), 1007–1023.

(9) Woon, D. E.; Dunning, T. H. Gaussian Basis Sets for Use in Correlated Molecular Calculations. III. The Atoms Aluminum through Argon. *J. Chem. Phys.* **1993**, *98* (2), 1358–1371.

(10) Woon, D. E.; Dunning, T. H. Gaussian Basis Sets for Use in Correlated Molecular Calculations. IV. Calculation of Static Electrical Response Properties. *J. Chem. Phys.* **1994**, *100* (4), 2975–2988.

(11) Woon, D. E.; Dunning, T. H. Gaussian Basis Sets for Use in Correlated Molecular Calculations. V. Core-valence Basis Sets for Boron through Neon. *J. Chem. Phys.* **1995**, *103* (11), 4572–4585.

(12) Sree Latha, G.; Durga Prasad, M. Lie-Algebraic Construction of Time Evolution Operator. Application to Intramolecular Vibrational Energy Relaxation. *J. Mol. Struct. Theochem* **1996**, *361*, 77–81.

(13) Prascher, B. P.; Woon, D. E.; Peterson, K. A.; Dunning, T. H.; Wilson, A. K. Gaussian Basis Sets for Use in Correlated Molecular Calculations. VII. Valence, Core-Valence, and Scalar Relativistic Basis Sets for Li, Be, Na, and Mg. *Theor. Chem. Acc.* **2011**, *128* (1), 69–82.

(14) Van Mourik, T.; Dunning, T. H. Gaussian Basis Sets for Use in Correlated Molecular Calculations. VIII. Standard and Augmented Sextuple Zeta Correlation Consistent Basis Sets for Aluminum through Argon. *Int. J. Quantum Chem.* **2000**, *76* (2), 205–221.

(15) Wilson, A. K.; Woon, D. E.; Peterson, K. A.; Dunning, T. H. Gaussian Basis Sets

for Use in Correlated Molecular Calculations. IX. The Atoms Gallium through Krypton. *J. Chem. Phys.* **1999**, *110* (16), 7667–7676.

(16) Dunning, T. H.; Peterson, K. A.; Wilson, A. K. Gaussian Basis Sets for Use in Correlated Molecular Calculations. X. The Atoms Aluminum through Argon Revisited. *J. Chem. Phys.* **2001**, *114* (21), 9244–9253.

(17) Rappoport, D.; Furche, F. Property-Optimized Gaussian Basis Sets for Molecular Response Calculations. *J. Chem. Phys.* **2010**, *133* (13), 134105.

(18) Weigend, F.; Ahlrichs, R. Balanced Basis Sets of Split Valence, Triple Zeta Valence and Quadruple Zeta Valence Quality for H to Rn: Design and Assessment of Accuracy. *Phys. Chem. Chem. Phys.* **2005**, *7* (18), 3297–3305.

(19) Weigend, F. Accurate Coulomb-Fitting Basis Sets for H to Rn. *Phys. Chem. Chem. Phys.* **2006**, *8* (9), 1057–1065.

(20) Hay, P. J.; Wadt, W. R. Ab Initio Effective Core Potentials for Molecular Calculations. Potentials for K to Au Including the Outermost Core Orbitals. *J. Chem. Phys.* **1985**, *82* (1), 299–310.

(21) Wadt, W. R.; Hay, P. J. Ab Initio Effective Core Potentials for Molecular Calculations. Potentials for Main Group Elements Na to Bi. *J. Chem. Phys.* **1985**, *82* (1), 284–298.

(22) Jansen, H. B.; Ros, P. Non-Empirical Molecular Orbital Calculations on the Protonation of Carbon Monoxide. *Chem. Phys. Lett.* **1969**, *3* (3), 140–143.

(23) Liu, B.; McLean, A. D. Accurate Calculation of the Attractive Interaction of Two

Ground State Helium Atoms. *J. Chem. Phys.* **1973**, *59* (8), 4557–4558.

(24) Boys, S. F.; Bernardi, F. The Calculation of Small Molecular Interactions by the Differences of Separate Total Energies. Some Procedures with Reduced Errors. *Mol. Phys.* **1970**, *19* (4), 553–566.

(25) Löwdin, P. O. Quantum Theory of Many-Particle Systems. III. Extension of the Hartree-Fock Scheme to Include Degenerate Systems and Correlation Effects. *Phys. Rev.* **1955**, *97* (6), 1509–1520.

(26) Schlegel, H. B. Potential Energy Curves Using Unrestricted Møller-Plesset Perturbation Theory with Spin Annihilation. *J. Chem. Phys.* **1986**, *84* (8), 4530–4534.

(27) Andrews, J. S.; Jayatilaka, D.; Bone, R. G. A.; Handy, N. C.; Amos, R. D. Spin Contamination in Single-Determinant Wavefunctions. *Chem. Phys. Lett.* **1991**, *183* (5), 423–431.

(28) Plakhutin, B. N.; Gorelik, E. V.; Breslavskaya, N. N. Koopmans' Theorem in the ROHF Method: Canonical Form for the Hartree-Fock Hamiltonian. *J. Chem. Phys.* **2006**, *125* (20), 204110.

(29) Roothaan, C. C. J. New Developments in Molecular Orbital Theory. *Rev. Mod. Phys.* **1951**, *23* (2), 69–89.

(30) Hall, G. G. The Molecular Orbital Theory of Chemical Valency. X. A Method of Calculating the Ionization Potentials of Conjugated Molecules. *Proc. R. Soc. London. Ser. A. Math. Phys. Sci.* **1952**, *213* (1112), 102–113.

(31) Møller, C.; Plesset, M. S. Note on an Approximation Treatment for Many-Electron Systems. *Phys. Rev.* **1934**, *46* (7), 618–622.

(32) Purvis, G. D.; Bartlett, R. J. A Full Coupled-Cluster Singles and Doubles Model: The Inclusion of Disconnected Triples. *J. Chem. Phys.* **1982**, *76* (4), 1910–1918.

(33) Raghavachari, K.; Trucks, G. W.; Pople, J. A.; Head-Gordon, M. A Fifth-Order Perturbation Comparison of Electron Correlation Theories. *Chem. Phys. Lett.* **1989**, *157* (6), 479–483.

(34) Hohenberg, P.; Kohn, W. Inhomogeneous Electron Gas. *Phys. Rev.* **1964**, *136* (3B), B864–B871.

(35) Kohn, W.; Sham, L. J. Self-Consistent Equations Including Exchange and Correlation Effects. *Phys. Rev.* **1965**, *140* (4A), A1133–A1138.

(36) Chong, D. P.; Gritsenko, O. V.; Baerends, E. J. Interpretation of the Kohn-Sham Orbital Energies as Approximate Vertical Ionization Potentials. *J. Chem. Phys.* **2002**, *116* (5), 1760–1772.

(37) Gritsenko, O. V.; Baerends, E. J. The Analog of Koopmans' Theorem in Spin-Density Functional Theory. *J. Chem. Phys.* **2002**, *117* (20), 9154–9159.

(38) Gritsenko, O. V.; Braïda, B.; Baerends, E. J. Physical Interpretation and Evaluation of the Kohn-Sham and Dyson Components of the ε-I Relations between the Kohn-Sham Orbital Energies and the Ionization Potentials. *J. Chem. Phys.* **2003**, *119* (4), 1937–1950.

(39) Gritsenko, O. V.; Baerends, E. J. The Spin-Unrestricted Molecular Kohn-Sham

Solution and the Analogue of Koopmans's Theorem for Open-Shell Molecules. *J. Chem. Phys.* **2004**, *120* (18), 8364–8372.

(40) Vosko, S. H.; Wilk, L.; Nusair, M. Accurate Spin-Dependent Electron Liquid Correlation Energies for Local Spin Density Calculations: A Critical Analysis. *Can. J. Phys.* **1980**, *58* (8), 1200–1211.

(41) Tao, J.; Perdew, J. P.; Staroverov, V. N.; Scuseria, G. E. Climbing the Density Functional Ladder: Nonempirical Meta–Generalized Gradient Approximation Designed for Molecules and Solids. *Phys. Rev. Lett.* **2003**, *91* (14), 146401.

(42) Csonka, G. I.; Perdew, J. P.; Ruzsinszky, A.; Philipsen, P. H. T.; Lebègue, S.; Paier, J.; Vydrov, O. A.; Ángyán, J. G. Assessing the Performance of Recent Density Functionals for Bulk Solids. *Phys. Rev. B - Condens. Matter Mater. Phys.* **2009**, *79* (15), 155107.

(43) Staroverov, V. N.; Scuseria, G. E.; Tao, J.; Perdew, J. P. Comparative Assessment of a New Nonempirical Density Functional: Molecules and Hydrogen-Bonded Complexes. *J. Chem. Phys.* **2003**, *119* (23), 12129–12137.

(44) Zhao, Y.; Truhlar, D. G. Benchmark Databases for Nonbonded Interactions and Their Use to Test Density Functional Theory. *J. Chem. Theory Comput.* **2005**, *1* (3), 415–432.

(45) Zhao, Y.; Truhlar, D. G. Design of Density Functionals That Are Broadly Accurate for Thermochemistry, Thermochemical Kinetics, and Nonbonded Interactions. *J. Phys. Chem. A* **2005**, *109* (25), 5656–5667.

(46) Becke, A. D. Density-Functional Thermochemistry. III. The Role of Exact

Exchange. *J. Chem. Phys.* **1993**, *98* (7), 5648–5652.

(47) Lee, C.; Yang, W.; Parr, R. G. Development of the Colle-Salvetti Correlation-Energy Formula into a Functional of the Electron Density. *Phys. Rev. B* **1988**, *37* (2), 785–789.

(48) Stephens, P. J.; Devlin, F. J.; Chabalowski, C. F.; Frisch, M. J. Ab Initio Calculation of Vibrational Absorption and Circular Dichroism Spectra Using Density Functional Force Fields. *J. Phys. Chem.* **1994**, *98* (45), 11623–11627.

(49) Marsman, M.; Paier, J.; Stroppa, A.; Kresse, G. Hybrid Functionals Applied to Extended Systems. *J. Phys. Condens. Matter* **2008**, *20* (6), 64201.

(50) Heyd, J.; Peralta, J. E.; Scuseria, G. E.; Martin, R. L. Energy Band Gaps and Lattice Parameters Evaluated with the Heyd-Scuseria-Ernzerhof Screened Hybrid Functional. *J. Chem. Phys.* **2005**, *123* (17), 174101.

(51) Brothers, E. N.; Izmaylov, A. F.; Normand, J. O.; Barone, V.; Scuseria, G. E. Accurate Solid-State Band Gaps via Screened Hybrid Electronic Structure Calculations. *J. Chem. Phys.* **2008**, *129* (1), 11102.

(52) Ehrlich, S.; Moellmann, J.; Grimme, S. Dispersion-Corrected Density Functional Theory for Aromatic Interactions in Complex Systems. *Acc. Chem. Res.* **2013**, *46* (4), 916–926.

(53) Grimme, S. Density Functional Theory with London Dispersion Corrections. *Wiley Interdiscip. Rev. Comput. Mol. Sci.* **2011**, *1* (2), 211–228.

(54) Goerigk, L.; Grimme, S. A Thorough Benchmark of Density Functional Methods

for General Main Group Thermochemistry, Kinetics, and Noncovalent Interactions. *Phys. Chem. Chem. Phys.* **2011**, *13* (14), 6670–6688.

(55) Grimme, S. Semiempirical GGA-Type Density Functional Constructed with a Long-Range Dispersion Correction. *J. Comput. Chem.* **2006**, *27* (15), 1787–1799.

(56) Chai, J.-D.; Head-Gordon, M. Long-Range Corrected Hybrid Density Functionals with Damped Atom-Atom Dispersion Corrections. *Phys. Chem. Chem. Phys.* **2008**, *10* (44), 6615–6620.

(57) Grimme, S.; Antony, J.; Ehrlich, S.; Krieg, H. A Consistent and Accurate Ab Initio Parametrization of Density Functional Dispersion Correction (DFT-D) for the 94 Elements H-Pu. *J. Chem. Phys.* **2010**, *132* (15), 154104.

(58) Perdew, J. P.; Zunger, A. Self-Interaction Correction to Density-Functional Approximations for Many-Electron Systems. *Phys. Rev. B* **1981**, *23* (10), 5048–5079.

(59) Temmerman, W. M.; Szotek, Z.; Winter, H. Self-Interaction-Corrected Electronic Structure of La_2CuO_4. *Phys. Rev. B* **1993**, *47* (17), 11533–11536.

(60) Strange, P.; Svane, A.; Temmerman, W. M.; Szotek, Z.; Winter, H. Understanding the Valency of Rare Earths from First-Principles Theory. *Nature* **1999**, *399* (6738), 756–758.

(61) Engel, E.; Schmid, R. N. Insulating Ground States of Transition-Metal Monoxides from Exact Exchange. *Phys. Rev. Lett.* **2009**, *103* (3), 036404.

(62) Tong, X. M.; Chu, S. I. Density-Functional Theory with Optimized Effective Potential and Self-Interaction Correction for Ground States and Autoionizing Resonances. *Phys. Rev. A - At. Mol. Opt. Phys.* **1997**, *55* (5), 3406–3416.

(63) Chu, S. I. Recent Development of Self-Interaction-Free Time-Dependent Density-Functional Theory for Nonperturbative Treatment of Atomic and Molecular Multiphoton Processes in Intense Laser Fields. *J. Chem. Phys.* **2005**, *123* (6), 62207.

(64) Ullrich, C. A.; Reinhard, P. G.; Suraud, E. Simplified Implementation of Self-Interaction Correction in Sodium Clusters. *Phys. Rev. A - At. Mol. Opt. Phys.* **2000**, *62* (5), 053202–053201.

(65) Telnov, D. A.; Heslar, J. T.; Chu, S. I. Strong-Field Ionization of Li and Be: A Time-Dependent Density Functional Theory with Self-Interaction Correction. *Chem. Phys.* **2011**, *391* (1), 88–91.

(66) Körzdörfer, T.; Mundt, M.; Kümmel, S. Electrical Response of Molecular Systems: The Power of Self-Interaction Corrected Kohn-Sham Theory. *Phys. Rev. Lett.* **2008**, *100* (13), 133004.

(67) Hofmann, D.; Körzdörfer, T.; Kümmel, S. Kohn-Sham Self-Interaction Correction in Real Time. *Phys. Rev. Lett.* **2012**, *108* (14), 133004.

(68) Hofmann, D.; Kümmel, S. Integer Particle Preference during Charge Transfer in Kohn-Sham Theory. *Phys. Rev. B - Condens. Matter Mater. Phys.* **2012**, *86* (20), 201109.

(69) Duffy, P.; Chong, D. P.; Casida, M. E.; Salahub, D. R. Assessment of Kohn-

Sham Density-Functional Orbitals as Approximate Dyson Orbitals for the Calculation of Electron-Momentum-Spectroscopy Scattering Cross Sections. *Phys. Rev. A* **1994**, *50* (6), 4707–4728.

(70) Pohl, A.; Reinhard, P. G.; Suraud, E. Angular Distribution of Electrons Emitted from Na Clusters. *Phys. Rev. A - At. Mol. Opt. Phys.* **2004**, *70* (2), 023202.

(71) Körzdörfer, T.; Kümmel, S.; Marom, N.; Kronik, L. When to Trust Photoelectron Spectra from Kohn-Sham Eigenvalues: The Case of Organic Semiconductors. *Phys. Rev. B - Condens. Matter Mater. Phys.* **2009**, *79* (20), 201205.

(72) Zhao, Y.; Truhlar, D. G. The M06 Suite of Density Functionals for Main Group Thermochemistry, Thermochemical Kinetics, Noncovalent Interactions, Excited States, and Transition Elements: Two New Functionals and Systematic Testing of Four M06-Class Functionals and 12 Other Function. *Theor. Chem. Acc.* **2008**, *120* (1), 215–241.

(73) Guidon, M.; Hutter, J.; Vandevondele, J. Auxiliary Density Matrix Methods for Hartree-Fock Exchange Calculations. *J. Chem. Theory Comput.* **2010**, *6* (8), 2348–2364.

(74) Zhao, Y.; Truhlar, D. G. A New Local Density Functional for Main-Group Thermochemistry, Transition Metal Bonding, Thermochemical Kinetics, and Noncovalent Interactions. *J. Chem. Phys.* **2006**, *125* (19), 194101.

(75) Walker, M.; Harvey, A. J. A.; Sen, A.; Dessent, C. E. H. Performance of M06, M06-2X, and M06-HF Density Functionals for Conformationally Flexible Anionic Clusters: M06 Functionals Perform Better than B3LYP for a Model

System with Dispersion and Ionic Hydrogen-Bonding Interactions. *J. Phys. Chem. A* **2013**, *117* (47), 12590–12600.

(76) Isegawa, M.; Neese, F.; Pantazis, D. A. Ionization Energies and Aqueous Redox Potentials of Organic Molecules: Comparison of DFT, Correlated Ab Initio Theory and Pair Natural Orbital Approaches. *J. Chem. Theory Comput.* **2016**, *12* (5), 2272–2284.

(77) Hilton, M. C.; Zhang, X.; Boyle, B. T.; Alegre-Requena, J. V.; Paton, R. S.; McNally, A. Heterobiaryl Synthesis by Contractive C–C Coupling via P(V) Intermediates. *Science* **2018**, *362* (6416), 799–804.

(78) Yu, H. S.; He, X.; Li, S. L.; Truhlar, D. G. MN15: A Kohn–Sham Global-Hybrid Exchange–Correlation Density Functional with Broad Accuracy for Multi-Reference and Single-Reference Systems and Noncovalent Interactions. *Chem. Sci.* **2016**, *7* (8), 5032–5051.

(79) Peverati, R.; Truhlar, D. G. Quest for a Universal Density Functional: The Accuracy of Density Functionals across a Broad Spectrum of Databases in Chemistry and Physics. *Philos. Trans. R. Soc. A Math. Phys. Eng. Sci.* **2014**, *372* (2011), 20120476.

(80) Zhang, W.; Truhlar, D. G.; Tang, M. Tests of Exchange-Correlation Functional Approximations against Reliable Experimental Data for Average Bond Energies of 3d Transition Metal Compounds. *J. Chem. Theory Comput.* **2013**, *9* (9), 3965–3977.

(81) Averkiev, B. B.; Zhao, Y.; Truhlar, D. G. Binding Energy of d^{10} Transition

Metals to Alkenes by Wave Function Theory and Density Functional Theory. *J. Mol. Catal. A Chem.* **2010**, *324* (1–2), 80–88.

(82) Xu, X.; Zhang, W.; Tang, M.; Truhlar, D. G. Do Practical Standard Coupled Cluster Calculations Agree Better than Kohn-Sham Calculations with Currently Available Functionals When Compared to the Best Available Experimental Data for Dissociation Energies of Bonds to 3d Transition Metals? *J. Chem. Theory Comput.* **2015**, *11* (5), 2036–2052.

(83) Hoyer, C. E.; Manni, G. L.; Truhlar, D. G.; Gagliardi, L. Controversial Electronic Structures and Energies of Fe_2, Fe_2^+, and Fe_2^- Resolved by RASPT2 Calculations. *J. Chem. Phys.* **2014**, *141* (20), 204309.

(84) Hu, L.; Chen, H. Assessment of DFT Methods for Computing Activation Energies of Mo/W-Mediated Reactions. *J. Chem. Theory Comput.* **2015**, *11* (10), 4601–4614.

(85) Sun, Y.; Chen, H. Performance of Density Functionals for Activation Energies of Re-Catalyzed Organic Reactions. *J. Chem. Theory Comput.* **2014**, *10* (2), 579–588.

(86) Sun, Y.; Chen, H. Performance of Density Functionals for Activation Energies of Zr-Mediated Reactions. *J. Chem. Theory Comput.* **2013**, *9* (11), 4735–4743.

(87) Moltved, K. A.; Kepp, K. P. Chemical Bond Energies of 3d Transition Metals Studied by Density Functional Theory. *J. Chem. Theory Comput.* **2018**, *14* (7), 3479–3492.

(88) Vogiatzis, K. D.; Polynski, M. V.; Kirkland, J. K.; Townsend, J.; Hashemi, A.;

Liu, C.; Pidko, E. A. Computational Approach to Molecular Catalysis by 3d Transition Metals: Challenges and Opportunities. *Chem. Rev.* **2019**, *119* (4), 2453–2523.

(89) Liu, M.; Yang, P.; Karunananda, M. K.; Wang, Y.; Liu, P.; Engle, K. M. C(Alkenyl)-H Activation via Six-Membered Palladacycles: Catalytic 1,3-Diene Synthesis. *J. Am. Chem. Soc.* **2018**, *140* (17), 5805–5813.

(90) Steinmetz, M.; Grimme, S. Benchmark Study of the Performance of Density Functional Theory for Bond Activations with (Ni,Pd)-Based Transition-Metal Catalysts. *ChemistryOpen* **2013**, *2* (3), 115–124.

(91) Huang, G.; Cheng, B.; Xu, L.; Li, Y.; Xia, Y. Mechanism of the Transition-Metal-Catalyzed Hydroarylation of Bromo-Alkynes Revisited: Hydrogen versus Bromine Migration. *Chem.: Eur. J.* **2012**, *18* (17), 5401–5415.

(92) Cramer, C. J.; Truhlar, D. G. Density Functional Theory for Transition Metals and Transition Metal Chemistry. *Phys. Chem. Chem. Phys.* **2009**, *11* (46), 10757.

(93) Benitez, D.; Shapiro, N. D.; Tkatchouk, E.; Wang, Y.; Goddard, W. A.; Toste, F. D. A Bonding Model for Gold(I) Carbene Complexes. *Nat. Chem.* **2009**, *1* (6), 482–486.

(94) Benitez, D.; Tkatchouk, E.; Gonzalez, A. Z.; Goddard, W. A.; Dean Toste, F. On the Impact of Steric and Electronic Properties of Ligands on Gold(l)-Catalyzed Cycloaddition Reactions. *Org. Lett.* **2009**, *11* (21), 4798–4801.

(95) Truhlar, D. G. Molecular Modeling of Complex Chemical Systems. *J. Am. Chem. Soc.* **2008**, *130* (50), 16824–16827.

(96) Zhao, Y.; Truhlar, D. G. Benchmark Energetic Data in a Model System for Grubbs II Metathesis Catalysis and Their Use for the Development, Assessment, and Validation of Electronic Structure Methods. *J. Chem. Theory Comput.* **2009**, *5* (2), 324–333.

(97) Weymuth, T.; Couzijn, E. P. A.; Chen, P.; Reiher, M. New Benchmark Set of Transition-Metal Coordination Reactions for the Assessment of Density Functionals. *J. Chem. Theory Comput.* **2014**, *10* (8), 3092–3103.

(98) Dandu, N. K.; Reed, J. A.; Odoh, S. O. Performance of Density Functional Theory for Predicting Methane-to-Methanol Conversion by a Tri-Copper Complex. *J. Phys. Chem. C* **2018**, *122* (2), 1024–1036.

(99) Landstrom, E. B.; Handa, S.; Aue, D. H.; Gallou, F.; Lipshutz, B. H. EvanPhos: A Ligand for Ppm Level Pd-Catalyzed Suzuki–Miyaura Couplings in Either Organic Solvent or Water. *Green Chem.* **2018**, *20* (15), 3436–3443.

(100) Guin, S.; Dolui, P.; Zhang, X.; Paul, S.; Singh, V. K.; Pradhan, S.; Chandrashekar, H. B.; Anjana, S. S.; Paton, R. S.; Maiti, D. Iterative Arylation of Amino Acids and Aliphatic Amines via δ-C(sp^3)−H Activation: Experimental and Computational Exploration. *Angew. Chem. Int. Ed.* **2019**, *58* (17), 5633–5638.

(101) Zhou, T.; Malakar, S.; Webb, S. L.; Krogh-Jespersen, K.; Goldman, A. S. Polar Molecules Catalyze CO Insertion into Metal-Alkyl Bonds through the Displacement of an Agostic C-H Bond. *Proc. Natl. Acad. Sci. U. S. A.* **2019**, *116* (9), 3419–3424.

(102) Luconi, L.; Demirci, U. B.; Peruzzini, M.; Giambastiani, G.; Rossin, A. Ammonia Borane and Hydrazine Bis(Borane) Dehydrogenation Mediated by an Unsymmetrical (PNN) Ruthenium Pincer Hydride: Metal–Ligand Cooperation for Hydrogen Production. *Sustain. Energy Fuels* **2019**.

(103) Achar, T. K.; Zhang, X.; Mondal, R.; Shanavas, M. S.; Maiti, S.; Maity, S.; Pal, N.; Paton, R. S.; Maiti, D. Palladium-Catalyzed Directed Meta-Selective C−H Allylation of Arenes: Unactivated Internal Olefins as Allyl Surrogates. *Angew. Chem. Int. Ed.* **2019**, *58* (30), 10353–10360.

(104) Asakawa, D.; Miyazato, A.; Rosu, F.; Gabelica, V. Influence of the Metals and Ligands in Dinuclear Complexes on Phosphopeptide Sequencing by Electron-Transfer Dissociation Tandem Mass Spectrometry. *Phys. Chem. Chem. Phys.* **2018**, *20* (41), 26597–26607.

(105) Bao, J. L.; Zhang, X.; Xu, X.; Truhlar, D. G. Predicting Bond Dissociation Energy and Bond Length for Bimetallic Diatomic Molecules: A Challenge for Electronic Structure Theory. *Phys. Chem. Chem. Phys.* **2017**, *19* (8), 5839–5854.

(106) Cramer, C. J.; Truhlar, D. G. Implicit Solvation Models: Equilibria, Structure, Spectra, and Dynamics. *Chem. Rev.* **1999**, *99* (8), 2161–2200.

(107) Klamt, A.; Schüürmann, G. COSMO: A New Approach to Dielectric Screening in Solvents with Explicit Expressions for the Screening Energy and Its Gradient. *J. Chem. Soc. Perkin Trans. 2* **1993**, No. 5, 799–805.

(108) Klamt, A. Conductor-like Screening Model for Real Solvents: A New Approach to the Quantitative Calculation of Solvation Phenomena. *J. Phys. Chem.* **1995**, *99*

(7), 2224–2235.

(109) Klamt, A.; Jonas, V.; Bürger, T.; Lohrenz, J. C. W. Refinement and Parametrization of COSMO-RS. *J. Phys. Chem. A* **1998**, *102* (26), 5074–5085.

(110) Mennucci, B.; Cancès, E.; Tomasi, J. Evaluation of Solvent Effects in Isotropic and Anisotropic Dielectrics and in Ionic Solutions with a Unified Integral Equation Method: Theoretical Bases, Computational Implementation, and Numerical Applications. *J. Phys. Chem. B* **2002**, *101* (49), 10506–10517.

(111) Cancès, E.; Mennucci, B.; Tomasi, J. A New Integral Equation Formalism for the Polarizable Continuum Model: Theoretical Background and Applications to Isotropic and Anisotropic Dielectrics. *J. Chem. Phys.* **1997**, *107* (8), 3032–3041.

(112) Cancès, E.; Mennucci, B. New Applications of Integral Equations Methods for Solvation Continuum Models: Ionic Solutions and Liquid Crystals. *J. Math. Chem.* **1998**, *23* (3–4), 309–326.

(113) Cossi, M.; Rega, N.; Scalmani, G.; Barone, V. Energies, Structures, and Electronic Properties of Molecules in Solution with the C-PCM Solvation Model. *J. Comput. Chem.* **2003**, *24* (6), 669–681.

(114) Barone, V.; Cossi, M. Quantum Calculation of Molecular Energies and Energy Gradients in Solution by a Conductor Solvent Model. *J. Phys. Chem. A* **1998**, *102* (11), 1995–2001.

(115) Kelly, C. P.; Cramer, C. J.; Truhlar, D. G. SM6: A Density Functional Theory Continuum Solvation Model for Calculating Aqueous Solvation Free Energies of Neutrals, Ions, and Solute-Water Clusters. *J. Chem. Theory Comput.* **2005**, *1* (6),

1133–1152.

(116) Marenich, A. V.; Olson, R. M.; Kelly, C. P.; Cramer, C. J.; Truhlar, D. G. Self-Consistent Reaction Field Model for Aqueous and Nonaqueous Solutions Based on Accurate Polarized Partial Charges. *J. Chem. Theory Comput.* **2007**, *3* (6), 2011–2033.

(117) Marenich, A. V.; Cramer, C. J.; Truhlar, D. G. Universal Solvation Model Based on Solute Electron Density and on a Continuum Model of the Solvent Defined by the Bulk Dielectric Constant and Atomic Surface Tensions. *J. Phys. Chem. B* **2009**, *113* (18), 6378–6396.

(118) Guerard, J. J.; Arey, J. S. Critical Evaluation of Implicit Solvent Models for Predicting Aqueous Oxidation Potentials of Neutral Organic Compounds. *J. Chem. Theory Comput.* **2013**, *9* (11), 5046–5058.

(119) Pelzer, H.; Wigner, E. P. Über Die Geschwindigkeitskonstante von Austauschreaktionen. *Part I Phys. Chem. Part II Solid State Phys.* **2011**, *15B* (1), 69–95.

(120) Eyeing, H. The Activated Complex and the Absolute Rate of Chemical Reactions. *Chem. Rev.* **1935**, *17* (1), 65–77.

(121) Evans, M. G.; Polanyi, M. Some Applications of the Transition State Method to the Calculation of Reaction Velocities, Especially in Solution. *Trans. Faraday Soc.* **1935**, *31*, 875–894.

(122) Truhlar, D. G.; Garrett, B. C.; Klippenstein, S. J. Current Status of Transition-State Theory. *J. Phys. Chem.* **1996**, *100* (31), 12771–12800.

(123) Hare, S. R.; Tantillo, D. J. Dynamic Behavior of Rearranging Carbocations - Implications for Terpene Biosynthesis. *Beilstein J. Org. Chem.* **2016**, *12*, 377–390.

(124) Woodward, R. B.; Baer, H. Studies on Diene-Addition Reactions. II. The Reaction of 6,6-Pentamethylenefulvene with Maleic Anhydride. *J. Am. Chem. Soc.* **1944**, *66* (4), 645–649.

(125) Kozuch, S.; Shaik, S. How to Conceptualize Catalytic Cycles? The Energetic Span Model. *Acc. Chem. Res.* **2011**, *44* (2), 101–110.

(126) Peng, Q.; Duarte, F.; Paton, R. S. Computing Organic Stereoselectivity-from Concepts to Quantitative Calculations and Predictions. *Chem. Soc. Rev.* **2016**, *45* (22), 6093–6107.

(127) Fang, L.; Saint-Denis, T. G.; Taylor, B. L. H.; Ahlquist, S.; Hong, K.; Liu, S.; Han, L.; Houk, K. N.; Yu, J. Q. Experimental and Computational Development of a Conformationally Flexible Template for the Meta-C-H Functionalization of Benzoic Acids. *J. Am. Chem. Soc.* **2017**, *139* (31), 10702–10714.

(128) Hansen, T. V; Stenstrom, Y. No Title. In *Organic Synthesis: Theory and Applications, Vol. 5*; Elsevier Science: Amsterdam, 2001; p 1.

(129) Dembitsky, V. M. Bioactive Cyclobutane-Containing Alkaloids. *J. Nat. Med.* **2008**, *62* (1), 1–33.

(130) Sergeiko, A.; Poroikov, V. V.; Hanus, L. O.; Dembitsky, V. M. Cyclobutane-Containing Alkaloids: Origin, Synthesis, and Biological Activities. *Open Med. Chem. J.* **2008**, *2* (1), 26–37.

(131) Namyslo, J. C.; Kaufmann, D. E. The Application of Cyclobutane Derivatives in Organic Synthesis. *Chem. Rev.* **2003**, *103* (4), 1485–1538.

(132) Seiser, T.; Saget, T.; Tran, D. N.; Cramer, N. Cyclobutanes in Catalysis. *Angew. Chem. Int. Ed.* **2011**, *50* (34), 7740–7752.

(133) Liebermann, C. Ueber Polythymochinon. *Berichte der Dtsch. Chem. Gesellschaft* **1877**, *10* (2), 2177–2179.

(134) Farid, S.; Shealer, S. E. Radical Cations: Photochemical and Ferric Ion-Induced Formation and Reactions of Indene Radical Cation. *J. Chem. Soc. Chem. Commun.* **1973**, *0* (18), 677–678.

(135) Kuwata, S.; Shigemitsu, Y.; Odaira, Y. Photosensitized Cyclodimerization of Phenyl Vinyl Ether. *J. Chem. Soc. Chem. Commun.* **1972**, *0* (1), 2.

(136) Caldwell, R. A.; Mizuno, K.; Hansen, P. E.; Vo, L. P.; Frentrup, M.; Ho, C. D. Photochemistry of the Phenanthrene-Stilbene System. Cycloaddition and Singlet-Sensitized Isomerization. *J. Am. Chem. Soc.* **1981**, *103* (24), 7263–7269.

(137) Bach, T.; Hehn, J. P. Photochemical Reactions as Key Steps in Natural Product Synthesis. *Angew. Chem. Int. Ed.* **2011**, *50* (5), 1000–1045.

(138) Hong, Y. J.; Tantillo, D. J. How Cyclobutanes Are Assembled in Nature-Insights from Quantum Chemistry. *Chem. Soc. Rev.* **2014**, *43* (14), 5042–5050.

(139) Poplata, S.; Tröster, A.; Zou, Y. Q.; Bach, T. Recent Advances in the Synthesis of Cyclobutanes by Olefin [2 +2] Photocycloaddition Reactions. *Chem. Rev.* **2016**, *116* (17), 9748–9815.

(140) Colomer, I.; Coura Barcelos, R.; Donohoe, T. J. Catalytic Hypervalent Iodine Promoters Lead to Styrene Dimerization and the Formation of Tri- and Tetrasubstituted Cyclobutanes. *Angew. Chem. Int. Ed.* **2016**, *55* (15), 4748–4752.

(141) Albrecht, Ł.; Dickmeiss, G.; Acosta, F. C.; Rodríguez-Escrich, C.; Davis, R. L.; Jørgensen, K. A. Asymmetric Organocatalytic Formal [2 + 2]-Cycloadditions via Bifunctional H-Bond Directing Dienamine Catalysis. *J. Am. Chem. Soc.* **2012**, *134* (5), 2543–2546.

(142) Nielsen, A. J.; Jenkins, H. A.; McNulty, J. Asymmetric Organocatalytic Stepwise [2+2] Entry to Tetra-Substituted Heterodimeric and Homochiral Cyclobutanes. *Chem.: Eur. J.* **2016**, *22* (27), 9111–9115.

(143) Prier, C. K.; Rankic, D. A.; MacMillan, D. W. C. Visible Light Photoredox Catalysis with Transition Metal Complexes: Applications in Organic Synthesis. *Chem. Rev.* **2013**, *113* (7), 5322–5363.

(144) Lautens, M.; Klute, W.; Tam, W. Transition Metal-Mediated Cycloaddition Reactions. *Chem. Rev.* **1996**, *96* (1), 49–92.

(145) Schmidt, V. A.; Hoyt, J. M.; Margulieux, G. W.; Chirik, P. J. Cobalt-Catalyzed [2π + 2π] Cycloadditions of Alkenes: Scope, Mechanism, and Elucidation of Electronic Structure of Catalytic Intermediates. *J. Am. Chem. Soc.* **2015**, *137* (24), 7903–7914.

(146) Chiba, K.; Miura, T.; Kim, S.; Kitano, Y.; Tada, M. Electrocatalytic Intermolecular Olefin Cross-Coupling by Anodically Induced Formal [2+2] Cycloaddition between Enol Ethers and Alkenes. *J. Am. Chem. Soc.* **2001**, *123*

(45), 11314–11315.

(147) Arata, M.; Miura, T.; Chiba, K. Electrocatalytic Formal [2+2] Cycloaddition Reactions between Anodically Activated Enyloxy Benzene and Alkenes. *Org. Lett.* **2007**, *9* (21), 4347–4350.

(148) Miura, T.; Kim, S.; Kitano, Y.; Tada, M.; Chiba, K. Electrochemical Enol Ether/Olefin Cross-Metathesis in a Lithium Perchlorate/Nitromethane Electrolyte Solution. *Angew. Chem. Int. Ed.* **2006**, *45* (9), 1461–1463.

(149) Chiba, K.; Tada, M. Diels-Alder Reaction of Quinones Generated in Situ by Electrochemical Oxidation in Lithium Perchlorate-Nitromethane. *J. Chem. Soc. Chem. Commun.* **1994**, 2485–2486.

(150) Gutekunst, W. R.; Baran, P. S. Applications of C–H Functionalization Logic to Cyclobutane Synthesis. *J. Org. Chem.* **2014**, *79* (6), 2430–2452.

(151) Wu, Q. F.; Wang, X. B.; Shen, P. X.; Yu, J. Q. Enantioselective C-H Arylation and Vinylation of Cyclobutyl Carboxylic Amides. *ACS Catal.* **2018**, *8* (3), 2577–2581.

(152) Hu, J.-L.; Feng, L.-W.; Wang, L.; Xie, Z.; Tang, Y.; Li, X. Enantioselective Construction of Cyclobutanes: A New and Concise Approach to the Total Synthesis of (+)-Piperarborenine B. *J. Am. Chem. Soc.* **2016**, *138* (40), 13151–13154.

(153) Yang, X.; Shan, G.; Yang, Z.; Huang, G.; Dong, G.; Sheng, C.; Rao, Y. One-Pot Synthesis of Quaternary Carbon Centered Cyclobutanes via Pd(II)-Catalyzed Cascade C(sp^3)-H Activations. *Chem. Commun.* **2017**, *53* (9), 1534–1537.

(154) Mascitti, V.; Corey, E. J. Total Synthesis of (±)-Pentacycloanammoxic Acid. *J. Am. Chem. Soc.* **2004**, *126* (48), 15664–15665.

(155) Lu, P.; Bach, T. Total Synthesis of (+)-Lactiflorin by an Intramolecular [2+2] Photocycloaddition. *Angew. Chem. Int. Ed.* **2012**, *51* (5), 1261–1264.

(156) Zhang, P.; Wang, Y.; Bao, R.; Luo, T.; Yang, Z.; Tang, Y. Enantioselective Biomimetic Total Syntheses of Katsumadain and Katsumadain C. *Org. Lett.* **2012**, *14* (1), 162–165.

(157) Reisman, S. E.; Ready, J. M.; Hasuoka, A.; Smith, C. J.; Wood, J. L. Total Synthesis of (±)-Welwitindolinone A Isonitrile. *J. Am. Chem. Soc.* **2006**, *128* (5), 1448–1449.

(158) Eberson, L. Catalysis by Electron Transfer in Organic Chemistry. *J. Mol. Catal.* **1983**, *20* (1), 27–52.

(159) Ischay, M. A.; Yoon, T. P. Accessing the Synthetic Chemistry of Radical Ions. *Eur. J. Org. Chem.* **2012**, *2012* (18), 3359–3372.

(160) Lin, S.; Lies, S. D.; Gravatt, C. S.; Yoon, T. P. Radical Cation Cycloadditions Using Cleavable Redox Auxiliaries. *Org. Lett.* **2017**, *19* (2), 368–371.

(161) Yamaguchi, Y.; Okada, Y.; Chiba, K. Understanding the Reactivity of Enol Ether Radical Cations: Investigation of Anodic Four-Membered Carbon Ring Formation. *J. Org. Chem.* **2013**, *78* (6), 2626–2638.

(162) Cortezano-Arellano, O.; Quintero, L.; Sartillo-Piscil, F. Total Synthesis of Cephalosporolide E via a Tandem Radical/Polar Crossover Reaction. The Use of

the Radical Cations under Nonoxidative Conditions in Total Synthesis. *J. Org. Chem.* **2015**, *80* (5), 2601–2608.

(163) Alehashem, M. S.; Lim, C. G.; Thomas, N. F. The Radical Cation Mediated Cleavage of Catharanthine Leading to the Vinblastine Type Alkaloids: Implications for Total Synthesis and Drug Design. *RSC Adv.* **2016**, *6* (22), 18002–18025.

(164) Bell, F. A.; Crellin, R. A.; Fujii, H.; Ledwith, A. Cation-Radicals: Metal-Catalysed Cyclodimerisation of Aromatic Enamines. *J. Chem. Soc. D Chem. Commun.* **1969**, No. 6, 251–252.

(165) Liu, L.-Q. Q.; Sun, D.-Q. Q.; Yang, J.-K. K. Efficient Additives to Improve the Catalytic Effects of Ferric(III) Chloride on the Reaction of N-Vinylcarbazole: Hydroquinone for Methanolysis, Hydrogen Peroxide for Cyclobutanation Respectively. *J. Phys. Org. Chem.* **2012**, *25* (4), 272–277.

(166) Yu, Y.; Fu, Y.; Zhong, F. Benign Catalysis with Iron: Facile Assembly of Cyclobutanes and Cyclohexenes: Via Intermolecular Radical Cation Cycloadditions. *Green Chem.* **2018**, *20* (8), 1743–1747.

(167) Riener, M.; Nicewicz, D. A. Synthesis of Cyclobutane Lignans via an Organic Single Electron Oxidant-Electron Relay System. *Chem. Sci.* **2013**, *4* (6), 2625–2629.

(168) Lu, Z.; Yoon, T. P. Visible Light Photocatalysis of [2+2] Styrene Cycloadditions by Energy Transfer. *Angew. Chem. Int. Ed.* **2012**, *51* (41), 10329–10332.

(169) Du, J.; Yoon, T. P. Crossed Intermolecular [2+2] Cycloadditions of Acyclic

Enones via Visible Light Photocatalysis. *J. Am. Chem. Soc.* **2009**, *131* (41), 14604–14605.

(170) Ischay, M. A.; Ament, M. S.; Yoon, T. P. Crossed Intermolecular [2 + 2] Cycloaddition of Styrenes by Visible Light Photocatalysis. *Chem. Sci.* **2012**, *3* (9), 2807–2811.

(171) Hurtley, A. E.; Lu, Z.; Yoon, T. P. Cycloaddition of 1,3-Dienes by Visible Light Photocatalysis. *Angew. Chem. Int. Ed.* **2014**, *53* (34), 8991–8994.

(172) Bauld, N. L.; Pabon, R. Cation Radical Catalyzed Olefin Cyclodimerization. *J. Am. Chem. Soc.* **1983**, *105* (3), 633–634.

(173) Gassman, P. G.; Singleton, D. A. Distinction between Aminium Cation Radical and Protic Acid Catalyzed Diels-Alder Reactions. *J. Am. Chem. Soc.* **1984**, *106* (25), 7993–7994.

(174) Reynolds, D. W.; Lorenz, K. T.; Chiou, H. S.; Bellville, D. J.; Pabon, R. A.; Bauld, N. L. Mechanistic Diagnosis of Aminium Salt Initiated Diels-Alder Cycloadditions in the Diene/Diene Format. *J. Am. Chem. Soc.* **1987**, *109* (16), 4960–4968.

(175) Bauld, N. L.; Yang, J.; Gao, D. Diels–Alder Cycloadditions of the N-Vinylcarbazole Radical Cation. *J. Chem. Soc. Perkin Trans. 2* **2000**, *0* (2), 207–210.

(176) Colomer, I.; Batchelor-Mcauley, C.; Odell, B.; Donohoe, T. J.; Compton, R. G. Hydrogen Bonding to Hexafluoroisopropanol Controls the Oxidative Strength of Hypervalent Iodine Reagents. *J. Am. Chem. Soc.* **2016**, *138* (28), 8855–8861.

(177) Ledwith, A. Cation Radicals in Electron Transfer Reactions. *Acc. Chem. Res.* **1972**, *5* (4), 133–139.

(178) Mattes, S. L.; Farid, S. Photooxygenation via Electron Transfer. 1,1-Dimethylindene. *J. Am. Chem. Soc.* **1982**, *104* (5), 1454–1456.

(179) Mattes, S. L.; Farid, S. Photosensitized Electron-Transfer Reactions. Interception of the Geminate Radical Ion Pair. *J. Am. Chem. Soc.* **1983**, *105* (5), 1386–1387.

(180) Mattes, S. L.; Farid, S. Photochemical Electron-Transfer Reactions of 1, 1 - Diarylethylenes. *J. Am. Chem. Soc.* **1986**, *108* (23), 7356–7361.

(181) Reynolds, D. W.; Harirchian, B.; Chiou, H. -S; Marsh, B. K.; Bauld, N. L. The Cation Radical Vinylcyclobutane Rearrangement. *J. Phys. Org. Chem.* **1989**, *2* (1), 57–88.

(182) Schepp, N. P.; Johnston, L. J. Nanosecond and Picosecond Dynamics of the Radical Cation Mediated Dimerization of 4-Methoxystyrene. *J. Am. Chem. Soc.* **1994**, *116* (15), 6895–6903.

(183) Johnston, L. J.; Schepp, N. P. No Title. In *Advances in Electron Transfer Vol. 6*; Mariano, P. S., Ed.; JAI Press: New York, 1996; pp 41–102.

(184) O'Neil, L. L.; Wiest, O. Acyclic or Long-Bond Intermediate in the Electron-Transfer-Catalyzed Dimerization of 4-Methoxystyrene. *J. Org. Chem.* **2006**, *71* (23), 8926–8933.

(185) Marquez, C. A.; Wang, H.; Fabbretti, F.; Metzger, J. O. Electron-Transfer-Catalyzed Dimerization of Trans-Anethole: Detection of the Distonic

Tetramethylene Radical Cation Intermediate by Extractive Electrospray Ionization Mass Spectrometry. *J. Am. Chem. Soc.* **2008**, *130* (51), 17208–17209.

(186) Chéron, N.; Jacquemin, D.; Fleurat-Lessard, P. A Qualitative Failure of B3LYP for Textbook Organic Reactions. *Phys. Chem. Chem. Phys.* **2012**, *14* (19), 7170–7175.

(187) Redfern, P. C.; Zapol, P.; Curtiss, L. A.; Raghavachari, K. Assessment of Gaussian-3 and Density Functional Theories for Enthalpies of Formation of C_1-C_{16} Alkanes. *J. Phys. Chem. A* **2000**, *104* (24), 5850–5854.

(188) Curtiss, L. A.; Redfern, P. C.; Raghavachari, K. Assessment of Gaussian-3 and Density-Functional Theories on the G3/05 Test Set of Experimental Energies. *J. Chem. Phys.* **2005**, *123* (12), 124107.

(189) Mantz, Y. A.; Gervasio, F. L.; Laino, T.; Parrinello, M. Charge Localization in Stacked Radical Cation DNA Base Pairs and the Benzene Dimer Studied by Self-Interaction Corrected Density-Functional Theory. *J. Phys. Chem. A* **2007**, *111* (1), 105–112.

(190) Close, D. M. One-Electron Oxidation of Individual DNA Bases and DNA Base Stacks. *J. Phys. Chem. A* **2010**, *114* (4), 1860–1867.

(191) Kumar, A.; Sevilla, M. D. Density Functional Theory Studies of the Extent of Hole Delocalization in One-Electron Oxidized Adenine and Guanine Base Stacks. *J. Phys. Chem. B* **2011**, *115* (17), 4990–5000.

(192) Frisch, M. J. .; Trucks, G. W. .; Schlegel, H. B. .; Scuseria, G. E. .; Robb, M. A. .; Cheeseman, J. R. .; Scalmani, G. .; Barone, V. .; Mennucci, B. .; Petersson,

G. A. .; et al. *Gaussian 09*, Revision E.01. Gaussian Inc. Wallingford CT. 2009. See Appendix 1 for full reference.

(193) Ditchfield, R.; Hehre, W. J.; Pople, J. A. Self-Consistent Molecular-Orbital Methods. IX. An Extended Gaussian-Type Basis for Molecular-Orbital Studies of Organic Molecules. *J. Chem. Phys.* **2004**, *54* (2), 724–728.

(194) Fukui, K. The Path of Chemical Reactions - The IRC Approach. *Acc. Chem. Res.* **1981**, *14* (12), 363–368.

(195) Fukui, K. Formulation of the Reaction Coordinate. *J. Phys. Chem.* **2005**, *74* (23), 4161–4163.

(196) Schäfer, A.; Horn, H.; Ahlrichs, R. Fully Optimized Contracted Gaussian Basis Sets for Atoms Li to Kr. *J. Chem. Phys.* **1992**, *97* (4), 2571–2577.

(197) Schäfer, A.; Huber, C.; Ahlrichs, R. Fully Optimized Contracted Gaussian Basis Sets of Triple Zeta Valence Quality for Atoms Li to Kr. *J. Chem. Phys.* **1994**, *100* (8), 5829–5835.

(198) Colomer, I.; Chamberlain, A. E. R.; Haughey, M. B.; Donohoe, T. J. Hexafluoroisopropanol as a Highly Versatile Solvent. *Nat. Rev. Chem.* **2017**, *1* (11), 0088.

(199) Eberson, L.; Hartshorn, M. P.; Persson, O.; Radner, F. Making Radical Cations Live Longer. *Chem. Commun.* **1996**, No. 18, 2105–2112.

(200) Gu, X.; Song, X.; Shao, C.; Zeng, P.; Lu, X.; Shen, X.; Yang, Q. Electrospinning of Poly(Butylene-Carbonate): Effect of Solvents on the Properties of the

Nanofibers Film. *Int. J. Electrochem. Sci.* **2014**, *9* (12), 8045–8056.

(201) Carraro, M.; Gardan, M.; Sartorel, A.; Maccato, C.; Bonchio, M. Hydrogen Peroxide Activation by Fluorophilic Polyoxotungstates for Fast and Selective Oxygen Transfer Catalysis. *Dalt. Trans.* **2016**, *45* (37), 14544–14548.

(202) Sigma-Aldrich. 1,1,1,3,3,3-Hexafluoro-2-propanol https://www.sigmaaldrich.com/catalog/product/aldrich/105228 (accessed Jun 6, 2017).

(203) Weast, R. C. *CRC Handbook of Chemistry and Physics*, 76th ed.; CRC Press: Boca Raton, FL, 1995.

(204) Richmond, E.; Yi, J.; Vuković, V. D.; Sajadi, F.; Rowley, C. N.; Moran, J. Ring-Opening Hydroarylation of Monosubstituted Cyclopropanes Enabled by Hexafluoroisopropanol. *Chem. Sci.* **2018**, *9* (30), 6411–6416.

(205) Grimme, S. Supramolecular Binding Thermodynamics by Dispersion-Corrected Density Functional Theory. *Chem.: Eur. J.* **2012**, *18* (32), 9955–9964.

(206) Funes-Ardoiz, I.; Paton, R. S. GoodVibes v1.0.1 http://doi.org/10.5281/zenodo.56091.

(207) Schrödinger, L. *The PyMOL Molecular Graphics Development Component, Version 1.8*; 2015.

(208) Wiest, O. Structure and [2+2] Cycloreversion of the Cyclobutane Radical Cation. *J. Phys. Chem. A* **1999**, *103* (39), 7907–7911.

(209) Weng, H.; Roth, H. D. Electron Transfer Photochemistry of Norbornadiene and

Quadricyclane. Nucleophilic Capture of Radical Cations, Free-Radical Rearrangements, and Hydrogen Abstraction. *J. Org. Chem.* **2005**, *60* (13), 4136–4145.

(210) Tang, B.; Simion, R.; Paton, R. S. Thermal and Photochemical Mechanisms for Cyclobutane Formation in Bielschowskysin Biosynthesis. *Synlett* **2015**, *26* (4), 501–507.

(211) Münster, N.; Parker, N. A.; van Dijk, L.; Paton, R. S.; Smith, M. D. Visible Light Photocatalysis of 6π Heterocyclization. *Angew. Chem. Int. Ed.* **2017**, *56* (32), 9468–9472.

(212) Gammack Yamagata, A. D.; Datta, S.; Jackson, K. E.; Stegbauer, L.; Paton, R. S.; Dixon, D. J. Enantioselective Desymmetrization of Prochiral Cyclohexanones by Organocatalytic Intramolecular Michael Additions to α,β-Unsaturated Esters. *Angew. Chem. Int. Ed.* **2015**, *54* (16), 4899–4903.

(213) Cramer, C. J.; Truhlar, D. G. A Universal Approach to Solvation Modeling. *Acc. Chem. Res.* **2008**, *41* (6), 760–768.

(214) Takano, Y.; Houk, K. N. Benchmarking the Conductor-like Polarizable Continuum Model (CPCM) for Aqueous Solvation Free Energies of Neutral and Ionic Organic Molecules. *J. Chem. Theory Comput.* **2005**, *1* (1), 70–77.

(215) Klamt, A.; Eckert, F.; Diedenhofen, M. Prediction of the Free Energy of Hydration of a Challenging Set of Pesticide-like Compounds. *J. Phys. Chem. B* **2009**, *113* (14), 4508–4510.

(216) Klamt, A.; Diedenhofen, M. Blind Prediction Test of Free Energies of Hydration

with COSMO-RS. *J. Comput. Aided. Mol. Des.* **2010**, *24* (4), 357–360.

(217) Reinisch, J.; Klamt, A. Prediction of Free Energies of Hydration with COSMO-RS on the SAMPL4 Data Set. *J. Comput. Aided. Mol. Des.* **2014**, *28* (3), 169–173.

(218) Marenich, A. V.; Cramer, C. J.; Truhlar, D. G. Performance of SM6, SM8, and SMD on the SAMPL1 Test Set for the Prediction of Small-Molecule Solvation Free Energies. *J. Phys. Chem. B* **2009**, *113* (14), 4538–4543.

(219) Ribeiro, R. F.; Marenich, A. V.; Cramer, C. J.; Truhlar, D. G. Prediction of SAMPL2 Aqueous Solvation Free Energies and Tautomeric Ratios Using the SM8, SM8AD, and SMD Solvation Models. *J. Comput. Aided. Mol. Des.* **2010**, *24* (4), 317–333.

(220) Soteras, I.; Orozco, M.; Luque, F. J. Performance of the IEF-MST Solvation Continuum Model in the SAMPL2 Blind Test Prediction of Hydration and Tautomerization Free Energies. *J. Comput. Aided. Mol. Des.* **2010**, *24* (4), 281–291.

(221) Sulea, T.; Wanapun, D.; Dennis, S.; Purisima, E. O. Prediction of SAMPL-1 Hydration Free Energies Using a Continuum Electrostatics-Dispersion Model. *J. Phys. Chem. B* **2009**, *113* (14), 4511–4520.

(222) Ho, J. Are Thermodynamic Cycles Necessary for Continuum Solvent Calculation of PK a s and Reduction Potentials? *Phys. Chem. Chem. Phys.* **2015**, *17* (4), 2859–2868.

(223) Klamt, A.; Mennucci, B.; Tomasi, J.; Barone, V.; Curutchet, C.; Orozco, M.;

Luque, F. J. On the Performance of Continuum Solvation Methods. A Comment on “Universal Approaches to Solvation Modeling.” *Acc. Chem. Res.* **2009**, *42* (4), 489–492.

(224) Baik, M. H.; Friesner, R. A. Computing Redox Potentials in Solution: Density Functional Theory as a Tool for Rational Design of Redox Agents. *J. Phys. Chem. A* **2002**, *106* (32), 7407–7412.

(225) Winget, P.; Cramer, C. J.; Truhlar, D. G. Computation of Equilibrium Oxidation and Reduction Potentials for Reversible and Dissociative Electron-Transfer Reactions in Solution. *Theor. Chem. Acc.* **2004**, *112* (4), 217–227.

(226) Fu, Y.; Liu, L.; Yu, H.-Z.; Wang, Y.-M.; Guo, Q.-X. Quantum-Chemical Predictions of Absolute Standard Redox Potentials of Diverse Organic Molecules and Free Radicals in Acetonitrile. *J. Am. Chem. Soc.* **2005**, *127* (19), 7227–7234.

(227) Schmidt Am Busch, M.; Knapp, E. W. One-Electron Reduction Potential for Oxygen- and Sulfur-Centered Organic Radicals in Protic and Aprotic Solvents. *J. Am. Chem. Soc.* **2005**, *127* (45), 15730–15737.

(228) Jaque, P.; Marenich, A. V.; Cramer, C. J.; Truhlar, D. G. Computational Electrochemistry: The Aqueous $Ru^{3+}|Ru^{2+}$ Reduction Potential. *J. Phys. Chem. C* **2007**, *111* (15), 5783–5799.

(229) Dutton, A. S.; Fukuto, J. M.; Houk, K. N. Theoretical Reduction Potentials for Nitrogen Oxides from CBS-QB3 Energetics and (C)PCM Solvation Calculations. *Inorg. Chem.* **2005**, *44* (11), 4024–4028.

(230) Hodgson, J. L.; Namazian, M.; Bottle, S. E.; Coote, M. L. One-Electron

Oxidation and Reduction Potentials of Nitroxide Antioxidants: A Theoretical Study. *J. Phys. Chem. A* **2007**, *111* (51), 13595–13605.

(231) Roy, L. E.; Jakubikova, E.; Graham Guthrie, M.; Batista, E. R. Calculation of One-Electron Redox Potentials Revisited. Is It Possible to Calculate Accurate Potentials with Density Functional Methods? *J. Phys. Chem. A* **2009**, *113* (24), 6745–6750.

(232) Gryn'ova, G.; Barakat, J. M.; Blinco, J. P.; Bottle, S. E.; Coote, M. L. Computational Design of Cyclic Nitroxides as Efficient Redox Mediators for Dye-Sensitized Solar Cells. *Chem.: Eur. J.* **2012**, *18* (24), 7582–7593.

(233) Marenich, A. V.; Majumdar, A.; Lenz, M.; Cramer, C. J.; Truhlar, D. G. Construction of Pourbaix Diagrams for Ruthenium-Based Water-Oxidation Catalysts by Density Functional Theory. *Angew. Chem. Int. Ed.* **2012**, *51* (51), 12810–12814.

(234) Psciuk, B. T.; Schlegel, H. B. Computational Prediction of One-Electron Reduction Potentials and Acid Dissociation Constants for Guanine Oxidation Intermediates and Products. *J. Phys. Chem. B* **2013**, *117* (32), 9518–9531.

(235) Marenich, A. V.; Ho, J.; Coote, M. L.; Cramer, C. J.; Truhlar, D. G. Computational Electrochemistry: Prediction of Liquid-Phase Reduction Potentials. *Phys. Chem. Chem. Phys.* **2014**, *16* (29), 15068–15106.

(236) Roth, H. G.; Romero, N. A.; Nicewicz, D. A.; Roth, H. G.; Romero, N. A.; Nicewicz, D. A.; Roth, H. G.; Romero, N. A.; Nicewicz, D. A. Experimental and Calculated Electrochemical Potentials of Common Organic Molecules for

Applications to Single-Electron Redox Chemistry. *Synlett* **2016**, *27* (05), 714–723.

(237) Pavlishchuk, V. V.; Addison, A. W. Conversion Constants for Redox Potentials Measured versus Different Reference Electrodes in Acetonitrile Solutions at 25°C. *Inorganica Chim. Acta* **2000**, *298* (1), 97–102.

(238) Isse, A. A.; Gennaro, A. Absolute Potential of the Standard Hydrogen Electrode and the Problem of Interconversion of Potentials in Different Solvents. *J. Phys. Chem. B* **2010**, *114* (23), 7894–7899.

(239) Chong, D.; Stewart, M.; Geiger, W. E. Cycloaddition Reactions of Unactivated Olefins Catalyzed by an Organorhenium Electron-Transfer Mediator. *J. Am. Chem. Soc.* **2009**, *131* (23), 7968–7969.

(240) Stewart, M. P.; Lam, K.; Chong, D.; Geiger, W. E. CElectron-Transfer Catalyzed Cycloaddition Reactions of Unactivated Cyclic Olefins in Weakly Coordinating Anion Electrolyte. *J. Electroanal. Chem.* **2015**, *743*, 68–77.

(241) Bickelhaupt, F. M. Understanding Reactivity with Kohn-Sham Molecular Orbital Theory: E2-SN2 Mechanistic Spectrum and Other Concepts. *J. Comput. Chem.* **1999**, *20* (1), 114–128.

(242) Fernández, I.; Bickelhaupt, F. M. The Activation Strain Model and Molecular Orbital Theory: Understanding and Designing Chemical Reactions. *Chem. Soc. Rev.* **2014**, *43* (14), 4953–4967.

(243) Wolters, L. P.; Bickelhaupt, F. M. The Activation Strain Model and Molecular Orbital Theory. *Wiley Interdiscip. Rev. Comput. Mol. Sci.* **2015**, *5* (4), 324–343.

(244) Bickelhaupt, F. M.; Houk, K. N. Analyzing Reaction Rates with the Distortion/Interaction-Activation Strain Model. *Angew. Chem. Int. Ed.* **2017**, *56* (34), 10070–10086.

(245) Ess, D. H.; Houk, K. N. Distortion/Interaction Energy Control of 1,3-Dipolar Cycloaddition Reactivity. *J. Am. Chem. Soc.* **2007**, *129* (35), 10646–10647.

(246) Cottrell, T. L. *The Strengths of Chemical Bonds*, 2nd Ed.; Butterworths, London, 1958.

(247) Benson, S. W. III - Bond Energies. *J. Chem. Educ.* **1965**, *42* (9), 502.

(248) Tan, J. S. J.; Paton, R. S. Frontier Molecular Orbital Effects Control the Hole-Catalyzed Racemization of Atropisomeric Biaryls. *Chem. Sci.* **2019**, *10* (8), 2285–2289.

(249) Tan, J. S. J.; Hirvonen, V.; Paton, R. S. Dynamic Intermediates in the Radical Cation Diels–Alder Cycloaddition: Lifetime and Suprafacial Stereoselectivity. *Org. Lett.* **2018**, *20* (10), 2821–2825.

(250) Marcus, R. A. On the Theory of Oxidation-Reduction Reactions Involving Electron Transfer. I. *J. Chem. Phys.* **1956**, *24* (5), 966–978.

(251) Marcus, R. A. On the Theory of Oxidation-Reduction Reactions Involving Electron Transfer. III. Applications to Data on the Rates of Organic Redox Reactions. *J. Chem. Phys.* **1957**, *26* (4), 872–877.

(252) Marcus, R. On the Theory of Oxidation-Reduction Reactions Involving Election Transfer V. Comparison and Properties of Electrochemical and Chemical Rate

Constants - Correction. *J. Phys. Chem.* **2007**, *67* (12), 2889–2889.

(253) Hush, N. S. Homogeneous and Heterogeneous Optical and Thermal Electron Transfer. *Electrochim. Acta* **1968**, *13* (5), 1005–1023.

(254) Closs, G. L.; Calcaterra, L. T.; Green, N. J.; Penfield, K. W.; Miller, J. R. Distance, Stereoelectronic Effects, and the Marcus Inverted Region in Intramolecular Electron Transfer in Organic Radical Anions. *J. Phys. Chem.* **1986**, *90* (16), 3673–3683.

(255) Han, C. C.; Wilbur, J. L.; Brauman, J. I. Kinetic Models for Gas-Phase Electron-Transfer Reactions between Nitrobenzenes. *J. Am. Chem. Soc.* **1992**, *114* (3), 887–893.

(256) Shannon, C. F.; Eads, D. D. Diffusion-Controlled Electron Transfer Reactions: Subpicosecond Fluorescence Measurements of Coumarin 1 Quenched by Aniline and N,N-Dimethylaniline. *J. Chem. Phys.* **1995**, *103* (13), 5208–5223.

(257) Eyler, J. R.; Richardson, D. E. Gas-Phase Electron Transfer: Direct Observation of Kinetic Barriers in Metallocene Self-Exchange Reactions. *J. Am. Chem. Soc.* **2005**, *107* (21), 6130–6131.

(258) Richardson, D. E. Potential Surfaces for Gas-Phase Electron-Transfer Reactions. *J. Phys. Chem.* **1986**, *90* (16), 3697–3700.

(259) Richardson, D. E.; Christ, C. S.; Sharpe, P.; Eyler, J. R. Gas-Phase Electron Transfer: Thermal Self-Exchange and Cross Reactions of Organometallic Molecules and Ions. *J. Am. Chem. Soc.* **1987**, *109* (13), 3894–3902.

(260) Appel, R. Tertiary Phosphane/Tetrachloromethane, a Versatile Reagent for Chlorination, Dehydration, and P–N Linkage. *Angew. Chem. Int. Ed.* **1975**, *14* (12), 801–811.

(261) Mitsunobu, O.; Yamada, M. Preparation of Esters of Carboxylic and Phosphoric Acid via Quaternary Phosphonium Salts. *Bull. Chem. Soc. Jpn.* **1967**, *40* (10), 2380–2382.

(262) Mitsunobu, O.; Eguchi, M. Preparation of Carboxylic Esters and Phosphoric Esters by the Activation of Alcohols. *Bull. Chem. Soc. Jpn.* **1971**, *44* (12), 3427–3430.

(263) Wittig, G.; Geissler, G. Zur Reaktionsweise Des Pentaphenyl-phosphors Und Einiger Derivate. *Justus Liebigs Ann. Chem.* **1953**, *580* (1), 44–57.

(264) Wittig, G.; Schöllkopf, U. Über Triphenyl-phosphin-methylene Als Olefinbildende Reagenzien (I. Mitteil.). *Chem. Ber.* **1954**, *87* (9), 1318–1330.

(265) Staudinger, H.; Hauser, E. Über Neue Organische Phosphorverbindungen IV Phosphinimine. *Helv. Chim. Acta* **1921**, *4* (1), 861–886.

(266) Staudinger, H.; Meyer, J. Ueber Neue Organische Phosphorverbindungen II. Phosphazine. *Helv. Chim. Acta* **1919**, *2* (1), 619–635.

(267) Scriven, E. F. V.; Turnbull, K. Azides: Their Preparation and Synthetic Uses. *Chem. Rev.* **1988**, *88* (2), 297–368.

(268) Pedley, J. B.; Marshall, E. M. Thermochemical Data for Gaseous Monoxides. *J. Phys. Chem. Ref. Data* **1983**, *12* (4), 967–1031.

(269) Van Kalkeren, H. A.; Blom, A. L.; Rutjes, F. P. J. T.; Huijbregts, M. A. J. On the Usefulness of Life Cycle Assessment in Early Chemical Methodology Development: The Case of Organophosphorus-Catalyzed Appel and Wittig Reactions. *Green Chem.* **2013**, *15* (5), 1255–1263.

(270) van Kalkeren, H. A.; van Delft, F. L.; Rutjes, F. P. J. T. J. T.; Van Kalkeren, H. A.; Van Delft, F. L.; Rutjes, F. P. J. T. J. T. Organophosphorus Catalysis to Bypass Phosphine Oxide Waste. *ChemSusChem* **2013**, *6* (9), 1615–1624.

(271) van Kalkeren, H. A.; Bruins, J. J.; Rutjes, F. P. J. T.; van Delft, F. L. Organophosphorus-Catalysed Staudinger Reduction. *Adv. Synth. Catal.* **2012**, *354* (8), 1417–1421.

(272) Mitzel, N. W.; Schier, A.; Beruda, H.; Schmidbaur, H. Phenylsilyl Chalcogenides, (Phenylsilyl)Amines and Related Phosphonium (Phenylsilyl)Methylides. *Chem. Ber.* **1992**, *125* (5), 1053–1059.

(273) Mitzel, N. W.; Angermaier, K.; Schmidbaur, H. Synthesis and Structure of N-Silylated Anilines. *Chem. Ber.* **1994**, *127* (5), 841–844.

(274) Li, P.; Wischert, R.; Métivier, P. Mild Reduction of Phosphine Oxides with Phosphites To Access Phosphines. *Angew. Chem. Int. Ed.* **2017**, *56* (50), 15989–15992.

(275) Buonomo, J. A.; Eiden, C. G.; Aldrich, C. C. Chemoselective Reduction of Phosphine Oxides by 1,3-Diphenyl-Disiloxane. *Chem.: Eur. J.* **2017**, *23* (58), 14434–14438.

(276) Provis-Evans, C. B.; Emanuelsson, E. A. C.; Webster, R. L. Rapid Metal-Free

Formation of Free Phosphines from Phosphine Oxides. *Adv. Synth. Catal.* **2018**, *360* (20), 3999–4004.

(277) Lenstra, D. C.; Wolf, J. J.; Mecinović, J. Catalytic Staudinger Reduction at Room Temperature. *J. Org. Chem.* **2019**, *84* (10), 6536–6545.

(278) Reichl, K. D.; Dunn, N. L.; Fastuca, N. J.; Radosevich, A. T. Biphilic Organophosphorus Catalysis: Regioselective Reductive Transposition of Allylic Bromides via PIII/PV Redox Cycling. *J. Am. Chem. Soc.* **2015**, *137* (16), 5292–5295.

(279) Lodewyk, M. W.; Siebert, M. R.; Tantillo, D. J. Computational Prediction of ^{1}H and ^{13}C Chemical Shifts: A Useful Tool for Natural Product, Mechanistic, and Synthetic Organic Chemistry. *Chem. Rev.* **2012**, *112* (3), 1839–1862.

(280) Cheeseman, J. R. A Comparison of Models for Calculating Nuclear Magnetic Resonance Shielding Tensors. *J. Chem. Phys.* **1996**, *104* (14), 5497–5509.

(281) Contreras-García, J.; Johnson, E. R.; Keinan, S.; Chaudret, R.; Piquemal, J. P.; Beratan, D. N.; Yang, W. NCIPLOT: A Program for Plotting Noncovalent Interaction Regions. *J. Chem. Theory Comput.* **2011**, *7* (3), 625–632.

(282) Berendsen, H. J. C.; van der Spoel, D.; van Drunen, R. GROMACS: A Message-Passing Parallel Molecular Dynamics Implementation. *Comput. Phys. Commun.* **1995**, *91* (1–3), 43–56.

(283) Lindahl, E.; Hess, B.; van der Spoel, D. GROMACS 3.0: A Package for Molecular Simulation and Trajectory Analysis. *J. Mol. Model.* **2001**, *7* (8), 306–317.

(284) Van Der Spoel, D.; Lindahl, E.; Hess, B.; Groenhof, G.; Mark, A. E.; Berendsen, H. J. C. GROMACS: Fast, Flexible, and Free. *J. Comput. Chem.* **2005**, *26* (16), 1701–1718.

(285) Hess, B.; Kutzner, C.; Van Der Spoel, D.; Lindahl, E. GRGMACS 4: Algorithms for Highly Efficient, Load-Balanced, and Scalable Molecular Simulation. *J. Chem. Theory Comput.* **2008**, *4* (3), 435–447.

(286) Pronk, S.; Páll, S.; Schulz, R.; Larsson, P.; Bjelkmar, P.; Apostolov, R.; Shirts, M. R.; Smith, J. C.; Kasson, P. M.; Van Der Spoel, D.; et al. GROMACS 4.5: A High-Throughput and Highly Parallel Open Source Molecular Simulation Toolkit. *Bioinformatics* **2013**, *29* (7), 845–854.

(287) Abraham, M. J.; Murtola, T.; Schulz, R.; Páll, S.; Smith, J. C.; Hess, B.; Lindah, E. Gromacs: High Performance Molecular Simulations through Multi-Level Parallelism from Laptops to Supercomputers. *SoftwareX* **2015**, *1–2*, 19–25.

(288) Jorgensen, W. L.; Tirado-Rives, J. The OPLS Potential Functions for Proteins. Energy Minimizations for Crystals of Cyclic Peptides and Crambin. *J. Am. Chem. Soc.* **1988**, *110* (6), 1657–1666.

(289) Jorgensen, W. L.; Maxwell, D. S.; Tirado-Rives, J. Development and Testing of the OPLS All-Atom Force Field on Conformational Energetics and Properties of Organic Liquids. *J. Am. Chem. Soc.* **1996**, *118* (45), 11225–11236.

(290) Schrödinger LLC. Schrödinger Release 2017-2: Maestro. New York, NY 2017.

(291) Bayly, C. I.; Cieplak, P.; Cornell, W. D.; Kollman, P. A. A Well-Behaved Electrostatic Potential Based Method Using Charge Restraints for Deriving

Atomic Charges: The RESP Model. *J. Phys. Chem.* **1993**, *97* (40), 10269–10280.

(292) Cornell, W. D.; Cieplak, P.; Bayly, C. I.; Kollman, P. A. Application of RESP Charges To Calculate Conformational Energies, Hydrogen Bond Energies, and Free Energies of Solvation. *J. Am. Chem. Soc.* **1993**, *115* (21), 9620–9631.

(293) Case, D. A.; Ben-Shalom, I. Y.; Brozell, S. R.; Cerutti, D. S.; Cheatham, III, T. E.; Cruzeiro, V. W. D.; Darden, T. A.; Duke, R. E.; Ghoreishi, D.; Gilson, M. K.; et al. Amber 2018. *Univeristy of California, San Francisco*. University of California, San Francisco 2018.

(294) van der Spoel, D.; van Maaren, P. J.; Caleman, C. GROMACS Molecule & Liquid Database. *Bioinformatics* **2012**, *28* (5), 752–753.

(295) Chen, S.; Yi, S.; Gao, W.; Zuo, C.; Hu, Z. Force Field Development for Organic Molecules: Modifying Dihedral and 1-n Pair Interaction Parameters. *J. Comput. Chem.* **2015**, *36* (6), 376–384.

(296) Duarte, F.; Paton, R. S. Molecular Recognition in Asymmetric Counteranion Catalysis: Understanding Chiral Phosphate-Mediated Desymmetrization. *J. Am. Chem. Soc.* **2017**, *139* (26), 8886–8896.

(297) Essmann, U.; Perera, L.; Berkowitz, M. L.; Darden, T.; Lee, H.; Pedersen, L. G. A Smooth Particle Mesh Ewald Method. *J. Chem. Phys.* **1995**, *103* (19), 8577–8593.

(298) Hess, B.; Bekker, H.; Berendsen, H. J. C.; Fraaije, J. G. E. M. LINCS: A Linear Constraint Solver for Molecular Simulations. *J. Comput. Chem.* **1997**, *18* (12), 1463–1472.

(299) Bussi, G.; Donadio, D.; Parrinello, M. Canonical Sampling through Velocity Rescaling. *J. Chem. Phys.* **2007**, *126* (1), 14101.

(300) Parrinello, M.; Rahman, A. Crystal Structure and Pair Potentials: A Molecular-Dynamics Study. *Phys. Rev. Lett.* **1980**, *45* (14), 1196–1199.

(301) Parrinello, M.; Rahman, A. Polymorphic Transitions in Single Crystals: A New Molecular Dynamics Method. *J. Appl. Phys.* **1981**, *52* (12), 7182–7190.

(302) Daura, X.; Gademann, K.; Jaun, B.; Seebach, D.; van Gunsteren, W. F.; Mark, A. E. Peptide Folding: When Simulation Meets Experiment. *Angew. Chem. Int. Ed.* **1999**, *38* (1/2), 236–240.

(303) Widauer, C.; Grützmacher, H.; Shevchenko, I.; Gramlich, V. Insights into the Staudinger Reaction: Experimental and Theoretical Studies on the Stabilization Ofcis-Phosphazides. *Eur. J. Inorg. Chem.* **1999**, *1999* (10), 1659–1664.

(304) Alajarin, M.; Conesa, C.; Rzepa, H. S. Ab Initio SCF-MO Study of the Staudinger Phosphorylation Reaction between a Phosphane and an Azide to Form a Phosphazene. *J. Chem. Soc. Perkin Trans. 2* **1999**, 1811–1814.

(305) Tian, W. Q.; Wang, Y. A. Mechanisms of Staudinger Reactions within Density Functional Theory. *J. Org. Chem.* **2004**, *69* (13), 4299–4308.

(306) Hérault, D.; Nguyen, D. H.; Nuel, D.; Buono, G. *Reduction of Secondary and Tertiary Phosphine Oxides to Phosphines*; Royal Society of Chemistry, 2015; Vol. 44, pp 2508–2528.

(307) Van Kalkeren, H. A.; Leenders, S. H. A. M.; Hommersom, C. R. A.; Rutjes, F. P.

J. T.; Van Delft, F. L. In Situ Phosphine Oxide Reduction: A Catalytic Appel Reaction. *Chem.: Eur. J.* **2011**, *17* (40), 11290–11295.

(308) Keglevich, G.; Kovacs, T. Silanes as Reagents for the Deoxygenation of Tertiary Phosphine Oxides A Case Study for the Deoxygenation of 5-Membered Cyclic Phosphine Oxides. *Curr. Green Chem.* **2014**, *1* (2), 182–188.

(309) Wu, H. C.; Yu, J. Q.; Spencer, J. B. Stereospecific Deoxygenation of Phosphine Oxides with Retention of Configuration Using Triphenylphosphine or Triethyl Phosphite as an Oxygen Acceptor. *Org. Lett.* **2004**, *6* (25), 4675–4678.

(310) Lao, Z.; Toy, P. H. Catalytic Wittig and Aza-Wittig Reactions. *Beilstein J. Org. Chem.* **2016**, *12* (1), 2577–2587.

(311) Fianchini, M.; O'Brien, C. J.; Chass, G. A. Reduction Rate of 1-Phenyl Phospholane 1-Oxide Enhanced by Silanol Byproducts: Comprehensive DFT Study and Kinetic Modeling Linked to Reagent Design. *J. Org. Chem.* **2019**, *84* (17), 10579–10592.

(312) Liu, Z.; Patel, C.; Harvey, J. N.; Sunoj, R. B. Mechanism and Reactivity in the Morita-Baylis-Hillman Reaction: The Challenge of Accurate Computations. *Phys. Chem. Chem. Phys.* **2017**, *19* (45), 30647–30657.

(313) Doggett, G. *Electronic Structure of Molecules*; Cornell University Press, 1980; Vol. 77.

(314) Muetterties, E. L.; Mahler, W.; Schmutzler, R. Stereochemistry of Phosphorus(V) Fluorides. *Inorg. Chem.* **1963**, *2* (3), 613–618.

(315) Hoffmann, R.; Woodward, R. B. The Conservation of Orbital Symmetry. *Acc. Chem. Res.* **1968**, *1* (1), 17–22.

(316) Adamo, C.; Barone, V. Exchange Functionals with Improved Long-Range Behavior and Adiabatic Connection Methods without Adjustable Parameters: The MPW and MPW1PW Models. *J. Chem. Phys.* **1998**, *108* (2), 664–675.

(317) Tantillo, D. CHEMical SHIft REpository with Coupling Constants Added Too http://cheshirenmr.info/index.htm (accessed Jul 1, 2017).

(318) Shepherd, E. D.; Dyson, B. S.; Hak, W. E.; Nguyen, Q. N. N.; Lee, M.; Kim, M. J.; Sohn, T. I.; Kim, D.; Burton, J. W.; Paton, R. S. Structure Determination of a Chloroenyne from Laurencia Majuscula Using Computational Methods and Total Synthesis. *J. Org. Chem.* **2019**, *84* (9), 4971–4991.

(319) Jameson, C. J.; De Dios, A.; Keith Jameson, A. Absolute Shielding Scale for 31P from Gas-Phase NMR Studies. *Chem. Phys. Lett.* **1990**, *167* (6), 575–582.

(320) Latypov, S. K.; Polyancev, F. M.; Yakhvarov, D. G.; Sinyashin, O. G. Quantum Chemical Calculations of ^{31}P NMR Chemical Shifts: Scopes and Limitations. *Phys. Chem. Chem. Phys.* **2015**, *17* (10), 6976–6987.

(321) Perdew, J. P.; Burke, K.; Ernzerhof, M. Generalized Gradient Approximation Made Simple. *Phys. Rev. Lett.* **1996**, *77* (18), 3865–3868.

(322) Perdew, J. P.; Burke, K.; Ernzerhof, M. Erratum: Generalized Gradient Approximation Made Simple (Physical Review Letters (1996) 77 (3865)). *Phys. Rev. Lett.* **1997**, *78* (8), 1396.

(323) Adamo, C.; Barone, V. Toward Reliable Density Functional Methods without Adjustable Parameters: The PBE0 Model. *J. Chem. Phys.* **1999**, *110* (13), 6158–6170.

(324) Ernzerhof, M.; Scuseria, G. E. Assessment of the Perdew-Burke-Ernzerhof Exchange-Correlation Functional. *J. Chem. Phys.* **1999**, *110* (11), 5029–5036.

(325) Labinger, J. A.; Bercaw, J. E. Understanding and Exploiting C-H Bond Activation. *Nature* **2002**, *417* (6888), 507–514.

(326) Wencel-Delord, J.; Glorius, F. C-H Bond Activation Enables the Rapid Construction and Late-Stage Diversification of Functional Molecules. *Nat. Chem.* **2013**, *5* (5), 369–375.

(327) Hennessy, E. J.; Buchwald, S. L. Synthesis of Substituted Oxindoles from α-Chloroacetanilides via Palladium-Catalyzed C-H Functionalization. *J. Am. Chem. Soc.* **2003**, *125* (40), 12084–12085.

(328) Faccini, F.; Motti, E.; Catellani, M. A New Reaction Sequence Involving Palladium-Catalyzed Unsymmetrical Aryl Coupling. *J. Am. Chem. Soc.* **2004**, *126* (1), 78–79.

(329) Grimster, N. P.; Gauntlett, C.; Godfrey, C. R. A.; Gaunt, M. J. Palladium-Catalyzed Intermolecular Alkenylation of Indoles by Solvent-Controlled Regioselective C-H Functionalization. *Angew. Chem. Int. Ed.* **2005**, *44* (20), 3125–3129.

(330) Campeau, L. C.; Rousseaux, S.; Fagnou, K. A Solution to the 2-Pyridyl Organometallic Cross-Coupling Problem: Regioselective Catalytic Direct

Arylation of Pyridine N-Oxides. *J. Am. Chem. Soc.* **2005**, *127* (51), 18020–18021.

(331) Chiong, H. A.; Pham, Q. N.; Daugulis, O. Two Methods for Direct Ortho-Arylation of Benzoic Acids. *J. Am. Chem. Soc.* **2007**, *129* (32), 9879–9884.

(332) Hull, K. L.; Sanford, M. S. Catalytic and Highly Regioselective Cross-Coupling of Aromatic C-H Substrates. *J. Am. Chem. Soc.* **2007**, *129* (39), 11904–11905.

(333) Wang, D. H.; Mei, T. S.; Yu, J. Q. Versatile Pd(II)-Catalyzed C-H Activation/Aryl-Aryl Coupling of Benzoic and Phenyl Acetic Acids. *J. Am. Chem. Soc.* **2008**, *130* (52), 17676–17677.

(334) Li, B. J.; Tian, S. L.; Fang, Z.; Shi, Z. J. Multiple C-H Activations to Construct Biologically Active Molecules in a Process Completely Free of Organohalogen and Organometallic Components. *Angew. Chem. Int. Ed.* **2008**, *47* (6), 1115–1118.

(335) Gao, P.; Guo, W.; Xue, J.; Zhao, Y.; Yuan, Y.; Xia, Y.; Shi, Z. Iridium(III)-Catalyzed Direct Arylation of C-H Bonds with Diaryliodonium Salts. *J. Am. Chem. Soc.* **2015**, *137* (38), 12231–12240.

(336) Seung, H. C.; Seung, J. H.; Chang, S. Palladium-Catalyzed C-H Functionalization of Pyridine N-Oxides: Highly Selective Alkenylation and Direct Arylation with Unactivated Arenes. *J. Am. Chem. Soc.* **2008**, *130* (29), 9254–9256.

(337) Rousseau, G.; Breit, B. Removable Directing Groups in Organic Synthesis and Catalysis. *Angew. Chem. Int. Ed.* **2011**, *50* (11), 2450–2494.

(338) Lin, C.; Shen, L. Recent Progress in Transition Metal-Catalyzed Regioselective Functionalization of Unactivated Alkenes/Alkynes Assisted by Bidentate Directing Groups. *ChemCatChem* **2019**, *11* (3), 961–968.

(339) Tiwari, V. K.; Kapur, M. Catalyst-Controlled Positional-Selectivity in C-H Functionalizations. *Org. Biomol. Chem.* **2019**, *17* (5), 1007–1026.

(340) Kittakoop, P.; Mahidol, C.; Ruchirawat, S. Alkaloids as Important Scaffolds in Therapeutic Drugs for the Treatments of Cancer, Tuberculosis, and Smoking Cessation. *Curr. Top. Med. Chem.* **2014**, *14* (2), 239–252.

(341) Cushnie, T. P. T.; Cushnie, B.; Lamb, A. J. Alkaloids: An Overview of Their Antibacterial, Antibiotic-Enhancing and Antivirulence Activities. *Int. J. Antimicrob. Agents* **2014**, *44* (5), 377–386.

(342) McGrath, N. A.; Brichacek, M.; Njardarson, J. T. A Graphical Journey of Innovative Organic Architectures That Have Improved Our Lives. *J. Chem. Educ.* **2010**, *87* (12), 1348–1349.

(343) Chen, X.; Engle, K. M.; Wang, D. H.; Jin-Quan, Y. Palladium(II)-CataIyzed C-H Aetivation/C-C Cross-Coupling Reactions: Versatility and Practicality. *Angew. Chem. Int. Ed.* **2009**, *48* (28), 5094–5115.

(344) Baudoin, O. Transition Metal-Catalyzed Arylation of Unactivated C(sp^3)–H Bonds. *Chem. Soc. Rev.* **2011**, *40* (10), 4902–4911.

(345) Li, H.; Li, B. J.; Shi, Z. J. Challenge and Progress: Palladium-Catalyzed sp^3 C-H Activation. *Catal. Sci. Technol.* **2011**, *1* (2), 191–206.

(346) White, M. C. Adding Aliphatic C-H Bond Oxidations to Synthesis. *Science* **2012**, *335* (6070), 807–809.

(347) Yamaguchi, J.; Yamaguchi, A. D.; Itami, K. C-H Bond Functionalization: Emerging Synthetic Tools for Natural Products and Pharmaceuticals. *Angew. Chem. Int. Ed.* **2012**, *51* (36), 8960–9009.

(348) Colby, D. A.; Bergman, R. G.; Ellman, J. A. Rhodium-Catalyzed C−C Bond Formation via Heteroatom-Directed C−H Bond Activation. *Chem. Rev.* **2010**, *110* (2), 624–655.

(349) Daugulis, O.; Roane, J.; Tran, L. D. Bidentate, Monoanionic Auxiliary-Directed Functionalization of Carbon-Hydrogen Bonds. *Acc. Chem. Res.* **2015**, *48* (4), 1053–1064.

(350) Lyons, T. W.; Sanford, M. S. Palladium-Catalyzed Ligand-Directed C−H Functionalization Reactions. *Chem. Rev.* **2010**, *110* (2), 1147–1169.

(351) Rouquet, G.; Chatani, N. Catalytic Functionalization of C(Sp^2)-H and C(sp^3)-H Bonds by Using Bidentate Directing Groups. *Angew. Chem. Int. Ed.* **2013**, *52* (45), 11726–11743.

(352) Chen, Z.; Wang, B.; Zhang, J.; Yu, W.; Liu, Z.; Zhang, Y. Transition Metal-Catalyzed C-H Bond Functionalizations by the Use of Diverse Directing Groups. *Org. Chem. Front.* **2015**, *2* (9), 1107–1295.

(353) He, G.; Wang, B.; Nack, W. A.; Chen, G. Syntheses and Transformations of α-Amino Acids via Palladium-Catalyzed Auxiliary-Directed sp^3 C-H Functionalization. *Acc. Chem. Res.* **2016**, *49* (4), 635–645.

(354) Lewis, J. C.; Coelho, P. S.; Arnold, F. H. Enzymatic Functionalization of Carbon-Hydrogen Bonds. *Chem. Soc. Rev.* **2011**, *40* (4), 2003–2021.

(355) Yoo, W. J.; Li, C. J. Cross-Dehydrogenative Coupling Reactions of sp^3-Hybridized C-H Bonds. In *Topics in current chemistry*; Springer Berlin Heidelberg, 2010; Vol. 292, pp 281–302.

(356) Yeung, C. S.; Dong, V. M. Catalytic Dehydrogenative Cross-Coupling: Forming Carbon−Carbon Bonds by Oxidizing Two Carbon−Hydrogen Bonds. *Chem. Rev.* **2011**, *111* (3), 1215–1292.

(357) Zhang, C.; Tang, C.; Jiao, N. Recent Advances in Copper-Catalyzed Dehydrogenative Functionalization via a Single Electron Transfer (SET) Process. *Chem. Soc. Rev.* **2012**, *41* (9), 3464–3484.

(358) Girard, S. A.; Knauber, T.; Li, C. J. The Cross-Dehydrogenative Coupling of C_{sp3}-H Bonds: A Versatile Strategy for C-C Bond Formations. *Angew. Chem. Int. Ed.* **2014**, *53* (1), 74–100.

(359) Spangler, J. E.; Kobayashi, Y.; Verma, P.; Wang, D. H.; Yu, J. Q. α-Arylation of Saturated Azacycles and N-Methylamines via Palladium(II)-Catalyzed C(sp^3)-H Coupling. *J. Am. Chem. Soc.* **2015**, *137* (37), 11876–11879.

(360) Chatani, N.; Asaumi, T.; Ikeda, T.; Yorimitsu, S.; Ishii, Y.; Kakiuchi, F.; Murai, S. Carbonylation at sp^3 C-H Bonds Adjacent to a Nitrogen Atom in Alkylamines Catalyzed by Rhodium Complexes. *J. Am. Chem. Soc.* **2000**, *122* (51), 12882–12883.

(361) McNally, A.; Haffemayer, B.; Collins, B. S. L.; Gaunt, M. J. Palladium-

Catalysed C-H Activation of Aliphatic Amines to Give Strained Nitrogen Heterocycles. *Nature* **2014**, *510* (7503), 129–133.

(362) Topczewski, J. J.; Cabrera, P. J.; Saper, N. I.; Sanford, M. S. Palladium-Catalysed Transannular C-H Functionalization of Alicyclic Amines. *Nature* **2016**, *531* (7593), 220–224.

(363) Calleja, J.; Pla, D.; Gorman, T. W.; Domingo, V.; Haffemayer, B.; Gaunt, M. J. A Steric Tethering Approach Enables Palladium-Catalysed C-H Activation of Primary Amino Alcohols. *Nat. Chem.* **2015**, *7* (12), 1009–1016.

(364) Huang, Z.; Wang, C.; Dong, G. A Hydrazone-Based Exo-Directing-Group Strategy for β C-H Oxidation of Aliphatic Amines. *Angew. Chem. Int. Ed.* **2016**, *55* (17), 5299–5303.

(365) Liu, Y.; Ge, H. Site-Selective C-H Arylation of Primary Aliphatic Amines Enabled by a Catalytic Transient Directing Group. *Nat. Chem.* **2017**, *9* (1), 26–32.

(366) Li, S.; Zhu, R. Y.; Xiao, K. J.; Yu, J. Q. Ligand-Enabled Arylation of γ-C-H Bonds. *Angew. Chem. Int. Ed.* **2016**, *55* (13), 4317–4321.

(367) Zaitsev, V. G.; Shabashov, D.; Daugulis, O. Highly Regioselective Arylation of sp^3 C-H Bonds Catalyzed by Palladium Acetate. *J. Am. Chem. Soc.* **2005**, *127* (38), 13154–13155.

(368) He, G.; Chen, G. A Practical Strategy for the Structural Diversification of Aliphatic Scaffolds through the Palladium-Catalyzed Picolinamide-Directed Remote Functionalization of Unactivated C(sp^3)-H Bonds. *Angew. Chem. Int.*

Ed. **2011**, *50* (22), 5192–5196.

(369) Wu, Y.; Chen, Y. Q.; Liu, T.; Eastgate, M. D.; Yu, J. Q. Pd-Catalyzed γ-C(sp^3)-H Arylation of Free Amines Using a Transient Directing Group. *J. Am. Chem. Soc.* **2016**, *138* (44), 14554–14557.

(370) Xu, Y.; Young, M. C.; Wang, C.; Magness, D. M.; Dong, G. Catalytic C(sp^3)−H Arylation of Free Primary Amines with an Exo Directing Group Generated In Situ. *Angew. Chem. Int. Ed.* **2016**, *55* (31), 9084–9087.

(371) Yada, A.; Liao, W.; Sato, Y.; Murakami, M. Buttressing Salicylaldehydes: A Multipurpose Directing Group for C(sp^3)−H Bond Activation. *Angew. Chem. Int. Ed.* **2017**, *56* (4), 1073–1076.

(372) Wang, Z. Q.; Hu, M.; Huang, X. C.; Gong, L. B.; Xie, Y. X.; Li, J. H. Direct α-Arylation of α-Amino Carbonyl Compounds with Indoles Using Visible Light Photoredox Catalysis. *J. Org. Chem.* **2012**, *77* (19), 8705–8711.

(373) Zhao, L.; Li, C. J. Functionalizing Glycine Derivatives by Direct C-C Bond Formation. *Angew. Chem. Int. Ed.* **2008**, *47* (37), 7075–7078.

(374) Zhao, L.; Basle, O.; Li, C.-J. Site-Specific C-Functionalization of Free-(NH) Peptides and Glycine Derivatives via Direct C-H Bond Functionalization. *Proc. Natl. Acad. Sci.* **2009**, *106* (11), 4106–4111.

(375) Osberger, T. J.; Rogness, D. C.; Kohrt, J. T.; Stepan, A. F.; White, M. C. Oxidative Diversification of Amino Acids and Peptides by Small-Molecule Iron Catalysis. *Nature* **2016**, *537* (7619), 214–219.

(376) Reddy, B. V. S.; Reddy, L. R.; Corey, E. J. Novel Acetoxylation and C-C Coupling Reactions at Unactivated Positions in α-Amino Acid Derivatives. *Org. Lett.* **2006**, *8* (15), 3391–3394.

(377) Ano, Y.; Tobisu, M.; Chatani, N. Palladium-Catalyzed Direct Ethynylation of C(sp^3)-H Bonds in Aliphatic Carboxylic Acid Derivatives. *J. Am. Chem. Soc.* **2011**, *133* (33), 12984–12986.

(378) Tran, L. D.; Daugulis, O. Nonnatural Amino Acid Synthesis by Using Carbon-Hydrogen Bond Functionalization Methodology. *Angew. Chem. Int. Ed.* **2012**, *51* (21), 5188–5191.

(379) He, G.; Zhang, S. Y.; Nack, W. A.; Li, Q.; Chen, G. Use of a Readily Removable Auxiliary Group for the Synthesis of Pyrrolidones by the Palladium-Catalyzed Intramolecular Amination of Unactivated γ C(sp^3)-H Bonds. *Angew. Chem. Int. Ed.* **2013**, *52* (42), 11124–11128.

(380) Fan, M.; Ma, D. Palladium-Catalyzed Direct Functionalization of 2-Aminobutanoic Acid Derivatives: Application of a Convenient and Versatile Auxiliary. *Angew. Chem. Int. Ed.* **2013**, *52* (46), 12152–12155.

(381) He, J.; Li, S.; Deng, Y.; Fu, H.; Laforteza, B. N.; Spangler, J. E.; Homs, A.; Yu, J. Q. Ligand-Controlled C(sp^3)-H Arylation and Olefination in Synthesis of Unnatural Chiral α-Amino Acids. *Science* **2014**, *343* (6176), 1216–1220.

(382) Gong, W.; Zhang, G.; Liu, T.; Giri, R.; Yu, J. Q. Site-Selective C(sp^3)-H Functionalization of Di-, Tri-, and Tetrapeptides at the N-Terminus. *J. Am. Chem. Soc.* **2014**, *136* (48), 16940–16946.

(383) He, G.; Zhang, S. Y.; Nack, W. A.; Pearson, R.; Rabb-Lynch, J.; Chen, G. Total Synthesis of Hibispeptin A via Pd-Catalyzed C(sp^3)-H Arylation with Sterically Hindered Aryl Iodides. *Org. Lett.* **2014**, *16* (24), 6488–6491.

(384) Zhang, Q.; Yin, X. S.; Chen, K.; Zhang, S. Q.; Shi, B. F. Stereoselective Synthesis of Chiral β-Fluoro α-Amino Acids via Pd(II)-Catalyzed Fluorination of Unactivated Methylene C(sp^3)-H Bonds: Scope and Mechanistic Studies. *J. Am. Chem. Soc.* **2015**, *137* (25), 8219–8226.

(385) Li, S.; Chen, G.; Feng, C. G.; Gong, W.; Yu, J. Q. Ligand-Enabled γ-C-H Olefination and Carbonylation: Construction of β-Quaternary Carbon Centers. *J. Am. Chem. Soc.* **2014**, *136* (14), 5267–5270.

(386) Deb, A.; Singh, S.; Seth, K.; Pimparkar, S.; Bhaskararao, B.; Guin, S.; Sunoj, R. B.; Maiti, D. Experimental and Computational Studies on Remote γ-C(sp^3)-H Silylation and Germanylation of Aliphatic Carboxamides. *ACS Catal.* **2017**, *7* (12), 8171–8175.

(387) Thrimurtulu, N.; Khan, S.; Maity, S.; Volla, C. M. R.; Maiti, D. Palladium Catalyzed Direct Aliphatic γC(sp^3)-H Alkenylation with Alkenes and Alkenyl Iodides. *Chem. Commun.* **2017**, *53* (92), 12457–12460.

(388) Dey, A.; Pimparkar, S.; Deb, A.; Guin, S.; Maiti, D. Chelation-Assisted Palladium-Catalyzed γ-Arylation of Aliphatic Carboxylic Acid Derivatives. *Adv. Synth. Catal.* **2017**, *359* (8), 1301–1307.

(389) Bauer, M.; Wang, W.; Lorion, M. M.; Dong, C.; Ackermann, L. Internal Peptide Late-Stage Diversification: Peptide-Isosteric Triazoles for Primary and

Secondary C(sp^3)−H Activation. *Angew. Chem. Int. Ed.* **2018**, *57* (1), 203–207.

(390) Guin, S.; Deb, A.; Dolui, P.; Chakraborty, S.; Singh, V. K.; Maiti, D. Promoting Highly Diastereoselective γ-C-H Chalcogenation of α-Amino Acids and Aliphatic Carboxylic Acids. *ACS Catal.* **2018**, *8* (4), 2664–2669.

(391) Zhang, X.; Lu, G.; Sun, M.; Mahankali, M.; Ma, Y.; Zhang, M.; Hua, W.; Hu, Y.; Wang, Q.; Chen, J.; et al. A General Strategy for Synthesis of Cyclophane-Braced Peptide Macrocycles via Palladium-Catalysed Intramolecular sp^3 C-H Arylation. *Nat. Chem.* **2018**, *10* (5), 540–548.

(392) Wang, W.; Lorion, M. M.; Martinazzoli, O.; Ackermann, L. BODIPY Peptide Labeling by Late-Stage C(sp^3)−H Activation. *Angew. Chem. Int. Ed.* **2018**, *57* (33), 10554–10558.

(393) Noisier, A. F. M.; Brimble, M. A. C–H Functionalization in the Synthesis of Amino Acids and Peptides. *Chem. Rev.* **2014**, *114* (18), 8775–8806.

(394) He, G.; Zhao, Y.; Zhang, S.; Lu, C.; Chen, G. Highly Efficient Syntheses of Azetidines, Pyrrolidines, and Indolines via Palladium Catalyzed Intramolecular Amination of C(sp^3)-H and C(Sp^2)-H Bonds at γ and δ Positions. *J. Am. Chem. Soc.* **2012**, *134* (1), 3–6.

(395) Nadres, E. T.; Daugulis, O. Heterocycle Synthesis via Direct C-H/N-H Coupling. *J. Am. Chem. Soc.* **2012**, *134* (1), 7–10.

(396) Cui, W.; Chen, S.; Wu, J. Q.; Zhao, X.; Hu, W.; Wang, H. Palladium-Catalyzed Remote C(sp^3)-H Arylation of 3-Pinanamine. *Org. Lett.* **2014**, *16* (16), 4288–4291.

(397) Xu, J. W.; Zhang, Z. Z.; Rao, W. H.; Shi, B. F. Site-Selective Alkenylation of δ-C(sp^3)-H Bonds with Alkynes via a Six-Membered Palladacycle. *J. Am. Chem. Soc.* **2016**, *138* (34), 10750–10753.

(398) Zhan, B. B.; Li, Y.; Xu, J. W.; Nie, X. L.; Fan, J.; Jin, L.; Shi, B. F. Site-Selective δ-C(Sp 3)−H Alkylation of Amino Acids and Peptides with Maleimides via a Six-Membered Palladacycle. *Angew. Chem. Int. Ed.* **2018**, *57* (20), 5858–5862.

(399) Chen, Y. Q.; Wang, Z.; Wu, Y.; Wisniewski, S. R.; Qiao, J. X.; Ewing, W. R.; Eastgate, M. D.; Yu, J. Q. Overcoming the Limitations of γ- And δ-C-H Arylation of Amines through Ligand Development. *J. Am. Chem. Soc.* **2018**, *140* (51), 17884–17894.

(400) Frisch, M. J.; Trucks, G. W.; Schlegel, H. B.; Scuseria, G. E.; Robb, M. A.; Cheeseman, J. R.; Scalmani, G.; Barone, V.; Mennucci, B.; Petersson, G. A.; et al. Gaussian 16, Revision A.01. 2016. See Appendix 1 for full reference.

(401) Andrae, D.; Häußermann, U.; Dolg, M.; Stoll, H.; Preuß, H. Energy-Adjustedab Initio Pseudopotentials for the Second and Third Row Transition Elements. *Theor. Chim. Acta* **1990**, *77* (2), 123–141.

(402) Peterson, K. A.; Figgen, D.; Goll, E.; Stoll, H.; Dolg, M. Systematically Convergent Basis Sets with Relativistic Pseudopotentials. II. Small-Core Pseudopotentials and Correlation Consistent Basis Sets for the Post-d Group 16–18 Elements. *J. Chem. Phys.* **2003**, *119* (21), 11113–11123.

(403) Mekareeya, A.; Walker, P. R.; Couce-Rios, A.; Campbell, C. D.; Steven, A.;

Paton, R. S.; Anderson, E. A. Mechanistic Insight into Palladium-Catalyzed Cycloisomerization: A Combined Experimental and Theoretical Study. *J. Am. Chem. Soc.* **2017**, *139* (29), 10104–10114.

(404) Deb, A.; Hazra, A.; Peng, Q.; Paton, R. S.; Maiti, D. Detailed Mechanistic Studies on Palladium-Catalyzed Selective C-H Olefination with Aliphatic Alkenes: A Significant Influence of Proton Shuttling. *J. Am. Chem. Soc.* **2017**, *139* (2), 763–775.

(405) Publishers, W.; Murov, S. Properties of Organic Solvents http://murov.info/orgsolvents.htm (accessed May 3, 2018).

(406) Haynes, W. M.; Lide, D. R.; Bruno, T. J. CRC Handbook 97 Ed. In *CRC handbook of chemistry and physics: a ready-reference book of chemical and physical data.*; Raton, B., Ed.; Florida: CRC Press., 2016; pp 3–364.

(407) Ulrich, N.; Endo, S.; Brown, T. N.; Watanabe, N.; Bronner, G.; Abraham, M. H.; Goss, K.-U. UFZ-LSER database v3.2.1 http://www.ufz.de/lserd (accessed Apr 30, 2018).

(408) Wang, X.; Pan, J.; Wu, J.; Liu, Z. Surface Tension of Dimethoxymethane and Methyl Tert-Butyl Ether. *J. Chem. Eng. Data* **2006**, *51* (4), 1394–1397.

(409) Glendening, E. D.; Reed, A. E.; Carpenter, J. E.; Weinhold, F. Gaussian NBO Version 3.1. *Gaussian Inc., Pittsburgh PA*. 2001, pp 2–3.

(410) Sosa, C.; Andzelm, J.; Elkin, B. C.; Wimmer, E.; Dobbs, K. D.; Dixon, D. A. A Local Density Functional Study of the Structure and Vibrational Frequencies of Molecular Transition-Metal Compounds. *J. Phys. Chem.* **1992**, *96* (16), 6630–

6636.

(411) Godbout, N.; Salahub, D. R.; Andzelm, J.; Wimmer, E. Optimization of Gaussian-Type Basis Sets for Local Spin Density Functional Calculations. Part I. Boron through Neon, Optimization Technique and Validation. *Can. J. Chem.* **1992**, *70* (2), 560–571.

(412) Skapski, A. C.; Smart, M. L. The Crystal Structure of Trimeric Palladium(II) Acetate. *J. Chem. Soc. D Chem. Commun.* **1970**, No. 11, 658b – 659.

(413) Bakhmutov, V. I.; Berry, J. F.; Cotton, F. A.; Ibragimov, S.; Murillo, C. A. Non-Trivial Behavior of Palladium(II) Acetate. *Dalt. Trans.* **2005**, No. 11, 1989–1992.

(414) Váňa, J.; Hanusek, J.; Sedlák, M. Bi and Trinuclear Complexes in Palladium Carboxylate-Assisted C-H Activation Reactions. *Dalt. Trans.* **2018**, *47* (5), 1378–1382.

(415) Diao, T.; White, P.; Guzei, I.; Stahl, S. S. Characterization of DMSO Coordination to Palladium(II) in Solution and Insights into the Aerobic Oxidation Catalyst, $Pd(DMSO)_2(TFA)_2$. *Inorg. Chem.* **2012**, *51* (21), 11898–11909.

(416) Sankaralingam, M.; Vadivelu, P.; Palaniandavar, M. Novel Nickel(II) Complexes of Sterically Modified Linear N4 Ligands: Effect of Ligand Stereoelectronic Factors and Solvent of Coordination on Nickel(II) Spin-State and Catalytic Alkane Hydroxylation. *Dalt. Trans.* **2017**, *46* (22), 7181–7193.

(417) Vana, J.; Lang, J.; Soltesova, M.; Hanusek, J.; Ruzicka, A.; Sedlak, M.;

Roithova, J. The Role of Trinuclear Species in a Palladium Acetate/Trifluoroacetic Acid Catalytic System. *Dalt. Trans.* **2017**, *46* (46), 16269–16275.

(418) Haines, B. E.; Berry, J. F.; Yu, J.-Q.; Musaev, D. G. Factors Controlling Stability and Reactivity of Dimeric Pd(II) Complexes in C–H Functionalization Catalysis. *ACS Catal.* **2016**, *6* (2), 829–839.

(419) Fekl, U.; Goldberg, K. I. Five-Coordinate Platinum(IV) Complex as a Precursor to a Novel Pt(II) Olefin Hydride Complex for Alkane Activation. *J. Am. Chem. Soc.* **2002**, *124* (24), 6804–6805.

(420) Crumpton, D. M.; Goldberg, K. I. Five-Coordinate Intermediates in Carbon-Carbon Reductive Elimination Reactions from Pt(IV). *J. Am. Chem. Soc.* **2000**, *122* (5), 962–963.

(421) Crumpton-Bregel, D. M.; Goldberg, K. I. Mechanisms of C-C and C-H Alkane Reductive Eliminations from Octahedral Pt(IV): Reaction via Five-Coordinate Intermediates or Direct Elimination? *J. Am. Chem. Soc.* **2003**, *125* (31), 9442–9456.

(422) Giri, R.; Lan, Y.; Liu, P.; Houk, K. N.; Yu, J. Q. Understanding Reactivity and Stereoselectivity in Palladium-Catalyzed Diastereoselective sp^3 C-H Bond Activation: Intermediate Characterization and Computational Studies. *J. Am. Chem. Soc.* **2012**, *134* (34), 14118–14126.

(423) Dang, Y.; Qu, S.; Nelson, J. W.; Pham, H. D.; Wang, Z. X.; Wang, X. The Mechanism of a Ligand-Promoted C(sp^3)-H Activation and Arylation Reaction

via Palladium Catalysis: Theoretical Demonstration of a Pd(II)/Pd(IV) Redox Manifold. *J. Am. Chem. Soc.* **2015**, *137* (5), 2006–2014.

(424) Rodríguez, N.; Romero-Revilla, J. A.; Fernández-Ibáñez, M. Á.; Carretero, J. C. Palladium-Catalyzed N-(2-Pyridyl)Sulfonyl-Directed C(sp^3)-H γ-Arylation of Amino Acid Derivatives. *Chem. Sci.* **2013**, *4* (1), 175–179.

(425) O'Duill, M. L.; Matsuura, R.; Wang, Y.; Turnbull, J. L.; Gurak, J. A.; Gao, D. W.; Lu, G.; Liu, P.; Engle, K. M. Tridentate Directing Groups Stabilize 6-Membered Palladacycles in Catalytic Alkene Hydrofunctionalization. *J. Am. Chem. Soc.* **2017**, *139* (44), 15576–15579.

(426) Liu, Z.; Wang, Y.; Wang, Z.; Zeng, T.; Liu, P.; Engle, K. M. Catalytic Intermolecular Carboamination of Unactivated Alkenes via Directed Aminopalladation. *J. Am. Chem. Soc.* **2017**, *139* (32), 11261–11270.

(427) Proutiere, F.; Schoenebeck, F. Orthogonal Selectivities under Pd(0) Catalysis with Solvent Polarity: An Interplay of Computational and Experimental Studies. *Synlett* **2012**, *23* (05), 645–648.

(428) Plata, R. E.; Singleton, D. A. A Case Study of the Mechanism of Alcohol-Mediated Morita Baylis-Hillman Reactions. the Importance of Experimental Observations. *J. Am. Chem. Soc.* **2015**, *137* (11), 3811–3826.

(429) Yang, Y. F.; Cheng, G. J.; Liu, P.; Leow, D.; Sun, T. Y.; Chen, P.; Zhang, X.; Yu, J. Q.; Wu, Y. D.; Houk, K. N. Palladium-Catalyzed Meta-Selective C-H Bond Activation with a Nitrile-Containing Template: Computational Study on Mechanism and Origins of Selectivity. *J. Am. Chem. Soc.* **2014**, *136* (1), 344–

355.

(430) Anand, M.; Sunoj, R. B.; Schaefer, H. F. Non-Innocent Additives in a Palladium(II)-Catalyzed C–H Bond Activation Reaction: Insights into Multimetallic Active Catalysts. *J. Am. Chem. Soc.* **2014**, *136* (15), 5535–5538.

(431) Abrams, D. J.; Provencher, P. A.; Sorensen, E. J. Recent Applications of C-H Functionalization in Complex Natural Product Synthesis. *Chem. Soc. Rev.* **2018**, *47* (23), 8925–8967.

(432) McMurray, L.; O'Hara, F.; Gaunt, M. J. Recent Developments in Natural Product Synthesis Using Metal-Catalysed C-H Bond Functionalisation. *Chem. Soc. Rev.* **2011**, *40* (4), 1885–1898.

(433) Zhang, J.; Kang, L. J.; Parker, T. C.; Blakey, S. B.; Luscombe, C. K.; Marder, S. R. Recent Developments in C–H Activation for Materials Science in the Center for Selective C–H Activation. *Molecules* **2018**, *23* (4), 922.

(434) Murahashi, S. Synthesis of Phthalimidines from Schiff Bases and Carbon Monoxide. *J. Am. Chem. Soc.* **1955**, *77* (23), 6403–6404.

(435) Ackermann, L.; Vicente, R.; Kapdi, A. R. Transition-Metal-Catalyzed Direct Arylation of (Hetero)Arenes by C-H Bond Cleavage. *Angew. Chem. Int. Ed.* **2009**, *48* (52), 9792–9826.

(436) Sigman, M. S.; Werner, E. W. Imparting Catalyst Control upon Classical Palladium-Catalyzed Alkenyl C-H Bond Functionalization Reactions. *Acc. Chem. Res.* **2012**, *45* (6), 874–884.

(437) Deb, A.; Bag, S.; Kancherla, R.; Maiti, D. Palladium-Catalyzed Aryl C-H Olefination with Unactivated, Aliphatic Alkenes. *J. Am. Chem. Soc.* **2014**, *136* (39), 13602–13605.

(438) Gemoets, H. P. L. L.; Kalvet, I.; Nyuchev, A. V.; Erdmann, N.; Hessel, V.; Schoenebeck, F.; Noël, T. Mild and Selective Base-Free C-H Arylation of Heteroarenes: Experiment and Computation. *Chem. Sci.* **2017**, *8* (2), 1046–1055.

(439) Tang, R. Y.; Li, G.; Yu, J. Q. Conformation-Induced Remote Meta-C-H Activation of Amines. *Nature* **2014**, *507* (7491), 215–220.

(440) Davis, H. J.; Mihai, M. T.; Phipps, R. J. Ion Pair-Directed Regiocontrol in Transition-Metal Catalysis: A Meta-Selective C-H Borylation of Aromatic Quaternary Ammonium Salts. *J. Am. Chem. Soc.* **2016**, *138* (39), 12759–12762.

(441) Ruan, Z.; Zhang, S. K.; Zhu, C.; Ruth, P. N.; Stalke, D.; Ackermann, L. Ruthenium(II)-Catalyzed Meta C−H Mono- and Difluoromethylations by Phosphine/Carboxylate Cooperation. *Angew. Chem. Int. Ed.* **2017**, *56* (8), 2045–2049.

(442) Dong, Z.; Wang, J.; Dong, G. Simple Amine-Directed Meta-Selective C-H Arylation via Pd/Norbornene Catalysis. *J. Am. Chem. Soc.* **2015**, *137* (18), 5887–5890.

(443) Saidi, O.; Marafie, J.; Ledger, A. E. W.; Liu, P. M.; Mahon, M. F.; Kociok-Köhn, G.; Whittlesey, M. K.; Frost, C. G. Ruthenium-Catalyzed Meta Sulfonation of 2-Phenylpyridines. *J. Am. Chem. Soc.* **2011**, *133* (48), 19298–19301.

(444) Bag, S.; Patra, T.; Modak, A.; Deb, A.; Maity, S.; Dutta, U.; Dey, A.; Kancherla, R.; Maji, A.; Hazra, A.; et al. Remote Para-C-H Functionalization of Arenes by a D-Shaped Biphenyl Template-Based Assembly. *J. Am. Chem. Soc.* **2015**, *137* (37), 11888–11891.

(445) Chemler, S. R.; Fuller, P. H. Heterocycle Synthesis by Copper Facilitated Addition of Heteroatoms to Alkenes, Alkynes and Arenes. *Chem. Soc. Rev.* **2007**, *36* (7), 1153–1160.

(446) Marshall, J. A. Synthesis and Reactions of Allylic, Allenic, Vinylic, and Arylmetal Reagents from Halides and Esters via Transient Organopalladium Intermediates. *Chem. Rev.* **2000**, *100* (8), 3163–3185.

(447) Yamamoto, Y.; Asao, N. Selective Reactions Using Allylic Metals. *Chem. Rev.* **1993**, *93* (6), 2207–2293.

(448) Kacprzynski, M. A.; May, T. L.; Kazane, S. A.; Hoveyda, A. H. Enantioselective Synthesis of Allylsilanes Bearing Tertiary and Quaternary Si-Substituted Carbons through Cu-Catalyzed Allylic Alkylations with Alkylzinc and Arylzinc Reagents. *Angew. Chem. Int. Ed.* **2007**, *46* (24), 4554–4558.

(449) Polet, D.; Rathgeb, X.; Falciola, C. A.; Langlois, J. B.; El Hajjaji, S.; Alexakis, A. Enantioselective Iridium-Catalyzed Allylic Arylation. *Chem.: Eur. J.* **2009**, *15* (5), 1205–1216.

(450) Selim, K. B.; Matsumoto, Y.; Yamada, K. I.; Tomioka, K. Efficient Chiral N-Heterocyclic Carbene/Copper(I)-Catalyzed Asymmetric Allylic Arylation with Aryl Grignard Reagents. *Angew. Chem. Int. Ed.* **2009**, *48* (46), 8733–8735.

(451) Ohmiya, H.; Yokokawa, N.; Sawamura, M. Copper-Catalyzed γ-Selective and Stereospecific Allyl-Aryl Coupling between (Z)-Acyclic and Cyclic Allylic Phosphates and Arylboronates. *Org. Lett.* **2010**, *12* (10), 2438–2440.

(452) Ohmiya, H.; Makida, Y.; Tanaka, T.; Sawamura, M. Palladium-Catalyzed γ -Selective and Stereospecific Allyl-Aryl Coupling between Allylic Acetates and Arylboronic Acids. *J. Am. Chem. Soc.* **2008**, *130* (51), 17276–17277.

(453) Nishikata, T.; Lipshutz, B. H. Allylic Ethers as Educts for Suzuki-Miyaura Couplings in Water at Room Temperature. *J. Am. Chem. Soc.* **2009**, *131* (34), 12103–12105.

(454) Ohmiya, H.; Makida, Y.; Li, D.; Tanabe, M.; Sawamura, M. Palladium-Catalyzed γ-Selective and Stereospecific Allyl-Aryl Coupling between Acyclic Allylic Esters and Arylboronic Acids. *J. Am. Chem. Soc.* **2010**, *132* (2), 879–889.

(455) Li, D.; Tanaka, T.; Ohmiya, H.; Sawamura, M. Synthesis of α-Arylated Allylsilanes through Palladium-Catalyzed γ-Selective Allyl-Aryl Coupling. *Org. Lett.* **2010**, *12* (15), 3344–3347.

(456) Yao, T.; Hirano, K.; Satoh, T.; Miura, M. Stereospecific Copper-Catalyzed C-H Allylation of Electron-Deficient Arenes with Allyl Phosphates. *Angew. Chem. Int. Ed.* **2011**, *50* (13), 2990–2994.

(457) Makida, Y.; Ohmiya, H.; Sawamura, M. Regio- and Stereocontrolled Introduction of Secondary Alkyl Groups to Electron-Deficient Arenes through Copper-Catalyzed Allylic Alkylation. *Angew. Chem. Int. Ed.* **2012**, *51* (17), 4122–4127.

(458) Cong, X.; Li, Y.; Wei, Y.; Zeng, X. Nickel-Catalyzed C-H Coupling with Allyl Phosphates: A Site-Selective Synthetic Route to Linear Allylarenes. *Org. Lett.* **2014**, *16* (15), 3926–3929.

(459) Fan, S.; Chen, F.; Zhang, X. Direct Palladium-Catalyzed Intermolecular Allylation of Highly Electron-Deficient Polyfluoroarenes. *Angew. Chem. Int. Ed.* **2011**, *50* (26), 5918–5923.

(460) Gavrilov, K. N.; Lyubimov, S. E.; Zheglov, S. V.; Benetsky, E. B.; Davankov, V. A. Enantioselective Pd-Catalysed Allylation with BINOL-Derived Monodentate Phosphite and Phosphoramidite Ligands. *J. Mol. Catal. A Chem.* **2005**, *231* (1–2), 255–260.

(461) Oi, S.; Tanaka, Y.; Inoue, Y. Ortho-Selective Allylation of 2-Pyridylarenes with Allyl Acetates Catalyzed by Ruthenium Complexes. *Organometallics* **2006**, *25* (20), 4773–4778.

(462) Kuninobu, Y.; Ohta, K.; Takai, K. Rhenium-Catalyzed Allylation of C-H Bonds of Benzoic and Acrylic Acids. *Chem. Commun.* **2011**, *47* (38), 10791–10793.

(463) Zhang, Y. J.; Skucas, E.; Krische, M. J. Direct Prenylation of Aromatic and α,β-Unsaturated Carboxamides via Iridium-Catalyzed C-H Oxidative Addition-Allene Insertion. *Org. Lett.* **2009**, *11* (18), 4248–4250.

(464) Wang, H.; Schröder, N.; Glorius, F. Mild Rhodium(III)-Catalyzed Direct C-H Allylation of Arenes with Allyl Carbonates. *Angew. Chem. Int. Ed.* **2013**, *52* (20), 5386–5389.

(465) Wang, H.; Beiring, B.; Yu, D. G.; Collins, K. D.; Glorius, F. Dendralene

Synthesis: Rhodium(III)-Catalyzed Alkenyl C-H Activation and Coupling Reaction with Allenyl Carbinol Carbonate. *Angew. Chem. Int. Ed.* **2013**, *52* (47), 12430–12434.

(466) Feng, C.; Feng, D.; Loh, T. P. Oxidant-Free Rh(III)-Catalyzed Direct C-H Olefination of Arenes with Allyl Acetates. *Org. Lett.* **2013**, *15* (14), 3670–3673.

(467) Qi, Z.; Li, X. Rhodium(III)-Catalyzed Coupling of Arenes with 7-Oxa/Azabenzonorbornadienes by C-H Activation. *Angew. Chem. Int. Ed.* **2013**, *52* (34), 8995–9000.

(468) Zeng, R.; Fu, C.; Ma, S. Highly Selective Mild Stepwise Allylation of N-Methoxybenzamides with Allenes. *J. Am. Chem. Soc.* **2012**, *134* (23), 9597–9600.

(469) Ye, B.; Cramer, N. A Tunable Class of Chiral Cp Ligands for Enantioselective Rhodium(III)-Catalyzed C-H Allylations of Benzamides. *J. Am. Chem. Soc.* **2013**, *135* (2), 636–639.

(470) Dai, H.; Yu, C.; Lu, C.; Yan, H. Rh^{III}-Catalyzed C-H Allylation of Amides and Domino Cycling Synthesis of 3,4-Dihydroisoquinolin-1(2H)-Ones with N-Bromosuccinimide. *Eur. J. Org. Chem.* **2016**, *2016* (7), 1255–1259.

(471) Barsu, N.; Kalsi, D.; Sundararaju, B. Carboxylate Assisted Ni-Catalyzed C-H Bond Allylation of Benzamides. *Chem.: Eur. J.* **2015**, *21* (26), 9364–9368.

(472) Goriya, Y.; Ramana, C. V. Ruthenium-Catalyzed C6-Propenylation Reactions of Substituted Pyridine Derivatives: Directed and Direct C-H Activation. *Chem.: Eur. J.* **2012**, *18* (42), 13288–13292.

(473) Kumar, G. S.; Kapur, M. Ruthenium-Catalyzed, Site-Selective C-H Allylation of Indoles with Allyl Alcohols as Coupling Partners. *Org. Lett.* **2016**, *18* (5), 1112–1115.

(474) Suzuki, Y.; Sun, B.; Sakata, K.; Yoshino, T.; Matsunaga, S.; Kanai, M. Dehydrative Direct C-H Allylation with Allylic Alcohols under [Cp^*Co^{III}] Catalysis. *Angew. Chem. Int. Ed.* **2015**, *54* (34), 9944–9947.

(475) Bunno, Y.; Murakami, N.; Suzuki, Y.; Kanai, M.; Yoshino, T.; Matsunaga, S. Cp^*Co^{III}-Catalyzed Dehydrative C-H Allylation of 6-Arylpurines and Aromatic Amides Using Allyl Alcohols in Fluorinated Alcohols. *Org. Lett.* **2016**, *18* (9), 2216–2219.

(476) Onodera, G.; Imajima, H.; Yamanashi, M.; Nishibayashi, Y.; Hidai, M.; Uemura, S. Ruthenium-Catalyzed Allylation of Aromatic Compounds and Allylic Ether Formation. *Organometallics* **2004**, *23* (24), 5841–5848.

(477) Gu, Y.; Tian, S. K. N-Alkylsulfonamides as Useful Carbon Electrophiles. *Synlett* **2013**, *24* (10), 1170–1185.

(478) Ouyang, K.; Hao, W.; Zhang, W.-X.; Xi, Z. Transition-Metal-Catalyzed Cleavage of C–N Single Bonds. *Chem. Rev.* **2015**, *115* (21), 12045–12090.

(479) Hiraki, K.; Matsunaga, T.; Kawano, H. Reactions of $RuClH(CO)(PPh_3)3$ with Allylic Amines: Insertions and an Unusual Carbon-Nitrogen Bond Cleavage of Allylic Amines. *Organometallics* **1994**, *13* (5), 1878–1885.

(480) Wu, X. S.; Chen, Y.; Li, M. B.; Zhou, M. G.; Tian, S. K. Direct Substitution of

Primary Allylic Amines with Sulfinate Salts. *J. Am. Chem. Soc.* **2012**, *134* (36), 14694–14697.

(481) Wang, Y.; Xu, J. K.; Gu, Y.; Tian, S. K. Catalytic Stereospecific Allylation of Protected Hydrazines with Enantioenriched Primary Allylic Amines. *Org. Chem. Front.* **2014**, *1* (7), 812–816.

(482) Yan, R.; Wang, Z. X. Ruthenium-Catalyzed C-H Allylation of Arenes with Allylic Amines. *Org. Biomol. Chem.* **2018**, *16* (21), 3961–3969.

(483) Mishra, N. K.; Sharma, S.; Park, J.; Han, S.; Kim, I. S. Recent Advances in Catalytic C(Sp^2)-H Allylation Reactions. *ACS Catal.* **2017**, *7* (4), 2821–2847.

(484) Manikandan, R.; Madasamy, P.; Jeganmohan, M. Ruthenium-Catalyzed Oxidant-Free Allylation of Aromatic Ketoximes with Allylic Acetates at Room Temperature. *Chem.: Eur. J.* **2015**, *21* (40), 13934–13938.

(485) Cajaraville, A.; López, S.; Varela, J. A.; Saá, C. Rh(III)-Catalyzed Tandem C-H Allylation and Oxidative Cyclization of Anilides: A New Entry to Indoles. *Org. Lett.* **2013**, *15* (17), 4576–4579.

(486) Liu, W.; Richter, S. C.; Zhang, Y.; Ackermann, L. Manganese(I)-Catalyzed Substitutive C−H Allylation. *Angew. Chem. Int. Ed.* **2016**, *55* (27), 7747–7750.

(487) Fang, Z.; Fu, C.; Ma, S. [$PdCl_2(MeCN)_2$]-Catalyzed Highly Regio- And Stereoselective Allylation of Electron-Rich Arenes with 2,3-Allenoates. *Chem.: Eur. J.* **2010**, *16* (13), 3910–3913.

(488) Nakanowatari, S.; Ackermann, L. Ruthenium(II)-Catalyzed C-H

Functionalizations with Allenes: Versatile Allenylations and Allylations. *Chem.: Eur. J.* **2015**, *21* (45), 16246–16251.

(489) Korkis, S. E.; Burns, D. J.; Lam, H. W. Rhodium-Catalyzed Oxidative C-H Allylation of Benzamides with 1,3-Dienes by Allyl-to-Allyl 1,4-Rh(III) Migration. *J. Am. Chem. Soc.* **2016**, *138* (37), 12252–12257.

(490) Maity, S.; Dolui, P.; Kancherla, R.; Maiti, D. Introducing Unactivated Acyclic Internal Aliphatic Olefins into a Cobalt Catalyzed Allylic Selective Dehydrogenative Heck Reaction. *Chem. Sci.* **2017**, *8* (7), 5181–5185.

(491) Maity, S.; Kancherla, R.; Dhawa, U.; Hoque, E.; Pimparkar, S.; Maiti, D. Switch to Allylic Selectivity in Cobalt-Catalyzed Dehydrogenative Heck Reactions with Unbiased Aliphatic Olefins. *ACS Catal.* **2016**, *6* (8), 5493–5499.

(492) Yamaguchi, T.; Kommagalla, Y.; Aihara, Y.; Chatani, N. Cobalt-Catalyzed Chelation Assisted C-H Allylation of Aromatic Amides with Unactivated Olefins. *Chem. Commun.* **2016**, *52* (66), 10129–10132.

(493) Basnet, P.; KC, S.; Dhungana, R. K.; Shrestha, B.; Boyle, T. J.; Giri, R. Synergistic Bimetallic Ni/Ag and Ni/Cu Catalysis for Regioselective γ,δ-Diarylation of Alkenyl Ketimines: Addressing β-H Elimination by in Situ Generation of Cationic Ni(II) Catalysts. *J. Am. Chem. Soc.* **2018**, *140* (46), 15586–15590.

(494) Leow, D.; Li, G.; Mei, T. S.; Yu, J. Q. Activation of Remote Meta-C-H Bonds Assisted by an End-on Template. *Nature* **2012**, *486* (7404), 518–522.

(495) Jayarajan, R.; Das, J.; Bag, S.; Chowdhury, R.; Maiti, D. Diverse *Meta*-C−H

Functionalization of Arenes across Different Linker Lengths. *Angew. Chem. Int. Ed.* **2018**, *57* (26), 7659–7663.

(496) Bag, S.; Jayarajan, R.; Dutta, U.; Chowdhury, R.; Mondal, R.; Maiti, D. Remote Meta-C–H Cyanation of Arenes Enabled by a Pyrimidine-Based Auxiliary. *Angew. Chem. Int. Ed.* **2017**, *56* (41), 12538–12542.

(497) Bag, S.; Jayarajan, R.; Mondal, R.; Maiti, D. Template-Assisted Meta-C−H Alkylation and Alkenylation of Arenes. *Angew. Chem. Int. Ed.* **2017**, *56* (12), 3182–3186.

(498) Chen, G.; Gong, W.; Zhuang, Z.; Andrä, M. S.; Chen, Y. Q.; Hong, X.; Yang, Y. F.; Liu, T.; Houk, K. N.; Yu, J. Q. Ligand-Accelerated Enantioselective Methylene C(sp^3)-H Bond Activation. *Science* **2016**, *353* (6303), 1023–1027.

(499) Cheng, G. J.; Yang, Y. F.; Liu, P.; Chen, P.; Sun, T. Y.; Li, G.; Zhang, X.; Houk, K. N.; Yu, J. Q.; Wu, Y. D. Role of N-Acyl Amino Acid Ligands in Pd(II)-Catalyzed Remote C-H Activation of Tethered Arenes. *J. Am. Chem. Soc.* **2014**, *136* (3), 894–897.

(500) Yang, Y. F.; Hong, X.; Yu, J. Q.; Houk, K. N. Experimental-Computational Synergy for Selective Pd(II)-Catalyzed C-H Activation of Aryl and Alkyl Groups. *Acc. Chem. Res.* **2017**, *50* (11), 2853–2860.

(501) Dutta, U.; Modak, A.; Bhaskararao, B.; Bera, M.; Bag, S.; Mondal, A.; Lupton, D. W.; Sunoj, R. B.; Maiti, D. Catalytic Arene Meta-C-H Functionalization Exploiting a Quinoline-Based Template. *ACS Catal.* **2017**, *7* (5), 3162–3168.

(502) Maji, A.; Guin, S.; Feng, S.; Dahiya, A.; Singh, V. K.; Liu, P.; Maiti, D.

Experimental and Computational Exploration of Para-Selective Silylation with a Hydrogen-Bonded Template. *Angew. Chem. Int. Ed.* **2017**, *56* (47), 14903–14907.

(503) Maji, A.; Dahiya, A.; Lu, G.; Bhattacharya, T.; Brochetta, M.; Zanoni, G.; Liu, P.; Maiti, D. H-Bonded Reusable Template Assisted Para-Selective Ketonisation Using Soft Electrophilic Vinyl Ethers. *Nat. Commun.* **2018**, *9* (1), 3582.

(504) Wheeler, S. E.; Houk, K. N.; Schleyer, P. V. R.; Allen, W. D. A Hierarchy of Homodesmotic Reactions for Thermochemistry. *J. Am. Chem. Soc.* **2009**, *131* (7), 2547–2560.

(505) Wheeler, S. E. Homodesmotic Reactions for Thermochemistry. *Wiley Interdiscip. Rev. Comput. Mol. Sci.* **2012**, *2* (2), 204–220.

(506) *Modern Acetylene Chemistry*; Stang, P. J., Diederich, F. E., Eds.; VCH, 1995.

(507) Drießen-Hölscher, B. *Application of Transition Metal Catalysts in Organic Synthesis*; Springer Berlin Heidelberg, 2011; Vol. 211.

(508) Kuhl, N.; Hopkinson, M. N.; Wencel-Delord, J.; Glorius, F. Beyond Directing Groups: Transition-Metal-Catalyzed C-H Activation of Simple Arenes. *Angew. Chem. Int. Ed.* **2012**, *51* (41), 10236–10254.

(509) Matsuyama, N.; Hirano, K.; Satoh, T.; Miura, M. Nickel-Catalyzed Direct Alkynylation of Azoles with Alkynyl Bromides. *Org. Lett.* **2009**, *11* (18), 4156–4159.

(510) Besselièvre, F.; Piguel, S. Copper as a Powerful Catalyst in the Direct

Alkynylation of Azoles. *Angew. Chem. Int. Ed.* **2009**, *48* (50), 9553–9556.

(511) Wei, Y.; Zhao, H.; Kan, J.; Su, W.; Hong, M. Copper-Catalyzed Direct Alkynylation of Electron-Deficient Polyfluoroarenes with Terminal Alkynes Using O_2 as an Oxidant. *J. Am. Chem. Soc.* **2010**, *132* (8), 2522–2523.

(512) Seregin, I. V.; Ryabova, V.; Gevorgyan, V. Direct Palladium-Catalyzed Alkynylation of N-Fused Heterocycles. *J. Am. Chem. Soc.* **2007**, *129* (25), 7742–7743.

(513) Tobisu, M.; Ano, Y.; Chatani, N. Palladium-Catalyzed Direct Alkynylation of C-H Bonds in Benzenes. *Org. Lett.* **2009**, *11* (15), 3250–3252.

(514) Xu, Y.-H.; Zhang, Q.-C.; He, T.; Meng, F.-F.; Loh, T.-P. Palladium-Catalyzed Direct Alkynylation of *N* -Vinylacetamides. *Adv. Synth. Catal.* **2014**, *356* (7), 1539–1543.

(515) Gu, Y.; Wang, X. Direct Palladium-Catalyzed C-3 Alkynylation of Indoles. *Tetrahedron Lett.* **2009**, *50* (7), 763–766.

(516) Brand, J. P.; Charpentier, J.; Waser, J. Direct Alkynylation of Indole and Pyrrole Heterocycles. *Angew. Chem. Int. Ed.* **2009**, *48* (49), 9346–9349.

(517) De Haro, T.; Nevado, C. Gold-Catalyzed Ethynylation of Arenes. *J. Am. Chem. Soc.* **2010**, *132* (5), 1512–1513.

(518) Zhou, J.; Shi, J.; Qi, Z.; Li, X.; Xu, H. E.; Yi, W. Mild and Efficient Ir(III)-Catalyzed Direct C-H Alkynylation of N-Phenoxyacetamides with Terminal Alkyne. *ACS Catal.* **2015**, *5* (11), 6999–7003.

(519) Li, G.; Liu, P.; Zhang, J.; Shi, D. Q.; Zhao, Y. Palladium-Catalyzed Direct: Ortho -Alkynylation of Arylalkylacid Derivatives at γ and δ Positions via an N, O - Bidentate Directing Group. *Org. Chem. Front.* **2017**, *4* (10), 1931–1934.

(520) Zhao, Y.; He, G.; Nack, W. A.; Chen, G. Palladium-Catalyzed Alkenylation and Alkynylation of Ortho-C(Sp^2)-H Bonds of Benzylamine Picolinamides. *Org. Lett.* **2012**, *14* (12), 2948–2951.

(521) Kim, S. H.; Park, S. H.; Chang, S. Palladium-Catalyzed Oxidative Alkynylation of Arene C-H Bond Using the Chelation-Assisted Strategy. *Tetrahedron* **2012**, *68* (26), 5162–5166.

(522) Zheng, Y.; Song, W. Pd-Catalyzed Site-Selective C(Sp^2)-H Olefination and Alkynylation of Phenylalanine Residues in Peptides. *Org. Lett.* **2019**, *21* (9), 3257–3260.

(523) Brand, J. P.; Waser, J. Para-Selective Gold-Catalyzed Direct Alkynylation of Anilines. *Org. Lett.* **2012**, *14* (3), 744–747.

(524) Wang, P.; Li, G. C.; Jain, P.; Farmer, M. E.; He, J.; Shen, P. X.; Yu, J. Q. Ligand-Promoted Meta-C-H Amination and Alkynylation. *J. Am. Chem. Soc.* **2016**, *138* (42), 14092–14099.

(525) Weibel, J.-M.; Blanc, A.; Pale, P. Ag-Mediated Reactions: Coupling and Heterocyclization Reactions. *Chem. Rev.* **2008**, *108* (8), 3149–3173.

(526) Daugulis, O.; Do, H. Q.; Shabashov, D. Palladium- and Copper-Catalyzed Arylation of Carbon-Hydrogen Bonds. *Acc. Chem. Res.* **2009**, *42* (8), 1074–1086.

(527) Lotz, M. D.; Camasso, N. M.; Canty, A. J.; Sanford, M. S. Role of Silver Salts in Palladium-Catalyzed Arene and Heteroarene C-H Functionalization Reactions. *Organometallics* **2017**, *36* (1), 165–171.

(528) Campeau, L. C.; Parisien, M.; Jean, A.; Fagnou, K. Catalytic Direct Arylation with Aryl Chlorides, Bromides, and Iodides: Intramolecular Studies Leading to New Intermolecular Reactions. *J. Am. Chem. Soc.* **2006**, *128* (2), 581–590.

(529) Lafrance, M.; Shore, D.; Fagnou, K. Mild and General Conditions for the Cross-Coupling of Aryl Halides with Pentafluorobenzene and Other Perfluoroaromatics. *Org. Lett.* **2006**, *8* (22), 5097–5100.

(530) Arroniz, C.; Denis, J. G.; Ironmonger, A.; Rassias, G.; Larrosa, I. An Organic Cation as a Silver(I) Analogue for the Arylation of Sp^2 and sp^3 C-H Bonds with Iodoarenes. *Chem. Sci.* **2014**, *5* (9), 3509–3514.

(531) Masui, K.; Ikegami, H.; Mori, A. Palladium-Catalyzed C-H Homocoupling of Thiophenes: Facile Construction of Bithiophene Structure. *J. Am. Chem. Soc.* **2004**, *126* (16), 5074–5075.

(532) Stuart, D. R.; Villemure, E.; Fagnou, K. Elements of Regiocontrol in Palladium-Catalyzed Oxidative Arene Cross-Coupling. *J. Am. Chem. Soc.* **2007**, *129* (40), 12072–12073.

(533) Potavathri, S.; Dumas, A. S.; Dwight, T. A.; Naumiec, G. R.; Hammann, J. M.; DeBoef, B. Oxidant-Controlled Regioselectivity in the Oxidative Arylation of N-Acetylindoles. *Tetrahedron Lett.* **2008**, *49* (25), 4050–4053.

(534) Li, H.; Liu, J.; Sun, C. L.; Li, B. J.; Shi, Z. J. Palladium-Catalyzed Cross-

Coupling of Polyfluoroarenes with Simple Arenes. *Org. Lett.* **2011**, *13* (2), 276–279.

(535) Wang, G. W.; Zhou, A. X.; Li, S. X.; Yang, S. D. Regio- and Stereoselective Allylic C-H Arylation with Electron-Deficient Arenes by 1,1′-Bi-2-Naphthol-Palladium Cooperation. *Org. Lett.* **2014**, *16* (11), 3118–3121.

(536) Preciado, S.; Mendive-Tapia, L.; Albericio, F.; Lavilla, R. Synthesis of C-2 Arylated Tryptophan Amino Acids and Related Compounds through Palladium-Catalyzed C-H Activation. *J. Org. Chem.* **2013**, *78* (16), 8129–8135.

(537) Paramonov, S. E.; Mychlo, E. V.; Troyanov, S. I.; Kuz'mina, N. P. Synthesis and Thermal Stability of Silver Carboxylates: Crystal Structure of Silver Pivalate. *Russ. J. Inorg. Chem.* **2000**, *45* (12), 1852–1856.

(538) Olson, L. P.; Whitcomb, D. R.; Rajeswaran, M.; Blanton, T. N.; Stwertka, B. J. The Simple yet Elusive Crystal Structure of Silver Acetate and the Role of the Ag–Ag Bond in the Formation of Silver Nanoparticles during the Thermally Induced Reduction of Silver Carboxylates. *Chem. Mater.* **2006**, *18* (6), 1667–1674.

(539) Schmidbaur, H.; Schier, A. Argentophilic Interactions. *Angew. Chem. Int. Ed.* **2015**, *54* (3), 746–784.

(540) Danheiser, R. L.; Kwasigroch, C. A.; Tsai, Y. M. Application of Allenylsilanes in [3+2] Annulation Approaches to Oxygen and Nitrogen Heterocycles. *J. Am. Chem. Soc.* **1985**, *107* (24), 7233–7235.

(541) Kanno, H.; Nakamura, K.; Noguchi, K.; Shibata, Y.; Tanaka, K. Rhodium-

Catalyzed Cycloisomerization of 2-Silylethynyl Phenols and Anilines via 1,2-Silicon Migration. *Org. Lett.* **2016**, *18* (7), 1654–1657.

(542) Dudnik, A. S.; Xia, Y.; Li, Y.; Gevorgyan, V. Computation-Guided Development of Au-Catalyzed Cycloisomerizations Proceeding via 1,2-Si or 1,2-H Migrations: Regiodivergent Synthesis of Silylfurans. *J. Am. Chem. Soc.* **2010**, *132* (22), 7645–7655.

(543) Li, T.; Zhang, L. Bifunctional Biphenyl-2-Ylphosphine Ligand Enables Tandem Gold-Catalyzed Propargylation of Aldehyde and Unexpected Cycloisomerization. *J. Am. Chem. Soc.* **2018**, *140* (50), 17439–17443.

(544) Taguchi, H.; Miyashita, H.; Tsubouchi, A.; Takeda, T. First Anionic Silyl Migration from Sp^2 Carbon to Carbonyl Oxygen. Stereospecific Allylation of (Z)-β-Trimethylsilyl-α,β-Unsaturated Ketones. *Chem. Commun.* **2002**, *2* (19), 2218–2219.

(545) Tsubouchi, A.; Sasaki, N.; Enatsu, S.; Takeda, T. Regio- and Stereoselective Preparation of (Z)-Silyl Enol Ethers by Three-Component Coupling Using α,β-Unsaturated Acylsilanes as Core Building Blocks. *Tetrahedron Lett.* **2013**, *54* (10), 1264–1267.

(546) Tsubouchi, A.; Matsuda, H.; Kira, T.; Takeda, T. Silyl Migration in Conjunction with Substitution on Silicon in Copper(I) *t*-Butoxide-Promoted Coupling between *o*-Silylphenyl Ketones and Organic Halides. *Chem. Lett.* **2009**, *38* (12), 1180–1181.

(547) Xi, P.; Yang, F.; Qin, S.; Zhao, D.; Lan, J.; Gao, G.; Hu, C.; You, J.

Palladium(II)-Catalyzed Oxidative C-H/C-H Cross-Coupling of Heteroarenes. *J. Am. Chem. Soc.* **2010**, *132* (6), 1822–1824.

(548) Martínez, Á. M.; Alonso, I.; Rodríguez, N.; Gómez Arrayás, R.; Carretero, J. C. Rhodium-Catalyzed Copper-Assisted Intermolecular Domino C−H Annulation of 1,3-Diynes with Picolinamides: Access to Pentacyclic π-Extended Systems. *Chem.: Eur. J.* **2019**, *25* (22), 5733–5742.

(549) Funes-Ardoiz, I.; Maseras, F. Computational Characterization of the Mechanism for the Oxidative Coupling of Benzoic Acid and Alkynes by Rhodium/Copper and Rhodium/Silver Systems. *Chem.: Eur. J.* **2018**, *24* (47), 12383–12388.

(550) Funes-Ardoiz, I.; Maseras, F. Cooperative Reductive Elimination: The Missing Piece in the Oxidative-Coupling Mechanistic Puzzle. *Angew. Chem. Int. Ed.* **2016**, *55* (8), 2764–2767.

(551) Holganza, M. K.; Trigoura, L.; Elfarra, S.; Seo, Y.; Oiler, J.; Xing, Y. Copper (II) Catalyzed Homocoupling and Heterocoupling of Terminal Alkynes. *Tetrahedron Lett.* **2019**, *60* (17), 1179–1181.

(552) Bai, R.; Zhang, G.; Yi, H.; Huang, Z.; Qi, X.; Liu, C.; Miller, J. T.; Kropf, A. J.; Bunel, E. E.; Lan, Y.; et al. Cu(II)-Cu(I) Synergistic Cooperation to Lead the Alkyne C-H Activation. *J. Am. Chem. Soc.* **2014**, *136* (48), 16760–16763.

(553) Zuidema, E.; Bolm, C. Sub-Mol % Catalyst Loading and Ligand-Acceleration in the Coppercatalyzed Coupling of Aryl Iodides and Terminal Alkyenes. *Chem.: Eur. J.* **2010**, *16* (14), 4181–4185.

(554) Zou, L. H.; Johansson, A. J.; Zuidema, E.; Bolm, C. Mechanistic Insights into

Copper-Catalyzed Sonogashira-Hagihara-Type Cross-Coupling Reactions: Sub-Mol % Catalyst Loadings and Ligand Effects. *Chem.: Eur. J.* **2013**, *19* (25), 8144–8152.

(555) He, C.; Ke, J.; Xu, H.; Lei, A. Synergistic Catalysis in the Sonogashira Coupling Reaction: Quantitative Kinetic Investigation of Transmetalation. *Angew. Chem. Int. Ed.* **2013**, *52* (5), 1527–1530.

(556) Zhang, G.; Yi, H.; Zhang, G.; Deng, Y.; Bai, R.; Zhang, H.; Miller, J. T.; Kropf, A. J.; Bunel, E. E.; Lei, A. Direct Observation of Reduction of Cu(II) to Cu(I) by Terminal Alkynes. *J. Am. Chem. Soc.* **2014**, *136* (3), 924–926.

(557) Shimizu, T.; Morisako, S.; Yamamoto, Y.; Kawachi, A. 1,2-Silyl Migration in 1-Halonaphthalenes Catalyzed by I_2. *Heteroat. Chem.* **2018**, *29* (4), e21434.

(558) Barczak, N. T.; Rooke, D. A.; Menard, Z. A.; Ferreira, E. M. Stereoselective Synthesis of Tetrasubstituted Olefins through a Halogen-Induced 1,2-Silyl Migration. *Angew. Chem. Int. Ed.* **2013**, *52* (29), 7579–7582.

(559) Zhao, R.; Zhang, R. Q. A New Insight into π-π Stacking Involving Remarkable Orbital Interactions. *Phys. Chem. Chem. Phys.* **2016**, *18* (36), 25452–25457.

(560) Zhao, R.; Zhang, R. Q. Intermolecular Orbital Interaction in π Systems. *Mol. Phys.* **2018**, *116* (7–8), 978–986.

(561) Neel, A. J.; Hilton, M. J.; Sigman, M. S.; Toste, F. D. Exploiting Non-Covalent π Interactions for Catalyst Design. *Nature* **2017**, *543* (7647), 637–646.

(562) Yamada, S. Cation-π Interactions in Organic Synthesis. *Chem. Rev.* **2018**, *118*

(23), 11353–11432.

(563) Xie, F.; Qi, Z.; Yu, S.; Li, X. Rh(III)- and Ir(III)-Catalyzed C-H Alkynylation of Arenes under Chelation Assistance. *J. Am. Chem. Soc.* **2014**, *136* (12), 4780–4787.

(564) Feng, C.; Loh, T. P. Rhodium-Catalyzed C-H Alkynylation of Arenes at Room Temperature. *Angew. Chem. Int. Ed.* **2014**, *53* (10), 2722–2726.

(565) Brun, E. M.; Gil, S.; Mestres, R.; Parra, M. A New Synthetic Method to 2-Pyridones. *Synthesis* **2000**, *2*, 273–280.

(566) Donets, P. A.; Cramer, N. Ligand-Controlled Regiodivergent Nickel-Catalyzed Annulation of Pyridones. *Angew. Chem. Int. Ed.* **2015**, *54* (2), 633–637.

(567) Joule, J. A.; Mills, K. Heterocyclic Chemistry at a Glance: Second Edition. In *Heterocyclic Chemistry at a Glance: Second Edition*; John Wiley & Sons, Ltd, 2012; pp 62–70.

(568) Ishikura, M.; Abe, T.; Choshi, T.; Hibino, S. Simple Indole Alkaloids and Those with a Nonrearranged Monoterpenoid Unit. *Nat. Prod. Rep.* **2015**, *32* (10), 1389–1471.

(569) Lukevics, E. Sila-Heterocycles in 2008. *Chem. Heterocycl. Compd.* **2008**, *44* (11), 1421–1428.

(570) Nagarajan, M.; Morrell, A.; Fort, B. C.; Meckley, M. R.; Antony, S.; Kohlhagen, G.; Pommier, Y.; Cushman, M. Synthesis and Anticancer Activity of Simplified Indenoisoquinoline Topoisomerase I Inhibitors Lacking Substituents on the

Aromatic Rings. *J. Med. Chem.* **2004**, *47* (23), 5651–5661.

(571) Cappelli, A.; Mohr, G. L. P.; Giuliani, G.; Galeazzi, S.; Anzini, M.; Mennuni, L.; Ferrari, F.; Makovec, F.; Kleinrath, E. M.; Langer, T.; et al. Further Studies on Imidazo[4,5-b]Pyridine AT1 Angiotensin II Receptor Antagonists. Effects of the Transformation of the 4-Phenylquinoline Backbone into 4-Phenylisoquinolinone or 1-Phenylindene Scaffolds. *J. Med. Chem.* **2006**, *49* (22), 6451–6464.

(572) Hirano, K.; Miura, M. A Lesson for Site-Selective C–H Functionalization on 2-Pyridones: Radical, Organometallic, Directing Group and Steric Controls. *Chem. Sci.* **2018**, *9* (1), 22–32.

(573) Jiang, J.; Ramozzi, R.; Morokuma, K. Rh^{III}-Catalyzed C(sp^3)-H Bond Activation by an External Base Metalation/Deprotonation Mechanism: A Theoretical Study. *Chem.: Eur. J.* **2015**, *21* (31), 11158–11164.

(574) Sarpong, R. C–H Functionalization/Activation in Organic Synthesis. *Beilstein J. Org. Chem.* **2016**, *12* (4), 2315–2316.

(575) Odani, R.; Hirano, K.; Satoh, T.; Miura, M. Copper-Mediated C6-Selective Dehydrogenative Heteroarylation of 2-Pyridones with 1,3-Azoles. *Angew. Chem. Int. Ed.* **2014**, *53* (40), 10784–10788.

(576) Zhang, L.; Zheng, X.; Chen, J.; Cheng, K.; Jin, L.; Jiang, X.; Yu, C. Ru(II)-Catalyzed C6-Selective C-H Amidation of 2-Pyridones. *Org. Chem. Front.* **2018**, *5* (20), 2969–2973.

(577) Ni, J.; Zhao, H.; Zhang, A. Manganese(I)-Catalyzed C–H 3,3-Difluoroallylation of Pyridones and Indoles. *Org. Lett.* **2017**, *19* (12), 3159–3162.

(578) Diesel, J.; Finogenova, A. M.; Cramer, N. Nickel-Catalyzed Enantioselective Pyridone C-H Functionalizations Enabled by a Bulky N-Heterocyclic Carbene Ligand. *J. Am. Chem. Soc.* **2018**, *140* (13), 4489–4493.

(579) Nakao, Y.; Idei, H.; Kanyiva, K. S.; Hiyama, T. Direct Alkenylation and Alkylation of Pyridone Derivatives by Ni/$AlMe_3$ Catalysis. *J. Am. Chem. Soc.* **2009**, *131* (44), 15996–15997.

(580) Tamura, R.; Yamada, Y.; Nakao, Y.; Hiyama, T. Alkylation of Pyridone Derivatives by Nickel/Lewis Acid Catalysis. *Angew. Chem. Int. Ed.* **2012**, *51* (23), 5679–5682.

(581) Gao, F.; Han, X.; Li, C.; Liu, L.; Cong, Z.; Liu, H. Cobalt(III)-Catalyzed Site-Selective C-H Amidation of Pyridones and Isoquinolones. *RSC Adv.* **2018**, *8* (57), 32659–32663.

(582) Chen, Y.; Wang, F.; Jia, A.; Li, X. Palladium-Catalyzed Selective Oxidative Olefination and Arylation of 2-Pyridones. *Chem. Sci.* **2012**, *3* (11), 3231.

(583) Maity, S.; Das, D.; Sarkar, S.; Samanta, R. Direct Pd(II)-Catalyzed Site-Selective C5-Arylation of 2-Pyridone Using Aryl Iodides. *Org. Lett.* **2018**, *20* (17), 5167–5171.

(584) Kwon, S.; Kang, D.; Hong, S. Rh^{I}-Catalyzed Site-Selective Decarbonylative Alkenylation and Arylation of Quinolones under Chelation Assistance. *Eur. J. Org. Chem.* **2015**, *2015* (17), 3671–3678.

(585) Lee, S.; Mah, S.; Hong, S. Catalyst Controlled Divergent C4/C8 Site-Selective C-H Arylation of Isoquinolones. *Org. Lett.* **2015**, *17* (15), 3864–3867.

(586) Shaikh, A. C.; Shinde, D. R.; Patil, N. T. Gold vs Rhodium Catalysis: Tuning Reactivity through Catalyst Control in the C-H Alkynylation of Isoquinolones. *Org. Lett.* **2016**, *18* (5), 1056–1059.

(587) Kwon, S.; Kang, D.; Hong, S. Rh I -Catalyzed Site-Selective Decarbonylative Alkenylation and Arylation of Quinolones under Chelation Assistance (Eur. J. Org. Chem. 17/2015) . *Eur. J. Org. Chem.* **2015**, *2015* (17), n/a-n/a.

(588) Choi, H.; Min, M.; Peng, Q.; Kang, D.; Paton, R. S.; Hong, S. Unraveling Innate Substrate Control in Site-Selective Palladium-Catalyzed C–H Heterocycle Functionalization. *Chem. Sci.* **2016**, *7* (6), 3900–3909.

(589) Nakatani, A.; Hirano, K.; Satoh, T.; Miura, M. Manganese-Mediated C3-Selective Direct Alkylation and Arylation of 2-Pyridones with Diethyl Malonates and Arylboronic Acids. *J. Org. Chem.* **2014**, *79* (3), 1377–1385.

(590) Miura, M.; Hirano, K.; Najib, A.; Tabuchi, S. Highly C3-Selective Direct Alkylation and Arylation of 2-Pyridones under Visible-Light-Promoted Photoredox Catalysis. *Heterocycles* **2016**, *92* (7), 1187.

(591) Modak, A.; Rana, S.; Maiti, D. Iron-Catalyzed Regioselective Direct Arylation at the C-3 Position of N-Alkyl-2-Pyridone. *J. Org. Chem.* **2015**, *80* (1), 296–303.

(592) Anagnostaki, E. E.; Fotiadou, A. D.; Demertzidou, V.; Zografos, A. L. Palladium Catalyzed C3-Arylation of 4-Hydroxy-2-Pyridones. *Chem. Commun.* **2014**, *50* (52), 6879–6882.

(593) Biswas, B.; Sugimoto, M.; Sakaki, S. C-H Bond Activation of Benzene and Methane by $M(\eta^2\text{-}O_2CH)_2$ (M = Pd or Pt). A Theoretical Study. *Organometallics*

2000, *19* (19), 3895–3908.

(594) Ryabov, A. D.; Sakodinskaya, I. K.; Yatsimirsky, A. K. Kinetics and Mechanism of Ortho-Palladation of Ring-Substituted NN-Dimethylbenzylamines. *J. Chem. Soc. Dalt. Trans.* **1985**, No. 12, 2629–2638.

(595) Min, M.; Choe, H.; Hong, S. Regioselective Cross-Dehydrogenative Coupling of Chromones and Non-Activated Arenes. *Asian J. Org. Chem.* **2012**, *1* (1), 47–50.

(596) Moon, Y.; Kwon, D.; Hong, S. Palladium-Catalyzed Dehydrogenation/Oxidative Cross-Coupling Sequence of β-Heteroatom-Substituted Ketones. *Angew. Chem. Int. Ed.* **2012**, *51* (45), 11333–11336.

(597) Moon, Y.; Hong, S. A Facile Route to Isoflavone Quinones via the Direct Cross-Coupling of Chromones and Quinones. *Chem. Commun.* **2012**, *48* (57), 7191–7193.

(598) Glover, B.; Harvey, K. A.; Liu, B.; Sharp, M. J.; Tymoschenko, M. F. Regioselective Palladium-Catalyzed Arylation of 3-Carboalkoxy Furan and Thiophene. *J. Heterocycl. Chem* **1989**, *26* (2), 301–304.

(599) Colletto, C.; Islam, S.; Juliá-Hernández, F.; Larrosa, I. Room-Temperature Direct β-Arylation of Thiophenes and Benzo[b]Thiophenes and Kinetic Evidence for a Heck-Type Pathway. *J. Am. Chem. Soc.* **2016**, *138* (5), 1677–1683.

(600) Kahl, H.; Wadewitz, T.; Winkelmann, J. *Surface Tension of Pure Liquids and Binary Liquid Mixtures*; Lechner, M. D., Ed.; Landolt-Börnstein - Group IV Physical Chemistry; Springer-Verlag: Berlin/Heidelberg, 2003; Vol. 48.

(601) Ohff, M.; Ohff, A.; Van Der Boon, M. E.; Milstein, D. Highly Active Pd(II) PCP-Type Catalysts for the Heck Reaction. *Chemtracts* **1998**, *11* (11), 845–849.

(602) Shaw, B. L.; Perera, S. D.; Staley, E. A. Highly Active, Stable, Catalysts for the Heck Reaction; Further Suggestions on the Mechanism. *Chem. Commun.* **1998**, No. 13, 1361–1362.

(603) Sehnal, P.; Taylor, R. J. K.; Fairlamb, L. J. S. Emergence of Palladium(IV) Chemistry in Synthesis and Catalysis. *Chem. Rev.* **2010**, *110* (2), 824–889.

(604) Herrmann, W. A.; Brossmer, C.; Reisinger, C. P.; Riermeier, T. H.; Öfele, K.; Beller, M. Palladacycles: Efficient New Catalysts for the Heck Vinylation of Aryl Halides. *Chem.: Eur. J.* **1997**, *3* (8), 1357–1364.

(605) Beller, M.; Fischer, H.; Herrmann, W. A.; Öfele, K.; Brossmer, C. Palladacycles as Efficient Catalysts for Aryl Coupling Reactions. *Angew. Chem. Int. Ed.* **1995**, *34* (17), 1848–1849.

(606) Miyazaki, F.; Yamaguchi, K.; Shibasaki, M. The Synthesis of a New Palladacycle Catalyst. Development of a High Performance Catalyst for Heck Reactions. *Tetrahedron Lett.* **1999**, *40* (41), 7379–7383.

(607) Heck, R. F. Palladium-Catalyzed Vinylation of Organic Halides. In *Organic Reactions*; John Wiley & Sons, Inc.: Hoboken, NJ, USA, 1982; pp 345–390.

(608) Davies, D. L.; Donald, S. M. A.; Al-Duaij, O.; Macgregor, S. A.; Pö, M. Electrophilic C-H Activation at {Cp*Ir}: Ancillary-Ligand Control of the Mechanism of C-H Activation. *J. Am. Chem. Soc.* **2006**, *128*, 4210–4211.

(609) Wang, L.; Carrow, B. P. Oligothiophene Synthesis by a General C-H Activation Mechanism: Electrophilic Concerted Metalation-Deprotonation (eCMD). *ACS Catal.* **2019**, *9* (8), 6821–6836.

(610) Amatore, C.; Jutand, A.; M'Barki, M. A. Evidence of the Formation of Zerovalent Palladium from $Pd(OAc)_2$ and Triphenylphosphine. *Organometallics* **1992**, *11* (9), 3009–3013.

(611) Ozawa, F.; Kubo, A.; Hayashi, T. Generation of Tertiary Phosphine-Coordinated Pd(0) Species from $Pd(OAc)_2$ in the Catalytic Heck Reaction. *Chem. Lett.* **2006**, *21* (11), 2177–2180.

(612) Amatore, C.; Carré, E.; Jutand, A.; M'Barki, M. A.; Kneisel, B. O.; Herbst-Irmer, R.; Pellinghelli, M. A.; Tiripicchio, A. Rates and Mechanism of the Formation of Zerovalent Palladium Complexes from Mixtures of $Pd(OAc)_2$ and Tertiary Phosphines and Their Reactivity in Oxidative Additions. *Organometallics* **1995**, *14* (4), 1818–1826.

(613) Shmidt, A. F.; Smirnov, V. V. The NMR Study of the Mechanism of Alkene Arylation with Anhydrides of Aromatic Acids. *Kinet. Catal.* **2002**, *43* (2), 195–198.

(614) Enders, M.; Kohl, G.; Pritzkow, H. Novel Heterobimetallic Compounds with Metal-Metal Bonds: The Use of Quinolyl-Substituted Metallocenes as Tridentate Ligands. *Organometallics* **2002**, *21* (6), 1111–1117.

(615) Köcher, S.; van Klink, G. P. M.; van Koten, G.; Lang, H. Ferrocene-Bridged Pd-NCN Pincer Complexes. *J. Organomet. Chem.* **2003**, *684* (1–2), 230–234.

(616) Negishi, E. I.; Takahashi, T.; Akiyoshi, K. 'Bis(TriphenyIphosphine)Palladium:' Its Generation, Characterization, and Reactions. *J. Chem. Soc. - Ser. Chem. Commun.* **1986**, No. 17, 1338–1339.

(617) Louie, J.; Hartwig, J. F. A Route to Pd^0 from Pd^{II} Metallaycles in Amination and Cross-Coupling Chemistry. *Angew. Chem. Int. Ed.* **1996**, *35* (20), 2359–2361.

(618) Benhaddou, R.; Czernecki, S.; Ville, G.; Zegar, A. A Kinetic Investigation of Some Electronic Factors and Ligand Effects in the Heck Reaction with Allylic Alcohols. *Organometallics* **1988**, *7* (12), 2435–2439.

(619) Fantasia, S.; Nolan, S. P. A General Synthetic Route to Mixed NHC-Phosphane Palladium(0) Complexes (NHC = N-Heterocyclic Carbene). *Chem.: Eur. J.* **2008**, *14* (23), 6987–6993.

(620) Hruszkewycz, D. P.; Balcells, D.; Guard, L. M.; Hazari, N.; Tilset, M. Insight into the Efficiency of Cinnamyl-Supported Precatalysts for the Suzuki-Miyaura Reaction: Observation of Pd(I) Dimers with Bridging Allyl Ligands during Catalysis. *J. Am. Chem. Soc.* **2014**, *136* (20), 7300–7316.

(621) Cui, X.; Fan, Y.; Hall, M. B.; Burgess, K. Mechanistic Insights into Iridium-Catalyzed Asymmetric Hydrogenation of Dienes. *Chem.: Eur. J.* **2005**, *11* (23), 6859–6868.

(622) Fan, Y.; Cui, X.; Burgess, K.; Hall, M. B. Electronic Effects Steer the Mechanism of Asymmetric Hydrogenations of Unfunctionalized Aryl-Substituted Alkenes. *J. Am. Chem. Soc.* **2004**, *126* (51), 16688–16689.

(623) Mazuela, J.; Norrby, P. O.; Andersson, P. G.; Pámies, O.; Diéguez, M.

Pyranoside Phosphite-Oxazoline Ligands for the Highly Versatile and Enantioselective Ir-Catalyzed Hydrogenation of Minimally Functionalized Olefins. A Combined Theoretical and Experimental Study. *J. Am. Chem. Soc.* **2011**, *133* (34), 13634–13645.

(624) Hopmann, K. H.; Bayer, A. On the Mechanism of Iridium-Catalyzed Asymmetric Hydrogenation of Imines and Alkenes: A Theoretical Study. *Organometallics* **2011**, *30* (9), 2483–2497.

(625) Church, T. L.; Rasmussen, T.; Andersson, P. G. Enantioselectivity in the Iridium-Catalyzed Hydrogenation of Unfunctionalized Olefins. *Organometallics* **2010**, *29* (24), 6769–6781.

(626) Davies, D. L.; Ellul, C. E.; MacGregor, S. A.; McMullin, C. L.; Singh, K. Experimental and DFT Studies Explain Solvent Control of C-H Activation and Product Selectivity in the Rh(III)-Catalyzed Formation of Neutral and Cationic Heterocycles. *J. Am. Chem. Soc.* **2015**, *137* (30), 9659–9669.

(627) Shin, K.; Park, S. W.; Chang, S. Cp^*Ir(III)-Catalyzed Mild and Broad C-H Arylation of Arenes and Alkenes with Aryldiazonium Salts Leading to the External Oxidant-Free Approach. *J. Am. Chem. Soc.* **2015**, *137* (26), 8584–8592.

(628) Hwang, H.; Kim, J.; Jeong, J.; Chang, S. Regioselective Introduction of Heteroatoms at the C-8 Position of Quinoline N-Oxides: Remote C-H Activation Using N-Oxide as a Stepping Stone. *J. Am. Chem. Soc.* **2014**, *136* (30), 10770–10776.

(629) Kim, J.; Park, S. W.; Baik, M. H.; Chang, S. Complete Switch of Selectivity in

the C-H Alkenylation and Hydroarylation Catalyzed by Iridium: The Role of Directing Groups. *J. Am. Chem. Soc.* **2015**, *137* (42), 13448–13451.

(630) Shibata, T.; Takano, H. Cationic Iridium-Catalyzed C-H Alkylation of 2-Substituted Pyridine N-Oxides with Acrylates. *Org. Chem. Front.* **2015**, *2* (4), 383–387.

(631) Shibata, T.; Tsuchikama, K.; Pan, S. Cationic Iridium-Catalyzed Synthesis Initiated by the Cleavage of C-H, N-H, and C-O Bonds. *Yuki Gosei Kagaku Kyokaishi/Journal Synth. Org. Chem.* **2013**, *71* (11), 1182–1194.

(632) Li, L.; Brennessel, W. W.; Jones, W. D. C-H Activation of Phenyl Imines and 2-Phenylpyridines with $[Cp^*MCl_2]_2$ (M) Ir, Rh): Regioselectivity, Kinetics, and Mechanism. *Organometallics* **2009**, *28* (12), 3492–3500.

(633) Connor, J. M.; Casey, C. P. Ring-Slippage Chemistry of Transition-Metal Cyclopentadienyl and Indenyi Complexes. *Chem. Rev.* **1987**, *87* (2), 307–318.

(634) Kuwabara, T.; Tezuka, R.; Ishikawa, M.; Yamazaki, T.; Kodama, S.; Ishii, Y. Ring Slippage and Dissociation of Pentamethylcyclopentadienyl Ligand in an (η^5-Cp^*)Ir Complex with a κ^3-*O,C,O* Tridentate Calix[4]Arene Ligand under Mild Conditions. *Organometallics* **2018**, *37* (12), 1829–1832.

(635) Campos, J.; Hintermair, U.; Brewster, T. P.; Takase, M. K.; Crabtree, R. H. Catalyst Activation by Loss of Cyclopentadienyl Ligands in Hydrogen Transfer Catalysis with Cp^*Ir^{III} Complexes. *ACS Catal.* **2014**, *4* (3), 973–985.

(636) Prinz, M.; Veiros, L. F.; Calhorda, M. J.; Romão, C. C.; Herdtweck, E.; Kühn, F. E.; Herrmann, W. A. Structural Preferences of Cyclopentadienyl and Indenyl

Rings in Iridium(I) Carbene Complexes. *J. Organomet. Chem.* **2006**, *691* (21), 4446–4458.

(637) Singleton, D. A.; Thomas, A. A. High-Precision Simultaneous Determination of Multiple Small Kinetic Isotope Effects at Natural Abundance. *J. Am. Chem. Soc.* **1995**, *117* (36), 9357–9358.

(638) Frantz, D. E.; Singleton, D. A.; Snyder, J. P. ^{13}C Kinetic Isotope Effects for the Addition of Lithium Dibutylcuprate to Cyclohexenone. Reductive Elimination Is Rate-Determining. *J. Am. Chem. Soc.* **1997**, *119* (14), 3383–3384.

(639) Beno, B. R.; Houk, K. N.; Singleton, D. A. Synchronous or Asynchronous? An "experimental" Transition State from a Direct Comparison of Experimental and Theoretical Kinetic Isotope Effects for a Diels-Alder Reaction. *J. Am. Chem. Soc.* **1996**, *118* (41), 9984–9985.

(640) Singleton, D. A.; Szymanski, M. J. Simultaneous Determination of Intermolecular and Intramolecular ^{13}C and ^{2}H Kinetic Isotope Effects at Natural Abundance. *J. Am. Chem. Soc.* **1999**, *121* (40), 9455–9456.

(641) Singleton, D. A.; Wang, Y.; Yang, H. W.; Romo, D. Mechanism and Origin of Stereoselectivity in Lewis Acid Catalyzed [2 + 2] Cycloadditions of Ketenes with Aldehydes. *Angew. Chem. Int. Ed.* **2002**, *41* (9), 1572–1575.

(642) Li, J.; Huang, R.; Xing, Y. K.; Qiu, G.; Tao, H. Y.; Wang, C. J. Catalytic Asymmetric Cascade Vinylogous Mukaiyama 1,6-Michael/Michael Addition of 2-Silyloxyfurans with Azoalkenes: Direct Approach to Fused Butyrolactones. *J. Am. Chem. Soc.* **2015**, *137* (32), 10124–10127.

(643) Rathbun, C. M.; Johnson, J. B. Rhodium-Catalyzed Acylation with Quinolinyl Ketones: Carbon-Carbon Single Bond Activation as the Turnover-Limiting Step of Catalysis. *J. Am. Chem. Soc.* **2011**, *133* (7), 2031–2033.

(644) Lee, D. H.; Kwon, K. H.; Yi, C. S. Dehydrative C-H Alkylation and Alkenylation of Phenols with Alcohols: Expedient Synthesis for Substituted Phenols and Benzofurans. *J. Am. Chem. Soc.* **2012**, *134* (17), 7325–7328.

(645) Lee, D. H.; Kwon, K. H.; Yi, C. S. Selective Catalytic C-H Alkylation of Alkenes with Alcohols. *Science* **2011**, *333* (6049), 1613–1616.

(646) Meyer, M. P. New Applications of Isotope Effects in the Determination of Organic Reaction Mechanisms. In *Advances in Physical Organic Chemistry*; Elsevier, 2012; Vol. 46, pp 57–120.

(647) van Dijk, L.; Ardkhean, R.; Sidera, M.; Karabiyikoglu, S.; Sari, Ö.; Claridge, T. D. W.; Paton, R. S.; Fletcher, S. P. Mechanistic Investigation of Rh(I)-Catalyzed Asymmetric Suzuki-Miyaura Coupling with Racemic Allyl Halides. *ChemRxiv* **2019**. https://doi.org/10.26434/chemrxiv.8208617.v1.

(648) Martí, S.; Roca, M.; Andrés, J.; Moliner, V.; Silla, E.; Tuñón, I.; Bertrán, J. Theoretical Insights in Enzyme Catalysis. *Chem. Soc. Rev.* **2004**, *33* (2), 98–107.

(649) Zhang, X.; Bennie, S. J.; van der Kamp, M. W.; Glowacki, D. R.; Manby, F. R.; Mulholland, A. J. Multiscale Analysis of Enantioselectivity in Enzyme-Catalysed 'Lethal Synthesis' Using Projector-Based Embedding. *R. Soc. Open Sci.* **2018**, *5* (2), 171390.

(650) Harrison, C. B.; O'Neil, L. L.; Wiest, O. Computational Studies of DNA

Photolyase. *J. Phys. Chem. A* **2005**, *109* (32), 7001–7012.

(651) Stare, J. Complete Sampling of an Enzyme Reaction Pathway: A Lesson from Gas Phase Simulations. *RSC Adv.* **2017**, *7* (15), 8740–8754.

(652) Meguro, A.; Motoyoshi, Y.; Teramoto, K.; Ueda, S.; Totsuka, Y.; Ando, Y.; Tomita, T.; Kim, S. Y.; Kimura, T.; Igarashi, M.; et al. An Unusual Terpene Cyclization Mechanism Involving a Carbon-Carbon Bond Rearrangement. *Angew. Chem. Int. Ed.* **2015**, *54* (14), 4353–4356.

(653) Korendovych, I. V.; DeGrado, W. F. Catalytic Efficiency of Designed Catalytic Proteins. *Curr. Opin. Struct. Biol.* **2014**, *27* (1), 113–121.

(654) Bolon, D. N.; Mayo, S. L. Enzyme-like Proteins by Computational Design. *Proc. Natl. Acad. Sci.* **2001**, *98* (25), 14274–14279.

(655) Nanda, V.; Koder, R. L. Designing Artificial Enzymes by Intuition and Computation. *Nat. Chem.* **2010**, *2* (1), 15–24.

(656) Steinhauser, M.; Hiermaier, S.; Steinhauser, M. O.; Hiermaier, S. A Review of Computational Methods in Materials Science: Examples from Shock-Wave and Polymer Physics. *Int. J. Mol. Sci.* **2009**, *10* (12), 5135–5216.

(657) Grimme, S.; Bannwarth, C.; Shushkov, P. A Robust and Accurate Tight-Binding Quantum Chemical Method for Structures, Vibrational Frequencies, and Noncovalent Interactions of Large Molecular Systems Parametrized for All spd-Block Elements (Z = 1-86). *J. Chem. Theory Comput.* **2017**, *13* (5), 1989–2009.

(658) Bannwarth, C.; Ehlert, S.; Grimme, S. GFN2-XTB - An Accurate and Broadly

Parametrized Self-Consistent Tight-Binding Quantum Chemical Method with Multipole Electrostatics and Density-Dependent Dispersion Contributions. *J. Chem. Theory Comput.* **2019**, *15* (3), 1652–1671.

(659) Gonzalez-James, O. M.; Kwan, E. E.; Singleton, D. A. Entropic Intermediates and Hidden Rate-Limiting Steps in Seemingly Concerted Cycloadditions. Observation, Prediction, and Origin of an Isotope Effect on Recrossing. *J. Am. Chem. Soc.* **2012**, *134* (4), 1914–1917.

(660) Xue, X. S.; Jamieson, C. S.; Garcia-Borràs, M.; Dong, X.; Yang, Z.; Houk, K. N. Ambimodal Trispericyclic Transition State and Dynamic Control of Periselectivity. *J. Am. Chem. Soc.* **2019**, *141* (3), 1217–1221.

(661) Villar López, R.; Faza, O. N.; Silva López, C. Dynamic Effects Responsible for High Selectivity in a [3,3] Sigmatropic Rearrangement Featuring a Bispericyclic Transition State. *J. Org. Chem.* **2017**, *82* (9), 4758–4765.

(662) Aziz, H. R.; Singleton, D. A. Concert along the Edge: Dynamics and the Nature of the Border between General and Specific Acid-Base Catalysis. *J. Am. Chem. Soc.* **2017**, *139* (16), 5965–5972.

(663) Nieves-Quinones, Y.; Singleton, D. A. Dynamics and the Regiochemistry of Nitration of Toluene. *J. Am. Chem. Soc.* **2016**, *138* (46), 15167–15176.

(664) Doubleday, C.; Boguslav, M.; Howell, C.; Korotkin, S. D.; Shaked, D. Trajectory Calculations for Bergman Cyclization Predict H/D Kinetic Isotope Effects Due to Nonstatistical Dynamics in the Product. *J. Am. Chem. Soc.* **2016**, *138* (24), 7476–7479.

(665) Yang, Z.; Jamieson, C. S.; Xue, X. S.; Garcia-Borràs, M.; Benton, T.; Dong, X.; Liu, F.; Houk, K. N. Mechanisms and Dynamics of Reactions Involving Entropic Intermediates. *Trends Chem.* **2019**, *1* (1), 22–34.

(666) Tantillo, D. J. Dynamic Effects on Organic Reactions. In *Reference Module in Chemistry, Molecular Sciences and Chemical Engineering*; Elsevier, 2018.

(667) Warshel, A.; Weiss, R. M. An Empirical Valence Bond Approach for Comparing Reactions in Solutions and in Enzymes. *J. Am. Chem. Soc.* **1980**, *102* (20), 6218–6226.

(668) Warshel, A.; Florian, J. The Empirical Valence Bond (EVB) Method. In *Encyclopedia of Computational Chemistry*; John Wiley & Sons, Ltd: Chichester, UK, 2004.

(669) Woo, T. K.; Cavallo, L.; Ziegler, T. Implementation of the IMOMM Methodology for Performing Combined QM/MM Molecular Dynamics Simulations and Frequency Calculations. *Theor. Chem. Acc.* **1998**, *100* (5–6), 307–313.

(670) Senn, H. M.; Thiel, W. QM/MM Methods for Biomolecular Systems. *Angew. Chem. Int. Ed.* **2009**, *48* (7), 1198–1229.

(671) Van Der Kamp, M. W.; Mulholland, A. J. Combined Quantum Mechanics/Molecular Mechanics (QM/MM) Methods in Computational Enzymology. *Biochemistry* **2013**, *52* (16), 2708–2728.

(672) Groenhof, G. Introduction to QM/MM Simulations; Humana Press, Totowa, NJ, 2013; pp 43–66.

(673) Ahmadi, S.; Barrios Herrera, L.; Chehelamirani, M.; Hostaš, J.; Jalife, S.; Salahub, D. R. Multiscale Modeling of Enzymes: QM-Cluster, QM/MM, and QM/MM/MD: A Tutorial Review. *Int. J. Quantum Chem.* **2018**, *118* (9), e25558.

(674) Manby, F. R.; Stella, M.; Goodpaster, J. D.; Miller, T. F. A Simple, Exact Density-Functional-Theory Embedding Scheme. *J. Chem. Theory Comput.* **2012**, *8* (8), 2564–2568.

(675) Lee, S. J. R. R.; Welborn, M.; Manby, F. R.; Miller, T. F. Projection-Based Wavefunction-in-DFT Embedding. *Acc. Chem. Res.* **2019**, *52*, 1359−1368.

(676) Li, C.; Zheng, X.; Su, N. Q.; Yang, W. Localized Orbital Scaling Correction for Systematic Elimination of Delocalization Error in Density Functional Approximations. *Natl. Sci. Rev.* **2018**, *5* (2), 203–215.

(677) Austin, A.; Petersson, G. A.; Frisch, M. J.; Dobek, F. J.; Scalmani, G.; Throssell, K. A Density Functional with Spherical Atom Dispersion Terms. *J. Chem. Theory Comput.* **2012**, *8* (12), 4989–5007.

(678) Grimme, S.; Ehrlich, S.; Goerigk, L. Effect of the Damping Function in Dispersion Corrected Density Functional Theory. *J. Comput. Chem.* **2011**, *32* (7), 1456–1465.

(679) Khorshidi, A.; Peterson, A. A. Amp: A Modular Approach to Machine Learning in Atomistic Simulations. *Comput. Phys. Commun.* **2016**, *207*, 310–324.

(680) Zhang, Y.-J.; Khorshidi, A.; Kastlunger, G.; Peterson, A. A. The Potential for Machine Learning in Hybrid QM/MM Calculations. *J. Chem. Phys.* **2018**, *148* (24), 241740.

(681) Handley, C. M.; Popelier, P. L. A. Potential Energy Surfaces Fitted by Artificial Neural Networks. *J. Phys. Chem. A* **2010**, *114* (10), 3371–3383.

(682) Behler, J. Perspective: Machine Learning Potentials for Atomistic Simulations. *J. Chem. Phys.* **2016**, *145* (17), 170901.

(683) Behler, J. Representing Potential Energy Surfaces by High-Dimensional Neural Network Potentials. *J. Phys. Condens. Matter* **2014**, *26* (18), 183001.

Appendix 1 Full *Gaussian* software citations

Full reference for *Gaussian 09* software used in this thesis

Gaussian 09, Revision D.01, M. J. Frisch, G. W. Trucks, H. B. Schlegel, G. E. Scuseria, M. A. Robb, J. R. Cheeseman, G. Scalmani, V. Barone, B. Mennucci, G. A. Petersson, H. Nakatsuji, M. Caricato, X. Li, H. P. Hratchian, A. F. Izmaylov, J. Bloino, G. Zheng, J. L. Sonnenberg, M. Hada, M. Ehara, K. Toyota, R. Fukuda, J. Hasegawa, M. Ishida, T. Nakajima, Y. Honda, O. Kitao, H. Nakai, T. Vreven, J. A. Montgomery, Jr., J. E. Peralta, F. Ogliaro, M. Bearpark, J. J. Heyd, E. Brothers, K. N. Kudin, V. N. Staroverov, R. Kobayashi, J. Normand, K. Raghavachari, A. Rendell, J. C. Burant, S. S. Iyengar, J. Tomasi, M. Cossi, N. Rega, J. M. Millam, M. Klene, J. E. Knox, J. B. Cross, V. Bakken, C. Adamo, J. Jaramillo, R. Gomperts, R. E. Stratmann, O. Yazyev, A. J. Austin, R. Cammi, C. Pomelli, J. W. Ochterski, R. L. Martin, K. Morokuma, V. G. Zakrzewski, G. A. Voth, P. Salvador, J. J. Dannenberg, S. Dapprich, A. D. Daniels, Ö. Farkas, J. B. Foresman, J. V. Ortiz, J. Cioslowski, and D. J. Fox, Gaussian, Inc., Wallingford CT, **2009**.

Full reference for *Gaussian 16* software used in this thesis

Gaussian 16, Revision A.01, Frisch, M. J.; Trucks, G. W.; Schlegel, H. B.; Scuseria, G. E.; Robb, M. A.; Cheeseman, J. R.; Scalmani, G.; Barone, V.; Mennucci, B.; Petersson, G. A.; Nakatsuji, H.; Caricato, M.; Li, X.; Hratchian, H. P.; Izmaylov, A. F.; Bloino, J.; Zheng, G.; Sonnenberg, J. L.; Hada, M.; Ehara, M.; Toyota, K.; Fukuda, R.; Hasegawa, J.; Ishida, M.; Nakajima, T.; Honda, Y.; Kitao, O.; Nakai, H.; Vreven, T.; Montgomery Jr., J. A.; Peralta, J. E.; Ogliaro, F.; Bearpark, M.; Heyd, J. J.; Brothers, E.; Kudin, K. N.; Staroverov, V. N.; Kobayashi, R.; Normand, J.; Raghavachari, K.; Rendell, A.; Burant, J. C.; Iyengar, S. S.; Tomasi, J.; Cossi, M.; Rega, N.; Millam, J. M.; Klene, M.; Knox, J. E.; Cross, J. B.; Bakken, V.; Adamo, C.; Jaramillo, J.; Gomperts, R.; Stratmann, R. E.; Yazyev, O.; Austin, A. J.; Cammi, R.; Pomelli, C.; Ochterski, J. W.; Martin, R. L.; Morokuma, K.; Zakrzewski, V. G.; Voth, G. A.; Salvador, P.; Dannenberg, J. J.; Dapprich, S.; Daniels, A. D.; Farkas, Ö.; Foresman, J. B.; Ortiz, J. V; Cioslowski, J.; Fox, D. J. Gaussian, Inc., Wallingford CT, **2016**.

Appendix 2 Absolute values (in hartrees) for optimised structures for cyclobutanation (Chapter 2)

Structure	E/au	ZPE/au	H/au	qh-G/au	SP DFT (MeCN)	SP DFT (HFIP)
Starting materials:						
1a_n	-463.275335	0.196779	-463.06578	-463.113618	-463.47216	-463.45545
1a_rc	-463.009101	0.196496	-462.79962	-462.848486	-463.26901	-463.24939
1b_n	-348.797531	0.163449	-348.624	-348.665962	-348.94416	-348.93471
1b_rc	-348.508642	0.162615	-348.33574	-348.378687	-348.72508	-348.71327
2a_n	-463.272892	0.197361	-463.06308	-463.110068	-463.46919	-463.45309
2a_rc	-463.002658	0.197471	-462.79254	-462.840538	-463.26241	-463.24302
Pathways for reaction P1:						
int1	-811.830601	0.361677	-811.4454	-811.51614	-812.22251	-812.2014
ts1	-811.8204	0.362952	-811.43567	-811.502488	-812.20993	-812.18829
ts1-c2	-811.819673	0.362972	-811.43472	-811.502623	-812.2087	-812.184
ts1-c3	-811.817037	0.363451	-811.43215	-811.498282	-812.20593	-812.18563
ts1-c4	-811.8155	0.36279	-811.43086	-811.4983	-812.2041	-812.1799
int2	-811.827989	0.364325	-811.44197	-811.50846	-812.21797	-812.19793
int2-c2	-811.820702	0.364306	-811.43435	-811.502244	-812.2152	-812.1903
ts2	-811.820847	0.363704	-811.43568	-811.502244	-812.21374	-812.18974
int3	-811.840226	0.365772	-811.45287	-811.519828	-812.22781	-812.2043
int3n	-812.112396	0.366062	-811.72494	-811.791592	-812.44141	-812.42075
ts2-an	-811.822963	0.364993	-811.4373	-811.501552	-812.2104	-812.1894
int3-an	-811.838653	0.3668	-811.4511	-811.515667	-812.2283	-812.2067
in3n-an	-812.084514	0.367041	-811.69673	-811.760614	-812.4152	-812.3964
ts3-an	-811.798775	0.362127	-811.41604	-811.480285	-812.1929	-812.1711
int4-an	-811.811886	0.364159	-811.42632	-811.492361	-812.2034	-812.1819
ts4-an	-811.801389	0.362955	-811.41779	-811.482102	-812.1954	-812.1735
int5-an	-811.867253	0.368185	-811.47845	-811.542769	-812.2565	-812.2351
int5n-an	-812.143694	0.36903	-811.75446	-811.817207	-812.4699	-812.4513
ts2-ph	-811.8229	0.364675	-811.4376	-811.501996	-812.2095	-812.1883

int3-ph	-811.83286	0.366611	-811.44559	-811.50995	-812.225	-812.2036
int3n-ph	-812.088345	0.366914	-811.70083	-811.764681	-812.4187	-812.3996
ts3-ph	-811.792234	0.361377	-811.40992	-811.475295	-812.1882	-812.1663
int4-ph	-811.795318	0.363464	-811.41061	-811.476306	-812.1893	-812.1674
ts4-ph	-811.791341	0.36199	-811.40858	-811.473359	-812.1883	-812.1662
int5-ph	-811.871577	0.367855	-811.48307	-811.547607	-812.259	-812.2374
int5n-ph	-812.148353	0.368384	-811.75961	-811.822937	-812.4746	-812.4559
int1'	-811.830818	0.361768	-811.44565	-811.516213	-812.2224	-812.2011
ts1'	-811.819644	0.362084	-811.4353	-811.503838	-812.2087	-812.1845
int2'	-811.828386	0.364445	-811.44207	-811.509328	-812.2171	-812.1934
ts2'	-811.820275	0.36361	-811.43523	-811.501806	-812.2145	-812.1908
int3'	-811.835024	0.365927	-811.44761	-811.514395	-812.2244	-812.2019
int3'n	-812.107687	0.367099	-811.71966	-811.784291	-812.4374	-812.4175
ts1'-c2	-811.819856	0.362392	-811.43541	-811.503368	-812.2088	-812.1851
int2'-c2	-811.826467	0.364267	-811.44032	-811.507619	-812.2142	-812.1906
ts1'-c3	-811.817539	0.363326	-811.43235	-811.499952	-812.2055	-812.1814
ts2'-c2	-811.823048	0.364276	-811.4376	-811.503233	-812.2148	-812.1918
ts2'-an	-811.819897	0.365019	-811.43414	-811.498971	-812.2058	-812.1834
int3'-an	-811.838475	0.367012	-811.45073	-811.51559	-812.2269	-812.2049
int3'n-an	-812.085137	0.366609	-811.69761	-811.762438	-812.415	-812.3962
ts3'-an	-811.80014	0.362153	-811.41738	-811.481938	-812.1934	-812.1709
int4'-an	-811.815056	0.365581	-811.42841	-811.493876	-812.2063	-812.1841
ts4'-an	-811.806516	0.362912	-811.42304	-811.487296	-812.1988	-812.1767
int5'-an	-811.870975	0.367156	-811.48281	-811.548353	-812.2599	-812.2382
int5'n-an	-812.146929	0.368206	-811.75824	-811.821732	-812.4733	-812.4546
ts2'-ph	-811.820292	0.364774	-811.43475	-811.499776	-812.2053	-812.183
int3'ph	-811.833694	0.366617	-811.44634	-811.511192	-812.224	-812.2023
int3'n-ph	-812.089823	0.367497	-811.70176	-811.765762	-812.4189	-812.3997
ts3'-ph	-811.794127	0.361621	-811.41172	-811.476599	-812.1897	-812.1678
int4'-ph	-811.795384	0.363123	-811.41112	-811.47655	-812.1897	-812.168
ts4'-ph	-811.792199	0.361989	-811.40945	-811.474224	-812.1889	-812.167

int5'-ph	-811.871393	0.367838	-811.48279	-811.547621	-812.2585	-812.2372
int5'n-ph	-812.147918	0.367895	-811.75948	-811.823266	-812.4739	-812.4552
ts1-g1	-811.809343	0.36205	-811.42516	-811.493286	-812.20077	-812.17717
ts1-g1-c2	-811.806243	0.361937	-811.42217	-811.490302	-812.19741	-812.17262
int3-g1	-811.831003	0.365911	-811.44365	-811.510568	-812.22339	-812.2003
int3n-g1	-812.10813	0.366794	-811.7204	-811.785243	-812.43726	-812.41714
ts1-g2	-811.807979	0.362206	-811.4238	-811.491482	-812.19861	-812.17524
ts1-g2-c2	-811.807962	0.362225	-811.42389	-811.490853	-812.19733	-812.17567
int3-g2	-811.836531	0.365899	-811.44902	-811.516229	-812.22909	-812.20503
int3n-g2	-812.112681	0.365856	-811.72627	-811.79125	-812.44314	-812.42185
Pathways for reaction P2:						
int6	-811.827255	0.362165	-811.44194	-811.511825	-812.2197	-812.1982
ts6	-811.8138	0.36304	-811.42878	-811.496384	-812.2023	-812.1785
int7	-811.821458	0.364966	-811.43464	-811.501867	-812.2103	-812.1865
ts6-c2	-811.811556	0.363612	-811.42618	-811.493393	-812.2	-812.1763
ts7	-811.81425	0.364527	-811.42861	-811.494203	-812.2074	-812.1843
int8	-811.829942	0.366245	-811.44256	-811.508156	-812.2191	-812.1968
int8n	-812.103398	0.367212	-811.71538	-811.779767	-812.4319	-812.4125
ts7-ph	-811.816532	0.364755	-811.4309	-811.496003	-812.2017	-812.1793
int8-ph	-811.838238	0.366265	-811.45098	-811.51638	-812.2284	-812.2067
int8n-ph	-812.094068	0.366732	-811.70647	-811.770992	-812.4232	-812.404
ts8-ph	-811.794574	0.361227	-811.41239	-811.477772	-812.1903	-812.1685
int9-ph	-811.795895	0.36251	-811.41197	-811.478259	-812.1903	-812.1686
ts9-ph	-811.792815	0.361418	-811.41043	-811.475878	-812.1895	-812.1677
int10-ph	-811.871577	0.367855	-811.48307	-811.547607	-812.259	-812.2374
int10n-ph	-812.148353	0.368384	-811.75961	-811.822937	-812.4746	-812.4559
int6'	-811.827223	0.362287	-811.44177	-811.51156	-812.2202	-812.1994
ts6'	-811.816034	0.363552	-811.43102	-811.496903	-812.2056	-812.1854
int7'	-811.82257	0.364928	-811.43621	-811.501884	-812.2118	-812.192
ts6'-c2	-811.8122	0.363485	-811.42696	-811.49451	-812.201	-812.176
ts7'	-811.813519	0.364032	-811.42817	-811.494741	-812.2074	-812.183

int8'	-811.834061	0.366916	-811.44593	-811.512015	-812.226	-812.203
int8'n	-812.110728	0.367118	-811.7227	-811.787491	-812.4403	-812.4199
ts7'-ph	-811.815113	0.365315	-811.42896	-811.493835	-812.201	-812.1797
int8'-ph	-811.831737	0.366662	-811.44426	-811.509192	-812.2221	-812.201
int8'n-ph	-812.086862	0.367373	-811.69885	-811.762683	-812.4154	-812.3969
ts8'-ph	-811.792113	0.362172	-811.40931	-811.473728	-812.1877	-812.1659
int9'-ph	-811.795116	0.363718	-811.41023	-811.475813	-812.1888	-812.1673
ts9'-ph	-811.791704	0.362283	-811.40872	-811.473405	-812.1884	-812.1667
int10'-ph	-811.871393	0.367834	-811.48279	-811.547629	-812.2585	-812.2372
int10'n-ph	-812.147918	0.367895	-811.75948	-811.823266	-812.4739	-812.4552
ts6-g1	-811.806884	0.362328	-811.42258	-811.490317	-812.19768	-812.17447
ts6-g1-c2	-811.801209	0.362155	-811.41696	-811.485182	-812.18942	-812.1657
int8-g1	-811.830732	0.366015	-811.44326	-811.510872	-812.22269	-812.19944
int8n-g1	-812.106868	0.366968	-811.7188	-811.784102	-812.43678	-812.4161
ts6-g2	-811.806139	0.363078	-811.42138	-811.488039	-812.1959	-812.17399
ts6-g2-c2	-811.8041	0.362342	-811.41965	-811.487872	-812.1943	-812.1705
int8-g2	-811.833643	0.365939	-811.44623	-811.512945	-812.22535	-812.20233
int8n-g2	-812.109777	0.366958	-811.72185	-811.786849	-812.43932	-812.41901
Pathways for reaction P3:						
int11	-811.826625	0.362542	-811.44104	-811.51056	-812.2177	-812.1961
ts11	-811.813906	0.363039	-811.42897	-811.496421	-812.2021	-812.1785
int12	-811.822145	0.364843	-811.43545	-811.50276	-812.2107	-812.1872
ts12	-811.814186	0.364325	-811.42866	-811.494366	-812.2064	-812.1832
int13	-811.830444	0.366665	-811.44273	-811.508102	-812.2179	-812.1958
int13n	-812.103733	0.367597	-811.7154	-811.779608	-812.4324	-812.413
ts11-c2	-811.8116	0.364027	-811.426	-811.492857	-812.2001	-812.1767
ts12-c2	-811.816141	0.363941	-811.43092	-811.497115	-812.2097	-812.1864
ts12-an	-811.815664	0.364822	-811.42982	-811.495274	-812.2022	-812.1796
int13-an	-811.844073	0.366597	-811.45654	-811.521647	-812.232	-812.2097
int13n-an	-812.090659	0.366581	-811.70308	-811.76784	-812.4198	-812.4012
ts13-an	-811.80345	0.36165	-811.42101	-811.485906	-812.1974	-812.1749

int14-an	-811.836459	0.366346	-811.44921	-811.514872	-812.226	-812.2039
ts14-an	-811.80629	0.362115	-811.42332	-811.488445	-812.2001	-812.1777
int15-an	-811.874038	0.367405	-811.48576	-811.550796	-812.2616	-812.2399
int15n-an	-812.147838	0.368062	-811.75919	-811.822966	-812.4744	-812.4555
ts14-an	-811.80629	0.362115	-811.42332	-811.488445	-812.2001	-812.1777
int11'	-811.827	0.36215	-811.44165	-811.511745	-812.2174	-812.1965
ts11'	-811.816072	0.363509	-811.43093	-811.497568	-812.2053	-812.1838
int12'	-811.823157	0.365312	-811.43643	-811.502025	-812.2127	-812.1929
ts12'	-811.815734	0.364673	-811.43002	-811.495472	-812.2072	-812.184
int13'	-811.833573	0.36636	-811.446	-811.512116	-812.2207	-812.1975
int13'n	-812.110248	0.366754	-811.72253	-811.787411	-812.4397	-812.4194
ts11'-c2	-811.812995	0.363386	-811.42782	-811.495166	-812.2023	-812.1773
ts12'-an	-811.814609	0.365472	-811.42843	-811.493023	-812.2014	-812.1802
int13'-an	-811.837248	0.366587	-811.44968	-811.514986	-812.2252	-812.2038
int13'n-an	-812.084122	0.366956	-811.69634	-811.760505	-812.4117	-812.394
ts13'-an	-811.800655	0.362275	-811.41767	-811.482339	-812.1948	-812.1726
int14'-an	-811.820047	0.365398	-811.43347	-811.499182	-812.2102	-812.1885
ts14'-an	-811.805417	0.362692	-811.42211	-811.486585	-812.1992	-812.1771
int15'-an	-811.8732	0.367256	-811.48503	-811.550182	-812.2607	-812.2391
int15'n-an	-812.1474	0.368324	-811.7586	-811.82221	-812.4737	-812.4549
ts11-g1	-811.80343	0.362753	-811.41872	-811.486308	-812.19289	-812.17057
ts11-g1-c2	-811.801585	0.36267	-811.41697	-811.48476	-812.19246	-812.16909
ts11-g2	-811.801221	0.362968	-811.41625	-811.484079	-812.19278	-812.16871
ts11-g2-c2	-811.800383	0.362453	-811.41585	-811.484087	-812.1904	-812.16621
Rotational barriers:						
ts-rot12	-811.812362	0.364997	-811.42647	-811.491979	-812.2048	-812.1799
ts-rot12'	-811.8152	0.364531	-811.4296	-811.495939	-812.2058	-812.181
ts-rot34	-811.812541	0.364335	-811.42716	-811.493012	-812.205	-812.18
ts-rot34'	-811.815556	0.364463	-811.42984	-811.496607	-812.2065	-812.1816

Table A2.1. Absolute values (in Hartrees) for SCF energy, zero-point vibrational energy (ZPE), enthalpy and quasi-harmonic Gibbs free energy (at 363K) for the SET-catalysed cyclobutanation.

Appendix 3 Absolute values (in hartrees) and imaginary frequencies (in cm^{-1}) for optimised structures for hydroxyphosphine-catalysed Staudinger reduction (Chapter 3)

	E/au	ZPE/au	H/au	qh-G/au	Im.Freq/cm^{-1}	SP ωB97X-D (MeCN)	SP MN15 (MeCN)
0. Starting materials:							
DBU	-461.992389	0.248855	-461.733	-461.774738	+	-462.1409628	-462.0706955
N_2	-109.48937	0.005705	-109.48036	-109.499089	+	-109.526411	-109.5295888
azide	-204.026862	0.050853	-203.970628	-203.999451	+	-204.0985572	-204.0836602
methylamine	-95.837706	0.064795	-95.768553	-95.792803	+	-95.87156402	-95.84779059
phenylsilane	-522.854847	0.116256	-522.730679	-522.766792	+	-522.9553098	-522.9102855
silylamine	-617.524537	0.163528	-617.350007	-617.393131	+	-617.6598139	-617.6046089
phosphonium_cation	-1228.424385	0.357095	-1228.046528	-1228.109859	+	-1228.783488	-1228.689573
silylanehydride_anion	-618.112321	0.16974	-617.931784	-617.974283	+	-618.2898356	-618.2290914
1_equatorial_catalyst:							
1a-eq	-1229.205456	0.366703	-1228.816985	-1228.885164	+	-1229.517081	-1229.425974
1a-eq-c2	-1229.2082	0.366999	-1228.8198	-1228.884403	+	-1229.520089	-1229.427865
1a-eq-c3	-1229.2067	0.366732	-1228.8183	-1228.883549	+	-1229.518698	-1229.426756
int1-eq	-1433.2465	0.419781	-1432.7991	-1432.876692	+	-1433.627403	-1433.519782
ts1-eq	-1433.226	0.419102	-1432.7805	-1432.855178	**-220.7185**	-1433.603415	-1433.493535
int2-eq	-1433.2477	0.420907	-1432.8009	-1432.874126	+	-1433.632447	-1433.52312
int3-eq	-1433.2533	0.42123	-1432.8061	-1432.879544	+	-1433.638177	-1433.529262
ts3-eq	-1433.2173	0.419278	-1432.7724	-1432.844593	**-443.5614**	-1433.60104	-1433.494639
int4-eq	-1433.3282	0.417686	-1432.8823	-1432.960911	+	-1433.717815	-1433.612812
int4'-eq	-1323.8339	0.411688	-1323.3981	-1323.467919	+	-1324.186834	-1324.078552
int5-eq	-1846.7063	0.529602	-1846.1441	-1846.230614	+	-1847.154235	-1846.997491
ts5-eq	-1846.6672	0.53132	-1846.105	-1846.187695	**-131.2725**	-1847.118665	-1846.96656
ts5u-eq	-1846.6515	0.533082	-1846.0871	-1846.170287	**-126.8519**	-1847.098992	-1846.944815
int6-eq	-1846.6823	0.533774	-1846.1173	-1846.201456	+	-1847.132987	-1846.981657
ts6-eq	-1846.6685	0.529687	-1846.108	-1846.190882	**-406.613**	-1847.115079	-1846.966173
int7-eq	-1846.7357	0.531576	-1846.172	-1846.257627	+	-1847.185224	-1847.030559

ts8-eq	-1846.7009	0.526695	-1846.142	-1846.228702	**-1135.4895**	-1847.143919	-1846.988894
int9-eq	-1846.7298	0.531904	-1846.1656	-1846.252205	+	-1847.181186	-1847.026786
ts6z-eq	-1846.6628	0.529476	-1846.1017	-1846.186033	**-183.948**	-1847.112192	-1846.96056
int6'-eq	-2308.7126	0.783994	-2307.8875	-2307.989453	+	-2309.301511	-2309.075343
ts6'-eq	-2308.7072	0.781736	-2307.8845	-2307.985805	**-849.8232**	-2309.297214	-2309.072355
int7'-eq	-2308.7098	0.786603	-2307.8822	-2307.983551	+	-2309.304223	-2309.077845
ts7'-eq	-2308.7072	0.781009	-2307.8852	-2307.98672	**-958.3155**	-2309.296392	-2309.071111
int8'-eq	-2308.7488	0.781417	-2307.9237	-2308.032114	+	-2309.340348	-2309.107829
ts10-eq	-1433.3143	0.412829	-1432.8735	-1432.952879	**-985.1693**	-1433.70187	-1433.596713
int11-eq	-1433.346	0.419552	-1432.8986	-1432.97649	+	-1433.734685	-1433.629397
int12-eq	-1846.7174	0.530796	-1846.1542	-1846.241108	+	-1847.167942	-1847.013257
ts10'-eq	-1323.8207	0.407157	-1323.3899	-1323.458624	**-988.9147**	-1324.171562	-1324.063067
ts10'-eq	-1323.8207	0.407157	-1323.3899	-1323.458624	**-988.9147**	-1324.171562	-1324.063067
int11'-eq	-1323.8525	0.412774	-1323.4161	-1323.484564	+	-1324.20469	-1324.096763
ts12-eq	-1846.683	0.533516	-1846.1195	-1846.200286	**-119.3873**	-1847.133635	-1846.981786
ts12-eq-c2	-1846.6778	0.5331	-1846.1147	-1846.195387	**-234.5104**	-1847.129355	-1846.978055
ts12-eq-c3	-1846.6773	0.533008	-1846.1143	-1846.195598	**-239.6948**	-1847.128615	-1846.976188
int13-eq	-1846.7292	0.530386	-1846.1661	-1846.253732	+	-1847.179514	-1847.024627
ts12n-eq	-1846.679	0.533049	-1846.1161	-1846.196458	+	-1847.130298	-1846.979437
ts12n-eq-c2	-1846.6709	0.532121	-1846.1086	-1846.189954	+	-1847.122052	-1846.970778
ts12n-eq-c3	-1846.6675	0.53232	-1846.105	-1846.186357	+	-1847.119605	-1846.969317
ts12n-eq-c4	-1846.6661	0.532476	-1846.1034	-1846.18447	+	-1847.1164	-1846.965468
ts12i-eq-c1	-1846.6622	0.532188	-1846.0997	-1846.181665	**-126.4394**	-1847.113786	-1846.962263
ts12i-eq-c2	-1846.6637	0.532456	-1846.1011	-1846.182258	**-230.6961**	-1847.114469	-1846.962796
ts12i-eq-c3	-1846.6604	0.532198	-1846.0979	-1846.179449	**-231.8471**	-1847.111188	-1846.959253
ts12o-eq-c1	-1846.6681	0.531273	-1846.1065	-1846.187781	**-90.8591**	-1847.122589	-1846.969852
ts12o-eq-c2	-1846.6583	0.528838	-1846.0984	-1846.181746	**-88.1088**	-1847.11463	-1846.963338
ts12o-eq-c3	-1846.6639	0.531433	-1846.1024	-1846.183333	**-278.6876**	-1847.113863	-1846.963604
ts12o-eq-c4	-1846.6604	0.530784	-1846.0992	-1846.180754	**-255.6696**	-1847.110186	-1846.959996
ts12o-eq-c5	-1846.6619	0.531663	-1846.1001	-1846.181044	**-389.7343**	-1847.110355	-1846.960499

ts12z-eq	-1846.6449	0.526192	-1846.088	-1846.170309	**-1222.3823**	-1847.099617	-1846.948307
int12b-eq	**-1941.3905**	**0.578932**	**-1940.7764**	**-1940.868483**	+	**-1941.875233**	**-1941.710007**
ts12b-eq	**-1941.355**	**0.580641**	**-1940.7412**	**-1940.828275**	**-114.9844**	**-1941.839931**	**-1941.677144**
int13b-eq	**-1941.4119**	**0.577846**	**-1940.7984**	**-1940.891258**	+	**-1941.896034**	**-1941.729633**
int12c-eq	**-2036.0699**	**0.627339**	**-2035.4047**	**-2035.50215**	+	**-2036.588001**	**-2036.410091**
ts12c-eq	**-2036.0239**	**0.628098**	**-2035.3598**	**-2035.451861**	**-125.0845**	**-2036.54113**	**-2036.369137**
int13c-eq	**-2036.0876**	**0.62499**	**-2035.4238**	**-2035.522791**	+	**-2036.60533**	**-2036.428398**
int12'-eq	-1942.5702	0.597933	-1941.9354	-1942.030982	+	-1943.050536	-1942.870035
ts12'-eq	-1942.5244	0.599634	-1941.8911	-1941.979091	**-324.094**	-1943.004824	-1942.829556
int13'-eq	-1942.5893	0.598648	-1941.9538	-1942.048878	+	-1943.067678	-1942.884488
ts12u-eq	-1846.6487	0.533343	-1846.0842	-1846.167427	**-129.7003**	-1847.098796	-1846.945634
2_catalyst_regeneration:							
6-axH	-1229.1985	0.366657	-1228.8112	-1228.874274	+	-1229.51800	-1229.422099
6-axH-2	-1229.184	0.365568	-1228.7974	-1228.861403	+	-1229.5	-1229.409483
6-eqH	-1229.1882	0.36539	-1228.8019	-1228.865347	+	-1229.508576	-1229.412354
int15-eq	-1691.1972	0.614532	-1690.5498	-1690.637669	+	-1691.6601	-1691.48974
ts15-eq	-1691.1804	0.61138	-1690.5367	-1690.622936	**-1036.0354**	-1691.639501	-1691.46899
int17-eq	-1691.2258	0.617356	-1690.5756	-1690.66295	+	-1691.681187	-1691.51581
int15-ax	-1691.2092	0.616082	-1690.5609	-1690.647149	+	-1691.670935	-1691.500537
ts15-ax	-1691.1426	0.61114	-1690.499	-1690.585404	**-658.5336**	-1691.603621	-1691.4313
int16-ax	-1691.1458	0.61561	-1690.4973	-1690.584569	+	-1691.610166	-1691.439174
int17-ax	-1691.2194	0.617878	-1690.5688	-1690.655669	+	-1691.672675	-1691.504942
ts18-1	-1229.1438	0.36429	-1228.7593	-1228.821475	**-71.1993**	-1229.468318	-1229.372577
ts18-2	-1229.143	0.362865	-1228.7595	-1228.822479	**-326.8518**	-1229.466958	-1229.371341
ts18-3	-1229.184	0.36527	-1228.7986	-1228.860529	**-27.0013**	-1229.505329	-1229.409152
ts19-1	-1229.1462	0.361888	-1228.7633	-1228.827263	**-1040.5248**	-1229.461553	-1229.364919
ts19-2	-1229.1458	0.361431	-1228.7632	-1228.82731	**-1225.5176**	-1229.462413	-1229.364395
3_axial_catalyst:							
1a-ax	-1229.1988	0.366664	-1228.8106	-1228.875139	+	-1229.510173	-1229.418026
int1-ax	-1433.235	0.418753	-1432.7884	-1432.866391	+	-1433.615977	-1433.508097
ts1-ax	-1433.2108	0.418373	-1432.7657	-1432.840918	**-250.6332**	-1433.589373	-1433.480092

int2-ax	-1433.2435	0.420782	-1432.7965	-1432.870378	+	-1433.629567	-1433.522206
ts3-ax	-1433.2013	0.418959	-1432.7564	-1432.829237	**-492.9689**	-1433.587133	-1433.482379
int4-ax	-1433.317	0.417299	-1432.8711	-1432.950772	+	-1433.706866	-1433.603033
int4'-ax	-1323.8208	0.410633	-1323.3856	-1323.456345	+	-1324.174273	-1324.066759
int5-ax	-1846.6923	0.528852	-1846.1303	-1846.218317	+	-1847.140959	-1846.986089
ts5-ax	-1846.6573	0.530151	-1846.0959	-1846.179596	**-196.7318**	-1847.11014	-1846.959851
int6-ax	-1846.6812	0.533373	-1846.1164	-1846.200897	+	-1847.13245	-1846.98254
ts6-ax	-1846.6617	0.529244	-1846.1009	-1846.185027	**-172.3124**	-1847.110202	-1846.959141
int7-ax	-1846.7463	0.532785	-1846.1807	-1846.267509	+	-1847.185914	-1847.034404
int11-ax	-1433.3445	0.419041	-1432.898	-1432.974709	+	-1433.733167	-1433.630325
int12-ax	-1846.7184	0.52964	-1846.1563	-1846.242733	+	-1847.167494	-1847.013059
ts12-ax	-1846.6644	0.531792	-1846.1023	-1846.183555	**-188.1784**	-1847.11757	-1846.966445
int13-ax	-1846.7401	0.531005	-1846.1765	-1846.264633	+	-1847.191754	-1847.035971
int12'-ax	-1942.5669	0.597921	-1941.9322	-1942.027223	+	-1943.047345	-1942.867435
ts12'-ax	-1942.5029	0.598358	-1941.8705	-1941.959293	**-256.8747**	-1942.985447	-1942.809865
int13'-ax	-1942.5901	0.598923	-1941.9543	-1942.049756	+	-1943.069934	-1942.888068
ts12''-ax	-1846.6715	0.531101	-1846.11	-1846.191286	**-177.1101**	-1847.122002	-1846.970903
4_reduction_of_aminophosphoranes:							
int11'-eq	-1323.8525	0.412774	-1323.4161	-1323.484564	+	-1324.20469	-1324.096763
int11'-ax	-1323.8501	0.412165	-1323.4144	-1323.482607	+	-1324.202004	-1324.096043
int11'-ax2	-1323.8427	0.412544	-1323.4065	-1323.475154	+	-1324.195876	-1324.088277
int11'-eq2	-1323.8443	0.412196	-1323.4082	-1323.477218	+	-1324.200399	-1324.091999
ts-rot-23	-1323.8158	0.412334	-1323.3808	-1323.447198	**-36.8574**	-1324.172233	-1324.064049
ts-rot-14	-1323.8047	0.410914	-1323.3707	-1323.437807	**-50.5266**	-1324.16061	-1324.053174
ts-rot-13	-1323.8382	0.412456	-1323.4029	-1323.469618	**-49.8874**	-1324.190661	-1324.083547
ts-rot-24	-1323.8311	0.412322	-1323.3958	-1323.462627	**-70.6256**	-1324.184961	-1324.076745
ts12-eq	-1846.683	0.533516	-1846.1195	-1846.200286	**-119.3873**	-1847.133635	-1846.981786
ts12-ax	-1846.6644	0.531792	-1846.1023	-1846.183555	**-188.1784**	-1847.11757	-1846.966445
ts12-eq2	-1846.6672	0.532019	-1846.1048	-1846.186834	**-116.9966**	-1847.119454	-1846.968849
ts12-ax2	-1846.6611	0.532764	-1846.0983	-1846.179101	**-209.7562**	-1847.114403	-1846.963107
5_alternative_mechanism:							

ts20-eq	-1433.2362	0.416918	-1432.7941	-1432.865983	**-751.3021**	-1433.619152	-1433.509316
int21-eq	-1433.2511	0.421282	-1432.8039	-1432.877324	+	-1433.637626	-1433.527655
int22-eq	-1956.1204	0.539007	-1955.5467	-1955.637959	+	-1956.603273	-1956.443539
ts22-eq	-1956.0884	0.538258	-1955.5166	-1955.60471	**-321.5157**	-1956.577073	-1956.426438
int23-eq	-1956.1458	0.535613	-1955.5741	-1955.668411	+	-1956.650167	-1956.496962
ts23-eq	-1956.1464	0.534098	-1955.5766	-1955.670358	**-112.9206**	-1956.645899	-1956.49369
int24-eq	-1956.2253	0.536633	-1955.6519	-1955.748056	+	-1956.712638	-1956.559898
int21-ax	-1433.2511	0.421444	-1432.8039	-1432.876745	+	-1433.639793	-1433.532787
int22-ax	-1956.1223	0.539671	-1955.5483	-1955.638355	+	-1956.605592	-1956.450519
ts22-ax	-1956.0912	0.539093	-1955.5188	-1955.606094	**-273.7801**	-1956.577043	-1956.42734
int23-ax	-1956.1484	0.535032	-1955.5771	-1955.672053	+	-1956.650608	-1956.496223
ts23-ax	-1956.1471	0.534358	-1955.577	-1955.671149	**-70.0813**	-1956.648611	-1956.495581
int24-ax	-1956.2346	0.538616	-1955.6599	-1955.754706	+	-1956.722	-1956.570709
6_MeO_catalyst_1b:							
1b	-1268.4962	0.394891	-1268.0783	-1268.14587	+	-1268.817377	-1268.718918
int1-MeO	-1472.5324	0.447731	-1472.0558	-1472.135616	+	-1472.921877	-1472.807591
ts1-MeO	-1472.5052	0.447897	-1472.0298	-1472.10626	**-254.4626**	-1472.892756	-1472.777756
int2-MeO	-1472.5288	0.450586	-1472.0512	-1472.126347	+	-1472.923261	-1472.808553
ts3-MeO	-1472.5018	0.447535	-1472.0269	-1472.102562	**-463.0892**	-1472.896881	-1472.782831
int4-MeO	-1472.6075	0.446494	-1472.1316	-1472.212006	+	-1473.006717	-1472.895468
int4'-MeO	-1363.113	0.439535	-1362.6478	-1362.720237	+	-1363.47528	-1363.360936
int5-MeO	-1885.9855	0.557417	-1885.3939	-1885.48385	+	-1886.44296	-1886.280124
ts5-MeO	-1885.95	0.559018	-1885.3584	-1885.444373	**-192.1519**	-1886.411429	-1886.252671
int6-MeO	-1885.9693	0.562193	-1885.3745	-1885.461347	+	-1886.429936	-1886.272208
int7-MeO	-1885.9723	0.560652	-1885.3788	-1885.465488	+	-1886.431809	-1886.275151
ts7-MeO	-1885.951	0.558495	-1885.3598	-1885.446489	**-155.1455**	-1886.41041	-1886.251388
int8-MeO	-1886.0417	0.561409	-1885.4462	-1885.535914	+	-1886.492604	-1886.334079
7_PPh3_catalyst:							
PPh3	-1036.0877	0.277271	-1035.7937	-1035.849812	+	-1036.335487	-1036.270703
H2O	-76.409532	0.021744	-76.384008	-76.402402	+	-76.44543719	-76.43320822
int1-pc	-1240.1266	0.329497	-1239.7745	-1239.842602	+	-1240.442641	-1240.362516

ts1-pc	-1240.0978	0.328379	-1239.7476	-1239.814091	**-262.0236**	-1240.412977	-1240.330688
int2-pc	-1240.1298	0.331268	-1239.7774	-1239.841883	+	-1240.45282	-1240.371813
ts3-pc	-1240.097	0.328709	-1239.747	-1239.811651	**-432.8572**	-1240.421141	-1240.342028
int4-pc	-1240.2023	0.327896	-1239.8509	-1239.921128	+	-1240.529809	-1240.452538
int4'-pc	-1130.7081	0.321387	-1130.3672	-1130.428386	+	-1130.99879	-1130.918202
int5-pc	-1653.5736	0.438574	-1653.1067	-1653.186945	+	-1653.961948	-1653.836572
ts5-pc	-1653.5584	0.44173	-1653.0906	-1653.164898	**-31.0218**	-1653.949748	-1653.825297
int6-pc	-1653.5735	0.442975	-1653.104	-1653.179021	+	-1653.961146	-1653.836111
ts6-pc	-1653.5361	0.437693	-1653.071	-1653.148164	**-583.2097**	-1653.92249	-1653.797699
int7-pc	-1653.6286	0.443435	-1653.1573	-1653.236031	+	-1654.007125	-1653.883504
ts6-pc-w	-1729.9756	0.461708	-1729.4847	-1729.565175	**-675.8505**	-1730.389105	-1730.254033
int7-pc-w	-1730.0511	0.468414	-1729.5519	-1729.635831	+	-1730.461933	-1730.326303
int5-w	-1207.1375	0.346489	-1206.7684	-1206.835965	+	-1207.459679	-1207.366602
ts5-w	-1207.1018	0.34538	-1206.7354	-1206.799123	**-224.9537**	-1207.420379	-1207.327858
int6-w	-1207.1282	0.349844	-1206.7574	-1206.820772	+	-1207.449504	-1207.360585
int7-w	-1207.1127	0.349395	-1206.7425	-1206.805923	+	-1207.43406	-1207.344786
ts7-w	-1207.1065	0.345814	-1206.7402	-1206.802783	**-912.956**	-1207.426669	-1207.337617
int8-w	-1207.1753	0.348687	-1206.8044	-1206.871545	+	-1207.499185	-1207.403407
int8'-w	-1111.3229	0.282066	-1111.0234	-1111.080773	+	-1111.617657	-1111.547158
ts7'-w	-1729.9454	0.469153	-1729.4487	-1729.525278	**-249.8947**	-1730.36501	-1730.233481
int9-w	-1634.1942	0.399624	-1633.7685	-1633.843037	+	-1634.583614	-1634.466662
ts9-w	-1634.1483	0.400479	-1633.7235	-1633.794771	**-201.918**	-1634.542266	-1634.429968
int10-w	-1634.1669	0.4024	-1633.7396	-1633.81161	+	-1634.55685	-1634.446588
ts10-w	-1634.1587	0.39913	-1633.7345	-1633.806978	**-156.9835**	-1634.547617	-1634.433647
int11-w	-1634.2154	0.402178	-1633.7872	-1633.862033	+	-1634.59692	-1634.485863

Appendix 4 Absolute values (in hartrees) and imaginary frequencies (in cm^{-1}) for optimised structures for δ-arylation (Chapter 4)

Structure	E/au	ZPE/au	H/au	qh-G/au	SP DFT (TBME)	ImFreq /cm^{-1}
Starting materials:						
1	-729.968887	0.341853	-729.60021	-729.679275	-730.885265	+
sm-1 - $Pd(TFA)_2$	-1178.318515	0.060493	-1178.2376	-1178.309077	-1179.642042	+
HTFA	-525.90441	0.04037	-525.85446	-525.89887	-526.575334	+
pyridine	-247.762761	0.089473	-247.66597	-247.704111	-248.071198	+
HI	-297.58318	0.005335	-297.57382	-297.599247	-297.586955	+
sm-1' - $Pd(TFA)_2(py)_2$	-1673.95914	0.244081	-1673.6783	-1673.782306	-1675.888255	+
$[Pd(TFA)_2]_2$	-2356.735982	0.123336	-2356.5716	-2356.686917	-2359.356276	+
$[Pd(TFA)_2]_3$	-3535.147025	0.186174	-3534.8983	-3535.058438	-3539.076728	+
ArI	-642.452756	0.123519	-642.31622	-642.369876	-642.880275	+
Ag_2CO_3	-556.727692	0.017256	-556.70052	-556.749839	-557.07963923	+
Pathway without pyridine ligand:						
A	-3943.294504	0.788308	-3942.4092	-3942.627445	-3947.711240	+
ts-A	-3943.241774	0.782901	-3942.3629	-3942.57849	-3947.652234	-1348.6927
B	-3943.251025	0.788085	-3942.3666	-3942.582852	-3947.664103	+
C	-3086.748426	0.466009	-3086.2138	-3086.379948	-3090.272882	+
int-1	-1908.345034	0.404572	-1907.8929	-1908.016055	-1910.578635	+
ts-1	-1908.32979	0.400691	-1907.8823	-1908.003846	-1910.556586	-197.3102
int-2	-1908.331012	0.403774	-1907.8796	-1908.002902	-1910.557829	+
int-3	-1382.415123	0.362564	-1382.0151	-1382.117512	-1383.984503	+
int-4	-1382.409747	0.361709	-1382.0106	-1382.112612	-1383.980311	+
ts-4	-1382.382482	0.357226	-1381.9887	-1382.088919	-1383.947170	-1413.066
int-5	-1382.397683	0.361725	-1381.9986	-1382.100732	-1383.964361	+
int-6	-1498.939203	0.444233	-1498.4533	-1498.564582	-1500.273756	+
ts-6	-1498.915736	0.444176	-1498.4309	-1498.539267	-1500.247698	-153.4792
int-7	-1498.929192	0.445017	-1498.4427	-1498.552903	-1500.260756	+
ts-7	-1498.917829	0.445413	-1498.4323	-1498.539302	-1500.250248	-264.4439

int-8	-1498.975689	0.446821	-1498.4881	-1498.597238	-1500.307462	+
int-9	-1727.288159	0.476923	-1726.7638	-1726.886036	-1729.280556	+
ts-9	-1727.260447	0.472307	-1726.7415	-1726.862309	-1729.246795	-1412.8
int-10	-1727.275647	0.476817	-1726.7514	-1726.874095	-1729.263882	+
int-11	-1843.817831	0.55929	-1843.2068	-1843.33841	-1845.574204	+
ts-11	-1843.794025	0.559109	-1843.1841	-1843.312942	-1845.547865	-154.7984
int-12	-1843.807344	0.56014	-1843.1957	-1843.326021	-1845.560782	+
ts-12	-1843.794662	0.560368	-1843.184	-1843.31127	-1845.548422	-264.5246
int-13	-1843.849056	0.561609	-1843.2366	-1843.36587	-1845.602114	+
int-14	-2072.15873	0.591842	-2071.5093	-2071.651746	-2074.571627	+
ts-14	-2072.133056	0.587093	-2071.4891	-2071.630185	-2074.539613	-1418.695
int-15	-2072.151155	0.591787	-2071.5017	-2071.644308	-2074.560538	+
int-16	-2188.698251	0.674641	-2187.9621	-2188.111875	-2190.872584	+
ts-16	-2188.671772	0.67382	-2187.9369	-2188.085877	-2190.846720	-161.358
int-17	-2188.691245	0.674902	-2187.9548	-2188.104679	-2190.865021	+
ts-17	-2188.670628	0.675537	-2187.9347	-2188.081475	-2190.844301	-269.7691
int-18	-2188.724769	0.676432	-2187.9873	-2188.136149	-2190.898783	+
Other TS conformers:						
ts-4-c2	-1382.378401	0.357169	-1381.9847	-1382.084971	-1383.942824	-1463.7223
ts-6-c2	-1498.914551	0.444174	-1498.4298	-1498.537958	-1500.246335	
ts-7-c2	-1498.906846	0.445104	-1498.4213	-1498.529071	-1500.240529	-149.0566
ts-9-c2	-1727.252822	0.47248	-1726.7338	-1726.85426	-1729.238585	
ts-9-c3	-1727.238281	0.470924	-1726.7202	-1726.842025	-1729.225716	-275.7268
ts-9a	-1727.256169	0.472419	-1726.7372	-1726.857388	-1729.241314	-1468.4218
ts-9a-c2	-1727.256943	0.472254	-1726.738	-1726.858914	-1729.243140	-1337.0955
ts-9a-c3	-1727.236504	0.470877	-1726.7185	-1726.840138	-1729.223271	-1419.4
ts-11-c2	-1843.793136	0.559211	-1843.1833	-1843.311596	-1845.546678	-1466.6123
ts-11a	-1843.794362	0.559058	-1843.1846	-1843.31306	-1845.547631	-1335.1556
ts-11a-c2	-1843.792825	0.55918	-1843.183	-1843.311622	-1845.546357	-148.5601
ts-12-c2	-1843.784298	0.559999	-1843.1737	-1843.3	-1845.539637	-158.6799
ts-12a	-1843.79577	0.561431	-1843.1846	-1843.31018	-1845.546309	-148.9423

ts-12a-c2	-1843.786595	0.560107	-1843.176	-1843.3	-1845.541285	-266.8948
ts-14-c2	-2072.130558	0.587322	-2071.4865	-2071.627241	-2074.537572	-296.9839
ts-16-c2	-2188.668142	0.674459	-2187.933	-2188.080302	-2190.840673	-266.7996
ts-17-c2	-2188.66291	0.675125	-2187.9271	-2188.075084	-2190.838728	-1471.6767
ts-17-c3	-2188.667674	0.675351	-2187.9319	-2188.078887	-2190.841007	-151.15600
ts-17-c4	-2188.667511	0.676001	-2187.9314	-2188.077331	-2190.838337	
ts-17-c5	-2188.654308	0.674779	-2187.9189	-2188.066452	-2190.827057	-249.9004
Pathway with pyridine ligand:						
int-4'	-1630.213178	0.453666	-1629.7138	-1629.832339	-1632.088801	-267.5227
ts-4'	-1630.16591	0.44849	-1629.6728	-1629.78823	-1632.041331	-270.3462
int-5'	-1104.271549	0.411573	-1103.8248	-1103.921267	-1105.4847000	+
ts-7'	-1746.69394	0.535902	-1746.1093	-1746.233232	-1748.325651	+
int-8'	-1746.788786	0.539053	-1746.2008	-1746.326492	-1748.425989	-1356.9381
int-9'	-1746.769913	0.538018	-1746.183	-1746.308063	-1748.403670	+
ts-9'	-1746.735932	0.533093	-1746.1545	-1746.278767	-1748.370295	-310.4541
int-10'	-1746.760532	0.538491	-1746.1733	-1746.298603	-1748.401135	+
int-13'	-2091.665624	0.655007	-2090.9523	-2091.094846	-2093.720383	+
int-14'	-2091.65048	0.652851	-2090.9385	-2091.083642	-2093.704809	-1403.9536
ts-14'	-2091.613357	0.647966	-2090.9069	-2091.051203	-2093.669270	+
int-15'	-2091.63819	0.653381	-2090.9259	-2091.071625	-2093.700360	+
int-19'	-2436.546862	0.76966	-2435.7084	-2435.872275	-2439.023104	+
Pathway with silver carbonate:						
int-9c	-2303.536004	0.554597	-2302.9208	-2303.070999	-2305.506123	+
ts-9c	-2303.479916	0.554941	-2302.8658	-2303.011907	-2305.447408	+

Table A4.1. Absolute values (in Hartrees) for SCF energy, zero-point vibrational energy (ZPE), enthalpy and quasi-harmonic Gibbs free energy (at 363K) for the substrate **2a**. For harmonic frequency analysis, a plus (+) sign indicates that the lowest frequency of the optimised structures is positive.

Structure	E/au	ZPE/au	H/au	qh-G/au	SP DFT (TBME)	Im Freq /cm^{-1}
Starting materials:						
1b	-651.521636	0.286607	-651.21192	-651.284798	-652.33686421	+

L2	-437.183553	0.127404	-437.044	-437.093431	-437.73370834	+
sm-1' - $Pd(TFA)_2(L2)_2$	-2052.81663	0.318364	-2052.452	-2052.57549	-2055.22010719	+
Pathway without pyridone ligand:						
Ab	-3786.403409	0.678759	-3785.6354	-3785.841145	-3790.61949042	+
ts-Ab	-3786.350209	0.672608	-3785.5894	-3785.791664	-3790.56295244	-1373.5267
Bb	-3786.362329	0.677682	-3785.5961	-3785.79873	-3790.57732455	+
Cb	-3008.304508	0.410499	-3007.8291	-3007.988716	-3011.72978045	+
int-4b	-1303.971637	0.30689	-1303.6308	-1303.727538	-1305.44221842	+
ts-4b	-1303.928713	0.302166	-1303.594	-1303.687328	-1305.39328200	-1459.3829
int-5b	-1303.950556	0.306923	-1303.6105	-1303.704919	-1305.41703403	+
int-6b	-1420.491634	0.389299	-1420.0648	-1420.169024	-1421.72632082	+
ts-6b	-1420.466462	0.389483	-1420.0405	-1420.141597	-1421.69778098	-150.8472
int-7b	-1420.485571	0.390235	-1420.0581	-1420.160541	-1421.71744848	+
ts-7b	-1420.466776	0.390487	-1420.0401	-1420.140476	-1421.70021210	-295.8827
int-8b	-1420.525028	0.391015	-1420.097	-1420.199983	-1421.75848694	+
Pathway with pyridone ligand:						
int-3b'	-1741.211636	0.436383	-1740.7289	-1740.849534	-1743.21981744	+
int-4b'	-1215.219402	0.393066	-1214.7901	-1214.889912	-1216.57283801	+
ts-4b'	-1215.206067	0.388551	-1214.7821	-1214.879772	-1216.55605398	-1204.9058
int-5b'	-1215.249222	0.393651	-1214.8194	-1214.919205	-1216.60046818	+
int-6b'	-1857.723834	0.518585	-1857.155	-1857.283552	-1859.49536392	+
ts-6b'	-1857.673982	0.517182	-1857.107	-1857.234398	-1859.44115352	-220.1806
int-7b'	-1857.709236	0.520382	-1857.1393	-1857.265658	-1859.47519397	+
ts-7b'	-1857.678623	0.518787	-1857.1103	-1857.237165	-1859.45089825	-274.963
int-8b'	-1857.738157	0.520384	-1857.168	-1857.295489	-1859.50887950	+
ts-9b'	-1560.084214	0.503317	-1559.5353	-1559.654055	-1561.85663961	-1194.2607
Pathway with silver carbonate:						
int-9b	-2414.55588	0.535778	-2413.9578	-2414.111833	-2416.64889907	+
ts-9b	-2414.512268	0.535216	-2413.9155	-2414.067976	-2416.60392944	-220.8506
int-10b	-2414.554457	0.538329	-2413.9547	-2414.106738	-2416.64786796	+

ts-10b	-2414.517406	0.537287	-2413.919	-2414.070585	-2416.61455369	-327.8454
int-11b	-2414.581944	0.539712	-2413.9809	-2414.133427	-2416.67648220	+
Cationic pathways with silver carbonate and ligand:						
Na^+ rct	-2019.759079	0.519972	-2019.1863	-2019.320319	-2021.62996259	+
Na^+ ts	-2019.692981	0.518841	-2019.1219	-2019.254262	-2021.56731297	-224.7822
Ag^+ rct	-2004.240092	0.517671	-2003.6685	-2003.806151	-2006.01162872	+
Ag^+ ts	-2004.211399	0.517934	-2003.641	-2003.77383	-2005.98320200	-147.7256
C–H activation TSs						
ts-4b'	-1215.216342	0.389049	-1214.7921	-1214.889196	-1216.56560028	-1274.8426
ts-4b'-c2	-1215.209311	0.389145	-1214.785	-1214.881908	-1216.55767352	-1202.7765
ts-4b'-c3	-1215.213267	0.389383	-1214.7887	-1214.885752	-1216.56260083	-1159.6763
ts-4b'-c4	-1215.206067	0.388551	-1214.7821	-1214.879772	-1216.55605398	-1204.9058
ts-4b	-1303.935607	0.302195	-1303.6008	-1303.694079	-1305.40090816	-1403.0514
ts-4b-c2	-1303.928713	0.302166	-1303.594	-1303.687328	-1305.39328200	-1459.3829
ts-4b-c3	-1303.932987	0.302483	-1303.598	-1303.691129	-1305.39819713	-1391.205
ts-4b-c4	-1303.925561	0.301735	-1303.5911	-1303.684798	-1305.39148299	-1454.0579
ts-4b'-py	-1551.721357	0.393329	-1551.2873	-1551.395944	-1553.49772055	-1074.4733
ts-4b'-py-c2	-1551.714436	0.393545	-1551.2804	-1551.388666	-1553.49059485	-907.8496
ts-4b'-py-c3	-1551.718593	0.39359	-1551.2843	-1551.392981	-1553.49565720	-928.9741
ts-4b'-py-c4	-1551.712733	0.393009	-1551.2788	-1551.388023	-1553.49122815	-729.0941
ts-4b''-py	-1551.720548	0.392608	-1551.287	-1551.396477	-1553.49321197	-1358.2501
ts-4b''-py-c2	-1551.716725	0.392967	-1551.2831	-1551.391793	-1553.48772247	-1371.6569
ts-4b''-py-c3	-1551.71868	0.392871	-1551.2849	-1551.394333	-1553.49132619	-1317.4028
ts-4b'-'py-c4	-1551.715779	0.392011	-1551.2826	-1551.392864	-1553.48773445	-1307.7334

Table A4.2. Absolute values (in Hartrees) for SCF energy, zero-point vibrational energy (ZPE), enthalpy and quasi-harmonic Gibbs free energy (at 363K) for the substrate **3a**. For harmonic frequency analysis, a plus (+) sign indicates that the lowest frequency of the optimised structures is positive.

Structure	E/au	ZPE/au	H/au	qh-G/au	SP DFT (TBME)	Im Freq /cm^{-1}
Regioselectivity study of substrate 4a						

4a-1	-1254.435262	0.417625	-1253.9806	-1254.081325	-1255.83322982	-1211.2001
4a-2-c1	-1254.429616	0.417526	-1253.9749	-1254.075648	-1255.82736203	-1207.274
4a-2-c2	-1254.432952	0.417831	-1253.9781	-1254.078471	-1255.83003608	-1402.362
Regioselectivity study of substrate 5a						
5a-1	-1331.711312	0.45341	-1331.2193	-1331.322343	-1333.20195926	-1242.3319
5a-2	-1331.655993	0.45387	-1331.1635	-1331.266705	-1333.14909231	-1435.667
5a-3	-1331.693185	0.453096	-1331.201	-1331.30516	-1333.18496260	-1164.3307
5a-4	-1331.693357	0.452364	-1331.2019	-1331.305871	-1333.18486761	-1413.2075
Regioselectivity study of substrate 6a						
6a-1	-1253.255431	0.398722	-1252.8225	-1252.917322	-1254.64525533	-1252.1656
6a-2	-1253.245734	0.397452	-1252.8133	-1252.909895	-1254.63635977	-1141.9363
Regioselectivity study of substrate 7a						
7a-1 (C–H)	-1369.701419	0.459961	-1369.2022	-1369.306684	-1371.23536456	-704.7933
7a-1 (OA)						
7a-2 (C–H)	-1369.706545	0.459753	-1369.2078	-1369.311749	-1371.24003927	-1144.4993
7a-2	-1369.706545	0.459753	-1369.2078	-1369.311749	-1371.24003927	-1144.4993

Table A4.3. Absolute values (in Hartrees) for SCF energy, zero-point vibrational energy (ZPE), enthalpy and quasi-harmonic Gibbs free energy (at 363K) for the regioselective TSs for C–H activation and oxidative addition of substrates **4a**, **5a**, **6a** and **7a**.

Appendix 5 Absolute values (in hartrees) and imaginary frequencies (in cm^{-1}) for optimised structures for allylation (Chapter 5)

	E/au	ZPE/au	H/au	qh-G/au	Im.Freq/cm^{-1}	SP ωB97X-D (MeCN)	SP MN15 (MeCN)
0. Starting materials:							
arene **1a**	-1426.5229	0.311509	-1426.1807	-1426.269	+	-1429.06227216	-1428.6919715
trans-hexene	-235.31399	0.16511	-235.13645	-235.18577	+	-235.88622142	-235.7628220
cis-hexene	-235.31226	0.165429	-235.13446	-235.18352	+	-235.88455969	-235.7610397
cyclo-hexene	-234.12832	0.146325	-233.97273	-234.01466	+	-234.68105898	-234.5687484
HOAc	-228.64453	0.062197	-228.57502	-228.61242	+	-229.13726389	-229.0706003
N-acetyl-norleucine	-593.15819	0.231435	-592.90548	-592.97546	+	-594.47065223	-594.2582931
$Pd(OAc)_2$	-583.80993	0.104326	-583.69012	-583.74848	+	-585.03620367	-584.6482919
$Pd_3(OAc)_6$	-1751.5873	0.317868	-1751.2218	-1751.3472	+	-1755.21537801	-1754.0473816
1. *meta*-allylation:							
int-1	-2010.361	0.417336	-2009.8966	-2010.0187	+	-2014.12074330	-2013.3624531
ts-1	-2010.3361	0.411975	-2009.8774	-2009.9989	-1136.100	-2014.09487408	-2013.3327515
int-2	-2010.3515	0.417256	-2009.8868	-2010.0103	+	-2014.11044997	-2013.3506657
int-1'	-2146.2068	0.522938	-2145.6315	-2145.763	+	-2150.30584854	-2149.465115
ts-1'	-2146.1909	0.517866	-2145.6212	-2145.7518	-1275.1147	-2150.28508610	-2149.445114
int-2'	-2146.2152	0.523642	-2145.6392	-2145.771	+	-2150.30936515	-2149.472983
int-3	-2017.0314	0.521084	-2016.458	-2016.5904	+	-2020.87263588	-2020.0563355
ts-3	-2017.0153	0.52024	-2016.4439	-2016.5742	-281.0309	-2020.85715946	-2020.04
int-4	-2017.0546	0.522503	-2016.481	-2016.6102	+	-2020.89515397	-2020.078034
ts-4	-2017.0395	0.52057	-2016.4685	-2016.5959	-95.8045	-2020.87256581	-2020.056365
int-5	-2017.0424	0.520722	-2016.4705	-2016.5995	+	-2020.87613345	-2020.059231
ts-5	-2017.0376	0.518443	-2016.4684	-2016.5963	-534.1546	-2020.86947612	-2020.053557
int-6	-2017.0487	0.51989	-2016.4775	-2016.6068	+	-2020.88145514	-2020.065211
int-7	-2017.0479	0.520931	-2016.4759	-2016.6053	+	-2020.88962226	-2020.069785
ts-7	-2017.043	0.516919	-2016.4754	-2016.6038	-960.7952	-2020.87758394	-2020.058839
int-8	-2017.0651	0.521465	-2016.492	-2016.6228	+	-2020.89597912	-2020.079392

ts-7'	-2017.0165	0.516398	-2016.4485	-2016.579	-975.0604	-2020.84680381	-2020.030891
2. Regioselectivity (*Z*-allylation vs styrenylation):							
ts-4a	-2017.0372	0.521116	-2016.4659	-2016.5927	-77.2317	-2020.87072244	-2020.05477
int-5a	-2017.0391	0.521107	-2016.4669	-2016.5956	+	-2020.87307361	-2020.056043
ts-5a	-2017.0339	0.518458	-2016.4648	-2016.5926	-516.2140	-2020.86630718	-2020.049971
int-6a	-2017.0456	0.519994	-2016.4743	-2016.6036	+	-2020.87970642	-2020.062662
ts-7a	-2017.0403	0.517241	-2016.4725	-2016.6006	-912.4642	-2020.87472779	-2020.056175
ts-4b	-2017.0195	0.520651	-2016.4483	-2016.5763	-49.4039	-2020.86277303	-2020.045129
int-5b	-2017.023	0.52038	-2016.4513	-2016.5812	+	-2020.86634486	-2020.04869
ts-5b	-2017.0233	0.517549	-2016.4542	-2016.5852	-244.3729	-2020.86046599	-2020.044136
int-6b	-2017.0272	0.518973	-2016.4564	-2016.5874	+	-2020.86030520	-2020.047355
ts-7b	-2016.9853	0.513883	-2016.4199	-2016.5499	-1493.0469	-2020.81104238	-2019.995037
3. Ligand identity in TDTS:							
ts-3-Ac-c1	-2017.01535	0.52024	-2016.44389	-2016.57418	-281.03090	-2020.85716	-2020.03997
ts-3-Ac-c2	-2017.01291	0.52006	-2016.44155	-2016.57193	-286.48340	-2020.85668	-2020.03961
ts-3-Ac-c3	-2017.01098	0.52017	-2016.43944	-2016.57063	-284.03240	-2020.85518	-2020.03759
ts-3-Ac-c4	-2017.01257	0.52013	-2016.44108	-2016.57153	-305.70220	-2020.85540	-2020.03868
ts-3-Ac-c5	-2017.00208	0.52015	-2016.43087	-2016.56047	-296.08770	-2020.85451	-2020.03664
ts-3-Ac-c6	-2017.00234	0.52011	-2016.43116	-2016.56056	-295.28320	-2020.85081	-2020.03394
ts3'_b-aa-c1	-2381.5373	0.689422	-2380.7825	-2380.9421	-284.2484	-2386.19788852	-2385.2342
ts3'_b-aa-c2	-2381.5378	0.689507	-2380.7832	-2380.9407	-283.7738	-2386.19729742	-2385.2348
ts3'_b-aa-c3	-2381.5322	0.689198	-2380.7775	-2380.9	-283.7067	-2386.19552260	-2385.2316
ts3'_b-aa-c4	-2381.5355	0.689509	-2380.7807	-2380.94	-281.9868	-2386.19596982	-2385.2323
ts3'_b-aa-c5	-2381.5321	0.689292	-2380.7774	-2380.9369	-304.8330	-2386.19465426	-2385.2314

ts3'_b-aa-c6	-2381.5357	0.689362	-2380.7812	-2380.9	-269.5971	-2386.19504216	-2385.2323
ts3'_b-aa-c7	-2381.5313	0.689485	-2380.7765	-2380.9	-281.9394	-2386.19432240	-2385.23
ts3'_b-aa-c8	-2381.5352	0.689671	-2380.7803	-2380.9386	-303.3393	-2386.19238004	-2385.2307
ts3'_b-aa-c9	-2381.5315	0.689867	-2380.7766	-2380.9346	-298.0564	-2386.19151425	-2385.2285
ts3'_b-aa-c10	-2381.5398	0.689694	-2380.7852	-2380.9421	-273.9343	-2386.19221804	-2385.2285
ts3'_b-aa-c11	-2381.538	0.68989	-2380.7833	-2380.9395	-301.0522	-2386.18994428	-2385.2285
ts3'_b-aa-c12	-2381.5373	0.689751	-2380.7825	-2380.9397	-281.9361	-2386.19017998	-2385.2268
3. Ligand non-participation in C–H activation and insertion:							
ts-1'a	-2146.1506	0.518113	-2145.5805	-2145.7119	-436.6324	-2150.25179663	-2149.412069
ts-1'b	-2374.8534	0.581988	-2374.211	-2374.3604	-1144.3739	-2379.42607373	-2378.5180592
ts-1'c1	-2374.8591	0.581302	-2374.2173	-2374.3664	-1121.5174	-2379.43433079	-2378.5270179
ts-1'c2	-2374.8622	0.581618	-2374.2202	-2374.3688	-1158.8650	-2379.43221037	-2378.5248558
ts-1'c3	-2374.8644	0.581842	-2374.2223	-2374.3706	-1167.8899	-2379.43111328	-2378.5238736
ts-1'c4	-2374.857	0.58183	-2374.2151	-2374.3631	-1158.6979	-2379.42807536	-2378.5198365
ts-1'c5	-2374.8399	0.581715	-2374.1982	-2374.3455	-1119.7362	-2379.41173753	-2378.5042266
4. Arene site selectivity (*ortho*- vs *para*-):							
ts-1o	-2010.3272	0.412335	-2009.8684	-2009.9894	-1136.4038	-2014.08095512	-2013.3227848
ts-1o-c2	-2010.3264	0.412728	-2009.8675	-2009.9873	-974.1986	-2014.07549514	-2013.3178916
ts-1o'	-2146.1916	0.518162	-2145.6217	-2145.7531	-1079.0146	-2150.28367525	-2149.445889
ts-3o	-2017.0025	0.520445	-2016.4309	-2016.5609	-330.9693	-2020.83578022	-2020.021731
int-4o	-2017.0373	0.523008	-2016.4633	-2016.5919	+	-2020.86780395	-2020.052957
ts-1p	-2010.3359	0.412169	-2009.8772	-2009.9984	-1147.9966	-2014.09219259	-2013.3325186
ts-1p-c2	-2010.3373	0.412306	-2009.8787	-2009.9992	-1129.4675	-2014.09091014	-2013.3321418
ts-1p'	-2146.1814	0.51829	-2145.6112	-2145.7425	-744.9454	-2150.27102572	-2149.431512
ts-3p	-2017.0115	0.520713	-2016.4399	-2016.5688	-293.7	-2020.85068341	-2020.036795
int-4p	-2017.0464	0.522973	-2016.4725	-2016.6014	+	-2020.88460750	-2020.068617
5. Boltzmann sampling for 1,2-migratory insertion:							
***trans*-d1-c1**	-2017.0126	0.520125	-2016.4411	-2016.5715	-305.7022	-2020.85540249	-2020.038678

***trans*-d1-c2**	-2017.0142	0.520158	-2016.4428	-2016.5728	-293.1491	-2020.85566193	-2020.039368
***trans*-d1-c3**	-2017.0123	0.519817	-2016.4412	-2016.5716	-277.2951	-2020.85328579	-2020.0377419
***trans*-d1-c4**	-2017.0126	0.52001	-2016.4412	-2016.5718	-316.8	-2020.85300091	-2020.036383
***trans*-d1-c5**	-2017.0149	0.520454	-2016.4434	-2016.5728	-316.9	-2020.85392791	-2020.037906
***trans*-d1-c6**	-2017.0085	0.519782	-2016.4373	-2016.568	-317.3912	-2020.85229877	-2020.034701
***trans*-d1-c7**	-2017.0144	0.520509	-2016.4428	-2016.5725	-315.0322	-2020.85308536	-2020.037854
***trans*-d1-c8**	-2017.0168	0.520816	-2016.4453	-2016.5736	-311.5392	-2020.85368267	-2020.038209
***trans*-d1-c9**	-2017.0095	0.519896	-2016.4383	-2016.5685	-337.4155	-2020.84905704	-2020.033366
***trans*-d2-c1**	-2017.0141	0.519663	-2016.4431	-2016.5733	-282.5387	-2020.85718	-2020.040593
***trans*-d2-c2**	-2017.0149	0.519612	-2016.444	-2016.5737	-308.8734	-2020.856582	-2020.040347
***trans*-d2-c3**	-2017.0173	0.520244	-2016.446	-2016.575	-288.8986	-2020.85666626	-2020.040614
***trans*-d2-c4**	-2017.0178	0.520381	-2016.4465	-2016.575	-304.4657	-2020.855951	-2020.040502
***trans*-d2-c5**	-2017.0128	0.519858	-2016.4416	-2016.5714	-282.6224	-2020.8542	-2020.037271
***trans*-d2-c6**	-2017.0146	0.519844	-2016.4436	-2016.5729	-284.4537	-2020.854195	-2020.038113
***trans*-d2-c7**	-2017.0111	0.51986	-2016.44	-2016.5701	-262.2307	-2020.85319709	-2020.037409
***trans*-d2-c8**	-2017.0147	0.519773	-2016.4438	-2016.573	-303.2176	-2020.853935	-2020.038479
***trans*-d2-c9**	-2017.0105	0.520114	-2016.4393	-2016.5688	-258.7607	-2020.85091759	-2020.035064
***cis*-d1-c1**	-2017.0114	0.51977	-2016.4403	-2016.5706	-293.1446	-2020.85454809	-2020.038653
***cis*-d1-c2**	-2017.0143	0.520243	-2016.443	-2016.5723	-289.5588	-2020.85460815	-2020.038579
***cis*-d1-c3**	-2017.0094	0.51988	-2016.4381	-2016.5686	-305.4801	-2020.85298719	-2020.036652
***cis*-d1-c4**	-2017.0128	0.520244	-2016.4414	-2016.571	-296.5738	-2020.85400716	-2020.037311
***cis*-d1-c5**	-2017.0132	0.520084	-2016.4421	-2016.5713	-287.1232	-2020.85342783	-2020.038021
***cis*-d1-c6**	-2017.012	0.520164	-2016.4418	-2016.5688	-295.7306	-2020.85327945	-2020.037221
***cis*-d1-c7**	-2017.012	0.520787	-2016.4405	-2016.5689	-300.2449	-2020.84805177	-2020.033502
***cis*-d1-c8**	-2017.0103	0.520806	-2016.4386	-2016.5674	-308.1908	-2020.84782328	-2020.03263
***cis*-d1-c9**	-2017.0051	0.52114	-2016.4333	-2016.5618	-314.0032	-2020.84019556	-2020.025393
***cis*-d2-c1**	-2017.0103	0.520114	-2016.4389	-2016.5691	-298.4609	-2020.85288539	-2020.037075
***cis*-d2-c2**	-2017.0109	0.520454	-2016.4393	-2016.5691	-300.5416	-2020.85324996	-2020.03695
***cis*-d2-c3**	-2017.0124	0.520431	-2016.4411	-2016.5702	-287.7811	-2020.85360314	-2020.038019
***cis*-d2-c4**	-2017.0117	0.520184	-2016.4404	-2016.5702	-300.4347	-2020.85217076	-2020.037598
***cis*-d2-c5**	-2017.0101	0.520328	-2016.4386	-2016.5687	-309.4578	-2020.85155613	-2020.036441

***cis*-d2-c6**	-2017.0079	0.520258	-2016.4364	-2016.5667	-313.6194	-2020.85126903	-2020.034999
***cis*-d2-c7**	-2017.0082	0.520327	-2016.4368	-2016.5657	-296.732	-2020.84989422	-2020.033341
***cis*-d2-c8**	-2017.0036	0.520716	-2016.4319	-2016.5615	-311.8461	-2020.84614435	-2020.028735
***cis*-d2-c9**	-2017.0028	0.520698	-2016.4311	-2016.5606	-316.5124	-2020.84448830	-2020.028321
cy-d1-c1	-2015.8245	0.500939	-2015.2752	-2015.3997	-309.5106	-2019.64627570	-2018.840491
cy-d1-c2	-2015.8233	0.501342	-2015.2737	-2015.398	-314.2776	-2019.64579942	-2018.839852
cy-d1-c3	-2015.8266	0.501253	-2015.2771	-2015.4006	-301.2641	-2019.64457672	-2018.840282
cy-d1-c4	-2015.821	0.501307	-2015.2712	-2015.3956	-292.1391	-2019.64289929	-2018.83771
cy-d2-c1	-2015.8236	0.500956	-2015.2744	-2015.3978	-304.458	-2019.64570310	-2018.839656
cy-d2-c2	-2015.8252	0.50095	-2015.276	-2015.3993	-291.53	-2019.64481242	-2018.840874
cy-d2-c3	-2015.8193	0.500887	-2015.2698	-2015.3941	-276.5101	-2019.64393051	-2018.838106
cy-d2-c4	-2015.8225	0.501028	-2015.2733	-2015.3965	-303.1028	-2019.644799	-2018.83868655
6. Isodesmic studies:							
pyridine	-247.76276	0.089473	-247.66596	-247.70411	+	-248.30904588	-248.2228936
ts-3-iso	-2264.7885	0.610871	-2264.1175	-2264.2672	-325.2881	-2269.16771081	-2268.26553
ts-3o-iso	-2264.8036	0.611869	-2264.1327	-2264.2776	-285.3699	-2269.16665412	-2268.26716
ts-3p-iso	-2264.7942	0.611633	-2264.123	-2264.2708	-310.8723	-2269.17001876	-2268.27014
7. *cis*-hexene product selectivity:							
***cis*-int-4**	-2017.0491	0.522286	-2016.4755	-2016.6050	+	-2020.89081831	-2020.074007
***cis*-ts-6**	-2017.0477	0.522116	-2016.4753	-2016.6026	-56.3933	-2020.88819118	-2020.071351
***cis*-int-7**	-2017.0458	0.521879	-2016.4733	-2016.6009	+	-2020.878591	-2020.062478
***cis*-ts-7**	-2017.04	0.517615	-2016.4721	-2016.5989	-894.6881	-2020.86995866	-2020.051674
***cis*-int-8**	-2017.0652	0.522118	-2016.4918	-2016.6211	+	-2020.88938870	-2020.07369804
***cis*-ts-6a**	-2017.0385	0.522431	-2016.4659	-2016.5931	-99.8893	-2020.87920898	-2020.061699
***cis*-int-7a**	-2017.0394	0.521802	-2016.467	-2016.5945	+	-2020.87708368	-2020.058029
***cis*-ts-7a**	-2017.0346	0.518017	-2016.4665	-2016.5928	-978.8647	-2020.86492859	-2020.046586
***cis*-int-8a**	-2017.0604	0.52288	-2016.4866	-2016.6149	+	-2020.88515958	-2020.069733
***cis*-ts-4b**	-2017.0163	0.520514	-2016.445	-2016.5739	-82.2613	-2020.86024466	-2020.041432
***cis*-int-5b**	-2017.0342	0.520372	-2016.4622	-2016.5930	+	-2020.87347141	-2020.056019
***cis*-ts-5b**	-2017.029	0.517817	-2016.4599	-2016.5898	-366.9912	-2020.86435208	-2020.049118
***cis*-int-6b**	-2017.0318	0.518939	-2016.4611	-2016.5918	+	-2020.86354955	-2020.05077

***cis*-ts-5b-c2**	-2017.0158	0.51803	-2016.4468	-2016.5756	-480.8873	-2020.85423166	-2020.038656
8. cyclohexene product selectivity:							
cy-int-4	-2015.8639	0.50327	-2015.3123	-2015.4358	+	-2019.68376601	-2018.876402
cy-ts-6a	-2015.8591	0.503392	-2015.3084	-2015.4297	-88.5455	-2019.67417990	-2018.868046
cy-int-7a	-2015.8591	0.502539	-2015.3084	-2015.4311	+	-2019.67414755	-2018.867609
cy-ts-7a	-2015.8477	0.498527	-2015.3017	-2015.4227	-1032.9256	-2019.65978358	-2018.851573
cy-int-8a	-2015.8717	0.503244	-2015.3201	-2015.4435	+	-2019.67805522	-2018.872553

Appendix 6 Absolute values (in hartrees) for optimised structures for alkynylation (Chapter 6)

Structure	E/au	ZPE/au	H/au	G/au	qh-G/au	SP ωB97X-D (MeCN)	SP MN15 (MeCN)
0_sm:							
1a	-1426.5229	0.311509	-1426.1822	-1426.271357	-1426.2667	-1429.04845440	-1428.6786329
1b	-3059.2496	0.12121	-3059.1129	-3059.171373	-3059.1703	-3059.73136747	-3059.9403307
1c	-485.35706	0.130012	-485.21303	-485.265131	-485.26489	-486.0681293	-485.9084379
1d	-2881.6333	0.101851	-2881.5201	-2881.570127	-2881.5693	-2882.07267838	-2882.3366382
HOAc	-228.64453	0.062197	-228.57532	-228.611767	-228.61143	-229.13351888	-229.0668662
Nacetylglycine	-436.25343	0.118206	-436.12243	-436.175678	-436.17305	-437.18030569	-437.0523413
HBr	-2575.0853	0.006123	-2575.0752	-2575.098797	-2575.0988	-2574.87712744	-2575.2352612
CuOAc2_monomer	-2096.9448	0.103478	-2096.8259	-2096.887377	-2096.884	-2097.7220570	-2097.862484
CuOAc2_dimer_singlet	-4193.9145	0.2089	-4193.6748	-4193.770684	-4193.7642	-4195.41435355	-4195.7209312
CuOAc2_dimer_triplet	-4193.9647	0.210384	-4193.7241	-4193.819467	-4193.8132	-4195.48133	-4195.770429
CuOAc_dimer_singlet	-3737.8511	0.105272	-3737.7284	-3737.7944	-3737.7912	-3738.42516828	-3738.851
CuOAc_dimer_triplet	-3737.7103	0.104279	-3737.5884	-3737.6552	-3737.6524	-3738.29887073	-3738.7162
CuBr2_monomer	-6789.8301	0.001703	-6789.8214	-6789.860471	-6789.8594	-6789.22792048	-6790.217605
CuBr2_dimer_singlet	-13579.701	0.004317	-13579.682	-13579.74594	-13579.743	-13578.47209	-13580.47502
CuBr2_dimer_triplet	-13579.72	0.003987	-13579.702	-13579.76965	-13579.764	-13578.50789	-13580.49347
AgBr_monomer	-2721.2253	0.000564	-2721.2202	-2721.251781	-2721.2518	-2721.36119518	-2721.3856319
AgBr_dimer	-5442.5245	0.001782	-5442.5131	-5442.563924	-5442.5627	-5442.77059613	-5442.8311465
AgOAc_monomer	-374.7487	0.050645	-374.68909	-374.734768	-374.73318	-375.57469470	-375.1751886

AgOAc_dimer	-749.614	0.104042	-749.49181	-749.561524	-749.55757	-751.22801036	-750.4392581
PdOAc2_trimer	-1751.5873	0.317868	-1751.2239	-1751.355928	-1751.3441	-1755.20433723	-1754.0362117
1_alkynylation_of_1b:							
int-1	-2010.361021	0.417336	-2009.8989	-2010.025439	-2010.0157	-2014.09960593	-2013.3417185
ts-1	-2010.33609	0.411975	-2009.8797	-2010.005994	-2009.9958	-2014.07504621	-2013.3134469
int-2	-2010.35148	0.417256	-2009.8891	-2010.01868	-2010.0072	-2014.0909700	-2013.3314472
int-1'	-1989.299016	0.40982	-1988.8469	-1988.96541	-1988.9582	-1992.99638924	-1992.242002
ts-1'	-1989.285298	0.404477	-1988.8388	-1988.957426	-1988.9496	-1992.98274427	-1992.226918
int-2'	-1989.308364	0.410403	-1988.8556	-1988.975621	-1988.9672	-1993.00391157	-1992.251518
int-3	-4840.971216	0.475881	-4840.4416	-4840.587747	-4840.5761	-4844.70115850	-4844.219901
ts-3	-4840.954399	0.475297	-4840.4262	-4840.571417	-4840.5599	-4844.69041408	-4844.205339
int-4	-4841.020565	0.477956	-4840.49	-4840.632214	-4840.6224	-4844.75555636	-4844.269364
ts-4	-4840.959972	0.476549	-4840.4307	-4840.573444	-4840.5632	-4844.70633991	-4844.221584
int-5	-4841.03872	0.477823	-4840.5075	-4840.652789	-4840.6415	-4844.77052705	-4844.288776
ts-3-c2	-4840.953808	0.475018	-4840.4258	-4840.570625	-4840.5593	-4844.69020998	-4844.205156
ts-4-c2	-4840.959568	0.476335	-4840.4304	-4840.57422	-4840.5633	-4844.70609086	-4844.222823
int-4'	-5215.84045	0.530066	-5215.2484	-5215.412349	-5215.4	-5220.36794079	-5219.492117
ts-4'	-5215.832056	0.529735	-5215.2409	-5215.402897	-5215.3907	-5220.35928688	-5219.483928
int-5'	-5215.865795	0.530375	-5215.2726	-5215.440323	-5215.4261	-5220.4013	-5219.519246
ts-3'z	-5215.75066	0.527466	-5215.1604	-5215.327817	-5215.3139	-5220.28972195	-5219.408864
ts-4'z	-5215.740197	0.526905	-5215.1501	-5215.322905	-5215.3057	-5220.28632879	-5219.406788
int-3r	-4840.966352	0.475466	-4840.4367	-4840.586257	-4840.5731	-4844.70196831	-4844.216596
ts-3r	-4840.95523	0.47543	-4840.4271	-4840.570658	-4840.5596	-4844.69151480	-4844.208097
int-4r	-4841.015859	0.477568	-4840.4854	-4840.629472	-4840.6187	-4844.75055601	-4844.265451
prd-TMS	-1910.712531	0.422586	-1910.2474	-1910.369467	-1910.36	-1913.930509	-1913.409386
1_alkynylation_of_1b (regioconvergence):							
int-4r'	-5215.832104	0.530422	-5215.2395	-5215.405033	-5215.3917	-5220.36410756	-5219.485658
ts-4r'	-5215.821896	0.529437	-5215.2308	-5215.394645	-5215.3817	-5220.35427898	-5219.47812
int-5r'	-5215.829729	0.529865	-5215.2374	-5215.403028	-5215.3898	-5220.36688210	-5219.489466
ts-5r'	-5215.800846	0.528577	-5215.2093	-5215.37938	-5215.3637	-5220.34501888	-5219.467047

int-6r'	-5215.871336	0.530833	-5215.2777	-5215.445362	-5215.4312	-5220.40546946	-5219.525982
2_alkynylation_of_1b_aa_ligand:							
ts-1'a	-1989.241518	0.404846	-1988.7947	-1988.914288	-1988.9057	-1992.93996133	-1992.185971
ts-1'b	-2217.946095	0.468797	-2217.4274	-2217.567499	-2217.5552	-2222.12071512	-2221.297634
ts-1'c	-2217.950755	0.467665	-2217.4326	-2217.575045	-2217.5616	-2222.1295546	-2221.3056348
ts3'a	-5048.547111	0.531403	-5047.9573	-5048.114495	-5048.1014	-5052.71629339	-5052.172854
ts3'b	-5048.564282	0.531205	-5047.9743	-5048.134568	-5048.1203	-5052.74047130	-5052.192636
ts3'c	-5048.571284	0.532029	-5047.9809	-5048.13779	-5048.1249	-5052.74364579	-5052.196485
3_alkynylation_of_1b_copper:							
prd-TMS-Cu	-4007.706141	0.528899	-4007.1194	-4007.27282	-4007.2619	-4011.68135651	-4011.302816
int-5'-Cu	-6728.989054	0.529306	-6728.3963	-6728.565912	-6728.5517	-6733.07561264	-6732.724159
ts-4'-Cu	-6937.993403	0.582236	-6937.3431	-6937.519912	-6937.5065	-6942.47112391	-6942.135956
ts-5r'-Cu	-6937.944999	0.581394	-6937.2949	-6937.474663	-6937.4599	-6942.43658511	-6942.099334
ts-4'-Cu-I	-6709.9488	0.529478	-6709.3577	-6709.5201	-6709.508	-6713.95378711	-6713.688
ts-5r'-Cu-I	-6709.9194	0.530303	-6709.3274	-6709.4906	-6709.4778	-6713.94078388	-6713.6704
4_arene_site_selectivity_ortho_para:							
ts-1o	-2010.327235	0.412335	-2009.8706	-2009.996525	-2009.9864	-2014.06251681	-2013.3048429
ts-1'o	-1989.275333	0.40504	-1988.8284	-1988.945718	-1988.9386	-1992.97006819	-1992.21543
ts-3o	-4840.950848	0.475039	-4840.4227	-4840.567922	-4840.5564	-4844.68267726	-4844.2002067
int-4o	-4841.005502	0.478328	-4840.4746	-4840.615898	-4840.6066	-4844.73707307	-4844.253322
ts-1p	-2010.335874	0.412169	-2009.8794	-2010.004978	-2009.9953	-2014.07305762	-2013.3139172
ts-1'p	-1989.285331	0.405046	-1988.8386	-1988.955232	-1988.9485	-1992.97998020	-1992.2270019
ts-3p	-4840.95513	0.47566	-4840.4269	-4840.568977	-4840.5592	-4844.68772197	-4844.2061858
int-4p	-4841.014183	0.478097	-4840.4835	-4840.625278	-4840.6157	-4844.74520831	-4844.2619844
pyridine	-247.762761	0.089473	-247.66632	-247.703094	-247.7031	-248.30299639	-248.2171106
ts-3-iso	-5088.733157	0.565521	-5088.1063	-5088.273417	-5088.2574	-5093.00230034	-5092.431749
ts-3o-iso	-5088.739269	0.566537	-5088.1119	-5088.273959	-5088.2602	-5093.00429760	-5092.43484
ts-3p-iso	-5088.737798	0.566374	-5088.1105	-5088.27522	-5088.2607	-5093.00522025	-5092.437843
5_alternative_oxidative_addition_TSs:							
ts-3-oa-c1	-4840.926859	0.475106	-4840.3986	-4840.542395	-4840.5316	-4844.65853300	-4844.176038

ts-3-oa-c2	-4840.916281	0.474524	-4840.3882	-4840.535615	-4840.5231	-4844.65155100	-4844.168891
ts-3-oa-c3	-4840.920333	0.475375	-4840.3919	-4840.536547	-4840.5252	-4844.65176600	-4844.169894
ts-3-oa-c4	-4840.913291	0.475415	-4840.3848	-4840.530401	-4840.5186	-4844.64899900	-4844.166361
6_ethynyltrimethylsilane_1c:							
ts-3H	-2267.064352	0.484575	-2266.5286	-2266.667859	-2266.6578	-2271.02940120	-2270.174764
int-4H	-2267.117887	0.487514	-2266.5796	-2266.716169	-2266.7075	-2271.08034834	-2270.225851
ts-4H	-2267.065965	0.485481	-2266.5297	-2266.667975	-2266.6581	-2271.03263981	-2270.176345
int-5H	-2267.080525	0.486262	-2266.5432	-2266.682216	-2266.6722	-2271.04173857	-2270.19011
ts-5H	-2267.058347	0.482448	-2266.5243	-2266.666613	-2266.655	-2271.02464274	-2270.168419
int-6H	-2267.112587	0.487541	-2266.5733	-2266.716186	-2266.7043	-2271.07262933	-2270.218973
ts-3rH	-2267.059619	0.484192	-2266.5242	-2266.663393	-2266.653	-2271.02667613	-2270.173159
int-4rH	-2267.110337	0.487008	-2266.5722	-2266.71284	-2266.7017	-2271.07618079	-2270.220442
7_bromoethynylbenzene_1d:							
int-3P	-4663.348539	0.45632	-4662.8422	-4662.982617	-4662.97	-4667.04108395	-4666.611194
ts-3P	-4663.334882	0.455895	-4662.8302	-4662.966822	-4662.9556	-4667.02770871	-4666.598967
int-4P	-4663.410381	0.458554	-4662.9032	-4663.037486	-4663.0277	-4667.10511821	-4666.673142
int-4'P	-5038.220005	0.511025	-5037.6508	-5037.806846	-5037.7944	-5042.70847151	-5041.885059
ts-4'P	-5038.213948	0.50998	-5037.6461	-5037.802513	-5037.7894	-5042.70363654	-5041.881219
int-5'P	-5038.246678	0.510894	-5037.677	-5037.836798	-5037.8225	-5042.73960204	-5041.913369
int-3rP	-4663.348567	0.456396	-4662.8424	-4662.981827	-4662.9697	-4667.03983832	-4666.610208
ts-3rP	-4663.334352	0.45606	-4662.8295	-4662.965766	-4662.9546	-4667.02827091	-4666.599432
int-4rP	-4663.408013	0.458631	-4662.9007	-4663.035552	-4663.0254	-4667.10120678	-4666.670752
int-4r'P	-5038.221148	0.51122	-5037.6518	-5037.809372	-5037.796	-5042.71271368	-5041.888975
ts-4r'P	-5038.203812	0.510319	-5037.6359	-5037.791775	-5037.7788	-5042.69533863	-5041.873737
int-5r'P	-5038.208472	0.51074	-5037.6393	-5037.798524	-5037.7844	-5042.70482600	-5041.88134
ts-5r'P	-5038.179023	0.508913	-5037.6113	-5037.773914	-5037.7576	-5042.68075194	-5041.853769
int-6r'P	-5038.253672	0.510711	-5037.6836	-5037.846764	-5037.8306	-5042.74558486	-5041.921402
Pd-1d2-c1	-5890.364189	0.205082	-5890.1328	-5890.219516	-5890.2141	-5891.64277896	-5891.906803
Pd-1d2-c2	-5890.359886	0.205108	-5890.1286	-5890.218338	-5890.2113	-5891.62582953	-5891.89701

Pd-1b2-c1	-6245.565123	0.242534	-6245.2867	-6245.39694	-6245.3888	-6246.93689409	-6247.085401
Pd-1b2-c2	-6245.56809	0.242148	-6245.292	-6245.39765	-6245.3897	-6246.92986787	-6247.081794

Appendix 7 Absolute values (in hartrees) for optimised structures for regiodivergent arylation of isoquinolone (Chapter 7). Solvents used for Pd-catalysis is dimethoxy-ethane and for Ir-catalysis is acetic acide.

Structure	E/au	ZPE/au	H/au	G/au	qh-G/au	SP ωB97X-D (Solvent)	SP MN15 (Solvent)
Palladium catalysis							
0_sm_prd:							
1a	-515.43269	0.169991	-515.24562	-515.30815	-515.30763	-516.543564	-516.376049
BF4_anion	-423.84049	0.014997	-423.81763	-423.85646	-423.85647	-424.7138954	-424.6685274
DME	-308.22683	0.141881	-308.07125	-308.12691	-308.12584	-308.912310	-308.802582
OPiv_anion	-345.7516	0.132714	-345.60462	-345.66029	-345.6594	-346.5989466	-346.4773461
HOPiv	-346.32547	0.146776	-346.16392	-346.22051	-346.21961	-347.0978885	-346.9711913
Ph2I_cation	-759.00954	0.181669	-758.80748	-758.88461	-758.87981	-760.894952	-759.934091
PhI	-528.14518	0.090724	-528.04359	-528.09468	-528.09464	-529.4533294	-528.5756867
PdOPiv2	-819.17098	0.273203	-818.86673	-818.96485	-818.95907	-820.9610434	-820.4506286
C3-prd	-746.00583	0.25142	-745.72932	-745.81072	-745.80807	-747.613098	-747.366593
C4-prd	-746.00701	0.251463	-745.73038	-745.8119	-745.80937	-747.615289	-747.368413
1_CMD_OA_RE_Pd2_neutral:							
C4-int1	-1334.6285	0.443908	-1334.1351	-1334.2752	-1334.2646	-1337.518468	-1336.838841
C4-ts1	-1334.5963	0.438682	-1334.1085	-1334.2479	-1334.2375	-1337.487361	-1336.806945
C4-int2	-1334.6151	0.444151	-1334.1212	-1334.2623	-1334.2516	-1337.504779	-1336.828225
C4-int3	-2093.2805	0.614849	-2092.5952	-2092.7814	-2092.7658	-2097.965086	-2096.336641
C4-ts3	-2093.25	0.613415	-2092.5667	-2092.752	-2092.7367	-2097.934345	-2096.306681
C4-int4	-2093.3031	0.61541	-2092.6176	-2092.8014	-2092.7868	-2097.981016	-2096.351175
C4-ts4	-2093.2838	0.614799	-2092.5996	-2092.7818	-2092.7674	-2097.961996	-2096.331192
C4-int5	-2093.3761	0.617472	-2092.6893	-2092.87	-2092.8568	-2098.052764	-2096.420462
C4-ts4b	-2093.2792	0.614623	-2092.595	-2092.7777	-2092.7631	-2097.957676	-2096.327766
C4-ts3b	-2093.2393	0.613592	-2092.5558	-2092.7411	-2092.7255	-2097.926489	-2096.298728
C4-ts3c	-2093.2322	0.61273	-2092.5491	-2092.7368	-2092.7199	-2097.922065	-2096.296123
C4-ts3d	-2093.2338	0.612529	-2092.5508	-2092.7393	-2092.7222	-2097.919613	-2096.292141
C4-ts3'a	-2171.2821	0.493961	-2170.7242	-2170.8965	-2170.8827	-2175.987067	-2174.437317

C4-ts3'b	-2171.2812	0.493557	-2170.7235	-2170.8969	-2170.8828	-2175.985693	-2174.43331
C4-ts3'c	-2171.2715	0.493656	-2170.7136	-2170.8893	-2170.8732	-2175.981357	-2174.431727
C4-ts4'	-2171.2906	0.493918	-2170.7326	-2170.908	-2170.892	-2175.994728	-2174.442124
C3-int1	-1334.6285	0.443907	-1334.1351	-1334.2752	-1334.2646	-1337.51847	-1336.838841
C3-ts1	-1334.5906	0.438395	-1334.1031	-1334.2432	-1334.2324	-1337.480157	-1336.800587
C3-int2	-1334.6184	0.44373	-1334.125	-1334.2672	-1334.2557	-1337.5081	-1336.827681
C8-int1	-1334.611	0.443472	-1334.1178	-1334.2584	-1334.2475	-1337.50445	-1336.826066
C8-ts1	-1334.5889	0.439437	-1334.1012	-1334.2346	-1334.2268	-1337.475863	-1336.801692
C8-ts1-c2	-1334.5874	0.438318	-1334.1	-1334.2381	-1334.2283	-1337.475366	-1336.796625
C8-ts1-c3	-1334.5867	0.439291	-1334.0989	-1334.2356	-1334.2259	-1337.473152	-1336.798081
C8-ts1-c4	-1334.5592	0.440891	-1334.0696	-1334.206	-1334.1967	-1337.453971	-1336.777948
C8-int2	-1334.6387	0.444668	-1334.1447	-1334.2819	-1334.2726	-1337.523534	-1336.847289
2_CMD_OA_RE_Pd2_cationic:							
int0-cat	-781.45376	0.282323	-781.14136	-781.23699	-781.23217	-783.217851	-782.7197608
C4-int1-cat	-1296.9154	0.453028	-1296.4138	-1296.5508	-1296.5412	-1299.77471	-1299.107805
C4-ts1-cat	-1296.8964	0.448337	-1296.4004	-1296.5342	-1296.5258	-1299.75528	-1299.085307
C4-int2-cat	-1296.9148	0.452972	-1296.4129	-1296.5531	-1296.5422	-1299.77392	-1299.10454
3_Heck_type_Pd2_neutral:							
H-int1	-1924.1818	0.592187	-1923.5224	-1923.7001	-1923.6862	-1928.52283	-1926.935917
H-ts1	-1924.1413	0.59001	-1923.4843	-1923.6618	-1923.648	-1928.48536	-1926.899821
H-ts1-c2	-1924.139	0.590411	-1923.4818	-1923.659	-1923.6452	-1928.48401	-1926.898252
H-int2	-1924.1793	0.591439	-1923.5204	-1923.7001	-1923.6851	-1928.51834	-1926.92977
H-C4-int3	-1911.4783	0.67212	-1910.7335	-1910.9185	-1910.9054	-1915.60928	-1914.728314
H-C4-ts3	-1911.4488	0.671071	-1910.7058	-1910.8885	-1910.8762	-1915.58145	-1914.7005
H-C4-int4	-1911.504	0.672333	-1910.759	-1910.9454	-1910.9317	-1915.64194	-1914.759282
H-C4-ts4	-2257.3374	0.80506	-2256.4453	-2256.6623	-2256.6453	-2262.26484	-2261.261883
H-C4-ts3-c2	-1911.4436	0.670942	-1910.7007	-1910.8852	-1910.8717	-1915.57814	-1914.700004

H-C4-ts3-c3	-1911.4507	0.671654	-1910.7075	-1910.8882	-1910.8765	-1915.57846	-1914.701504
H-C4-ts3-c4	-1911.4472	0.671044	-1910.7042	-1910.8864	-1910.8744	-1915.58222	-1914.699582
H-C4-ts3-c5	-1911.4418	0.67066	-1910.6992	-1910.8822	-1910.8696	-1915.57523	-1914.696049
H-C4-ts3-c6	-1911.4403	0.670951	-1910.6974	-1910.8813	-1910.8679	-1915.5759	-1914.695683
H-C3-ts3	-1911.4431	0.671286	-1910.7	-1910.8827	-1910.87	-1915.58087	-1914.699886
H-C3-int4	-1911.4842	0.672863	-1910.7391	-1910.922	-1910.91	-1915.61765	-1914.736923
H-C3-ts3-c2	-1911.4473	0.671511	-1910.7042	-1910.8848	-1910.8734	-1915.58241	-1914.700558
H-C3-ts3-c3	-1911.4461	0.671281	-1910.7031	-1910.8867	-1910.8737	-1915.58118	-1914.698474
H-C3-ts3-c4	-1911.4356	0.671161	-1910.6925	-1910.8749	-1910.8627	-1915.57954	-1914.69714
H-C3-ts3-c5	-1911.44	0.671097	-1910.6971	-1910.8798	-1910.8673	-1915.57807	-1914.696554
H-C3-ts3-c6	-1911.4368	0.671067	-1910.6939	-1910.8766	-1910.8641	-1915.57472	-1914.689568
H-C8-ts3	-1911.42	0.670124	-1910.6776	-1910.8632	-1910.8493	-1915.56062	-1914.67943
H-C8-ts3'	-1911.4078	0.669712	-1910.666	-1910.8469	-1910.8358	-1915.53167	-1914.655516
4_Heck_type_Pd2_cationic:							
H-int1-cat	-1578.2026	0.455921	-1577.6954	-1577.8394	-1577.8286	-1581.8458	-1580.37926
H-ts1-cat	-1578.1828	0.454661	-1577.6762	-1577.823	-1577.8114	-1581.82531	-1580.357399
H-int2-cat	-1578.1964	0.455151	-1577.6885	-1577.8372	-1577.825	-1581.84224	-1580.372463
H-C4-int3-cat	-1565.4901	0.535511	-1564.8963	-1565.051	-1565.041	-1568.9287	-1568.166792
H-C4-ts3-cat	-1565.4823	0.535103	-1564.8899	-1565.042	-1565.0326	-1568.91858	-1568.156859
H-C4-int4-cat	-1565.5499	0.537906	-1564.9545	-1565.1073	-1565.0974	-1568.99105	-1568.224922
H-C3-int3-cat	-1565.4865	0.535099	-1564.8928	-1565.0503	-1565.0389	-1568.93097	-1568.165769
H-C3-ts3-cat	-1565.4767	0.534479	-1564.8846	-1565.0394	-1565.0287	-1568.91941	-1568.153649
H-C3-int4-cat	-1565.5122	0.535932	-1564.9179	-1565.0744	-1565.0631	-1568.95945	-1568.194033

H-C8-ts3-cat	-1565.4705	0.534667	-1564.8786	-1565.0311	-1565.0211	-1568.90768	-1568.146535
H-C8-ts3'-cat	-1565.4605	0.534406	-1564.8689	-1565.019	-1565.0107	-1568.89084	-1568.131223
H-C8-ts3'-c2-cat	-1565.4305	0.532177	-1564.8403	-1564.9937	-1564.9843	-1568.8659	-1568.104519
H-C8-ts3''-cat	-1565.4605	0.533897	-1564.8691	-1565.0218	-1565.0122	-1568.88785	-1568.133048
5_OA_CMD_RE_Pd2_neutral:							
HC-C4-int3	-1911.4735	0.671983	-1910.7289	-1910.9126	-1910.9002	-1915.61141	-1914.730429
HC-C4-ts3	-1911.4508	0.667169	-1910.7114	-1910.8958	-1910.8824	-1915.58537	-1914.703819
HC-C4-int4	-1911.4708	0.672075	-1910.7256	-1910.9141	-1910.8991	-1915.60316	-1914.724282
HC-C4-ts4	-1911.4638	0.67168	-1910.7202	-1910.9037	-1910.8908	-1915.59343	-1914.714977
HC-C4-int5	-1911.5603	0.6739	-1910.8142	-1910.9989	-1910.9853	-1915.68677	-1914.808328
HC-C3-int3	-1911.4735	0.671984	-1910.7289	-1910.9126	-1910.9002	-1915.61142	-1914.730429
HC-C3-ts3	-1911.4382	0.666877	-1910.6992	-1910.8834	-1910.87	-1915.57288	-1914.692184
HC-C3-int4	-1911.4741	0.672445	-1910.729	-1910.9151	-1910.9011	-1915.60434	-1914.726622
HC-C8-ts3	-1911.4099	0.667569	-1910.6702	-1910.8552	-1910.8413	-1915.54976	-1914.668779
HC-C8-ts3-c2	-1911.4131	0.667113	-1910.6741	-1910.8568	-1910.844	-1915.54634	-1914.667363
HC-C8-ts3-cat	-1565.4782	0.531741	-1564.8893	-1565.0415	-1565.0315	-1568.91223	-1568.15225
6_Heck_type_Pd0_neutral:							
Pd(DME)2	-744.14592	0.286179	-743.82869	-743.9314	-743.92346	-745.776243	-745.2927561
H0-int2	-1232.7406	0.318248	-1232.3842	-1232.5024	-1232.4931	-1235.58876	-1234.240207
H0-C4-int3	-1220.0354	0.397793	-1219.5935	-1219.7212	-1219.7118	-1222.6787	-1222.037763
H0-C4-ts3	-1220.0078	0.397245	-1219.5675	-1219.6918	-1219.6835	-1222.65264	-1222.010461
H0-C4-int4	-1220.0454	0.39946	-1219.6029	-1219.7274	-1219.7191	-1222.68596	-1222.04532

H0-C3-int3	-1220.0371	0.398232	-1219.5951	-1219.7211	-1219.7126	-1222.6819	-1222.040583
H0-C3-ts3	-1220.013	0.397204	-1219.5729	-1219.6971	-1219.6889	-1222.6575	-1222.016228
H0-C3-int4	-1220.0472	0.399491	-1219.6046	-1219.729	-1219.7208	-1222.68679	-1222.046177
7_Heck_type_Pd0_cationic:							
H0-int2-cat	-1195.0468	0.327278	-1194.6822	-1194.797	-1194.789	-1197.86194	-1196.524069
H0-C3-int3-cat	-1182.3422	0.406943	-1181.8923	-1182.0147	-1182.0077	-1184.95739	-1184.326385
H0-C3-ts3-cat	-1182.3194	0.40664	-1181.871	-1181.9908	-1181.9846	-1184.93123	-1184.299904
H0-C3-int4-cat	-1182.3475	0.407482	-1181.8976	-1182.0193	-1182.0123	-1184.95242	-1184.32428
H0-C4-int3-cat	-1182.3422	0.406943	-1181.8923	-1182.0147	-1182.0077	-1184.95739	-1184.326386
H0-C4-ts3-cat	-1182.3148	0.406354	-1181.8666	-1181.9866	-1181.9803	-1184.92782	-1184.296558
H0-C4-int4-cat	-1182.3441	0.408226	-1181.8935	-1182.0161	-1182.0086	-1184.95506	-1184.323504
Iridium catalysis							
0_sm_prd:							
1a	-515.43269	0.169991	-515.2472	-515.30507	-515.30461	-516.5349727	-516.3674211
BF4_anion	-423.84049	0.014997	-423.81821	-423.85457	-423.85457	-424.7103018	-424.6649355
OAc_anion	-228.05929	0.048235	-228.00369	-228.04311	-228.0421	-228.6456961	-228.5822406
HOAc	-228.64453	0.062196	-228.57472	-228.6138	-228.61341	-229.1315628	-229.0647707
Ph2I_cation	-759.00954	0.181669	-758.8093	-758.88079	-758.87634	-760.8848747	-759.9240493
PhI	-528.14518	0.090724	-528.04452	-528.09217	-528.09214	-529.4486981	-528.5710762
C8-prd	-745.99909	0.25095	-745.72527	-745.8007	-745.79811	-747.5969839	-747.3503962
1_CMD_OA_RE_Ir_neutral:							
Ir-cat1	-1178.3658	0.390123	-1177.932	-1178.0555	-1178.0486	-1180.85984	-1180.317478
Ir-cat2	-949.69129	0.32639	-949.32884	-949.43583	-949.43036	-951.7115397	-951.2376535
C4-int20	-1465.1418	0.499208	-1464.5911	-1464.7287	-1464.7213	-1468.256118	-1467.609338
C4-ts20b	-1465.0992	0.493167	-1464.5546	-1464.6919	-1464.6851	-1468.213429	-1467.568178
C4-ts20	-1465.1257	0.493431	-1464.5808	-1464.7188	-1464.7112	-1468.234006	-1467.587541

C4-int21	-1465.1488	0.498463	-1464.5984	-1464.7381	-1464.7304	-1468.255995	-1467.609718
c3-ts20	-1465.1199	0.493743	-1464.575	-1464.712	-1464.7047	-1468.22867	-1467.584426
C8-ts20	-1465.1133	0.493352	-1464.5688	-1464.7058	-1464.6987	-1468.221357	-1467.578611
C8-ts20b	-1465.0816	0.494096	-1464.5363	-1464.6736	-1464.6664	-1468.205677	-1467.561064
C8-ts20c	-1465.0758	0.49307	-1464.5317	-1464.6672	-1464.661	-1468.204818	-1467.559602
2_CMD_OA_RE_Ir_cationic:							
Ir-cat+	-950.09595	0.339112	-949.72025	-949.83031	-949.82308	-952.1717434	-951.6887173
C3-int10	-1236.8792	0.447335	-1236.3877	-1236.5094	-1236.5035	-1239.572325	-1238.985581
C3-ts10	-1236.8293	0.440593	-1236.3443	-1236.4681	-1236.461	-1239.529694	-1238.938348
C3-int11	-1236.8435	0.445491	-1236.3529	-1236.4791	-1236.4714	-1239.536119	-1238.950257
C3-ts10b	-1465.5079	0.505285	-1464.9505	-1465.0918	-1465.0827	-1468.67438	-1468.020532
C4-int10	-1236.8788	0.447346	-1236.3871	-1236.5098	-1236.5031	-1239.571778	-1238.984872
C4-ts10	-1236.8293	0.440962	-1236.3438	-1236.4688	-1236.4611	-1239.53252	-1238.940589
C4-int11	-1236.8414	0.446039	-1236.3499	-1236.4788	-1236.4699	-1239.543732	-1238.95638
C4-ts10b	-1465.5149	0.505362	-1464.9573	-1465.0988	-1465.0899	-1468.680663	-1468.024874
C8-int10	-1236.8956	0.447678	-1236.4037	-1236.5271	-1236.52	-1239.585235	-1239.000129
C8-ts10	-1236.8588	0.442318	-1236.3726	-1236.4943	-1236.4881	-1239.543976	-1238.959
C8-int11	-1236.8955	0.447481	-1236.4035	-1236.5269	-1236.5204	-1239.573874	-1238.991593
C8-ts10b	-1465.5203	0.505644	-1464.963	-1465.1013	-1465.0938	-1468.674381	-1468.022267
C8-int12-g1	-1995.5365	0.618525	-1994.8549	-1995.018	-1995.0075	-2000.017506	-1998.478903
C8-ts12-g1	-1995.4866	0.618051	-1994.8065	-1994.9651	-1994.9566	-1999.965646	-1998.428717
C8-int13-g1	-1995.5316	0.619746	-1994.8497	-1995.0085	-1994.9996	-2000.013719	-1998.477308
C8-ts12-g1-c2	-1995.4852	0.617678	-1994.8054	-1994.9647	-1994.9559	-1999.962919	-1998.426473
C8-ts12-g1-c3	-1995.4808	0.617192	-1994.8011	-1994.9626	-1994.9526	-1999.961179	-1998.424956
C8-ts12-g1-c4	-1995.4883	0.616517	-1994.8095	-1994.9702	-1994.9605	-1999.95093	-1998.420039
C8-int14-g1	-1467.4025	0.527293	-1466.8237	-1466.9592	-1466.9527	-1470.574129	-1469.917784
C8-ts14-g1	-1467.3874	0.526803	-1466.81	-1466.9426	-1466.937	-1470.557736	-1469.900428
C8-ts14-g1-c2	-1467.3513	0.524863	-1466.7754	-1466.9106	-1466.9037	-1470.521324	-1469.864668

C8-int15-g1	-1467.4552	0.528634	-1466.8751	-1467.0111	-1467.0047	-1470.63227	-1469.96893
C8-ts12-g2	-1995.4921	0.616456	-1994.813	-1994.9765	-1994.9653	-1999.952919	-1998.421624
C8-ts12-g2-c2	-1995.4817	0.617968	-1994.8019	-1994.96	-1994.9517	-1999.958102	-1998.424468
C8-ts12-g2-c3	-1995.487	0.617793	-1994.8072	-1994.9658	-1994.9573	-1999.954871	-1998.42402
C8-ts12-g2-c4	-1995.4464	0.616318	-1994.7676	-1994.9301	-1994.9194	-1999.940933	-1998.401548
C8-int14-g2	-1467.4001	0.527474	-1466.8212	-1466.9566	-1466.9501	-1470.578931	-1469.917299
C8-ts14-g2	-1467.3858	0.526307	-1466.8086	-1466.9432	-1466.9365	-1470.563295	-1469.90224
C8-int15-g2	-1467.4544	0.528714	-1466.8744	-1467.0096	-1467.0032	-1470.638538	-1469.974981
C8-ts12a	-1995.436	0.614744	-1994.7591	-1994.9221	-1994.9106	-1999.896018	-1998.36425
C8-ts12b	-1995.4333	0.61487	-1994.7562	-1994.9178	-1994.907	-1999.893802	-1998.361617
C8-ts12c	-1995.4218	0.616345	-1994.7439	-1994.9028	-1994.8929	-1999.893699	-1998.362093
C8-ts12d	-1995.4177	0.616073	-1994.7399	-1994.8989	-1994.8893	-1999.894269	-1998.360784
C8-ts12e	-1995.3776	0.614904	-1994.7006	-1994.8613	-1994.8509	-1999.865177	-1998.332744
2_CMD_OA_RE_Ir_cationic:							
H-int12	-1708.7607	0.51055	-1708.195	-1708.344	-1708.3339	-1712.625468	-1711.190338
H-ts12	-1708.7024	0.509749	-1708.1386	-1708.2835	-1708.2748	-1712.56349	-1711.132243
H-int13	-1708.7457	0.511711	-1708.18	-1708.3246	-1708.3157	-1712.606369	-1711.176461
H-ts12-c2	-1708.6954	0.509111	-1708.1318	-1708.279	-1708.2692	-1712.555851	-1711.126587